Oscar Camara Tommaso Mansi
Mihaela Pop Kawal Rhode
Maxime Sermesant Alistair Young (Eds.)

# Statistical Atlases and Computational Models of the Heart

## Imaging and Modelling Challenges

LNCS 7746

Third International Workshop, STACOM 2012
Held in Conjunction with MICCAI 2012
Nice, France, October 2012, Revised Selected Papers

Springer

Lecture Notes in Computer Science 7746

*Commenced Publication in 1973*
Founding and Former Series Editors:
Gerhard Goos, Juris Hartmanis, and Jan van Leeuwen

Oscar Camara  Tommaso Mansi
Mihaela Pop  Kawal Rhode
Maxime Sermesant  Alistair Young (Eds.)

# Statistical Atlases and Computational Models of the Heart

## Imaging and Modelling Challenges

Third International Workshop, STACOM 2012
Held in Conjunction with MICCAI 2012
Nice, France, October 5, 2012
Revised Selected Papers

Springer

Volume Editors

Oscar Camara
Universitat Pompeu Fabra, Barcelona, Spain
E-mail: oscar.camara@upf.edu

Tommaso Mansi
Siemens Corporation, Corporate Technology, Princeton, NJ, USA
E-mail: tommaso.mansi@siemens.com

Mihaela Pop
University of Toronto, ON, Canada
E-mail: mihaela.pop@utoronto.ca

Kawal Rhode
King's College London, UK
E-mail: kawal.rhode@kcl.ac.uk

Maxime Sermesant
INRIA - Asclepios Research Project, Sophia Antipolis Cedex, France
E-mail: maxime.sermesant@inria.fr

Alistair Young
University of Auckland, New Zealand
E-mail: a.young@auckland.ac.nz

ISSN 0302-9743 e-ISSN 1611-3349
ISBN 978-3-642-36960-5 e-ISBN 978-3-642-36961-2
DOI 10.1007/978-3-642-36961-2
Springer Heidelberg Dordrecht London New York

Library of Congress Control Number: 2013932345

CR Subject Classification (1998): J.3, H.4, H.5.1-2, H.1.2, I.2.10

LNCS Sublibrary: SL 6 – Image Processing, Computer Vision, Pattern Recognition, and Graphics



*Typesetting:* Camera-ready by author, data conversion by Scientific Publishing Services, Chennai, India

Printed on acid-free paper

Springer is part of Springer Science+Business Media (www.springer.com)

# Preface

This year's edition of STACOM 2012 was held in conjunction with the MICCAI conference (Nice, France), and followed the last two editions: STACOM 2010 (held in 2010, Beijing, China) and STACOM 2011 (Toronto, Canada). The main purpose was to provide a forum for the discussion of the latest developments in the areas of statistical atlases and computational imaging and modeling of the heart. This broad aim included: cardiac mapping, image processing, atlas construction, statistical modeling of cardiac function across different patient populations, cardiac computational physiology, model personalization, ontological schemata for data and results, atlas-based functional analysis, integrated functional and structural analyses, as well as the clinical applicability of these methods. STACOM 2012 again drew in participants from around the world, with 42 papers accepted and published by Springer in this volume of *Lecture Notes in Computer Science*.

The integration of cardiac models in preclinical and clinical platforms is important for understanding disease, evaluating the treatment, and planning an intervention. However, significant clinical translation of these tools is constrained by the lack of complete and rigorous technical and clinical validation as well as benchmarking of the developed tools. To validate the models, available ground-truth data capturing generic knowledge on healthy and pathological hearts are required. Several efforts are now established to provide Web-accessible structural and functional experimental datasets for clinical, research, and educational purposes. We believe that these approaches will only be effectively developed through collaboration across the full research scope of the cardiac imaging and modelling communities.

In addition to regular papers focused on the main themes, STACOM 2012 was also enhanced by four different challenges for participants to test their computational tools on given data: a Computational Fluid Dynamics (CFD) Challenge (organized by Siemens Corporation, Corporate Technology, King's College London, and Open Source Medical Software Corporation US), a Delayed Enhancement Magnetic Resonance Imaging (DE-MRI) Segmentation Challenge (organized by King's College London and KU Leuven), a Cardiac Motion Analysis Challenge (organized by Philips Research Medisys, INRIA, CHU Caena and Cyceron, KU Leuven) and a Cardiac Landmark Challenge (organized by the University of Auckland). Each challenge is briefly described below.

*CFD Challenge* — Advances in medical imaging and computational fluid dynamics (CFD) techniques make it possible to simulate blood flow and pressure in cardiovascular models built from patient data. In particular, image-based CFD techniques enable the calculation of pressure gradients through an aortic coarctation noninvasively and for various physiological states. However, the wide range of available software, modeling formulations and approaches to boundary

condition specification make it difficult to assess the consistency and repeatability of computational predictions. As a first step to ward gauging the ability of CFD methods to make reliable predictions in the clinic, the STACOM 2012 CFD Challenge set out to assess the variability in the calculation of the pressure gradient through a moderate thoracic aortic coarctation model under resting conditions. A geometrical model of the ascending aorta, aortic arch, descending aorta, and upper branch vessels of a young patient was provided to participants. Additionally, inflow boundary condition and flow splits in the branches were also provided, along with systolic and diastolic proximal pressures. The participants were asked to reproduce all the given data and to compute the average and peak pressure gradient through the coarctation. The computed pressure gradient will be compared with a clinically measured surrogate of the pressure gradient through the coarctation: i.e., the difference between pressure cuff measurements taken in the arm (representative of pressure proximal to the coarctation) and in the leg (representative of pressure distal to the coarctation). The challenge attracted six participant groups and these proceedings contain the details of the methodologies and results obtained by each of these participating groups, as well as reflections on the challenges derived from the lack of absolute ground truth data in clinical measurements.

*DE-MRI Segmentation Challenge* — Delayed-enhancement magnetic resonance imaging (DE-MRI) is a powerful tool for detecting fibrosis/scar in the myocardium of the heart. Recently there has been much interest in quantifying left ventricular fibrosis/scar with many useful applications including cardiac resynchronization therapy guidance, ventricular tachycardia ablation therapy guidance, and investigation of remodeling following myocardial infarction. The STACOM 2012 DE-MRI Segmentation Challenge made available 30 DE-MRI datasets to participants for segmentation of enhanced regions from post-myocardial infarction patients (15) and pigs (15) that had been subjected to myocardial ischemia. Of each of these 15 datasets, 5 were provided as training samples with manual annotation of enhanced regions made by experienced observers. The provided data included the DE-MRI ventricle scan and a segmentation of the myocardium. Ground truth was established by using manual segmentations from experienced clinical observers. The aim of the challenge was to create a standard dataset for benchmarking of DE-MRI segmentation algorithms and to compare different state-of-the-art algorithms. The challenge attracted five participants and these proceedings contain the details of the methodologies and results from each of these participating groups. A collation study of this segmentation challenge is also included in these proceedings.

*LV Landmark Detection Challenge* — Anatomical landmark annotation of the heart plays a significant role in cardiac MR analysis. It enables more robust and accurate functional and structural analysis of the heart. Yet, this prerequisite step for an automated cardiac MRI segmentation method is usually determined by tedious and subjective manual positioning. At the STACOM 2012 workshop, the Cardiac Atlas Project provided 100 cardiac MR images for a fully automated detection of anatomical landmarks of the heart, which include mitral valve, RV

insert and LV center points. To help participants develop and evaluat their methods, another 100 patient images were made available for training, accompanied with landmarks determined by expert observers. The training and validation cases were randomly selected from the same cohort. The challenge attracted nine participants of which two submitted their detection results. Details of their methods are presented in these proceedings.

*Motion Analysis Challenge* — This year, the second cardiac Motion Analysis Challenge (cMAC2) focused on 3D ultrasound. For any modality, validation of myocardial motion and deformation quantification algorithms is a challenging task that requires reference databases with controlled ground truth. In the case of ultrasound, ground truth motion cannot be obtained through manual landmarking of the data. For this reason, the focus was on phantom data, including synthetic images and in vitro acquisitions. The synthetic images proposed in this challenge combined an electromechanical model with an ultrasound imaging model. We provided ten sequences spanning different values of the global conductivity, global contractility, and electrical delay parameters of the 3D electromechanical model. In the current dataset, a single probe design was considered. Scatterers were randomly placed in the myocardial geometry and moved along the cardiac cycle according to the result of the mechanical simulation. The approach accelerated the convolution of a 3D point spread function (PSF) by multiple 1D convolutions and allowed the generation of more realistic ultrasound datasets. These data included ground truth on the motion field so that each challenger can report quantitative results. Ground truth motion was provided as a series of volumetric meshes. For the physical phantom, a Polyvinyl alcohol was produced by repeated freezing and thawing of PVA solution (with addition of graphite) in a cylindrical shape. One extremity of the cylinder was fixed. The other extremity was moved by a piston imposing both rotation and longitudinal compression. Ground truth data for the phantom set-up were captured using microsonometry (which gave the distance between crystals pairs embedded in the gel and is therefore considered as ground truth for radial, circumferential, and longitudinal strains). The cMAC2 challenge attracted 7 participant groups.

We hope that the results obtained by these four challenges, together with all regular paper contributions, will act to accelerate progress in the important areas of heart function and structure analysis.

October 2012

Oscar Camara
Tommaso Mansi
Mihaela Pop
Kawal Rhode
Maxime Sermesant
Alistair Young

# Organization

We would like to thank the Program Committee, the additional reviewers, and all participants for their time and effort, as well as our sponsors: King's College London Wellcome Trust/EPSRC Medical Engineering Centre (UK); Siemens Corporation, Corporate Technology (USA) and Scimedia-BrainVision (Japan and USA).

## Chairs

| | |
|---|---|
| Oscar Camara | Universitat Pompeu Fabra, Barcelona, Spain |
| Tommaso Mansi | Siemens Corporation, Corporate Technology, Imaging and Computer Vision, Princeton, USA |
| Mihaela Pop | University of Toronto, Canada |
| Kawal Rhode | King's College London, UK |
| Maxime Sermesant | Inria, Sophia Antipolis, France |
| Alistair Young | University of Auckland, New Zealand |

## Program Committee

| | |
|---|---|
| Leon Axel | New York University, USA |
| Nicholas Ayache | Inria, France |
| Piet Claus | KUL Leuven, Belgium |
| Mathieu De Craene | Philips, France |
| Hervé Delingette | INRIA, France |
| Alberto Figueroa | King's College London, UK |
| Peter Hunter | University of Auckland, New Zealand |
| Reza Razavi | King's College London, UK |
| Puneet Sharma | Siemens Corporation, Corporate Technology, USA |
| Nic Smith | King's College London, UK |
| Nathan Wilson | Open Source Medical Software Corporation, USA |
| Graham Wright | University of Toronto, Sunnybrook Research Institute, Canada |

## Challenges: Organizing Teams

| | |
|---|---|
| *Landmark Challenge*: | A. Young, A. Suinesiaputra |
| *CFD Challenge:* | T. Mansi, A. Figueroa, N. Wilson, P. Sharma |

| | |
|---|---|
| *Motion Tracking Challenge*: | M. de Craene, P. Allain, E. Saloux, A. Manrique, H. Delingette, S. Marchesseau, A. Prakosa, M. Sermesant, H. Gao, J. D'hooge |
| *DE-MRI Segmentation Challenge*: | K. Rhode, R. Karim, P. Claus |

## Additional Referees

We would like to acknowledge the following reviewers who, in addition to the Workshop Chairs and Program Committee members, provided scientific feedback to the participants on their papers: Constantine Butakoff, Ruben Cardenes, Piet Claus, Nicolas Duchateau, Bogdan Georgescu, Lucian Itu, Rashed Karim, Garry Liu, Stéphanie Marchesseau, Kristin McLeod, Viorel Mihalef, Ali Pashaei, Gemma Piella, Adityo Prakosa, Saikiran Rapaka, Avan Suinesiaputra, Nicolas Toussaint, Robert Xu, Chong Zhang, Xudong Zheng.

## Sponsoring Institutions

The STACOM workshop received sponsorship from King's College London Wellcome Trust/EPSRC Medical Engineering Centre; (UK); Siemens Corporation, Corporate Technology (USA) and Scimedia/BrainVision (USA and Japan).

# Table of Contents

## CFD Challenge

Study on Hemodynamics in Patient-Specific Thoracic Aortic Coarctation Model . . . . . 1
*Wenyu Fu and Aike Qiao*

Quantitative Hemodynamic Evaluation in Children with Coarctation of Aorta: Phase Contrast Cardiovascular MRI versus Computational Fluid Dynamics . . . . . 9
*Prahlad G. Menon, Kerem Pekkan, and Shobhit Madan*

A Lattice Boltzmann Simulation of Hemodynamics in a Patient-Specific Aortic Coarctation Model . . . . . 17
*Amanda Peters Randles, Moritz Bächer, Hanspeter Pfister, and Efthimios Kaxiras*

A 1D Lumped-Parameter/3D CFD Approach for Pressure Drop in the Aortic Coarctation . . . . . 26
*Eduardo Soudah, Maurizio Bordone, Pooyan Dadvand, and Riccardo Rossi*

Aortic Coarctation Simulation Based on the Lattice Boltzmann Method: Benchmark Results . . . . . 34
*Thomas Henn, Vincent Heuveline, Mathias J. Krause, and Sebastian Ritterbusch*

CFD Challenge: Hemodynamic Simulation of a Patient-Specific Aortic Coarctation Model with Adjoint-Based Calibrated Windkessel Elements . . . . . 44
*Mahmoud Ismail, Michael W. Gee, and Wolfgang A. Wall*

## DE-MRI Segmentation Challenge

Supervised Learning Modelization and Segmentation of Cardiac Scar in Delayed Enhanced MRI . . . . . 53
*Laura Lara, Sergio Vera, Frederic Perez, Nico Lanconelli, Rita Morisi, Bruno Donini, Dario Turco, Cristiana Corsi, Claudio Lamberti, Giovana Gavidia, Maurizio Bordone, Eduardo Soudah, Nick Curzen, James Rosengarten, John Morgan, Javier Herrero, and Miguel A. González Ballester*

Healthy and Scar Myocardial Tissue Classification in DE-MRI ..... 62
*Xènia Albà, Rosa M. Figueras i Ventura, Karim Lekadir, and Alejandro F. Frangi*

Infarct Segmentation of the Left Ventricle Using Graph-Cuts ..... 71
*Rashed Karim, Zhong Chen, Samantha Obom, Ying-Liang Ma, Prince Acheampong, Harminder Gill, Jaspal Gill, C. Aldo Rinaldi, Mark O'Neill, Reza Razavi, Tobias Schaeffter, and Kawal S. Rhode*

Hierarchical Conditional Random Fields for Myocardium Infarction Detection ..... 80
*Zahra Karimaghaloo, Hassan Rivaz, and Tal Arbel*

Mixture-Model-Based Segmentation of Myocardial Delayed Enhancement MRI ..... 87
*Anja Hennemuth, Ola Friman, Markus Huellebrand, and Heinz-Otto Peitgen*

Infarct Segmentation Challenge on Delayed Enhancement MRI of the Left Ventricle ..... 97
*Rashed Karim, Piet Claus, Zhong Chen, R. James Housden, Samantha Obom, Harminder Gill, YingLiang Ma, Prince Acheampong, Mark O'Neill, Reza Razavi, Tobias Schaeffter, and Kawal S. Rhode*

## LV Landmark Detection Challenge

Discriminative Context Modeling Using Auxiliary Markers for LV Landmark Detection from a Single MR Image ..... 105
*Xiaoguang Lu and Marie-Pierre Jolly*

Landmark Detection in Cardiac MRI Using Learned Local Image Statistics ..... 115
*Dwarikanath Mahapatra*

## Motion Tracking Analysis Challenge

Computational and Physical Phantom Setups for the Second Cardiac Motion Analysis Challenge (cMAC2) ..... 125
*Mathieu De Craene, Pascal Allain, Hang Gao, Adityo Prakosa, Stephanie Marchesseau, Oudom Somphone, Loic Hilpert, Alain Manrique, Hervé Delingette, Sherif Makram-Ebeid, Nicolas Villain, Jan D'hooge, Maxime Sermesant, and Eric Saloux*

Temporal Diffeomorphic Free Form Deformation to Quantify Changes Induced by Left and Right Bundle Branch Block and Pacing ..... 134
*Gemma Piella, Antonio R. Porras, Mathieu De Craene, Nicolas Duchateau, and Alejandro F. Frangi*

Three-Dimensional Cardiac Motion Estimation Based on Non-rigid Image Registration Using a Novel Transformation Model Adapted to the Heart ..... 142
*Brecht Heyde, Daniel Barbosa, Piet Claus, Frederik Maes, and Jan D'hooge*

Motion Estimation in 3D Echocardiography Using Smooth Field Registration ..... 151
*Oudom Somphone, Cécile Dufour, Benoît Mory, Loïc Hilpert, Sherif Makram-Ebeid, Nicolas Villain, Mathieu De Craene, Pascal Allain, and Eric Saloux*

Monogenic Phase Based Optical Flow Computation for Myocardial Motion Analysis in 3D Echocardiography ..... 159
*Martino Alessandrini, Hervé Liebgott, Daniel Barbosa, and Olivier Bernard*

Quadrature Filter Based Motion Analysis for 3D Ultrasound Sequences ..... 169
*Lennart Tautz, Anja Hennemuth, and Heinz-Otto Peitgen*

Evaluation of iLogDemons Algorithm for Cardiac Motion Tracking in Synthetic Ultrasound Sequence ..... 178
*Adityo Prakosa, Kristin McLeod, Maxime Sermesant, and Xavier Pennec*

## Regular Papers

An Atlas for Cardiac MRI Regional Wall Motion and Infarct Scoring ... 188
*Pau Medrano-Gracia, Avan Suinesiaputra, Brett Cowan, David Bluemke, Alejandro Frangi, Daniel Lee, João Lima, and Alistair Young*

Real-Time Catheter Extraction from 2D X-Ray Fluoroscopic and 3D Echocardiographic Images for Cardiac Interventions ..... 198
*Xianliang Wu, James Housden, Yingliang Ma, Daniel Rueckert, and Kawal S. Rhode*

Measurement of Myocardial Structure: 3D Structure Tensor Analysis of High Resolution MRI Quantitatively Compared to DT-MRI ..... 207
*Stephen Gilbert, Mark Trew, Bruce Smaill, Aleksandra Radjenovic, and Olivier Bernus*

A Fast and Noise-Robust Method for Computation of Intravascular Pressure Difference Maps from 4D PC-MRI Data ..... 215
*Sebastian Meier, Anja Hennemuth, Johann Drexl, Jelena Bock, Bernd Jung, and Tobias Preusser*

Robust and Accurate Diaphragm Border Detection in Cardiac X-Ray Angiographies ..... 225
*Simeon Petkov, Adriana Romero, Xavier Carrillo Suarez, Petia Radeva, and Carlo Gatta*

Modeling of the Optical Behavior of Myocardial Fibers in Polarized Light Imaging ..... 235
*Paul Audain Desrosiers, Gabrielle Michalowicz, Pierre-Simon Jouk, Yves Usson, and Yuemin Zhu*

Quantification of Transvalvular Flow through Composite Gaussian Surfaces from Temporally Interleaved Multi-view 3D Colour Doppler Images ..... 245
*Alberto Gómez, Daniel Giese, Kuberan Pushparajah, John Simpson, Tobias Schaeffter, and Graeme P. Penney*

What a Difference in Biomechanics Cardiac Fiber Makes ..... 253
*Debora Gil, Agnés Borràs, Ruth Aris, Mariano Vázquez, Pierre Lafortune, Guillaume Houzeaux, Jazmin Aguado, Manel Ballester, Chi Hion Li, and Francesc Carreras*

Generalized Step Criterion Edge Detectors for Kalman Filter Based Left Ventricle Tracking in 3D+T Echocardiography ..... 261
*Engin Dikici and Fredrik Orderud*

Multi-resolution DT-MRI Cardiac Tractography ..... 270
*Ferran Poveda, Debora Gil, and Enric Martí-Godia*

From Image to Personalized Cardiac Simulation: Encoding Anatomical Structures into a Model-Based Segmentation Framework ..... 278
*Hannes Nickisch, Hans Barschdorf, Frank M. Weber, Martin W. Krueger, Olaf Dössel, and Jürgen Weese*

A Near-Incompressible Poly-affine Motion Model for Cardiac Function Analysis ..... 288
*Kristin McLeod, Christof Seiler, Maxime Sermesant, and Xavier Pennec*

Towards Real-Time Computation of Cardiac Electrophysiology for Training Simulator ..... 298
*Hugo Talbot, Christian Duriez, Hadrien Courtecuisse, Jatin Relan, Maxime Sermesant, Stéphane Cotin, and Hervé Delingette*

Automated Personalised Human Left Ventricular FE Models to Investigate Heart Failure Mechanics . . . . . 307
*Vicky Y. Wang, Corné Hoogendoorn, Alejandro F. Frangi, B.R. Cowan, Peter J. Hunter, Alistair A. Young, and Martyn P. Nash*

Feasibility Study of Looped-Catheter-Based 2D-3D Image Registration of CT and X-Rays for Cardiac Catheterization Procedures in a Phantom Experiment . . . . . 317
*Michael V.N. Truong, Graeme P. Penney, and Kawal S. Rhode*

A Pre-clinical Framework to Characterize Peri-infarct Remodelling Using *in vivo* $T_1$ Maps and CARTO Data . . . . . 326
*Mihaela Pop, Samuel Oduneye, Nilesh Ghugre, Elnaz Shokrolahi, Jen Barry, Yuesong Yang, Sudip Ghate, Roey Flor, Ilan Lashevsky, Eugene Crystal, and Graham A. Wright*

Exercise Induced Inter-individual Variation of Right Ventricular Pressures: Simulations Using a Modular Model of the Cardiovascular System . . . . . 336
*Catalina Tobon-Gomez, Georgina Palau-Caballero, Marta Sitges, and Bart H. Bijnens*

Improving Clinical Translation of Cardiovascular Circulatory Models through an Intuitive Graphical User Interface to CircAdapt, Presenting Simulation Results as Clinical Images and Signals . . . . . 345
*Georgina Palau-Caballero, Catalina Tobon-Gomez, Vedrana Balicevic, Constantine Butakoff, Sven Loncaric, Marta Sitges, and Bart H. Bijnens*

Integrating Fiber Orientation Constraint into a Spatio-temporal FEM Model for Heart Borders and Motion Tracking in Dynamic MRI . . . . . 355
*Răzvan Stoica, Jérôme Pousin, Christopher Casta, Pierre Croisille, Yue-Min Zhu, and Patrick Clarysse*

*In vivo* Contact EP Data and *ex vivo* MR-Based Computer Models: Registration and Model-Dependent Errors . . . . . 364
*Mihaela Pop, Maxime Sermesant, Roey Flor, Charles Pierre, Tommaso Mansi, Samuel Oduneye, Jen Barry, Yves Coudiere, Eugene Crystal, Nicholas Ayache, and Graham A. Wright*

Understanding Hemodynamics and Its Determinant Factors in Type B Aortic Dissections Using an Equivalent Lumped Model . . . . . 375
*Paula Rudenick, Bart Bijnens, Constantine Butakoff, David García-Dorado, and Arturo Evangelista*

**Author Index** . . . . . 383

# Study on Hemodynamics in Patient-Specific Thoracic Aortic Coarctation Model

Wenyu Fu[1,2] and Aike Qiao[2,*]

[1] Beijing Union University, Beijing 100020, China
[2] Beijing University of Technology, Beijing 100124, China

**Abstract.** In order to assess the variability in the calculation of the pressure gradient through a moderate thoracic aortic coarctation (MTAC), a 3D finite element model of MTAC was constructed, which includes the ascending aorta, the aortic arch, the descending aorta, and the three large branches (the innominate artery, the left common carotid artery, and the left subclavian artery), as well as with a coarctation in the descending aorta. The surface model of MTAC in STL format was imported into ANSYS ICEM CFD12.1 to generate volume mesh. A finite element model suitable for hemodynamics analysis of patient-specific MTAC was established. Numerical simulation of hemodynamics in this model was performed by means of Computational fluid dynamics (CFD) using ANSYS CFX12.1. The temporal distributions of homodynamic variables such as streamlines, wall pressure, velocity vector and wall shear stress in the arteries were analyzed during a cardiac cycle. The maximum and the average of pressure gradient in a cardiac cycle through a MTAC are 13 mmHg and 2.84 mmHg respectively. The pressure difference between the systolic and the diastolic in a cardiac cycle proximal to the coarctation is about 38 mmHg, which is smaller than the difference between the recorded systolic and diastolic pressures of 115 and 65 mmHg (i.e. the difference is 115-65=50). Similarly, the pressure gradient through the coarctation under exercise conditions could be predicted via modifying the inflow and outflow boundary conditions under resting conditions. CFD techniques make it possible to obtain information (such as pressure when the patient is under exercise condition) which is difficult to get in clinic practice or in experiment based on patient-specific data.

**Keywords:** Thoracic aortic coarctation, MRA image, Computational fluid dynamics, Pressure gradient, Hemodynamics.

* Common first author and corresponding: Aike Qiao, Email:qak@bjut.edu.cn. This work was supported by National Natural Science Foundation of China (10972016, 81171107), Higher School Specialized Research Fund for the Doctoral Program Funding Issue (20111103110012) and Natural Science Foundation of Beijing (KZ201210005006, 3092004).

O. Camara et al. (Eds.): STACOM 2012, LNCS 7746, pp. 1–8, 2013.

## 1 Introduction

Coarctation of the aorta (CoA), which usually occurs in the thoracic segments of the aorta, often leads to hypertension. It can be treated with percutaneous balloon angioplasty or stent implantation. The CoA can be expanded to the normal value after treatment and the pressure gradient through CoA will decrease. Studies have shown that hemodynamic parameters such as wall pressure, flow velocity and wall shear stress (WSS) are closely related to vascular geometry[1-3]. Therefore, hemodynamic analysis can be performed and then applied to predict the variability in the calculation of the pressure gradient through a thoracic aortic coarctation model. Numerical simulation of hemodynamics is an important investigation approach in biomechanical field where construction of accurate and effective patient-specific model is a key point. Many researchers have performed numerical simulations of blood flow in human thoracic aorta[4-7]. However, numerical simulation based on model with several large arteries and CoA is rare. In order to assess the variability in the calculation of the pressure gradient through a moderate thoracic aortic coarctation (MTAC), a 3D finite element model of MTAC was constructed, which includes the ascending aorta, the aortic arch, the descending aorta, and the three large branches (the innominate artery, the left common carotid artery, and the left subclavian artery), as well as with a coarctation in the descending aorta. Numerical simulation of hemodynamics in this model was performed by means of Computational fluid dynamics (CFD) using ANSYS CFX12. 1.

## 2 Construction of Finite Element Model

Gadolinium-enhanced MR angiography (MRA) of an 8 years old female with a moderate thoracic aortic coarctation (approximately 65% of area reduction) was obtained from a 1.5-T GE Signa scanner. Data of aortic vessel was extracted by image segmentation. Then surface model of thoracic aorta was exported in STL format (shown in Fig.1). The number of faces and points in the .stl file is 114,514 and 57,259, respectively. The STL file was imported into ANSYS ICEMCFD 12.1. Volume meshes were generated by using mesh types of unstructural tetrahedron and prism. To improve accuracy of calculation near the boundary layer, progressively finer meshes were generated in the normal direction of vessel wall. The total number of the meshes is 4,170,327 and the total number of the nodes is 1,318,788. Meshes in a cross-section is shown in Fig.2.

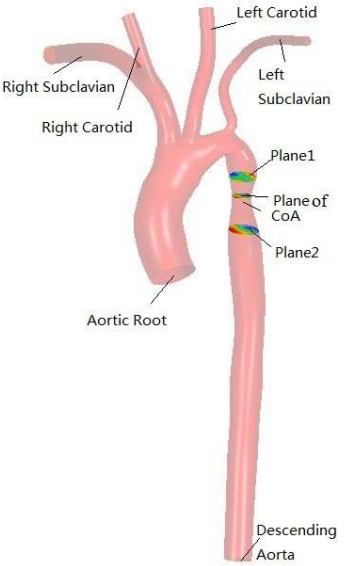


**Fig. 1.** 3D model of aorta

**Fig. 2.** Meshes in a cross-section

## 3 Calculation Method

Volume mesh file was imported into ANSYS CFX 12.1 to perform the numerical simulation. The following assumptions were employed in this numerical study: non-permeability, rigid wall; incompressible Newtonian fluid; pulsatile and laminar flow. Viscosity and density of blood are 0.004Pa•s and 1000kg/m3 respectively. Heart rate is 86 beats/min with the cardiac cycle T of 0.7s. Womersley number based on the thoracic aorta diameter is 5.78. The average value of Reynolds number is 1076 based on the entrance flow velocity and the thoracic aortic diameter.

The flow rate in the ascending aorta is shown in Fig.3 and it is used as inlet boundary condition. This implies a flat velocity profile is assigned at the aortic inlet[8]. No-slip condition is applied to vascular wall. Blood pressure was set to 0Pa in all the outlet sections.

The discrete form of differential equations governing the blood flow is upwind scheme. Residual convergence criteria of mass and momentum are set to 10-5. The time step in calculation is 0.005s. Because the number of volume mesh is more than four million, parallel calculation was used to reduce running time. Run mode in CFX is "PVM Local Parallel". Personal computer was used to perform simulation calculation. Its CPU is Intel Core i5-2400 (4 cores) and its main frequency is 3.10G. Memory is 8GB. Convergence solutions were obtained after 3 cycles and about 13 hours calculation.

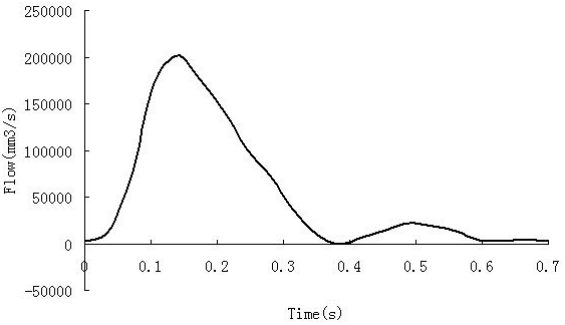


**Fig. 3.** Flow at entrance in a cardiac cycle

## 4 Calculation Result

As shown in Table 1, peak pressure gradient and time-averaged pressure gradient between Plane1 and Plane2 (as shown in Fig.1) are 13 mmHg and 2.84 mmHg respectively. Systolic pressure and diastolic pressure in ascending aorta are 115 mmHg and 77 mmHg respectively. The difference between systolic pressure and diastolic pressure is 38 mmHg, which is bigger than the value given in the CFD challenge measurements (115-65 =50mmHg).

**Table 1.** Results requested by the CFD challenge

| | |
|---|---|
| Peak pressure difference between Plane 1 and Plane 2 | 13 mmHg |
| Mean pressure difference between Plane 1 and Plane 2 | 2.84 mmHg |
| Pressure in ascending aorta (Systolic/Diastolic) | 115/77 mmHg |

Flow splits in supra-aortic and descending aorta are shown in Table 2. The number in the second row in Table 2 is the data given by the CFD challenge measurements. The number in the third row in Table 2 is the data obtained from the simulation calculation. It can be found that there is relatively big error of blood flow through descending aorta (58.8-41.73=17.07).

**Table 2.** % of ascending aortic flow through various branches of the aortic model

| Location | $Q_{IA}$ | $Q_{LCCA}$ | $Q_{LSA}$ | $Q_{DAO}$ |
|---|---|---|---|---|
| % Ascending Aortic Flow(Measurement) | 25.6 | 11.3 | 4.26 | 58.8 |
| % Ascending Aortic Flow(Calculation) | 37.21 | 17.18 | 3.88 | 41.73 |

$Q_{IA}$: flow through the innominate artery; $Q_{LCCA}$: flow through the left common carotid artery; $Q_{LSA}$: flow through the left subclavian artery; $Q_{DAo}$: flow through descending aorta;

Several typical moments (0.08s and 0.14s, systolic acceleration phase; 0.25s, systolic deceleration phase; 0.49s and 0.6s, diastolic phase) were selected to show the calculation results of velocity, pressure and WSS.

Streamlines (partial model was shown for clarity) at different moments in a cardiac cycle were shown in Fig.4 which shows a vortex in the end of the aortic arch and before the descending thoracic aortic coarctation. It is obvious that blood flow velocity is the biggest in the region of aortic coarctation. The maximum is about 2.981m/s at the moment of 0.14s in a cardiac cycle. Blood flow velocity near the inner parts of the aortic arch is bigger than that near the outer parts of the aortic arch in the phase of systole. The flow characteristics in the thoracic aorta with coarctation and without coarctation are significantly different (refer to [9] for the analysis of flow characteristics without coarctation)

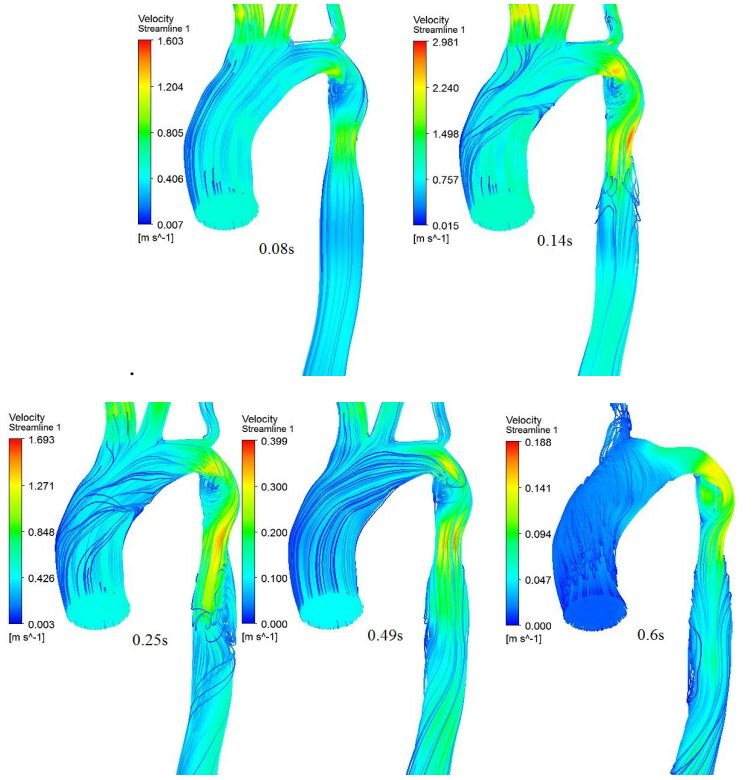


**Fig. 4.** Streamlines of blood flow within a cardiac cycle

To obtain the pressure gradient through the coarctation, two planes were defined before the coarctation and after the coarctation as shown in Fig.1 (Plane1 and Plane2). The maximum of the pressure gradient in a cardiac cycle is 13 mmHg and the average of the pressure gradient in a cardiac cycle is 2.84 mmHg. As shown in Fig.5, pressure

gradient between Plane 1 and Plane 2 changes over time. The range of pressure gradient in systole is bigger than that in diastole as shown. In the acceleration phase of systole, pressure gradient increases gradually (0s to 0.14s). In the decreasing phase of systole (0.14s to 0.32s), pressure gradient decreases gradually. In the phase of diastole, pressure gradient between Plane 1 and Plane 2 aorta becomes almost identical.

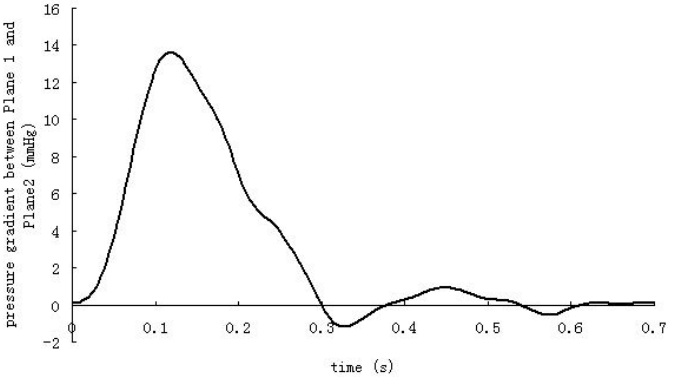


**Fig. 5.** Pressure gradient between Plane 1 and Plane 2 at different moment in a cardiac cycle

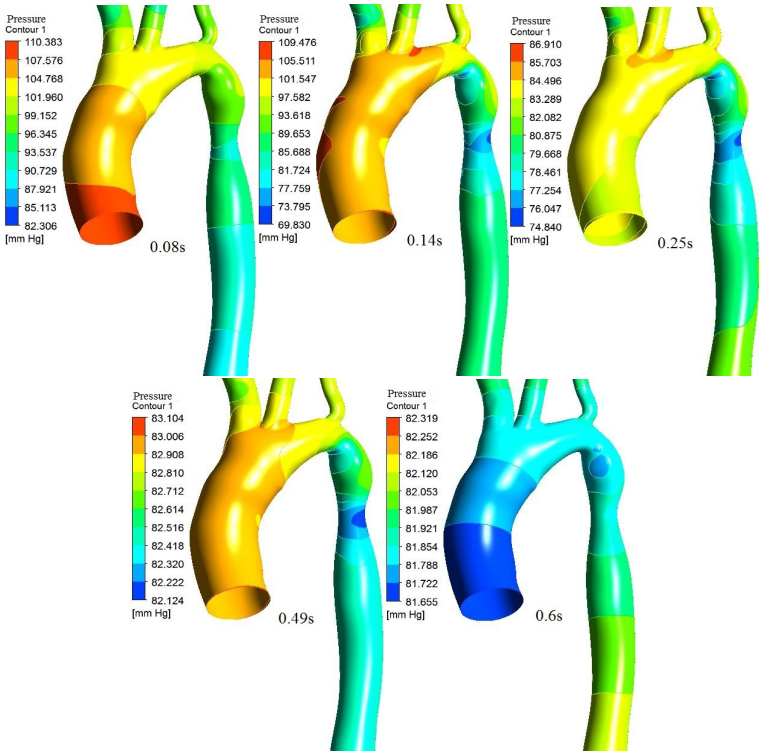


**Fig. 6.** Wall pressure at different moment in a cardiac cycle

The range of wall pressure fluctuation in systole is bigger than that in diastole as shown in Fig. 6. In the accelerated phase of systole, wall pressure decreases gradually from proximal end to distal end (0.08s, 0.14s). On the whole, wall pressure decreases from ascending aorta to the location of MATC in the decreasing phase of systole (0.25s). In the phase of diastole fluctuation of wall pressure is not big. In the latter half phase of diastole, change of wall pressures between ascending aorta and descending aorta is very small.

As shown in Fig.7, the largest WSS in systole appears in the outer wall of the thoracic aortic coarctation. Maximum of WSS in systole is larger than that in diastole by about two orders of magnitude. WSSs on the inner wall of the aortic arch are significantly larger than WSSs on the outer wall of the aortic arch in the acceleration phase of systole (0.08s, 0.14s, 0.25s, 0.49s) and their absolute values are also very high (the maximum is about 126 Pa at 0.14s). The maximum of WSS changes from dozens Pa to hundreds Pa at different moments.

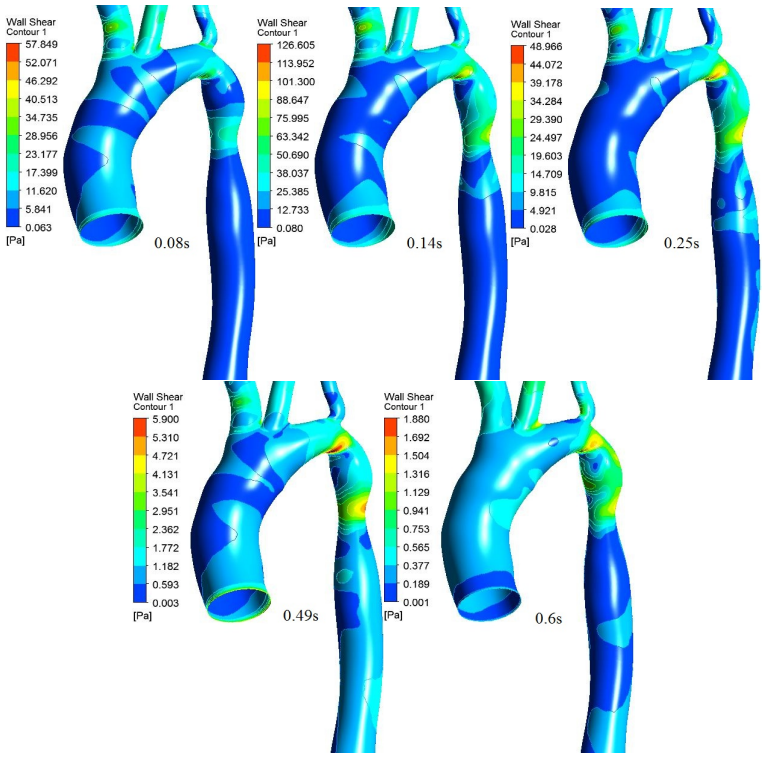


**Fig. 7.** Wall shear stress distribution within a cardiac cycle

## 5 Conclusions

With the construction and simulation of patient-specific model of thoracic aorta, distribution and changes of hemodynamics in blood flow field were obtained. Thoracic

aortic model with coarctation based on the MRA images has digital and personalized features. This kind of model can be used for calculation of hemodynamics in the thoracic aorta and predication of pressure gradient of section with coarctation. It is noteworthy that boundary conditions for outlets were established with 0 Pa. The outlet boundary conditions not only represent the domain of interest (the main aorta),but also include smaller arteries, arterioles and capillaries. Now 0 pressures are used for all the outlets, so the flow split in supra-aortic and descending aorta is controlled solely by flow resistance in the branches of interest. The resistance of the downstream vascular beds is not considered. This is the main reason why there is a big error in the data of rate of flow between measurement and calculation in Table 2. So the setup of boundary conditions for outlets used now is not very appropriate. If the pressure at the outlets could be obtained at different moments in a cardiac cycle, boundary conditions of outlets could be set up with the pressure waves in a cardiac cycle. It may be closer to the real physiological state.

## References

1. Borghi, A., Wood, N.B., Mohiaddin, R.H., et al.: Fluid-solid interaction simulation of flow and stress pattern in thoracoabdominal aneurysms: A patient-specific study. Journal of Fluids and Structures 24, 270–280 (2008)
2. Cai, Y., Xu, S., Jing, Z., et al.: Effect of Geometry Configuration of Abdominal Aortic Aneurysm on Hemodynamics by 3D Numerical Analysis. Journal of Medical Biomechanics 23, 140–146 (2008)
3. Fu, W.Y., Meng, X.L., Gu, Z.Y., Qiao, A.K.: Construction and Analysis of Human Thoracic Aorta Based on CT Images. Journal of Beijing University of Technology 37(5), 788–793 (2011)
4. Hoi, Y., Woodward, S.H., Kim, M., et al.: Validation of CFD Simulations of Cerebral Aneurysms with Implication of Geometric Variations. Journal of Biomechanical Engineering 128(12), 843–851 (2006)
5. Shahcheragh, N., Dwyer, H.A., Cheer, A.Y., et al.: Unsteady and Three-Dimensional Simulation of Blood Flow in the Human Aortic Arch. Journal of Biomechanical Engineering 124(8), 378–387 (2002)
6. Canstein, C., Cachot, P., Faust, A., et al.: 3D MR Flow Analysis in Realistic Rap-id-Prototyping Model Systems of the Thoracic Aorta: Comparison with In Vivo Data and Computational Fluid Dynamics in Identical Vessel Geometries. Magnetic Resonance in Medicine 59, 535–546 (2008)
7. Wood, N.B., Weston, S.J., Kilner, P.J., et al.: Combined MR Imaging and CFD Simulation of Flow in the Human Descending Aorta. Journal of Magnetic Resonance Imaging 13, 699–713 (2001)
8. Nerem, R.M.: Vascular fluid mechanics, the arterial wall, and atherosclerosis. Journal of Biomechanical Engineering 114(3), 274–282 (1992)
9. Lin, Y., Jing, Z., Zhao, Z., et al.: Three Dimensional Simulation of Pulsatile Blood Flow in Human Thoracic Aorta. Academic Journal of Second Military Medical University 27(8), 867–875 (2006)

# Quantitative Hemodynamic Evaluation in Children with Coarctation of Aorta: Phase Contrast Cardiovascular MRI versus Computational Fluid Dynamics

Prahlad G. Menon[1], Kerem Pekkan[2], and Shobhit Madan[2]

[1] Department of Biomedical Engineering, Carnegie Mellon University, Pittsburgh, PA
[2] Department of Radiology, Children's Hospital of Pittsburgh of the University of Pittsburgh Medical Center, Pittsburgh, PA
pgmenon@andrew.cmu.edu

**Abstract.** Pressure gradient across coarctation of aorta (CoA) is conventionally computed from phase contrast magnetic resonance imaging (PC-MRI) by applying the Bernoulli equation to the peak blood flow velocity measurement obtained just distal to the aortic narrowing. In order to test the validity and accuracy of the Bernoulli flow assumptions of negligible viscous forces in assessment of pressure gradients across the coarctation, we sought to determine pressure information from patient-specific computational fluid dynamics (CFD) simulation, modeling Newtonian, viscous, incompressible blood flow under steady and pulsatile inflow conditions. The transient high velocity jet observed though a moderate thoracic aortic coarctation model (65% area reduction) reconstructed from magnetic resonance angiography scans of an 8-year old female patient provided for the 2012 STACOM CFD challenge, was studied over a cardiac cycle under patient-specific flow conditions. Descending aorta hemodynamics was contrasted with a geometrically and dynamically comparable normal aorta simulation. The peak velocity of the modeled CoA jet (6.99 m/s) was observed to occur ~2 cm distal to the site of coarctation. The magnitude of this velocity was found to be similar to appropriately dynamically scaled clinical observations (6.00±0.6 m/s) of peak velocity obtained from PC-MRI data on three pre-surgical CoA patients, evaluated at Children's Hospital of Pittsburgh. Bernoulli pressure gradient across the CoA computed using the CFD velocity field at the peak-systole instant of pulsatile flow grossly overestimated the true gradient predicted from CFD (30 mm Hg) when unsteady jet wake effects were more pronounced, but underestimated the CFD pressure gradient at steady time-averaged inflow conditions (5.8 mm Hg). Based on this pilot study, CFD determined flow fields are a more reliable clinical indicator of pressure gradient which considers viscous flow and complex jet wake interactions affecting hemodynamics downstream of CoA.

**Keywords:** Coarctation of Aorta, Computational Fluid Dynamics, Phase Contrast Magnetic Resonance Imaging, Pressure Gradient.

O. Camara et al. (Eds.): STACOM 2012, LNCS 7746, pp. 9–16, 2013.

# 1 Introduction

Coarctation of aorta (CoA), one of the most commonly encountered congenital cardiovascular diseases, is characterized by aortic narrowing, resulting in differential blood flow and systolic pressure gradient between the upper and lower extremities. Significant pressure-loss across the coarctation, turbulent jet flows [1], and hypertension in the proximal circulation characterize this condition, which could potentially result in major adverse cardiovascular events if left undetected. Therefore, CoA requires comprehensive qualitative and quantitative evaluation of pressure gradients, collateral flow, and velocity across the coarctation in order to assess its severity for timely disease management. Morphological evaluation of coarctation and functional assessment of collateral flow at various levels of the descending aorta (DAo) is routinely performed [2] with phase contrast magnetic resonance imaging (PC-MRI). Pressure gradient (in mm Hg) is computed from peak blood flow velocity measurements (in m/s) obtained just before and after the aortic narrowing, using the Bernoulli's equation. In order to test the validity and accuracy of the Bernoulli flow assumptions of negligible viscous forces in assessment of pressure gradients across the coarctation, given that turbulent jet flows are observed, we sought to determine pressure information from patient-specific computational fluid dynamics (CFD) simulation, modeling Newtonian, viscous, incompressible flow. We examine the transient jet flow observed over a cardiac cycle though a moderate thoracic aortic coarctation model (65% area reduction) reconstructed from magnetic resonance angiography scans of an 8-year old female patient (BSA = 0.94 $m^2$), as provided for the 2012 STACOM CFD challenge.

The paper is further organized as follows. In Section 2, the computational methods are briefly explained followed by the nature of the supporting clinical study that was conducted. In Section 3, pressure gradient results obtained with CFD are presented along with analyzed flow structures in the DAo, drawing attention to differences that exist between the flow structures seen past the CoA and those seen in a normal aorta. Section 5 concludes with a short note on the limitations of this study and the focus of present studies.

# 2 Methods

## 2.1 Computational Methods

Direct numerical simulation (DNS) was performed to solve the Navier–Stokes equations using a second-order accurate, finite difference method; this solver has been used extensively for image-based hemodynamic modeling and incorporates a validated multi-grid artificial compressibility numerical solver [3, 4] simulating incompressible and Newtonian blood flow with constant hemodynamic properties ($\rho$ = 1000 kg/$m^3$, $\mu = 4 \times 10^{-3}$ Pa.s). Flow is simulated on a high-resolution unstructured Cartesian immersed boundary grid. In this study, the resulting 3D CFD grid had ~200,000 uniformly spaced nodes, with an average node spacing resolution of 0.03 mm, which was generated after immersing the surface model in a Cartesian grid of 228 x 118 x 387 cubical elements. This solver has been employed for DNS jet flow characterization studies in the past [5] for a range

of flow regimes (laminar to turbulent) which were validated against particle image velocimetry (PIV) quantitative flow measurements and flow visualization techniques [6]. The temporal resolution was considered as 0.01 simulation time units i.e. $O(10^{-4})$ sec. Computations were performed using normalized spatial and temporal units. The mean aortic annulus diameter of 1.61 cm was used to achieve spatial normalization, and the mean inflow Reynolds number (Re = 1070) was used in order to obtain temporal normalization. The cardiac cycle was discretized into 21 steps per cycle (0.7 seconds, ~86 BPM) and a second order interpolation scheme was employed in order to obtain inlet conditions based on the input discrete cardiac cycle data. Simulations were conducted using a Poiseuille inflow velocity profile having a mean-velocity varying as per the PC-MRI obtained cardiac output waveform (3.245 L/min, seen in Figure 1) , without extending the inlet. A mass-flow split type outflow boundary condition is employed in the solver, with a 42.2% - 58.8% flow split between the head-and-neck vessels and the DAo. Simulation data was gathered for the 5th cardiac cycle, in order to ensure damping of initial transients.

As a case control, a similar steady inflow hemodynamics simulation was conducted for a normal aorta model (idealized model) which was dynamically scaled (by inlet Re) to match the steady time-averaged inflow of the simulated CoA case, considering the same outflow boundary splits and similar grid resolution. The jet across the coarctation was analyzed for downstream velocity and helicity and compared with the normal model in order to visualize alteration of vortical flow structures in the DAo. Further, the pressure gradient in the normal model, across a length equivalent in size and location to the simulated CoA case, was computed in order to arrive at a qualitative as well as quantitative comparison between normal and pathological cases.

### 2.2 Clinical Study

Following approval from the Institutional Review Board, we collected retrospective cardiac MRI data on children pre-repair for CoA, evaluated at Children's Hospital of Pittsburgh. PC-MRI velocity field data in children between the ages 5 and 18 were collected over a period of 2 years. For this study, three cases having focal CoA with narrowing of the isthmus and proximal DAo were examined. Pressure drops across the coarctation were computed based on Bernoulli principle using peak velocity measurement, V, obtained from PC-MRI data as $4 \times V^2 = \Delta P$ [7]. The results of the patient study were dynamically scaled to match the flow regime and peak-systole cardiac output of the CFD modeled CoA case. Dynamically scaling of the collected patient-specific velocity data was achieved in a two step procedure: a) First the velocity at the coarctation was scaled up or down appropriately by scaling the extent of narrowing (area as a percentage of area at the hiatus) to be equivalent to the 65% narrowing seen in the simulated CoA case, given the inverse relationship between velocity and the square of diameter at a cross-section; let us reference this computed velocity as $v_{65\%}$. b) Next, since each patient had a different peak flow cardiac output, the velocity expected at the inlet to the ascending aorta (AAo) was computed for a diameter of 16.1 mm (i.e. diameter of inlet to the CoA CFD model) and the ratio of

this computed velocity with the inlet profile-average velocity of the CoA CFD model (0.99 m/s at peak systole) was obtained, while accounting for the applied 58.8% mass-flow split boundary condition at the DAo. This ratio was applied to $v_{65\%}$ in order to finally obtain the velocity expected at the coarctation given that the patient had an identical cardiac output at peak-systole as modeled in the CFD simulation.

## 3 Results and Discussion

Based on analysis from the clinical investigation, patients with ~30% focal extent of coarctation were expected to have peak velocity distal to the CoA of 1.75±0.25 m/s i.e Bernoulli pressure drop of 12.25±0.25 mm Hg with collateral flows ranging between 5 and 20 mL/beat, depending upon the extent of collateral vessel development during the time of diagnosis. Extrapolating this clinical investigation using the principles of dynamical scaling, patients with a similar focal extent and location of CoA as the modeled patient (65%) are expected to have peak velocity distal to the CoA of 6.00±0.6 m/s (see Table 1) i.e. pressure drop of 144±1.5 mm Hg by the $4\times V^2$ formulation. The velocity range was close to the peak systole velocity observed distal to the CoA from CFD, whereas the pressure gradient was far greater than the CFD result.

**Table 1.** Summary of clinical study along with dynamical scaling procedure

| Patient no | Age | Sex | Collateral Flow (mL/beat) | Peak Velocity at CoA (m/s) | Peak Velocity at Hiatus (m/s) | Isthmus (cm) | Hiatus (cm) | % CoA narrowing |
|---|---|---|---|---|---|---|---|---|
| CoA001 | 11 yr 7.6 mo | F | 5.00 | 1.30 | 0.40 | 0.40 | 1.50 | 73 |
| CoA002 | 12 yr 8 mo | M | 6.80 | 1.75 | 0.80 | 1.00 | 1.36 | 26 |
| CoA003 | 13 yr 0 mo | M | 20.00 | 1.50 | 0.90 | 1.30 | 1.45 | 31 |

| Dynamical Scaling | | | |
|---|---|---|---|
| Patient no | Peak velocity expected at 65% narrowing ($v_{65\%}$, m/s) | AAo peak velocity at 16.1 mm inlet - given 58.8% DAo split (m/s) | Peak velocity at 65% CoA matched to modeled patient CoA peak cardiac output (m/s) |
| CoA001 | 0.75 | 0.14 | 5.47 |
| CoA002 | 7.72 | 1.15 | 6.66 |
| CoA003 | 5.82 | 0.98 | 5.86 |
| | | ***Mean +- Standard Deviation =*** | ***6.00 +- 0.60 m/s*** |

The peak systole and the running average (equivalent to a time-averaged steady inlet flow simulation) flow fields for the simulated CoA case are presented for comparison in Figure 1. Using the instantaneous pulsatile CFD pressure field at the peak systole, pressure drop across the CoA computed at two reference planes (depicted in Table 2), was ~30 mm Hg. At end diastole, 0.36 mm Hg pressure drop was observed. In comparison, peak systole pressure drop computed using Bernoulli principle across the coarctation using the peak CFD velocities observed in the plane distal

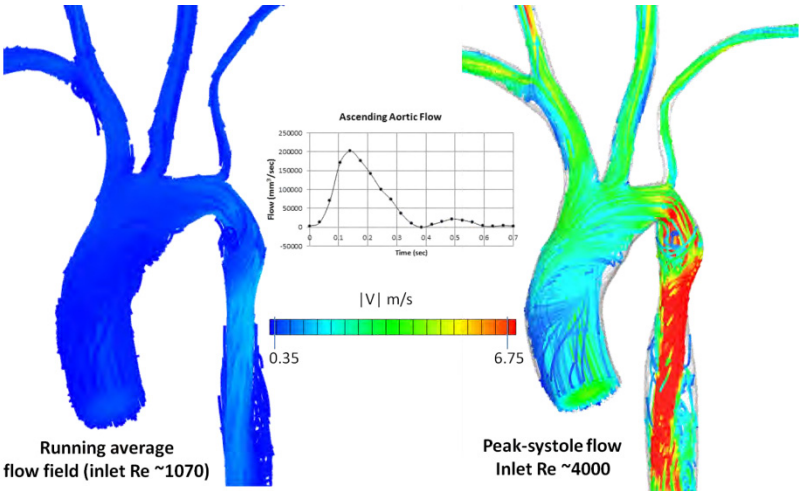


**Fig. 1.** Stream traces computed by time integration of the velocity field in Tecplot (Bellevue, WA) colored by velocity magnitude, |V|, for a mean ascending aortic velocity of 0.265 m/s, Re 1070 (left) obtained from the running average pulsatile flow field; and at the peak systole instant of the prescribed pulsatile cardiac output (right) having average inlet velocity of ~1 m/s.

to the level of the coarctation (6.78 m/s from CFD) and proximal to it (4.93 m/s from CFD), was ~81 mm Hg, which was again a gross overestimation of the true CFD pressure gradient.

The pressure fields at peak systole and end-diastole are colored onto the observed flow stream traces plotted at their respective times instants of the cardiac cycle, in Figure 2A. These pressure results have also been summarized in Table 2.

**Table 2.** Peak and time-averaged CFD pressure gradient between two reference planes in the CoA model. AAo (inlet) pressures corresponding to peak systole and end-diastole pressures of 115 and 65 mm Hg proximal to the CoA, respectively, are also indicated.

| | | |
|---|---|---|
| Peak pressure difference | 30.02 mm Hg | *Peak Systole (mm Hg)* |
| Mean pressure difference | 5.81 mm Hg | |
| Flow splits in supra-aortic and DAo | 25.6/11.3/4.3/58.8 (%) | |
| Pressure in AAo (Systolic/Diastolic) | 147/65.5 mm Hg | 87 115 143 171 |

The peak velocity observed from CFD data in the peak-systole jet was 6.99 m/s, which was ~10% higher than that observed at the neck of the coarctation. The running average flow field obtained from pulsatile flow simulation and the corresponding steady inflow centerline velocity and pressure profiles were found to match with a corresponding maximum CoA jet velocity of 1.45 m/s, indicating that the quasi-steady assumption is a reasonable approximation for mean flow of the cardiac cycle.

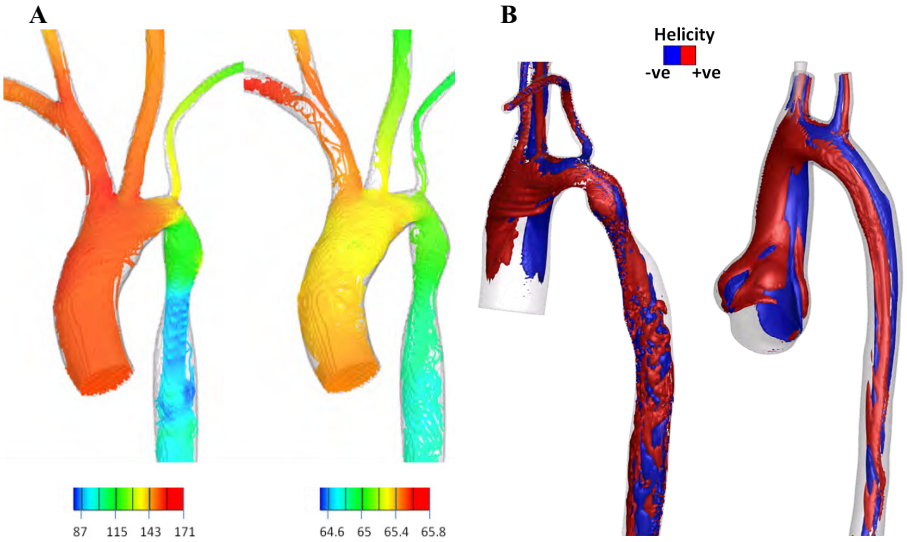


**Fig. 2.** A) Stream traces computed by time integration of the velocity field colored by pressure at end-systole (left) and end-diastole (right), in mm Hg. B) Helicity isocontours computed at peak systole flow instant of the CoA case (left) and the normal aorta case simulated at steady Re 1070 inflow conditions. Helical flow patterns transform into a turbulent jet wake past the CoA whereas they remain helical at the DAo of the normal aorta, therefore indicating a striking disparity in downstream hemodynamics.

In order to evaluate the influence that CFD inflow velocity profiles prescribed at the inlet of the aorta models have in hemodynamics observed, peak systole velocities were compared for a parabolic Poiseuille flow (peak velocity = 2x mean) and a plug flow boundary velocity profile. Peak velocities past the CoA at multiple cross sections were found to match within +-0.4 m/s.

The pressure drop obtained from the time-average steady inflow CFD model (~5.8 mm Hg) were underestimated by the Bernoulli estimates computed from the same velocity field (~1 mm Hg). This is expected on account of neglected viscous frictional losses in the Bernoulli formulation. The corresponding CFD pressure drop observed across the isthmus of the normal aorta model, considering similar reference planes for data extraction, was ~5 mm Hg, for the identical steady inflow Re.

In order to compare the nature of vortical structures in the DAo flow field between the CoA case and the normal aorta case, helicity was computed as a flow derived parameter and rendered as isocontours (see Figure 2B) for time-averaged inflow conditions (Re 1070). Helicity was computed as the normalized magnitude of the dot product between vorticity and velocity vectors at each node in the computed flow field. Positive helicity (highlighted red) indicates right handed vortical structures and negative helicity (highlighted blue) indicates left handed vortical structures. Helicity in the DAo is regarded as a contributor to optimizing naturally occurring transport processes in the cardiovascular system, avoiding excessive energy dissipation. Further, statistically significant differences are known to exist in the helical content of aortic flows at different phases of the cardiac cycle. Helical flow patterns were observed in the AAo and transverse arch of both CoA and normal cases, but these patterns were more pronounced in the DAo of the normal aorta model. In contrast, the DAo past the coarctation case did not demonstrate such coherent helical flow but rather complex shedding vortical flow characteristic of a turbulent jet wake.

Flow induced wall shear stress (WSS) is believed to play an important role in the initiation and progression of vascular diseases. Increased WSS was seen at the isthmus of the normal aorta and pathological CoA CFD models. A comparison was made between the running time average pulsatile WSS field in the CoA case and the normal aorta simulation at steady inflow conditions (Figure 3). The increased WSS in the CoA case was nearly twice as high at the coarctation (46-48 dynes / $cm^2$) than that expected in the normal aorta.

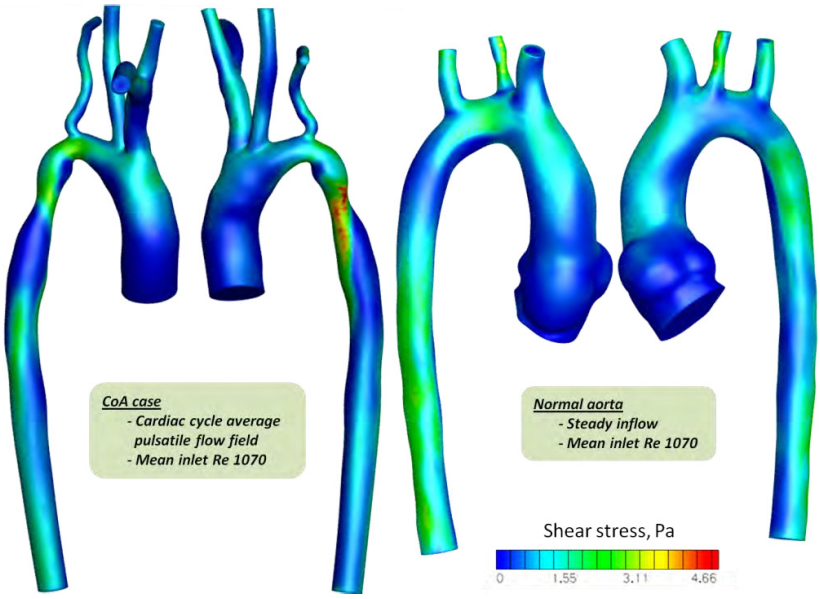


**Fig. 3.** Surface plots of the time averaged WSS field obtained from the pulsatile CoA simulation (left) and the steady inflow normal aorta simulation, at the corresponding time-averaged Reynolds number (right)

## 4 Conclusions

CFD is a powerful tool for simulation of altered hemodynamics in pathological anatomies and is adopted in this study as a diagnostic technique for evaluating blood velocity and pressure gradients across a patient-specific CoA. The downstream hemodynamics and helicity observed in the DAo of the normal aorta model were significantly different than that observed in the jet wake of the CoA case. The peak velocity of the modeled CoA jet was observed to occur ~2 cm distal to the site of coarctation and the magnitude of this velocity was found to match clinical observations after appropriate dynamical scaling. The 65% stenosis in the simulated CoA led to a multifold increase in expected pressure gradient and peak DAo velocity in comparison with a normal aorta. The primary conclusion of this study is that Bernoulli estimated pressure drops overestimate the true pressure drop computed using CFD at the peak-systole instant of the pulsatile flow model when complex jet wake effects are pronounced, and underestimate it when compared using a time-averaged steady flow field. Based on this pilot study, CFD determined flow fields are a more reliable clinical indicator of pressure gradient that consider viscous flow and complex jet wake interactions affecting hemodynamics downstream of CoA. Patient-specific CFD modeling for a larger sample size is required in order to confirm this hypothesis. Since collateral flow is an important clinical indicator for determining severity and timing of surgical management, future CFD studies on anatomical models that include reconstructions of major collateral vessels along with their respective PC-MRI determined mass-flow splits, is warranted for more realistic examination of DAo hemodynamics.

**Acknowledgements.** We acknowledge funding from the 2011-12 Dowd-ICES fellowship award and the Pittsburgh Supercomputing Center (allocation CCR080013) for facilitating the parallel CFD simulations presented in this work.

## References

1. Arzani, A., et al.: In vivo validation of numerical prediction for turbulence intensity in an aortic coarctation. Ann. Biomed. Eng. 40(4), 860–870 (2012)
2. Madan, S., Mandal, S., Tadros, S.S.: Magnetic Resonance Angiography Basics to Future. In: Shabana, W. (ed.) Magnetic Resonance Angiography of Aortic Diseases in Children. InTech (2012)
3. Payli, R., et al.: High Performance Clinical Computing on the TeraGrid: Patient-Specific Hemodynamic Analysis and Surgical Planning. In: TeraGrid 2007 Conference 2007, Madison, WI (2007)
4. Pekkan, K., et al.: Embryonic intra-cardiac flow fields at 3 idealized ventricular morphologies. In: APS, Milwaukee, USA (2009)
5. Menon, P.G., et al.: Device specific analysis of neonatal aortic outflow cannula jet flows for improved cardiopulmonary bypass hemodynamics. In: 64th Annual Meeting of the APS Division of Fluid Dynamics, Baltimore, Maryland (2011)
6. Menon, P.G., et al.: Device specific aortic outflow cannula jets studied using 2D PIV and high-performance 3D CFD simulation. In: ASME Summer Bioengineering Conference, Fajardo, Puerto Rico (2012)
7. Konen, E., et al.: Coarctation of the aorta before and after correction: the role of cardiovascular MRI. AJR Am. J. Roentgenol. 182(5), 1333–1339 (2004)

# A Lattice Boltzmann Simulation of Hemodynamics in a Patient-Specific Aortic Coarctation Model

Amanda Peters Randles*, Moritz Bächer, Hanspeter Pfister, and Efthimios Kaxiras

School of Engineering and Applied Sciences,
Harvard University
Cambridge, MA, USA 02138
apeters@fas.harvard.edu
hemo.seas.harvard.edu

**Abstract.** In this paper, we propose a system to determine the pressure gradient at rest in the aorta. We developed a technique to efficiently initialize a regular simulation grid from a patient-specific aortic triangulated model. On this grid we employ the lattice Boltzmann method to resolve the characteristic fluid flow through the vessel. The inflow rates, as measured physiologically, are imposed providing accurate pulsatile flow. The simulation required a resolution of at least 20 microns to ensure a convergence of the pressure calculation. HARVEY, a large-scale parallel code, was run on the IBM Blue Gene/Q supercomputer to model the flow at this high resolution. We analyze and evaluate the strengths and weaknesses of our system.

**Keywords:** computational fluid dynamics, coarctation of the aorta, lattice boltzmann, parallel computing.

## 1 Introduction

Coarctation of the aorta (CoA) can pose a significant problem as this narrowing of the aorta can inhibit blood flow through the artery. CoA accounts for 8%-11% of congenital heart defects, which makes it affect tens of thousands of patients annually in the Western world [1]. Hence, there is a need to efficiently diagnose the degree of arterial narrowing so that preventative action such as balloon angioplasty or stent implantation can be taken [2]. These methods serve to alleviate the pressure gradient through the coarctation in order to reduce the burden on the heart.

An obstruction is characterized as significant when the peak to peak systolic pressure gradient across the coarcted vessel is measured at greater than 20 mmHg. This pressure gradient is not only determined by the size of the narrowing but also factors such as the flowrate of the fluid and the size, number, and placement of collateral vessels [2]. The physiological state of the patient can also

* Corresponding author.

O. Camara et al. (Eds.): STACOM 2012, LNCS 7746, pp. 17–25, 2013.

contribute to an increase in the pressure gradient if, e.g., the patient is in an exercised state due to the associated elevation in heart rate. When the patient is at rest, clinicians can easily measure the pressure gradient; however, this measurement is difficult to obtain under exercise conditions. This difficulty causes simulation to play a key role in determining the pressure gradient non-invasively.

In this paper, we discuss a method for using data from medical imaging alongside a lattice Boltzmann fluid model to simulate blood flow and pressure in a model built from patient data. We will present the methods to impose a regular grid and model the fluid flow using parameters provided from patient data. We use the provided inflow waveform to produce realistic pulsatile flow that upholds the measured flow distribution via velocity imposed boundary conditions at the inlets and outlets.

## 2 Data

The data used in this paper was provided by the STACOM CFD Challenge for the simulation of hemodynamics in a patient-specific aorta coarctation model. The geometry of the vessels were obtained through gadolinium-enhances MR angiography (MRA) with a 1.5-T GE Signa scanner. A segmented STL file was provided defining the ascending aorta, arch, descending aorta, and upper branch vessels. Flow rates were measured by PC-MRI sequence encoding and provided for the course of a cardiac cycle as well as the percent of flow seen in each branch of the model [1].

## 3 Computational Fluid Dynamics (CFD) Framework

In this work, we use the lattice Boltzmann method (LBM) as the basis of our simulation [3]. The LBM has proven to be a strong alternative to simulations derived from the Navier-Stokes equation of continuum mechanics. In recent years, its ease of handling complex geometries and parallelization has made it increasingly popular. Unlike conventional CFD methods based on the discretization of macroscopic continuum equations, the LBM constructs a simplified kinetic model incorporating the essential physics and preserving macroscopically averaged quantities like mass and momentum [4].

In this model, the volume of a 3-dimensional mesh is filled with a regular array of lattice points on which a minimal form of the classical Boltzmann is simultaneously solved for a set of fictitious particles [3]. These particles represent the collective motion of a group of physical particles and the dynamics are such that they ensure hydrodynamic behavior in the continuum limit.

### 3.1 Algorithm

The fundamental quantity is the probability density function defining the likelihood of finding particles at a specific location, at a specific time, traveling along a specific velocity path. In this work, we use the 19-speed velocity model, D3Q19,

in which the discrete velocities, $c_i$, connect lattice points to the first and second topological neighbors [4]. The distribution function is advanced through (1) [3].

In each time step, the particles advect along the straight trajectories defined by the discretized velocities. Fluid-fluid collisions are then handled through a relaxation towards a local equilibrium, shown on the right side of (1). In this work, we leverage the Bhatnager-Gross-Krook (BGK) operator, a collision operator which relaxes to equilibrium on a single time scale [5]. The equilibrium distribution is defined through a second-order Hermite expansion of a local Maxwellian with density $\rho$ and speed $u$ as shown in (2) [6]. The relaxation frequency $\omega$ is related to the kinematic viscosity of the fluid through (3) [7].

$$f(x + c_i \Delta t, t + \Delta t) = f(x, t) - \omega \Delta t (f(x, t) - f^{eq}(x, t)). \tag{1}$$

$$f_i^{eq} = w_i \rho \left\{ 1 + \frac{\xi_i \cdot u}{c_s^2} + \frac{uu : (\xi\xi - c_s^2 I)}{2c_s^2} \right\}. \tag{2}$$

$$\nu = c_s^2 \Delta t (\frac{1}{\omega} - \frac{1}{2}) \tag{3}$$

In (2), $w$ denotes the quadrature weight normalized to unity and the speed of sound is a lattice constant: $c_s^2 = \frac{1}{3}$. $I$ is the unit tensor in Cartesian space.

A key advantage of the LBM is that macroscopic quantities such as density are moments of the distribution function. This means that they can be calculated based on its summation and therefore are available entirely locally. In the study of CoA, the fluid pressure is particularly important.

Pressure can be easily recovered through the ideal gas relation: $P = c_s^2 \rho$. This means that the value is available locally which is particularly advantageous as this means they do not require solving an expensive Poisson problem as in other CFD methods [8].

### 3.2 Boundary Conditions

As prescribed by the challenge definition, we employ rigid walls in this simulation. At the wall, we impose a no-slip boundary condition through the use of a full bounce-back method. To this end, the velocity of any particle which is set to advect to a lattice point designated as a wall node is reversed. In this case, the directions of post-collisional particles are reversed if the prescribed velocity points to a lattice point designated as a wall node as shown in Fig. 1. The curved vessels are shaped on the regular (axis-aligned) grid via a staircase representation as opposed to the body-fitted grids found in direct Navier-Stokes solvers. This does come at the expense of numerical accuracy, which has been shown to degrade to first order [3]. This representation is improved systematically by increasing the resolution of the mesh via increased density of lattice points.

In this model, there is one inlet for the aorta and multiple outlets for each of the collateral vessels. The imposition of the boundary conditions is based on the knowledge of local flow profiles as provided by the measured patient-specific data

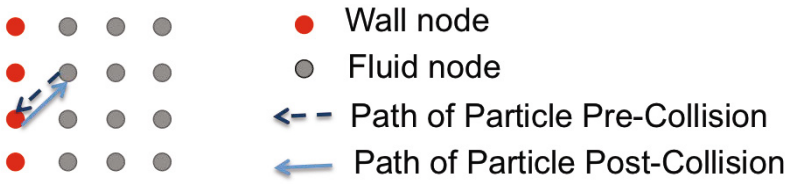


**Fig. 1.** Bounceback boundary condition. The no-slip boundary is enforced by reversing the direction of each particle just inside the wall boundary.

of this challenge. We employ a simple method of imposing a plug flow profile based on the flow rates. The inlet condition comes from the aortic flow measured by a phase-constract (PC) MRI sequence providing the inlet flow over the course of one cardiac cycle [1]. Any node defined as an inlet node has it's velocity set based on the time point in the simulation ensuring proper pulsatile flow that matches the measured data.

For the outlet condition, flow rate is determined based on the percent of flow through the various branches in the model as measured with the PC MRI as well. This allows us to calculate the flow rate at each branch and subsequent outlet. For most of the vessels, we are thus able to use clinically measured values for the outflows. In order to determine flow going through the right subclavian and right common carotid outlet faces, we use the empirical procedure based on the following assertion from previous studies: "in the coronary system we assume the physiological condition that the pressure drop in each vessel is driven by the oxygen request from the tissues nourished by the vessel" [8]. That means that we use flow splitting conditions of $\phi_1/\phi_2 = S_1/S_2$ in which $\phi_1$ and $\phi_2$ denote the outgoing flow rates and $S_1$ and $S_2$ the corresponding sectional areas. Coupling the incoming flow rate with the known flow splitting at each bifurcation allows us to impose consistent outflow conditions.

## 4 Simulation

The simulation of blood flow in the patient specific data involves the following five steps:

1. Acquisition of medical imaging data
2. Image segmentation to identify vessel geometry
3. Grid initialization
4. Flow simulation
5. Data analysis and simulation

In this work, the first two steps were provided by the competition framework. In this section, we illustrate how we handle (3) as a pre-processing routing, step (4) with our HARVEY code, and (5) with a separate visualization routine coupled with the use of Paraview [9].

### 4.1 Initializing the Regular Simulation Grid

To guarantee a proper initialization of our simulation grid, we require the patient's triangulated vessel geometry to be a closed, 2-manifold with no overlaps of interior volume. We start by computing the axis-aligned bounding box (AABB) of the input geometry offset by $\varepsilon$ (we use $\varepsilon = 1.8c_i\Delta t$) on each side, then discretize the box's volume into a regular grid of targeted resolution. Note that we choose $\varepsilon$ to be slightly bigger than the length of the diagonal of a regular grid cube ($\varepsilon > \sqrt{3}c_i\Delta t$). With this choice, we guarantee that every interior grid point has a neighbor not only in any 6-neighborhood but in any diagonal grid direction also.

Next, we classify each grid point to either be inside or outside of the given vessel geometry. Note that it would be prohibitively slow to run an inside-outside test for each individual grid point. We therefore correctly initialize the grid points falling inside the union of all sphere-swept triangles (the volume of a sphere-swept triangle is given by the union of all spheres of radius $\varepsilon$ with centers on the triangle) and then "fill in" the inside-outside classification for all remaining grid points. More specifically, we iterate over all vessel triangles: for each triangle, we compute the grid points that overlap with its AABB offset by $\varepsilon$ and then check them against its sphere-swept bounding volume. For the remaining grid points, we then compute the closest point on the triangle and – if the point hasn't been initialized yet or the current point is closer to the vessel geometry than the previously initialized one – classify it as either inside or outside using the angle weighted pseudonormal approach by Bærentzen and Aanæs [10]. Note that [10] guarantees a correct inside-outside classification for points with respect to non-convex geometries provided that we know their closest points on the mesh. After a run through all triangles, we can guarantee to find the correct closest points for all grid points falling in the union of the sphere-swept triangles, hence, to correctly classify them using [10]. By using a radius of $\varepsilon$ to sweep the triangles, we can further guarantee to correctly initialize at least two inside grid points in any 6-neighborhood and diagonal grid direction within a distance $\varepsilon$ of the vessel's boundary. Finally, we "fill in" the remaining grid points by looping over the three grid indices (that are monotonously decreasing or increasing in their respective dimension) and classifying all grid points as inside if the loop index of the most inner loop has crossed the grid boundary an odd number of times.

This classification is then refined into wall, inlet, and outlet points by using the grid point's 6-neighborhood (if at least one of its six neighbors are classified as outside, we have a wall point) together with proximity information to inlet or outlet triangles. The remaining grid points are either "fluid" nodes (inside the wall), or "dead" (outside and not considered).

### 4.2 Flow Simulation

The HARVEY simulation package is designed to handle complex geometries and to run large-scale simulations on high performance hardware resources. It has been developed from the ground up with parallel efficiency in mind to enable

high resolution runs. The mesh is Cartesian which enables straightforward data handling. It is written in C and uses MPI as the communication library. This code takes advantage of optimizations such as a) hand loop unrolling b) Single Instruction, Multiple Data (SIMD) intrinsics c) removal of redundant operations d) non-blocking communication [11]. The domain is split such that each processor handles a set division of the Cartesian mesh. In HARVEY a double buffer approach is used in which a starting distribution of fluid particles is initialized for each lattice point. The advection step propagates the particles to adjacent lattice points and stores these values in a temporary distribution function. This is the data exchanged with the neighboring processors, and subsequently used for the collision step. The result of the collision step is then used to update the local portion of the original array containing the distribution function for each lattice point. In this manner, HARVEY acts as a typical stencil code that draws information from its neighbors, updates its local value, and pushes this data to the neighbors, however, the data accessed in the temporary data structure is from another phase space as well as from another lattice location.

This double buffer approach further increases the already large memory demand of the simulation. In the case of this data set when simulated at a 200 micron resolution, there are 64,435 fluid voxels in a bounding box of 11,254,320 voxels. For each lattice point, there are two buffers that make up the bulk of the memory requirements. These buffers store the density data for each discrete velocity at each lattice point as a floating point number. For a 200 micron resolution simulation, this requires at least three gigabytes of memory. While some commodity desktops may now be able to meet the memory needs for 200 microns, this becomes increasingly difficult at finer resolutions. For a 20 micron simulation, 3 terabytes of data are necessary. This is feel beyond the capabilities of traditional computers and requires the use of large-scale platforms such as the IBM Blue Gene/Q described in a following section, especially when simulating full heartbeats.

The second issue is the runtime for the simulation to complete. At high resolutions, the LBM requires rather small time steps on the order of $10^{-6}$ seconds resulting in the need for 700,000 time steps to complete one heartbeat. The computation of the solution of the LBM equations for each lattice point in a serial manner can take from hours to days at these resolutions. In order to drastically decrease our time to solution, we leverage a parallel implementation that allows us to simulate the full cardiac cycle in minutes.

For the work in this challenge, we relied on the IBM Blue Gene/Q architecture. Similar to previous Blue Gene systems, it is built on a system-on-a-chip backbone and has expanded options for threading and memory access. The Blue Gene/Q system has a 64-bit PowerPC processor operating at 1.6 GHz frequency. Each node consists of 16 cores with 4 potential threads per core. There are capabilities for a 4-wide double precision FPU SIMD resulting in a 204.8 GFlop/s peak performance per node [12]. Memory per node is expanded to 16 gigabytes. In this work, we used 256 processors on 16 nodes of Blue Gene/Q for our simulations. The resulting velocity distribution is shown in Fig. 2. This is at 0.14 seconds in a 100 micron resolution simulation.

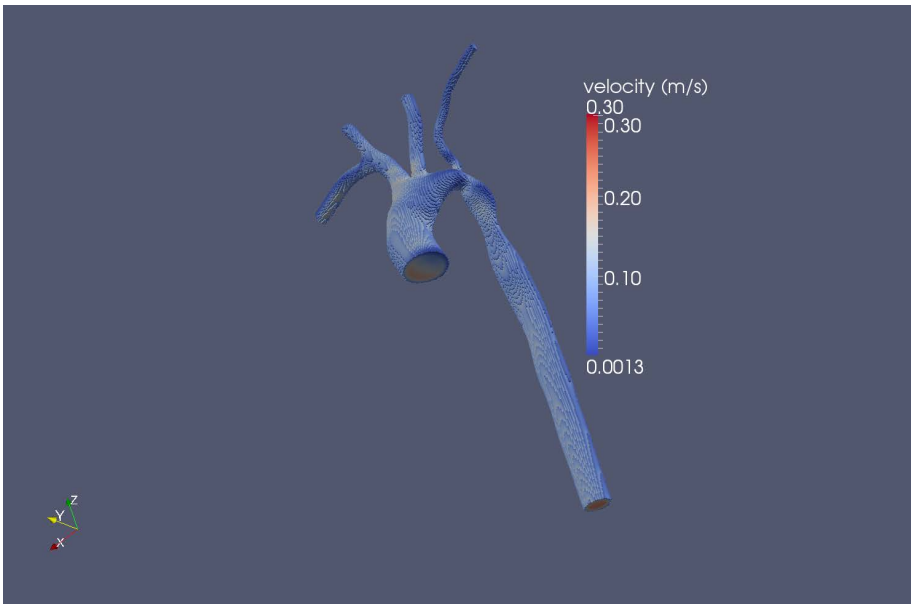


**Fig. 2.** Mapping showing the velocity distribution at .14 seconds in a 100 micron resolution simulation

### 4.3 Data Analysis and Visualization

The distribution function, $f$, at each lattice point is saved at a set time interval during the simulation allowing for post processing of the data to determine relevant macroscopic properties. It is during the post processing stage that the data is shifted from lattice units to SI units to allow for analysis of factor like fluid velocity, density, and pressure gradients. Only a subsample of time points are recorded and used for visualization and analysis. In this case, checkpoints were invoked every 20000 time steps. Paraview from Kitware is used to view the results [9].

## 5 Results

We assume rigid walls as well as the Newtonian behavior of the blood. The physical density is set at .001 g/mm$^3$ and the dynamic viscosity is .004 gr/mm/s.

We measure the mean pressure gradient between the upper and lower body by taking the difference of the average pressure of the fluid in the plane at the proximal and distal locations. The results of simulations at three different resolutions are provided in Table 1. The pressure proximal to the coarctation is measured at 113.1 mmHg (systolic) and 62.3 mmHg (diastolic) which corresponds well to the measured values of 115 mmHg and 65 mmHg respectively.

**Table 1.** Mean pressure gradient at different mesh resolutions

| Resolution | Pressure Gradient at Diastole | Pressure Gradient at Systole |
|---|---|---|
| $200\mu m$ | 10.1 mmHg | 12.2 mmHg |
| $100\mu m$ | 8.7 mmHg | 10.9 mmHg |
| $50\mu m$ | 8.1 mmHg | 10.4mmHg |
| $20\mu m$ | 8.2 mmHg | 10.3 mmHg |

**Table 2.** Required simulation results

| | |
|---|---|
| Peak pressure difference between Plane 1 and Plane 2 | 10.6 mmHg |
| Mean pressure difference between Plane 1 and Plane 2 | 9.2 mmHg |
| Flow splits in supra-aortic and DAo | 40% and 60% |
| Pressure in AAo(Systolic/Diastolic) | 10.3mmHg/8.2mmHg |

## 6 Conclusion

We have presented a system to simulate blood flow in a patient specific geometry in order to measure the pressure gradient in the aorta. The system imposes a regular grid on the vessel geometry derived from the segmentation of MRA data and uses HARVEY, a lattice Boltzmann application, to model the blood flow through the arteries and to derive the fluid pressure gradients.

We have tested our system on the provided datasets from the STACOM'12 CFD Challenge and analyzed the results. This has been a useful exercise to assist in validating our application. Our preliminary results demonstrate a 8.2 mmHg pressure differential at diastole and 10.3 mmHg at systole.

**Acknowledgments.** The authors would like to thank Dr. Hudong Chen and Dr. Raoyang Zhang of EXA Corporation for their helpful discussions. This work was supported by the Department of Energy's Computational Science Graduate Fellowship, grant number DOE CSGF DE-FG02-97ER25308. We would like to thank the LLNL Support Team for access to their Blue Gene/Q system.

## References

1. Figueroa, A., Mansi, T., Sharma, P., Wilson, D.N.: CFD challenge: Simulation of hemodynamics in a patient-specific aortic coarctation model (2012), `http://www.vascularmodel.org/miccai2012/`
2. Rao, P.: Coarctation of the aorta. Current Cardiology Reports 7, 425–434 (2005), doi:10.1007/s11886-005-0060-0
3. Succi, S.: The Lattice Boltzmann Equation for Fluid Dynamics and Beyond. Oxford University Press (2001)
4. Chen, S., Doolean, G.D.: Lattice Boltzmann method for fluid flow. Annual Review Fluid Mechanics 30, 329–364 (1998)

5. Bhatnagar, P., Gross, E., Krook, M.: A model for collision processes in gases. Physics Review Letters 94, 511 (1954)
6. Zhang, R., Shan, X., Chen, H.: Efficient kinetic method for fluid simulation beyond the Navier-Stokes equation. Physics Review E 74, 1–7 (2006)
7. Peters, A., Melchionna, S., Kaxiras, E., Lätt, J., Sircar, J., Bernaschi, M., Bison, M., Succi, S.: Multiscale simulation of cardiovascular flows on the IBM Blue Gene/P: Full heart-circulation system at red-blood cell resolution. In: Proceedings of the 2010 ACM/IEEE International Conference for High Performance Computing, Networking, Storage and Analysis, SC 2010, pp. 1–10. IEEE Computer Society (2010)
8. Melchionna, S., Bernaschi, M., Succi, S., Kaxiras, E., Rybicki, F.J., Mitsouras, D., Coskun, A.U., Feldman, C.L.: Hydrokinetic approach to large-scale cardiovascular blood flow. Computer Physics Communications 181(3), 462–472 (2010)
9. Henderson, A.: Paraview guide, a parallel visualization application (2007)
10. Bærentzen, J.A., Anaæs, H.: Signed distance computation using the angle weighted pseudonormal. IEEE Transactions on Visualization and Computer Graphics 11(3), 243–253 (2005)
11. Peters Randles, A., Kale, V., Gropp, W., Kaxiras, E.: Performance analysis of the Lattice Boltzmann model beyond Navier-Stokes. Manuscript submitted for publication (2012)
12. Haring, R.A., Ohmacht, M., Fox, T.W., Gschwind, M.K., Satterfield, D.L., Sugavanam, K., Coteus, P.W., Heidelberger, P., Blumrich, M.A., Wisniewski, R.W., Gara, A., Chiu, G.L.T., Boyle, P.A., Chist, N.H., Kim, C.: The IBM Blue Gene/Q compute chip, vol. 32, pp. 48–60. IEEE Computer Society, Los Alamitos (2012)

# A 1D Lumped-Parameter/3D CFD Approach for Pressure Drop in the Aortic Coarctation

Eduardo Soudah, Maurizio Bordone, Pooyan Dadvand, and Riccardo Rossi

CIMNE Biomedical Engineering Department. Centre Internacional de Mètodes Numèrics en Enginyeria. Edifici C1, Campus Nord-UPC, Gran Capità, s/n, 08034 Barcelona

**Abstract.** Aortic Coarctation is a congenital constriction of the aorta that increases blood pressure above the constriction and hinders the flow below it. Based on a 3D surface mesh of a moderate thoracic coarctation, a high quality volume mesh is created using an optimal tetrahedral aspect ratio for whole domain. In order to quantify the severity of this constriction, a coupled 1D lumped-parameter/3D CFD approach is used to calculate the pressure drop through the coarctation. The CFD computation is performed assuming that the arterial wall is rigid and the blood is considered a homogeneous Newtonian fluid with density r = 0.001 gr/mm3 and a dynamic viscosity m = 0.004 gr/mm/sec in laminar flow. The boundary conditions of the 3D model (inlet and outlet conditions) have been calculated using a 1D model. Parallelization procedures will be used in order to increase the performance of the CFD calculations.

**Keywords:** Aortic coarctation, pressure drop, lumped model, 1D/3D coupled method.

## 1 Introduction

Coarctation of the Aorta (CoA) is one of the most common congenital heart defects, and in the western world every year tens thousands of new cases are registered. In this pathology, the aorta narrows in the area where the ductus arteriosus inserts and de-pends where is this narrow the CoA is classified as:

1. Preductal coarctation if the narrowing is proximal to the ductus arteriosus. This condition could be life-threatening is the constriction is severe. This type of deformation is due to an intracardiac anomaly during fetal life. The blood flow is not regular on the left side of the heart producing a hypoplastic development of the aorta.
2. Ductal coarctation if the narrowing occurs at the insertion of the ductus arteriosus.
3. Postductal coarctation if the narrowing is distal to the insertion of the ductus arteriosus. This deformation could lead to an impaired blood flow in the lower part of the body. This condition is most common in adult beings. It can produce hypertension in the upper side of the body and insufficient peaks in the lower part. The deformation is generated during the fetal life as an extension of a muscular artery (ductus arteriosus) into an elastic artery (aorta).

O. Camara et al. (Eds.): STACOM 2012, LNCS 7746, pp. 26–33, 2013.

Many clinical, pharmacological tests and analysis could be performed in order to study and treat of the CoA in the best way. The goal standard of the CoA treatment is the gradient pressure generated by the constriction in the ductus arteriosus. According to the pressure drop the clinicians determinate the best treatment for this patient. This pressure drop changes when the blood flow is modified by stress or exercises and is hard to be reproduced in a clinical way. Medical Imaging techniques and Mathematical Methods and Computational Fluid Dynamics (CFD) tools could reproduce a lot of different conditions if the problem is well known.

## 2 Methods

### 2.1 Geometry and Mesh

The geometry of study is obtained by an 8-year old female patient. It is possible to note a moderate coarctation of about 65% of area reduction. Image data come from Gadolinium-enhanced MR angiography (MRA) with the subject in the supine position. The scanner is a Signa 1.5-T GE that has a time of images acquisition of approximately 20 seconds, in which the patient holds her breath. The model includes the ascending aorta, aortic arch, descending aorta, right and left subclavia and finally right and left carotid in .STL format (surface mesh).

To generate the 3D volume mesh GiD software [1] has been used. GiD is a CAD system that features the widely used for mesh generation. For generating a 3D volume mesh from the STL file, we have used an isosurface stuffing procedure. This technique is ideal to generate a volume mesh with quality warranty of the elements, this mean angle and volume bounds are guaranteed.

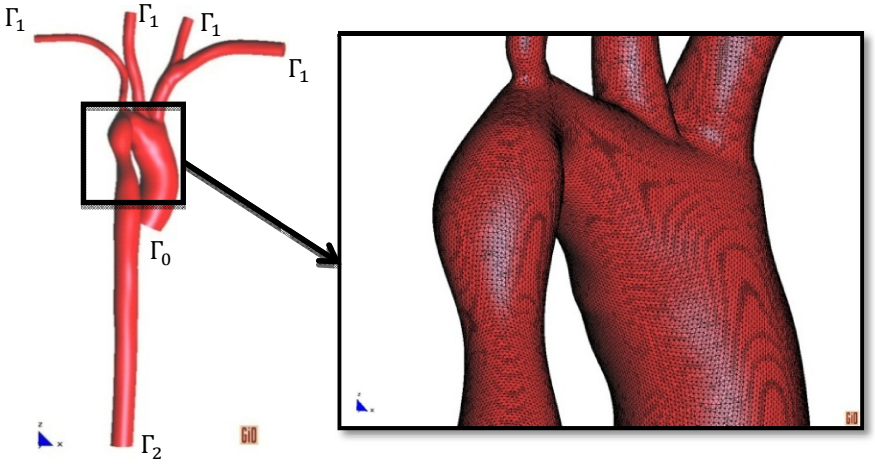


**Fig. 1.** Representation of the 3D model rendering of stl model in the XZ plane. Detail of surface mesh. $\Gamma_0$: inlet section (Aortic Root), $\Gamma_1$: outlet sections (Supra-aortic arteries) and $\Gamma_2$: outlet section (Descending aorta).

This technique increases the quality of the tetrahedral elements for computational simulations preserving the original shape and dimensions of original model. Using this method we have obtained a smooth element and an aspect radio for whole of the meshes upper than 0.9 (ideal ratio=1 for an equilateral triangle). This algorithm generates tetrahedral form a small set of precomputed stencils, and the boundary mesh is guaranteed to be a geometrically and topologically accurate approximation of the isosurface[1,2]. The result of the iso-stuffing procedure is a volume mesh of 6,423,037 tetrahedral elements and 356,835 triangular elements with 1,167,825 nodes. The original surface mesh has 114,514 triangle elements and 57,259 nodes. Figure 1 shows the rendering of .stl model and 3D volume mesh.

## 2.2 1D Model Geometry

A 1D model replica of the 8-year old female patient has been created according to the model developed in [5]. For the following arteries: ascending aorta, aortic arch, innominate artery; left common carotid artery, left subclavia artery and descending aorta, the radius was measured directly from the 3D geometry. A 1D segment (thoracic coarctation artery) was created to define the aorta coarctation with a 65% of area reduction. For the rest of the arteries, the radius was scaled using the $f_R$ factor and the length of the arteries was scaled using $f_L$ factor. Arterial wall thickness and Young modulus values were taken directly from [5].

$$f_R = \frac{R_{Aorta}^{8-year}}{R_{Aorta}^{[5]}} \qquad f_l = \frac{l_{Aorta}^{8-year}}{l_{Aorta}^{[5]}} \tag{1}$$

## 2.3 Boundary Conditions: Inlet Condition

Realistic boundary conditions are essential for a good performance and a realistic result for the simulation. For this, blood flow data was acquired using 2D cardiac-gated, respiratory compensated phase-contrast (PC) cine sequence with through-plane encoding. Figure 2 shows the inlet flow in $mm^3$/sec. Through the flow profile measurement in the aortic root (inlet section $\Gamma_0$) the mean velocity describes in figure 2 is calculated. The inlet velocity profile is prescribed as uniform and flat in the inlet surface $\Gamma_0$.

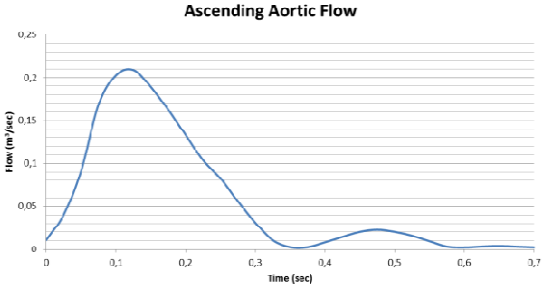


**Fig. 2.** Input data: aortic root flow profile

During the acquisition procedure the patient breathed freely and each scan lasted approximately 3 min. The flow data is the results of a PC-MRI sequence encoding 20 phases over the cardiac cycle. Heartbeat has a frequency of 86 beats per minute (T=0.7 sec) and the cardiac output was 3,245 L/min.

### 2.4 Boundary Conditions: Pressure Profile

Through a measurement via sphygmometer was possible to register the upper-body systolic and diastolic pressure and values were of 115 and 65 mmHg. To determinate a realistic pressure profile in the outlet ($\Gamma_1$, $\Gamma_2$) of the 3D model, a 1D lumped arterial model was used [4, 5]. The 1D outflow boundary conditions on ($\Gamma_1$, $\Gamma_2$) were modeled using the relation:

$$Q_{1D} = \frac{P_{1D} - P_{out}}{R_p} \tag{2}$$

where $Q_{1D}$ and $P_{1D}$ are the flow rate and pressure at the outlet of the 1-D terminal branch, and $P_{out}$ and $R_p$ are the outlet pressure and the peripheral resistance to the flow determined by [5]. The 1D model was fitted according the pressure values of the 8-year old female patient based on original model and calibration tests [6].

### 2.5 CFD Specifications

The CFD computation is performed assuming that the arterial wall is rigid and the blood is considered an homogeneous Newtonian fluid with density $\rho = 1000$ k g/m and a dynamic viscosity $\mu = 0.004$ kg/(sec·m) in laminar flow. A coupled 1D lumped-parameter/3D CFD approach was performed using KRATOS [7]. KRATOS is a fluid dynamics and multi-physics simulation environment based on the stabilized Finite Element Method that solved the 3D Navier–Stokes equations.

$$\begin{aligned} &\rho\frac{\partial \boldsymbol{u}}{\partial t} + \rho\boldsymbol{u}\cdot\nabla\boldsymbol{u} - \mu\triangle\boldsymbol{u} + \nabla P = \mathbf{f}, \\ &\operatorname{div}\boldsymbol{u} = 0, \end{aligned} \tag{3}$$

that we assume to hold in the 3D domain where **u** is the velocity vector, **f** is the fluid forces and **p** is the pressure. For the 1D model, the model has been deduced using the same equations by making the following assumptions: axial symmetry, radial displacements, and constant pressure on each section, no body forces and dominance of axial velocity. Also, in the absence of branching, a short section of an artery may be considered a cylindrical compliant tube. In order to close the system equations (Eq.3) for the 1D, we provide a relation for the pressure completed with a pressure–area (Eq.4) relation previously. It assumes a thin, homogeneous and elastic arterial wall and it takes the form:

$$P = P_{ext} + \Psi(A, A_o, \beta) \Longrightarrow \Psi = \beta\frac{\sqrt{A}-\sqrt{A_0}}{A_0} \Longrightarrow \frac{Eh_0\sqrt{\pi}}{1-\xi^2} \tag{4}$$

where $\mathbf{A_o}$ and $\mathbf{h_o}$ are the sectional area and wall thickness at the reference state ($\mathbf{P_o}$, $\mathbf{U_o}$), with $\mathbf{P_o}$ and $\mathbf{U_o}$ assumed to be zero, **E** is the Young's modulus and $\boldsymbol{\xi}$ is the Poisson's ratio, typically taken to be $\xi$=0.5, since biological tissue is practically incompressible. The parameter $\boldsymbol{\beta}$ is related to the speed of pulse wave propagation, **c** (Eq.5), through Formaggia[5],

$$c = \frac{\beta}{3\rho A_o} A^{\frac{3}{2}} \tag{5}$$

### 2.6 1D-3D Coupling

A coupled 1D/3D CFD approach employed in this work is shown in figure 3. At every time step $t^n$, we compute the velocity and pressure using the 1D approach over whole domain $\Omega_{1D}$, and the variables over the interface sections ($\Gamma_1$, $\Gamma_2$) of the $\Omega_{1D}$-$\Omega_{3D}$ are determined. Then 3D problem is solved in $\Omega_{3D}$ using the boundary conditions obtained in $\Gamma_1$, $\Gamma_2$ sections and the pressure drop is calculated. The variables computed in the interface sections ($\Gamma_1$, $\Gamma_2$) are updated according to the 1D-3D problem solution to account the effect of the vessel elasticity. For the next time step $t^{n+1}$, the process is repeated until the final time simulation is reached.

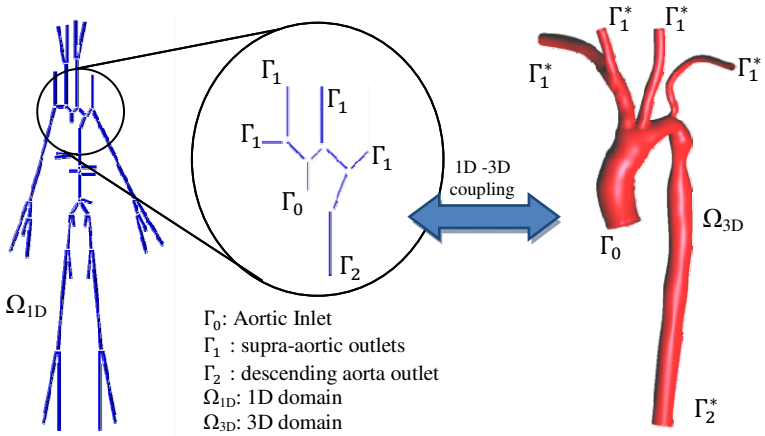


**Fig. 3.** 1D-3D coupled approach schematics. Variables in the interface surfaces (*) are modified to account for vessel elasticity effects. On the left side, the 1D model of the 8-year old female patient. (551 elements and 586 nodes).

To perform the simulation for the 1D and 3D approaches, we set the computational time step to 0.001 sec for a total of 1400 computational step. The total time of the simulation was of 1.4 sec in order to perform 2 complete heart cycles. We start the simulation with 50 initial steps in order to stabilize the initial condition solution. For the 1D approach second-order Taylor-Galerkin scheme and an explicit four-order Runge-Kutta time-integration scheme have been implemented. This scheme is

appropriate for this kind of problem because of it can propagate waves of different frequencies without suffering from excessive dispersion and diffusion errors. For the 3D approach, time integration method chosen was a Backward Euler, using a Bi Conjugate Gradient Non-symmetric solver in order to accelerate the calculation time performance [8]. We used a pressure stabilization of 4º order and automatic velocity advection stabilization. Turbulence model was not included, but we used a laminar formulation. Parallelization procedures have been used in order to increase the performance of the CFD calculations [9]. Figure 4 shows the final pressure profiles imposed at the interface surfaces (*).

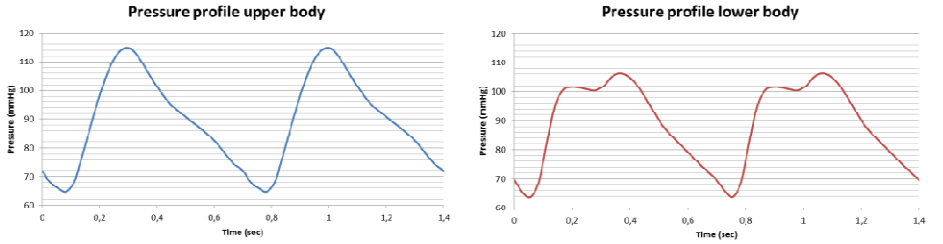


**Fig. 4.** On the left pressure profile imposed at $\Gamma_1^*$ and on the right pressure profile imposed at $\Gamma_2^*$

# 3 Results

## 3.1 Branches Flow Distribution Analysis

To obtain the flow distributions in all the branches of the domain, we have calculated the flow values along the cycle time for the four outlets($\Gamma_1$, $\Gamma_2$) of the system related to the inlet flow. Table 1 shows the percentage of ascending aortic flow through the outlet sections of the aortic model as measured via PC-MRI and calculated via CFD, and the error between the CFD and the PC-MRI measurement.

**Table 1.** % of ascending aortic flow through the outlet sections of the aortic model as measured via PC-MRI and calculated via CFD and the error. QIA: flow through innominate artery; QLCCA: flow through left common carotid artery, QLSA: flow through left subclavia artery; QDAo: flow through descending aorta.

| Section | QIA | QLCCA | QLSA | QDAo |
|---|---|---|---|---|
| % CFD (Aortic Flow) | 29.28 | 13.72 | 4.30 | 52.7 |
| % PC-MRI (Aortic Flow) | 25.6 | 11.3 | 4.26 | 58.8 |
| % Error CFD-PC-MRI | 3.68 | 2.42 | 0.04 | 6.1 |

Figure 5 shows the results of the volumetric flow at the four outlets of the system calculated via CFD.

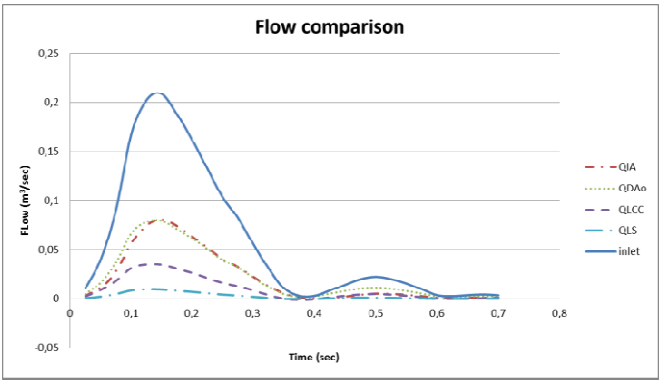


**Fig. 5.** Out flow: comparison calculated with CFD. QIA: flow through innominate artery; QLCCA: flow through left common carotid artery, QLSA: flow through left subclavia artery; QDAo: flow through descending aorta

### 3.2 Pressure Analysis

To evaluate the pressure gradient, the average value of the pressure for all time steps between at the proximal (P1) and distal section (P2) is calculated:

Plane 1 (P1) with a normal of (0.00, 0.27, 0.96)

Plane 2 (P2) with a normal of (0.00, 0.14, 0.99)

Figure 6 shows the pressure gradient obtained for P1 and P2. The maximum value of the pressure gradient (15,459 mmHg) is reached in the systolic phase.

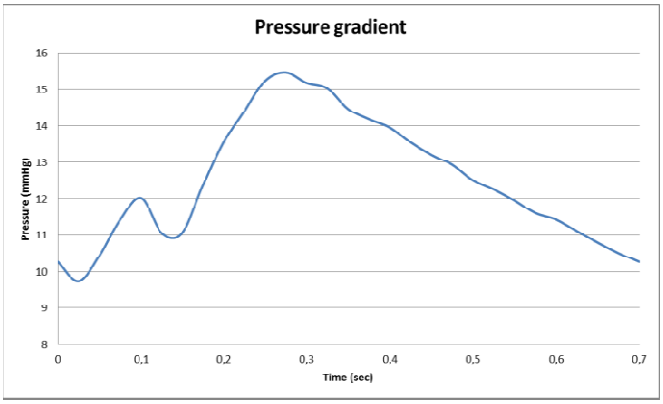


**Fig. 6.** Pressure drop (P1-P2)

## 4 Discussion

The preliminary results show a good agreement with the pathological values; however an improvement of the methodology should be required to obtain a better approximation to the values measured using PC MRI at the outlets. The maximum error reached is 6% in the flow of the descending aorta; meanwhile the error in the supra-aortic arteries is less than 4%. Future work will be focused on the enhancement of the 1D lumped-3D coupling procedure, using physiological flow inlet profiles. These improvements, in conjunction with a fine adjustment of the lumped 1D model parameters, seem necessary to obtain a more accurate flow solution in the aortic arch and in the narrowing of the aorta. This will lead to a better computation of the pressure drop and the volumetric flow through artery outlets.

## References

1. GiD. The personal pre and postprocessor, CIMNE (2011), http://www.gidhome.com
2. Labelle, F., Shewchuk, J.R.: Isosurface Stuffing: Fast Tetrahedral Meshes with Good Dihedral Angles. ACM Transactions on Graphics 26(3) (August 2007); Special issue on Proceedings of SIGGRAPH 2007
3. Soudah, E., Pennecot, J., Pérez, J.S., Bordone, M., Oñate, E.: Medical-GiD: From Medical Images to Simualtion, 4D MRI Flow Analysis. In: Computational Vision and Medical Image Processing, VIP Image 2009, pp. 9–14. CRC Press, Porto (2009)
4. Soudah, E., Oñate, E.: Validation of the one-dimensional numerical model in the ascending-descending aorta with real flow profile. In: 8th World Congress on Computational Mechanics (WCCM8). 5th European Congress on Computational Methods in Applied Sciences and Engineering (ECCOMAS 2008), Lido Island, Venice, Italy, June 30-July 4 (2008)
5. Formaggia, L., Lamponi, D., Quarteroni, A.: One dimensional models for blood flow in arteries. Journal of Engineering Mathematics 47(3-4), 251–276 (2003)
6. Matthys, K.S., Alastruey, J., Peiro, J., Khir, A.W., Segers, P., Verdonck, P.R., Parker, K.H., Sherwin, S.J.: Pulse wave propagation in a model human arterial network: Assessment of 1-D numerical simulations against in vitro measurements. J. Biomech. 40(15), 3476–3486 (2007)
7. Dadvand, P., Rossi, R., Oñate, E.: An object-oriented environment for developing finite element codes for multi-disciplinary applications. Archives of Computational Methods in Engineering 17(3), 253–297 (2010) ISSN: 1134-3060
8. Barrett, R., et al.: Templates for the Solution of Linear Systems: Building Blocks for Iterative Methods, 2nd edn. SIAM, Philadelphia (1994)
9. Dadvand, P., Rossi, R., Gil, M., Martorell, X., Cotela, J., Juanpere, E., Idelsohn, S.R., Oñate, E.: Migration of a generic multi-physics framework to HPC environments. Computers and Fluids (to be published 2012)

# Aortic Coarctation Simulation Based on the Lattice Boltzmann Method: Benchmark Results

Thomas Henn[1], Vincent Heuveline[1], Mathias J. Krause[2], and Sebastian Ritterbusch[1]

[1] Engineering Mathematics and Computing Lab, Karlsruhe Institute for Technology (KIT), Kaiserstrasse 12, 76131 Karlsruhe, Germany
[2] Institute for Algebra and Geometry Karlsruhe Institute of Technology (KIT), Kaiserstr. 93, 76128 Karlsruhe, Germany

**Abstract.** We investigate a patient specific blood flow simulation through a transverse aortic arch with a moderate thoracic aortic coarctation, where particular attention is paid to the blood pressure gradient through the coarctation. The challenge in this context is the complex geometry containing a stenosis, which results in complex flow patterns. The fluid is assumed to be incompressible and Newtonian. Its dynamic is usually described by an Navier-Stokes equation with appropriate boundary conditions. Instead, we modeled the problem mesoscopically by a family of BGK-Boltzmann equations those solutions reaches that of a corresponding Navier-Stokes system in a certain limit. For discretization we take advantage of lattice Boltzmann methods, which are realized within the open-source library OpenLB. A realistic transient flow profile of the cardiac output for a human at rest was used to specify the inflow boundary condition at the aortic root, whereas the outflow at the descending aorta was modeled by a pressure boundary condition. A short introduction to lattice Boltzmann methods is provided and especially the used boundary conditions are introduced in detail. The exact simulation setup is stated and the obtained results are discussed.

## 1 Introduction

Patient-specific numerical simulations of human organs open new opportunities for medical diagnosis and therapy. They are even more advantageous, if they do not require additional radiating screenings, but are based on computer tomography imaging from standard procedures. In the case of the human respiratory system, numerical simulations of air flow have already proven to be accurate in the United Airways project [1]. Therefore, an adaption of the concept to human blood flow is highly appreciated.

An anomaly in the human cardiovascular system, such as a coarctation of the aorta, obstructs the body's supply of nutrients and stresses the heart. In

O. Camara et al. (Eds.): STACOM 2012, LNCS 7746, pp. 34–43, 2013.

particular, the narrowing can lead to an intense drop in pressure, which directly affects the health of the patient. This pathological case accounts approximately one out of ten of all congenital heart defects, and is usually corrected surgically or by use of a catheter.

A conventional measurement of the pressure drop under resting conditions is an easy task for a clinician, but measuring the pressure gradient under exercise conditions is more challenging. Usually artificial stress is created by administering a drug to increase heart rate and contractibility. As this may have unwanted side-effects, it opens up a range of applications for CFD techniques. By simulation of a section of the blood system mimicking the real situation, the health-endangering measurements can be shifted into a virtual model. In this paper we investigate to what extent the *lattice Boltzmann method* (LBM) is of significance for the present medical case of an eight year old female patient. It is worth mentioning that the used model is likely to be expanded by an elastic model of the aorta geometry to achieve more realistic results.

## 2 Modelling

Let $\Omega \subset \mathbb{R}^3$ be a bounded domain representing the aorta, $[t_0, t_1]$ a considered time interval and $p : \Omega \times [t_0, t_1] \to \mathbb{R}$ denotes the physical pressure. We denote by $\rho \in \mathbb{R}$ the mass density of the blood which is constant due to the incompressibility of the fluid. And let $\mu \in \mathbb{R}^3$ be the viscosity of the blood. The aorta inlet area is denoted by $\Sigma_{in} \subset \partial\Omega$ and the aorta outlet area is $\Sigma_{out} \subset \partial\Omega$ which contains the outlet areas of the brachiocephalic artery, left common carotid artery, left subclavian artery and aorta. The outer normal vector on $\partial\Omega$ is denoted by $n$. Shear rates in large arteries are typically sufficiently large to assume that blood behaves as a Newtonian fluid, [2]. Therefore, blood flow in the thoracic aorta and the three major branches is governed by the time dependent Navier-Stokes equations, see below.

*Problem 1.* Find the fluid velocity $\boldsymbol{u} \in [L^2(\Omega \times [t_0, t_1])]^3$ and the pressure $p \in L^2(\Omega \times [t_0, t_1])$ that fulfill the incompressible Navier-Stokes equations

$$\frac{\partial \boldsymbol{u}}{\partial t} + (\boldsymbol{u} \cdot \nabla)\boldsymbol{u} - \mu \triangle \boldsymbol{u} = -\frac{1}{\rho}\nabla p \qquad \text{in } \Omega \times [t_0, t_1], \tag{1}$$

$$\nabla \boldsymbol{u} = 0 \qquad \text{in } \Omega \times [t_0, t_1], \tag{2}$$

with the appropriate boundary conditions, where $I$ denotes the unity matrix.

*Dirichlet condition*

$$\boldsymbol{u} = \boldsymbol{g} \qquad \text{on } \Sigma_{in} \times [t_0, t_1], \tag{3}$$

"*do nothing*" *condition*

$$(-Ip + \mu \nabla \boldsymbol{u}) \cdot \boldsymbol{n} = 0 \qquad \text{on } \Sigma_{out} \times [t_0, t_1], \tag{4}$$

$no - slip$ *condition*

$$\boldsymbol{u} = 0 \qquad \text{on } \partial\Omega \backslash \overline{\Sigma_{in} \cup \Sigma_{out}} \times [t_0, t_1]. \tag{5}$$

The non-linearity of the problem w.r.t. $\boldsymbol{u}$ comes from the term $(\boldsymbol{u} \cdot \nabla)\boldsymbol{u}$ in the PDE (1). According to [3], [4] in case of stationarity and a sufficiently smooth right hand side there exists at most one strong solution for the velocity $\boldsymbol{u}$, whereas the solution for the pressure is only defined up to an additive constant [5].

## 3 Lattice Boltzmann Method

The subclass of lattice Boltzmann methods considered here enables the simulation of the dynamics of incompressible Newtonian fluids which is usually described macroscopically by an initial value problem governed by a Navier-Stokes equation. Instead of directly computing the quantities of interests, which are the fluid velocity $\boldsymbol{u} = \boldsymbol{u}(t, \boldsymbol{r})$ and fluid pressure $p = p(t, \boldsymbol{r})$ where $\boldsymbol{r} \in \Omega$ and $t \in [t_0, t_1] \subseteq \mathbb{R}$, a lattice Boltzmann numerical model simulates the dynamics of particle distribution functions $f : [t_0, t_1] \times \Omega \times \mathbb{R}^3 \to \mathbb{R}_{\geq 0}$ in a phase space $\Omega \times \mathbb{R}^3$ with position $\boldsymbol{r} \in \Omega$ and particle velocity $\boldsymbol{v} \in \mathbb{R}^3$. The continuous transient phase space is replaced by a discrete space with a spacing of $\Delta r = h$ for the positions, a set of $q \in \mathbb{N}$ vectors $\boldsymbol{v_i} \in \mathcal{O}(h^{-1})$ for the velocities and a spacing of $\Delta t = h^2$ for time. The resulting discrete phase space is called the lattice and is labeled with the term *DdQq*. To reflect the discretization of the velocity space, the continuous distribution function $f$ is replaced by a set of $q$ distribution functions $f_i : [t_0, t_1] \times \Omega \to \mathbb{R}_{\geq 0}$ $(i = 0, 1, ..., q-1)$, representing an average value of $f$ in the vicinity of the velocity $\boldsymbol{v}_i$. Detailed derivations of various LBM can be found in the literature, e.g. in [6]. The iterative process in an LB algorithm can be written in two steps as follows, the *collision step* (6) and the *streaming step* (7):

$$\widetilde{f}_i(t, \boldsymbol{r}) = f_i(t, \boldsymbol{r}) - \frac{1}{3\nu + 1/2} \left( f_i(t, \boldsymbol{r}) - M_{f_i}^{eq}(t, \boldsymbol{r}) \right) , \tag{6}$$

$$f_i(t + h^2, \boldsymbol{r} + h^2 \boldsymbol{v}_i) = \widetilde{f}_i(t, \boldsymbol{r}) \tag{7}$$

for $i = 0, 1, ..., q-1$, where

$$M_{f_i}^{eq}(t, \boldsymbol{r}) := \frac{w_i}{w} \rho_{f_i} \left( 1 + 3h^2 \, \boldsymbol{v}_i \cdot \boldsymbol{u}_{f_i} - \frac{3}{2} h^2 \boldsymbol{u}_{f_i}^2 + \frac{9}{2} h^4 \left( \boldsymbol{v}_i \cdot \boldsymbol{u}_{f_i} \right)^2 \right),$$

is a discretized *Maxwell distribution* with moments $\rho$ and $\boldsymbol{u}$ which are given according to

$$\rho := \sum_{i=0}^{q-1} f_i \quad \text{and} \quad \rho \boldsymbol{u} := \sum_{i=0}^{q-1} \boldsymbol{v}_i f_i.$$

Here the variable $\boldsymbol{u}$ is the discrete fluid velocity and $\rho$ the discrete mass density. The kinematic fluid viscosity $\nu = \mu / \rho$ is assumed to be given, and the terms $w_i / w$, $\boldsymbol{v_i} h$ $(i = 0, 1, ..., q-1)$ are constants depending on the used *lattice Boltzmann method*. For more detailed information concerning *lattice Boltzmann methods* we refer to [7]. The discrete fluid velocity $\boldsymbol{u}$ and the discrete mass density $\rho$ can be related to the solution of a macroscopic initial value problem governed by an incompressible Navier-Stokes equation as shown in [8].

# 4 Numerical Study

## 4.1 Simulation Setup

A given surface $\partial\Omega$ of an aorta with a moderate thoracic aortic coarctation is voxelized by 5 different resolutions, reaching from $235 \times 118 \times 402$ to $1168 \times 582 \times 2002$ voxels (*cf.* Figure 1). Recorded data of 20 measurements of the ascending aortic flow is interpolated by cubic splines with periodic boundary conditions. A smooth start-up phase is added to suppress undesired pressure fluctuation. The resulting function is illustrated in Figure 2. A velocity boundary condition, as introduced by Skordos in [9], with a Poiseuille flow profile reflecting the measured flow volume is set at the ascending aortic opening. The blood flow through the upper branch vessels was experimentally measured as a percentage of the ascending aortic flow. Therefore the flow through the left carotid artery is set to be 11.3 % of the aortic flow, whereas the flow through the left subclavian artery is set to be 4.26 %. For the right carotid and the right subclavian only a combined value of 25.6 % was available. Hence the flow through these two arteries was calculated depending on the areas of the openings and chosen to be 10.9 % and 14.7 %, respectively. The boundary conditions at the descending aorta is set as pressure condition, i.e. the pressure is fixed to 0 mmHg for all times. A full-way bounce back condition is assigned to the remaining surface. The blood is assumed to be Newtonian with a density of $\rho = 0.001\,\mathrm{gr/mm^3}$ and a dynamic viscosity of $\mu = 0.004\,\mathrm{gr/mm/s}$. A $D3Q19$ BGK-Lattice Boltzmann Method, supported by a Smagorinsky turbulence model with constant $C_S = 0.12$, was used. The simulations were executed using the open-source library OpenLB[1]. Computation times vary between approx. 1.5 hours on 64 Intel Xeon X5650@2.67GHz cores for the smallest resolution and 6 days occupying 512 AMD Opteron@2.6GHz cores for the highest resolution.

## 4.2 Results

Two cardiac cycles have been simulated and the pressure drop at the aortic coarctation was determined by calculation of the spatial pressure average in two planes $\pi_1$ and $\pi_2$ (*cf.* Figure 1). The absolute pressure over time at the ascending aorta and the pressure drop around the coarctation are shown in Figures 3 and 4 for different spatial resolutions. It is found that with increasing resolution the resulting curves become less smooth. This effect is more pronounced in the graphs of the pressure drop and may be due to the fact that with increasing resolution small turbulence become more significant, which otherwise are smoothed.

Figure 1 shows streamlines representing the flow and velocity $\boldsymbol{u}$ at the time of highest inflow. As expected the velocity increases in the coarctation. The flow is predominantly laminar except for turbulence in the areas before and after the coarctation.

[1] `http://www.openlb.org`

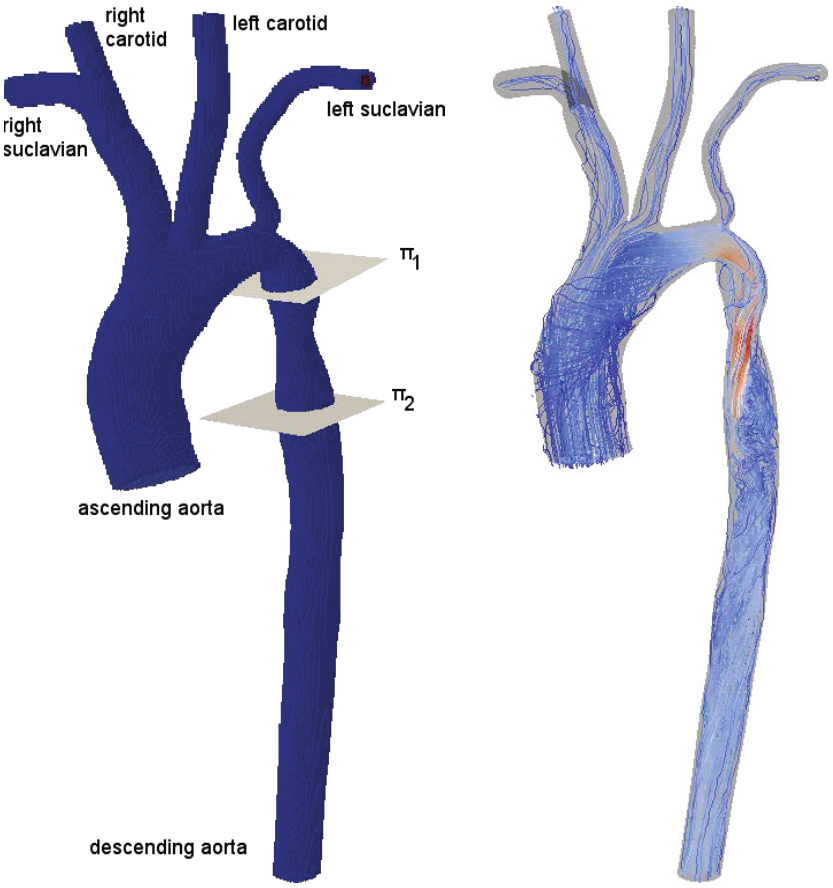


**Fig. 1.** Voxelized geometry $\Omega_h$ of the aortic arc with spacial resolution of $235 \times 118 \times 402$ voxels and flow visualizations at the point of time of highest flow rate. Color indicates the flow velocity $\|\boldsymbol{u}\|$.

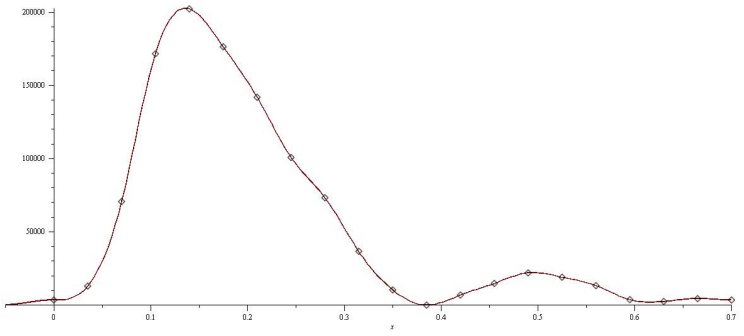


**Fig. 2.** Cubic spline interpolation of the provided flow information at the ascending aorta [ml $s^{-1}$/s]. The marked points represent the measured data.

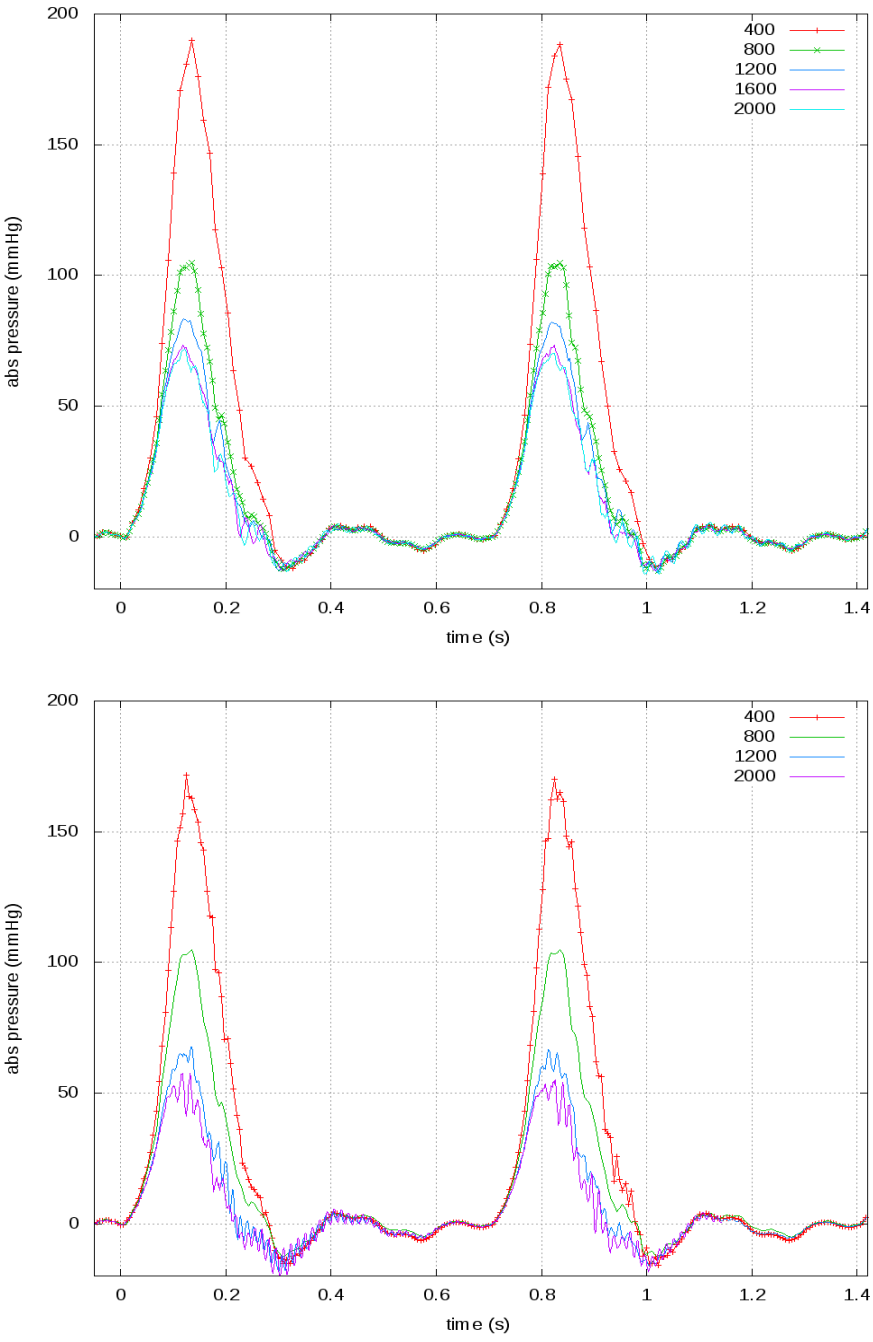


**Fig. 3.** The absolute pressure over time at the ascending aorta is shown for different spacial resolutions. The upper graph shows the resulting curve for the higher time resolution. The according time-step sizes can be found in Table 1.

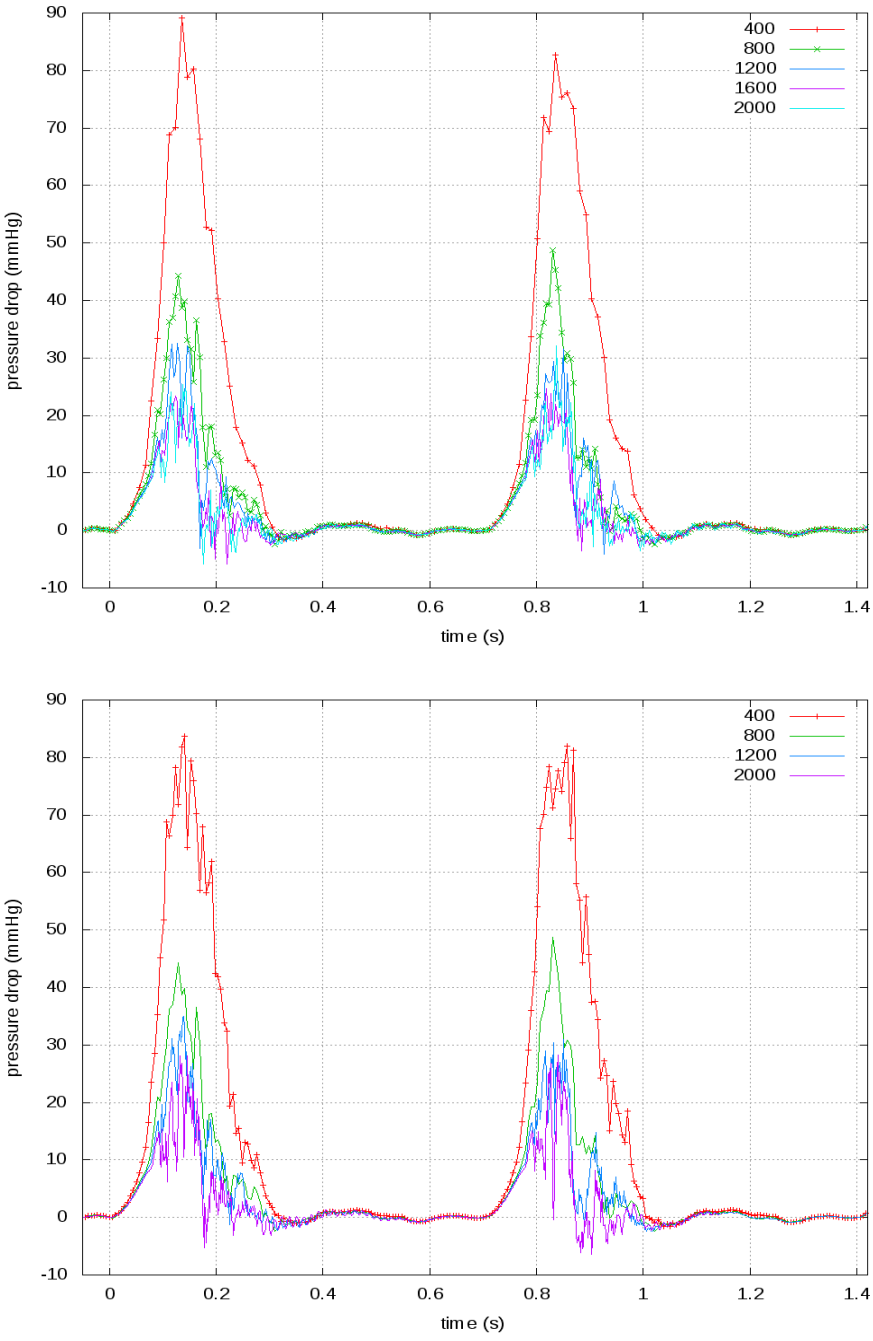


**Fig. 4.** The pressure drop between the planes $\pi_1$ and $\pi_2$ around the coarctation are shown for different spatial resolutions. The upper graph shows the resulting curve for the higher time resolution. The according time-step sizes can be found in Table 1.

**Table 1.** Computed values for pressure and flow both cycles; $Q_{\mathrm{IA}}$: flow through innominate artery; $Q_{\mathrm{LCCA}}$: flow through left common carotid artery; $Q_{\mathrm{LSA}}$: flow through left subclavian artery; $Q_{\mathrm{DAo}}$: flow through descending aorta; $Q_{\mathrm{AAo}}$ flow through ascending aorta; The values for the systolic and diastolic pressure have been adjusted to fit the experimentally taken values of 115/65 mmHg.

| | Spatial Resolution | 235 × 118 × 402 | | 468 × 234 × 802 | | 702 × 350 × 1202 | | 935 × 466 × 1602 | 1168 × 582 × 2002 | |
|---|---|---|---|---|---|---|---|---|---|---|
| | Time Resolution [s] | $5.64 \cdot 10^{-6}$ | $2.28 \cdot 10^{-6}$ | $2.28 \cdot 10^{-6}$ | $1.41 \cdot 10^{-6}$ | $1.88 \cdot 10^{-6}$ | $9.41 \cdot 10^{-7}$ | $1.41 \cdot 10^{-6}$ | $1.13 \cdot 10^{-6}$ | $5.64 \cdot 10^{-7}$ |
| First cycle | Peak pressure difference [mmHg] | 80.249 | 83.642 | 44.256 | 51.635 | 32.519 | 35.011 | 23.325 | 24.707 | 28.150 |
| | Mean pressure difference [mmHg] | 13.674 | 13.772 | 5.889 | 5.713 | 3.887 | 3.864 | 2.566 | 2.585 | 2.689 |
| | Flow splits ($Q_{\mathrm{IA}}/Q_{\mathrm{LCCA}}/Q_{\mathrm{LSA}}/Q_{\mathrm{DAo}}$) [% of $Q_{\mathrm{AA}}$] | 19.6/6.9/2.5/60.5 | 20.1/7.0/2.5/60.5 | 28.0/12.1/5.7/62.2 | 28.0/12.1/5.7/62.0 | 31.4/13.6/6.6/64.3 | 30.4/13.3/6.5/61.7 | 30.4/13.3/6.5/61.7 | 32.9/14.5/7.1/67.2 | 33.0/14.5/7.17/66.9 |
| | Pressure in AAo (Sys/Dia) [mmHg] | 250.508/65 | 232.761/65 | 166.039/65 | 154.197/65 | 144.565/65 | 128.201/65 | 134.273/65 | 131.535/65 | 116.97/65 |
| Second cycle | Peak pressure difference [mmHg] | 82.657 | 83.643 | 48.804 | 50.422 | 29.400 | 30.353 | 24.738 | 32.108 | 28.224 |
| | Mean pressure difference [mmHg] | 14.242 | 14.119 | 5.405 | 5.943 | 4.008 | 3.568 | 2.601 | 2.788 | — |
| | Flow splits ($Q_{\mathrm{IA}}/Q_{\mathrm{LCCA}}/Q_{\mathrm{LSA}}/Q_{\mathrm{DAo}}$) [% of $Q_{\mathrm{AAo}}$] | 20.0/6.9/2.5/60.5 | 20.1/7.0/2.5/60.5 | 28.0/12.1/5.7/62.2 | 28.0/12.2/5.7/61.9 | 31.5/13.5/6.6/64.6 | 31.5/13.5/6.6/64.3 | 32.4/14.2/7.0/65.8 | 33.0/14.5/7.2/67.4 | — |
| | Pressure in AAo (Sys/Dia) [mmHg] | 248.890/65 | 231.070/65 | 165.767/65 | 150.614/65 | 141.946/65 | 128.239/65 | 135.052/65 | 129.683/65 | 115.479/65 |
| | Processors | 64 Intel Xeon X5650 @2.67GHz | | | 128 Intel Xeon X5355 @2.66GHz | | | 512 AMD Opteron @2.6GHz | | |
| | Computation time [s] | 5121.92 | 10305.40 | 51100.74 | 49407.26 | 94928.75 | 189891.79 | 72905.32 | 163573.81 | cancelled after 6 days |

In Table 1 the peak and mean pressure difference around the coarctation, the flow splits through the upper arteries and the descending aorta as a percentage of the flow through the ascending aorta and systolic and diastolic pressure in the ascending aorta are listed for all simulations. As the pressure is only determined up to an additive constant when solving the Navier-Stokes equations in our context, the values of the absolute pressure at the ascending aorta have been shifted to fit the measured systolic and diastolic pressure of 115 mmHg and 65 mmHg. It is found that the pressure is decreasing with increasing spatial and time discretization.

Assuming the measured systolic pressure of 115 mmHg as solution, we obtain the *experimental order of convergence* (EOC) for $0 < h_1 < h_2$, which is defined by

$$EOC\,(h_1, h_2) := \frac{\ln\,(err_{h1}/err_{h2})}{\ln\,(h_1/h_2)},$$

where $err_h = p_h^{sys} - 115$ is the error of the computed systolic pressure with respect to the measured value for a given spacing $h$.

| $h_2$ | $h_1$ | EOC |
|---|---|---|
| 1/402 | 1/802 | 1.413 |
| 1/802 | 1/1202 | 1.436 |
| 1/1202 | 1/1602 | 1.261 |
| 1/1602 | 1/2002 | 1.008 |

From this table we see that this lattice Boltzmann method yields a systolic pressure $p_h^{sys}$ of linear order. For the highest spatial and time resolution we obtain $p_h^{sys} = 116.97$ mmHg.

## 5 Conclusion

In this paper, we presented how lattice Boltzmann methods can be used for hemodynamic simulations in an aortic model. Here, a discrete Boltzmann equation is solved to simulate a Newtonian fluid on a mesoscopic scale. Since the numerical solution depends on the spatial discretization (note that the temporal resolution is coupled to the spatial resolution *cf.* Section 3), we have experimentally found a linear convergence of the solution $p$ in $h$. The numerical investigations have shown that this approach may well be used for patient-specific simulations, because for high temporal and spatial resolution of the solution space, we obtain realistic values for the pressure (see right column of Table 1). These results could be further improved by extension of the underlying model, *e.g.* by a Windkessel approach.

**Acknowledgment.** This work is supported by the German "Federal Ministry of Education and Research (BMBF)": BMBF-Fördermassnahme KMU-innovativ: Informations- und Kommunikationstechnologie, Forschungsbereich Softwaresysteme und Wissens-verarbeitung, Gesundheit und Medizintechnik. Support code 01|S11031B.

We would like to express thanks to our colleague Dr. Andreas Helfrich-Schkarbanenko for the numerous discussions and careful proof reading.

## References

1. Krause, M.J., Gengenbach, T., Mayer, R., Zimney, S., Heuveline, V.: How to Breathe Life into CT-Data. Computer Aided Medical Engineering (4), 29–33 (2011)
2. Fung, Y.-C.: Biomechanics: mechanical properties of living tissues. Springer, New York (1981)
3. Sohr, H.: The Navier-Stokes Equations. Birkhäuser, Basel (2001)
4. Temam, R.: Navier-Stokes Equations and Nonlinear Functional Analysis (CBMS-NSF Regional Conference Series in Applied Mathematics). Society for Industrial and Applied Mathematics (1987)
5. Marion, M., Temam, R.: Navier-stokes equations: Theory and approximation. In: Ciarlet, P., Lions, J. (eds.) Numerical Methods for Solids (Part 3) Numerical Methods for Fluids (Part 1). Handbook of Numerical Analysis, vol. 6, pp. 503–689. Elsevier (1998)
6. Sukop, M.C., Thorne, D.T.: Lattice Boltzmann Modeling: An Introduction for Geoscientists and Engineers. Springer (2010)
7. Krause, M.J.: Fluid Flow Simulation and Optimisation with Lattice Boltzmann Methods on High Performance Computers: Application to the Human Respiratory System. PhD thesis, Karlsruhe Institute of Technology (KIT), Universität Karlsruhe (TH), Kaiserstraße 12, 76131 Karlsruhe, Germany (July 2010), http://digbib.ubka.uni-karlsruhe.de/volltexte/1000019768
8. Junk, M., Klar, A.: Discretizations for the incompressible navier–stokes equations based on the lattice boltzmann method. SIAM Journal on Scientific Computing 22(1), 1–19 (2000)
9. Skordos, P.A.: Initial and boundary conditions for the lattice boltzmann method. Phys. Rev. E 48, 4823–4842 (1993)

# CFD Challenge: Hemodynamic Simulation of a Patient-Specific Aortic Coarctation Model with Adjoint-Based Calibrated Windkessel Elements

Mahmoud Ismail[1,2], Michael W. Gee[2,3], and Wolfgang A. Wall[1,2]

[1] Institute for Computational Mechanics, Technische Universität München, Germany
[2] Center for Computational Biomedical Engineering, Technische Universität München, Germany
[3] Mechanics and High Performance Group, Technische Universität München, Germany
wall@lnm.mw.tum.de

**Abstract.** This work presents our approach for modelling the CFD challenge example of the aortic coarctation of an 8 year old child. The three-dimensional fluid domain was modeled as described in the challenge as an incompressible Newtonian fluid. A residual-based variational multiscale finite element method is used to solve the 3D fluid field. The boundaries were treated with 3-element windkessel models. The windkessel elements were tuned using an adjoint based method to fit the pressure and flowrate values reported by the challenge. A mesh refinement was performend to ensure the spatial convergence of the presented results. Finally, pressure values at $\pi_1$ and $\pi_2$ slices are reported.

## 1 Introduction

In this work we present our approach for modelling the CFD challenge of the aortic coarctation of an eight year old child. The 3D domain is modeled using a version of the residual-based variational multiscale finite element method developed in [1]. The boundaries are treated using 3-element windkessel models and flowrate conditions. All flowrates and windkessel elements were tuned to fit the pressure and flowrate values reported in the challenge. The tuning of the windkessel elements is done using an adjoint based method previously developed in [2]. Furthermore, a mesh refinement analysis was performed to ensure the spatial convergence of our results. Detailed pressure values at the points of interest (slice $\pi_1$ and slice $\pi_2$) and the average flowrate percentages within each artery are reported at the end of this report.

## 2 Governing Equations and Boundary Conditions

### 2.1 3D Flow Domain

Fluid motion in a domain $\Omega$ is defined in the form of incompressible flow, via incompressible Navier-Stokes equations. The boundary $\Gamma$ to $\Omega$ is defined as

$$\Gamma = \Gamma_{\mathrm{D}} \cup \Gamma_{\mathrm{N}},$$

O. Camara et al. (Eds.): STACOM 2012, LNCS 7746, pp. 44–52, 2013.

where $\Gamma_{\mathrm{D}}$ and $\Gamma_{\mathrm{N}}$ are the Dirichlet and Neumann parts of the boundary, respectively. Dirichlet boundary conditions are prescribed on $\Gamma_{\mathrm{D}}$ as $\mathbf{u} = \mathbf{u}_{\mathrm{D}}$, where $\mathbf{u}$ is the velocity of the fluid. The Neumann boundary is defined as

$$-u_n^{\mathrm{in}}\mathbf{u} - p\mathbf{n} + 2\nu\varepsilon(\mathbf{u}) \cdot \mathbf{n} = \mathbf{h}, \tag{1}$$

where $u_n^{\mathrm{in}} = \frac{u_n - |u_n|}{2}$, $u_n$ is the normal velocity defined as $u_n = \mathbf{u}\cdot\mathbf{n}$, $p$ the pressure, and $\varepsilon(\mathbf{u})$ is the rate-of-deformation tensor given by $\varepsilon(\mathbf{u}) = \frac{1}{2}\left(\nabla\mathbf{u} + (\nabla\mathbf{u})^{\mathrm{T}}\right)$.

The 3D domain is discretized using a residual-based variational multiscale finite element method developed in [1], where the density is simply set to be constant.

### 2.2 Flowrate Boundary Conditions

The flowrate boundary conditions in this work are modeled using Womersley velocity shape profiles which yield

$$u_n(r) = 2\frac{Q_0}{A}\left[1 + \left(\frac{r_i}{r_0}\right)^2\right] + \sum_{k=1}^{N} \mathrm{Real}\left\{\frac{Q_k}{A}\left[\frac{J_0(z) - J_0\left(\frac{r_i}{r_0}z\right)}{zJ_0(z) - 2J_1(z)}\right] ze^{i(k\omega t - \phi_k)}\right\} \tag{2}$$

where $A$ is the cross-sectional area, $r_i$ the radial coordinate, $r_0$ the radius of the boundary surface, $\alpha = r_0\sqrt{\frac{\omega}{\nu}}$ the Womersley number, $\omega$ the angular frequency, $\nu$ the kinematic viscosity, and $z = \alpha i^{3/2}$. $J_0$ and $J_1$ are Bessel functions of the first kind. A Fourier analysis of the flowrate ($Q$) yields $Q_k$ and $\phi_k$:

$$Q = Q_0 + \sum_{k=1}^{N} Q_k cos(k\omega t - \phi_k).$$

Since the aforementioned profiles are defined for circular geometries, the profiles are mapped to the arbitrary closed boundary as was originally proposed in [4].

### 2.3 3-Element Windkessel Model

The 3-element windkessel model (see Figure 1) yields the following differential equation

$$\mathbf{N} := p_{in} + CR_p\frac{dp_{in}}{dt} + CR_p\frac{dp_C^-}{dt} - p_{out} - (R_p + R_s)q_{in} - CR_sR_p\frac{dq_{in}}{dt} = 0, \tag{3}$$

where $p_{in}$ is the pressure at the windkessel inlet, $C$ the systemic capacitance, $R_p$ the peripheral resistance, $R_s$ the systemic resistance, and $q_{in}$ the flow entering the windkessel model. The pressures $p_C^-$ and $p_{out}$ are set to zero. Throughout this work $p_{in}$ and $q_{in}$ are renamed to $p$ and $q$, respectively.

The windkessel models are coupled to the 3D domain using a Dirichlet to Neumann coupling approach as in [3].

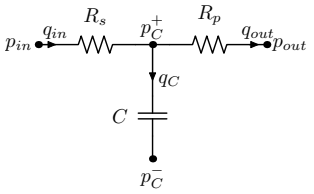


**Fig. 1.** Circuit representation of a three-element windkessel model

## 3 Modeling Approach

For all simulation blood was assumed to incompressible Newtonian fluid with a density $\rho = 0.001\,\mathrm{g/mm^3}$ and dynamic viscosity $\mu = 0.004\,\mathrm{g/s/m}$, as is requested by the CFD challenge.

### 3.1 Physiological Analysis

Looking deeper into the coarctation of the given geometry, it is observed that the coarctation is not only positioned between slices $\pi_1$ and $\pi_2$ but also a clear constriction of the aorta is observed in the section between the left common carotid artery and just after the left subclavian artery, as illustrated in Figure 2(a). Thus a rise in the blood pressure must be observed with in the section combining the aortic root, right subclavian, right common carotid, and left common carotid (see Region 1 in Figure 2(b)). Since the first aortic constriction ends just after the bifurcation of the left subclavian, a drop in the pressure of the left subclavian must be observed (see Region 2 in Figure 2(b)). Due to the severe constriction just after the left subclavian bifurcation, another drop in the blood pressue must be observed within region 3 (see Figure 2(b)). A drop in the blood pressure must also be observed in the descending aorta due to the constriction between $\pi_1$ and $\pi_2$ slices (see Region 4 in Figure 2(b)). This analysis is supported by the average volumetric flowrates reported by the challenge, where a low flowrate is reported within the left subclavian, where as the other upper branching arteries have elevated flowrate values. In addition to the geometrical observations, The systolic blood pressure in a healthy 8 year old female child is expected to be around 125 mmHg where as the diastolic blood pressure is expected to be around 87 mmHg [7]. The reported blood pressure in the challenge is 65 mmHg and 115 mmHg for both diastolic and systolic blood pressure, respectively. Thus, we suspect that the 115/65 mmHg blood pressure, measured using the sphygmometer, is measured at the left arm of the patient, i.e. the pressure recorded is within the left brachial artery. Thus we can conclude that the pressure at the outlet boundary of the left subclavian artery should be close to the 115/65 mmHg.

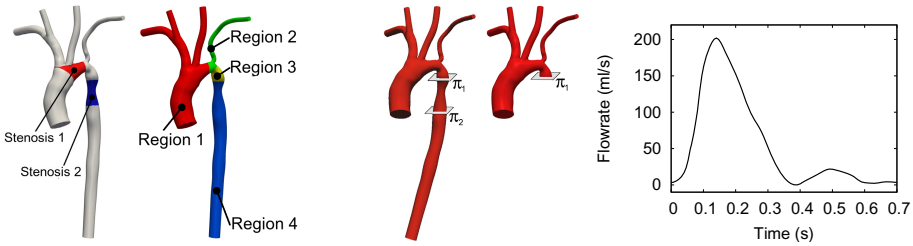


**Fig. 2.** (a) Different stenoses regions within the aortic coarctation, (b) different pressure regions within the coarctation, (c) Complete aortic Coarctation showing $\pi_1$ and $\pi_2$ plane, (d) aortic coarctation trimmed at $\pi_1$ where the systolic and diastolic pressures are measured and (e) the measured flowrate at the aortic root

### 3.2 Tuning the Windkessel Boundary Conditions

To simulate the aortic coarctation in Figure 2(a), the challenge measured cardiac output (shown in Figure 2(e)) was prescribed at the aortic root. Velocity profiles at the aortic root are more complex than the parabolic and Womersley ones [5]. Nevertheless, a Womersley velocity profile was prescribed at the inlet of the aortic root because it has a profile that we concider to be more reasonable close approximation to the complex flow conditions at the aortic root. The outlet boundaries are modeled using 3-element windkessel models.

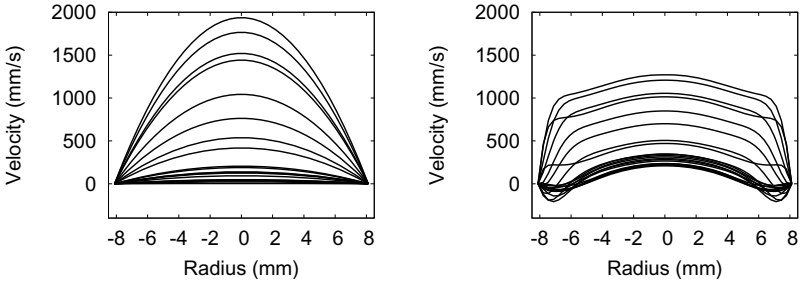


**Fig. 3.** Velocity profiles at the inlet of the aortic root represented in a parabolic profile shape (a) and Womersley profile shape (b)

For calibration of the windkessel models, only the aortic section between the aortic root and $\pi_1$ was considered (as shown in Figure 2(d)). We assume that the pressure has small variations within sections perpendicular to the center line. This means that the trimmed aortic geometry has similar pressure values at the $\pi_1$ section as the complete aortic geometry, and thus both problems have similar upper body windkessel elements. The windkessel elements were calibrated at the

outlets of the trimmed geometry using the adjoint method described in [2]. The following objective functions and design variables were chosen for tuning the windkessel elements:

$$L(u,\phi) = \begin{vmatrix} P_{\mathrm{LS}}^{\mathrm{sys}} - 115\,\mathrm{mmHg} \\ P_{\mathrm{LS}}^{\mathrm{dia}} - 65\,\mathrm{mmHg} \\ Q_{\pi_1}^{\mathrm{avg}} - 0.588 Q_{\mathrm{AA}}^{\mathrm{avg}} \\ Q_{\mathrm{LC}}^{\mathrm{avg}} - 0.113 Q_{\mathrm{AA}}^{\mathrm{avg}} \\ Q_{\mathrm{RC}}^{\mathrm{avg}} - 0.113 Q_{\mathrm{AA}}^{\mathrm{avg}} \\ Q_{\mathrm{RS}}^{\mathrm{avg}} - 0.143 Q_{\mathrm{AA}}^{\mathrm{avg}} \end{vmatrix} = 0 \quad ; \phi = \begin{vmatrix} R_{\mathrm{LS}} \\ C_{\mathrm{LS}} \\ R_{\pi_1} \\ R_{\mathrm{LC}} \\ R_{\mathrm{RC}} \\ R_{\mathrm{RS}} \end{vmatrix}, \tag{4}$$

where $L(u,\phi)$ are the design functions, $\phi$ the design variables, and $u$ the state variables. In Equation (4), AA stands for ascending aorta (aortic root), LS for left subclavian artery, LC for left carotid artery, RC for right carotid artery, RS for right subclavian artery. The total windkessel resistance is defined as $R = R_s + R_p$. The wanted average flowrate percentages and pressure values in Equation 4 are reported in the challenge. The initial windkessel parameters are evaluated by assuming the flowrate at each boundary is equal to the percentage reported in the challenge multiplied by the flowrate at the aortic root. In addition to that we assumed that the all outlets have a systolic pressure of 115 mmHg and a diastolic pressure of 65 mmHg. The windkessel elements are then applied onto the geometry in Figure 2(d). The flowrate curves produced from the simulated model in Figure 2(d) where corrected by a factor to meet the reported average flowrates and then used to further calibrate the initial windkessel elements. Finally the evaluated capacitances at RS, RC, LC, and $\pi_1$ are fixed and the tuning shown in equation 4 is performed.

The final tuned windkessel parameters are shown in Table 1. It is important to point to the fact that the results in Table 1 reproduce the pressure and flowrate values, at the boundaries of the trimmed aorta, as were reported by the challenge within a 2.6% tolerance.

The windkessel parameters are then prescribed to the left subclavian, left carotid, right carotid, and right subclavian boundaries of the full oartic geometry (see Figure 2(a)). The windkessel parameters at the abdominal aorta were evaluated after estimating the resistance of the section between $\pi_1$ and the outlet of the abdominal aorta through a CFD simulation using the simulated flowrate at $\pi_1$ of the geometry in Figure 2(d).

**Table 1.** Tuned windkessel parameters that reproduced the reported pressure and flowrate values. (all units are in mm, g, s)

| Boundary | $R_s$ | $R_p$ | $C$ |
|---|---|---|---|
| Left subclavian | 0.010313 | 5.275347 | 0.139334 |
| Left carotid | 0.017608 | 1.936892 | 0.456585 |
| Right carotid | 0.019892 | 1.934809 | 0.453177 |
| Right subclavian | 0.007989 | 1.509068 | 0.603330 |
| $\pi_1$ | 0.034707 | 0.347407 | 1.831837 |
| Abdominal Aorta | 0.027240 | 0.347407 | 1.831837 |

The resistance within the descending aorta was estimated to be 0.0075 and was then subtracted from $R_s^{\pi_1}$ to produce $R_s^{\mathrm{DA}}$. $R_p^{\mathrm{DA}}$ and $C^{\mathrm{DA}}$ are set equal to $R_p^{\pi_1}$ and $C^{\pi_1}$, respectively. Final results of the full aortic coarctation are shown in Section 5.

## 4 Mesh Analysis

After performing a nondimensional analysis of turbulent effects within the reported geometry using the reported flowrate in the challenge two meshes were generated. Both of the meshes were meshed using hybrid meshes with dominating hexahedral elements, using the commercial mesher Harpoon (Sharc Ltd, Manchester, UK). Tetrahedral, prism, and pyramid elements are also part of the meshes but the hexahedral elements dominate. All of the elements use linear interpolations for both velocity and pressure degrees of freedom (DOFs). Mesh 1 (see Figure 4(b)) features element edge length of 0.28 mm. Taking a time step size of 0.5 ms the CFL number of mesh 1 is thus 3.5. Mesh 1 resulted in a total of 921,671 elements, 653,629 nodes, and 2,614,516 DOFs. Mesh 2 (see Figure 4(c)) features element edge length of 0.09 mm. Taking a time step size of 0.1 ms the CFL number of mesh 2 yields 1. Mesh 2 resulted in a total of 5,246,414 elements, 4,205,977 nodes, and 16,823,908 DOFs. In both meshes a three element boundary layer was linearly expanded into the fluid domain, starting from the aortic wall.

All of the computations were performed using our parallel multiphysics inhouse code BACI [6]. The results presented in Figure 5 show minor differences between the pressure values of the two meshes. This indicates that mesh 1 yields sufficiently good results and is thus consequently used for all of the computations. Figure 6 shows a significant pressure differences at $\pi_2$ section during peak flowrate (time=0.14 s). However the plane averaged pressure in plane $\pi_2$ at t=0.14 s is 5779.74 Pa and 5910.5 Pa for the coarse and the fine mesh, respectively. This means that the plane averaged pressure at $\pi_2$ matches between the two meshes with in 2.21% difference. Furthermore the pressure drop between $\pi_1$ and $\pi_2$ matches between the fine and coarse mesh with an error of 12.89% (see Table 2)

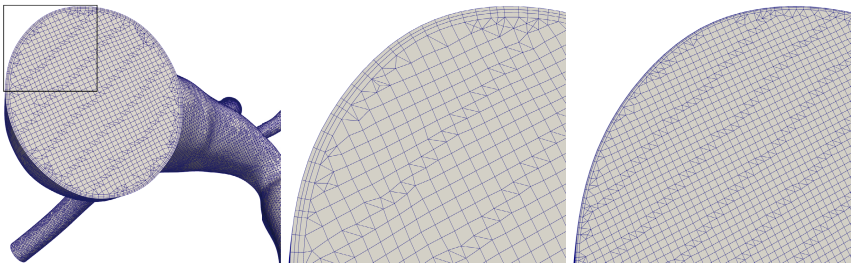


**Fig. 4.** Meshed aortic geometry (a) and corresponding coarse (b) and the fine (c) meshes at the inlet of the aortic root

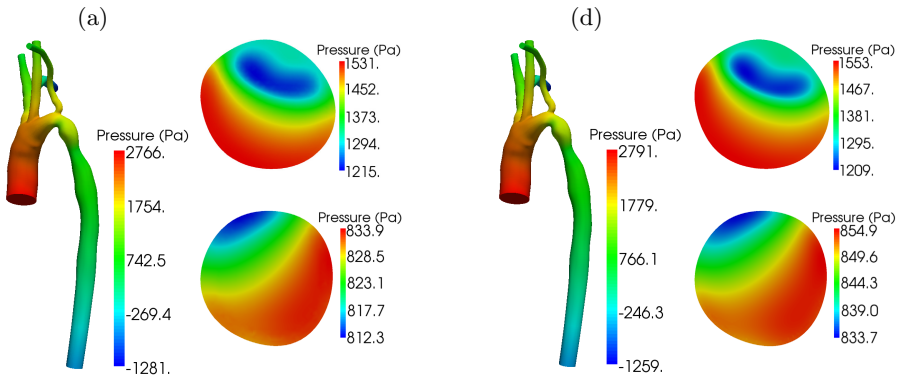


**Fig. 5.** Aortic pressure distribution for the coarse mesh (a) and its corresponding pressure values at $\pi_1$ (upper) and $\pi_2$ (lower). Aortic pressure distribution for the fine mesh (b) and its corresponding pressure values at $\pi_1$ (upper) and $\pi_2$ (lower). All values are presented at $t = 0.08\,\mathrm{s}$.

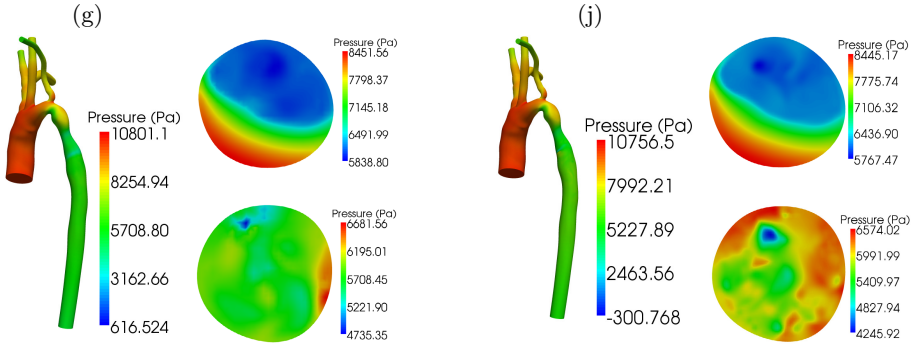


**Fig. 6.** Aortic pressure distribution for the coarse mesh (a) and its corresponding pressure values at $\pi_1$ (upper) and $\pi_2$ (lower). Aortic pressure distribution for the fine mesh (b) and its corresponding pressure values at $\pi_1$ (upper) and $\pi_2$ (lower). All values are presented at $t = 0.14\,\mathrm{s}$.

**Table 2.** Plane averaged pressure at different slices at time t=0.14 s

| Coarse mesh | | | Fine mesh | | |
|---|---|---|---|---|---|
| $P_{\pi_1}$ (Pa) | $P_{\pi_2}$ (Pa) | $P_{\pi_1} - P_{\pi_2}$ (Pa) | $P_{\pi_1}$ (Pa) | $P_{\pi_2}$ (Pa) | $P_{\pi_1} - P_{\pi_2}$ (Pa) |
| 6702.24 | 5779.74 | 922.5 | 6727.64 | 5910.5 | 817.15 |

## 5 Results

The plane averaged pressure values at sections $\pi_1$ and $\pi_2$ are presented in Figure 7. The detailed systolic and diastolic pressure values at the $\pi_1$ and $\pi_2$ slices,

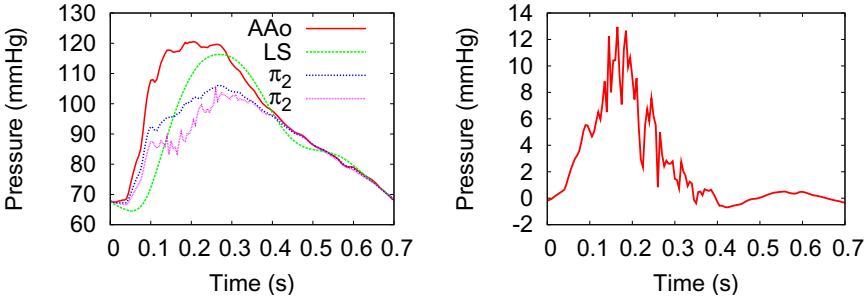


**Fig. 7.** (a) Plane averaged pressure values over a cardiac cycle at the aortic root (AAo), left subclavian (LS), plane $\pi_1$ and plane $\pi_2$. (b) Plane averaged pressure difference between $\pi_1$ and $\pi_2$.

**Table 3.** Simulated results as required by the challenge. All values shown in brackets are measured and reported by the challenge. Values outside the brackets are resulted from the CFD simulation.

| | | | | |
|---|---|---|---|---|
| Peak pressure difference between Plane 1 and Plane 2 | 12.94 mmHg | | | |
| Mean pressure difference between Plane 1 and Plane 2 | 2.29 mmHg | | | |
| Flow splits in | Brachiocephalic | Left carotid | Left subclavian | Descending Aorta |
| | 26.25 (25.6) | 11.62 (11.3) | 4.21 (4.26) | 57.92 (58.8) |
| Pressure in ascending aorta (Systolic/Diastolic) | 120.5/67.39 mmHg | | | |
| Pressure in left subclavian (Systolic/Diastolic) | 116.3/64.5 mmHg (115/65 mmHg) | | | |

the simulated flowrate percentages, the aortic root pressure, and the left subclavian pressure are shown in Table 3.

## 6 Discussion

We started our modeling approach with a detailed geometrical and physiological analysis of the aortic coarctation, where we predicted four pressure regions (as shown in Figure 2(b)). We then calibrated the windkessel boundary conditions using our newly developed adjoint method. The final computed CFD results showed that our modeling and physiological analysis are reasonable. This observed from the results presented in Figure 7(a), where large pressure drops can be observed between the different regions shown in Figure 2(b). The calibrated windkessel boundaries were successful in reproducing the flowrates measured by the challenge with an error smaller than 2.6% (see Table 3). The systolic and diastolic measurements of the sphygmometer, which are reported in the challenge, were also well reproduced at the left subclavian artery with an error of

1.63 mmHg and 0.5 mmHg for the systolic and diastolic pressure, respectively. (see Table 3 and Figure 7(a)). The pressure drop between plain $\pi_1$ and $\pi_2$ are reported in Table 3. Furthermore we showed, via performing a mesh analysis, that the mesh chosen in our study yields good results. This is clearly observed in the results presented in Figure 5, Figure 6, and Table 2. Here the difference in the pressure drop between the fine and coarse mesh was found to be 12.8%.

## References

1. Gravemeier, V., Wall, W.A.: Residual-based variational multiscale methods for laminar, transitional and turbulent variable-density flow at low Mach number. International Journal for Numerical Methods in Fluids 65, 1260–1278 (2011)
2. Ismail, M., Wall, W.A., Gee, M.W.: Adjoint-based Inverse Analysis of Windkessel Parameters for Patient-Specific Vascular Models. Journal of Computational Physics (2012) (in press)
3. Vignon-Clementel, I.E., Figueroa, C.A., Jansen, K.E., Taylor, C.A.: Outflow boundary conditions for three-dimensional finite element modeling of blood flow and pressure in arteries. Computer Methods in Applied Mechanics and Engineering 195, 3776–3796 (2006)
4. Mynard, J.P., Nithiarasu, P.: A 1D arterial blood flow model incorporating ventricular pressure, aortic valve and regional coronary flow using the locally conservative Galerkin (LCG) method. Communications in Numerical Methods in Engineering 24, 367–417 (2008)
5. Segadal, L.: Velocity distribution model for normal blood flow in the human ascending aorta. Medical and Biological Engineering and Computing 29(5), 489–492 (1991)
6. Wall, W.A., Gee, M.W.: BACI: A parallel multiphysics finite element environment. Institute for Computational Mechanics, Technische Universität München, Germany (2012)
7. The fourth report on the Diagnosis, Evaluation, and Treatment of High Blood Pressure in Children and Adolescents, National Heart Lung and Blood Institute, USA (2005)

# Supervised Learning Modelization and Segmentation of Cardiac Scar in Delayed Enhanced MRI

Laura Lara[1], Sergio Vera[1], Frederic Perez[1], Nico Lanconelli[2], Rita Morisi[2], Bruno Donini[2], Dario Turco[2], Cristiana Corsi[2], Claudio Lamberti[2], Giovana Gavidia[3], Maurizio Bordone[3], Eduardo Soudah[3], Nick Curzen[4], James Rosengarten[4], John Morgan[4], Javier Herrero[1], and Miguel A. González Ballester[1]

[1] Alma IT Systems, Barcelona, Spain
[2] Alma Mater Studiorum, University of Bologna, Italy
[3] Centre Internacional de Mètodes Numèrics en Enginyeria, Barcelona, Spain
[4] University Hospital, Southampton, UK

**Abstract.** Delayed Enhancement Magnetic Resonance Imaging can be used to non-invasively differentiate viable from non-viable myocardium within the Left Ventricle in patients suffering from myocardial diseases. Automated segmentation of scarified tissue can be used to accurately quantify the percentage of myocardium affected. This paper presents a method for cardiac scar detection and segmentation based on supervised learning and level set segmentation. First, a model of the appearance of scar tissue is trained using a Support Vector Machines classifier on image-derived descriptors. Based on the areas detected by the classifier, an accurate segmentation is performed using a segmentation method based on level sets.

**Keywords:** Myocardial Scar, Support Vector Machine, Level Set, Segmentation.

## 1 Introduction

Cardiovascular diseases remain the biggest cause of death worldwide. Myocardial scar appears when myocardium cells become nonfunctional after being affected by cardiovascular diseases, such as infarct. Delayed Enhancement Magnetic Resonance Imaging (DE-MRI) images allow a good visualization of the scar tissue, due to the higher concentrations of gadolinium contrast present on the scar compared to healthy myocardium, which appear some minutes after the administration of the contrast agent. DE-MRI protocol requires the patient to hold breathing during scans to minimize errors due to motion. Elderly people cannot hold breathing for too long and hence, DE-MRI studies have often limited depth resolution (Fig. 1), making the segmentation of the cardiac scar a challenging task.

Scar segmentation in DE-MRI images has been approached as a threshold selection problem. Indeed, most methods for scar segmentation rely on some thresholding scheme based on the intensity of the healthy myocardium or the blood pool [7]. A comprehensive review of scar segmentation methods can be found in [5]. Those methods assume that the voxel intensity of the scar/myocardium/blood pool follows a certain

O. Camara et al. (Eds.): STACOM 2012, LNCS 7746, pp. 53–61, 2013.

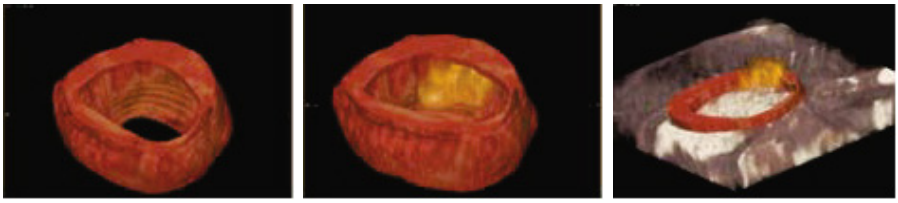

(a) (b) (c)

**Fig. 1.** Three-dimensional volume rendering of a myocardium section (a), the myocardium and the scar (b), the original MRI, myocardium and scar (c)

probability density function (usually Gaussian) that can be used to identify scar from non scar voxels.

Let $G$ be a Gaussian distribution with mean $\mu$ and standard deviation $\sigma$, any values greater than $\mu + \alpha\sigma$ will be selected as scar segmentation. Here, $\alpha$ acts as a parameter that regulates how much of the Gaussian distribution is considered healthy (or scarred) myocardium. Most methods only differ from the selected multiplier and the area where the Gaussian distribution is being assumed.

However, those approaches, have several flaws. First, it is supposed that the area of the scar will be small relative to the area of the healthy myocardium. While this can be assumed to be true, certain areas of the myocardium in some patients may not comply to this condition. Even more, this implies that the presence of a scar in the myocardium is implicitly assumed. Secondly, this kind of thresholding mechanisms does not consider spatial coherence in the segmented area. Voxels may be selected as scar regardless of the value assigned to neighboring pixels. This in turn generates artifacts due to noise or bright voxels in the myocardium mask, that can produce unconnected scar/noise segments. This forces some authors to post-process the segmentation in order to provide spatial coherence and/or remove noisy false positives [10].

Our approach uses a Support Vector Machine classifier to detect the presence of scar in the image. The output of the classifier is used as a initial seed for an intensity-based level set algorithm that can segment the scar considering spatial properties, thus generating more continuous segmentations. This is even more important in images such as typical DE-MRI volumes where the z-spatial coordinate has big spacing.

## 2 Methods

Starting from a gadolinium enhanced MRI image, the first step in order to segment the cardiac scar is to obtain a segmentation of the myocardium. Our method performs the segmentation of the myocardium walls with a semi-automatic step. With the binary segmentation of the myocardium, the final segmentation of the scar tissue is obtained via a supervised classifier and a level set refinement step.

### 2.1 Detection of the Scars

A semi-automatic procedure for the detection of the scars in DE-MRI images is proposed, where the user must provide an initial seed within the blood pool (one seed per

study). The software is based on a Support Vector Machine (SVM) classifier, which is able to detect scars on the basis of features of the objects segmented in the image. The training of the system is achieved by using images manually annotated by doctors. Our software can be divided in two major stages:

First, the region of interest in the image is identified in order to reduce the search area [4]. Here, the purpose is to select from the image the regions where scars are usually located. In order to achieve this, the seed provided by the user is used. The choice of this seed is not very critical, as any point within the blood pool can be used as starting point. From the seed, a region growing algorithm is used to segment the left ventricle. Morphological operations [2,6] are then performed for removing spurious signals. The minimal bounding circle of the segmented object is then computed for each slice. In this way an estimate of the external surface of the ventricle can be computed. In order to choose a region where scars are located and reduce at the same time the area of the image to be analyzed, an inner and an outer radius, starting from the minimal bounding circle are computed. The annulus between these two circles is the region where the scars should be located.

In a second step, a set of objects within this region are selected based on Otsu threshold [7]. Features are extracted from those objects, and they are used as inputs to the classifier to assign a label as *scar* or *no scar*. We consider features based on grey-level:

**Average grey level:** mean intensity value of the area.
**Entropy:** statistical measure of randomness that can be used in order to obtain information about the texture of an image defined by $E = -\sum_{i=1}^{n} p_i \log_2 p_i$. where $p_i$ are the probabilities of pixel intensities.

and features connected to the morphology (shape of the object):

**Area:** number of pixels in each object.
**Bounding Box:** width and height of the minimum rectangle containing the object.
**Majox Axis:** length of the major axis of the ellipse that has the same normalized second central moment of the object.
**Minor Axis:** length of the minor axis of the ellipse with the same second central moment of the region considered.
**Eccentricity:** eccentricity of the ellipse that has the same second moment of the considered object. It provides a measure of how the object shape is similar to a circle.
**ConvexArea:** area of the object's convex hull.
**Euler number:** As this is calculated for each object segmented, this equals to $1 - \#holes$ in the object.

Figure 2 shows two examples of the distribution of some of the considered features, for *scar* and *no scar* objects. It is worth noting that the overlapping of the two classes is significant in both cases, as expected. The same behavior can be observed also for the other features. As a consequence, we cannot use only a few features for discriminating scars from false positives, an extensive set of features is needed instead.

Some tests were performed using different classifiers, in order to assess their performance on our validation set. In particular, we tested the following classifiers:

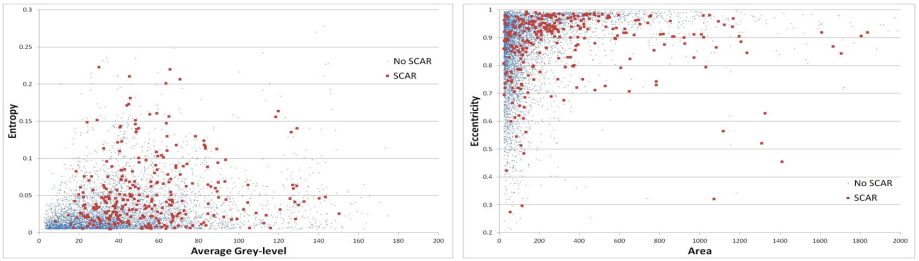


(a) (b)

**Fig. 2.** Scatter plots of some features for *scar* objects (red) and *no scar* (blue). Entropy versus average grey level (a). Eccentricity versus area (b).

1. Support Vector Machine with polynomial kernel ($2^{nd}$ degree).
2. K-Nearest Neighbors (KNN) classifier with 5 nearest neighbors.
3. Linear Bayesian discriminant classifier.
4. Linear perceptron classifier.

Table 1 shows the performance of the various classifiers with the set of features selected.

**Table 1.** Performance of the classifiers, as estimated on our validation set, in terms of average error, sensitivity and false-positive rate

| | SVM | KNN | Bayesian | Perceptron |
|---|---|---|---|---|
| Average error | $0.147 \pm 0.008$ | $0.152 \pm 0.005$ | $0.137 \pm 0.005$ | $0.19 \pm 0.05$ |
| Average sensitivity | $20\% \pm 3\%$ | $14\% \pm 2\%$ | $15\% \pm 3\%$ | $24\% \pm 14\%$ |
| Average false positive | $0.04 \pm 0.01$ | $0.038 \pm 0.006$ | $0.034 \pm 0.007$ | $0.10 \pm 0.07$ |

Results indicate similar performance between all classifiers. However, SVM provides the best trade-off between average error and sensitivity.

### 2.2 Segmentation of the Scars

Level sets segmentation methods [3,8] are implicit methods for tracking the evolution of contours and surfaces. The main advantage of level sets is that arbitrarily complex shapes, as in the scar, can be modeled and topological changes in the evolution front such as merging and splitting are handled implicitly. Level set contours get attracted to specific image features while their evolution is also controlled by other forces such as propagation and smoothness forces. This generates smoother, more continuous segmentations when compared to pure intensity methods such as simple thresholding or region growing schemes which also provide spatial coherence, but are prone to leakage.

The previously detected scar contour from the SVM is used as initialization for the level set. The feature image that drives the level set is targeted to be attracted to intensity values learned in the training phase of the method. The selection of this type of level set is not casual. The scar has no well-defined boundaries with the blood pool and other (bright) areas of the heart, so edges of the scar are hard to use in the segmentation step. Fortunately, we can use the myocardium segmentation to constrain the level set evolution inside the mask.

From the myocardium image area, a speed image (propagation term) is generated that allows the level set to grow in areas where the image intensity is within the window defined by the input from the SVM, and to shrink outside of that window. Let $I(x)$ be a input image, $U$ the upper intensity and $L$ the lower intensity bounds, the speed image $P(x)$ is defined as:

$$P(x) = \begin{cases} I(x) - L & \text{if } I(x) < \frac{U+L}{2} \\ U - I(x) & \text{otherwise} \end{cases} . \tag{1}$$

The values of $U$ and $L$ are computed from the gray level intensity statistics of the objects selected by the SVM classifier with the training data. From all the regions that exit the classifier we compute the mean and standard deviation of the intensity values. With this values $U$ and $L$ are computed as $\mu \pm 5\sigma$ to mimic the behaviour of a 5-SD method [1]. The evolution of the level set is controlled by the equation:

$$\phi_t + \beta P(x)|\nabla\phi| = \gamma Z(x)\kappa|\nabla\phi| \ . \tag{2}$$

Where $\phi_t$, $\nabla\phi$, are the level set boundary at iteration $t$ and its gradient; $P(x)$, $Z(x)$, are the propagation (speed) and curvature terms, and $\beta$, $\gamma$ and $\kappa$ are scalar weights that control the influence of each term. The curvature term provides a smoothness condition while at the same time allows to remove spurious or isolated noise voxels with high curvature term, that might be detected by the SVM as scar.

## 3 Results

To evaluate our method we participated in the STACOM 2012 DE-MRI segmentation challenge [9]. Data available for the challenge consists of 30 different DE-MRI images, divided in two datasets. Fifteen images belong to human patients and the other 15 images are from pigs. Each group is divided into 5 training images with MRI, myocardium mask and scar ground truth (GT) and the remaining 10 studies only include MRI and myocardium mask. Given that a segmentation of the myocardium is provided by the challenge organization, we use the provided myocardium segmentations instead of our own cumputed segmentations. Human data was captured with a 1.5T MRI while pig data was captured with a 3.0T scanner. Ground truth was generated slice by slice as the consensus of two radiologists for pig data while for human data the STAPLE [11] of three operator segmentations was used. In order to evaluate the quality of the segmentation, the standard Dice coefficient has been calculated with respect to the ground truth. The Dice coefficient measures the degree of overlap between two sets (or two segmentations) $A$ and $B$, and is defined as:

$$\mathrm{Dice}(A, B) = \frac{2|A \cap B|}{|A| + |B|} \quad . \tag{3}$$

Dice values are in the range of 0 (no overlap) to 1 (representing full overlap). For each volume we also compute the percentage of myocardium affected by the scar and compare this value with the percentage of the myocardium computed using the ground truth. Notice that this second metric is not necessarily related to the Dice score. Instead this metric is related with the size of the scar and the difference between GT and segmented scar. At the time of writing this article only the results of the training set are known. Results are shown in Table 1.

**Table 2.** Results for each training dataset. overlap scores and difference between percentage of myocardium affected area. Volumes labeled with *a* are from pig data while the ones labeled *p* are from human data.

| Volume | Dice Score | %GT | %Seg | Difference |
|---|---|---|---|---|
| a1 | 0.59 | 7.6 | 6.3 | 1.2 |
| a2 | 0.57 | 11.0 | 8.0 | 3.0 |
| a3 | 0.60 | 8.1 | 16.3 | -8.2 |
| a4 | 0.61 | 8.6 | 5.3 | 3.3 |
| a5 | 0.81 | 12.4 | 15.1 | -2.7 |
| p4 | 0.45 | 10.0 | 5.2 | 4.8 |
| p5 | 0.38 | 1.9 | 3.4 | -1.4 |
| p7 | 0.57 | 8.2 | 12.3 | -4.1 |
| p11 | 0.76 | 12.4 | 14.3 | -1.9 |
| p13 | 0.70 | 14.1 | 11.0 | 3.1 |
| | Mean: $0.60 \pm 0.12$ | | | RMSE: 3.89 |

Results show a more stability in percentage of myocardium affected than in DICE score. Differences in image quality and ground truth selection criteria might explain reduction in the overlap measurements. While some scans show a clearly distinguishable scar, others show little contrast in the damaged tissue as exemplified in Fig. 3. The method defined in this article will perform better in the presence of good contrasted scar tissue.

Figure 4 shows the segmentation results in green, compared with the scar ground truth (orange). It can be seen that segmented scar results improve when the myocardium is clearly darker than the scar. It is worth noting also that the level set has a tendency to under-segment the scar, compared with the provided ground truth scar.

The criterion to differentiate scar from non scar tissue also affects the overlap results, and is a source of discrepancies due to the high inter-observer variability. The method presented herein selects brighter areas of the myocardium as scar. However, the ground truth seems to be more selective at times, with some brighter areas of the myocardium

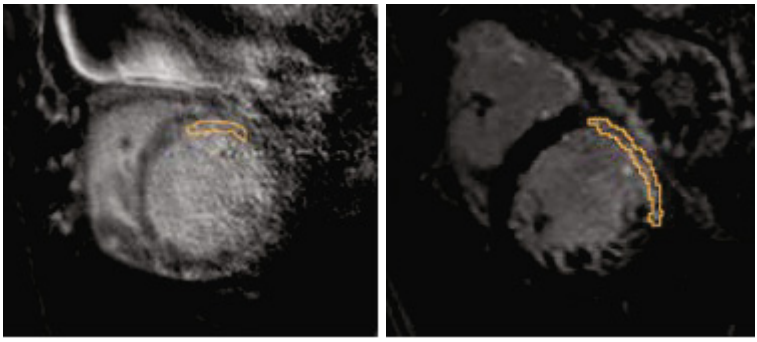

(a) (b)

**Fig. 3.** Examples of scars (orange outlines) from the datasets. Left image shows a scar with little contrast with the myocardium, while in the right image the scar is clearly noticeable.

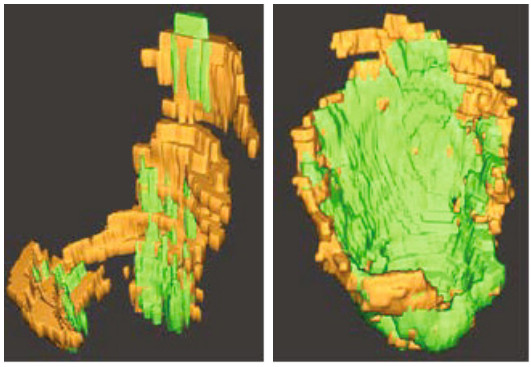

(a) (b)

**Fig. 4.** Isosurface representation of ground truth (orange) and segmentation results (green). (a): low contrast volume, (b): high contrast volume.

not being marked as scar GT (Fig. 5). Our clinical collaborators disagreed with the provided GT in several datasets. This is, however, expected given the nature of the ground truths provided for the challenge.

The worst performing case with an overlap score of 0.38 presents similar intensity values for myocardium and scar. Also, the upper segment of the myocardium mask includes fibrotic tissue that is not scar tissue. This circumstances confuses the SVM stage creating false scar seeds and reducing drastically the overlap index (Fig. 6(a)). In some cases the classifiers detects wrong scar segments due to the presence of bright voxels in the myocardium mask, like when the mask includes non myocardium areas (blood pool). A proposed improvement to this issue is the inclusion in the classifier of additional shape-related features.

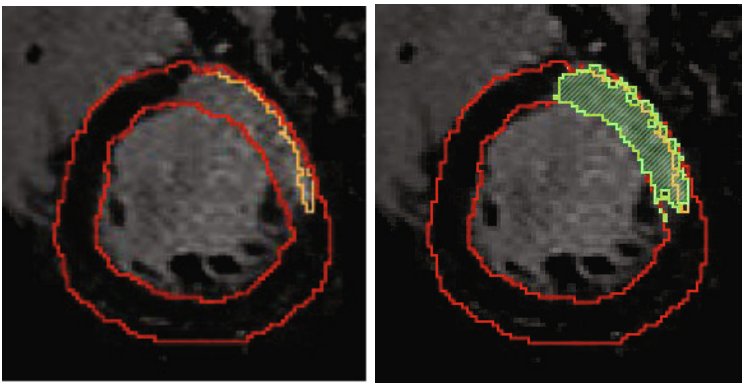

(a) (b)

**Fig. 5.** Scar discrepancies. Myocardium (red) bright areas not selected as scar ground truth in orange (b). Our method will include this area (green) as scar (b).

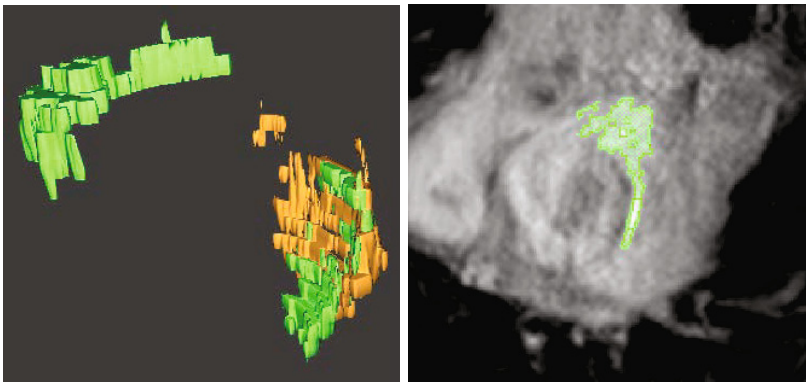

(a) (b)

**Fig. 6.** Wrongly detected seed generates a false positive scar segment. 3D view upper green iso-surface (a). The same area in a 2D slice (b).

## 4 Conclusions

We have presented a method for the detection and segmentation of myocardial scar in DE-MRI data. While overlap values for the rest of the test data remain yet unknown, overlap values for the training data seem promising, and the percentage of myocardium affected by scar results, a relevant clinical measurement, are good, in spite of having a small training set. It seems evidenced that inter-observer variability may be an issue to address in order to create a gold standard in the definition of the scar contour. Finally, the presence of fat and other non scarified fibrotic tissue in the myocardium area, might hinder the performance of the method.

**Acknowledgements.** this work is partially supported by CHIRON - EU JU ARTEMIS Grant #2009-1-100228.

## References

1. Amado, L.C., Gerber, B.L., Gupta, S.N., Rettmann, D.W., Szarf, G., Schock, R., Nasir, K., Kraitchman, D.L., Lima, J.A.: Accurate and objective infarct sizing by contrast-enhanced magnetic resonance imaging in a canine myocardial infarction model. Journal of the American College of Cardiology 44(12), 2383–2389 (2004)
2. Bankman, I.: Handbook of Medical Imaging, Processing and Analysis. Academic Press (2000)
3. Chan, T.F., Vese, L.A.: Active contours without edges. IEEE Transactions on Image Processing 10(2), 266–277 (2001)
4. Ciofolo, C., Fradkin, M.: Segmentation of Pathologic Hearts in Long-Axis Late-Enhancement MRI. In: Metaxas, D., Axel, L., Fichtinger, G., Székely, G. (eds.) MICCAI 2008, Part I. LNCS, vol. 5241, pp. 186–193. Springer, Heidelberg (2008)
5. Kolipaka, A., Chatzimavroudis, G.P., White, R.D., O'Donnell, T.P., Setser, R.M.: Segmentation of non-viable myocardium in delayed enhancement magnetic resonance images. The International Journal of Cardiovascular Imaging (formerly Cardiac Imaging) 21, 303–311 (2005)
6. Landini, L., Positano, V., Santarelli, M.F.: 3D medical image processing. In: Image Processing in Radiology. Medical Radiology, pp. 67–85 (2008)
7. Otsu, N.: A Threshold Selection Method from Gray-level Histograms. IEEE Transactions on Systems, Man and Cybernetics 9(1), 62–66 (1979)
8. Sethian, J.: Level set methods and fast marching methods: Evolving interfaces in computational geometry, fluid mechanics, computer vision, and materials science 18(1), 89–92 (1999)
9. STACOM2012: Statistical atlases and computational models of the heart (2012), `http://www.physense.org/stacom2012/`
10. Tao, Q., Milles, J., Zeppenfeld, K., Lamb, H.J., Bax, J.J., Reiber, J.H., van der Geest, R.J.: Automated segmentation of myocardial scar in late enhancement mri using combined intensity and spatial information. Magnetic Resonance in Medicine 64(2), 586–594 (2010)
11. Warfield, S.K., Zou, K.H., Wells, W.M.: Simultaneous truth and performance level estimation (staple): An algorithm for the validation of image segmentation. IEEE TMI 23, 903–921 (2004)

# Healthy and Scar Myocardial Tissue Classification in DE-MRI

Xènia Albà[1,2], Rosa M. Figueras i Ventura[1,2], Karim Lekadir[1,2], and Alejandro F. Frangi[1,2,3,⋆]

[1] Center for Computational Imaging & Simulation Technologies in Biomedicine (CISTIB), Universitat Pompeu Fabra, Barcelona, Spain
[2] Networking Center on Biomedical Research (CIBER-BBN), Barcelona, Spain
[3] Department of Mechanical Engineering, University of Sheffield, Sheffield, UK

**Abstract.** We propose an automatic technique to segment scar and classify the myocardial tissue of the left ventricle from Delay Enhancement (DE) MRI. The method uses multiple region growing with two types of regions and automatic seed initialization. The region growing criteria is based on intensity distance and the seed initialization is based on a thresholding technique. We refine the obtained segmentation with some morphological operators and geometrical constraints to further define the infarcted area. Thanks to the use of two types of regions when performing the region growing, we are able to segment and classify the healthy and pathological tissues. We have also a third type of tissue in our classification, which includes tissue areas that deserve special attention from medical experts: border-zone tissue or myocardial segmentation errors.

## 1 Introduction

Magnetic Resonance Imaging (MRI) plays an important role for the assessment of cardiac viability [1]. To this end, Delay Enhancement MRI (DE-MRI) has established itself as a standard imaging protocol in clinical practice to localize and quantify myocardial scar tissue [2]. Due to the large amount of information and in order to remove operator bias, user interaction needs to be reduced or eliminated where possible.

The purpose of our work is to automatically locate the infarcted tissue inside the left ventricle in short axis DE-MRI. First, the left ventricle borders need to be segmented. Following this, tissues inside the myocardium have to be classified.

The first step, segmentation of the myocardium, can be solved in different ways: registering CINE segmentations to DE images [3, 4] or trying to directly segment DE-MRI. The first approach benefits from higher contrast in CINE,

⋆ This research has been partially funded by the Industrial and Technological Development Center (CDTI) under the CENIT-cvREMOD program, by the European Commission's project euHeart (FP7-ICT-224495) and by the Spanish Ministry of Science and Innovation (TIN2011-28067). Alejandro F. Frangi is partially funded by the ICREA-Academia programme.

O. Camara et al. (Eds.): STACOM 2012, LNCS 7746, pp. 62–70, 2013.

but introduces segmentation errors due to slice misalignment and inconsistency in the number of slices. The second one if performed with the right priors can solve these inconsistencies and correct slice misalignments [5].

Once the myocardium contours have been obtained, the scar has to be located. The theory behind the delay enhancement analysis is that the image intensity of the scar is significantly higher than that of healthy myocardial tissue. However, the detection and quantification of the pathological tissues is a difficult task and several issues have to be solved. The contrast between the different tissues is related to the acquisition system and time, which are not always optimal. Moreover, depending on the pathology, the shape and extension of pathological areas, their location with respect to myocardium contours and the keenness of their borders diverge a lot. All this factors make the segmentation difficult and prone to intra and inter-observer variability. Considering this, the development of an automated segmentation of the infarct extent is needed.

Based on the theory behind the DE-MRI, an intuitive method for the detection of the scar is the application of a threshold two or three standard deviations above the average intensity value of a healthy myocardial region [2, 6], or using other metrics [7, 8]. Another approach is to apply clusters [9], or classify myocardial tissue using a support vector machine [3, 10]. The main disadvantage of these methods is the absence of spatial information. Hsu et al. [11] perform a feature analysis after the initial thresholding studying the 3-D connectivity to remove false positive segmentations. In [12], the authors combine both intensity thresholding and spatial information. To avoid the choice of a threshold, the fuzzy c-means algorithm, which provide a membership degree to the class of enhanced pixels, can be applied to the pixels only inside the myocardium [9] or both myocardium and blood pool [13]. Moreover, [14] proposed an algorithm that combines a histogram analysis with a constrained watershed segmentation as part of a combined analysis of coronary arteries, myocardial perfusion, and delay enhancement based on MRI. Elagouni *et al.* [15] use fuzzy thresholding followed by region analysis. In [16], the pathological tissue in the myocardium wall is identified using a MAP-based classifier based on the visual appearance and spatial interaction of the LV pathological tissue as well as healthy tissue.

We propose an automatic technique to classify the myocardial tissues of the left ventricle from DE-MRI. Our method uses a region growing algorithm based on intensity distance with automatic seed selection to segment the healthy tissue, the scar and a third type of tissue (which for most patients is ischemic viable tissue or border-zone tissue). To define the final infarcted area, a post-processing is applied based on morphological operators and location constraints.

The data used in the paper is provided by the STACOM-DEMRI Challenge. The challenge dataset consists of 30 DE-MRI datasets for segmentation of enhanced regions from post-myocardial infarction patients (15) and pigs (15) that have suffered from myocardial ischaemia. The dataset includes the myocardial segmentations and, of each of these 15 datasets, 5 are provided as training samples with manual annotations of the scar.

## 2 Methodology

Assuming that the myocardium contours have already been obtained, our scar segmentation method consists of five steps, as illustrated in Fig. 1. The automated algorithm selects seeds based on the intensity, and defines a region growing algorithm to, finally, segment the healthy tissue, the scar and a third type of tissue, which would include border-zone tissue and/or myocardial segmentation errors. We have also used some geometrical rules based on morphological operators to define the final infarcted area. This section provides detailed description of the method, describing it step by step.


**Fig. 1.** Block scheme of the scar segmentation method

### 2.1 Pre-processing

The preprocessing step is divided in two parts. On the one hand, some of the myocardial segmentations provided by the STACOM-DEMRI challenge have small segmentation errors. Typically, these consist of: single pixels that are not inside the myocardium but that are marked as such (islands), or pixels inside the myocardium not included in the mask (holes). This is a necessary step for the seed selection and posterior region growing. On the other hand, we have also performed a pre-processing to the DE-MRI slices consisting on an enhancement method to improve the contrast: we have applied a sigmoid function to the gray levels of the image (see Fig. 2).

### 2.2 Automatic Seed Selection

After the pre-processing step, we proceed to automatically select the seeds that will be used for the region growing algorithm: two seeds at most for scar tissue

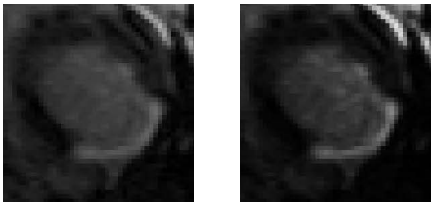

**Fig. 2.** Application of sigmoid function: original (left) and processed image (right)

and two at most for healthy tissue. To do so, we consider as scar candidates any pixel $v_i$ in slice $i$ with coordinates $(x, y)$ if:

$$v_i(x, y) \text{ is "scar candidate" if } v_i(x, y) > \mu_i + 2\sigma_i, \quad (1)$$

where $\mu$ is the mean gray level value of the myocardium and $\sigma$ is the standard deviation of the gray levels inside the myocardium in the slice that is being analyzed. This gives us a first approximation of possible locations of scar (Fig. 3a). We discard as scar candidates very thin and elongated regions which are near the epicardium, as they often come from errors in the segmentation of the myocardium. We choose the brightest pixels in the one or two bigger regions (single pixels or small islands are discarded) as seeds for scar region growing, and the darkest pixels in the myocardium which are outside the preliminary scar zone and which are inside connected big regions as seeds for the healthy region growing, as depicted in Fig. 3b. With the selected seeds, our method has then from one to four seeds to grow, depending on whether it found no scar, one scar and one healthy region, two scar regions and one healthy or two scar regions and two healthy regions. The possible use of two seeds for scar, instead of just one, solves the problem of having two disconnected regions.

### 2.3 Region Growing

Region growing is a pixel-based image segmentation method. A region is iteratively grown by comparing all unallocated neighboring pixels to the region [17]. Starting with the seeds chosen as explained in Sec. 2.2, we apply the region growing algorithm, which takes pixels and compares them with its neighbors using an intensity distance related to the standard deviation.

The region growing is performed independently for every seed (the scar ones and healthy). During this step, we do not control if regions overlap or not, the region iteratively grows by comparing all unallocated neighboring pixels to the region. The difference between a pixel intensity value and the region mean is used as a measure of similarity. The pixel with the smallest difference is allocated to the respective region. The process grows the region until the stopping criteria

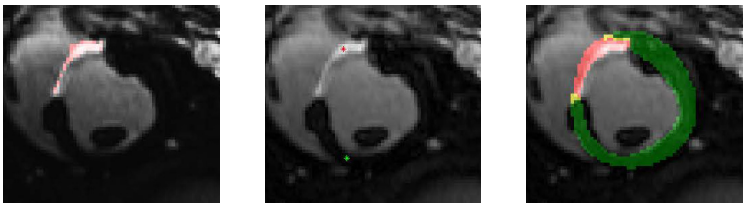

(a) (b) (c)

**Fig. 3.** Evolution of the algorithm: (a) shows the candidate pixels for scar seeds, (b) shows the seeds for scar tissue (red dot) and healthy tissue (green dot) and (c) shows the three labels: red for "scar", green for "healthy" and yellow for "other"

is met. The regions will, in most of the cases, overlap in some parts of the myocardium. Also, in some cases, some parts of the myocardium are not included neither in the healthy regions nor in the scar ones.

### 2.4 Region Labeling

Once the region growing algorithm has defined the (possibly overlapping) healthy and scar regions, we proceed to label each pixel as "scar", "healthy" or "other", where "other" could include border-zone and segmentation errors. The labeling uses the following rules:

$$\begin{cases} v_i(x,y) \text{ is "scar"} & \text{if} \quad v_i(x,y) \in R_s \ \& \ \notin R_h, \\ v_i(x,y) \text{ is "healthy"} & \text{if} \quad v_i(x,y) \notin R_s \ \& \ \in R_h, \\ v_i(x,y) \text{ is "other"} & \text{if} \quad \text{otherwise}, \end{cases} \tag{2}$$

where $R_s$ are the scar regions and $R_h$ are the healthy regions. As can be seen from above expressions, we label as "scar" any pixel which is included only in the scar regions. Similarly, "healthy" label is assigned to every pixel which is only included in the "healthy" regions. Any other pixel (included both in healthy and scar regions or not included in any region) is labeled as "other".

A second labeling step is performed for the tissue labeled in the previous step as "other":

$$\begin{cases} v_i(x,y) \in \text{"other" is "scar"} & \text{if} \quad v_i(x,y) \text{ neighbor with "scar"}, \\ v_i(x,y) \in \text{"other" is "other"} & \text{if} \quad \text{otherwise}, \end{cases} \tag{3}$$

where we consider as part of the scar tissue labeled as "other" which is in contact with "scar".

This gives us a myocardium with three labels, "scar" for pixels considered as scar, "healthy" for pixels considered as healthy tissue, and "other" for pixels that are either viable ischemic tissue or miss-segmentations, as shown in Fig. 3c.

### 2.5 Post-processing

Once we have the labeling, we want to fill the small holes so that there are no isolated pixels in any region. We perform the hole filling both for the regions labeled as "scar" and for the regions labeled as "healthy". Also, we exclude from scar all regions that are too small proportional to the area of the myocardium, which often come from noise in the acquisition, and the connected regions, which were not considered very small but that are attached to the epicardial or endocardial contours and that are very thin and elongated, considering them segmentation errors. Finally, we relabel as scar some patchy, dark regions without contrast which are fully surrounded by enhanced regions, which are consistent with microvascular obstruction and thus should belong to the infarct (see Fig. 5).

**Table 1.** DSC between automatic and manual segmentations

| | 1 | 2 | 3 | 4 | 5 | Average |
|---|---|---|---|---|---|---|
| PIGS | 0.6739 | 0.6072 | 0.8164 | 0.8615 | 0.8070 | 0.7532 |
| HUMANS | 0.4400 | 0.5600 | 0.6395 | 0.4048 | 0.6703 | 0.5429 |

## 3 Results

The STACOM-DEMRI Challenge dataset consists of 30 DE-MRI volumes for segmentation of enhanced regions from post-myocardial infarction patients (15) and pigs (15) that have been subjected to myocardial ischaemia. However, only 5 pigs and 5 humans are provided as training samples with manual annotations for the scar and these 10 volumes have been used to validate our method.

Validation of the method is done by comparing the automatic segmentation results with the manual ones from one observer by calculating the Dice similarity coefficient (DSC) (measuring the degree of area overlap). DSC is always between 0 and 1, with higher DSC indicating better match between automatic and manual segmentations. DSC is 0 for situations in which one of the segmentations shows scar and the other does not, and it is 1 when there is perfect agreement in the segmentations, including the cases where both segmentations show no scar. Table 1 shows the average DSC of each subject.

Figs. 4 and 5 show some visual results for scar segmentation, both for pigs and humans. In the figures, we can compare manual segmentation (top row) with our segmentation (bottom row). The DSC value between the automatically identified and manually defined regions are also shown below each slice. The first two columns of Fig. 4 show cases that have properly worked, the borders

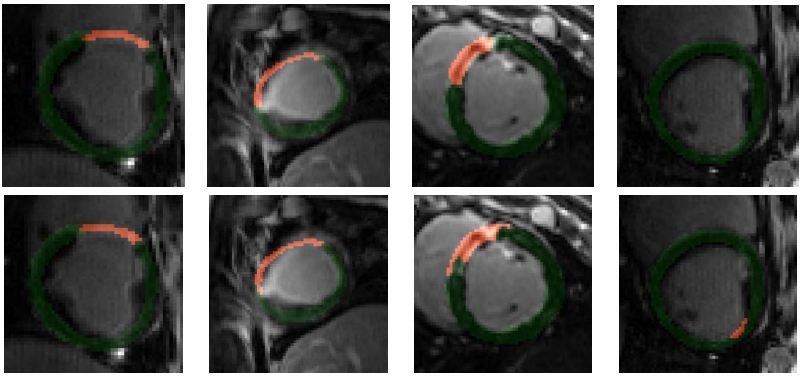


**Fig. 4.** Examples of our proposed scar location approach (bottom) compared with the manual ground truth (top) for the pig dataset and its DSC value

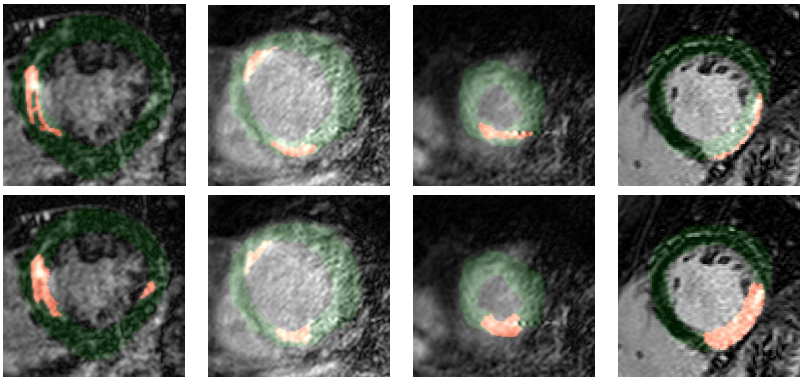


**Fig. 5.** Examples of our proposed scar location approach (bottom) compared with the manual ground truth (top) for the human dataset and its DSC value

of the scar have been accurately defined. The third column shows a case where the segmentation could have errors due to lack of penetration, but it performs quite well thanks to the double seed initialization and the hole filling. It can be noticed that the DSC is sensitive to the scar size observing the first three values of the measure. Finally, the fourth column of Fig. 4 depicts an error that comes from a bad segmentation of the myocardium, which makes our algorithm fail and detect as scar tissue next to the myocardium.

Fig. 5 shows some segmentations performed on the human dataset. The first column shows a case with correct scar detection, filling the holes without contrast inside the scar that come probably from microvascular obstruction, even though the ground truth provided does not consider these holes as scar. The second column shows an example of double scar detection thanks to the use of two scar and two healthy tissue seeds. The third column shows a typical example of the segmentations being affected by a low contrast and acquisition artifacts. Finally, the fourth column gives a clear example of false positive scar detection due to incorrect myocardial segmentation: a large amount of what seems to be blood pool has been included in the myocardium, and our algorithm has annotated this region, which is exactly next to the real scar, as scar.

Our algorithm is fast enough to be used in real time: the average computational time for one slice is between 0.1 and 4 seconds (depending on the resolution and if any scar seed is detected) when executed in Matlab in a Intel(R) Core(TM)2 Quad CPI Q6600 @ 2.40GHz with windows 7. This makes it usable in clinical scenarios, especially if we consider the fact that the code can be further optimized and refined.

## 4 Conclusions

We have presented a fully automatic method to segment scar in DE-MRI images. This method has three characteristics that make it very interesting for clinical

practice: it does not require training, it can be used in real time and includes three types of tissue in the labeling: "scar", "healthy" and "other", which includes both possible areas of ischemic viable tissue and voxels that are not really myocardium but were included probably due to segmentation errors.

Our segmentation method is fast enough to be used in real time in a clinical scenario. The most time consuming step of the processing would be the manual segmentation of the myocardium. Using a fast automatic myocardial segmentation, such as the one presented in [5], would help to improve this.

Segmentation results using this method look promising. False positives often come from myocardial segmentation errors. Also, we would like to point out that often, when performing an undersegmentation of a scar, the undersegmented voxels are labeled as "other" and not as healthy. This is important because it indicates to the clinicians that in this area we do not consider the tissue as fully healthy, and that it should be analyzed with caution. Further analysis and evaluation of the performance of this method with a larger dataset has to be performed in order to test its full potential.

## References

[1] Vogel-Claussen, J., Rochitte, C., Wu, K.C., Kamel, I.R., Foo, T.K., Lima, J.A.C., Bluemke, D.: Delayed enhancement MR imaging: Utility in myocardial assessment. RadioGraphics 26, 795–810 (2006)

[2] Kim, R.J., Fieno, D.S., Parrish, T.B., Harris, K., Chen, E., Simonetti, O., Bundy, J., Finn, J.P., Klocke, F.J., Judd, R.M.: Relationship of MRI delayed contrast enhancement to irreversible injury, infarct age, and contractile function. Circulation 100, 1992–2002 (1999)

[3] Dikici, E., O'Donnell, T., Setser, R., White, R.D.: Quantification of Delayed Enhancement MR Images. In: Barillot, C., Haynor, D.R., Hellier, P. (eds.) MICCAI 2004. LNCS, vol. 3216, pp. 250–257. Springer, Heidelberg (2004)

[4] Berbari, R.E., Kachenoura, N., Frouin, F., Herment, A., Mousseaux, E., Bloch, I.: An automated quantification of the transmural myocardial infarct extent using cardiac DE-MR images. In: Proc. Int. Conf. IEEE Engineering in Medicine and Biology Society (EMBS) (2009)

[5] Albà, X., Figueras i Ventura, R., Lekadir, K., Frangi, A.F.: Conical deformable model for myocardial segmentation in late-enhanced MRI. In: IEEE International Symposium on Biomedical Imaging (ISBI) (2012)

[6] Heiberg, E., Engblom, H., Engvall, J., Hedström, E., Ugander, M., Arheden, H.: Semi-automatic quantification of myocardial infarction from delayed contrast enhanced magnetic resonance imaging. Scandinavian Cardiovascular Journal 39, 267–275 (2005)

[7] Breeuwer, M., Paetsch, I., Nagel, E., Muthupillai, R., Flamm, S., Plein, S., Ridgway, J.: The detection of normal, ischemic and infarcted myocardial tissue using MRI. Computer Assisted Radiology and Surgery 1256, 1153–1158 (2003)

[8] Kolipaka, A., Chatzimavroudis, G.P., White, R.D., O'Donnell, T.P., Setser, R.M.: Segmentation of non-viable myocardium in delayed enhancement magnetic resonance images. International Journal of Cardiovascular Imaging 21, 303–311 (2005)

[9] Positano, V., Pingitore, A., Giorgetti, A., Favilli, B., Santarelli, M., Landini, L., Marzullo, P., Lombardi, M.: A fast and effective method to assess myocardial necrosis by means of contrast magnetic resonance imaging. Journal of Cardiovascular Magnetic Resonance 7, 487–494 (2005)
[10] O'Donnell, T.P., Xu, N., Setser, R.M., White, R.D.: Semi-automatic segmentation of nonviable cardiac tissue using cine and delayed enhancement magnetic resonance images. In: Proc. SPIE Medical Imaging, vol. 5031, pp. 242–251 (2003)
[11] Hsu, L.Y., Natanzon, A., Kellman, P., Hirsch, G.A., Aletras, A.H., Arai, A.E.: Quantitative myocardial infarction on delayed enhancement MRI. Part I: animal validation of an automated feature analysis and combined thresholding infarct sizing algorithm. Journal Magnetic Resonance Imaging 23, 298–308 (2006)
[12] Tao, Q., Milles, J., Zeppenfeld, K., Lamb, H.J., Bax, J.J., Reiber, J.H., van der Geest, R.J.: Automated segmentation of myocardial scar in late enhancement MRI using combined intensity and spatial information. Magnetic Resonance in Medicine 64, 586–594 (2010)
[13] Kachenoura, N., Redheuil, A., Herment, A., Mousseaux, E., Frouin, F.: Robust assessment of the transmural extent of myocardial infarction in late gadolinium-enhanced MRI studies using appropriate angular and circumferential subdivision of the myocardium. European Radiology 18, 2140–2147 (2008)
[14] Hennemuth, A., Seeger, A., Friman, O., Miller, S., Klumpp, B., Oeltze, S., Peitgen, H.: A comprehensive approach to the analysis of contrast enhanced cardiac MR images. IEEE Transactions on Medical Imaging 27, 1592–1610 (2008)
[15] Elagouni, K., Ciofolo-Veit, C., Mory, B.: Automatic segmentation of pathological tissues in cardiac MRI. In: IEEE International Symposium on Biomedical Imaging (ISBI), pp. 472–475 (2010)
[16] Elnakib, A., Beache, G.M., Nitzken, M., Gimel'jarb, G., EI-Baz, A.: A new framework for automated identification of pathological tissues in contrast enhanced cardiac magnetic resonance images. In: IEEE International Symposium on Biomedical Imaging (ISBI), pp. 1272–1275 (2011)
[17] Adams, R., Bischof, L.: Seeded region growing. IEEE Transactions on Pattern Analysis and Machine Intelligence 16(6), 641–647 (1994)

# Infarct Segmentation of the Left Ventricle Using Graph-Cuts

Rashed Karim[1], Zhong Chen[1,2], Samantha Obom[1], Ying-Liang Ma[1], Prince Acheampong[1], Harminder Gill[1], Jaspal Gill[1], C. Aldo Rinaldi[2], Mark O'Neill[1,2], Reza Razavi[1,2], Tobias Schaeffter[1], and Kawal S. Rhode[1]

[1] Division of Imaging Sciences and Biomedical Engineering, King's College London, United Kingdom
[2] Department of Cardiology, Guy's and St. Thomas' NHS Foundation Trust, London, United Kingdom

**Abstract.** Delayed-enhancement magnetic resonance imaging (DE-MRI) is an effective technique for imaging left ventricular (LV) infarct. Existing techniques for LV infarct segmentation are primarily threshold-based making them prone to high user variability. In this work, we propose a segmentation algorithm that can learn from training images and segment based on this training model. This is implemented as a Markov random field (MRF) based energy formulation solved using graph-cuts. A good agreement was found with the Full-Width-at-Half-Maximum (FWHM) technique.

**Keywords:** Segmentation, Delayed-enhancement MRI, Left ventricle, Graph-cuts.

## 1 Introduction

Acute and chronic infarction in the myocardium has important prognostic implications in patients suffering from heart diseases. There is growing evidence suggesting that the use of Cardiovascular Magnetic Resonance CMR using DE-MRI sequences can be considered the gold-standard modality for assessment of infarct. However, the optimal technique for quantifying DE in DE-MRI is still debatable. An excellent survey and evaluation of these techniques can be found in [1]. The two highly used techniques, owing to their ease of implementation and simplicity, is the FWHM and standard-deviation (SD) techniques. The latter fixes infarct to be a certain number of standard deviations from healthy myocardium, and the former defines infarct to be above half of the maximal signal within infarct. Although there is now strong evidence that the FWHM technique is highly reproducible [1] and at least one body of work establishing correlation with histology studies [2], it still remains unclear why the chosen half of the maximal signal in FWHM would universally conjure the right quantification for infarct in DE-MRI.

In this work, we present a segmentation method for the data provided as part of the MICCAI challenge on ventricle DE-MRI data from humans and animals.

O. Camara et al. (Eds.): STACOM 2012, LNCS 7746, pp. 71–79, 2013.

It is based on a probabilistic tissue intensity model of DE-MRI data, which is derived both from training and the unseen data. The algorithm uses a Markov random field (MRF)-based energy formulation that is solved using graph-cuts [3]. The method of graph-cuts has shown high accuracy, simultaneous ROI detection, and scalability to three dimensions in segmenting structures [4]. It has been applied in a wide variety of segmentation problems arising in computer vision and medical image processing [5,6,7]. It is used in this work to efficiently solve the MRF model. The main advantages of employing the graph-cut technique in ventricle DE-MRI quantification are the following: 1) Uses a training model and thus the algorithm can be trained prior to suit to the quality of enhancement in the test cohort, and 2) Regions of infarct segmented are generally continuous and free from *salt-and-pepper* holes commonly encountered in thresholding techniques such as FWHM and SD.

## 2 Methods

The segmentation of infarct from DE-MRI can be described as assigning a label $f_p \in \{0, 1\}$ to every voxel $p$ in the search space of the image. The search space for infarct is myocardium and a binary segmentation is assumed to be readily available. Voxels representing infarct tissue are assigned the foreground class label $f_p = 1$ and non-infarct or healthy tissues are assigned background class label $f_p = 0$. Given the observed intensities in the search space of the image and prior knowledge about infarcts, the segmentation problem can be solved using a probabilistic framework where the maximum *a posteriori* (MAP) estimate is computed using Bayes' theorem:

$$\arg\max_{\mathbf{f}} P(\mathbf{f}|\mathbf{I}) = \frac{P(\mathbf{I}|\mathbf{f})P(\mathbf{f})}{P(\mathbf{I})} \tag{1}$$

where $\mathbf{f}$ is the total label configuration and $\mathbf{I}$ are all observed intensities within the search space. The image likelihood $P(\mathbf{I}|\mathbf{f})$ describes how likely is the observed image given a label configuration $\mathbf{f}$. The prior $P(\mathbf{f})$ encodes any prior knowledge of the tissue class labels (i.e. healthy and infarct tissue classes).

The MAP estimate allows to determine the most likely label configuration $\mathbf{f}$, given the observed intensities $\mathbf{I}$. To make numerical computation more convenient, the MAP formulation is transformed to one involving only summations. This is possible by taking the negative logarithm of Eq. 1:

$$\hat{\mathbf{f}} = \arg\min_{\mathbf{f}} \{-\ln P(\mathbf{I}|\mathbf{f}) - \ln P(\mathbf{f})\} \tag{2}$$

where $\hat{\mathbf{f}}$ is the optimal labelling. The prior probability $P(\mathbf{I})$ can be ignored as it is independent from the labelling $\mathbf{f}$. Note that the segmentation problem is now an energy minimization problem, following from (2):

$$\hat{\mathbf{f}} = \arg\min_{\mathbf{f}} \{\lambda E_{\text{data}}(\mathbf{f}) + E_{\text{prior}}(\mathbf{f})\} \tag{3}$$

The weighting term $\lambda$ weighs the relative contribution of the energy terms: $E_{\text{data}}$ is the data term which measures the disagreement between a prior probabilistic (i.e. training) model and the observed data, and $E_{\text{prior}}$ is a smoothness term penalizing any discontinuities within a tissue class. It achieves this by penalizing discontinuities between adjacent voxel pairs in a neighbourhood system. Eq. 3 is commonly represented in existing literature as an energy function over the entire image as:

$$E(f) = \lambda \sum_{p \in \mathcal{P}} D_p(f_p) + \sum_{\{p,q\} \in N} V_{p,q}(f_p, f_q) \tag{4}$$

Here $D$ and $V$ are terms corresponding to $E_{\text{data}}$ and $E_{\text{prior}}$ respectively of Eq. 3.

For MRF-based energy functions such as the one in Eq. 4, global optimization methods are computationally inefficient to be applied to medical image segmentation, especially with 3D free-breathing images. Other optimization schemes such as the Iterated Conditional Modes (ICM), widely applied in medical image segmentation, is well known to suffer from local minima trapping. The graph-cut method employed in this work, is now a widely used technique for minimizing context-dependent MRF problems as the one suggested here.

In the graph-cut implementation of [3], a close approximation of the global minimum is guaranteed and this is most desirable in DE-MRI we seek a global optimal solution (i.e. segmentation of infarct) based on the observed and training data. Indeed, a locally optimal solution would yield regions with inconsistent segmentations. In the graph formulation, the MRF-based energy function in Eq. 4 is coded into the edge-weights. The cost of the graph *cut*, partitioning the graph into two sets of nodes each belonging to a separate class: scar or healthy, is equal to the total energy of the corresponding segmentations. The problem is thus to find the cut with the least cost thus yielding the optimal segmentation.

### 2.1 Integration of Information in Edge-Weights

In the graph-cut method, the graph constructed from the infarct search space (i.e. region of myocardium) contains $t$-links and $n$-links. The $t$-links connect each voxel in the image to the tissue label classes namely healthy and infarct. The $n$-links are links between adjacent voxels that enforce smoothness in a local neighbourhood. The $t$ and $n$-links correspond to the data term $E_{\text{data}}$ and smoothness terms $E_{\text{prior}}$ of Eq. 3 respectively. The $t$-links are the major contributing term and is what drives most of the segmentation process. It is sensible that the weights assigned to these links are derived from a tissue prior such as a probabilistic model of healthy and infarct tissues.

**Tissue Intensity Prior:** For integrating prior knowledge about healthy and infarct tissues, tissue intensities are modelled in each class. In the healthy tissue (i.e. non-infarct) class, tissue intensities are modelled from from the unseen image. As the segmentation of myocardium is assumed to be available, tissues

lying outside myocardium are modelled using a multi-modal Gaussian mixture model. The number of modes is left variable as it is often unclear what would be the ideal and optimal number of tissue modes within the healthy class.

For infarct tissue class, the *enhancement ratio* of the mean intensity of infarct to blood-pool is modelled from the training data. These can be readily obtained from manually segmented infarct images. The ratio is modelled with a uni-modal Gaussian distribution. The data term of Eq. 3 and thus the $t$-link in the graph-cut is obtained from the aforementioned intensity distributions: $P(I_p|f_p = 1)$ for infarct and $P(I_p|f_p = 0)$ for healthy, and thus before we insert this information as edge-weights we must have:

$$D_p(f_p) = -\ln P(I_p|f_p) \tag{5}$$

**Tissue Continuity Prior:** The smoothness term $V$ in Eq. 3 ensure that segmented regions remain smooth and continuous. Neighbouring adjacent voxels with similar intensities incur an exponentially high *cut* cost if they are classified into separate tissue classes. The Lorentzian error norm [6] is employed, which is a robust metric for measuring intensity differences within a neighbourhood:

$$\varphi(p, q) = 1 + \frac{1}{2}\left(\frac{|I_p - I_q|}{\sigma}\right)^2 \tag{6}$$

The implementation of the graph-cut algorithm used is the one found in [8].

## 3 Results

### 3.1 Challenge Data

The data provided as part of this challenge was acquired using a standard 1.5T scanner and a 32 -channel coil (Philips Healthcare, Best, Netherlands). These were both from human ($n = 10$) and pig ($n = 10$). In the human set, the pixel resolution was reconstructed to $1.3 \times 1.3 \times 2$ mm$^3$. For the animal data, the resolution of the images provided were $1.7 \times 1.7 \times 6$ mm$^3$. Segmentation of the myocardium was also provided for each scan. These were manually annotated by a clinical expert. Also a set of training data ($n = 5$) were provided for both the patient and animal cohorts. This included expert segmentations of infarct within the myocardial contour. A sample of the datasets provided can be seen in Fig. 1.

### 3.2 Comparison with Gold-Standard

The FWHM is now established as a gold-standard for quantifying infarct in DE-MRI scans of the ventricle with good correlation shown against histology studies [2,1]. Results from the proposed algorithm were evaluated quantitatively against segmentations from the FWHM technique. Details on the implementation of

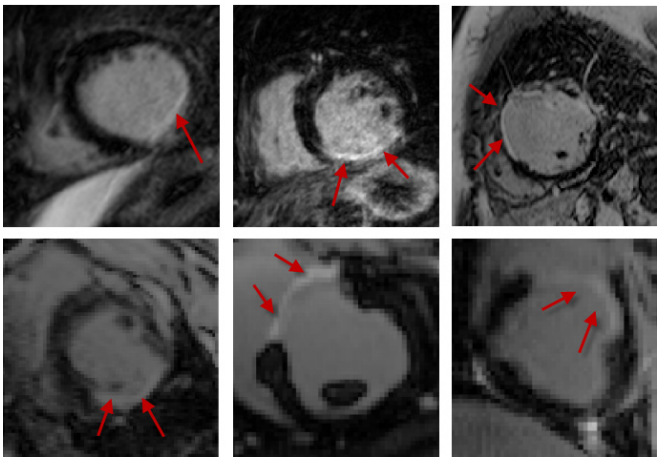

**Fig. 1.** Sample of the human (top row) and animal pig (bottom row) DE-MRI data provided to participants as part of the challenge. Red arrows indicate areas of enhancement.

FWHM can be found in [2]. Infarct was defined as signal intensities $T$ where: $T > 0.5 \times T_{\max}$, here $T_{\max}$ is the (mean) peak signal intensity within myocardium.

Infarct was quantified using both FWHM and the proposed algorithm. For comparison, the amount of infarct detected represented as percentage of myocardium was determined in both the methods. These comparisons are shown in the Bland-Altman plots of Fig. 2 for the human data set and 3 for the animal data set. In these plots, the percentage difference (vertical axis) is plotted against the average (horizontal axis) of the two techniques. Furthermore, the two techniques are also compared using the Dice overlap measure [9] in Table 1. We see good agreement in both human (Mean difference in measurements = -0.9%) and animal (Mean difference = -1.4 %) datasets. Note that a negative percentage indicates under-estimation of infarct by the proposed algorithm. There was also good pixel-by-pixel correlation in both human (Mean dice = 93/100) and animal (Mean dice = 87/100) datasets.

### 3.3 Performance

The human DE-MRI images were segmented in all but 1 case successfully using the proposed graph-cut algorithm. Segmentations were evaluated both qualitatively and quantitatively. A successful segmentation was defined as one where the algorithm was able to produce a result *and* had good correlation (Dice > 0.7) with FWHM. See Fig. 4 for a sample of the segmentations generated by the algorithm. The segmentations were computed in less than 5 seconds on a 2.5 Ghz PC. There was no operator input during the entire segmentation process. However, it is essential that a correct segmentation of the myocardium is provided as this defines its search space.

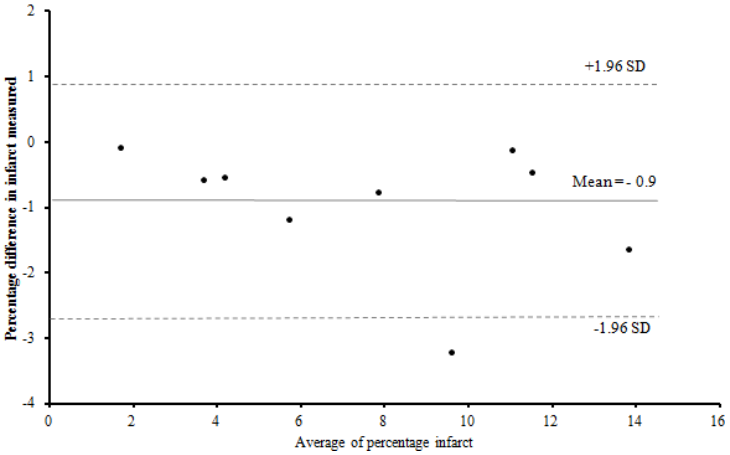


**Fig. 2.** Patient data-set: Bland-Altman plot showing difference in measurements (infarct detected as percentage of myocardium) in FWHM and proposed algorithm. A negative percentage indicates under-estimation of infarct by the proposed algorithm.

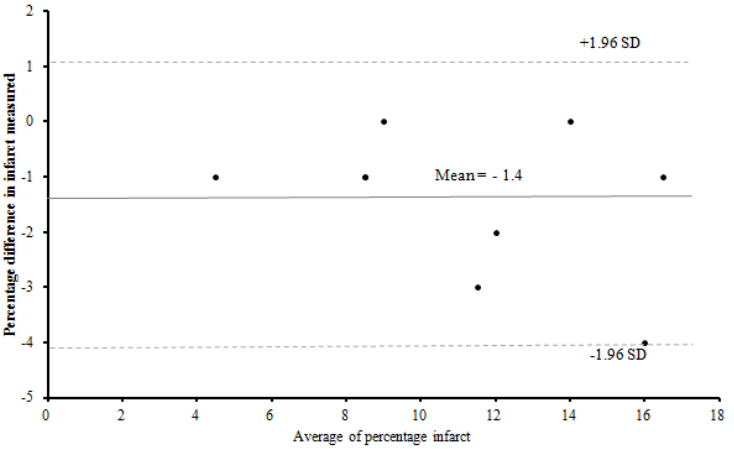


**Fig. 3.** Animal data-set: Bland-Altman plot showing difference in measurements (infarct detected as percentage of myocardium) in FWHM and proposed algorithm. A negative percentage indicates under-estimation of infarct by the proposed algorithm.

In the animal DE-MRI images, segmentations were obtained in all but 2 cases successfully. Similar to the human data, segmentations were computed in less than 5 seconds with no operator input. Fig. 5 shows a sample of the output generated by the algorithm.

**Table 1.** Dice overlap comparison with FWHM technique

| No. | Human | Animal |
|---|---|---|
| 1 | 80 | 90 |
| 2 | 90 | 95 |
| 3 | 91 | 98 |
| 4 | 95 | 92 |
| 5 | 93 | 95 |
| 6 | 98 | 75 |
| 7 | 92 | 89 |
| 8 | 95 | 77 |
| 9 | 94 | 72 |
| 10 | 97 | 50 |
| Mean | 93 (5) | 87 (10) |

The Dice overlap between FWHM and the algorithm for human and animal data sets. The Dice ranges between 0 and 100 where 100 represents perfect overlap.

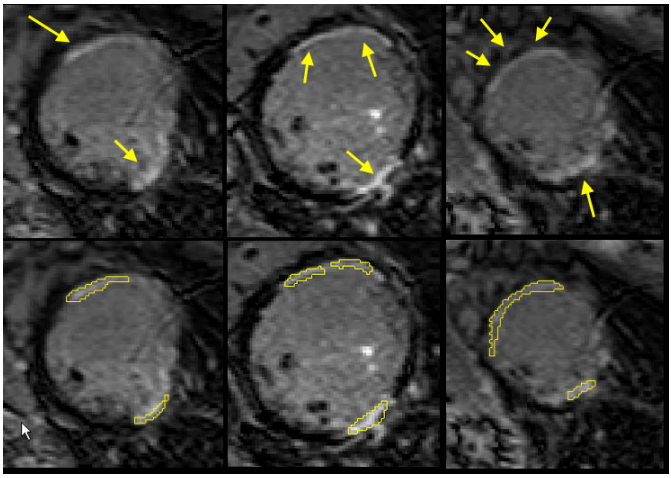

**Fig. 4.** Patient data: Original DE-MRI scans (top row) and their corresponding graph-cut segmentations (bottom row)

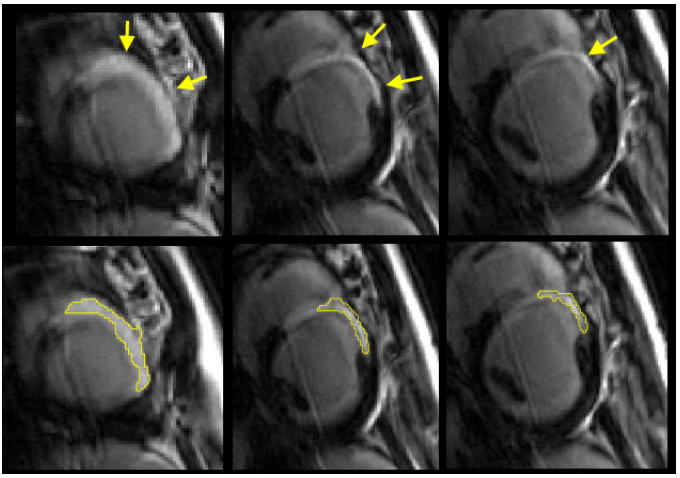

**Fig. 5.** Animal data: Original DE-MRI scans (top row) and their corresponding graph-cut segmentations (bottom row)

### 3.4 Conclusions

The proposed work employs a graph-cut implementation to maximize the MAP estimate and obtain the most likely (i.e. optimal) segmentation for infarct, given the observed and training data. The algorithm was tested on both patient and animal DE-MRI by utilizing the training data from each separately. Results from the algorithm were verified by a clinician qualitatively and were deemed suitable for clinical applications. Furthermore, quantitative validation with FWHM, currently the gold-standard in infarct quantification, shows good agreement.

Quantification of acute and chronic infarction in the myocardium is a challenging problem and has important prognostic implications in patients suffering from heart-related illnesses. Existing techniques rely on setting a standard cut-off intensity value for infarct and it is yet not clear why fixing a global intensity value would generate accurate segmentations. Given the quality of images obtained in clinical practice and as seen in the mix provided within this challenge, it is becoming clear that techniques which exploit local information are more likely to generate accurate segmentations. Furthermore, any quantification algorithm intended to be used in clinical practice must be tested against multi-center studies. Future work will further include a more detailed quantitative evaluation with ground-truth information.

**Acknowledgements.** The authors would like to thank the members of the Division of Biomedical Engineering and Imaging Sciences, Kings College London, who assisted with this study. This work was funded by a research grant from the Medical Engineering Council (MEC) of UK.

## References

1. Flett, A., Hasleton, J., Cook, C., Hausenloy, D., Quarta, G., Ariti, C., Muthurangu, V., Moon, J.: Evaluation of techniques for the quantification of myocardial scar of differing etiology using cardiac magnetic resonance. JACC Cardiovascular Imaging 4(2), 150 (2011)
2. Amado, L., Gerber, B., Gupta, S., Rettmann, D., Szarf, G., Schock, R., Nasir, K., Kraitchman, D., Lima, J.: Accurate and objective infarct sizing by contrast- enhanced magnetic resonance imaging in a canine myocardial infarction model. Journal of the American College of Cardiology 44(12), 2383–2389 (2004)
3. Boykov, Y., Veksler, O., Zabih, R.: Fast approximate energy minimization via graph cuts. IEEE Transactions on Pattern Analysis and Machine Intelligence, 1222–1239 (2001)
4. Boykov, Y., Funka-Lea, G.: Graph cuts and efficient nd image segmentation. International Journal of Computer Vision 70(2), 109–131 (2006)
5. Rother, C., Kolmogorov, V., Blake, A.: Grabcut: Interactive foreground extraction using iterated graph cuts. ACM Transactions on Graphics (TOG) 23, 309–314 (2004)
6. Song, Z., Tustison, N., Avants, B., Gee, J.C.: Integrated Graph Cuts for Brain MRI Segmentation. In: Larsen, R., Nielsen, M., Sporring, J. (eds.) MICCAI 2006. LNCS, vol. 4191, pp. 831–838. Springer, Heidelberg (2006)
7. van der Lijn, F., den Heijer, T., Breteler, M., Niessen, W.: Hippocampus segmentation in MR images using atlas registration, voxel classification, and graph cuts. NeuroImage 43(4), 708–720 (2008)
8. Boykov, Y.: University of western ontario vision group wiki page. Source code for implementation of the max-flow/min-cut problem (January 2010)
9. Dice, L.: Measures of the amount of ecologic association between species. Ecology 26(3), 297–302 (1945)

# Hierarchical Conditional Random Fields for Myocardium Infarction Detection

Zahra Karimaghaloo[1], Hassan Rivaz[2], and Tal Arbel[1]

[1] Center for intelligence machine, McGill university, Montreal, Canada
[2] Brain Imaging Center, McGill University, Montreal, Canada

**Abstract.** Accurate detection and delineation of myocardium infarction is important for treatment planning in patients with heart disease. Delayed contrast enhanced magnetic resonance imaging (DE-MRI) is a well established technique for the assessment of myocardial infarction. However, manual delineation of myocardium infarction in DE-MRI is both time consuming and prone to intra and inter rater variability. In this paper, we present an automatic, probabilistic framework for segmentation of myocardium infarction using Hierarchical Conditional Random Fields (HCRFs). In each level, a CRF classifier with up to triplet clique potentials is learnt. Furthermore, incorporation of spin image features in the second level allows for better learning the neighbourhood characteristics. The performance of the HCRF classifier on 5 animal scans and 5 human scans shows promising results.

## 1 Introduction

In patients with chronic ischemic heart disease, the myocardium infarction size is used to evaluate the performance of treatment strategies. Hence, detection and segmentation of myocardium infarction is of great importance in scientific studies and clinical trials. Contrast enhanced magnetic resonance imaging has been widely used for this purpose. However, in addition to being laborious and time consuming, manual detection is prone to intra - and - inter expert variability making the analysis of the results very complicated. Therefore, it is desirable to have a fully automatic segmentation scheme for infarction detection in studies with large ensemble of patient data. The previous work mainly suggest using threshold based methods other non-probabilistic approaches to address this problem [1,2]. In contrary, we propose a fully automatic and probabilistic approach based on Hierarchical Conditional Random Fileds (HCRF) [3,4]. Our HCRF framework includes a first level CRF classifier with unary, pairwise and triplet potentials to obtain infarction candidates, and a second level CRF classifier with the incorporation of spin image features.

## 2 Method

The goal of image classification or segmentation is to assign each voxel in the image a label, from a finite set of possible labels. Let us denote $\mathbf{x}_i \in \Re^d$ as the

O. Camara et al. (Eds.): STACOM 2012, LNCS 7746, pp. 80–86, 2013.

observation vector (e.g. intensity values) at the voxel $i$ and $y_i \in \{1, 0\}$ as the label of the $i^{th}$ instance (e.g. infarct vs. non-infarct). Given a test image, $X$, the goal of a probabilistic classifier is to infer the posterior distribution of its labels given the observations, i.e $p(Y|X)$ where $X = \{\mathbf{x}_i\}_1^n$, $Y = \{y_i\}_1^n$ and $n$ is the total number of voxels. Since the labels of neighbouring voxels are typically correlated, neighbourhood information is incorporated by building a graphical model, G(V;E), where voxels are represented by a set of nodes (V) and the relationships among them are represented by edges (E).

### 2.1 First Level CRF

At the first level of inference, we develop a Conditional Random Field (CRF) [5] classifier at the voxel level. A CRF is a discriminant graphical model that directly estimates the parameters of the conditional posterior, $p(Y|X)$, by learning a mapping from observations to class labels. Conventional CRF is generally formulated as energy functions defined on unary and pairwise cliques. In this work we go beyond the pairwise interactions by also considering triplet interactions in the energy function:

$$p(Y|X) = \frac{1}{Z} \exp(\sum_{i=1}^{n} \phi(y_i|X) + \sum_{j \in N_i} \varphi(y_i, y_j|X) + \sum_{j,k \in N_i} \psi(y_i, y_j, y_k|X))) \quad (1)$$

where $Z$ is the normalization term. $\phi$, $\varphi$ and $\psi$ are the *unary* , *pairwise* and *triplet* potentials at the voxel level respectively. The unary potential is modeled as:

$$\phi(y_i|X) = \log\ p(y_i|\mathbf{x}_i) = \log(\sigma(g(\mathbf{x}_i))) \quad (2)$$

where $\mathbf{x}_i$ is the observation vector at voxel $i$ and $\sigma$ denotes the sigmoid function. Similar to [6], we use a Relevance Vector Machine (RVM) classifier to model $p(y_i|\mathbf{x}_i)$. RVM [7] is a discriminant classifier that models the probability distribution of the labels by learning the decision boundary $g(\mathbf{x}_i)$ within a Bayesian framework. The RVM classifier has a several advantages: 1- It can provide a good generalization performance comparable to SVM. 2- It can obtain a sparser model and use a wider kernel function than SVM. 3- It does not need the estimation of the error/margin tradeoff parameters. 4- It is much easier to be implemented. Hence, RVM has been applied more and more in various fields [8].

The pairwise and triplet potentials in a CRF model permits learning the relationships between the labels of neighbouring nodes given the observed data and/or incorporating prior knowledge on their labels. The final inference in the first level is obtained with finding the best labeling that maximizes Eq. 1. This is achieved through a graph cut optimization framework [9].

### 2.2 Second Level CRF

After the fist level of CRF, a novel intensity-domain descriptor called *spin image* [10,11] is computed for all of the remaining voxels. The spin image is a

two-dimensional histogram encoding the distribution of image brightness values in the neighbourhood of a particular reference (center) point. The two dimensions of the histogram are $d$, distance from the center point, and $i$, the intensity value. The slice of the spin image corresponding to a fixed $d$ is simply the histogram of the intensity values of pixels located at a distance d from the center. Fig. 1 shows the principle behind the construction of spin images.

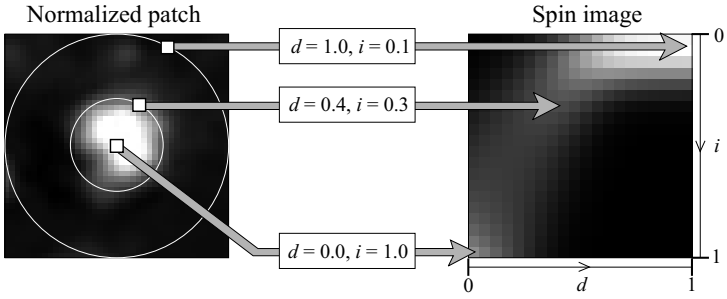


**Fig. 1.** The original image and its spin image descriptor are shown in the left and right images respectively. Each white circle in the left image correspond to a constant d (i.e. a vertical line in the right image). The mapping between three sample pairs is shown as well (Figure from [10] ).

Given a query image, after applying the first level CRF, the spin image descriptors of the remaining voxels are computed. Similar to the first level (Eq. 1), a CRF classifier is trained where besides the intensity at each voxel, the spin image features are used as well. Likewise, the final inference is performed via a graph cut optimization framework [9].

## 3 Experiments and Results

### 3.1 Data Pre-processing

The contrast enhanced MRI data was acquired from 15 human patients and 15 pigs with varying amounts of infarction. The MRI image intensity can vary significantly due to variations in acquisition protocols, scanner differences, etc. As a result, intensity normalization plays an important role in standardizing the tissue intensities across different MRI volumes. In our study, the intensity range of all volumes is normalized using a method suggested by Nyul *et al.* [12] (The intensity profile of the human data and that of the animal data are normalized separately). 5 MRI volumes from each group are used as the training data.

In principal any discriminant classifier can be used for modeling the unary potential. In our analysis, the unary potential in the first level is modeled using an RVM classifier for both human and animal data. Similarly, the unary potential in the second level is also modeled using an RVM classifier for the human data.

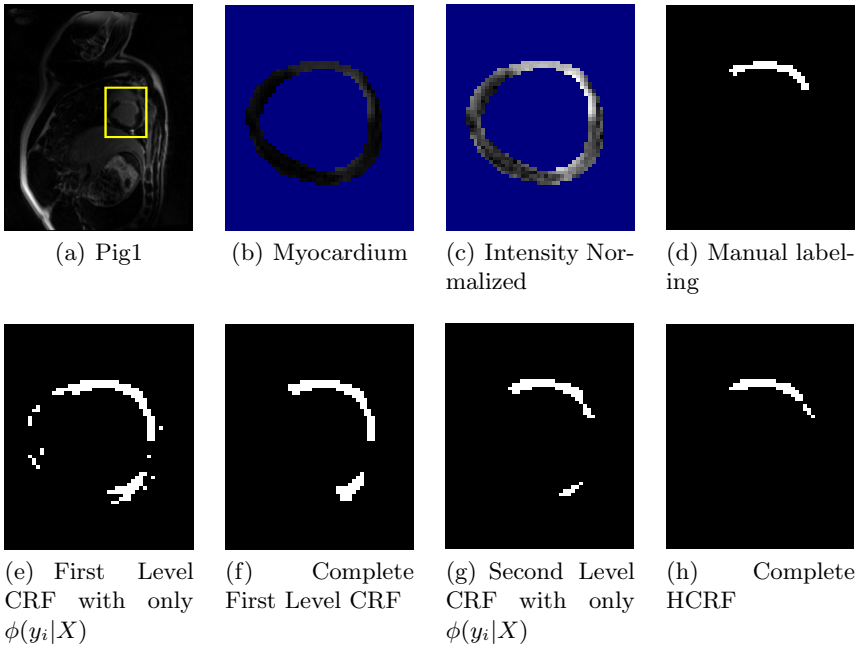

(a) Pig1 (b) Myocardium (c) Intensity Normalized (d) Manual labeling

(e) First Level CRF with only $\phi(y_i|X)$ (f) Complete First Level CRF (g) Second Level CRF with only $\phi(y_i|X)$ (h) Complete HCRF

**Fig. 2.** The performance of the different components of the proposed HCRF classifier shown for two example slices from pig data. The shown images are: the delayed MRI (a), the delayed MRI only showing the myocardium tissue (b), Nyul intensity normalization of the myocardium (c), the manual labels of myocardium infarction (d), the classification results using only the unary potential (e), the classification result using the complete CRF model (Unary, pairwise and triplet potentials) at the first level (f), the classification result of the second level with using only the unary potential (g), the classification result of the complete HCRF model (h).

However, it was observed that for the animal data modelling the unary potential with a KNN classifier yields better results. Furthermore, in human cases there is a large number of pixels to be analyzed due to the large size of the myocardium (compared to the animal cases) which cannot be processed at once because of computational limitations and training complexity. Therefore, we adapted a boosting technique to select an efficient subset of training samples for learning the unary classifier [13]. This strategy both decreases the training time and increases the learning efficiency by incorporating the harder samples in to the training set.

### 3.2 Qualitative Results

Fig. 2 and Fig. 3 show examples of the performance of the various components of the HCRF framework for the animal and human cases, respectively. Comparing Fig.2 (b) and Fig.2 (c) (similarly Fig.3 (b) and Fig.3 (c)), we observe the effect

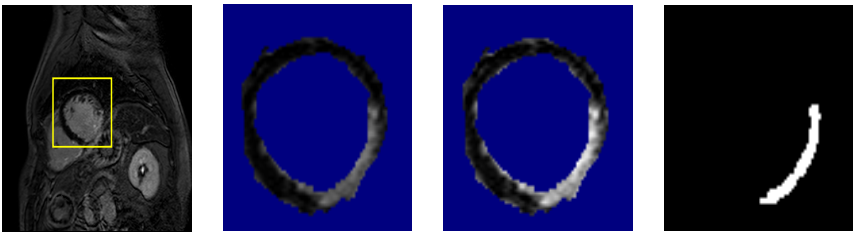

(a) Patient11 (b) Myocardium (c) Intensity Normalized (d) Manual labeling

(e) First Level CRF with only $\phi(y_i|X)$ (f) Complete First Level CRF (g) Second Level CRF with only $\phi(y_i|X)$ (h) Complete HCRF

**Fig. 3.** The performance of the different components of the proposed HCRF classifier shown for one example slice from human data. The shown images are: the delayed MRI (a), the delayed MRI only showing the myocardium tissue (b), Nyul intensity normalization of the myocardium (c), the manual labels of myocardium infarction (d), the classification results using only the unary potential (e), the classification result using the complete CRF model (Unary, pairwise and triplet potentials) at the first level (f), the classification result of the second level with using only the unary potential (g), the classification result of the complete HCRF model (h).

of the intensity normalization on enhancing the contrast between the infarction and the healthy tissues. Furthermore, it is observed that the result of the unary potential (Fig.2 (e) and Fig.3 (e)) in the first level yields too many false positives which are removed by adding the neighbourhood information through the incorporation of the pair-wise and triplet potentials (Fig.2 (f) and Fig.3 (f)). In the second level, by effectively learning the neighbourhood characteristics through the incorporation of the spin image feature, more false positives are removed (Fig.2 (g) and Fig.3 (g)). Finally, the complete HCRF model yields very similar results to the manual labelling (Fig.2 (h) and Fig.3 (h)).

### 3.3 Quantitative Results

The performance of different components of our HCRF model is also quantitatively evaluated in Table 1 and Table 2. Let us denote True Positive, False

**Table 1.** Leave one out cross validation results for different components of the model for animal data. The first and second columns show the first level CRF using only the unary ($CRF_1(\phi)$) and the combination of the unary, pairwise and triplet potentials ($CRF_1(\phi, \varphi, \psi)$), respectively. The third column shows the classification result of the second level CRF using only the unary term ($CRF_2(\phi)$ ). Finally, the last column (HCRF) is the proposed hierarchical model.

| | $CRF_1(\phi)$ | $CRF_1(\phi, \varphi, \psi)$ | $CRF_2(\phi)$ | **HCRF** |
|---|---|---|---|---|
| Sensitivity | 0.91 | 0.89 | 0.76 | 0.74 |
| FPR | 0.22 | 0.10 | 0.08 | 0.06 |
| PPV | 0.27 | 0.43 | 0.49 | 0.53 |

**Table 2.** Leave one out cross validation results for different components of the model for human data. The first and second columns show the first level CRF using only the unary ($CRF_1(\phi)$) and the combination of the unary, pairwise and triplet potentials ($CRF_1(\phi, \varphi, \psi)$) respectively. The third column shows the classification result of the second level CRF using only the unary term ($CRF_2(\phi)$ ). Finally, the last column (HCRF) is the proposed hierarchical model.

| | $CRF_1(\phi)$ | $CRF_1(\phi, \varphi, \psi)$ | $CRF_2(\phi)$ | **HCRF** |
|---|---|---|---|---|
| Sensitivity | 0.86 | 0.84 | 0.68 | 0.65 |
| FPR | 0.21 | 0.13 | 0.09 | 0.07 |
| PPV | 0.31 | 0.42 | 0.48 | 0.51 |

Positive, True Negative and False negative pixels with TP, FP, TN and FN. The following metrics are calculated for comparison:

$$\text{Sensitivity rate} = \frac{TP}{TP+FN},$$
$$\text{False Positive Rate (FPR)} = \frac{FP}{FP+TN},$$
$$\text{Positive Predictive Value (PPV)} = \frac{TP}{TP+FP}.$$

As expected, the complete HCRF model has lowest FPR and highest PPV while maintaining the sensitivity in an acceptable range.

## 4 Discussion

In this paper a Hierarchical Conditional Random Field (HCRF) classifier is proposed to address the myocardium infarction segmentation. The proposed model has yielded promising results on the training cases of both human and pig data. The learnt model can be improved by including more training data

as 5 cases might not be enough to well represent a population. Specifically, for patients 4 and 5 (and possibly patient 6) we observed poor segmentation results as their intensity profiles are very different from that of the rest of available training patients.

## References

1. Hsu, L., Ingkanisorn, W., Kellman, P., Aletras, A., Arai, A.: Quantitative myocardial infarction on delayed enhancement MRI. Part I clinical application of an automated feature analysis and combined thresholding infarct sizing algorithm. Journal of Magnetic Resonance, 309–314 (2006)
2. Positano, V., Pingitore, A., Giorgetti, A., Favilli, B., Santarelli, M.F., Landini, L., Marzullo, P., Lombardi, M.: A fast and effective method to assess myocardial necrosis by means of contrast magnetic resonance imaging. Journal of Cardiovascular Magnetic Resonance, 487–494 (2005)
3. Kumar, S., Hebert, M.: A hierarchical field framework for unified context-based classification. In: International Conference on Computer Vision, pp. 1284–1291 (2005)
4. Karimaghaloo, Z., Arnold, D.L., Collins, D.L., Arbel, T.: Hierarchical Conditional Random Fields for Detection of Gad-Enhancing Lesions in Multiple Sclerosis. In: Ayache, N., Delingette, H., Golland, P., Mori, K. (eds.) MICCAI 2012, Part II. LNCS, vol. 7511, pp. 379–386. Springer, Heidelberg (2012)
5. Lafferty, J., McCallum, A., Pereira, F.: Conditional random fields: probabilistic models for segmenting and labeling sequence data. In: Conference on Machine Learning, pp. 282–289 (2001)
6. Karimaghaloo, Z., Shah, M., Francis, S., Arnold, D., Collins, D., Arbel, T.: Automatic detection of Gadolinium-enhancing multiple sclerosis lesions in brain MRI using conditional random fields. Transaction on Medical Imaging 31, 1181–1194 (2012)
7. Tipping, M.: Sparse Bayesian learning and the relevance vector machine. Journal on Machine Learning Research 1, 211–244 (2001)
8. Agarwal, A., Triggs, B.: Recovering 3D human pose from monocular images. Pattern Analysis and Machine Intelligence
9. Woodford, O.J., Torr, P.S., Reid, I., Fitzgibbon, A.: Global stereo reconstruction under second order smoothness priors. In: Computer Vision and Pattern Recognition (2008)
10. Lazebnik, S., Schmid, C., Ponce, J.: A sparse texture representation using local affine regions. Pattern Analysis and Machine Intelligence 27, 1265–1278 (2005)
11. Rivaz, H., Collins, D.L.: Self-similarity Weighted Mutual Information: A New Nonrigid Image Registration Metric. In: Ayache, N., Delingette, H., Golland, P., Mori, K. (eds.) MICCAI 2012, Part III. LNCS, vol. 7512, pp. 91–98. Springer, Heidelberg (2012)
12. Nyul, L., Udupa, J.: On standardizing the MR image intensity scale. Computer Assisted Tomography 42, 1072–1081 (1999)
13. Kalal, Z., Matas, J., Mikolajczyk, K.: Weighted sampling for large-scale boosting. In: British Machine Vision Conference (2008)

# Mixture-Model-Based Segmentation of Myocardial Delayed Enhancement MRI

Anja Hennemuth, Ola Friman, Markus Huellebrand, and Heinz-Otto Peitgen

Fraunhofer MEVIS,
Universitaetsallee 29, 28359 Bremen, Germany

**Abstract.** Myocardial viability assessment is an important task in the diagnosis of coronary heart disease. The measurement of the delayed enhancement effect, the accumulation of contrast agent in defective tissue, has become the gold standard for detecting necrotic tissue with MRI. The purpose of the presented work was to provide a segmentation and quantification method for delayed enhancement MRI. To this end, a suitable mixture model for the myocardial intensity distribution is determined based on expectation maximization and the comparison of the fit accuracy. The subsequent watershed-based segmentation uses the intensity threshold information derived from this model. Preliminary results are derived from an analysis of datasets provided by the STACOM challenge organizers. The segmentation provided reasonable results in all datasets, but the method strongly depends on the underlying myocardium segmentation.

## 1 Introduction

Viability assessment with MR imaging has become a gold standard for the detection of necrotic and fibrotic myocardial tissue. Its prognostic value in patients with coronary artery disease has been proven [1]. For the segmentation and quantification of myocardial regions, which exhibit delayed enhancement, commercially available tools offer basic methods such as thresholding two or three standard deviations above the average intensity value of a healthy myocardial region [2]. There exist different approaches to compute a threshold automatically [3], apply clustering methods [4], or classify myocardial voxels based on support vector machines [5].

The arterial vessels supplying the myocardium run from the epicardial surface inward. A shortening of blood supply is strongest at the vessel endings close to the endocardial surface. Therefore, in coronary artery disease infarctions start subendocardially and grow from the inner to the outer part of the myocardium. This fact has been considered in the approach of [6], who perform a feature analysis after the initial thresholding. In addition to checking the subendocardial distance, a 3D connectivity analysis is applied to remove false positive segmentations.

For therapy decisions, it is important to know the transmurality, the degree of penetration of myocardium with infarction from endocardium to the outer

O. Camara et al. (Eds.): STACOM 2012, LNCS 7746, pp. 87–96, 2013.

surface [7]. Newer approaches combine simple thresholding with the proposed assumptions about the typical scar shape and location to determine the actual extent of the diseased tissue region [8]. Elagouni et al. combine the proposed mixture model approach with a so-called *Fast Region Competition* [9]. This corresponds closely to an automatic seed detection with a subsequent region growing applying the threshold model derived from the mixture model.

The segmentation of microvascular obstructions, which occur in scans acquired in the early delayed enhancement phase, are only covered by few approaches. Hsu et al. include microvascular obstructions into the delayed enhancement segmentation via the assumption that they must be included in the outmost contour of the segmentation [6]. Saering et al. add the assumption of an intensity below two standard deviations of healthy myocardium [10].

The proposed approach integrates approaches from own previous work. It is based on assumptions on intensity distributions in myocardial delayed enhancement images, spatial properties of myocardial infarctions, and contrast agent distribution in diseased tissue.

### 1.1 Method

The presented dection and quantification method for myocardial infarctions is based on a segmentation of the heart muscle. Because the provided myocardial segmentations are coarse estimates, an interactive contour editing step is performed before the actual detection of delayed enhancement areas. The approach then combines a mixture model analysis of the myocardial intensities with a constrained watershed segmentation.

According to Dietrich et al. [11], the intensity distribution in MR image data depends on the actual acquisition parameters as well as the reconstruction algorithm. It can be either a Gaussian, a Rayleigh distribution, or a non-central $\chi$-distribution. These distributions are closely related to the Rician distribution shown in equation 1.

$$p(x|\mu,\sigma) = \frac{x}{2\pi\sigma^2}\int_0^{2\pi} e^{-\frac{\mu^2+x^2-2\mu x\cos\phi}{2\sigma^2}}d\phi \tag{1}$$

$$p(x|\mu,\sigma) = \frac{x}{\sigma^2}e^{-\frac{\mu^2+x^2}{2\sigma^2}}I_0\left(\frac{\mu x}{\sigma^2}\right) \text{ with} \tag{2}$$

$$I_0(x) = \frac{1}{2\pi}\int_0^{2\pi} e^{x\cos\alpha}d\alpha \tag{3}$$

$I_0$ is the modified zeroth order Bessel function of the first kind. For $\mu = 0$, corresponding with low intensities in the magnitude image, the Rician function takes the simpler form of the Rayleigh function (Eq. 4).

$$p(x|\sigma) = \frac{x}{\sigma^2}e^{-\frac{x^2}{2\sigma^2}} \tag{4}$$

For large $x$ the asymptotic form of the Bessel function is [12]:

$$I_0(x) \approx \frac{e^x}{\sqrt{2\pi x}}\left[1+\frac{1}{8x}+\frac{1\cdot 9}{2!(8x)^2}+\frac{1\cdot 9\cdot 25}{3!(8x)^3}+\cdots\right] \tag{5}$$

Thus, for large values of $\mu$, $P(x|\mu,\sigma)$ approximates a Gaussian (Eq. 6).

$$\begin{aligned} p(x|\mu,\sigma) &\approx \frac{x}{\sigma^2} e^{-\frac{\mu^2+x^2}{2\sigma^2}} \frac{e^{\frac{\mu x}{\sigma^2}}}{\sqrt{2\pi\frac{\mu x}{\sigma^2}}} \left[ 1 + \underbrace{\frac{1}{8\frac{\mu x}{\sigma^2}} + \frac{1\cdot 9}{2!\left(8\frac{\mu x}{\sigma^2}\right)^2} + \frac{1\cdot 9\cdot 25}{3!\left(8\frac{\mu A}{\sigma^2}\right)^3} + \cdots}_{\longrightarrow 0} \right] \\ &\approx \frac{1}{\sqrt{2\pi}\sigma} e^{-\frac{(x-\mu)^2}{2\sigma^2}} \sqrt{\frac{x}{\mu}}, \text{ with} x \approx \mu \\ &\approx \frac{1}{\sqrt{2\pi}\sigma} e^{-\frac{(A-\mu)^2}{2\sigma^2}} \end{aligned} \tag{6}$$

If $\sigma = 1$ the Rician is equivalent to a non-central $\chi$-distribution with two degrees of freedom.

In DE-MRI data myocardium normally appears dark to medium intense whereas the diseased myocardial tissue is supposed to show enhanced intensity values. For the intensity distribution of the myocardium in DE-MRI data, we therefore consider the following three models:

**Rician distribution.** Myocardial intensity distribution without delayed enhancement.

**Rician-Gaussian mixture.** Intensity distribution for diseased myocardium in conventional acquisitions and special cases of $\chi$-distributions if there are necrotic tissue regions.

**Gaussian mixture.** Intensity distribution for diseased myocardium in image data with Gaussian-distributed intensities.

It is normally desirable to choose either the Rician-Gaussian or the Gaussian mixture model depending on prior knowledge about the image sequence that was applied for data acquisition. If the Gaussian mixture is suitable for the given data, it is preferable because of the lower calculation expense for the parameter determination.

Generally, the mixture model fit can be formulated as the task of maximizing the likelihood of a given set of observations $X = \{x_1, ..., x_N\}$ with frequencies $h(x)$ by optimizing the parameters of the applied mixture model. Assuming that we have a set of two classes $C = \{c_{myo}, c_{DE}\}$ with a corresponding parameter set $\Omega = \{\theta_{myo}, \theta_{DE}\}$ that defines the fitted distributions, the likelihood to optimize is:

$$L(\Omega|X,C) = \ln\left(\prod_{x\in X} p(x,C|\Omega)^{h(x)}\right)$$

and the expected log-likelihood can be formulated as follows:

$$
\begin{aligned}
E_c\left[\ln\left(L\right)\right] &= E_c\left[\ln\left(\prod_{x\in X} p(x,C|\Omega)^{h(x)}\right)\middle| x\right] \\
&= E_c\left[\sum_{x\in X} h(x)\ln\left(p(x,C|\Omega)\right)\middle| x\right] \\
&= \sum_{x\in X} h(x) E_c\left[\ln\left(p(x,C|\Omega)\right)\right)] \\
&= \sum_{x\in X} h(x) \sum_{c\in C} p(c|x,\Omega)\ln(p(x|c,\Omega)p(c|\Omega))
\end{aligned}
$$

The optimal parameter set is then calculated with Expectation Maximization [13–15].

The STACOM data was delivered without additional information regarding the MRI sequence used for the image acquisition. Thus all three suggested distributions are fitted to the myocardial histogram in order to determine the optimal model. The best model is then chosen according to the average fit error.

The actual segmentation of the tissue regions that exhibit delayed enhancement uses a partial volume model derived from the fitted mixture model as shown in Figure 1. It is combined with a watershed-based segmentation approach that is derived from the assumptions about location and shape of myocardial infarctions. Necrotic tissue regions, which are visible in delayed enhancement images, are usually attached to the subendocardial border and form compact crescent

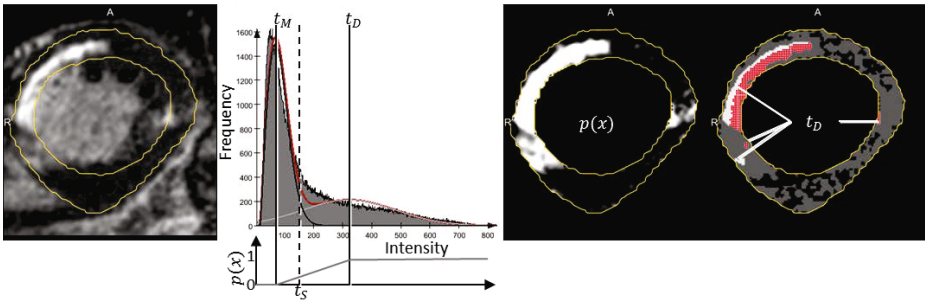


**Fig. 1.** Calculation of the partial volume model and the segmentation thresholds from the mixture model analysis. The leftmost image shows the original image with the myocardium segmentation. The resulting mixture model and derived thresholds are depicted in the diagram. The images on the right side of the diagram present the application of the partial volume function $p(x)$ and the threshold $t_D$, which is used for the detection of the seed points. Seed points are depicted as red dots. The rightmost image shows that they only appear in those regions located in the inner part of the myocardium.

shaped regions [16]. Taking this into account, in a first step seed voxels $v$ with an intensity value $x$ higher than the determined threshold $t_D$ are determined in the subendocardial layer of the myocardium. For these voxels the distance $d$ from the endocardial wall (*endo*) is shorter than that from the epicardial wall (*epi*):

$$\left(\frac{d(v, endo)}{d(epi, endo)} \leq 0.5\right) \wedge (p(x) = 1) \tag{7}$$

In the special case where the intersection $t_S$ of the two fitted distributions is not located between the maxima $t_M$ and $t_D$ we apply $t_S := t_D$. The seed voxels $v$ are used to define the basins included into the initial segmentation mask.
In an ensuing connected-component analysis, small noisy structures are identified and removed from the segmentation result.

Microvascular obstructions are not included in the initial segmentation. To add these so-called no-reflow areas, the image $I$ is divided into the sets $I_S$, $I_B$, and $I_H$. $I_S = S_{WT} \cup S_{BP}$ is the combination of the initial segmentation mask $S_{WT}$ delivered by the watershed transform and the bloodpool mask $S_{BP}$. $I_B$ contains the voxels not included in $I_S$ with a path to the image border that does not contain voxels of $I_S$, whereas $I_H = (I \setminus I_S) \setminus I_B$ contains those voxels of $I \setminus I_S$ without such a path. The final segmentation $I_R(v)$ can then be described as follows:

$$I_R(v) = \begin{cases} 1, & (v \in S_{WT} \cup I_H) \wedge (d(v, I_B) > 3) \\ p(x), & (v \in S_{WT} \cup I_H) \wedge (d(v, I_B) \leq 3) \\ 0, & v \notin S_{WT} \cup I_H \end{cases}, \; d(v, I_B) = \min_{v_i \in I_B} d(v, v_i) \tag{8}$$

$d(v, I_B)$ calculates the minimal voxel distance of the $v$ to the outer voxel set $I_B$. This method results in the filling of holes in the segmentation. Furthermore, the function $p(x)$ calculates wrong values for the delayed enhancement portion of the voxel at the transition from delayed enhancement to no-reflow areas. $I_R$ corrects these values as well.

## 2 Results

The presented methods have been evaluated with 30 DE-MRI data sets from post-myocardial infarction patients (15) and pigs (15), which have been provided by the organizers of the STACOM workshop.

Ground truth data is provided through manual segmentations from clinical experts. For the training phase, manual reference delineations of five patient datasets and five animal datasets are available.
The animal datasets have an in-plane resolution of $1.791 \times 1.791\,\text{mm}^2$ and a spacing between slices of 6 mm. In the patient datasets of the training set the in-plane resolution varies between $0.625 \times 0.625\,\text{mm}^2$ and $1.293 \times 1.293\,\text{mm}^2$. The spacing between slices is 2 to 8 mm.

The computation time was between 5 and 15 seconds per dataset, and the major part of this time was needed for the calculation of the Rice function

parameters. Infarct regions were detected in all training datasets. Either the mixture of two Gaussians or the Rician-Gaussian mixture model were chosen as the best description of the given myocardial intensity distribution (cf. Fig. **??**).

**Table 1.** Dice coefficients for the assessment of the overlap between the manual segmentations by experts and the automatic segmentations from the presented algorithm

| **Animals** | | **Humans** | |
|---|---|---|---|
| Case | Dice | Case | Dice |
| 1 | 0.56 | 11 | 0.67 |
| 2 | 0.65 | 13 | 0.47 |
| 3 | 0.78 | 4 | 0.52 |
| 4 | 0.84 | 5 | 0.47 |
| 5 | 0.75 | 7 | 0.38 |

Table 1 shows the results of the comparison of the manually determined groundtruth data using the Dice coefficient $D$. The overlap between the segmentation results is calculated as $D = \frac{2|V_{\text{man}} \cap V_{\text{auto}}|}{|V_{\text{man}}|+|V_{\text{auto}}|}$.

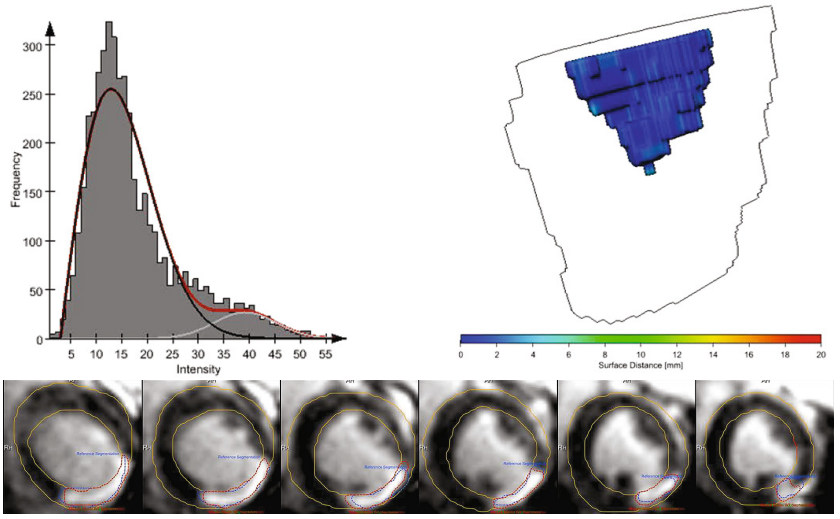


**Fig. 2.** Mixture model fit and surface distance comparison for animal 4. The grey area in the diagram represents the myocardial histograms. The red curve is the sum of the black curve and the white curve. These curves represent the intensity distributions of healthy and diseased myocardium according to the fitted mixture model. The 3D visualization of the segmentation right of the diagram is colored according to the distance from the ground truth. In the 2D views the reference segmentation is shown as a blue contour whereas the mixture model segmentation contour as well as the initial seed points are colored red. For this case the Rician-Gaussian mixture was chosen as the best model, and the segmentation result matches the reference segmentation very well.

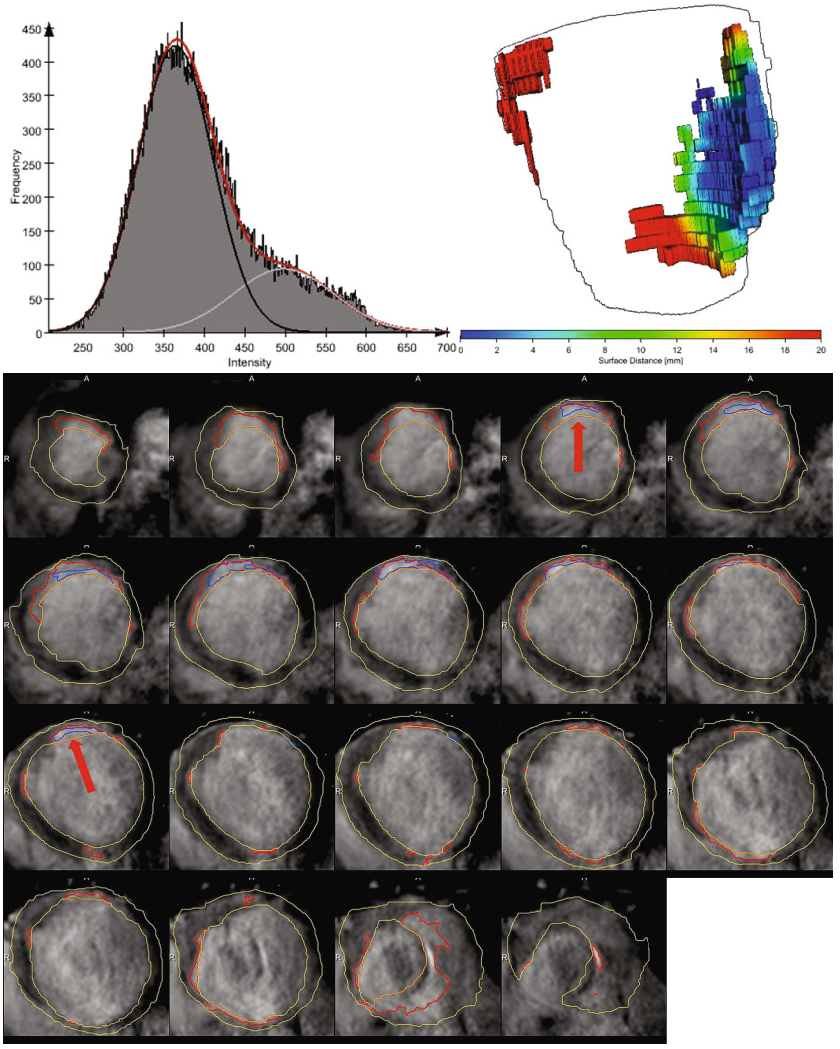


**Fig. 3.** Mixture model fit and surface distance comparison for patient 5. The diagram shows the histogram (grey area) and the fitted mixture model (black curve: healthy myocardium, white curve: DE, red curve: sum ). In the 3D visualization the color of the segmentation surface indicates the distance from the ground truth. In the 2D views, the segmentation results are shown as contours (blue: reference, red: mixture model segmentation). The red dots show the automatically detected segmentation seed points. For this case, the Gaussian mixture was as good as the Rician-Gaussian. However, the comparison with the reference segmentation clearly shows the overestimation of the infarct area by the mixture model segmentation.

To this end, a threshold of 0.75 was applied to derive a binary mask from the partial volume map that is originally provided by the algorithm. This mask was also used to calculate and visualize the surface distance between the ground truth and the result of the presented approach.

Figure 2 and 3 show the results for animal 4 and human 5. In the animal case, the Rician-Gaussian mixture model provided the best fit, and the segmentation overlap with the ground truth segmentation is very good. For the human case however, the Gaussian mixture suitable model for the myocardial intensity distribution. Although, the location of the detected infarction matches the ground truth very well, the extent of the segmented region clearly exceeds the reference result.

## 3 Discussion

Although there was an agreement between the automatic segmentation and the ground truth in all training cases, the overlap according to the Dice coefficient was moderate. The visual inspection as presented in Figure 3 showed that this was generally caused by an overestimation of infarct regions through the algorithm. For patient 5, delayed enhancement was even detected at locations, which were not identified by the expert.

A major weakness of the method is the strong dependence on the underlying myocardium segmentation. If the endocardial border is inaccurate, the algorithm tends to add blood pool voxels to the segmentation. Furthermore, partial volume effects close to the outflow tract can lead to false results as shown in Figure 4.

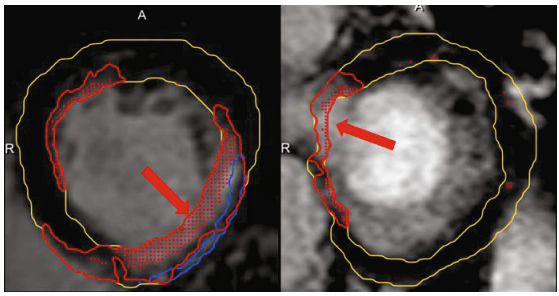


**Fig. 4.** Segmentation problems based on inappropriate assumptions. On the image slices above, the given myocardium segmentation is shown as a yellow contour. The reference segmentation is shown as a blue contour. The seed points as well as the resulting contour of the mixture model segmentation are colored red. The image on the left shows a strong overestimation of the infarct segmentation caused by the assumption that relevant infarct regions are located subendocardial. In this case, the provided myocardium segmentation is so coarse that this supposition is not suitable. The image on the right shows an inclusion of the outflow tract into the delayed enhancement segmentation. The original method does not consider the inclusion of such regions in the myocardium segmentation and has to be extended in order to recognize this.

One method to make the method more robust against the inclusion of blood-pool voxels is to extend the mixture model with a Gaussian that represents the blood pool intensities. Figure **??** shows an example for the improvement achieved with the integration of an additional compartment in the intensity distribution model. To make the method more robust against errors in the outflow tract region, it could be helpful to apply location assumptions not only about the relative position within the myocardial wall but also about the position relative to the heart anatomy.

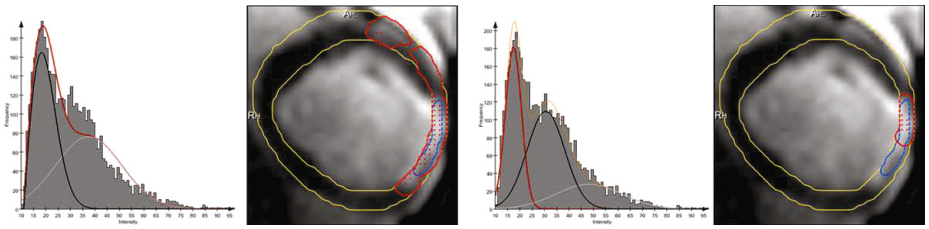

**Fig. 5.** Comparison of the results achieved with the intensity distribution models consisting of two (left) and three (right) Gaussians respectively. In the right image the red region, which represents the result of the automatic segmentation, matches the blue reference segmentation much better than in the left image.

## 4 Conclusions

We presented an approach for the segmentation of delayed myocardial enhancement in patients with coronary artery disease. The approach is based on the selection of a model for the myocardial intensity distribution. If a mixture model is the best description of the given intensity distribution, it is used to derive the thresholds and the partial volume function for the segmentation and quantification of the delayed enhancement regions. The segmentation is performed with automatically determined seed points and a watershed transform. The application to the training data of the STACOM DE-MRI challenge resulted in a moderate overlap with the provided ground truth data. Future work should therefore focus on enhancing the robustness against input segmentation through advanced segmentation constraints.

## References

1. Gerber, B.L., Rousseau, M.F., Ahn, S.A., le Polain de Waroux, J.B., Pouleur, A.C., Phlips, T., Vancraeynest, D., Pasquet, A., Vanoverschelde, J.L.J.: Prognostic value of myocardial viability by delayed-enhanced magnetic resonance in patients with coronary artery disease and low ejection fraction: impact of revascularization therapy. J. Am. Coll. Cardiol. 59(9), 825–835 (2012)

2. Kim, R., Fieno, D., Parrish, T., Harris, K., Chen, E., Simonetti, O., Bundy, J., Finn, J., Klocke, F., Judd, R.: Relationship of MRI delayed contrast enhancement to irreversible injury, infarct age, and contractile function. Circulation 100(19), 1992–2002 (1999)
3. Kolipaka, A., Chatzimavroudis, G., White, R., O'Donnell, T., Setser, R.: Segmentation of non-viable myocardium in delayed enhancement magnetic resonance images. Int. J. Cardiovasc. Imaging 21(2-3), 303–311 (2005)
4. Positano, V., Pingitore, A., Giorgetti, A., Favilli, B., Santarelli, M., Landini, L., Marzullo, P., Lombardi, M.: A Fast and Effective Method to Assess Myocardial Necrosis by Means of Contrast Magnetic Resonance Imaging. Journal of Cardiovascular Magnetic Resonance 7(2), 487–494 (2005)
5. O'Donnell, T., Xu, N., Setser, R., White, R.: Semi-automatic segmentation of nonviable cardiac tissue using cine and delayed enhancement magnetic resonance images. In: Proceedings of SPIE, vol. 5031, p. 242 (2003)
6. Hsu, L., Natanzon, A., Kellman, P., Hirsch, G., Aletras, A., Arai, A.: Quantitative myocardial infarction on delayed enhancement MRI, part I: animal validation of an automated feature analysis and combined thresholding infarct sizing algorithm. J. Magn. Reson. Imaging 23, 298–308 (2006)
7. Choi, K., Kim, R., Gubernikoff, G., Vargas, J., Parker, M., Judd, R.: Transmural Extent of Acute Myocardial Infarction Predicts Long-Term Improvement in Contractile Function. Circulation 104(10), 1101–1107 (2001)
8. Tao, Q., Milles, J., Zeppenfeld, K., Lamb, H., Bax, J., Reiber, J., van der Geest, R.: Automated segmentation of myocardial scar in late enhancement MRI using combined intensity and spatial information. Magn. Reson. Med. 64(2), 586–594 (2010)
9. Elagouni, K., Ciofolo-Veit, C., Mory, B.: Automatic segmentation of pathological tissue in cardiac MRI. In: Proceedings of the IEEE International Symposium on Biomedical Imaging, pp. 472–475 (2010)
10. Saering, D., Ehrhardt, J., Stork, A., Bansmann, P., Lund, G., Handels, H.: Analysis of the Left Ventricle after Myocardial Infarction combining 4D Cine-MR and 3D DE-MR Image Sequences. In: Bildverarbeitung fuer die Medizin, pp. 56–60 (2006)
11. Dietrich, O., Raya, J., Reeder, S., Ingrisch, M., Reiser, M., Schoenberg, S.: Influence of multichannel combination, parallel imaging and other reconstruction techniques on MRI noise characteristics. Magn. Reson. Imaging 26(6), 754–762 (2008)
12. Abramowitz, M., Stegun, I.A.: Handbook of Mathematical Functions. Dover Publications (1965)
13. Hennemuth, A., Seeger, A., Friman, O., Miller, S., Klumpp, B., Oeltze, S., Peitgen, H.O.: A comprehensive approach to the analysis of contrast enhanced cardiac MR images. IEEE Trans. Med. Imaging 27(11), 1592–1610 (2008)
14. Friman, O., Hennemuth, A., Peitgen, H.O.: A Rician-Gaussian Mixture Model for Segmenting Delayed Enhancement MRI Images. In: ISMRM 2008, p. 1040 (2008)
15. Hennemuth, A., Friman, O., Huellebrand, M., Peitgen, H., Mahnken, A.: Semi-Automatic Quantification of Late Enhancement in CT and MRI Images. In: ISMRM 2012, p. 1251 (2012)
16. Hunold, P., Schlosser, T., Barkhausen, J.: Magnetic resonance cardiac perfusion imaging-a clinical perspective. Eur. Radiol. 16(8), 1779–1788 (2006)

# Infarct Segmentation Challenge on Delayed Enhancement MRI of the Left Ventricle

Rashed Karim[1], Piet Claus[3], Zhong Chen[1,2], R. James Housden[1], Samantha Obom[1], Harminder Gill[1], YingLiang Ma[1], Prince Acheampong[1], Mark O'Neill[1,2], Reza Razavi[1,2], Tobias Schaeffter[1], and Kawal S. Rhode[1]

[1] Division of Imaging Sciences and Biomedical Engineering, King's College London, United Kingdom
[2] Department of Cardiology, Guy's and St. Thomas' NHS Foundation Trust, London, United Kingdom
[3] Cardiovascular Imaging and Dynamics, Department of Cardiovascular Sciences, KULeuven, Leuven, Belgium

**Abstract.** This paper presents collated results from the Delayed Enhancement MRI (DE-MRI) segmentation challenge at MICCAI 2012. DE-MRI Images from fifteen patients and fifteen pigs were randomly selected from two different imaging centres. Three independent sets of manual segmentations were obtained for each image and included in this study. A ground truth consensus segmentation based on all human rater segmentations was obtained using an Expectation-Maximization (EM) method (the STAPLE method). Automated segmentations from five groups contributed to this challenge.

**Keywords:** Segmentation, Delayed-Enhancement MRI, Left ventricle, Segmentation Challenge.

## 1 Introduction

In this era of timely access to the cardiac catheterization lab, treatment of myocardial infarction shifts from survival to reducing infarct size, post-reperfusion myocardial vascular obstruction (MVO) and hemorrhage. In this setting, Contrast-Enhanced Magnetic Resonance Imaging (CE-MRI) has become an indispensable imaging modality to assess MVO, usually imaged a few minutes after contrast administration and also infarct size, assessed after 15 minutes and hence referred to as Delayed Enhancement MRI (DE-MRI) [1]. In the last decade infarct size assessed with DE-MRI has been increasingly used as a primary end-point in clinical studies. Moreover, interventions target the infarct border zone, and the use of fluoroscopy augmented with MRI-based anatomical models of the heart and infarct areas are entering the clinical work-flow (e.g. for VT ablation or localized delivery in cell-based therapies). These developments require both a relatively fast and accurate segmentation of the infarct region.

Manual delineation of the enhanced myocardial regions is relatively time consuming and requires training. Though expert consensus on delineation of myocardial infarction on DE-MRI can be reached, manual delineations still suffer

O. Camara et al. (Eds.): STACOM 2012, LNCS 7746, pp. 97–104, 2013.

from inter- and intra-observer variability. Automated thresholding based on the full-width half maximum signal intensity or a number of standard deviations above normal myocardial signal intensity, remain acquisition dependent.

In this challenge, DE-MRI images of left ventricles containing infarct regions, from both human and porcine studies, were provided to the participating groups along with a given myocardial segmentation. To minimize inter-observer variability in the ground-truth infarct segmentations, a probabilistic estimate was computed for each dataset from three different expert delineations.

## 2 Methods

### 2.1 MRI Data

Cardiac DE-MRI images were collected at two centers (King's College London (KCL) and Katholieke Universiteit Leuven (KUL)), providing fifteen human and fifteen porcine datasets. For all datasets a short axis stack of DE-MRI images covering the left ventricle were provided together with a mask of the left-ventricular myocardium. A sample of the datasets can be seen in Fig. 1.

The human datasets were randomly selected patients with a known history of ischaemic cardiomyopathy and under assessment for implantable cardioverter defibrillator (ICD) for primary or secondary preventions after infarction. In addition to this, the patients chosen had a history of myocardial infarction at least 3 months prior to their MRI scan along with evidence of significant coronary artery disease on angiography and evidence of left ventricular impaired systolic function on echocardiography. The images were acquired on a clinical 1.5T MRI unit (Achieva, Philips, The Netherlands)

The fifteen porcine studies were randomly selected from an experimental database of a pre-clinical model of chronic myocardial ischemia [2], with either left-anterior descending or left-circumflex artery induced lesions. Datasets were acquired six weeks after the induction of the coronary lesion on a clinical 3T MRI unit (Trio, Siemens, Erlangen, Germany). Details of the acquisition can be found in Table 1.

### 2.2 Raters

There were five automated raters or algorithms (UPF, MCG, MVS, KCL, ALM) and three expert human raters (HA, HB, HC) taking part in this study. Brief descriptions of the algorithms are given in Table 2.

### 2.3 Evaluation

The accuracy and performance of each algorithm was evaluated by comparing its segmentations against the human raters. For rater segmentations, the Simultaneous Truth And Performance Level Estimation (STAPLE) method [3] was used to obtain a single ground truth. STAPLE estimates the ground truth by forming

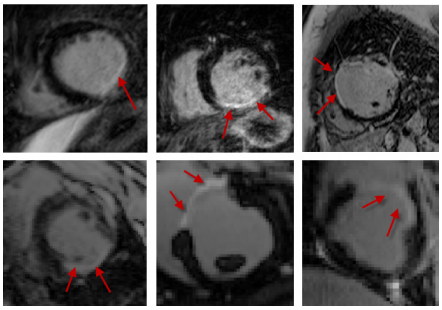

**Fig. 1.** Sample of the human (top row) and animal (bottom row) DE-MRI data provided to participants as part of the challenge. Red arrows indicate areas of enhancement.

**Table 1.** Image acquisition

| | **KCL** | **KUL** |
|---|---|---|
| **Scanner type** | Philips Achieva 1.5T | Siemens Trio 3.0T |
| **Sequence** | Segmented 2D, Inversion recovery Gradient Echo ECG triggered, breathold | Segmented 3D Inversion recovery Gradient Echo ECG triggered, breathold |
| **TI, TR, TE, FA** | 280 ms, 3.4 ms, 2.0 ms, 25° | 340-370 ms, 2.19 ms, 0.78 ms, 15° |
| **Voxel size** | $1.8 \times 1.8 \times 8$ mm | $1.8 \times 1.8 \times 6$ mm |
| **Interleaving** | Every RR | Every other RR |

Image acquisition parameters for the challenge DE-MRI data. Abbreviations: TI - Inversion time, TR - Repetition time, TE - Echo time, FA - Flip angle.

an optimal combination of the segmentations, by weighting each segmentation depending upon the estimated performance level, together with a prior model that can account for the spatial distribution of structures and spatial homogeneity constraint. In this work, the threshold set on the probabilities obtained from STAPLE was 0.7 and above for a pixel to be labeled as scar.

In addition to computing STAPLE of human rater segmentations, the STAPLE of all submissions was also computed with a leave-one-out approach. For example, UPF was tested against the STAPLE of KCL, MVS, MCG, ALM combined. This assessed how the submissions fared between themselves. To assess similarity between segmentations the Dice co-efficient was used [4]:

$$\mathcal{D} = \frac{2|X \cap T|}{|X| \cup |T|} \tag{1}$$

where $X$ and $T$ are sets of pixels belonging to the algorithm's output and ground truth respectively. The Dice is normalized to 100 for convenience. Furthermore,

**Table 2.** Algorithms presented at the challenge

| Algo. | Description | Auto or Semi-auto |
|---|---|---|
| UPF | Region growing and morphology | Auto |
| MCG | Conditional Random Fields (CRF) | Auto |
| MV | Gaussian mixture, EM-algorithm, Watershed transformation | Auto |
| KCL | Markov Random Fields, Graph-cuts | Auto |
| ALM | Support Vector Machines followed with Level-set evolution | Semi-auto |

Institution abbreviations: UPF - Universitat Pompeu Fabra, MCG - McGill University, MV - Mevis Fraunhofer, KCL - King's College London, ALM - Alma IT Systems.

the amount of infarct detected ($V_{\mathrm{IF}}$) represented as percentage of myocardium $V_{\mathrm{MYO}}$ was determined in all methods as:

$$\mathrm{IF}\% = \frac{V_{\mathrm{IF}}}{V_{\mathrm{MYO}}} \times 100\% \tag{2}$$

## 3 Results

Following the submission of results from each group of the challenge, segmentations were evaluated against the human rater segmentations using Dice and infarct volumes. The human and porcine images were analyzed separately.

### 3.1 Human Patient Datasets

Segmentations were compared to ground truth and between themselves with a leave-one-out approach (see example dataset in Fig. 2). Dice results can be seen in Fig. 3. To measure how much the infarct volumes (expressed as a percentage of total myocardium) differ from the human raters' segmentations, Bland-Altman plots are presented in Fig. 4.

### 3.2 Porcine Datasets

Similar to the patient datasets, segmentations were compared between ground truth and with the leave-one-out approach. An example on a dataset can be found in Fig. 5. The Dice comparison is given in Fig. 6. Difference in percentage of infarct volumes is shown in the Bland-Altman plots of Fig. 7.

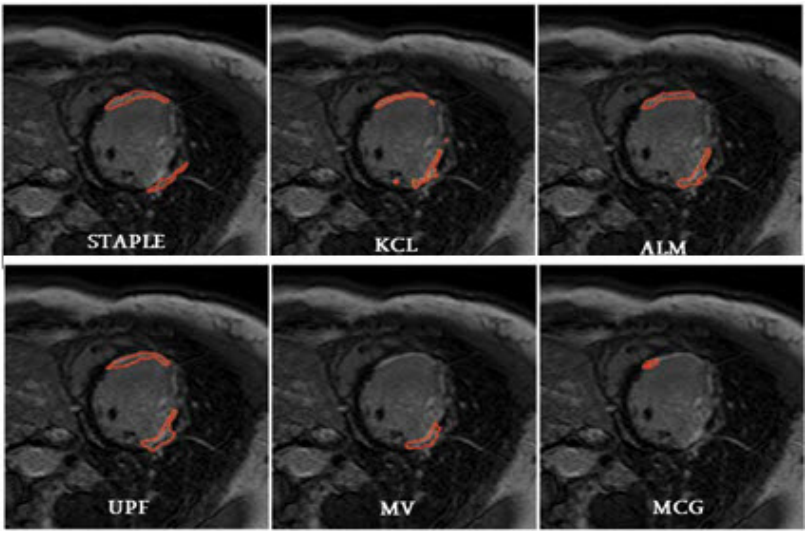


**Fig. 2.** Human Dataset: comparing STAPLE with submissions in a single slice of an example dataset

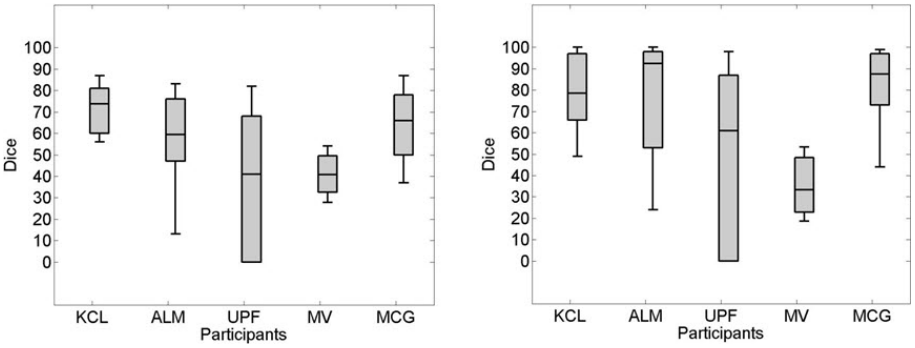


**Fig. 3.** Human Datasets: comparing segmentations from each submission using Dice - (Left) against STAPLE ground-truth, and (Right) against STAPLE of leave-one-out for each submission. For example, UPF here is tested against the STAPLE of KCL, MVS, MCG, ALM. Each box in the plot represents lower, middle and upper quartiles.

### 3.3 Discussion

A collation study for the DE-MRI segmentation of enhanced tissue representing fibrosis and scar has been presented in this work. A ground-truth segmentation was generated using the STAPLE algorithm combining three human rater segmentations. The performance of each algorithm taking part in the study was compared to the STAPLE estimate of the ground truth. Each algorithm's output was also compared to segmentations from other algorithms using a leave-one-out

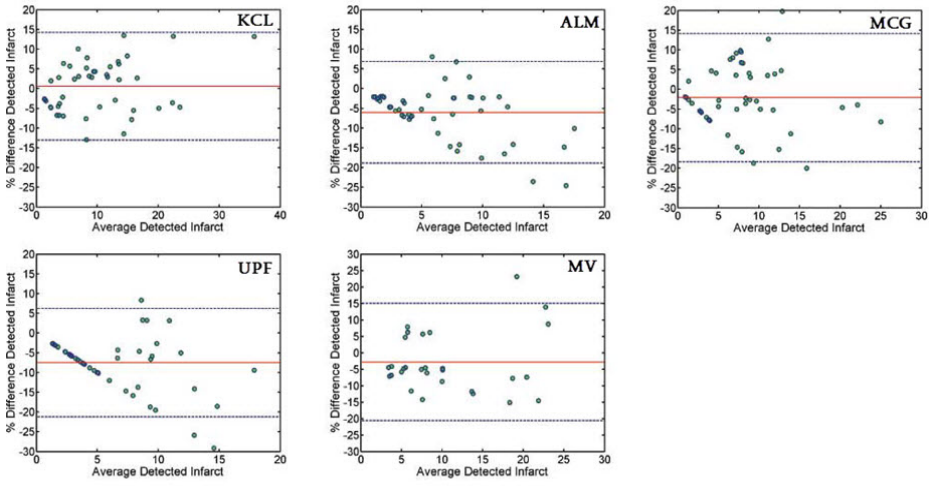


**Fig. 4.** Human Datasets: Bland-Altman plots showing differences in infarct volumes (%) in segmentations of each submission against STAPLE of human raters. The solid line shows the mean and the dashed lines show ±2 standard deviations.

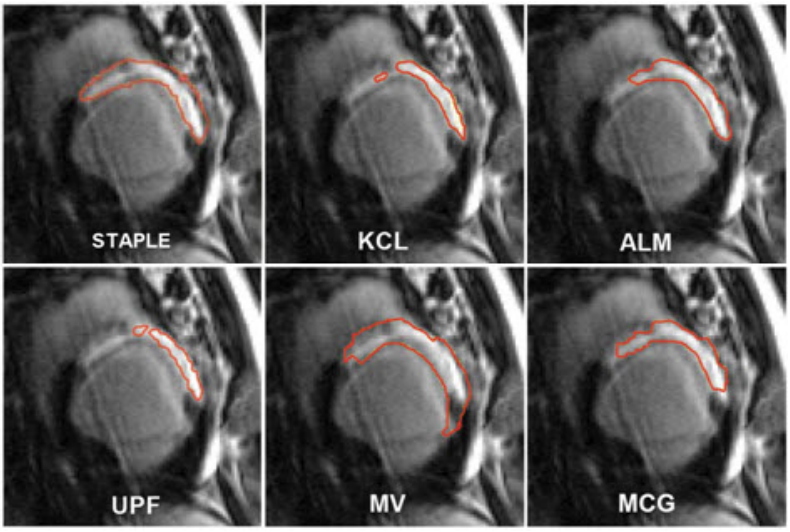


**Fig. 5.** Porcine Dataset: comparing STAPLE with submissions in a single slice of an example dataset

STAPLE result. The STAPLE method is able to resolve disagreement between human raters especially in regions where it is difficult to assert on infarction. In the ventricle, this is especially within the left ventricular outflow tract (LVOT) where fibrotic tissue making up the valve is not infarcted. Furthermore, using

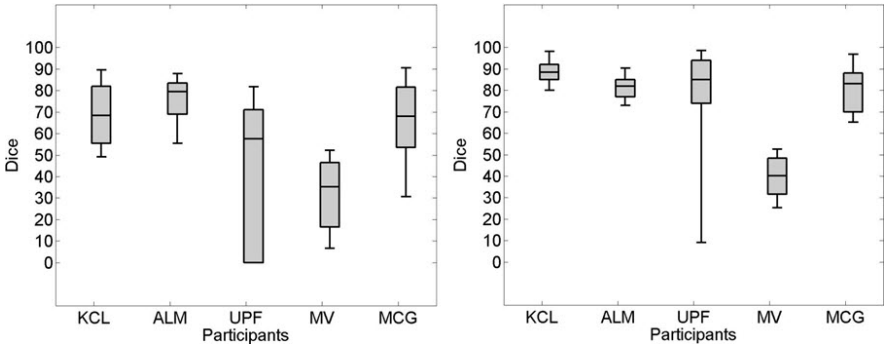


**Fig. 6.** Porcine Datasets: comparing segmentations from each submission using Dice - (Left) against STAPLE ground-truth, and (Right) against STAPLE of leave-one-out for each submission. Each box in the plot represents lower, middle and upper quartiles.

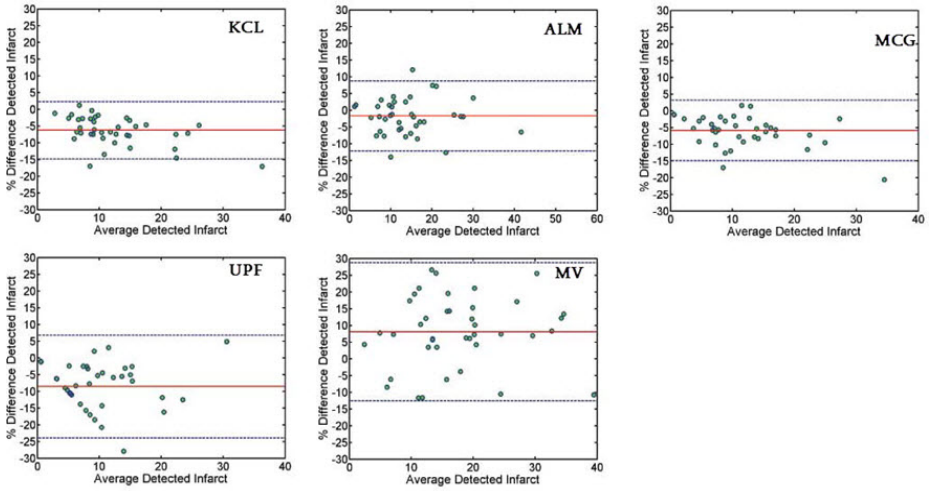


**Fig. 7.** Porcine Datasets: Bland-Altman plots showing differences in infarct volumes (%) in segmentations of each submission against STAPLE of human raters. The solid line shows the mean and the dashed lines show ±2 standard deviations.

the STAPLE result of the algorithms' outputs (i.e. leave-one-out approach), each algorithm's performance can be measured against the others and this reveals interesting insights into whether certain algorithms are computing scar in a similar fashion.

It was observed that in general, porcine scans produced better segmentations compared to human scans. One major contributing factor is the quality of porcine scans, providing excellent contrast for infarcted regions. In human datasets, it is often challenging to obtain good contrast due to the nature of the scan. For example, incorrect selection of inversion time causes myocardium

not to be nulled properly and if the patient cannot hold their breath during the scan it produces breathing artefacts. For patient scans, obtaining a Dice of 80 or above was challenging for all submissions. When considering infarct volumes, submissions differed by a maximum of approximately ±15% and ±10% for patient and porcine scans respectively. This further shows that segmenting patient scans was far more challenging.

The Dice used in this study has several limitations. It can be over-sensitive to a small mis-match. An alternative approach for comparison is thus considered. Comparing infarct using percentage volumes has become a simple and standard approach. Infarct volumes are computed on selected slices and represented in the difference plots of Figs. 4 and 7. Some patterns are notable, for example the data points which appear on a straight line in Fig. 4 (MCG and UPF) and Fig. 7 (UPF). This is due to the submission recording a zero volume for each of those data points and thus selected slice, resulting in a straight-line on the difference-vs-average plot.

A second limitation is the inter-observer variation of human rater segmentations. There was less variation in the porcine datasets than the human datasets. All datasets were segmented by individuals with experience working on these scans. They were segmented using ITK-SNAP (www.itk-snap.org) [5] which is a commonly used tool for performing manual segmentations.

### 3.4 Conclusions

The presented work reports on the preliminary results of the ventricle DE-MRI segmentation challenge at the MICCAI 2012 meeting. Future work will look to provide a more extensive analysis of the submitted results.

**Acknowledgements** The authors would like to thank the members of the Division of Biomedical Engineering and Imaging Sciences, King's College London, who assisted with this study. This work was funded by a research grant from the Medical Engineering Council (MEC), UK.

## References

1. Kellman, P., Arai, A.: Cardiac imaging techniques for physicians: Late enhancement. Journal of Magnetic Resonance Imaging 36(3), 529–542 (2012)
2. Wu, M., D'hooge, J., Ganame, J., Ferferieva, V., Sipido, K., Maes, F., Dymarkowski, S., Bogaert, J., Rademakers, F., Claus, P.: Non-invasive characterization of the area-at-risk using magnetic resonance imaging in chronic ischaemia. Cardiovascular Research 89(1), 166–174 (2011)
3. Warfield, S., Zou, K., Wells, W.: Simultaneous truth and performance level estimation (staple): an algorithm for the validation of image segmentation. IEEE Transactions on Medical Imaging 23(7), 903–921 (2004)
4. Dice, L.: Measures of the amount of ecologic association between species. Ecology 26(3), 297–302 (1945)
5. Yushkevich, P.A., Piven, J., Cody Hazlett, H., Gimpel Smith, R., Ho, S., Gee, J.C., Gerig, G.: User-guided 3D active contour segmentation of anatomical structures: Significantly improved efficiency and reliability. Neuroimage 31(3), 1116–1128 (2006)

# Discriminative Context Modeling Using Auxiliary Markers for LV Landmark Detection from a Single MR Image

Xiaoguang Lu* and Marie-Pierre Jolly

Siemens Corporation, Corporate Technology, Princeton, NJ, USA
xiaoguang.lu@siemens.com

**Abstract.** Cardiac magnetic resonance imaging (MRI) is a key diagnostic tool for non-invasive assessment of the function and structure of the cardiovascular system in clinical practice. Cardiac landmarks provide strong cues to navigate the complex heart anatomy, extract and evaluate morphological and functional features for diagnosis and disease monitoring. A fully automatic method is presented to detect cardiac landmarks from individual images using a learning-based approach to model discriminative context. In addition to the target landmarks, auxiliary markers are taken into consideration to construct context with more discriminative power. The presented approach is evaluated on the STACOM2012 database, containing 100 independent test cases. Automatic landmark detection targets include two mitral valve landmarks in a long axis image, two RV insert landmarks in a short-axis image, and one central axis point in an LV base image.

## 1 Introduction

Cardiac Magnetic Resonance (MR) imaging plays a vital role as a powerful non-invasive tool in clinical applications for diagnosis, prognosis, and therapy of cardiovascular diseases [1]. However, due to large data variations and complexity of the heart, automated analysis of cardiac images for quantification and modeling is essential but challenging [2].

Typical cardiac MR studies contain both long-axis and short-axis slices to provide complementary and comprehensive views. Cardiac landmarks are helpful in accurate and efficient 3D modeling and functional analysis of the heart [3–5], comprehensive heart navigation, common clinical cardiovascular MR imaging plane prescription, etc. However, it poses a great challenge to fully automatically detect landmarks from MR images due to the wide dynamic image intensity range, various heart shapes across patients and populations, etc.

We present a unified approach to detecting cardiac landmarks by exploring contextual geometry and image information. Cardiac landmarks are converted into parameterized bounding box representations, which fit into an object detection framework. Such representations embed not only individual landmarks

* Corresponding author.

O. Camara et al. (Eds.): STACOM 2012, LNCS 7746, pp. 105–114, 2013.

but also their context, which contains rich information to distinguish the cardiac landmark from its background and other anatomical structures. We apply a learning-based method to train detectors on context built from expert annotations in order to handle complex appearance and heterogeneous characteristics of anatomical features in medical images, as the complex prior knowledge is implicitly encoded into context. Learning based object detection approaches have been demonstrated to be successful in many applications [6, 7]. The presented approach provides a large flexibility to be applied to a wide range of anatomical structures and is fully automated.

To help reduce the ambiguity and complexity presented in the landmark detection task, we introduce auxiliary markers present in the same image as the target landmarks. These auxiliary markers along with the target landmarks take into account more contextual information present in the image and jointly lead to more discriminative power from the background. The auxiliary markers bear anatomical correlations with the target landmarks, providing clinically justifiable evidence to help landmark detection. With such better constrained contextual representations, parameter search ranges during online detection are greatly reduced, model learning complexity decreases for training, and the resulting contextual models are more powerful to lead to more accurate landmark detection results.

As part of the Statistical Atlases and Computational Models (STACOM) of the Heart 2012 workshop, the Cardiac Atlas Project [8] is running an LV Landmark Detection Challenge. The proposed method is evaluated on this landmark challenge dataset to automatically detect anatomical landmark points from cardiac MRI images. The target landmark points include two mitral valve points on a long-axis view image, two RV insert points on a short-axis image and the base central axis point on a short-axis base image. Our algorithm is focused on landmark detection in a single image.

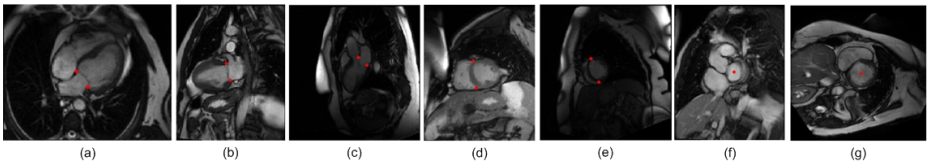


**Fig. 1.** Target Landmarks (red dots): two mitral valve points (a-c), two RV insert points (d,e), and one base central axis point (f,g)

## 2 Context-Based Landmark Detection

### 2.1 Learning-Based Detection Framework

A unified framework is developed to detect cardiac landmarks from MR images. Both target landmarks and auxiliary markers are integrated to construct context to feed into the same object detection framework. Such context is represented

by a bounding box as an object with 5 parameters (2 translations, 1 orientation, and 2 scales), as shown in Fig. 2. Each combination of such 5 parameters is one hypothesis, corresponding to one bounding box, and therefore one (oriented) image patch. A probabilistic learning approach [9] is applied to solve a two-class (object vs. background) classification task on such hypotheses. As each contextual bounding box has a bijective mapping with the target landmarks and auxiliary markers due to construction design, the target landmark positions can be inferred from the bounding box.

A 2D object (bounding box) parameter set consists of five degrees of freedom. Exhaustively searching in this 5-dimensional space is prohibitive for online applications. Therefore, we adopt the marginal space search strategy, where we design a series of detectors that estimate object parameters at a number of sequential stages in the order of complexity, i.e., translation, orientation, and scale, as the parameter degrees of freedom increase [10]. Different stages utilize different image features. Multiple hypotheses are maintained between algorithm stages, which quickly removes false hypotheses at the earlier stages while propagating the right hypotheses to the final stage. Only one hypothesis is consolidated as the final detection result.

Probabilistic boosting trees [9] are used for each detector to differentiate between the object and background. The classifier is a tree-based structure with which the posterior probabilities of the presence of the object of interest are calculated from image data. The nodes in the tree are constructed by a combination of simple classifiers using boosting techniques [9].

Each detector selects a set of discriminative features that are used to distinguish the object from the background from a large pool of features. For the classifiers at the translation stage, we choose Haar wavelet-like features [6], which are efficiently calculated using integral image-based techniques. For the classifiers at the orientation and scale stages, steerable features [10] are applied, because their computation does not require image rotation and re-scaling, which are computationally expensive, especially when the hypothesis search space is large.

### 2.2 Context Modeling with Auxiliary Markers

Auxiliary markers are bonded with the target landmarks at the anatomical level, thereby jointly providing more representational power for the target landmarks and discriminative power from the background. Selection of auxiliary markers depends on the target landmarks.

**Context Modeling for Mitral Valve Landmarks.** For each long-axis image, the two mitral valve points are combined to build one object. We associate a two-dimensional bounding box with this contextual object. The LV apex is introduced as the auxiliary marker to determine the orientation of the contextual bounding box, as shown in Fig. 2(a). Each bounding box is specified by a five-parameter set $\Theta$, containing two positions $< x, y >$, one orientation $< \phi >$, and two scales $< s_x, s_y >$. Although the positions are the targets, orientation and

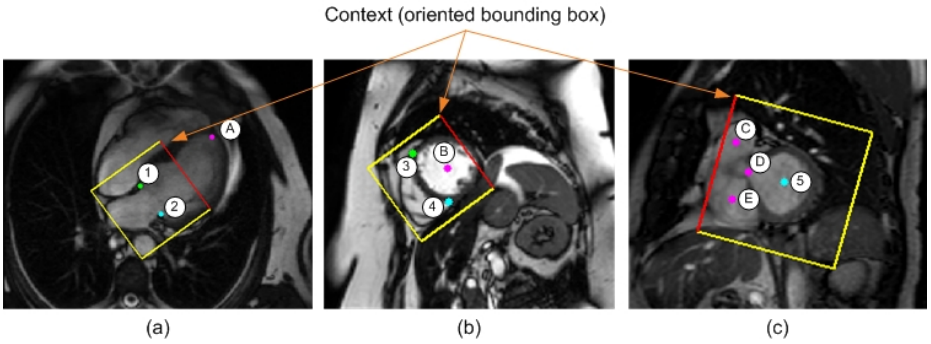


**Fig. 2.** Context construction with auxiliary markers for (a) Mitral valve, (b) RV insert, and (c) Base central axis. Markers 1-5 are the target landmarks. A-E are the auxiliary markers. Both target landmarks and auxiliary markers are used to construct context for each target, which is represented as an oriented bounding box. The red edge of the bounding box indicates the box orientation. And mapping between the marker positions and the context (bounding box) parameters is bijective by design.

scales are useful in encoding proper and consistent context learned during offline training process, where a set of contextual models/classifiers are obtained.

For mitral valve landmark detection, due to its complexity across different cardiac phases and views, we adopted a joint modeling scheme proposed by Lu et al. [7]. In addition to building context for mitral valve, context of apex and joint context for the pair of <mitral valve, apex> are also constructed as shown in Fig. 3, which are used for inter-marker validation. Let $< x_a, y_a >$, $< x_{b1}, y_{b1} >$, and $< x_{b2}, y_{b2} >$ denote the positions of the apex, and two mitral valve points, respectively.

The contextual parameters for the mitral valve are: position $\{(x_{b1} + x_{b2})/2, (y_{b1} + y_{b2})/2\}$; orientation {orthogonal to the line segment connecting the two mitral valve points, and pointing toward the apex}; and scales $\{s_b, s_b\}$, where $s_b = \sqrt{(y_{b2} - y_{b1})^2 + (x_{b2} - x_{b1})^2} * \alpha$, where $\alpha$ is a factor that can be used to adjust the contextual range and set to 2.4 in our experiments. Selection of $\alpha$ is a tradeoff between rich context and noise.

For the apex, the context parameters are constructed as: position $\{x_a, y_a\}$; orientation $\{arctan((y_a - (y_{b1}+y_{b2})/2)/(x_a - (x_{b1}+x_{b2})/2))\}$; and scales $\{s_a, s_a\}$, where $s_a = \sqrt{((y_{b2} - y_{b1})^2 + (x_{b2} - x_{b1})^2)} * \beta$ ($\beta$ is set to 2.4 in our experiments).

Let $< x_{mv}, y_{mv} >$ be the mitral valve center position (i.e., $\{(x_{b1}+x_{b2})/2, (y_{b1}+y_{b2})/2\}$). For joint context: positions $\{(x_a + x_{mv})/2, (y_a + y_{mv})/2\}$; orientation {center of mitral valve ($< x_{mv}, y_{mv} >$) pointing to the apex}; and scales $\{s_{J_x}, s_{J_y}\}$, where

$$s_{J_x} = \sqrt{((y_{mv} - y_a)^2 + (x_{mv} - x_a)^2)} * \gamma, s_{J_y} = \sqrt{(y_{b2} - y_{b1})^2 + (x_{b2} - x_{b1})^2} * \eta,$$

with $\gamma$=1.5 and $\eta$=4.8 in our experiments.

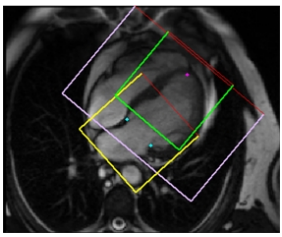

**Fig. 3.** Auxiliary context (represented by bounding boxes, where the red edge indicates the orientation) for mitral valve landmark detection. In addition to the mitral valve context (yellow), apex context (green) and joint context (purple) are taken into consideration for mitral valve landmark detection.

**Context Modeling for RV Insert Landmarks.** For each short-axis image, two RV insert points are combined to build one object. The LV center is introduced as the auxiliary marker to determine the orientation of the contextual bounding box. For RV inserts, the anterior and inferior landmarks are identified with the following context modeling. Let $< x_{an}, y_{an} >$, $< x_{in}, y_{in} >$, and $< x_{LV}, y_{LV} >$ denote the positions of the RV insert anterior, RV insert inferior, and LV center, respectively. See Fig. 2(b) for an example.

The contextual parameter set for RV inserts is: position $\{(x_{an}+x_{in})/2, (y_{an}+y_{in})/2\}$; orientation {orthogonal to the line segment connecting RV insert anterior and RV insert inferior, and pointing toward the LV}; and scales $\{s_{ins}, s_{ins}\}$, where $s_{ins} = \sqrt{(x_{an}-x_{in})^2+(y_{an}-y_{in})^2} * \zeta$. $\zeta$ is set to 1.5 in our experiments.

**Context Modeling for Base Central Axis Point.** For the base central axis point $(< x_{BC}, y_{BC} >)$ in each short-axis image, three auxiliary markers are introduced as illustrated in Fig. 2(c): one marker $(< x_{AV}, y_{AV} >)$ for LVOT, one marker $(< x_{PA}, y_{PA} >)$ at the pulmonary artery side in RV, and one marker $(< x_{RA}, y_{RA} >)$ at the right atrium side in RV. These three additional markers help determine the orientation and scale for the contextual bounding box of the base central point. The contextual parameter set for the base central point is: position $\{x_{BC}, y_{BC}\}$; orientation $\{(< x_{BC}, y_{BC} >)$ pointing to $(< x_{AV}, y_{AV} >)\}$; and scales $\{s_{BC}, s_{BC}\}$, where $s_{BC} = \rho * (\sqrt{(x_{PA}-x_{BC})^2+(y_{PA}-y_{BC})^2} + \sqrt{(x_{RA}-x_{BC})^2+(y_{RA}-y_{BC})^2})/2$. $\rho$ is set to 2.4 in our experiments.

## 3 Experiments

We evaluate our algorithm on the STACOM LV landmark detection challenge data sets, which are attributed to the Cardiac Atlas Project [8]. In this database, a full set of 4D cine-MRI in long-axis and short-axis views from 200 patients are provided. The entire database is partitioned into 2 sets at random: training set (100 patients) and validation set (100 patients). Our landmark detection algorithm are tested on the 100 patients from the validation set without landmark

annotations. In total, the validation set contains 6835 long-axis images for mitral valves, 645 short axis images for RV insert points, and 100 short-axis images for base central axis points. Long axis images consist of different chamber views, namely, 4-chamber, 3-chamber, and 2-chamber views. Short axis images for RV inserts cover a wide range across the left ventricle, leading to significant variations on RV appearance presented in the images. Short axis images for base central axis point detection show significantly different anatomic structures around the LV base according to different acquisition positions such as with/without LVOT and splitting of RV.

On the training set with 100 patients, the target landmarks are annotated by experts. We extracted 6920 long axis images with mitral valve points, 670 short axis images with RV insert points, and 100 short axis images with base central points from the training set; and annotated auxiliary markers (A-E in Fig. 2) to build and learn landmark context. In addition, we have collected and annotated 8304 long axis images for mitral valves, 891 short axis images for RV inserts, and 479 short axis images for base central axis point in our own database. By combining STACOM and self-collected data, our training database is composed of 15224 long axis images (mitral valve), 1561 short axis images for RV inserts, and 579 short axis images for base central axis points.

Our algorithm is applied to each individual image in the validation set in a fully automated fashion. The algorithm detects the objects of 'Mitral valve', 'RV insert', and 'LV base center' on respective long axis and short axis images. With each object detected, the corresponding landmarks that are used to built object context are inferred based on reverse object/context modeling process, i.e., calculating landmark positions from the detected parameterized bounding box. Our algorithm also calculated a confidence score (ranging from 0 to 1) as an outcome from the probabilistic boosting trees for each detection result. The detection results whose scores are below 0.3 are rejected. For mitral valve landmarks, 2.6% of total detections were rejected. No rejections were obtained on RV inserts and base central axis points. We computed the Euclidean distance between the detected landmark position and its corresponding ground truth as the detection error for each landmark. Performance is summarized in Table 1 and Fig. 4 (rejected cases, if any, are not included). Fig. 5 shows examples of the detection results. In addition to the large parameter search space, cardiac MR images in a large population present a large variation of appearance intensities along with the anatomy shape changes across the heart beat cycle, which poses a great challenge to landmark detection from a single image. On the average, it took about 0.39, 0.14, and 0.11 seconds to detect the two mitral valve points, two RV insert points and the base central axis point in a single long/short axis image on a quad-core 2.53GHz CPU, respectively.

## 4 Discussion

In the entire MR acquisition, in addition to image context that has been explored in our method, there are a great deal of other cues that can be integrated (when

**Table 1.** Average distance of the detected landmarks from the ground truth positions on the validation set. Distances are in mm.

| | Mean | Std | Median |
|---|---|---|---|
| Mitral valves | 3.5 | 5.6 | 2.6 |
| RV inserts | 7.9 | 11.5 | 4.7 |
| Base central axis point | 6.2 | 4.0 | 5.4 |

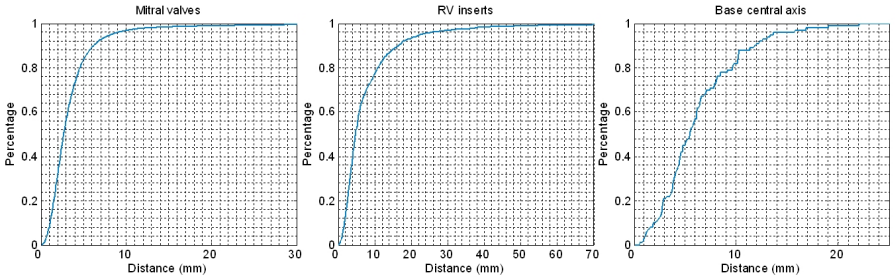


**Fig. 4.** Accuracy percentage evaluation results. A point on the curve shows the percentage (vertical coordinate) of cases where distance of the automatic detection results from ground truth is less than a distance value (horizontal coordinate).

available) after applying our landmark detection algorithm on each individual image to further improve landmark detection results. For example, temporal coherence presented in a long axis slice sequence can be exploited to help with mitral valve point detection consistency; deformable registration can also be utilized to guide mitral valve detection across the sequence; for landmark detection in a short axis stack, e.g., RV inserts, spatial coherence across the stack can help remove outliers and better constrain the search range, see Fig. 6 for an example. However, in order to demonstrate the capacity of our context modeling approach, these cues are not taken into account in our experimental results and we are focused on landmark detection in a single image in this manuscript.

In our experiments, a confidence threshold (0.3) was set in advance to reject cases with low scores. We empirically set this value the same for all three landmark detection applications. This threshold can vary for different applications and be refined through cross validations to balance the accuracy and false alarms. Due to task/classification complexities and different decision boundaries learned from probabilistic boosting trees, the detection results showed that 2.6% of total detections were rejected for Mitral Valve markers, and no rejections were observed for RV inserts and base central axis points. Fig. 7 presents representative examples of those cases that got rejected for mitral valve point detection. The low confidence scores on these cases are due to unfamiliar image appearance compared to the training data such as intensity distributions and/or anatomy geometric parameters (location/orientation/scale) that are not covered by the training set, as our online detection search range is derived from the training set

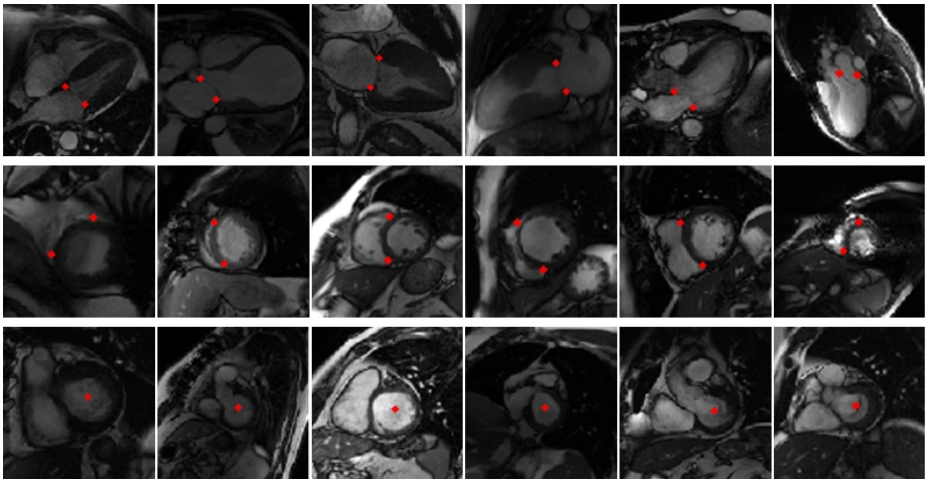

**Fig. 5.** Examples of automatic landmark detection results (red dots) on various cases. Mitral valve points (top); RV insert points (middle); base central axis point (bottom).

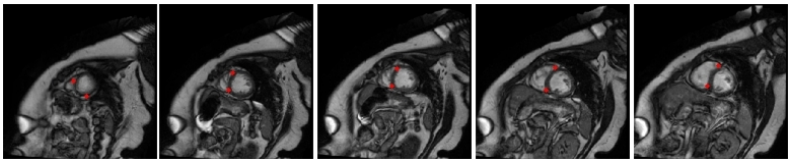

**Fig. 6.** Spatial coherence. RV insert point detection results (red dots) on five slices from the same short axis stack. The detection algorithm is applied on each individual image independently. The detected landmarks are off on the left-most image, where RV insert starts to lose context as getting close to the apex. However, if taking into account the detection results from all the other slices in the same short axis stack by enforcing the spatial coherence, such detection errors can be automatically identified and corrected or better constrained.

(even though certain small relaxations were introduced to make the parameter search range more robust.)

Determining a sufficient number of training samples depends on the marker detection complexities in different applications due to anatomy and image variations. On the RV insert point detection, we partitioned our self-collected training data sets into four parts at random, and trained the landmark detector by combining 2, 3, and 4 parts (i.e., 50%, 75%, and 100%) of all self-collected training data and tested on the 100 annotated STACOM cases. We observed that although after 3 parts (75%), a great deal of mis-detections were removed, the landmark detection accuracy continued to increase even with all training data included, no accuracy saturation was reached. This could also partially be attributed to the data distribution across multiple vendors in the STACOM database.

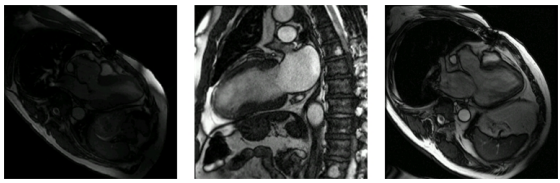

**Fig. 7.** Examples of images with low confidence scores (less than 0.3 in our experiment) due to large variations of intensities and/or geometric parameters of the anatomy from the training set

The proposed context modeling approach is data driven, therefore performance is heavily dependent on the training set, not only on the number of training samples, but more importantly on the training data distribution coverage to accommodate the data variations in real practice. Our training database contains both self-collected data that was mainly collected from Siemens scanners and STACOM database acquired from multiple vendors. Data distribution across vendors is highly unbalanced. On one hand, experimental results showed robustness and generalization capabilities of the proposed approach to handle such unbalanced distribution. On the other hand, due to the variety of MR acquisition sequences, protocols and reconstruction methods adopted by different vendors, image intensity distributions were significantly different. Therefore, images acquired by different vendor scanners with significant appearance variations from the training data pose challenges to the detectors. However, if such data is included into training, our modeling approach is able to detect correctly. Much more data from multiple vendors beyond this STACOM challenge database collection is needed to further analyze with respect to this vendor factor and generate statistically significant quantitative measurement.

This STACOM LV landmark detection challenge contains a set for apex axis point detection. Image examples are provided in Fig. 8. Although the proposed approach is not restricted to the landmarks presented in our experiments, large amount of contextual variations present in the apex axis marker detection task and limited number of annotated images (100 provided in the STACOM database) pose challenges to directly application of the proposed method (especially on single image only). However, cues from other available images during the same acquisition are of great help to constrain the search range with spatial coherence for marker position inference.

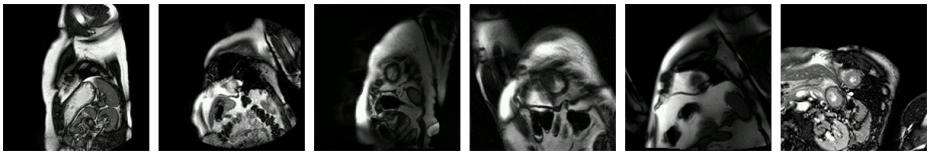

**Fig. 8.** Image examples for apex axis point detection in this STACOM challenge

## 5 Conclusions

We have proposed a unified approach to exploring contextual information and integrated it with a learning-based object detection framework. Auxiliary markers are introduced for context construction and modeling. We have developed a fully automatic system to detect multiple cardiac landmarks in both MR long-axis and short-axis images. The principle of the proposed approach is generic and able to be adapted to a wide range of landmark detection tasks through concrete context design for different applications.

## References

1. Finn, J.P., Nael, K., Deshpande, V., Ratib, O., Laub, G.: Cardiac MR imaging: State of the technology. Radiology 241(2), 338–354 (2006)
2. Frangi, A., Niessen, W., Viergever, M.: Three-dimensional modeling for functional analysis of cardiac images: A review. IEEE Trans. on Medical Imaging 20(1), 2–25 (2001)
3. Young, A., Cowan, B., Thrupp, S., Hedley, W., Dell'Italia, L.: Left ventricular mass and volume: Fast calculation with guide-point modeling on MR images. Radiology 216(2), 597–602 (2000)
4. Jolly, M.-P., Guetter, C., Lu, X., Xue, H., Guehring, J.: Automatic Segmentation of the Myocardium in Cine MR Images Using Deformable Registration. In: Camara, O., Konukoglu, E., Pop, M., Rhode, K., Sermesant, M., Young, A. (eds.) STACOM 2011. LNCS, vol. 7085, pp. 98–108. Springer, Heidelberg (2012)
5. Cerqueira, M., Weissman, N., Dilsizian, V., Jacobs, A., Kaul, S., Laskey, W., Pennell, D., Rumberger, J., Ryan, T., Verani, M.: Standardized myocardial segmentation and nomenclature for tomographic imaging of the heart. Circulation 105(4), 539–542 (2002)
6. Viola, P., Jones, M.J.: Robust real-time face detection. International Journal of Computer Vision 57(2), 137–154 (2004)
7. Lu, X., Georgescu, B., Jolly, M.-P., Guehring, J., Young, A., Cowan, B., Littmann, A., Comaniciu, D.: Cardiac Anchoring in MRI through Context Modeling. In: Jiang, T., Navab, N., Pluim, J.P.W., Viergever, M.A. (eds.) MICCAI 2010, Part I. LNCS, vol. 6361, pp. 383–390. Springer, Heidelberg (2010)
8. Fonseca, C., Backhaus, M., Bluemke, D., Britten, R., Chung, J., Cowan, B.R., Dinov, I., Finn, J., Hunter, P., Kadish, A., Lee, D., Lima, J., Medrano-Gracia, P., Shivkumar, K., Suinesiaputra, A., Tao, W., Young, A.: The cardiac atlas project - an imaging database for computational modeling and statistical atlases of the heart. Bioinformatics 27(16), 2288–2295 (2011)
9. Tu, Z.: Probabilistic boosting-tree: Learning discriminative models for classification, recognition, and clustering. In: Proc. ICCV, pp. 1589–1596 (2005)
10. Zheng, Y., Barbu, A., Georgescu, B., Scheuering, M., Comaniciu, D.: Fast automatic heart chamber segmentation from 3D CT data using marginal space learning and steerable features. In: Proc. ICCV (2007)

# Landmark Detection in Cardiac MRI Using Learned Local Image Statistics

Dwarikanath Mahapatra*

Department of Computer Science, ETH Zurich, Switzerland
dwarikanath.mahapatra@inf.ethz.ch

**Abstract.** We propose a supervised learning approach for detecting landmarks in cardiac images from different views. A set of candidate landmark points are obtained using morphological operations and graph cut segmentation. The final landmarks are determined using random forests (RF) classifiers which were trained on low level features derived from the neighborhood of annotated landmarks on training images. We use features like intensity, texture, shape asymmetry and context information for landmark detection. Experimental results on the STACOM LV landmark detection challenge dataset show that our approaching is promising with room for further improvement.

## 1 Introduction

Cardiac magnetic resonance imaging (MRI) has acquired great significance because MRI enables complete analysis of cardiac function. To overcome high inter-observer variability in interpretation of images there is a need for automatic detection of cardiac landmarks (like apex, mitral valve). Further, such automatic detection can act as a good initialization for LV segmentation.

Stralen et al. [12] proposed a method for detecting left ventricle (LV) long axis and mitral valve plane in 3D ultrasound images using circular Hough transform and dynamic programming. Fourier Mellin Transform (FMT) was used in [11] for LV localization. The template and search image are transformed into a rotation and scale invariant representation using FMT. This enables fast landmark detection using a cascade of linear detectors. In [5] a classification method to detect structures in ultrasound images is proposed. Haar features are extracted and fed to a boosted cascade of weak classifiers for detection. Karavides et al [6] detect landmarks in 3D echocardiograms using Haar features and two cascades of Adaboost classifiers. Lu et al.[10] adopt a similar approach, but with the addition of steerable features. Apart from the heart, other anatomies also appear in the same slice which can lead to ambiguities in landmark detection. To resolve such ambiguities context information was used in [9]. Context appearance is derived from its local image features like shape and appearance. The method aims to exploit the correlation of appearance and shape between different landmarks.

* Corresponding author.

O. Camara et al. (Eds.): STACOM 2012, LNCS 7746, pp. 115–124, 2013.

We propose a learning based classification approach for LV landmark detection that makes use of local appearance and context features. Local appearance information was derived from intensity, texture and shape features. Context information was included in the form of difference in curvature values over a neighborhood. These features are learned from a set of annotated training images identifying the landmark locations. The rest of the paper is organized as follows. In Section 2 we describe our feature extraction and landmark detection approach, followed by results and discussion in Section 3, and conclude with Section 4

## 2 Method

Our approach to detect landmarks consists of two stages. First we automatically segment the LV or RV as the case may be. All the edge points on the segmented LV/RV are examined for landmark points using random forests (RF) classifiers. This gives a set of candidate landmark points, and the two points (for mitral valve and right ventricular points) or one point (for apex and base central axis points) with the maximum votes is selected as the landmark points.

### 2.1 Segmenting the LV and RV

Although there are many methods in literature for LV segmentation, we desire a method that requires minimal user involvement and is fast. We use a combination of morphological operations and graph cuts to obtain the LV boundary from a test image. All the image intensities in the training and test set are normalized to lie between 0 and 1 using the 95−th percentile intensity value such that all intensities above this value are 1. The test image ($I$) is first thresholded such that pixels with intensities above $th$ are set to 1 and all other pixels are set to 0. The threshold is given by

$$th = \mu + \gamma \times \sigma^2, \tag{1}$$

where $\mu$ is the mean image intensity, $\sigma^2$ is the standard deviation and $\gamma = 2$ is a constant set empirically by testing over a large number of training images.

The morphological image opening operation (erosion followed by dilation) is applied to the thresholded image $I_{th}$ using the *imopen* function in MATLAB to get $I_{open}$. For *imopen* a disk structuring element of size 3 is generated using the *strel* command in MATLAB. All the connected components in $I_{open}$ are extracted. For each cluster of pixels we determine their intensity distributions. Previously, in the set of normalized training images we manually identify regions of the LV/RV and determine the intensity distribution over its pixels. The intensity distributions of the connected regions in $I_{open}$ are matched with this reference distribution using the Bhattacharya metric. The region with the closest match to the reference distribution is the region of interest (ROI).

One limitation of thresholding is that neighboring regions of the LV are also clustered with the LV, and *imopen* is unable to remove the connections between

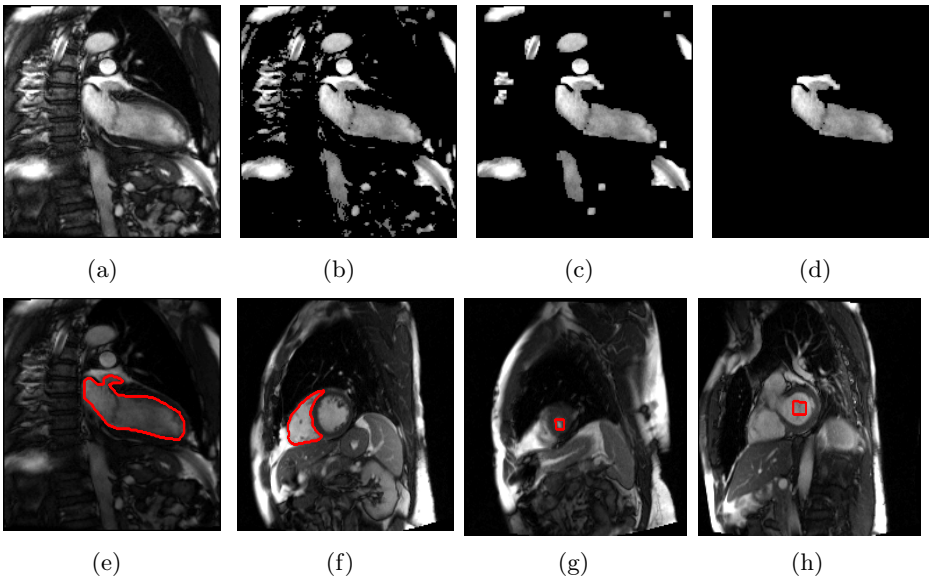


**Fig. 1.** Results of different stages of LV segmentation: (a) Original Image; (b) thresholded image; (c) morphological opening; (d) connected components; extracted edge for (e) LV and (f) RV; search areas for (g) ACA and (h) BCA

these regions. The pixels in the extracted region (from $I_{open}$) are again assigned labels as ROI or non-ROI using graphcuts [3]. The ROI intensity distribution previously calculated is used to determine penalties for ROI label. Similarly a reference distribution for non-ROI regions are also determined to calculate the penalty for non-ROI label. Note that only those pixels in the extracted region are labeled and not all pixels in the image. This gives a segmented ROI in which we identify the edge points. These edge points are then further classified as landmark or non-landmark using a trained RF classifier.

Figure 1 shows the results of different steps for extracting LV in a long axis (LA) image. Figure 1 (a) shows the original image followed by the thresholded image $I_{th}$ in Fig. 1 (b). Figure 1 (c) shows the image after morphological image opening ($I_{open}$) and Fig. 1 (d) shows the extracted LV region using connected component analysis. As pointed out previously neighboring anatomical structures are also extracted. The result after graphcut segmentation is shown in Fig. 1 (e) with the edge points identified by the red line. This approach also works well for the RV insert points (Fig. 1 (f)). However for the apex and base central points, we do not apply graph cuts. After extracting the desired region using connected components, the center of this region is determined and a search area is defined as a bounding box of size $25 \times 25$ around this center. Figures 1 (g) and (h) show the search areas (red rectangle) for base and apex central points. The candidate search points are then classified in the next stage using RF classifiers.

### 2.2 Landmark Detection Using RF Classifiers

The training set provides us with annotated images that identify landmarks on the mitral valves (MV), right ventricular inserts (RVI), centers of apex central axis (ACA) and base central axis (BCA). For each of the annotated points we extract features from a $35 \times 35$ neighborhood and use them to train the RF classifier. The following features are used for training.

**Intensity and Texture Features:** The mean, variance, skewness and kurtosis of intensity values are calculated for the patch around the landmarks to get the first set of features. Texture maps of the patch are obtained along four directions $(0°, 45°, 90°, 135°)$ using Gabor filters. Gabor filters conform to the receptive field properties of cortical cells, capture rich visual properties like spatial frequency characteristics and orientation, and are robust to noise by incorporating Gaussian smoothing. The Gabor filter bank is represented as

$$g_{\gamma,\omega}(x,y) = a^{\gamma} g\left(a^{\gamma}\left(x\cos\left(\omega\psi\right) + y\sin\left(\omega\psi\right)\right) a^{\gamma}\left(-x\sin\left(\omega\psi\right) + y\cos\left(\omega\psi\right)\right)\right) \tag{2}$$

where $\gamma = 0, \cdots, \Gamma - 1, \omega = 0, \cdots, \Omega - 1$. The mother function $g$ is a Gaussian defined as:

$$g(x,y) = \left(\frac{1}{2\pi\sigma_x\sigma_y}\right) \exp\left[-\frac{1}{2}\left(\frac{x^2}{\sigma_x^2} + \frac{y^2}{\sigma_y^2}\right) + 2\pi j W x\right] \tag{3}$$

$\Gamma = 4$ is the total orientations, $\Omega = 2$ is the number of scales, the rotation factor is $\psi = \pi/\Omega$ and the scaling factor is $a = (U_h/U_l)^{1/\Gamma - 1}$. $U_h$ and $U_l$ determine the frequency range of the filter bank and $W$ is a shifting parameter in the frequency domain.

In [7] texture anisotropy was used as a feature to identify tumorous regions in brain images. While they calculate anisotropy using local gradient differences and gray level dependence histograms, we use entropy to measure anisotropy. The texture maps are divided into 8 equal parts corresponding to 8 sectors of a circle, and entropy determined for each sector. Figure 2 (a) shows an illustration of the sectors in a circle that are used to compute the entropy. A higher entropy value indicates wider distribution of texture values (hence high anisotropy), while low entropy indicates lower anisotropy. The texture anisotropy for sector $r$ is

$$Tex^r_{Anisotropy} = -\sum_{tex} p^r_{tex} \log p^r_{tex}. \tag{4}$$

$p^r_{tex}$ denotes the distribution of texture values in sector $r$. Values of $tex$ lie between 0 and 1. Thus the number of texture features are 32 (8 entropy values from each of 4 oriented filters).

**Shape Asymmetry:** We extend the concept of asymmetry (or anisotropy) to shape features. Here instead of texture we operate on image curvature values. The entropy of curvature values is determined from 8 sectors of each slice to give us 8 values for shape asymmetry. If the curvature values have a wide distribution

it indicates greater asymmetry in shape, leading to a higher entropy value. On the other hand low entropy values indicates less shape asymmetry. The shape asymmetry measure for a sector $r$ is given by

$$Shape^{r}_{Asymmetry} = -\sum_{\theta} p^{r}_{\theta} \log p^{r}_{\theta}. \tag{5}$$

$p^{r}_{\theta}$ denotes the probability distribution of curvature values in sector $r$. Values of $\theta$ lie in the range $\{-180°, 180°\}$.

**Context Information.** Belongie et al. [2] proposed a shape context method using distribution of relative distances for matching shapes. In [13] Tu propose "auto-context" which integrates image and contextual information from a set of trained classifiers and use it to segment brain structures from MRI. Auto context was used by Li et al. in [8] to segment the human prostate gland from computed tomography (CT) images. Object interaction priors were used in [1] for inter-vertebral disc segmentation using graph cuts. Context comes from a variety of sources. Since the human anatomy is standard, and image acquisition procedures are the same presence of one organ leads to a strong cue about the presence of another organ in medical images. We aim to capture the contextual relationship between the landmarks and its neighborhood through curvature values. Basically context information provides information of one set of objects from another set of objects. Previous works have incorporated statistical models from large training data to include context information. However, these approaches require complex modeling and inference methods. For every labeled landmark we examine a neighborhood of $35 \times 35$ and sample a few points from it. The sampling location are shown in Fig. 2 (b) (red 'X's). From the image center rays at intervals of 45° are drawn, and points are sampled on these rays. The maximum distance along rays at $0°, 90°, 180°, 270°$ is 17 pixels (since the neighborhood is of size $35 \times 35$) and points are sampled at distances of $2, 7, 12, 17$ pixels. The maximum distance along rays at $45°, 135°, 225°, 315°$ is $17\sqrt{2} = 24$ pixels and points are sampled at distances of $3, 8, 13, 18, 23$ pixels. This gives 36 sampled points on each slice.

At each sampled point we calculate the difference in feature values with respect to the central point (i.e., the landmark pixel) and include it in a feature vector. This gives 36 values for a single slice.

$$Cont = f(i) - f(n_i), \forall n \in N_i \tag{6}$$

where $f$ is the feature value, $n_i$ is the sampled neighboring points, and $N_i$ denotes the whole in the neighborhood of the labeled voxel $i$.

For context information we can use any or all of the previously mentioned features (intensity, texture or shape). However in practice we find that shape context features provides the maximum discrimination ability in comparison to other features. Inclusion of intensity and texture context features increases the length of the feature vector (also the computation time), but does not lead to a significant increase in accuracy of landmark detection over shape features.

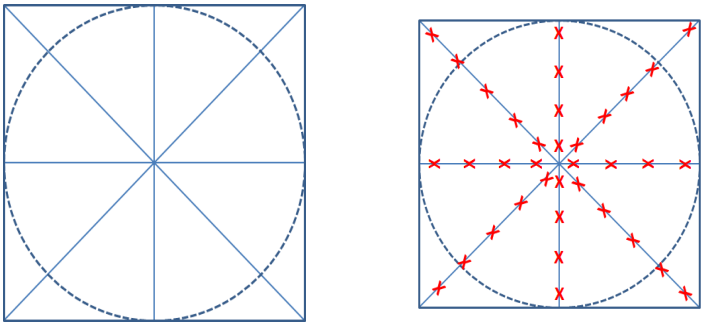

(a) (b)

**Fig. 2.** (a) Illustration of sectors for entropy calculation in texture anisotropy and shape asymmetry; (b) sampling locations to derive context information

Therefore we include only the shape context features in the final feature vector. Here we clarify that to derive context information we use only shape features, while for incorporating low level information we use shape, texture and intensity features. The final landmark(s) among the candidate points are those which have the maximum number of votes by the RF classifier.

## 3 Experimental Results and Discussion

We use the database of STACOM LV landmark detection challenge workshop 2012 [4]. The training data consists of 100 patients with the images acquired in the LA and SA. Our classifiers were trained on features derived from all the 100 datasets. We test our method on 4 validation datasets of the STACOM landmark detection challenge - validations sets $1, 2, 3, 4$- a total of 80 patients. The extracted feature vectors for each point are 80 dimensional $(4+32+8+36)$. While the manual annotations gave us positive samples, we automatically extract background points in the landmarks' vicinity to get sufficient negative samples to train the RF classifier. For each landmark type (MV,RVI,ACA and BCA) we have different sets of classifiers. All the classifiers had 50 trees.

For every dataset there is only one ACA and BCA point, while there are many RVI and MV points depending upon the number of acquired images. In order to calculate the error measures the Euclidean distance between the detected landmark and the actual landmark is determined. The performance is summarized in Table 1. Figure 3 gives the error distributions for each type of landmark point. A major percentage of the errors is within 10 mm for all cases. However there are cases of high error, particularly for MV points.

Figure 4 shows the detected landmarks by our method (green 'x') and the actual landmarks as red 'x' for patient number 95. Visual results and error measures show that our method is promising and detects landmarks quite close to the actual position. We implemented the whole method in MATLAB on a Pentium Core 2 Duo, 2.66 GHz processor. The average time to detect landmarks

**Table 1.** Average error measures for landmark detection on 4 validation datasets comprising 80 patients. Values are given for mean±standard, minimum, maximum and median error. Values are in units of mm.

| | Mean±std | min | max | median |
|---|---|---|---|---|
| ACA | 5.66±5.39 | 0.60 | 33.48 | 4.16 |
| BCA | 7.01±7.99 | 0.25 | 52.28 | 4.51 |
| MV | 5.67±5.83 | 0.02 | 64.66 | 4.19 |
| RVI | 6.79±5.49 | 0.14 | 45.56 | 5.44 |

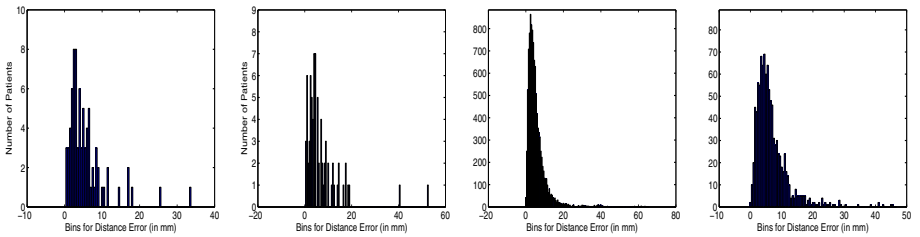


**Fig. 3.** Distribution of landmark errors for: (a) ACA; (b) BCA; (c) MV; (d) RVI

in a $192 \times 152$ pixel image was 23 seconds, thus indicating scope for a faster and efficient approach. The generation of candidate landmark points took less than 2 seconds on an average.

**Importance of Different Features.** Figure 5 shows error measures for different feature combinations on the training dataset. For single features $Int$ performs worst and $Cont$ gives the best results. For two feature combination the lowest error is given by $Cont + Shape$. In the case of three features, all combinations having $Cont$ give similar results highlighting the discriminative power of context information.

Our method also has limitations. It is particularly sensitive to the accuracy of segmentation as it provides candidate points for landmark detection. Segmentation accuracy depends upon threshold value, efficacy of the image opening step and of connected component analysis. We select $\gamma = 2$ (Eqn. 1) after visual examination of the results over more than 50 images from SA and LA views. The disk size in the *imopen* operation was fixed through similar examination.

Initially we tried to localize the ROI using a machine learning approach. We divided the training images into 64 square blocks and extracted the previously mentioned features for blocks containing the annotated landmark (landmark block) as well as blocks not containing the landmark (background blocks). Context information was derived with respect to the central pixel in the block. If a test block is denoted landmark by the RF classifier, we subdivide it into 4 sub-blocks and

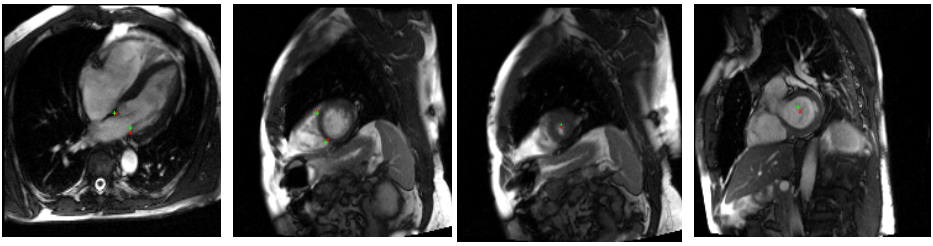

(a) (b) (c) (d)

**Fig. 4.** Results of landmark detection: (a) MV (average error= 2.6 pixels); (b) RVI (average error= 1.9 pixels); (c) ACA (average error= 1.2 pixels); (d) BCA (average error= 2.1 pixels)

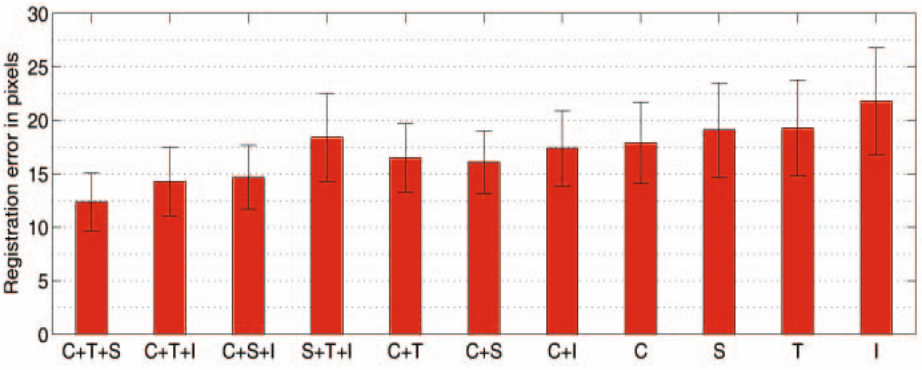


**Fig. 5.** Error measures(mean and standard deviation) for MV detection using different feature combinations.$C$-Context;$S$-Shape;$T$-Texture;$I$-Intensity

check for the presence of landmark from these 4 sub-blocks. Finally each pixel of the identified sub-block is analyzed for the presence of a landmark. We extract features from a $35 \times 35$ neighborhood of each pixel and train different set of classifiers for each stage. But such an approach required many computations in MATLAB. Since our features use entropy based measures sufficient samples are needed for an accurate feature value. Thus smaller blocks give erroneous values. Alternatively, larger blocks result in more computations when we analyzed each pixel's neighborhood. This approach gave fairly good results for LV and RV landmarks, but poor results for ACA and BCA points as there were not sufficient samples to train a accurate classifier that can distinguish between landmark and background blocks. In order to overcome this limitation we used morphological operations and graph cuts to find a set of candidate points for each landmark.

## 4 Conclusion

We have proposed a method to detect landmarks in cardiac MRI using a combination of graphcut segmentation, low level feature information and machine learning techniques. An initial set of candidate landmark points is obtained by thresholding, connected component analysis and graphcut segmentation. The final landmarks are identified with the help of RF classifiers trained on manual annotations of landmark points. For accurate landmark detection low level image features like intensity, texture anisotropy, shape asymmetry and context information was derived from neighborhoods of annotated landmarks. Training was performed on data from 66 patients. Results on 5 test patient databases show our approach is promising for the purpose of detecting the appropriate landmarks. But there is also scope for speeding up the detection of candidate points as well as identifying the final landmark.

## References

1. Ben Ayed, I., Punithakumar, K., Garvin, G., Romano, W., Li, S.: Graph Cuts with Invariant Object-Interaction Priors: Application to Intervertebral Disc Segmentation. In: Székely, G., Hahn, H.K. (eds.) IPMI 2011. LNCS, vol. 6801, pp. 221–232. Springer, Heidelberg (2011)
2. Belongie, S., Malik, J., Puzicha, J.: Shape matching and object recognition using shape contexts. IEEE Trans. Patt. Anal. Mach. Intell. 24(24), 509–522 (2002)
3. Boykov, Y., Funka-Lea, G.: Graph cuts and efficient N-D image segmentation. Intl. J. Comp. Vis. 70(2), 109–131 (2006)
4. Fonseca, C., Backhaus, M., Bluemke, D., Britten, R., Chung, J., Cowan, B., Dinov, I., Finn, J., Hunter, P., Kadish, A., Lee, D., Lima, J., Medrano-Gracia, P., Shivkumar, K., Suinesiaputra, A., Tao, W., Young, A.: The cardiac atlas project - an imaging database for computational modeling and statistical atlases of the heart. Bioinformatics 27(16), 2288–2295 (2011)
5. Georgescu, B., Zhou, X., Comaniciu, D., Gupta, A.: Database guided segmentation of anatomical structures with complex appearance. In: CVPR, pp. 429–436 (2005)
6. Karavides, T., Leung, K., Paclik, P., Hendriks, E., Bosch, J.: Database guided detection of anatomical landmark points in 3D images of the heart. In: ISBI, pp. 1089–1092 (2010)
7. Kovalev, V., Petrou, M., Bondar, Y.: Texture anisotropy in 3D images. IEEE Trans. Imag. Proc. 8(3), 346–360 (1999)
8. Li, W., Liao, S., Feng, Q., Chen, W., Shen, D.: Learning Image Context for Segmentation of Prostate in CT-Guided Radiotherapy. In: Fichtinger, G., Martel, A., Peters, T. (eds.) MICCAI 2011, Part III. LNCS, vol. 6893, pp. 570–578. Springer, Heidelberg (2011)
9. Lu, X., Georgescu, B., Littmann, A., Mueller, E., Comaniciu, D.: Discriminative Joint Context for Automatic Landmark Set Detection from a Single Cardiac MR Long Axis Slice. In: Ayache, N., Delingette, H., Sermesant, M. (eds.) FIMH 2009. LNCS, vol. 5528, pp. 457–465. Springer, Heidelberg (2009)
10. Lu, X., Georgescu, B., Zheng, Y., Otsuki, J., Comaniciu, D.: AutoMPR: Automatic detection of standard plane in 3D echocardiography. In: ISBI, pp. 1279–1282 (2008)

11. Ma, M., Bosch, J., Reiber, J., Lelieveldt, B.: Fully automatic estimation of object pose for segmentation initialization: application to cardiac MR and echocardiography. In: SPIE Medical Imaging (2007)
12. Van Stralen, M., Leung, K., Voormolen, M., de Jong, N., van der Steen, A., Reiber, J., Bosch, J.G.: Time continuous detection of the left ventricular long axis and the mitral valve plane in 3-D echocardiography. Ultrasound in Med. Bio. 34(2), 196–207 (2008)
13. Tu, Z., Bai, X.: Auto-context and its application to high-level vision tasks and 3D brain image segmentation. IEEE Trans. Patt. Anal. Mach. Intell. 32(10), 1744–1757 (2010)

# Computational and Physical Phantom Setups for the Second Cardiac Motion Analysis Challenge (cMAC2)

Mathieu De Craene[1], Pascal Allain[1], Hang Gao[4], Adityo Prakosa[5], Stephanie Marchesseau[5], Oudom Somphone[1], Loic Hilpert[2], Alain Manrique[3], Hervé Delingette[5], Sherif Makram-Ebeid[1], Nicolas Villain[1], Jan D'hooge[4], Maxime Sermesant[5], and Eric Saloux[2]

[1] Philips Research Medisys, France
[2] Department of Cardiology, University Hospital of Caen, Caen, France
[3] Department of Human Investigations, GIP Cyceron, Caen, France
[4] Laboratory of Cardiovascular Imaging and Dynamics, University of Leuven, Leuven, Belgium
[5] Inria, Asclepios Research Project, Sophia Antipolis, France

**Abstract.** This paper describes the data setup of the second cardiac Motion Analysis Challenge (cMac2). The purpose of this challenge is to initiate a public data repository for the benchmark of motion and strain quantification algorithms on 3D ultrasound images. The data currently includes synthetic images that combine ultrasound and biomechanical simulators. We also collected sonomicrometry curves and ultrasound images acquired on a Polyvinyl alcohol phantom.

## 1 Introduction

Being a wide-spread modality, echocardiography plays a key role in the assessment of cardiac function. When it comes to quantifying local motion and strain, the validation of Doppler-based or speckle-tracking measurements becomes critical. Accuracy, sensitivity and reproducibility of any quantification algorithm should be known as a function of the signal to noise ratio before applying it for diagnostic purposes. However, the construction of a ground truth for motion and strain is a challenging task. Indeed, obtaining ground truth from manual measurements requires to track anatomical landmarks over time. Taking the spatial derivative of these trajectories to compute strain amplifies intra- and inter-observer errors.

### 1.1 Existing Validation Strategies

Several alternatives have been proposed to construct ground truth for motion and strain quantification from ultrasound (US) images.

*Another modality* can be taken as reference (e.g. tagged Magnetic Resonance (MR) [1]). While this approach can enhance consistency between the two modalities, differences could raise from some bias introduced by the reference modality.

O. Camara et al. (Eds.): STACOM 2012, LNCS 7746, pp. 125–133, 2013.

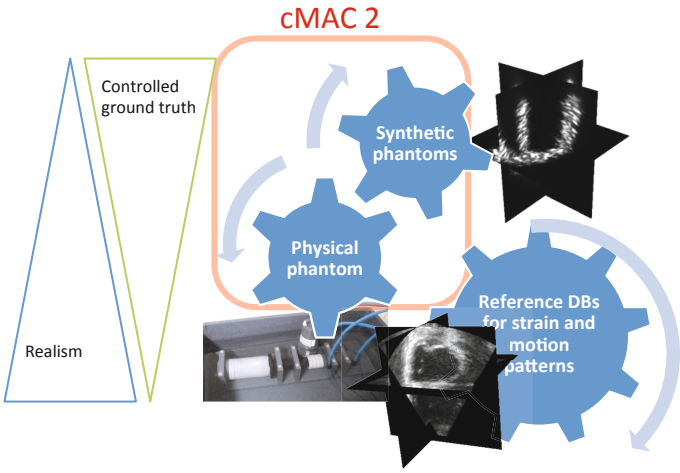


**Fig. 1.** Global picture of ultrasound-based motion and deformation validation. Covering the whole spectrum between data realism and controlled ground truth requires covering, on the long term, phantom and patient data. This year cMAC2 challenge will be restricted to synthetic images and in vitro phantom to focus on a reliable ground truth motion field.

*Sonomicrometry* is an alternative for strain validation [2] and measures at a high frame rate the time taken by an acoustic wave to travel between pairs of crystals. Time measurements can be converted to distances if the propagation velocity of the medium is known. However, this data is only available at few locations in the entire volume.

*Computational Phantoms.* To provide highly controlled ground truth datasets, several authors proposed to simulate the US imaging pipeline. While of limited realism, the advantage is to provide data where the exact underlying motion field is known and controlled. The Field [3] package provides a library for the calculation of pressure fields from arbitrarily shaped, apodized, and excited US transducers. It can generate the spatial impulse response specific to an US system with known characteristics. Recently, Gao *et al.* [4] proposed a fast approach for generating 3D US sequences in less than an hour. It accelerates the convolution of a 3D point spread function (PSF) by multiple 1D convolutions while preserving the resulting image quality. Elen *et al.* [5] applied this simulation technology to an ellipsoid model of the left ventricle (LV) with torsion, longitudinal and radial deformation mapped to the characteristics of a healthy subject. For inclusion of more realistic geometries and motion, Duan *et al.* [6] integrated a realistic electro-mechanical model in the simulation process.

*Physical Phantoms.* Alternatively to simulated data, ground truth can be obtained on physical phantoms, which motion and deformations can be mechanically controlled [7]. Although the geometry of phantoms are often simplified,

the obtained image quality reflects the challenges of a real US imaging system. Polyvinyl alcohol (PVA) gels [8] were proposed as a tissue-mimicking material for MR and US. As the number of freeze-thaw cycles affects the properties of the material, locally stiffer inclusions can be embedded for quantifying the localizability of lesions for several spatial and stiffness extents [9].

### 1.2 Standardization Context in Echocardiography

Public dissemination of validation data is a key issue. Without systematic data access, reproducibility of the findings of the different motion and strain quantification techniques can be hardly verified by independent experts. Recently, the European Association of Echocardiography (EAE) launched a joint initiative with the American Society of Echocardiography ASE to involve manufacturers and software developers in a programme aimed to standardize quantitation of myocardial deformation (strain) among vendors[1]. In this context, different vendors and academic partners regularly meet at cardiac imaging conferences to agree on standard data and formats. The investigations of the task force are currently limited to 2D US imaging.

### 1.3 Contribution of cMAC Challenges

*At last year STACOM workshop*, a motion challenge was proposed [10], including data collected from healthy volunteers and *in vitro* phantoms. Magnetic resonance (MR) images were acquired using 3D cine and tagging protocols [10]. 3D US images were also collected for the phantom and the volunteers. Although of high quality and realism, the main difficulty for this dataset was the construction of ground truth data for comparing the different motion algorithms. The retained solution was to manually track tag crossings by two observers. The obtained ground truth trajectories on 8 landmarks were then reported on the US space of coordinates. Because of variations in heart rate between MR and US acquisitions, only the end-systolic and end-diastolic results were compared.

Since the focus of *this year cMAC challenge* is 3D US, our objective was to propose a 3DUS database with highly reliable ground truth on motion and deformation, without requiring another imaging modality or manual measurements to build the ground truth. Physical and computational phantoms are two elements of a complete validation strategy illustrated in Fig. 1. When adding patient images, the resulting database covers the full spectrum from accurate ground truth to fully realistic data. As a first step towards this goal, we propose in this paper a computational phantom obtained from combining an US imaging modeling package [4] with a bio-mechanical model [11,12]. We also designed a physical phantom able of dissociating compression and torsion for separately quantifying the accuracy on these two deformation modes. The phantom is made of PVA gel for further allowing local inclusions with different mechanical properties.

[1] `http://bit.ly/esc-news`

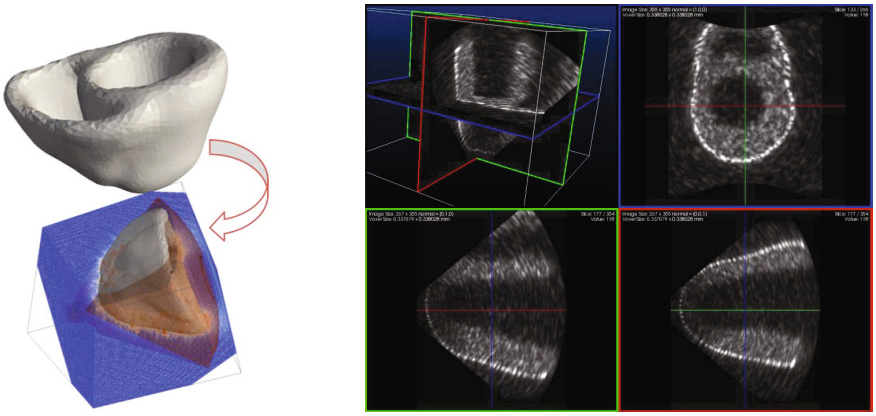

(a) (b)

**Fig. 2.** Synthetic 3DUS image generation process: (a) Mapping from the simulation volumetric meshes into the 3D US imaging space and (b) obtained image

## 2 Computational Phantom

The synthetic images proposed in this challenge combine an electro-mechanical model described in [11,12] with an US imaging model from [4]. We provide 10 sequences spanning different values of electrical activation, conductivity and contractility parameters. Global conductivity is the conduction velocity of the electrophysiology model and global contractility is the maximum value of the fibre active stress. For electrical delay, both LBBB and RBBB cases were considered with or without pacing in different AHA regions. A summary of the simulation parameters for each case is given in Table 1. In the current dataset, a single probe design was considered. Scatterers were randomly placed in the myocardial geometry and moved along the cardiac cycle according to the result of the mechanical simulation. A single rigid transformation was used to map the sequence of volumetric meshes to the synthetic US field of view, as illustrated in Fig. 2(a). The US modeling pipeline is fully described in [4].

The 3D Point Spread Function (PSF) considered in the current dataset was obtained by rotating a 2D beam profile to get 3D images on the assumption that PSF in azimuth and elevation are the same. Scatterers in the background were placed randomly at each frame to ensure there is no frame to frame correlation in the blood pool. As an additional challenge, scatterers with a high reflectivity were placed around the epicardium to mimic pericardium. This layer moves at a slower rate than the myocardium to render the difficulty brought by an intense pericardium tissue moving at a different speed than the myocardium next to it. An example of 3D US image generated for this challenge is shown in Fig. 2(b).

**Table 1.** Simulation parameters for the synthetic database

| Case | Initial Electrical Activation Position | Global Conductivity (cm/s) | Global Contractility (dimensionless) |
|---|---|---|---|
| 1 | Normal | 50 | 0.09 |
| 8 | RBBB | 30 | 0.05 |
| 12 | LBBB | 30 | 0.05 |
| 20 | LBBB+Pacing(AHA 5) | 30 | 0.05 |
| 22 | LBBB+Pacing(AHA 6) | 30 | 0.09 |
| 28 | LBBB+Pacing(AHA 7) | 30 | 0.05 |
| 36 | LBBB+Pacing(AHA 12) | 30 | 0.05 |
| 44 | RBBB+Pacing(AHA 9) | 30 | 0.05 |
| 60 | BV Pacing(AHA 3+6) | 30 | 0.05 |
| 88 | BV Pacing(AHA 14+7) | 30 | 0.05 |

## 3 Physical Phantom

The phantom was made of a single cylindrical cavity. This shape was produced by repeated freezing and thawing of a PVA solution (with addition of graphite).

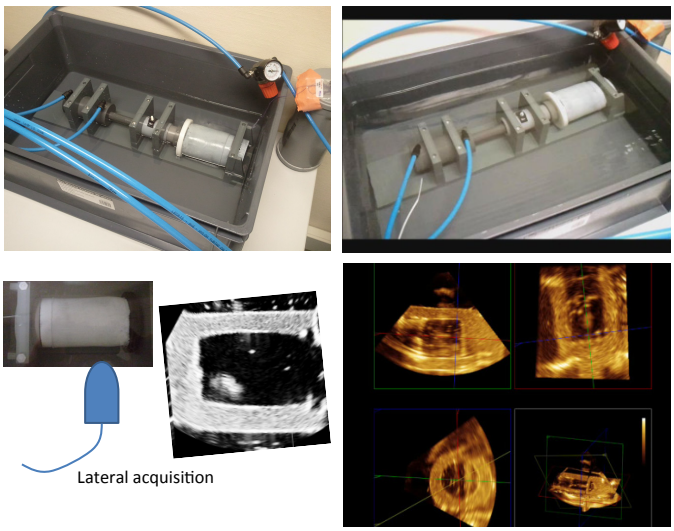


**Fig. 3.** Physical phantom setup. Top: The PVA phantom is placed in a water-filled aquarium. The pneumatic mechanical part is MR compatible and can dissociate or combine compression and rotation. Bottom left: images were acquired from a lateral position of the probe. Bottom right: obtained 3D US image.

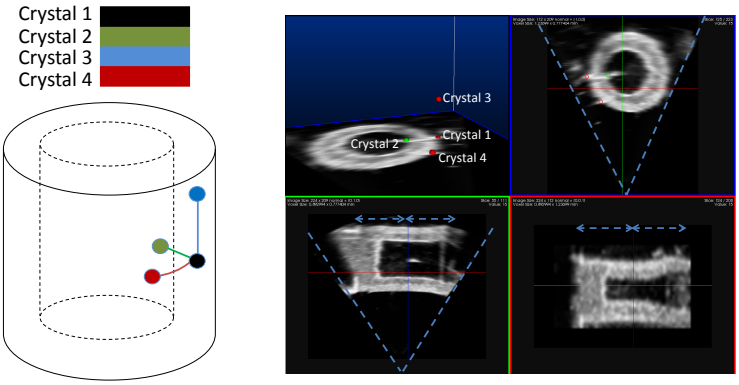


(a) (b)

**Fig. 4.** Location of the sonomicrometry crystals. (a) Four crystals were placed to capture radial, circumferential and longitudinal length changes. (b) The crystals can be manually landmarked in the image space to compute the same length changes from the intensity-based tracking result. Blue arrows indicate that the crystals are placed at half the height of the cylinder.

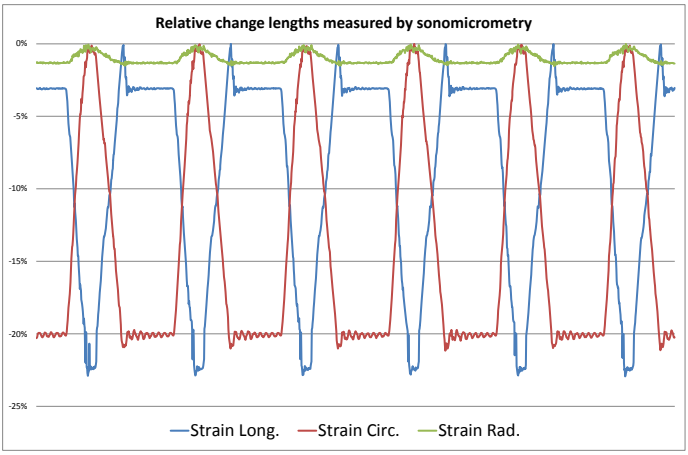


**Fig. 5.** Pairwise distances between crystals as provided by sonomicrometry

A pneumatic part is mounted at the top and allows varying compression and torsion modes jointly or separately. The mechanical controller is linked to an EEG simulator. The phantom is fully MR compatible. For this challenge, 3D US data was acquired with a Philips 3D X5 probe. In the current setup, data was acquired from a lateral position, as indicated in Fig. 3. Ground truth data for deformation was captured using sonomicrometry. It gives the distance between crystals pairs embedded in the gel and will therefore approximate radial,

circumferential and longitudinal strain values. Crystals were placed at a position and using a pattern plotted in Fig. 4. Since the correspondence between image and sonomicrometry coordinate systems is unknown, the four crystals were manually landmarked by an expert and their location in the image was provided to all challengers. The distances between pairs of crystals give an approximation of radial, circumferential and longitudinal strains. Fig. 5 plots the relative length changes over time ($\Delta L(t)/L(t_0)$) for the first provided dataset.

## 4 Discussion and Conclusions

This paper presented a small database containing both synthetic and phantom datasets. Synthetic images were obtained by combining a biventricular geometry with biomechanical and US imaging models. Although these images do not reproduce faithfully all artifacts inherent to real US images, the true motion field is known densely in the whole myocardial volume. In future work, various settings will be generated for realistic probe designs. The relative intensity of the myocardial wall and the blood pool will be modulated to produce several scenarios of signal to noise ratios.

Regarding mechanical simulations, the current challenge modeled different activation patterns producing normal and impaired motion and deformation. This will help to determine if currently available image processing algorithms can detect and quantify dyssynchrony in the LV. Besides assysnchrony, another pathology we intend to include in the database is the presence of ischemic or stunned segments with reduced or null contractility. These segments should follow the vascularization territories corresponding to the main branches of the coronary tree (left, right and circumflex coronary arteries).

On the physical phantom, ground truth is currently available as pairwise distance curves returned by the sonomicrometry system. This has three main limitations.

First, this information is extremely sparse (4 spatial locations only). To circumvent this, we intend to complement the database by tagged MR acquisitions giving dense markers, the tags crossings, in the myocardium. To this end, we will use the same acquisition protocol as in the first cMAC challenge [10].

Second, sonomicrometry provides ground truth on deformation and not on trajectories. This would be a desirable feature as verifying the accuracy on the motion field is an intermediate step before quantifying strain accuracy. On the physical phantom, there are two ways to construct ground truth trajectories: one is to manually track tags crossings [10]. An alternative could be to use the sonomicrometry system to reconstruct trajectories by means of triangulation techniques using fixed crystals. This approach was followed by Gorman *et al.* [13], who applied a multidimensional scaling algorithm for tracking the three-dimensional geometry of the mitral valve using sonomicrometry.

Third, sonomicrometry crystals do not give access to the infinitesimal Lagrangian strain tensor, but measure relative length changes approximating strain values. For the "circumferential" direction, microsonometry measures the straight

distance between crystals rather than the arc length, as desired for circumferential strain. Despite these limitations, the accuracy of image tracking algorithms can still be quantified if the distances are measured consistently in image and sonomicrometry spaces.

This dataset is only meant as a first step to help the medical imaging processing community to construct reference databases for the validation of motion and strain quantification algorithms from 3D US images. Although embryonic, we hope it will be an opportunity to strengthen a community including physicians and engineers around this challenging topic. All the data generated in this context is hosted on the cardiac atlas project page[2] and publicly available through email request to help constructing an open validation framework for US-based 3D strain measurements.

## References

1. Amundsen, B., Crosby, J., Steen, P., Torp, H., Slørdahl, S., Støylen, A.: Regional myocardial long-axis strain and strain rate measured by different tissue doppler and speckle tracking echocardiography methods: a comparison with tagged magnetic resonance imaging. European Journal of Echocardiography 10(2), 229–237 (2009)
2. Amundsen, B., Helle-Valle, T., Edvardsen, T., Torp, H., Crosby, J., Lyseggen, E., Støylen, A., Ihlen, H., Lima, J., Smiseth, O., et al.: Noninvasive myocardial strain measurement by speckle tracking echocardiography: validation against sonomicrometry and tagged magnetic resonance imaging. Journal of the American College of Cardiology 47(4), 789–793 (2006)
3. Jensen, J.: A new calculation procedure for spatial impulse responses in ultrasound. The Journal of the Acoustical Society of America 105(6), 3266–3274 (1999)
4. Gao, H., Choi, H., Claus, P., Boonen, S., Jaecques, S., Van Lenthe, G., Van Der Perre, G., Lauriks, W., D'hooge, J.: A fast convolution-based methodology to simulate 2-D/3-D cardiac ultrasound images. IEEE Transactions on Ultrasonics, Ferroelectrics and Frequency Control 56(2), 404–409 (2009)
5. Elen, A., Choi, H., Loeckx, D., Gao, H., Claus, P., Suetens, P., Maes, F., D'hooge, J.: Three-dimensional cardiac strain estimation using spatio–temporal elastic registration of ultrasound images: A feasibility study. IEEE Transactions on Medical Imaging 27(11), 1580–1591 (2008)
6. Duan, Q., Moireau, P., Angelini, E.D., Chapelle, D., Laine, A.F.: Simulation of 3D Ultrasound with a Realistic Electro-mechanical Model of the Heart. In: Sachse, F.B., Seemann, G. (eds.) FIHM 2007. LNCS, vol. 4466, pp. 463–473. Springer, Heidelberg (2007)
7. Lesniak-Plewinska, B., Cygan, S., Kaluzynski, K., D'hooge, J., Zmigrodzki, J., Kowalik, E., Kordybach, M., Kowalski, M.: A dual-chamber, thick-walled cardiac phantom for use in cardiac motion and deformation imaging by ultrasound. Ultrasound in Medicine & Biology 36(7), 1145–1156 (2010)
8. Surry, K., Austin, H., Fenster, A., Peters, T.: Poly (vinyl alcohol) cryogel phantoms for use in ultrasound and MR imaging. Physics in Medicine and Biology 49, 5529 (2004)

[2] `http://www.cardiacatlas.org/`

9. Heyde, B., Cygan, S., Choi, H., Lesniak-Plewinska, B., Barbosa, D., Elen, A., Claus, P., Loeckx, D., Kaluzynski, K., D'hooge, J.: Regional cardiac motion and strain estimation in three-dimensional echocardiography: A validation study in thick-walled univentricular phantoms. IEEE Transactions on Ultrasonics, Ferroelectrics and Frequency Control, 668–682 (2011)
10. Tobon-Gomez, C., De Craene, M., Dahl, A., Kapetanakis, S., Carr-White, G., Lutz, A., Rasche, V., Etyngier, P., Kozerke, S., Schaeffter, T., Riccobene, C., Martelli, Y., Camara, O., Frangi, A.F., Rhode, K.S.: A Multimodal Database for the $1^{st}$ Cardiac Motion Analysis Challenge. In: Camara, O., Konukoglu, E., Pop, M., Rhode, K., Sermesant, M., Young, A. (eds.) STACOM 2011. LNCS, vol. 7085, pp. 33–44. Springer, Heidelberg (2012)
11. Sermesant, M., Chabiniok, R., Chinchapatnam, P., Mansi, T., Billet, F., Moireau, P., Peyrat, J., Wong, K., Relan, J., Rhode, K., et al.: Patient-specific electromechanical models of the heart for the prediction of pacing acute effects in CRT: A preliminary clinical validation. Medical Image Analysis, 201–215 (2011)
12. Marchesseau, S., Delingette, H., Sermesant, M., Rhode, K., Duckett, S.G., Rinaldi, C.A., Razavi, R., Ayache, N.: Cardiac Mechanical Parameter Calibration Based on the Unscented Transform. In: Ayache, N., Delingette, H., Golland, P., Mori, K. (eds.) MICCAI 2012, Part II. LNCS, vol. 7511, pp. 41–48. Springer, Heidelberg (2012)
13. Gorman III, J., Gupta, K., Streicher, J., Gorman, R., Jackson, B., Ratcliffe, M., Bogen, D., Edmunds, L., et al.: Dynamic three-dimensional imaging of the mitral valve and left ventricle by rapid sonomicrometry array localization. The Journal of Thoracic and Cardiovascular Surgery 112(3), 712–724 (1996)

# Temporal Diffeomorphic Free Form Deformation to Quantify Changes Induced by Left and Right Bundle Branch Block and Pacing

Gemma Piella[1,2], Antonio R. Porras[1,2], Mathieu De Craene[3], Nicolas Duchateau[4], and Alejandro F. Frangi[1,2,5]

CISTIB
[1] DTIC, Universitat Pompeu Fabra
[2] CIBER-BBN, Barcelona, Spain
[3] Philips Research, Medisys, Suresnes, France
[4] Hospital Clínic, IDIBAPS, Universitat de Barcelona, Spain
[5] University of Sheffield, United Kingdom

**Abstract.** This paper presents motion and deformation quantification results obtained from *synthetic* and *in vitro* phantom data provided by the second *cardiac Motion Analysis Challenge* at STACOM-MICCAI. We applied the Temporal Diffeomorphic Free Form Deformation (TDFFD) algorithm to the datasets. This algorithm builds upon a diffeomorphic version of the FFD, to provide a $3D + t$ continuous and differentiable transform. The similarity metric includes a comparison between consecutive images, and between a reference and each of the following images.

Motion and strain accuracy were evaluated on synthetic 3D ultrasound sequences with known ground truth motion. Experiments were also conducted on *in vitro* acquisitions.

## 1 Introduction

Estimation of motion and strain gives insight into cardiac function by quantifying how a given pathology affects global and local deformation of the myocardium. This provides useful information for diagnosis, treatment, and follow-up of cardiac diseases. In clinical routine, motion and strain are often obtained from ultrasound (US) images because it is safe, non-invasive and cost-effective. Although 3D acquisition systems are increasingly used, 3D US images have lower quality and temporal resolution than the 2D ones, thus making their processing more challenging. Nonetheless, processing 3D has the advantage of providing the whole motion and deformation of heart, unlike 2D for which only the projection of these parameters on the observation plane is available. This is particularly important for an accurate quantification, due to the cardiac architecture (e.g., fiber orientation) which imposes by itself motion and deformation to be 3D.

In this paper, we use the Temporal Diffeomorphic Free Form Deformation (TDFFD) algorithm [1,2] and apply it to the synthetic and *in vitro* data provided by the second *cardiac Motion Analysis Challenge (cMAC2)* with the underlying purpose of estimating its accuracy and comparing it to the other motion estimation algorithms submitted to the challenge. The TDFFD models the velocities

O. Camara et al. (Eds.): STACOM 2012, LNCS 7746, pp. 134–141, 2013.

continuously in time and space as a sum of B-spline kernels. In contrast to [1], we use a similarity metric which takes into account the physics of US images. The rationale behind this new metric is that speckle remains temporally consistent for small deformations and can be used as a feature for motion tracking, while tissue and blood pool intensities are globally preserved over the cardiac cycle. Therefore, the proposed metric includes a comparison both between consecutive images (based on the correlated speckle noise as in [3]) and a comparison to the first frame (using mean square error as in [1]). We present and discuss displacement and strain quantification results on the cMAC2 dataset.

In previous work, the accuracy of the TDFFD algorithm was validated (in addition to be tested on patient data) on ground truth data with normal motion from synthetic US images [1] and tagged magnetic resonance imaging provided by the 1st cMAC challenge [6]. Here, the data consists of synthetic images representing different configurations observable in the clinical practice, in the context of cardiac resynchronization therapy (CRT): normal heart, dyssynchronous ones with left bundle branch block (LBBB) and right bundle branch block (RBBB), and with different pacing configurations, for which dyssynchrony is expected to be reduced or corrected. The objective is to check the ability of our algorithm to estimate accurate and physiologically meaningful motion (displacement) and deformation (strain), in both healthy and pathological cases.

## 2 Methods

### 2.1 cMAC2 Database

The synthetic images combine the US imaging model described in [4] with the electro-mechanical model presented in [5]. There are in total 10 sequences simulating one normal heart as well as RBBB abd LBBB cases with and without pacing in different regions of the heart. This data includes ground truth on the motion field. For the synthetic data, volumetric meshes were provided for each frame. More details about the database and its contruction are given in the webpage of the challenge[1].

In vitro images were acquired using a polyvinyl alcohol cryogel phantom and a Philips 3D X5 probe. Ground truth data was generated using microsonometry. Microsonometry measures distances and hence can be used as ground truth for radial, circumferential and longitudinal strains. Further details about the in vitro image generation can be found in the challenge webpage.

### 2.2 Motion Quantification

We use the TDFFD algorithm described in [1] to reconstruct trajectories in the cardiac cycle. The velocity field is represented as a continuous and differentiable 4D vector field using B-splines. The temporal smoothness of the velocity field guarantees to recover temporally smooth transformation. Another advantage is

[1] http://www.physense.org/stacom2012/

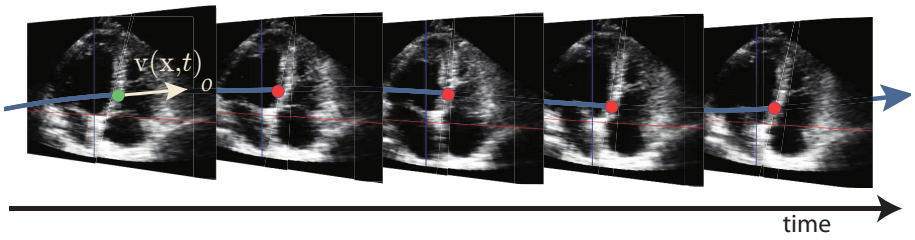


**Fig. 1.** The optimization of velocity at one time point depends on all previous times

that trajectories are not restricted to the discrete set of imaging time points, thus can be evaluated for any continuous time.

The diffeomorphic mapping $\boldsymbol{\varphi} : \Omega \times \mathcal{T} \rightarrow \Omega,\ \Omega \subset \mathbb{R}^3,\ \mathcal{T} \subset \mathbb{R}^+$ is related to the time-varying velocity field $\mathbf{v} : \Omega \times \mathcal{T} \rightarrow \mathbb{R}^3$ by

$$\boldsymbol{\varphi}_n^m(\mathbf{x};\mathbf{p}) = \mathbf{x} + \int_n^m \mathbf{v}(\boldsymbol{\varphi}_n^t(\mathbf{x};\mathbf{p}), t; \mathbf{p})\mathrm{d}t\,, \tag{1}$$

with $\boldsymbol{\varphi}_0^0 = \mathbf{id}$, where $\boldsymbol{\varphi}_m^n(\mathbf{x})$ stands for the transport of a coordinate $\mathbf{x}$ at time $n$ to time $m$, and $\mathbf{p}$ is the vector of parameters (i.e., B-spline velocity coefficients assigned to all control points). At each time step, the optimization of the velocity field evaluates image intensities through all previous times, thus providing a more robust estimation. This is illustrated in Fig. 1.

The similarity metric used in [1] was the squared intensity differences between each image and the first image in the sequence. This choice was shown to avoid the accumulation of motion errors leading to drift effects. In [6], the metric was extended to include also the squared intensity differences between consecutive image pairs with the aim of improving the sensitivity to small incremental displacements. Here, we propose another approach using a combination of two similarity terms: the first one compares images over the entire cardiac cycle as in [1,6], while the second one compares images at adjacent time points using an US-specific metric which considers speckle tracking information as proposed by Cohen *et al.* in [3]. This second metric has inherent robustness to speckle decorrelation, which makes it a suitable metric for fully-developed speckle noise.

For the metric computation, we consider two randomly drawn set of samples. The first one is $\{\mathbf{x}_j \in \Omega_0,\ j = 1, \ldots, J\}$, where $\Omega_0$ is the subdomain of $\Omega$ at time $t = 0$, enclosing the region of interest (e.g., the left ventricle domain). The second one is $\{(\mathbf{y}_k, n_k), \mathbf{y}_k \in \Omega_{n_k},\ k = 1, \ldots, K,\ n_k \in [0, N-2]\}$, where $\Omega_{n_k}$ is the subdomain of $\Omega$ at time $t = n_k$ and $N$ is the number of frames in the sequence. The proposed metric is then defined as

$$M(\mathbf{p}) = \sum_{n=1}^{N-1}\sum_{j=1}^{J}\left(\Delta_0^n(\mathbf{x}_j;\mathbf{p})\right)^2 + \lambda\sum_{k=1}^{K}\left(\ln\left(\exp 2\Delta_{n_k}^{n_k+1}(\mathbf{y}_k;\mathbf{p}) + 1\right) - \Delta_{n_k}^{n_k+1}(\mathbf{y}_k;\mathbf{p})\right), \tag{2}$$

where $\lambda$ is a constant factor balancing the metric terms, $\Delta_l^m(\cdot;\mathbf{p})$ is the intensity difference between homologous points at $t = m$ and $t = l$, i.e.,

$$\Delta_l^m(\cdot;\mathbf{p}) = I_m\big(\boldsymbol{\varphi}_l^m(\cdot;\mathbf{p})\big) - I_l(\cdot)\,. \tag{3}$$

The second term of Eq. 2 is able to make use of speckle tracking information, whereas the first term of Eq. 2, can ensure that small errors in registration results do not add up causing significant errors over the entire cardiac cycle.

### 2.3 Strain Quantification

The strain is estimated from the spatial derivative of the reconstructed displacement field. Let $\nabla\mathbf{u}(\mathbf{x},t)$ be the spatial gradient of displacement $\mathbf{u}(\mathbf{x},t)$, the strain tensor can then be obtained by

$$\boldsymbol{\epsilon}(\mathbf{x},t) = \frac{1}{2}\big(\nabla\mathbf{u}(\mathbf{x},t)^T + \nabla\mathbf{u}(\mathbf{x},t) - \nabla\mathbf{u}(\mathbf{x},t)^T\nabla\mathbf{u}(\mathbf{x},t)\big)\,, \tag{4}$$

where superindex $^T$ denotes transposition. The strain tensor is then projected on a set of local directions: radial, circumferential and longitudinal. The strain data is averaged over 17 regions in accordance with the standard division of the left ventricle proposed by the American Heart Association (AHA) [7]. The local directions are defined on the mesh of the first frame (corresponding to end-systole). Since strain is computed in a Lagrangian space of coordinates, local directions and AHA segments only need to be defined at the first frame.

We use centered differences on the mesh to approximate the spatial derivatives of the displacement. The radial direction is obtained from the normal to the mesh at each node of the surface. The longitudinal direction is defined as perpendicular to the radial direction while maximizing the scalar product with the apex-base vector. The circumferential direction is then obtained by the cross product of radial and longitudinal directions.

## 3 Results

Experiments were performed first on a set of synthetic 3D US sequences to evaluate the accuracy of the TDFFD algorithm with respect to known ground truth displacement. For the B-spline grid resolution, we used one control point per frame in the temporal direction and 5 control points in the short-axis and long-axis directions. The factor $\lambda$ in Eq. 2 is computed (for each sequence) as the ratio of the values of the first term of Eq. 2 to the second term, at the first iteration of the optimization process.

### 3.1 Synthetic Data

For all cases, we computed the error between true and recovered displacements. The median of the peak magnitude of the difference between the ground truth

**Table 1.** Median (with first and third quartiles) of the peak errors (in mm) of the proposed image registration for each case in the dataset

| Case | | Median Peak Error (1st-3rd quartiles) |
|---|---|---|
| 1 | Normal | $1.49(1.19 - 1.60)$ |
| 8 | RBBB | $0.71(0.62 - 0.83)$ |
| 12 | LBBB | $0.66(0.57 - 0.78)$ |
| 20 | LBBB+Pacing 5 | $0.76(0.65 - 0.85)$ |
| 22 | LBBB+Pacing 6 | $1.38(1.12 - 1.48)$ |
| 28 | LBBB+Pacing 7 | $0.80(0.66 - 0.87)$ |
| 36 | LBBB+Pacing 12 | $0.78(0.60 - 0.92)$ |
| 44 | RBBB+Pacing 9 | $0.74(0.67 - 0.78)$ |
| 60 | LBBB+Pacing 3+6 | $0.71(0.63 - 0.82)$ |
| 88 | LBBB+Pacing 7+14 | $0.71(0.66 - 0.79)$ |

displacement field and the one obtained by our algorithm are summarized in Table 1 for each case. The median peak error was obtained by computing the median of the maximum error at each AHA segment.

Fig. 2 plots the mean registration error (over all cases) for each segment and direction. Fig. 3 shows displacement magnitude and circumferential strain for cases 1 (normal), 12 (LBBB) and 22 (LBBB with pacing at AHA segment 6) for the AHA segments at the septum and lateral wall. Displacement magnitudes for case 12 are reduced with respect to the other cases. Moreover, dyssynchrony can be observed for this case between septal segments (2, 3, 8 and 9) and lateral segments (5, 6, 11 and 12), which contract about 20% of the cycle later. When looking at displacements for case 22, this temporal difference in reduced for almost 10% of the cycle and displacement results are similar to the ones obtained for case 1. As for circumferential strain, while rather uniform strain patterns are observed for the normal case, an overall reduction of its magnitude is found for case 12, and its value is almost zero for septal segments during the whole cycle (probably due to the LBBB). In case 22, circumferential strain magnitude is increased with respect to case 12 and more similar to case 1, presenting contraction at septal segments.

### 3.2 Phantom Data

On phantom data, ground truth was provided as distance between pairs of sonomicrometry crystals. These distances give an approximation of radial, circumferential and longitudinal strains. Crystals positions were provided in the image space of coordinates. We computed the trajectories and the pairwise distances corresponding to those given by the ground truth.

Fig. 4 plots on the top row the three strains as provided by sonomicrometry for each acquisition, and on the bottom row the ones obtained by our TDFFD algorithm. As expected, the magnitude of global deformation is reduced with compression. Radial strain is almost zero and, unlike in myocardial tissue, the

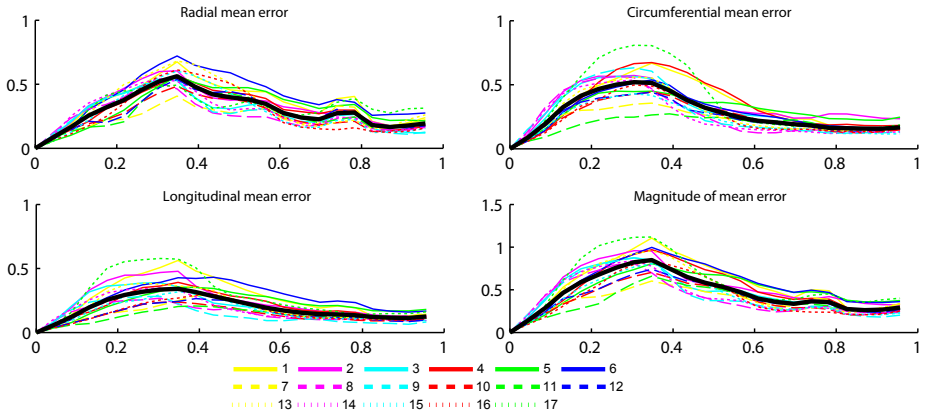


**Fig. 2.** Segmental displacement error (in millimiters), average over all cases. From top to bottom and from left to right: radial, circumferential, longitudinal and overall. Thick black curve corresponds to the median error for all segments. The horizontal axis is the normalized cardiac time (from 0 to 1).

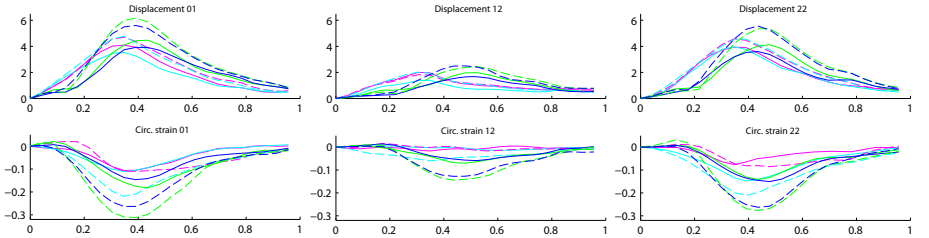


**Fig. 3.** Displacement (top) and circumferential strain (bottom) for case 1 (normal), 12 (LBBB) and 22 (LBBB with pacing at AHA segment 6) for septum and lateral wall segments. The horizontal axis is the normalized cardiac time (from 0 to 1).

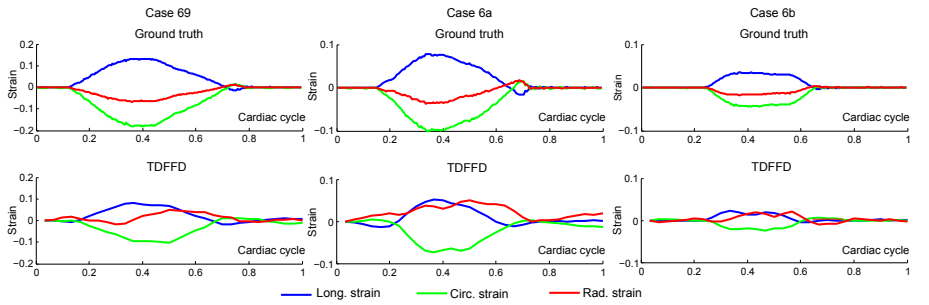


**Fig. 4.** Strain in radial, circumferential and longitudinal directions from sonomicrometry crystals (top) and from tracking on the 3D US sequences (bottom). The horizontal axis is the normalized cardiac time (from 0 to 1).

longitudinal strain takes positive values. One can see that circumferential and longitudinal strain curves from ground truth and from our algorithn are similar in amplitude and shape.

## 4 Conclusions

In this paper, the TDFFD algorithm was extended to include an US-specific metric that considers the correlated speckle noise between consecutive images and has inherent robustness to speckle decorrelation. The use of both this sequential metric and the non-sequential one results in a good compromise between low error values over the contraction period and low temporal drifts in the last phases. Preliminar motion and deformation results were reported for the phantom data provided by the cMAC2. Overall, mean displacement error was below 1 mm. Uniform strain patterns were observed over all myocardial segments for the normal case, as physiologically expected. Comparing the normal with the LBBB case (with and without pacing), the capability to recover dyssynchrony as assessed by the ground truth it is shown.

**Acknowledgments.** This research has been partially funded by the Spanish Industrial and Technological Development Center (CDTI) under the CENIT Programme (cvREMOD Project), the Spanish Ministry of Science and Innovation (Ref. TIN2009-14536-C02-01), Plan E and FEDER, and the European Community's Seventh Framework Program (FP7/2007-2013) under the euHeart project (FP7-ICT-2007-2-224495). ARP is funded by the Spanish Government with an FPU grant.

## References

1. De Craene, M., Piella, G., Camara, O., Duchateau, N., Silva, E., Doltra, A., D'hooge, J., Brugada, J., Sitges, M., Frangi, A.F.: Temporal diffeomorphic free-form deformation: application to motion and strain estimation from 3D echocardiography. Med. Image Anal. 16(2), 427–450 (2012)
2. De Craene, M., Piella, G.: An implementation of the TDFFD and LDFFD algorithms. Insight Journal (2012), `http://hdl.handle.net/10380/3345`
3. Cohen, B., Dinstein, I.: New maximum likelihood motion estimation schemes for noisy ultrasound images. Pattern Recogn. 35(2), 455–463 (2002)
4. Gao, H., Choi, H.F., Claus, P., Boonen, S., Jaecques, S., van Lenthe, G., Van Der Perre, G., Lauriks, W., D'hooge, J.: A fast convolution-based methodology to simulate 2-D/3-D cardiac ultrasound images. IEEE Trans. Ultrason., Ferroelect., Freq. Contr. 56(2), 404–409 (2009)
5. Sermesant, M., Chabiniok, R., Chinchapatnam, P., Mansi, T., Billet, F., Moireau, P., Peyrat, J., Wong, K., Relan, J., Rhode, K., Ginks, M., Lambiase, P., Delingette, H., Sorine, M., Rinaldi, C., Chapelle, D., Razavi, R., Ayache, N.: Patient-specific electromechanical models of the heart for the prediction of pacing acute effects in crt: A preliminary clinical validation. Med. Image Anal. 16(1), 201–215 (2012)

6. De Craene, M., Tobon-Gomez, C., Butakoff, C., Duchateau, N., Piella, G., Rhode, K.S., Frangi, A.F.: Temporal Diffeomorphic Free Form Deformation (TDFFD) Applied to Motion and Deformation Quantification of Tagged MRI Sequences. In: Camara, O., Konukoglu, E., Pop, M., Rhode, K., Sermesant, M., Young, A. (eds.) STACOM 2011. LNCS, vol. 7085, pp. 68–77. Springer, Heidelberg (2012)
7. Cerqueira, M.D., Weissman, N.J., Dilsizian, V., Jacobs, A.K., Kaul, S., Laskey, W.K., Pennell, D.J., Rumberger, J.A., Ryan, T., Verani, M.S.: Standardized myocardial segmentation and nomenclature for tomographic imaging of the heart: a statement for healthcare professionals from the cardiac imaging committee of the council on clinical cardiology of the American Heart Association. Circulation 105(4), 539–542 (2002)

# Three-Dimensional Cardiac Motion Estimation Based on Non-rigid Image Registration Using a Novel Transformation Model Adapted to the Heart

Brecht Heyde[1], Daniel Barbosa[1], Piet Claus[1], Frederik Maes[2], and Jan D'hooge[1,3]

[1] Cardiovascular Imaging and Dynamics, University of Leuven, Leuven, Belgium
brecht.heyde@med.kuleuven.be
[2] Medical Image Computing, University of Leuven, Leuven, Belgium
[3] Medical Imaging Lab, Norwegian Institute for Science & Technology, Trondheim, Norway

**Abstract.** We present a novel method for tracking myocardial motion from volumetric ultrasound data based on non-rigid image registration using an anatomical free-form deformation model. Traditionally, the B-spline control points of such a model are defined on a rectangular grid in Cartesian space. This arrangement may be suboptimal as it treats the blood pool and myocardium similarly and as it enforces spatial smoothness in non-physiological directions. In this work, the basis functions are locally oriented along the radial, longitudinal and circumferential direction of the endocardium. This formulation allows us to model the left ventricular motion more naturally. We obtained encouraging accuracy results for the simulated models, with average errors of 0.8±0.6mm (10% relatively) and 0.5±0.4mm (15% relatively) compared to the ground truth in high and low contractility models respectively.

**Keywords:** Non-rigid registration, anatomical deformation model, motion, echocardiography.

## 1 Introduction

Various automated methods have been developed to objectively assess regional cardiac deformation using echocardiography. Image registration methods using free-form deformation (FFD) models have been an attractive approach. Traditionally, this FFD model is formulated in Cartesian space (Fig. 1a), and has already been shown to be successful for cardiac motion estimation of ultrasound data [1,2,3]. However, this topology may be suboptimal as it treats the blood pool and the myocardium similarly, and as it intrinsically imposes spatial smoothness in non-physiologic directions.

For the analysis of MR images, other transformation models more closely matching the left ventricle (LV) shape and motion have previously been proposed

O. Camara et al. (Eds.): STACOM 2012, LNCS 7746, pp. 142–150, 2013.

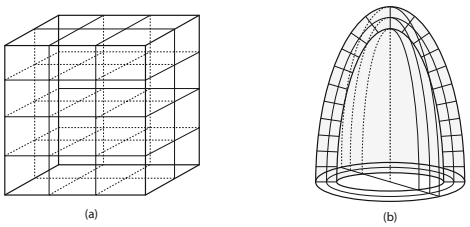


**Fig. 1.** Free form deformations with the B-spline support (a) defined on a cubic lattice in Cartesian space or (b) shaped according to the endocardium in anatomical space

(cylindrical e.g. [4], prolate spheroidal e.g. [5], or extended cylindrical e.g. [6]). However, these geometrical transformation models do not necessarily follow the true anatomy of the heart and are often applied to stacks of 2D short-axis MR data, where motion is not estimated in the apical regions. Furthermore, their application on 4D echocardiography is currently underexplored.

In this paper we propose a novel anatomical FFD (AFFD) model where the local basis functions are locally oriented along the radial ($r$), longitudinal ($l$) and circumferential ($c$) direction of the endocardium. Furthermore, our model can also track tissue in the apical regions. Please note that our description in $[r, l, c]$ coordinates is different compared to the description in prolate spheroidal coordinates $[\lambda, \mu, \theta]$ by Li *et al.* [5] since the local $r$-direction does not neccesarily coincide with the $\mu$-direction as the LV shape is only approximately prolate spheroidal. Moreover, in this work subsequent frames are registered with each other in a pairwise fashion as opposed to the methodology described by Li *et al.* in which the model is always deformed towards the initial (undeformed) state. While this may be reliable for MR, a frame-to-frame registration may be better for echocardiography due to speckle decorrelation over the cardiac cycle.

## 2 Methods

### 2.1 Traditional Cartesian FFD Formulation

Myocardial displacement of a point $\mathbf{r} = [x, y, z]$ between two frames $f$ and $f+1$, can be modelled with a three-dimensional third order B-spline tensor-product [7], defined on a cubic lattice (Fig. 1a):

$$\mathbf{u}_{f\to f+1}(\mathbf{r}) = \sum_{i\in N_i}\sum_{j\in N_j}\sum_{k\in N_k} \mu_{ijk}\beta_x^3(\frac{x-s_i}{\sigma_x})\beta_y^3(\frac{y-s_j}{\sigma_y})\beta_z^3(\frac{z-s_k}{\sigma_z}) \qquad (1)$$

with $s_\xi$ and $\sigma_\xi$ the control point location and spacing respectively, and $N_\xi$ the set of control points within the compact support of the B-spline $\beta_\xi$ ($\xi \in \{x, y, z\}$).

The sum-of-squared differences was used as an image similarity metric for intra-modality registration. The optimal inter-frame transformation field $\mathbf{T}(\mathbf{r}) = \mathbf{r} + \mathbf{u}_{f\to f+1}(\mathbf{r})$ was estimated iteratively with a LBFGSB optimizer [8] as this

optimizer was found to give a good performance for optimization of a large amount of parameters while also eliminating the need for storing the inverse of the Hessian matrix during the optimization routine. In order to capture small deformations, the model complexity was gradually increased using a coarse-to-fine refinement strategy, halving the B-spline grid with a factor of two in every stage. Regularization was performed during the optimization process by the addition of a smoothness penalty based on the 3D equivalent of the bending energy of a 2D thin sheet of metal [9] in the cost function $E$:

$$E = \frac{1}{d} \sum_{\mathbf{r} \in I_f} \left[ I_f(\mathbf{r}) - I_{f+1}(\mathbf{T}(\mathbf{r})) \right]^2 + \frac{\alpha}{d} \sum_{\mathbf{r} \in I_f} \left\| \frac{\partial^2 \mathbf{T}(\mathbf{r})}{\partial \mathbf{r}^2} \right\|^2 \tag{2}$$

with $d$ the number of points $\mathbf{r}$, and $\alpha$ a factor to modulate the influence of the smoothness penalty.

The choice of these registration components have all been proven useful for myocardial motion estimation [1,2,3]. In practice, subsequent images $I_f$ were registered to each other in a pair-wise fashion. The total displacement of a point $\mathbf{r}$ was found by concatenating the resulting $\mathbf{T}(\mathbf{r})$ over the cardiac cycle.

### 2.2 Anatomical FFD Formulation

The AFFD B-spline grid is organized locally according to the shape of the endocardium (Fig. 1b). Due to the locally varying grid topology, it becomes evident that the mathematical formulation of the B-spline grid locations, their local neighborhood and grid refinement schemes are complex. In effect, the evaluation of (1) in this local coordinate system is not straightforward.

An alternative implementation for an anatomical organized grid is to transform the images to *anatomical* coordinates first, such that the overlying grid becomes a cubic lattice similar to the Cartesian formulation. The next sections describe the details of the anatomical unfolding process.

**Endocardial Surface Parametrization.** In order to map the curved endocardial surface to a plane, an elegant parametrization is required which allows a uniform sampling along the $l$- and $c$-direction. Given the ellipsoidal shape of the LV, a natural choice to describe its geometry would be in prolate spheroidal coordinates $[\lambda, \mu, \theta]$ (Fig. 2a). In order to account for local shape differences, $\lambda$ is parametrized as a spherical harmonics (SH) expansion series:

$$\lambda(\mu, \theta) = \sum_{q=0}^{\infty} \sum_{m=-q}^{q} c_{qm} \, Y_{qm}(\mu, \theta); \quad Y_{qm} = \sqrt{\frac{2q+1}{4\pi} \frac{(q-m)!}{(q+m)!}} P_{qm}(cos\,\mu) e^{im\theta} \tag{3}$$

with $Y_{qm}$ and $P_{qm}$ the SH basis functions and the Legendre functions respectively. This SH parametrization has several advantages. It is efficient as it can generate a wide variety of shapes even for low SH orders $q$ and surface derivatives can be calculated analytically. Given a sparse sampling of the LV surface with $d$

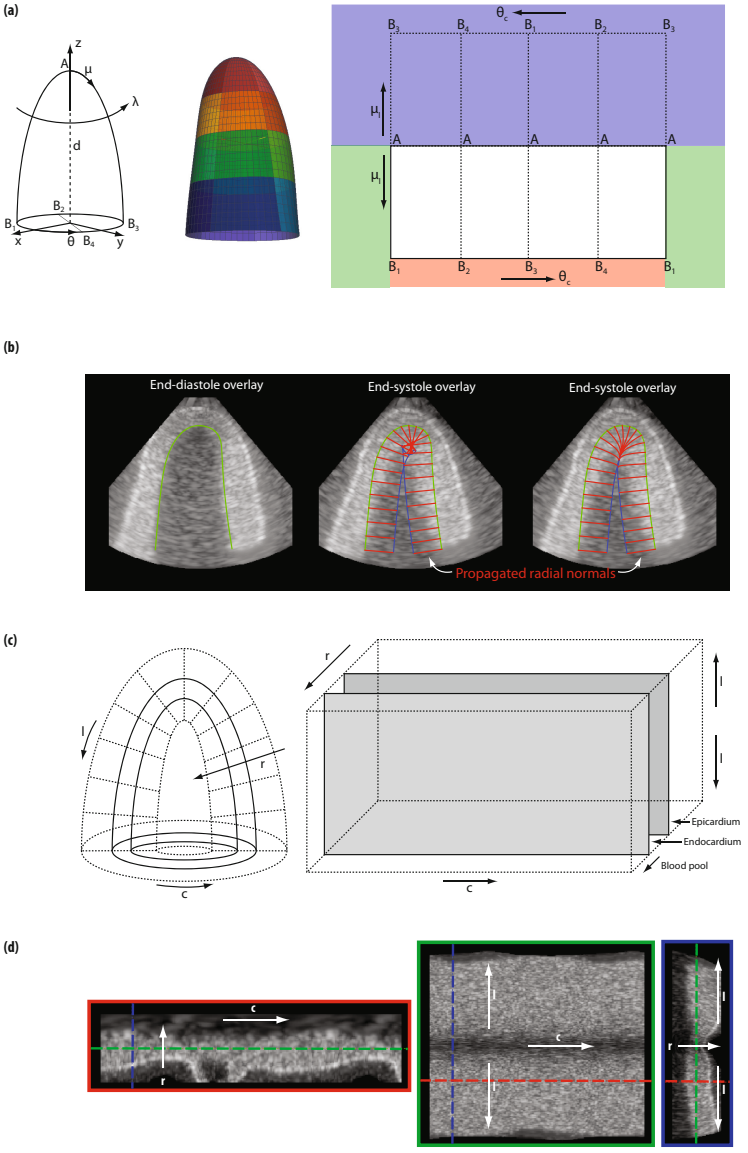


**Fig. 2.** Overview of the different steps to unfold the left ventricle into anatomical space. (a) Endocardial surface parametrization in Cartesian space *(left)* with the associated segmental color-coded sampled surface *(middle)*; and the sampling strategy in anatomical space *(right)*, (b) Propagation of the radial direction from the endocardial surface, (c) Radial expansion strategy in Cartesian space *(left)* and the resulting mapping in anatomical space *(right)*, and (d) Illustration of the transformed volumetric image in anatomical space.

points, the expansion coefficients $c_{qm}$ completely define the endocardial surface and can be found by minimizing the following objective function:

$$F(\lambda) = \sum_d \left(\lambda(\mu_d, \theta_d) - \lambda_d(\mu_d, \theta_d)\right)^2 \tag{4}$$

where $\lambda_d$ is the $\lambda$ coordinate of the $d$th point. These points can come from manual contouring (in clinical practice) or from a given mesh. Please note that the considered endocardial surface is not necessarily a prolate spheroid.

**Endocardial Surface Sampling Strategy.** After surface parametrization, the endocardium is sampled in a select number of angles along the $l$ and $c$ direction, by linear sampling of $\mu_l \in \left[0, \frac{\pi}{2}\right]$ and $\theta_c \in [0, 2\pi]$ respectively. In order to keep a comparable resolution after unwrapping the surface, the number of circumferential $\theta_c$ samples is equal to the mid-ventricular circumference length in voxels, and the number of longitudinal $\mu_l$ samples is equal to the average base-to-apex length along the surface in voxels (Fig. 2a, white zone).

In order to account for longitudinal motion near the base, the endocardium is oversampled in the $\mu_l$ direction by extending the mesh along the longitudinal direction of the base. For the images considered in this challenge, a fixed value of 20% was used (Fig. 2a, red zone).

It is important that the mapping preserves the topology of the endocardium. In order to enforce circumferential continuity at the $\theta_c$=0, $\theta_c$=2$\pi$ borders, a small part of the image was copied on either side (Fig. 2a, green zone). The size of this copy was equal to the B-spline support extend at the coarsest transformation model scale, i.e. $\left[\frac{-n-1}{2}s, \frac{n+1}{2}s\right]$ voxels with a B-spline degree $n$. Longitudinal continuity near the apex was ensured by mirroring a shifted ($\Delta\theta$=$\pi$) copy of the current image at the apex (Fig. 2a, blue zone).

**Radial Expansion Strategy.** The image is further resampled by propagating the endocardial surface $S$ along the surface normal, i.e. in the radial direction $\mathbf{n_r}$. As such, the endocardial surface is propagated both inwards towards the blood pool as outwards towards the epicardium to ensure that the full myocardium remains inside the transformed image during the whole cardiac cycle.

The normals of the surface $\mathbf{n}_r, \mathbf{n}_l, \mathbf{n}_c$ can be calculated analytically by using (3) and

$$\mathbf{n}_l = \frac{\partial \mathbf{r}}{\partial \mu} = \frac{\partial \mathbf{r}}{\partial \lambda}\frac{\partial \lambda}{\partial \mu} + \frac{\partial \mathbf{r}}{\partial \theta}\frac{\partial \theta}{\partial \mu} + \frac{\partial \mathbf{r}}{\partial \mu}\frac{\partial \mu}{\partial \mu}; \quad \mathbf{n}_c = \frac{\partial \mathbf{r}}{\partial \theta} = sim; \quad \mathbf{n}_r = \mathbf{n}_l \otimes \mathbf{n}_c \tag{5}$$

where $\mathbf{n}_c$ is calculated in a similar fashion as $\mathbf{n}_l$. However, simply expanding the surface towards the blood pool along a fixed direction may lead to tissue folding in cartesian space. This situation often occurs near the apex or at locations with a high curvature (Fig. 2b, *middle*). The radial direction should therefore not be kept constant, but rather evolve dynamically towards the inner cavity.

In practice, this can be solved by posing the propagation process as a diffusion problem for each component of $\mathbf{n}_r$:

$$\frac{\partial \mathbf{n}_r}{\partial t} = \beta \nabla^2 \mathbf{n}_r;\ \mathbf{n}_{r,0}^{S} \overset{(5)}{=} \mathbf{n}_r,\ \mathbf{n}_{r,0}^{\Omega \backslash S} = 0,\ \mathbf{n}_{r,t}^{S} \overset{(5)}{=} \mathbf{n}_r \tag{6}$$

where $\mathbf{n}_{r,t}^{S}$ corresponds to the radial direction at time $t$ on the endocardial surface $S$, and $\Omega \backslash S$ corresponds to entire image domain excluding the endocardial surface. In practice, 200 iterations proved to be a good trade-off between calculation time and desired accuracy. Following the calculated streamlines, the surface is propagated in both directions (Fig. 2b *right* for endocardial propagation in 2D), and a 3D stack in anatomical space is generated (Fig. 2c).

This expansion strategy can also be thought of in terms of electrostatics in which the endocardial surface would have a constant charge. Accordingly, isopotential surfaces can be computed by solving the Laplace equation. Expanding the endocardial surface then becomes equivalent to moving this surface along the electrical field lines, i.e. along the normals of these isosurfaces.

**Motion and Strain Estimation.** In practice, motion is estimated by transforming the image sequence $I$ to an anatomical equivalent image sequence $\hat{I}$ in $[r, l, c]$ coordinates (Fig. 2d) as described above. A linear interpolation procedure is used to resample the original image. Subsequent images are then registered in a pairwise fashion by using the method described in section 2.1 since the overlaying lattice is now cubic. Similarly, a series of points $\mathbf{p}_f$ representing a region-of-interest for motion estimation, can be mapped to $\hat{\mathbf{p}}_f$, and propagated over time using the obtained registration results. Finally, the deformed points $\hat{\mathbf{p}}_{f+1}$ are then mapped back to cartesian coordinates $\mathbf{p}_{f+1}$ for motion estimation and visualisation.

Since the provided ground-truth mesh was not organised in the r/l/c direction, the same anatomical mapping strategy described above was used to populate the myocardium with points in the cardiac directions for strain calculation ($n_r$=5, $n_l$=30, $n_c$=60). Strain along a cardiac direction could then be estimated by using the unit length extension $\epsilon = (L - L_0)/L_0$, with $L_0$ and $L$, the initial and current length between neighboring points in the considered direction.

## 3 Experiments and Results

All the simulated datasets provided for this challenge (image size: 355x355x267 for x,y,z resp.) were transformed to anatomical space with $\theta_c$=191 and $\mu_l$=327. In order to evaluate the performance of the motion estimation, the ground truth displacement $\mathbf{T}^{GT}(\mathbf{p}_f)$ provided for the reference mesh and the estimated displacement $\mathbf{T}(\mathbf{p}_f)$ were compared in every frame $f$ according to

$$\delta_{p,f} = \left\| \mathbf{T}^{GT}(\mathbf{p}_f) - \mathbf{T}(\mathbf{p}_f) \right\| \tag{7}$$

Only points of the ground truth mesh belonging to the left ventricle (segments 1-17) were considered.

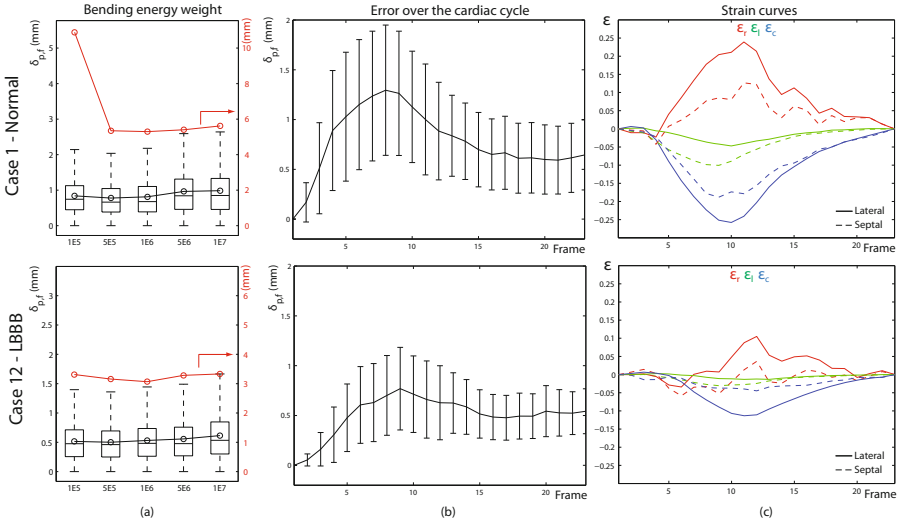


**Fig. 3.** (a) Influence of the bending energy weight $\alpha$ on the error $\delta_{p,f}$ for (top) case 1 and (bottom) case 12. The black and red line correspond to the average and the maximum error over the cardiac cycle respectively, (b) The dispersion of the errors ($\mu \pm \sigma$) and (c) the resulting strain curves in the lateral and septal segment (for $\alpha$=5E5).

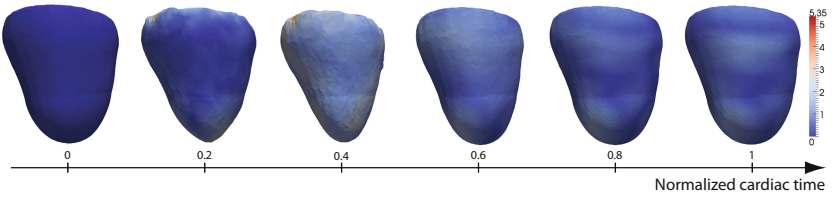


**Fig. 4.** Visualisation of the registration results for case 1 (lateral view). The color overlay on the deformed LV represents the magnitude of the registration error $\delta_{p,f}$(mm).

First, the weight of the bending energy $\alpha$ was optimized using two training datasets with a normal motion pattern (case 1) and motion in the presence of a left bundle branch block (LBBB; case 12) by varying its contribution between 1E5 and 1E7. Third order B-splines and three refinement stages with a final B-spline grid spacing of 10x10x10 voxels were used in all cases (on average corresponding to 3.4 x 3.4 x 3.4mm in the original image sequence $I$). An optimal weight of $\alpha$=5E5 was found (Fig. 3a).

Next, all datasets were processed using these parameter settings and the error $\delta_{p,f}$ over the cardiac cycle was assessed using (7). The dispersion of the errors and the resulting strain curves for two cases are shown in Fig. 3b and c respectively. Fig. 4 shows the registration results for case 1. Table 1 summarizes the obtained accuracy results, and analyses which segments contain the largest errors. The amount and range of the outliers are also indicated.

**Table 1.** Mean($\mu$)±std($\sigma$) errors $\delta_{d,f}$ in $mm$ for the different datasets. The number of outliers (in %), their range ($min - max$) and the two segments (AHA 17 segment model) containing the most outliers are also indicated. * = higher contractility.

| Case | Description | $\mu \pm \sigma$[mm] | Outliers | | | |
|---|---|---|---|---|---|---|
| | | | min[mm] | max[mm] | count(%) | segments(%) |
| 1* | Normal | 0.78±0.57 | 2.04 | 5.35 | 3.67 | 17(24) 13(21) |
| 8 | RBBB | 0.51±0.35 | 1.35 | 2.99 | 2.47 | 17(18) 6(13) |
| 12 | LBBB | 0.50±0.35 | 1.36 | 3.16 | 2.29 | 17(18) 1(15) |
| 20 | LBBB (Pacing 5) | 0.51±0.35 | 1.37 | 2.98 | 2.23 | 17(18) 1(13) |
| 22* | LBBB (Pacing 6) | 0.75±0.57 | 2.08 | 4.76 | 3.11 | 17(17) 13(16) |
| 28 | LBBB (Pacing 7) | 0.51±0.35 | 1.39 | 3.24 | 2.01 | 17(21) 1(16) |
| 36 | LBBB (Pacing 12) | 0.51±0.35 | 1.40 | 3.14 | 2.15 | 17(22) 1(15) |
| 44 | RBBB (Pacing 9) | 0.50±0.34 | 1.29 | 3.17 | 2.83 | 17(18) 1(12) |
| 60 | BV (Pacing 3+6) | 0.50±0.34 | 1.36 | 2.88 | 2.08 | 17(21) 1(14) |
| 88 | BV (Pacing 14+7) | 0.48±0.35 | 1.34 | 3.54 | 2.35 | 1(17) 17(15) |

## 4 Discussion and Conclusions

Table 1 shows that the obtained average errors for all the processed data were in the sub-mm range. For the datasets with a high contractility (case 1 and 22), errors were 0.8±0.6mm (this corresponds to an error relative to the present motion of approximately 10%), while the error was 0.5±0.4mm for the other datasets with a lower global contractility (relative error approximately 15%).

Our method was also able to detect differences in model contractility. An example of the obtained strain curves is given in Fig. 3c (case 1 vs case 12). However, for the LBBB dataset (case 12) we didn't observe any peak strain timing differences between the lateral and segmental wall. The underlying reasons remain unclear since no specific details of the applied electromechanical model were given (e.g. the affected segments, the contractility delay or the degree of impairment). Furthermore, the apparent small motion amplitude from the model makes it intrinsically harder to assess strain differences between segments.

Two other observations can be inferred from table 1. First, the average errors within the two data groups, i.e. low and high contractility, are very similar. This may be due to the low intra-model variability. For example, looking at the ground truth data of case 12 (no pacing) and case 36 (with pacing), both models only differ at most 1mm in segment 12 (where the pacing occurs). Given the fact that the average thickness of this segment is 15mm and that the motion difference is very localized, this subtle difference may be too difficult to pick up, most likely because of the particularly low SNR of these datasets. Secondly, the largest errors mostly occured in the apical region (segments 17 and 13), where the method underestimated motion during systole. Segment 1 (base) was another site with major errors. This may be due to an unsmooth motion of the ground truth mesh at the base. This particular electromechanical model behavior remains unclear to the authors.

Moreover, Fig. 3a showed that the obtained average errors are robust to changes in the bending energy penalty weight within the currently assessed range, which was preselected based on experience. In this in-silico setup, the contribution of this term thus appears low. This may be due to the low ground truth deformations, intrinsically leading to a low inter-frame bending energy. Indeed, in the high contractility model (case 1, Fig. 3a *top*), the influence becomes higher. The maximum error increased substantially up to 10.9mm (*left*) and 5.62mm (*right*). It is expected that this trend continues beyond the assessed range. Obviously, increasing the influence of the smoothness constraint too much restricts the motion while decreasing it leads to too much degrees of freedom.

In conclusion, this paper presented a novel registration approach using a transformation model adapted to the heart shape. We obtained encouraging accuracy results with average errors of 0.8±0.6mm and 0.5±0.4mm compared to the ground truth in high and low contractility models respectively.

## References

1. Elen, A., Choi, H., Loeckx, D., Gao, H., Claus, P., Suetens, P., Maes, F., D'hooge, J.: 3D cardiac strain estimation using spatio-temporal elastic registration of ultrasound images: a feasibility study. IEEE Trans. Med. Imaging 27(11), 1580–1591 (2008)
2. Heyde, B., Cygan, S., Choi, H., Lesniak-Plewinska, B., Barbosa, D., Elen, A., Claus, P., Loeckx, D., Kaluzynski, K., D'hooge, J.: Regional cardiac motion and strain estimation in three-dimensional echocardiography: A validation study in thick-walled univentricular phantoms. IEEE Trans. Ultrason. Freq. Control 59(4), 668–682 (2012)
3. De Craene, M., Piella, G., Camara, O., Duchateau, N., Silva, E., Doltra, A., D'hooge, J., Brugada, J., Sitges, M., Frangi, A.: Temporal diffeomorphic free-form deformation: application to motion and strain estimation from 3D echocardiography. Med. Image Analysis 16(2), 427–450 (2012)
4. Deng, X., Denney, T.: Three-dimensional myocardial strain reconstruction from tagged MRI using a cylindrical B-spline model. IEEE Trans. Med. Imaging 23(7), 861–867 (2004)
5. Li, J., Denney, T.: Left ventricular motion reconstruction with a prolate spheroidal B-spline model. Phys. Med. Biol. 51(3), 517–537 (2006)
6. Lin, N., Duncan, J.: Generalized robust point matching using an extended free-form deformation model: application to cardiac images. In: ISBI - International Symposium on Biomedical Imaging, vol. 1, pp. 320–323 (2004)
7. Kybic, J., Unser, M.: Fast parametric elastic image registration. IEEE Trans. Image Process. 12(11), 1427–1442 (2003)
8. Byrd, R., Lu, P., Nocedal, J., Zhu, C.: A limited memory algorithm for bound constrained optimization. SIAM Journal on Scientific Computing 16(5), 1190–1208 (1995)
9. Rueckert, D., Sonoda, L., Hill, D., Leach, M., Hawkes, D.: Nonrigid registration using free-form deformations: application to breast MR images. IEEE Trans. Med. Imaging 18(8), 712–721 (1999)

# Motion Estimation in 3D Echocardiography Using Smooth Field Registration

Oudom Somphone[1], Cécile Dufour[1], Benoît Mory[1], Loïc Hilpert[2], Sherif Makram-Ebeid[1], Nicolas Villain[1], Mathieu De Craene[1], Pascal Allain[1], and Eric Saloux[2]

[1] Medisys, Philips Research, Suresnes, France
[2] Department of Cardiology, University Hospital of Caen, Caen, France

**Abstract.** This paper describes an algorithm for motion and deformation quantification of 3D cardiac ultrasound sequences. The algorithm is based on the assumption that the deformation field is smooth inside the myocardium. Thus, we assume that the displacement field can be represented as the convolution of an unknown field with a Gaussian kernel. We apply our algorithm to datasets with reliable ground truth: a set of synthetic sequences with known trajectories and a set of sequences of a mechanical phantom implanted with microsonometry crystals.

**Keywords:** Motion Estimation, Myocardial Motion, 3D Cardiac Ultrasound, Demons, Phantom, Microsonometry.

## 1 Introduction

Quantifying heart function at a local scale is an important challenge for the diagnosis of heart diseases. For example, locally ischemic segments will have impaired contractility in a region whose size and location depend on vascularization territories from the coronary tree. Another example is local assynchrony induced by conduction defects in the Purkinje tree. Besides the importance of quantifying heart function at a local level, deformation (strain) is preferred to motion since it is less influenced by surrounding tissue.

Several imaging modalities offer the possibility to quantify strain noninvasively. Tissue Doppler Imaging (TDI) [1] measures tissue velocities (hence strain rate) in a 2D plane. However, they give a projection of the strain tensor in the direction of the ultrasound beam. Speckle tracking [2] was proposed as an alternative to quantify displacement independently from the acquisition angle. Because of the orientation of the fibers architecture within the ventricular wall [3], motion and deformation of myocardial tissue are intrinsically three dimensional. 2D speckle tracking are therefore limited by out of plane motion, disturbing the tracking of speckle over time and calling for multiple acquisitions with the limitations and challenges of combining information from different heart cycles.

3D speckle tracking therefore has the potential to overcome limitations of both TDI and 2D speckle tracking. However, thorough validation needs to be conducted for quantifying the impact of different imaging settings on accuracy

O. Camara et al. (Eds.): STACOM 2012, LNCS 7746, pp. 151–158, 2013.

and localizability of this technique. Byram *et al.* [4] studied the effects of frame rate, kernel size, and data type on 3D tracking performances. They reported increasing accuracy in motion accuracy with frame rate, up to 200 Hz, at which the accuracy stabilizes. Heyde *et al.* [5] quantified strain accuracy for a non-rigid registration method on a thick-walled cardiac phantom. Local inclusions were placed for various stiffness ratios between materials mimicking normal and pathological tissues. They reported to recover full transmural inclusions down to 17 mm in diameter, for a stiffness ration of at least 5:2.

In this paper, we quantify the accuracy on motion and strain of a *demons*-based image registration algorithm. Motion accuracy was quantified on simulated ultrasound data for different contractility and pacing settings. Strain accuracy was quantified from in vitro phantom images by comparing relative length changes to distances measured by sonomicrometry. All data was acquired in the context of the cardiac motion analysis challenge at STACOM 2012.

## 2 Motion Estimation with Smooth Registration

In this section, we give a brief description of the *Smooth Registration* approach that we use to perform motion estimation, and the subsequent *demons*-like algorithm. Demons have been previously used by Mansi *et al* to estimate myocardial strain from 3D cine and tagged MRI sequences [6].

### 2.1 Variational Formulation

Considering the problem of registering two images $R$ and $T$, referred to as the reference and the template respectively, we adopt a fluid-like regularization, which can be approximated by Gaussian linear filtering, as in the well-known *demons* algorithm [7]. The displacement field $\mathbf{u}$ that transforms $T$ towards $R$ is assumed to be the result of the component-wise convolution of an unknown non-rigid field $\mathbf{v}$ with a spatial Gaussian kernel $\omega_\sigma$:

$$\mathbf{u}(\mathbf{x}) = \omega_\sigma * \mathbf{v}(\mathbf{x}) = \int_\Omega \omega_\sigma(\mathbf{x} - \mathbf{y})\mathbf{v}(\mathbf{y})\ d\mathbf{y} \tag{1}$$

where $\Omega \subset \mathbb{R}^3$ is the domain of definition of $\mathbf{u}$ and $\sigma$ is the scale of the kernel; the larger $\sigma$, the smoother $\mathbf{u}$. This field representation was introduced in [8] in the context of template-to-image registration. It is then injected within a classical Sum of Squared Differences formulation, consisting in the minimization of the following cost functional with respect to $\mathbf{v}$:

$$E(\mathbf{v}) = \int_\Omega \Big[R(\mathbf{x}) - T(\mathbf{x} + \mathbf{u}(\mathbf{x}))\Big]^2\ d\mathbf{x} \tag{2}$$

Note that although the optimal displacement $\mathbf{u}$ warps the later frame towards the earlier one, it represents the motion field at the instant of $R$.

### 2.2 A Simple Algorithm

The optimization is done by gradient descent; basic calculus of variations results in the following evolution equation:

$$\frac{\partial \mathbf{v}}{\partial t} = -\nabla_{\mathbf{v}} E = -\omega_\sigma * \nabla_{\mathbf{u}} E \tag{3}$$

where $\nabla_{\mathbf{u}} E$ is the gradient of $E$ w.r.t. $\mathbf{u}$:

$$\nabla_{\mathbf{u}} E(\mathbf{x}) = -\Big[R(\mathbf{x}) - T(\mathbf{x} + \mathbf{u}(\mathbf{x}))\Big] \nabla T(\mathbf{x} + \mathbf{u}(\mathbf{x})) \tag{4}$$

It appears that the gradient w.r.t. $\mathbf{v}$ is simply obtained by filtering the gradient w.r.t. $\mathbf{u}$ with a Gaussian kernel. This leads to the *demons*-like iterative scheme detailed in Algorithm 1 below.

**Algorithm 1.** Smooth Registration - Gradient Descent Scheme

Set $i = 0$ and $\mathbf{v}^0 = \mathbf{0}$
**repeat**
  Compute $\mathbf{u}^i = \omega_\sigma * \mathbf{v}^i$
  **for** all $\mathbf{x} \in \Omega$ **do**
    Compute $T(\mathbf{x} + \mathbf{u}^i(\mathbf{x}))$ and $\nabla T(\mathbf{x} + \mathbf{u}^i(\mathbf{x}))$ by interpolation
    Compute $\nabla_{\mathbf{u}^i} E(\mathbf{x})$ according to (4)
  Smooth the result to obtain the incremental update $\delta \mathbf{v}^i = -\omega_\sigma * \nabla_{\mathbf{u}^i} E$
  Update $\mathbf{v}^{i+1} = \mathbf{v}^i + \delta t . \delta \mathbf{v}^i$
  $i = i + 1$
**until** *steady state*;

This gradient descent scheme is embedded into a multiresolution strategy.

### 2.3 Myocardium Mask

Regularizing the displacement field as in (1) may corrupt the estimation inside the myocardium with the influence of features located outside of the myocardium. This is particularly critical at the interface between the pericardium – which is fixed – and the epicardium, where motion may be underestimated. To deal with this issue, we introduce a mask, provided by a prior segmentation of the myocardium, by substituting the Gaussian filtering with a normalized convolution. The displacement field becomes:

$$\mathbf{u} = \omega_\sigma * (\mathbf{v}, \chi) \;\widehat{=}\; \frac{\omega_\sigma * (\chi \mathbf{v})}{\omega_\sigma * \chi} \tag{5}$$

where $\chi$ is the characteristic function of the myocardium (1 inside and 0 outside). Replacing (1) by (5) in the previous calculus leads to the following gradient:

$$\nabla_{\mathbf{v}} E = \chi \left( \omega_\sigma * \frac{\nabla_{\mathbf{u}} E}{\omega_\sigma * \chi} \right) \tag{6}$$

The subsequent modified scheme is presented in Algorithm 2 below.

**Algorithm 2.** Masked Smooth Registration - Gradient Descent Scheme

Set $i = 0$ and $\mathbf{v}^0 = \mathbf{0}$;
**repeat**
  Compute $\mathbf{u}^i = \omega_\sigma * (\mathbf{v}^i, \chi)$
  **for** all $\mathbf{x} \in \Omega$ **do**
    Compute $T(\mathbf{x} + \mathbf{u}^i(\mathbf{x}))$ and $\nabla T(\mathbf{x} + \mathbf{u}^i(\mathbf{x}))$ by interpolation
    Compute $\nabla_{\mathbf{u}^i} E(\mathbf{x})$ according to (4)
    Divide $\nabla_{\mathbf{u}^i} E(\mathbf{x})$ by $\omega_\sigma * \chi(\mathbf{x})$
  Smooth and mask the result to obtain the incremental update
  $\delta \mathbf{v}^i = -\chi \left( \omega_\sigma * \frac{\nabla_{\mathbf{u}^i} E}{\omega_\sigma * \chi} \right)$
  Update $\mathbf{v}^{i+1} = \mathbf{v}^i + \delta t . \delta \mathbf{v}^i$
  $i = i + 1$
**until** *steady state*;

### 2.4 Tracking Trajectories

Tracking trajectories along a sequence can be done by applying the above algorithm using two strategies (see Fig. 1):

(i) registering every frame $I^{(t)}$ towards the initial frame $I^{(0)}$;
(ii) registering every frame $I^{(t)}$ towards the previous frame $I^{(t-1)}$ and compose frame-to-frame displacements.

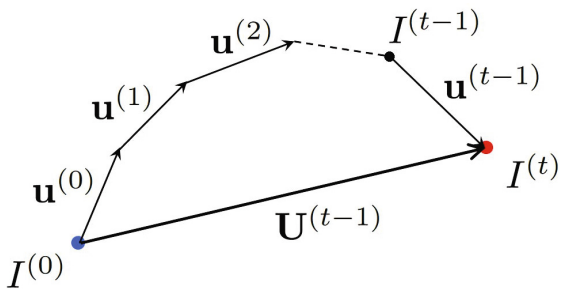


**Fig. 1.** Tracking trajectories along a sequence. Registering frames $I^{(t)}$ as template and $I^{(0)}$ as reference results in the displacement field $\mathbf{U}^{(t-1)}$. Registering frames $I^{(t)}$ as template and $I^{(t-1)}$ as reference results in the displacement field $\mathbf{u}^{(t-1)}$.

Strategy (i) may seem more suitable since it avoids the frame-to-frame error accumulation inherent to strategy (ii). However, it leaves out the temporal coherence of the sequence, since the estimation of each $\mathbf{U}^{(t)}$ is dependent of $I^{(0)}$ only and does not take the previous frames into account. This latter drawback being critical, we chose strategy (ii).

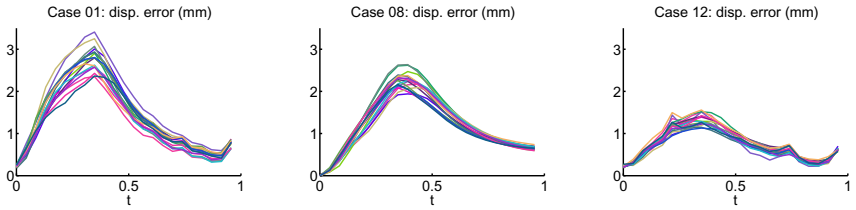


**Fig. 2.** Synthetic cases. Average error on displacement as a function of time for the 17 AHA segments in the 3 first cases of the database.

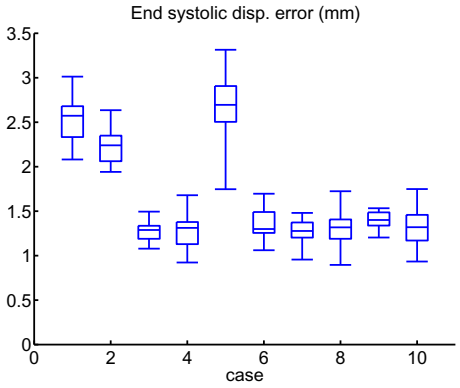


**Fig. 3.** Synthetic cases. Box plots showing the dispersion of displacement error (in mm) measured at the end of systole for each case.

## 3 Experiments

We applied the method described in Sect. 2 on the synthetic and the phantom data provided for the cMAC2 challenge. Details on the data setup can be found on the cMAC2 challenge web page[1]. We processed all provided data i.e. the 10 simultations with provided ground truth on the motion fields and the 3 phantom datasets with ground truth provided at 4 spatial locations as distances measured by sonomicrometry. The computation time was in the order of 8 minutes for each processed sequence.

### 3.1 Results on Synthetic Data

On synthetic data, we evaluated the accuracy of our algorithm to estimate the trajectories of material points given on the volumetric mesh. Error magnitude was plotted over time for each of the 17 American Heart Association (AHA) segments in the Left Ventricle (LV). The curves (one per segment) are plotted in

[1] `http://bit.ly/motionchallenge`

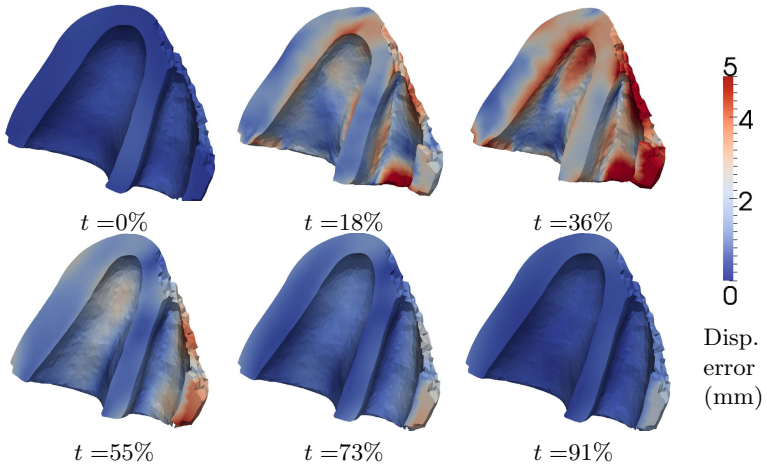


**Fig. 4.** Synthetic cases. Displacement error plotted at 6 frames of the cardiac cycle (times goes from top left, early systole, to bottom right, late diastole.

Fig. 2 for the 3 first cases of the database. Since the first case models a healthy subject, it showed the largest displacements. The error was higher on this case than for the other subjects (see Fig. 2), indicating that the error increases with the magnitude of the displacement to be estimated. The same tendency appears in the temporal evolution of the error curves within each subject. Indeed, the error increases over systole, up to frame #10, for all cases before decreasing over diastole. The latter indicates the absence of drift in the trajectories estimated by our algorithm.

To observe the error dispersion over all subjects, we plotted the range of error magnitudes at the end of systole for each subject. The resulting plot is shown in Fig. 3. For most cases, the median error at the end of systole was below 1.5 mm. Three cases exhibited higher errors: the first one, as previously commented, and two outliers: the second and the fifth cases. Finally, to examine the spatial distribution of errors over time, we plotted the error on the trajectories as a color map for each frame of the cardiac cycle (see Fig. 4). Only the LV was tracked, which explains the high error values appearing in the right ventricle. The highest error values appeared close to the apex and can be explained by high reverberation artifacts observable on the simulated images.

### 3.2 Results on Phantom Data

On phantom data, ground truth was provided as pairwise distances measured between sonomicrometry crystals. Crystals positions were also provided by the challenge organizers in the image space of coordinates. We computed the trajectories and the pairwise distances matching those given by the ground truth. These distances are not strictly equivalent to strain but are a good surrogate of radial, circumferential and longitudinal deformations. Fig. 5 plots on the top

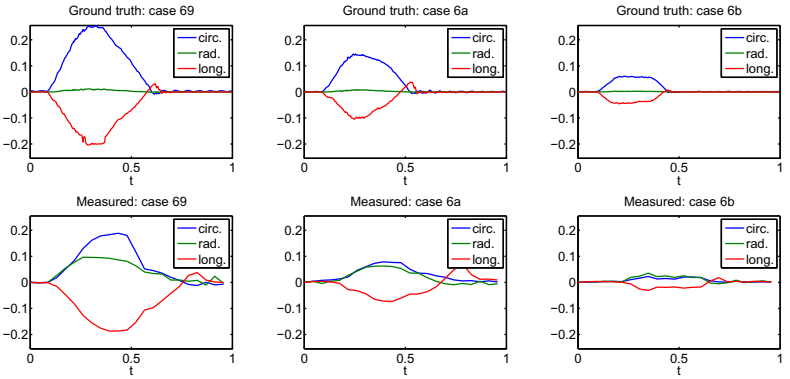


**Fig. 5.** Top: relative length changes over time between sonomicrometry crystals in radial, circumferential and longitudinal directions. Bottom: The same relative length changes measured by tracking on the 3D US image.

line the three distances as provided by sonomicrometry for each provided acquisition. It can be observed that, unlike in real myocardial tissue, the circumferencial strain takes positive values over the cardiac cycle. Radial strain showed positive values, but of one order of magnitude smaller than the two other distances. The magnitude of the global deformation was mechanically reduced over each acquisition, as confirmed by the decreasing amplitude of the sonomicrometry curves.

In comparison to the ground truth, we observe that image-based tracking (bottom line of Fig. 5) correctly estimated both the amplitude and the pattern of longitudinal strain. Only in the last acquisition, imaging noise disturbed the temporal pattern of the estimated curve with respect to ground truth. Circumferential strain was underestimated in all three acquisitions but the relative magnitude of peak-systolic circumferential strain matched the decreasing tendency of the ground truth. Finally, estimates of radial strain values are not in agreement with the values reported by the ground truth.

When averaging radial strain values on the axial slice containing the two crystals, we obtained values of respectively 10, 7 and 3.5 % for each acquisition. These values are significantly higher than the ones reported by sonomicrometry. Further experiments and validation on the estimated trajectories are required to understand this disagreement.

## 4 Conclusion

We proposed a *demons*-like algorithm that performs a normalized convolution of the estimated motion field in the region of interest (myocardial mask). The method is fast and processes an entire 3D sequence is about 7 minutes. Our experiments on the cMAC2 synthetic data gave a median accuracy around 1.5

mm at the end of systole for 7 cases over 10. On the phantom dataset, longitudinal strain values were comparable in amplitude and pattern to distances measured by sonomicrometry. The relative amplitude and the temporal pattern of circumferential strain values were in accordance with sonomicrometry. Important differences were observed in radial strain values that require further investigation.

## References

1. Sutherland, G., Di Salvo, G., Claus, P., D'hooge, J., Bijnens, B.: Strain and strain rate imaging: a new clinical approach to quantifying regional myocardial function. Journal of the American Society of Echocardiography 17(7), 788–802 (2004)
2. Mondillo, S., Galderisi, M., Mele, D., Cameli, M., Lomoriello, V., Zacà, V., Ballo, P., D'Andrea, A., Muraru, D., Losi, M., et al.: Speckle-tracking echocardiography: a new technique for assessing myocardial function. Ultrasound in Medicine 30(1), 71 (2011)
3. Greenbaum, R., Ho, S., Gibson, D., Becker, A., Anderson, R.: Left ventricular fibre architecture in man. British Heart Journal 45(3), 248–263 (1981)
4. Byram, B., Holley, G., Giannantonio, D., Trahey, G.: 3-D phantom and in vivo cardiac speckle tracking using a matrix array and raw echo data. IEEE Transactions on Ultrasonics, Ferroelectrics and Frequency Control 57(4), 839–854 (2010)
5. Heyde, B., Cygan, S., Choi, H., Lesniak-Plewinska, B., Barbosa, D., Elen, A., Claus, P., Loeckx, D., Kaluzynski, K., D'hooge, J.: Regional cardiac motion and strain estimation in three-dimensional echocardiography: A validation study in thick-walled univentricular phantoms. IEEE Transactions on Ultrasonics, Ferroelectrics and Frequency Control (2011)
6. Mansi, T., Pennec, X., Sermesant, M., Delingette, H., Ayache, N.: iLogDemons: A Demons-Based Registration Algorithm for Tracking Incompressible Elastic Biological Tissues. International Journal of Computer Vision 92(1), 92–111 (2011)
7. Thirion, J.P.: Image matching as a diffusion process: an analogy with Maxwell's Demons. Medical Image Analysis 2(3), 243–260 (1998)
8. Mory, B., Somphone, O., Prevost, R., Ardon, R.: Real-Time 3D Image Segmentation by User-Constrained Template Deformation. In: Ayache, N., Delingette, H., Golland, P., Mori, K. (eds.) MICCAI 2012, Part I. LNCS, vol. 7510, pp. 561–568. Springer, Heidelberg (2012)

# Monogenic Phase Based Optical Flow Computation for Myocardial Motion Analysis in 3D Echocardiography

Martino Alessandrini[1], Hervé Liebgott[1], Daniel Barbosa[1,2], Olivier Bernard[1]

[1] CREATIS, CNRS UMR 5220, INSERM U630, INSA-Lyon, Villeurbanne, France
alessandrini@creatis.insa-lyon.fr
[2] Lab. on Cardiovascular Imaging and Dynamics, KU Leuven, Leuven, Belgium

**Abstract.** We present a method for the analysis of heart motion from 3D cardiac ultrasound sequences. The algorithm exploits the monogenic signal theory, recently introduced as a N-dimensional generalization of the analytic signal. The displacement is computed locally by tracking variations in the monogenic phase. A 3D local affine displacement model accounts for typical motions as contraction/expansion and shearing. A coarse-to-fine B-spline scheme allows a robust and effective computation of the model parameters and a pyramidal refinement scheme helps in dealing with large motions. The independence of the monogenic phase on the local energy makes the algorithm insensitive to the time variant changes of image intensity that are often observed on echocardiographic sequences. The performance of our method is evaluated on 10 realistic simulated 3D echocardiographic sequences, showing good tracking accuracy (average error: $0.68 \pm 0.5$ to $1.27 \pm 0.9$ mm).

## 1 Introduction

Three dimensional cardiac ultrasound provides a real time low cost and non invasive technique for the assessment of myocardial elasticity and contractility. Nowadays, this analysis mainly relies on the visual inspection of the ultrasound sequences by the physician. In this context, the availability of automated motion analysis techniques would be an highly desirable alternative to such a practice that, besides being intrinsically subjective, is extremely time demanding [1]. Some of the methods developed to this end exploit the standard brightness constancy assumption [2]. Nevertheless, this can be an arguable choice as far as medical ultrasound is concerned. Indeed, temporal variations in the local echo strength are likely to occur due to the changes in the angle between the myocardial fibers and direction of propagation of the ultrasonic beam [3]. Methods looking for the maximum correlation between speckle patches [4] may also be inadequate due to the relative low frame rate of 3D ultrasound scanners [5].

To overcome this issues, most recent techniques base their motion estimates on features that are maximally insensitive to brightness fluctuations and more strictly correlated with the image structure. They include the mutual information [5] and the monogenic phase [6]. The monogenic signal has been recently

O. Camara et al. (Eds.): STACOM 2012, LNCS 7746, pp. 159–168, 2013.

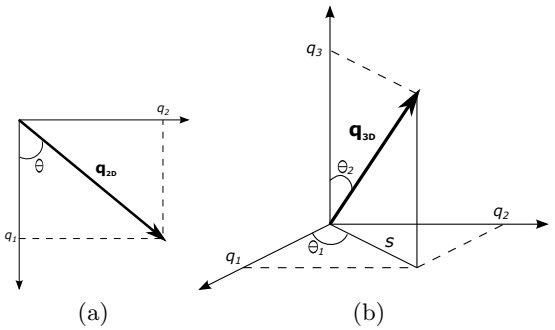


**Fig. 1.** (a) Traditional representation of the monogenic orientation for 2D images. (b) Monogenic orientation for 3D data.

introduced by Felsberg as an nD generalization of the analytic signal (see [7] and references therein). Similarly to the latter, it provides both local energy and phase features. Additionally, it provides the feature of monogenic orientation, representing the direction of maximum energy variation. Orientation and phase can be shown to be uncorrelated with the energy content and this property makes them valuable features for developing robust applications targeted to medical ultrasound.

In this paper, we propose a motion estimation algorithm replacing the traditional brightness constancy with the more suitable conservation of the monogenic phase. The motion is the estimated by solving the optical flow equation locally on a sliding spatial window. A local affine model accounts for typical cardiac motions as contraction/expansion and shearing. A coarse-to-fine B-spline scheme allows a robust and effective computation of the model parameters. In order to estimate large motions, a multi-scale pyramidal refinement approach is adopted.

The paper is organized as follows. In Section 2 some details on the 3D monogenic signal are given and an original noise robust computation of the monogenic orientation is described. In Section 3 the proposed monogenic phase optical flow algorithm is described. In Section 4 some implementation details are given. The obtained results are presented in Section 5. Finally, some conclusions are drawn in Section 6.

## 2 Monogenic Signal Computation

In this section we define the monogenic signal and illustrate the most practical aspects of its implementation. For a more rigorous derivation we address the reader to [7] and the references therein. Note that the presented formulation is slightly different from the original one as 3D volumes are here considered instead of 2D images.

The monogenic signal of a 3D grey valued image $I : \Omega \to \mathbb{R}, \Omega \subset \mathbb{R}^3$, is obtained from the responses to four 3D spherical quadrature filters (SQFs). The SQFs consist of one *even* rotation invariant bandpass $b_e(\mathbf{x}; \lambda_0)$ filter and three *odd* bandpass

filters $b_{o1}(\mathbf{x};\lambda_0)$, $b_{o2}(\mathbf{x};\lambda_0)$ and $b_{o3}(\mathbf{x};\lambda_0)$, where $\mathbf{x}=[x_1,x_2,x_3]^T$ is the pixel position and $\lambda_0$ is the filter wavelength, defined as the reciprocal of the normalized center frequency $f_0$.

The odd filters are computed from the Riesz transform of the even one. In the frequency domain it is:

$$B_{ok}(\boldsymbol{\omega}) = \mathcal{R}_k(\boldsymbol{\omega}) \cdot B_e(\boldsymbol{\omega}), \qquad \mathcal{R}_k(\boldsymbol{\omega}) = -\frac{j\omega_k}{|\boldsymbol{\omega}|} \tag{1}$$

where $\boldsymbol{\omega}=[\omega_1,\omega_2,\omega_3]^T$ is the normalized angular frequency and $\mathcal{R}_k(\boldsymbol{\omega})$ is the Riesz transform along the direction $k=\{1,2,3\}$. In this paper, as recommended in [7], the difference of Poisson (DoP) kernel is adopted:

$$B_e(\boldsymbol{\omega}) = \exp\left(-2\pi|\boldsymbol{\omega}|s_f\right) - \exp\left(-2\pi|\boldsymbol{\omega}|s_c\right), \quad s_f < s_c. \tag{2}$$

From the four filter responses the image features of amplitude $A(\mathbf{x})$, monogenic phase $\phi(\mathbf{x})$, and the two orientations $\theta_1(\mathbf{x})$, $\theta_2(\mathbf{x})$ can be obtained:

$$A(\mathbf{x}) = \sqrt{p^2(\mathbf{x}) + |\mathbf{q}(\mathbf{x})|^2}, \qquad \phi(\mathbf{x}) = \arctan\left(\frac{|\mathbf{q}(\mathbf{x})|}{p(\mathbf{x})}\right) \tag{3}$$

$$\theta_1(\mathbf{x}) = \arctan\left(\frac{q_2(\mathbf{x})}{q_1(\mathbf{x})}\right), \qquad \theta_2(\mathbf{x}) = \arctan\left(\frac{s(\mathbf{x})}{q_3(\mathbf{x})}\right)$$

where $p(\mathbf{x}) = (I * b_e)(\mathbf{x})$, $q_1(\mathbf{x}) = (I * b_{o1})(\mathbf{x})$, $q_2(\mathbf{x}) = (I * b_{o2})(\mathbf{x})$, $q_3(\mathbf{x}) = (I * b_{o3})(\mathbf{x})$, $\mathbf{q}(\mathbf{x}) = [q_1(\mathbf{x}), q_2(\mathbf{x}), q_3(\mathbf{x})]^T$ and $s(\mathbf{x}) = \sqrt{q_1(\mathbf{x})^2 + q_2(\mathbf{x})^2}$. Note that passing from two to three dimensions implies replacing the single monogenic orientation with the two angles $\theta_1$ and $\theta_2$, needed to define the direction of $\mathbf{q}$ in the 3D space (cf. Fig. 1).

Despite a theoretically justified derivation of the above quantities requires the employment of complex mathematical concepts, otherwise they can be given a simple and intuitive interpretation. Namely, monogenic amplitude $A$ and phase $\phi$ correspond to the analogous quantities of the analytic signal once the standard Hilbert transform has been replaced with the *directional Hilbert transform* along $\mathbf{n}=\mathbf{q}/|\mathbf{q}|$ (see next section for its definition). In turn, the two angles $\theta_1$ and $\theta_2$ define the direction of maximum image energy variation.

The unit vector $\mathbf{n}$ and the two monogenic orientations are related by (cf. Fig. 1):

$$\mathbf{n} = [\cos(\theta_1)\sin(\theta_2), \sin(\theta_1)\sin(\theta_2), \cos(\theta_2)]^T. \tag{4}$$

The dependency on $\mathbf{x}$ is omitted in the sequel for brevity sake. The *phase vector* $\mathbf{r}=\phi\cdot\mathbf{n}$ is commonly used to represent monogenic phase and orientation in a concise form [7].

### 2.1 Robust Orientation Computation

In order to improve the robustness against image noise, in this study we replace the classical orientation estimate in (3) with a robust least squares one [8].

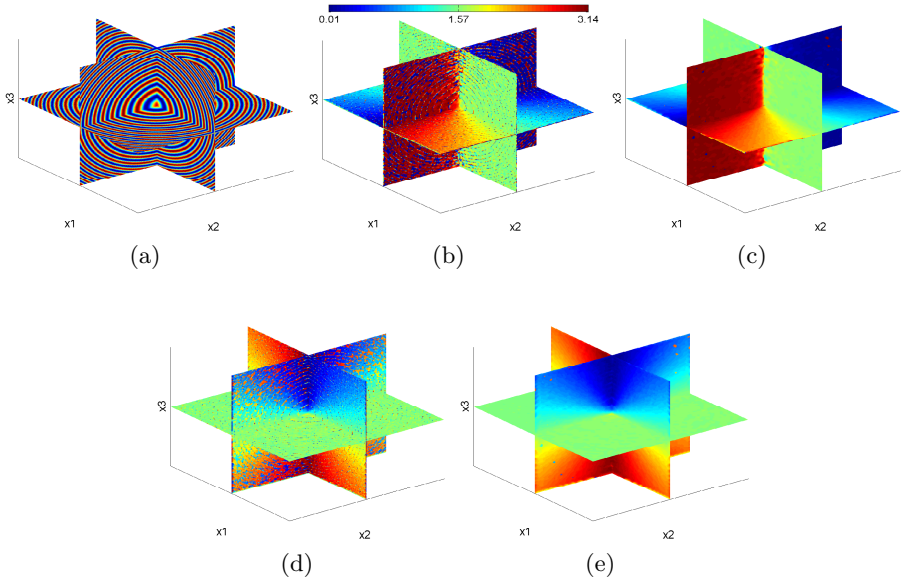


**Fig. 2.** (a) Test image: a 3D chirp image containing full $[0, 2\pi]$ rotations in $\theta_1$ and $\theta_2$ and a linearly increasing frequency in the outwards direction. A 10dB additive Gaussian noise has been added to evaluate the robustness of the adopted orientation estimates. (b) point-wise estimate of $\theta_1$. (c) least-squares estimate of $\theta_1$. (d) point-wise estimate of $\theta_2$. (e) least-squares estimate of $\theta_2$. The increased robustness with respect to noise is evident.

This is obtained as the value maximizing the directional Hilbert transform $\mathcal{H}_{\mathbf{u}}I(\mathbf{x})$ averaged over a local neighborhood $v_\sigma$:

$$\mathbf{n}(\mathbf{x}) = \arg \max_{||\mathbf{u}||=1} \int_\Omega v_\sigma(\mathbf{x}' - \mathbf{x}) \cdot |\mathcal{H}_{\mathbf{u}}I(\mathbf{x}')|^2 d\mathbf{x}' \tag{5}$$

where $v_\sigma$ corresponds here to a Gaussian kernel with variance $\sigma^2$ and the directional Hilbert transform is defined in the frequency domain as $\mathcal{H}_{\mathbf{u}}(\boldsymbol{\omega}) = \boldsymbol{\omega}^T\mathbf{u}/|\boldsymbol{\omega}|$. It can be shown that (5) corresponds to the pointwise solution (3) if $v_\sigma(\mathbf{x}) = \delta(\mathbf{x})$.

The optimization problem (5) is solved by the eigenvector associated to the largest eigenvalue of the $3 \times 3$ matrix $\mathbf{T}(\mathbf{x})$, with entries:

$$[\mathbf{T}(\mathbf{x})]_{nm} = \int_\Omega v_\sigma(\mathbf{x}' - \mathbf{x}) q_n(\mathbf{x}') q_m(\mathbf{x}') d\mathbf{x}' \tag{6}$$

with $n, m = \{1, 2, 3\}$. Matrix $\mathbf{T}$ can be assimilated to a Riesz-transform counterpart of the standard structure tensor.

Rigorously, the eigenvalue problem should be solved iteratively on all the voxels of the image, which would increase tremendously the computational burden.

Here, to avoid this shortcoming we derive an analytical solution based on the hypothesis that the image structure is locally 1D[1]. By doing so, the only eigenvalue of (6) is $\lambda = [\mathbf{T}]_{11} + [\mathbf{T}]_{22} + [\mathbf{T}]_{33}$, and the two monogenic orientations are defined by:

$$\theta_1 = \arctan\left\{\frac{([\mathbf{T}]_{22} + [\mathbf{T}]_{33}) \cdot [\mathbf{T}]_{23} + [\mathbf{T}]_{13} \cdot [\mathbf{T}]_{12}}{([\mathbf{T}]_{11} + [\mathbf{T}]_{33}) \cdot [\mathbf{T}]_{13} + [\mathbf{T}]_{23} \cdot [\mathbf{T}]_{12}}\right\}; \tag{7}$$
$$\theta_2 = \arctan\left\{\frac{([\mathbf{T}]_{11} + [\mathbf{T}]_{22})}{([\mathbf{T}]_{13} \cdot \sin(\theta_1) + [\mathbf{T}]_{23} \cdot \cos(\theta_1))}\right\}.$$

The derivation of (7) is omitted here for reasons of space.

Due to the averaging operation in (5), this alternative estimate is expected to be less sensitive to image noise as compared to the traditional one. An example of this property is given in Fig. 2.

## 3 Multiscale Optical Flow Computation from the Monogenic Phase

As in [7], the displacement field $\mathbf{d}(\mathbf{x}) = [d_1(\mathbf{x}), d_2(\mathbf{x}), d_3(\mathbf{x})]^T$ along $x_1$ $x_2$ and $x_3$ between two frames is estimated by replacing the traditional brightness constancy assumption with the more robust *monogenic phase constancy assumption*. This can be conveniently expressed in terms of the monogenic phase vector $\mathbf{r} = [r_1, r_2, r_3]$ as $\mathbf{r}(t+1, \mathbf{x}) = \mathbf{r}(t, \mathbf{x} - \mathbf{d})$. Assuming small displacements the first order Taylor expansion can be used $\mathbf{r}(t, \mathbf{x} - \mathbf{d}) = \mathbf{r}(t, \mathbf{x}) - \mathbf{J} \cdot \mathbf{d}$, where $\mathbf{J}$ is the Jacobian matrix of $\mathbf{r}$. Then, assuming all pixels translate of the same quantity $\mathbf{d}_0$ within a local window $w$ centered in $\mathbf{x}_0 = [x_{10}, x_{20}, x_{30}]$, the following linear system of equations is obtained:

$$\langle \mathbf{J} \rangle_w \mathbf{d}_0 = -\langle \mathbf{r}_t \rangle_w, \quad \mathbf{J} = \begin{bmatrix} r_{1x_1} & r_{1x_2} & r_{1x_3} \\ r_{2x_1} & r_{2x_2} & r_{2x_3} \\ r_{3x_1} & r_{3x_2} & r_{3x_3} \end{bmatrix} \tag{8}$$

where $(\cdot)_t$ denotes the time derivative, $\langle \mathbf{v} \rangle_w = \int_\Omega w(\mathbf{x} - \mathbf{x}_0)\mathbf{v}(\mathbf{x})d\mathbf{x}$ and $r_{ix_k} = \partial_{x_k} r_i$. Assuming 1D structures [7], the matrix $\mathbf{J}$ is rewritten a function of its only eigenvalue $f$ and eigenvector $\mathbf{n}$, *i.e.* $\mathbf{J} = f\mathbf{n}\mathbf{n}^T$. In particular, it can be shown that $\mathbf{n}$ is the same as in (4), while the $f =< \nabla\phi, \mathbf{n} >$, with $\nabla = [\partial_{x_1}, \partial_{x_2}, \partial_{x_3}]^T$. Resulting from the derivative of the monogenic phase, $f$ is called *monogenic frequency*.

The required terms to solve (8) are then $\mathbf{r}_t$, $f$ and $\mathbf{n}$. The first two are computed as in [7]:

$$f = \frac{p\nabla^T\mathbf{q} - \mathbf{q}^T\nabla p}{p^2 + |\mathbf{q}|^2}, \quad \mathbf{r}_t = \frac{p_t\mathbf{q}_{t+1} - \mathbf{q}_t p_{t+1}}{|p_t\mathbf{q}_{t+1} - \mathbf{q}_t p_{t+1}|} \arctan\left(\frac{|p_t\mathbf{q}_{t+1} - \mathbf{q}_t p_{t+1}|}{p_t p_{t+1} + \mathbf{q}_t^T\mathbf{q}_{t+1}}\right) \tag{9}$$

[1] This assumption holds as long as the image does not contain sharp features at the observation scale $\sigma$. This is a reasonable approximation on cardiac images due to the natural regularity of the heart contours. We also note that the 1D assumption is itself primal in the formulation of the monogenic signal theory [9].

where subscripts "t" and "t + 1" denote the time instant, while $\mathbf{n}$ is computed from the monogenic orientations (7) by means of (4).

### 3.1 Affine Model

The simple translation model in (8) is too restrictive in a general context. Also, its validity is heavily dependent on the choice of the size of $w$. To encompass this limitation, we employ an affine model for the local displacement, accounting for rotation, expansion, compression and shear. Considering for simplicity a window centered at $(x_{10}, x_{20}, x_{30}) = (0, 0, 0)$, the affine model is:

$$\mathbf{d}(\mathbf{x}) = \mathbf{A}(\mathbf{x})\mathbf{u}, \tag{10}$$

$$\mathbf{A} = \begin{bmatrix} 1 & 0 & 0 & x_1 & x_2 & x_3 & 0 & 0 & 0 & 0 & 0 & 0 \\ 0 & 1 & 0 & 0 & 0 & 0 & x_1 & x_2 & x_3 & 0 & 0 & 0 \\ 0 & 0 & 1 & 0 & 0 & 0 & 0 & 0 & 0 & x_1 & x_2 & x_3 \end{bmatrix} \tag{11}$$

$$\mathbf{u} = [d_{10}, d_{20}, d_{30}, d_{1x_1}, d_{1x_2}, d_{1x_3}, d_{2x_1}, d_{2x_2}, d_{2x_3}, d_{3x_1}, d_{3x_2}, d_{3x_3}]^T \tag{12}$$

where $\mathbf{I}$ is the $3 \times 3$ identity matrix and $\mathbf{u}$ is the new unknown vector: $d_{10}$, $d_{20}$ and $d_{30}$ correspond to the translation of the window center and the other entries are the first order spatial derivatives ($d_{ix_k} = \partial_{x_k} d_i$). Plugging (10) into (8) leads to an underdetermined system of equations. whose least-squares solution is $\mathbf{b} = \mathbf{M}\mathbf{u}$, with $\mathbf{b} = -\left\langle \mathbf{A}^T\mathbf{J}^T\mathbf{r}_t \right\rangle_w$ and $\mathbf{M} = \left\langle \mathbf{A}^T\mathbf{J}^T\mathbf{J}\mathbf{A} \right\rangle_w$. It can be shown that the entries of $\mathbf{M}$ and $\mathbf{b}$ are the local moments of orders zero to two of the spatial and temporal derivatives of the phase vector components [10].

Let's note also that, as the first order spatial derivatives of the displacement are also computed, the Lagrangian strain tensor can be directly obtained from the latter, with no need of further numerical differencing.

### 3.2 Multiscale Choice of the Window Size

The choice of the window size is a tedious issue connected with local techniques: the assumed motion model (translational or affine) may not hold when the window is too big, otherwise, the adoption of an excessively small window may result in the well known *aperture problem*. To circumvent this issue we apply a 3D extension of the multiscale choice of the window size proposed in [10]. This is based on the possibility to compute the image moments, *i.e.* the entries of the system matrix $\mathbf{M}$ and the vector $\mathbf{b}$, at multiple scales by using an efficient B-spline *coarse to fine* strategy [10]. In particular, they are obtained from window functions $w$ which are progressively scaled and subsampled by a factor 2 in each dimension. Namely, at scale $j$, the window $w^j(\mathbf{x} - \mathbf{x}_0) = w((\mathbf{x} - 2^j\mathbf{x}_0)/2^j)$ is employed, where $w$ is written as the separable product of three B-spline functions.

By doing so, at each scale $J_f \leq j \leq J_c$ ($J_f \geq 0$) a solution $\mathbf{u}^j$ can be computed. Among the considered scales, the $\mathbf{u}^j$ producing the smallest residual error $||\mathbf{M}\mathbf{u}^j - \mathbf{b}||_{\ell 2}/|w|_{\ell 1}$ is retained as the final displacement estimate. Whenever necessary, bi-cubic interpolation is employed to have a dense motion field. With this strategy, the scale providing the most consistent motion estimate is selected.

### 3.3 Iterative Displacement Refinement

The hypothesis of small displacements employed in differential techniques may be inadequate whenever the displacement is big or the image intensity profile is non-linear. This problem becomes crucial when 3D ultrasound imaging is concerned, due to the low acquisition frame rate.

To overcome this limitation, we implement here a coarse to fine refinement of the displacement estimate. We exploit a coarse sub-sampled representation of the image to obtain a rough estimate of the displacement. The current estimate is then employed to undo the motion and the incremental displacement is computed on the image at the finer scale. The required multi-resolution representation of the images is obtained via B-spline decomposition. Fifth order B-spline functions are employed. This strategy is observed to improve considerably the precision of the estimate.

## 4 Implementation Details

The pseudo-code of the proposed algorithm is presented in Algorithm 1. Function `ComputeBsplineImagePyramid` generates a pyramid of images at scales $s = 1, \cdots, N_p$ using B-spline decomposition. $I^s$ denotes the image at scale $s$. The wavelength for the SQF was fixed at $\lambda_0 = 0.1$ Hz$^{-1}$. The multiscale window choice of Section 3.2 was implemented by considering 5-th order B-splines and

**Algorithm 1:** Multiscale Monogenic Optical Flow

**Input**: two subsequent frames: $I_1$, $I_2$
parameters: $\lambda_0$, $J_f$, $J_c$, $N_p$, $k$, $\sigma$.
**Output**: displacement $\mathbf{d}$ between $I_1$ and $I_2$

$\mathbf{d} = 0$; `/* set initial displacement */`
`ComputeBsplineImagePyramid`($I_1$,$I_2$)
**for** $n = 1 : N_p$ **do**
  $s = N_p - n + 1$; `/* scale in the B-spline pyramid of Section 3.3 */`
  $[B_e, B_{o1}, B_{o2}, B_{o3}]$ = `ComputeSQF`($\lambda_0$); `/* see (1) and (2) */`
  $[p_1, \mathbf{q}_1]$ = `MonogenSignal`($I_1^s$,$B_e$,$B_{o1}$,$B_{o2}$,$B_{o3}$);
  $[p_2, \mathbf{q}_2]$ = `MonogenSignal`($I_2^s$,$B_e$,$B_{o1}$,$B_{o2}$,$B_{o3}$)
  $f$ = `MonogenFreq`($p_1$,$\mathbf{q}_1$); `/* see (9) */`
  $[\theta_1, \theta_2]$ = `MonogenOrient`($\mathbf{q}_1$,$\sigma$); `/* see (7) */`
  $\mathbf{r}_t$ = `TimeDer`($p_1$,$p_2$,$\mathbf{q}_1$,$\mathbf{q}_2$); `/* see (9) */`
  $\mathbf{J}$ = `JacobianMatrix`($f$,$\theta_1$,$\theta_2$); `/* see (8) */`
  $\Delta\mathbf{d}$ = `MultiscaleOF`($\mathbf{J}$,$\mathbf{r}_t$,$J_c$,$J_f$); `/* increment, see Section 3.2 */`
  $\mathbf{d} = \mathbf{d} + \Delta\mathbf{d}$; `/* estimate refinement */`
  $I_2^{s-1}$ = `Interp`($I_2^{s-1}$,$\mathbf{x} + \mathbf{d}$); `/* subtract motion before refinement */`

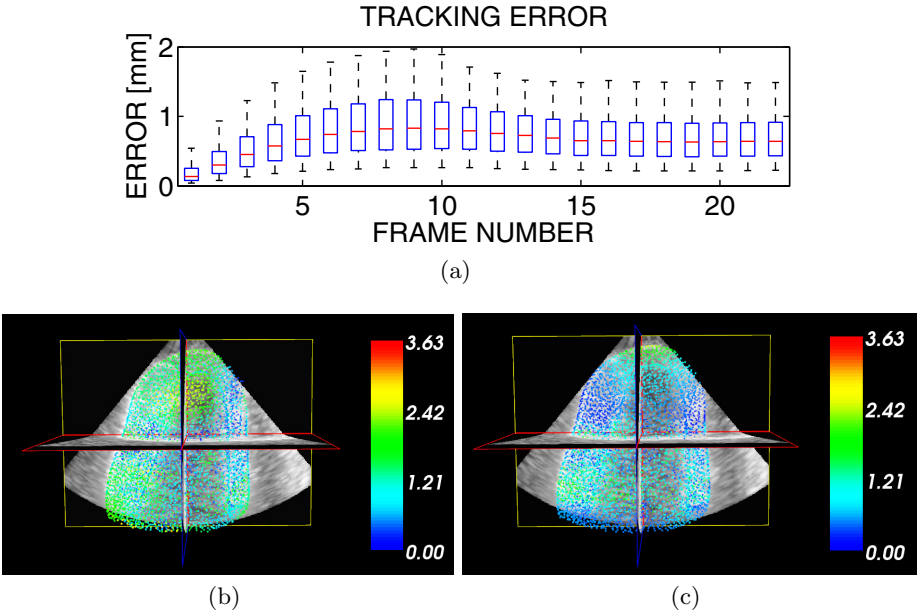


**Fig. 3.** (a) Tracking error on the 2nd simulated sequence (named case08). Lower and upper limits of the box represent 25th and 75th percentile while the whiskers the 5th and 95th. (b) Error map corresponding to the end-systole and close to the end diastole in (c). The scatterers positions correspond the true one while the color indicates the estimation error.

scales $j = \{3, 4\}$. A Gaussian kernel of standard deviation $\sigma = 1$ was employed for the robust orientation computation of Section 2.1.

## 5 Results

The performance was evaluated on a set of 10 simulated 3D echocardiographic sequences. The heart motion was simulated by displacing a set of point scatterers according to the electromechanical model of the myocardium proposed by Sermesant *et al.* [11]. From the time varying scatter map the ultrasound image formation was then simulated with the COLE software developed by Gao *et al.* [12]. Each sequence represents an entire cardiac cycle (from the initial end-diastolic state (ED1) to the subsequent end-diastole (ED2)) and was obtained from a different configuration of the parameters of the electromechanical model (namely electrical activation position, global conductivity and contractility). The precise parameters configuration for each sequence is reported in the STACOM2012 challenge site [13].

We evaluate the performance of our algorithm by measuring the error in tracking the scatterers employed in the simulation. Namely, let's denote by $\bar{\mathbf{x}}_k^i$

**Table 1.** Tracking errors overview for all the sequences, in millimeters

| sequence ID | 01 | 08 | 12 | 20 | 22 | 28 | 36 | 44 | 60 | 88 |
|---|---|---|---|---|---|---|---|---|---|---|
| **Full cardiac cycle** | | | | | | | | | | |
| mean value | 1.27 | 0.70 | 0.69 | 0.68 | 1.23 | 0.72 | 0.68 | 0.71 | 0.68 | 0.68 |
| standard deviation | 0.87 | 0.47 | 0.48 | 0.46 | 0.87 | 0.49 | 0.46 | 0.47 | 0.48 | 0.47 |
| 5th percentile | 0.08 | 0.06 | 0.04 | 0.05 | 0.06 | 0.04 | 0.04 | 0.06 | 0.04 | 0.04 |
| 95th percentile | 2.92 | 1.59 | 1.60 | 1.55 | 2.87 | 1.65 | 1.57 | 1.60 | 1.60 | 1.57 |
| **End-systole (ES)** | | | | | | | | | | |
| mean value | 1.87 | 0.93 | 0.94 | 0.94 | 1.87 | 0.98 | 0.95 | 0.94 | 0.95 | 0.97 |
| standard deviation | 1.05 | 0.53 | 0.51 | 0.50 | 1.01 | 0.54 | 0.51 | 0.52 | 0.50 | 0.52 |
| 5th percentile | 0.57 | 0.27 | 0.28 | 0.29 | 0.58 | 0.28 | 0.27 | 0.27 | 0.29 | 0.31 |
| 95th percentile | 3.92 | 1.97 | 1.91 | 1.88 | 3.80 | 2.04 | 1.92 | 1.91 | 1.88 | 1.93 |
| **End-diastole 2 (ED2)** | | | | | | | | | | |
| mean value | 1.19 | 0.72 | 0.74 | 0.72 | 1.20 | 0.78 | 0.70 | 0.74 | 0.72 | 0.73 |
| standard deviation | 0.69 | 0.40 | 0.43 | 0.41 | 0.65 | 0.42 | 0.39 | 0.43 | 0.42 | 0.40 |
| 5th percentile | 0.38 | 0.23 | 0.24 | 0.23 | 0.40 | 0.25 | 0.23 | 0.22 | 0.22 | 0.24 |
| 95th percentile | 2.45 | 1.49 | 1.59 | 1.50 | 2.46 | 1.58 | 1.47 | 1.57 | 1.56 | 1.51 |

the true position of the $i$-th scatterer at time $k$ and by $\mathbf{x}_k^i$ the estimated one. The latter is obtained from the computed motion field $\mathbf{d}_{k-1}^k$ between frame $k-1$ and $k$ as: $\mathbf{x}_k^i = \mathbf{x}_{k-1}^i + \mathbf{d}_{k-1}^k(\mathbf{x}_{k-1}^i)$, with $\mathbf{x}_0^i = \bar{\mathbf{x}}_0^i$. The measured error is $\epsilon_k^i = |\mathbf{x}_k^i - \bar{\mathbf{x}}_k^i|$. Only scatterers belonging to the left ventricle were considered in the error computation. These were selected according to the American Heart Association (AHA) subdivision. The error behavior over time on the second simulated sequence, is represented in the boxplot of Fig. 3(a). As expected, the largest estimation error corresponds to the end-systolic instant, where the maximum displacement from the rest condition happens. Nevertheless, let's note that the average error remains much smaller with respect to the true maximum displacement, that in the end-systolic instant reaches the value of 3.93mm. The spatial error distribution corresponding to the worst (end-systole) and one of the best (close to the end of the cycle) cases is reported in Fig. 3(b)–(c). A summary of the average errors obtained on all the sequences is given in Table 1.

The computation time for each volume (size $267\times355\times355$ pixels$^3$) is of 40 seconds on a MATLAB implementation executed on a desktop pc with a 3.47GHz Intel Xeon X5690 processor, 12 Gb of RAM and running Windows 7.

## 6 Conclusion

A novel algorithm for myocardial motion analysis on 3D echocardiographic images has been presented. Results on simulated sequences show a good precision and a competitive execution time.

## References

1. D'hooge, J., Heimdal, A., Jamal, F., Kukulski, T., Bijnens, B., Rademakers, F., Hatle, L., Suetens, P., Sutherland, G.R.: Regional strain and strain rate measurements by cardiac ultrasound: Principles, implementation and limitations. Eur. J. Echocardiogr. 1(3), 154–170 (2000)
2. Ledesma-Carbayo, M., Kybic, J., Desco, M., Santos, A., Suhling, M., Hunziker, P., Unser, M.: Spatio-temporal nonrigid registration for ultrasound cardiac motion estimation. IEEE TMI 24(9), 1113–1126 (2005)
3. Noble, J., Boukerroui, D.: Ultrasound image segmentation: a survey. IEEE TMI 25(8), 987–1010 (2006)
4. Duan, Q., Angelini, E.D., Herz, S.L., Ingrassia, C.M., Costa, K.D., Holmes, J.W., Homma, S., Laine, A.F.: Region-based endocardium tracking on real-time three-dimensional ultrasound. UMB 35(2), 256–265 (2009)
5. Elen, A., Choi, H.F., Loeckx, D., Gao, H., Claus, P., Suetens, P., Maes, F., D'hooge, J.: Three-dimensional cardiac strain estimation using spatio temporal elastic registration of ultrasound images: A feasibility study. IEEE TMI 27(11), 1580–1591 (2008)
6. Grau, V., Becher, H., Noble, J.: Registration of multiview real-time 3-D echocardiographic sequences. IEEE TMI 26(9), 1154–1165 (2007)
7. Felsberg, M.: Optical Flow Estimation from Monogenic Phase. In: Jähne, B., Mester, R., Barth, E., Scharr, H. (eds.) IWCM 2004. LNCS, vol. 3417, pp. 1–13. Springer, Heidelberg (2007)
8. Chenouard, N., Unser, M.: 3D steerable wavelets and monogenic analysis for bioimaging. In: IEEE ISBI, pp. 2132–2135 (2011)
9. Felsberg, M., Sommer, G.: The monogenic signal. IEEE Transactions on Signal Processing 49(12), 3136–3144 (2001)
10. Sühling, M., Arigovindan, M., Jansen, C., Hunziker, P., Unser, M.: Myocardial motion analysis from b-mode echocardiograms. IEEE TIP 14(4), 525–536 (2005)
11. Sermesant, M., Chabiniok, R., Chinchapatnam, P., Mansi, T., Billet, F., Moireau, P., Peyrat, J., Wong, K., Relan, J., Rhode, K., Ginks, M., Lambiase, P., Delingette, H., Sorine, M., Rinaldi, C., Chapelle, D., Razavi, R., Ayache, N.: Patient-specific electromechanical models of the heart for the prediction of pacing acute effects in crt: A preliminary clinical validation. MedIA 16(1), 201–215 (2012)
12. Gao, H., Choi, H.F., Claus, P., Boonen, S., Jaecques, S., van Lenthe, G., Van Der Perre, G., Lauriks, W., D'hooge, J.: A fast convolution-based methodology to simulate 2-D/3-D cardiac ultrasound images. IEEE UFFC 56(2), 404–409 (2009)
13. STACOM2012: `http://www.physense.org/stacom2012/`

# Quadrature Filter Based Motion Analysis for 3D Ultrasound Sequences

Lennart Tautz, Anja Hennemuth, and Heinz-Otto Peitgen

Fraunhofer MEVIS, Bremen, Germany

**Abstract.** Analysis of echocardiograms is a valuable tool for assessing myocardial function and diseases. Processing of ultrasound data is challenging due to noise levels and depth-dependent quality of structure edges. We propose to adapt a method based on quadrature filters that is invariant to changes in intensity and has been successfully applied to MRI data earlier. Quadrature-filter-based registration derives the spatial deformation between two images from the local phase shift. Because the local phase is intensity-invariant and requires inhomogeneity, e.g., noise and intensity variations, to properly pick up phase shifts, it is well suited for ultrasound data. A multi-resolution and multi-scale scheme is used to cover different scales of deformations. The type and strength of regularization of the dense deformation field can be specified for each level, allowing for weighting of global and local motion. To speed up the registration, deformation fields are determined slice-wise for three orientations of the original data and subsequently combined into a true 3D deformation field. The method is evaluated with the data and ground truth provided by the *Cardiac Motion Analysis Challenge* at STACOM 2012.

**Keywords:** Ultrasound, Morphon, Registration, Quadrature filter.

## 1 Introduction

Much effort is still dedicated to ultrasound motion tracking algorithms. Many different approaches have been proposed that can be coarsely divided into intensity-based algorithms that are purely driven by the data, and model-based algorithms that add knowledge about the underlying anatomy and heart mechanics. Wang et al. [6] used a multi-model approach to incorporate information from both data and prior model knowledge, which requires a learning phase with manual expert segmentations. Zhang et al. [7] propose an intensity-based method with temporal smoothness constraints.

With the progress of ultrasound imaging technology, the resolution and amount of acquired data is constantly increasing. While this allows to derive dense motion fields from the data to assess local deformations, the analysis of this spatially and temporally extensive data is expensive, as the motion tracking challenge at STACOM 2011 showed [5]. State-of-the-art motion analysis techniques require computational resources that are not available in most clinical environments.

O. Camara et al. (Eds.): STACOM 2012, LNCS 7746, pp. 169–177, 2013.

We propose a fully-automatic and purely data-driven approach that uses quadrature-filter-based registration [1] to derive motion fields from adjacent time frames. Instead of processing the whole 3D volume at once, displacements are computed for 2D slices. These displacements are combined to a true 3D displacement field, which makes the algorithm highly suitable for parallel processing. It is robust to noise and to variations in intensity, and avoids obscuring pathologies by over-regularization because it does not make physiological assumptions on spatial or temporal smoothness. This approach is based on the implementation from [2] and has been previously applied to different types of cardiac images, including MRI perfusion [3], MRI tagging and 3D+t cardiac ultrasound [4].

For reliable and beneficial analysis of myocardial motion in cardiac ultrasound, tracking and deformation quantification algorithms have to be validated against appropriate ground truth. Because manual landmarking in ultrasound images is unfeasible, efforts have been focused on phantom data where motion patterns and deformations are known. The *Cardiac Motion Analysis Challenge* at STACOM 2012 provides a framework to validate motion tracking algorithms against synthetic and in-vitro phantom data.

## 2 Materials and Methods

### 2.1 Image Data

Twelve data sets were provided by the organizers of the STACOM 2012 challenge and included synthetic phantom images as well as images of a hardware phantom.

**Synthetic Data.** The synthetic images were created from the combination of an electro-mechanical model with an ultrasound imaging model and simulate different electrical and contraction parameters. Each of the nine data sets had an extent of 267x355x355 over 23 time frames, with a voxel size of 0.33x0.33x0.33 and unknown temporal resolution. A segmentation of the heart was provided as ground-truth for evaluation. Figure 1 shows one of the data sets and the associated heart model mesh.

**Phantom Data.** The hardware phantom consists of a cylinder that has been subjected to motion. Microcrystals were embedded in the phantom to provide ground truth landmarks in tagged MR and microsonometry imaging. Each of the three data sets had an extent of 224x112x209 over 30 time frames, with a voxel size of 0.89x1.23x0.77 and unknown temporal resolution. Figure 2 shows a time frame of one phantom data set.

### 2.2 Method

Our proposed method calculates a dense deformation field to non-rigidly align adjacent time frames. It is purely data-driven and thus applicable without prior training or modeling steps. However, the registration scheme has to be adapted to the data to reflect noise characteristics, image dimensions and scale of deformations.

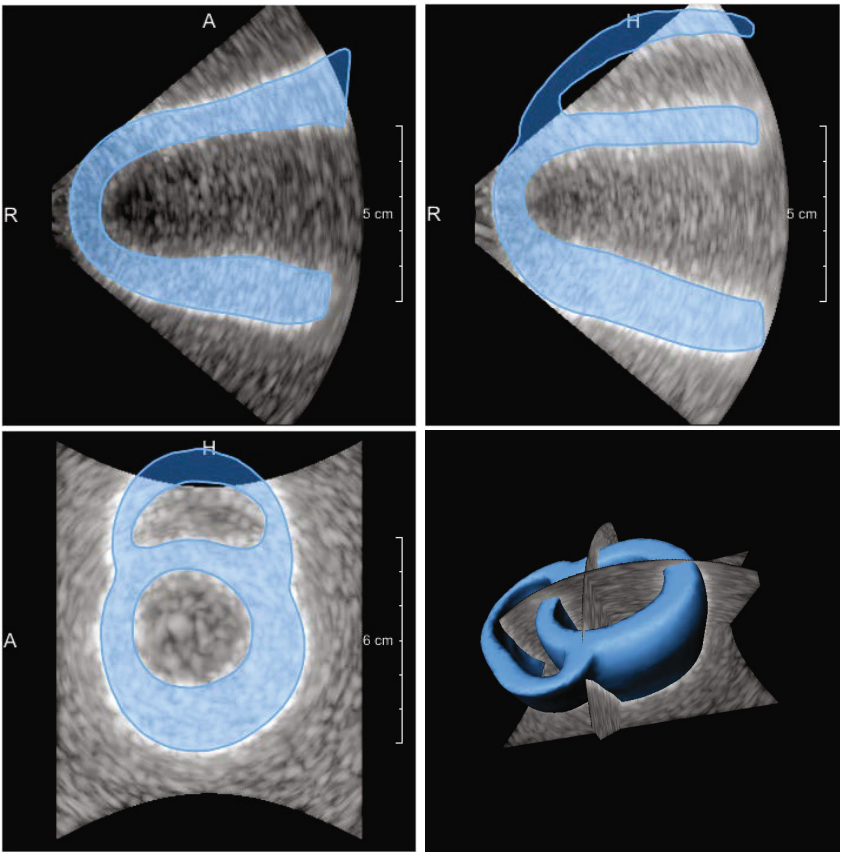


**Fig. 1.** Orthogonal views of synthetic data set *case22*, and segmentation mesh that was provided for the synthetic data sets. The mesh is also overlaid on the ultrasound data. Note that the heart model is not fully covered by the cone-shaped acquisition range of the simulated ultrasound unit.

**Background.** Phase-based image registration makes use of the Fourier Shift Theorem, which states that the Fourier transforms of a signal $f(x)$ and a shifted signal $f(x-d)$ are related via a phase factor by $\mathcal{F}\{f(x-d)\} = e^{-jd\omega}\mathcal{F}\{f(x)\}$. For two signals $f_1(x) = f(x)$ and $f_2(x) = f(x-d)$, $d$ is proportional to $\arg\left(\mathcal{F}\{f_1(x)\}\overline{\mathcal{F}\{f_2(x)\}}\right)$, with $\overline{\ }$ denoting the complex conjugate. By using the *local* phase $\phi(x)$, derived from the complex analytical signal $f_a(x) = A(x)e^{j\phi(x)}$ of $f(x)$, the above approach can be used to estimate non-stationary shifts in 1D. The analytic signal is in practice estimated by applying a quadrature filter $q(x)$. This has a band-pass character that determines the scale of the structures or shifts of interest. To generalize this 1D construct to higher dimensions, we use a set of quadrature filters with different orientations $\hat{\mathbf{n}}_i$. The displacement $\hat{d}_i(\mathbf{x})$ of a deformed image $J(\mathbf{x}) = I(\mathbf{x} + \mathbf{d}(\mathbf{x}))$ along the orientation $\hat{\mathbf{n}}_i$ can then be estimated using

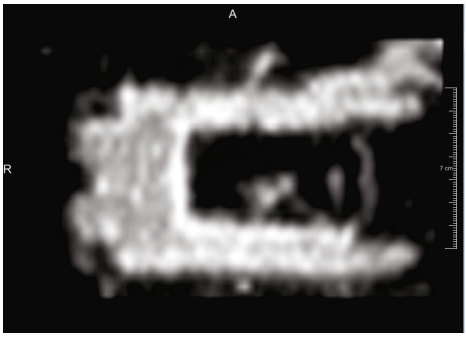


**Fig. 2.** Time frame 15 of phantom data set *images6b*

$$p_{IJ}^{(i)}(\mathbf{x}) = (I * q^{(i)})(\mathbf{x})\,\overline{(J * q^{(i)})(\mathbf{x})}. \tag{1}$$

$$\hat{d}_i(\mathbf{x}) \propto \arg\left(p_{IJ}^{(i)}(\mathbf{x})\right) \tag{2}$$

A confidence measure $c_i(\mathbf{x})$ based on the similarity of the filter responses is associated with the estimate in each filter direction,

$$c_i(\mathbf{x}) = \sqrt{\left|p_{IJ}^{(i)}(\mathbf{x})\right|}\left[1 + \cos\left(\arg\left(p_{IJ}^{(i)}(\mathbf{x})\right)\right)\right] \tag{3}$$

and the summation of the individual measures leads to a combined confidence measure $c(\mathbf{x})$. A first estimate of the complete deformation field can be formulated by weighting the displacement estimates with the associated confidence measures,

$$\mathbf{d}(\mathbf{x}) = \frac{\sum_i c_i(\mathbf{x}) d_i(\mathbf{x}) \hat{\mathbf{n}}_i}{\sum_i c_i(\mathbf{x})}. \tag{4}$$

This deformation field should be subjected to a spatial regularization to reflect the elasticity of biological tissue, and to incorporate the confidence measure to converge to the most certain field,

$$\mathbf{d}_{reg}(\mathbf{x}) = \frac{[\mathbf{d}(\mathbf{x})c(\mathbf{x})] * g(\mathbf{x}; \sigma^2)}{c(\mathbf{x}) * g(\mathbf{x}; \sigma^2)}. \tag{5}$$

To estimate large deformations, the displacement estimation outlined above must be implemented in a scale space, and it is also necessary to iterate the estimation several times on each scale to refine the estimation. The deformation estimates are accumulated in $\mathbf{d}_{tot}(\mathbf{x})$ as

$$\mathbf{d}_{tot}(\mathbf{x}) \leftarrow \mathbf{d}_{tot}(\mathbf{x}) + \frac{c(\mathbf{x})}{c_{tot}(\mathbf{x}) + c(\mathbf{x})}\,\mathbf{d}_{reg}(\mathbf{x}), \tag{6}$$

where $c_{tot}(\mathbf{x})$ is an accumulated confidence measure that is updated for each iteration as

$$c_{tot}(\mathbf{x}) \leftarrow \frac{c_{tot}^2(\mathbf{x}) + c^2(\mathbf{x})}{c_{tot}(\mathbf{x}) + c(\mathbf{x})}. \tag{7}$$

After convergence, $\mathbf{d}_{tot}(\mathbf{x})$ is the final estimate of the true deformation field $\mathbf{d}(\mathbf{x})$.

**Implementation.** To derive the motion fields from the ultrasound data, the image data is analyzed slice-wise with a set of four 2D filters in orthogonal directions. We do not employ a true 3D registration for performance reasons. The convolution with the quadrature filter kernels is the computationally most expensive step of our approach, so it is highly desirable to avoid convolutions with 3D kernels and use a strategy of distributed 2D convolutions instead. Thus, the total motion field is obtained by combining three 2D motion vector fields from orthogonal directions, which can be computed independently. Because each 3D vector component is present in two fields, out-of-plane motion and other artifacts can be compensated for by combining the corresponding components.

We apply log-normal quadrature filters in a 14-scale scale space created by two different center frequencies and seven resolution scale steps with a resample factor of 0.63. It should be noted that the frequencies are not related to the noise properties of the images, but were selected to give the scale-space scheme good coverage of motions with different magnitudes. On scales with downsampled resolution three iterations are performed, while only two are carried out on scales with the original resolution to reduce computation time. An overview of the parameters is given in Table 1.

The regularization of the deformation field is performed using a Gaussian kernel, whose parameters were empirically optimized to produce reasonably smooth deformation fields without removing local distortions that can represent pathologies.

For each of the three orthogonal slice orientations, a stack of slice-wise 2-component vector fields is calculated. Each slice in this vector field stack represents the motion between two adjacent time frames. These partial motion fields are reformatted to the transversal orientation. Every orientation contributes to two components of the final 3D vector that is determined by averaging the respective components. The data sets are downsampled by a factor of 2.5 for processing to compensate for their size and the increased noise level and upsampled with linear interpolation afterwards.

## 3 Results

The synthetic data sets were processed and compared with the provided comparison framework. This framework consists of ground-truth meshes for all time frames and source code that calculates the error between the ground-truth displacement and the displacement of our method for all mesh points. Table 2 shows the error statistics for these data sets over all time frames. The deformation field for data set *case01* had an erroneous region just below the apex, which

**Table 1.** Morphon parameters

| Resolution Level | Resolution Iterations | Sigma [voxels] |
|---|---|---|
| 0 | 142 | 2 | 3 |
| 1 | 89 | 3 | 3 |
| 2 | 56 | 3 | 3 |
| 3 | 35 | 3 | 3 |
| 4 | 22 | 3 | 3 |
| 5 | 13 | 3 | 3 |
| 6 | 8 | 3 | 3 |

**Table 2.** Error values for synthetic data sets

| Data Set | Minimum | $q_{25}$ | $q_{50}$ | $q_{75}$ | $q_{95}$ | Maximum | Average | Standard Deviation |
|---|---|---|---|---|---|---|---|---|
| case01 | 0.02 | 1.9 | 3.88 | 6.91 | 11.36 | 21082.1 | 11.19 | 209.44 |
| case08 | 0.004 | 1.15 | 2.01 | 3.13 | 5.13 | 11.17 | 1.79 | 1.56 |
| case12 | 0.002 | 1.19 | 2.06 | 3.2 | 5.17 | 10.57 | 1.83 | 1.57 |
| case20 | 0.005 | 1.17 | 2.04 | 3.2 | 5.23 | 9.98 | 1.83 | 1.59 |
| case22 | 0.009 | 1.71 | 3.62 | 6.55 | 10.56 | 16.86 | 3.88 | 3.24 |
| case28 | 0.006 | 1.18 | 2.02 | 3.18 | 5.13 | 9.88 | 1.81 | 1.56 |
| case36 | 0.006 | 1.18 | 2.05 | 3.2 | 5.25 | 10.23 | 1.84 | 1.59 |
| case44 | 0.004 | 1.21 | 2.05 | 3.18 | 5.19 | 10.69 | 1.84 | 1.57 |
| case60 | 0.006 | 1.09 | 1.99 | 3.16 | 5.22 | 10.05 | 1.78 | 1.61 |

caused the high maximum error. Figures 3 and 4 show motion estimation errors at selected time frames from two data sets.

The phantom data sets were processed as well, but lack evaluation because no segmentation was provided for them.

Computation time is about four hours for one synthetic data set, and about two hours for one phantom data set. The processing was done on a 3 GHz PC with 8 GB of memory.

## 4 Discussion

We have identified two major contributing factors for motion estimation errors in the synthetic data: (a) motion at thin structures, and (b) motion near the conus boundaries. Factor (a) influences the estimation of apical and right-ventrical motion in particular. Because the synthetic data sets do not cover the whole heart (Fig. 1), factor (b) affects all regions except for the septum. The cut-off heart regions disturb our approach, because in contrast to model-based approaches, no anatomical information is available to compensate the influence of the image background. The filter field of view and the regularization could be extended by a background mask that prevents excessive propagation from the background regions into the central motion field.

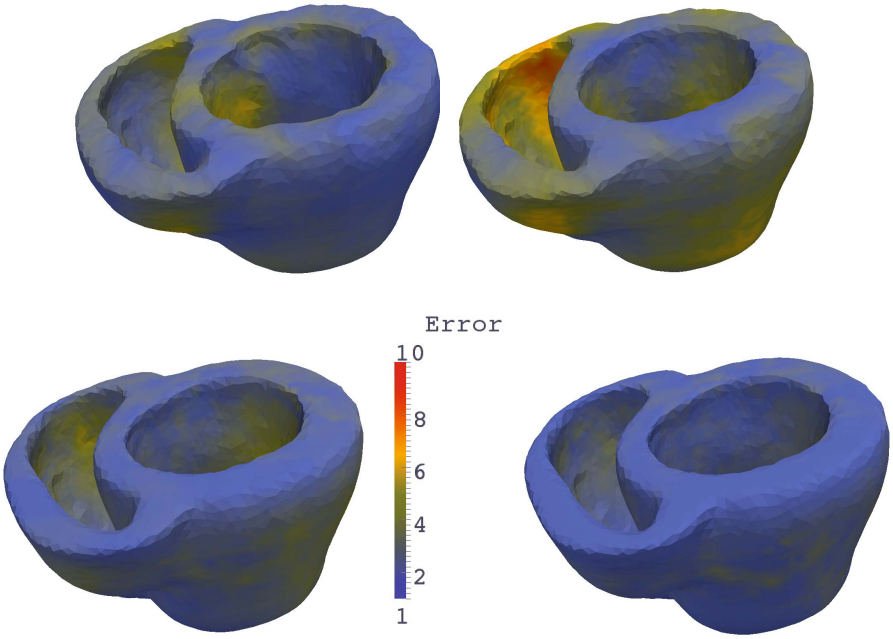


**Fig. 3.** Displacement error overlaid as color on the mesh of data set *case08* at time frame 1. From left to right and top to bottom time frames 4, 8, 12 and 16. Blue to green represents 0 to 5mm error, green to orange 5 to 6.5mm error, and orange to red marks above 6.5mm error. The largest errors occur at the posterior right ventricle wall.

Although the scale space we used provides good coverage of all motion, it is still computationally expensive. To save computation time, a reduced scale space should be designed that delivers a comparable performance. Parallel processing of the individual orientations and slices could be implemented on the GPU or in a cluster architecture.

To compute strain curves, the deformation fields are used with respect to a reference frame, typically the first frame. Because the frame-to-frame motion field inherently contains errors, concatenation of the relative fields will propagate the errors towards the sequence end. A temporal regularization, e.g., simple temporal smoothing or an additional constraint that material point trajectories should by cyclic, could be added to reduce these errors.

## 5 Conclusions

We introduced an algorithmic approach for the analysis of myocardial motion based on cardiac ultrasound data. The method is a phase-based approach, which applies quadrature filters to derive dense motion fields between subsequent image time frames. The algorithm was applied to the data sets provided by the STACOM 2012 challenge, and provided satisfactory results. Motion estimation

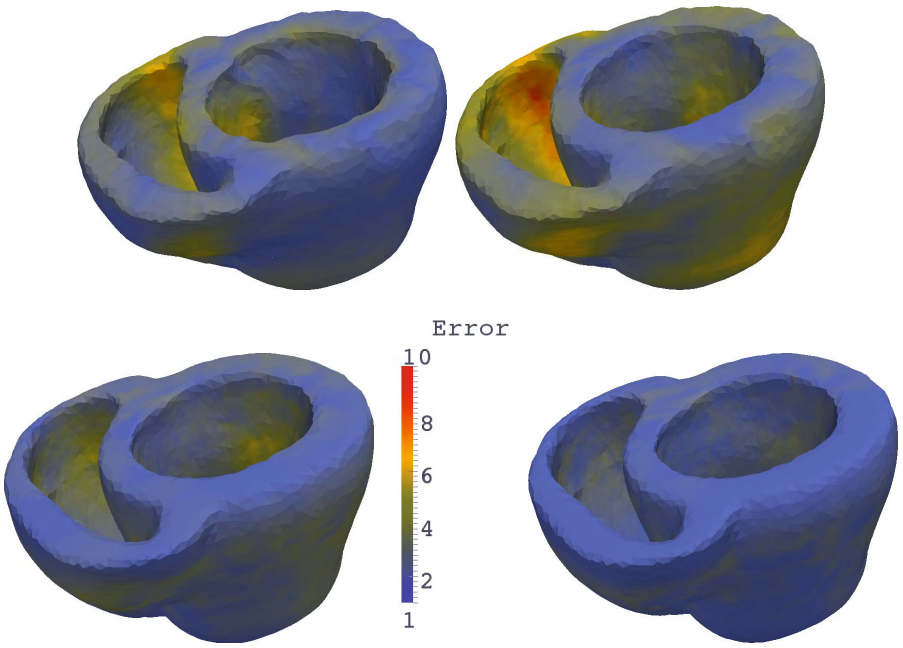


**Fig. 4.** Displacement error overlaid as color on the mesh of data set *case44* at time frame 1. From left to right and top to bottom time frames 4, 8, 12 and 16. Blue to green represents 0 to 5mm error, green to orange 5 to 6.5mm error, and orange to red marks above 6.5mm error. The largest errors occur at the posterior right ventricle wall.

performance outside the image center is limited by the data set field of view. The algorithm has to be improved with respect to this and the error causes discussed above to provide a clinically applicable method.

## References

1. Knutsson, H., Andersson, M.: Morphons: Segmentation using elastic canvas and paint on priors. In: Symposium on Image Analysis, SSBA 2005, pp. 73–76 (2005)
2. Petterson, J.: Automatic Generation of Patient Specific Models for Hip Surgery Simulation. Ph.D. thesis, Linköping University (2006)
3. Tautz, L., Hennemuth, A., Andersson, M., Seeger, A., Knutsson, H., Friman, O.: Phase-based non-rigid registration of myocardial perfusion MRI image sequences. In: 2010 IEEE International Symposium on Biomedical Imaging: From Nano to Macro, pp. 516–519 (April 2010)
4. Tautz, L., Hennemuth, A., Peitgen, H.-O.: Motion Analysis with Quadrature Filter Based Registration of Tagged MRI Sequences. In: Camara, O., Konukoglu, E., Pop, M., Rhode, K., Sermesant, M., Young, A. (eds.) STACOM 2011. LNCS, vol. 7085, pp. 78–87. Springer, Heidelberg (2012)

5. Tobon-Gomez, C., De Craene, M., McLeod, K., Tautz, L., Shi, W., Hennemuth, A., Prakosa, A., Wang, H., Carr-White, G., Kapetanakis, S., Lutz, A., Rasche, V., Schaeffter, T., Butakoff, C., Friman, O., Mansi, T., Sermesant, M., Zhuang, X., Ourselin, S., Peitgen, H.O., Pennec, X., Razavi, R., Rueckert, D., Frangi, A., Rhode, K.: Evaluation of current algorithms for myocardial tracking and deformation: 1st cardiac motion analysis challenge (2012) (submittted)
6. Wang, Y., Georgescu, B., Houle, H., Comaniciu, D.: Volumetric Myocardial Mechanics from 3D+t Ultrasound Data with Multi-model Tracking. In: Camara, O., Pop, M., Rhode, K., Sermesant, M., Smith, N., Young, A. (eds.) STACOM-CESC 2010. LNCS, vol. 6364, pp. 184–193. Springer, Heidelberg (2010)
7. Zhang, Z., Song, X., Sahn, D.J.: Cardiac Motion Estimation from 3D Echocardiography with Spatiotemporal Regularization. In: Metaxas, D.N., Axel, L. (eds.) FIMH 2011. LNCS, vol. 6666, pp. 350–358. Springer, Heidelberg (2011)

# Evaluation of iLogDemons Algorithm for Cardiac Motion Tracking in Synthetic Ultrasound Sequence

Adityo Prakosa, Kristin McLeod, Maxime Sermesant, and Xavier Pennec

Inria Méditerranée, Asclepios Project, Sophia Antipolis, France

**Abstract.** In this paper, we evaluate the iLogDemons algorithm for the STACOM 2012 cardiac motion tracking challenge. This algorithm was previously applied to the STACOM 2011 cardiac motion challenge to track the left-ventricle heart tissue in a data-set of volunteers. Even though the previous application showed reasonable results with respect to quality of the registration and computed strain curves; quantitative evaluation of the algorithm in an objective manner is still not trivial. Applying the algorithm to the STACOM 2012 synthetic ultrasound sequence helps to objectively evaluate the algorithm since the ground truth motion is provided. Different configurations of the iLogDemons parameters are used and the estimated left ventricle motion is compared to the ground truth motion. Using this application, quantitative measurements of the motion error are calculated and optimal parameters of the algorithm can be found.

## 1 Introduction

Understanding cardiac motion dynamics through the heart beat is fundamental for providing useful insights into cardiac diseases. Analyzing medical images is one way to better understand the complex dynamics of the heart and in recent years, cardiac motion tracking algorithms have been developed to attempt to estimate the observed motion. We refer the reader to [2] for the state of the art on cardiac motion tracking. A cardiac motion tracking challenge was introduced in the STACOM 2011 MICCAI workshop which allowed participants to apply algorithms to a given data-set of healthy volunteers with cine-magnetic resonance, ultrasound, and tagged-magnetic resonance image sequences. In this work we describe the application of the incompressible log-domain demons algorithm (iLogDemons for short) to a set of synthetic ultrasound image sequences for which the ground truth deformation is known and provided for training within the STACOM 2012 MICCAI cardiac motion tracking challenge. From this we are able to compute the error between the ground truth and the estimated deformation for the training data.

## 2 Methodology

The iLogDemons algorithm is a consistent and efficient framework for tracking left-ventricle heart tissue through the cardiac cycle using an elastic, incompressible

O. Camara et al. (Eds.): STACOM 2012, LNCS 7746, pp. 178–187, 2013.

non-linear registration algorithm based on the LogDemons algorithm [3,2]. Applying a non-linear registration to pairs of medical images is a common method to estimate the motion and the deformation of the tissue in the image.

### 2.1 LogDemons

The LogDemons [6] non-linear registration aligns a template image $T(\mathbf{x})$ to a reference image $R(\mathbf{x})$ by estimating a dense non-linear transformation $\phi(\mathbf{x})$, where $\mathbf{x} \in \mathbb{R}^3$ is the space coordinate. This transformation $\phi(\mathbf{x})$ is associated with the displacement vector field $\mathbf{u}(\mathbf{x})$ and is parameterized by the stationary velocity vector field $\mathbf{v}(\mathbf{x})$, $\phi(\mathbf{x}) = \mathbf{x} + \mathbf{u}(\mathbf{x}) = \exp(\mathbf{v}(\mathbf{x}))$. This ensures the invertibility of the deformation. The LogDemons algorithm contains two steps, which are the *optimization* and the *regularization* step. The *optimization* step finds the intermediate correspondence transformation $\phi_c(\mathbf{x}) = \exp(\mathbf{v}_c(\mathbf{x})) = \phi(\mathbf{x}) \circ \exp(\delta\mathbf{v}(\mathbf{x})))$ by minimizing the LogDemons energy

$$\varepsilon(\mathbf{v}, \mathbf{v}_c) = \frac{\| R - T \circ \exp(\mathbf{v}_c) \|^2_{L_2}}{\lambda_i^2} + \frac{\| \log(\exp(-\mathbf{v}) \circ \exp(\mathbf{v}_c)) \|^2_{L_2}}{\lambda_x^2} + \frac{\| \nabla \mathbf{v} \|^2}{\lambda_d^2}$$

with respect to $\mathbf{v}_c(\mathbf{x})$, where $\lambda_i^2$ is the parameter that estimates the noise in the image $\lambda_i^2(\mathbf{x}) = |R(\mathbf{x}) - T \circ \phi(\mathbf{x})|^2$, $\lambda_x^2$ is the parameter that controls the uncertainty of the correspondences and $\lambda_d^2$ is the parameter that controls the regularization strength. $\mathbf{v}_c$ parameterizes the intermediate transformation $\phi_c(\mathbf{x})$ which models the voxel correspondences of the two images without considering the regularity of the transformation. The optimal update velocity writes

$$\delta\mathbf{v}(\mathbf{x}) = -\frac{R(\mathbf{x}) - T \circ \phi(\mathbf{x})}{\| J(\mathbf{x}) \|^2 + \lambda_i^2/\lambda_x^2} J(\mathbf{x}),$$

where $J(\mathbf{x})$ is the symmetric gradient $J(\mathbf{x}) = (\nabla R(\mathbf{x}) + \nabla(T \circ \phi(\mathbf{x})))/2$. The correspondence velocity $\mathbf{v}_c$ is updated using the the Baker-Campbell-Hausdorff (BCH) formula $\mathbf{v}_c = Z(\mathbf{v}_c, \delta\mathbf{v})$ [6]. Finally, the optimal regularized transformation $\phi(\mathbf{x})$ is estimated in the *regularization step* by minimizing the LogDemons energy with respect to $\mathbf{v}$, which is approximated by smoothing the correspondence velocity $\mathbf{v}_c$ with a Gaussian kernel $G_\sigma$.

### 2.2 iLogDemons

iLogDemons adds physiological constraints; *elasticity* and *incompressibility*, to the LogDemons algorithm. It proposes an *elastic* regularizer to filter the correspondence velocities by the elastic-like kernel: $\mathbf{v} = \left(G_\sigma Id + \frac{\sigma^2\kappa}{1+\kappa} HG_\sigma\right) \star \mathbf{v}_c = G_{\sigma,\kappa} \star \mathbf{v}_c$, where $HG_\sigma$ is the Hessian of the Gaussian kernel $G_\sigma$ and $G_{\sigma,\kappa}$ is the elastic-like vector filter. *Incompressibility* is achieved by constraining the stationary velocity field $\mathbf{v}(\mathbf{x})$ to be divergence-free. The complete algorithm of the iLogDemons is described in Algorithm 1.

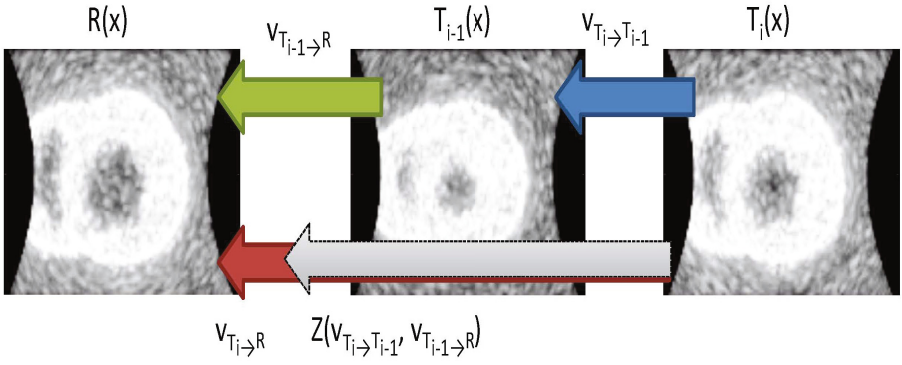


**Fig. 1.** The concatenation of the velocity field $\mathbf{v}_{T_i \to T_{i-1}}$ and $\mathbf{v}_{T_{i-1} \to R}$ using the BCH formula is used to initiate the registration of the template image $T_i(\mathbf{x})$ to the reference image $R(\mathbf{x})$

**Algorithm 1.** iLogDemons: Incompressible Elastic LogDemons Registration

**Require:** Stationary velocity field $\mathbf{v}^0$. Usually $\mathbf{v}^0 = \mathbf{0}$ i.e. $\phi^0 = Id$.

1: **loop** {*over n until convergence*}
2: Compute the update velocity: $\delta\mathbf{v}^n$ (see [2]).
3: Fluid-like regularization: $\delta\mathbf{v}^n \leftarrow G_{\sigma_f} \star \delta\mathbf{v}^n$ , $G_{\sigma_f}$ is a Gaussian kernel.
4: Update the correspondence velocity using the Baker-Campbell-Hausdorff (BCH) formula: $\mathbf{v}^n \leftarrow Z(\mathbf{v}^{n-1}, \delta\mathbf{v}^n)$ (see [6]).
5: Elastic-like regularization: $\mathbf{v}^n \leftarrow G_{\sigma,\kappa} \star \mathbf{v}^n$ (see [2]).
6: Solve: $\Delta p = \nabla \cdot \mathbf{v}^n$ with 0-Dirichlet boundary conditions. This is done in order to achieve the incompressibility.
7: Project the velocity field: $\mathbf{v}^n \leftarrow \mathbf{v}^n - \nabla p$.
8: Update the warped image $T \circ \phi^n = T \circ \exp(\mathbf{v}^n)$.
9: **return** $\mathbf{v}$, $\phi = \exp(\mathbf{v})$ and $\phi^{-1} = \exp(-\mathbf{v})$.

### 2.3 Cardiac Motion Tracking Strategy

We initialize the registration of the template image $T_i(\mathbf{x})$ at frame $i$ to the reference image $R(\mathbf{x})$ with the concatenation of the previous frame $(i-1)$ to reference velocity field $\mathbf{v}_{T_{i-1} \to R}$ and the current-to-previous frame velocity field $\mathbf{v}_{T_i \to T_{i-1}}$ by $Z(\mathbf{v}_{T_{i-1} \to R}, \mathbf{v}_{T_i \to T_{i-1}})$ with $Z$ is the BCH operation, as a strategy to track the myocardium (cf. Fig. 1) [2]. The final registration is always calculated to the same end diastolic reference image $R(x)$.

## 3 Application to Challenge Data

### 3.1 Algorithm Parameter Setting

We used the standard parameters that were used previously in [3]. However, since the ground truth motion is available for the synthetic ultrasound sequence

**Table 1.** iLogDemons parameters used in the application

| **Input parameters:** | **Value** |
|---|---|
| Multi-resolution levels (frame-by-frame registration) | 3 |
| Multi-resolution levels (refinement step) | 2 |
| Number of iterations / level | 100 |
| $\sigma_f$ update field in $mm$ | 0.5 |
| $\kappa_f$ update field in $mm$ | 0 |
| $\sigma$ stationary velocity field in $mm$ | 1 or 1.5 or 2 |
| $\kappa$ stationary velocity field in $mm$ | 1 |
| Incompressibility update field (0-Disable,1-Enable) | 0 |
| Incompressibility velocity field (0-Disable,1-Enable) | 1 or 0 |

provided, we also tested different parameters of the iLogDemons as described in Table 3.1.

iLogDemons non-rigid registration was previously applied to the STACOM 2011 challenge data-set [5,3]. It showed reasonable results in term of the alignment of the registered frames in the cardiac sequence with the reference end diastolic image. Using the estimated transformations, it could also track the myocardium along the cardiac cycle. The calculated strain curve was also comparable to literature for healthy strain values [4].

### 3.2 Simulated Ultrasound Cardiac Sequence Data

The simulated data-set consisted of 10 synthetic ultrasound sequences with 23 frames per case, with image spatial resolution of 267×355×355, and isotropic voxel size of 0.33 mm. For each sequence, the left ventricle (LV) is almost fully visible while the right ventricle is only partially visible in the ultrasound acquisition cone. To compensate for the part of the LV which is out-of-window region, we artificially expanded the acquisition pyramid. The boundary voxels were copied to fill this region and additional noise was also added. The data-set contains different motion and deformation patterns (normal, LBBB, RBBB, pacing) with the ground truth deformation provided as the deformation of volumetric meshes in a cardiac cycle (See [1] for further details on the synthetic data-set).

### 3.3 Application to the Synthetic Data

In order to find the optimal parameters of the algorithm that are able to handle large deformations, we processed the first case of the ultrasound synthetic data-set since it simulates normal heart motion with large contraction. We launched the parameters that were used previously in [3] to the full resolution data-set. We also applied our algorithm on down-sampled images to reduce the computational time. We down-sampled the data to a resolution of 88×117×117 with isotropic voxel size of 1.02 mm The computation time of the whole sequence processing

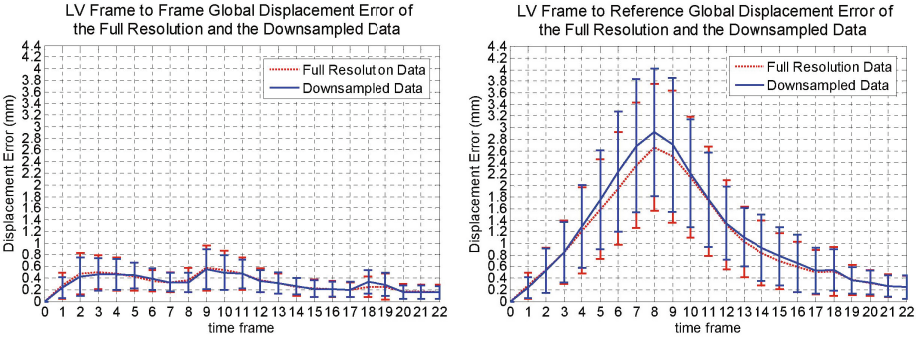


**Fig. 2.** The registration error (calculated using the method described in Section. 3.4 ) of the full resolution and down-sampled dataset of the first case are compared. They show relatively small difference. .

was reduced from the order of days to hours. The current implementation can be optimized to handle large volumes by improving the memory access scheme since the addition of computation time of current implementation is not caused by the addition of computational complexity. One configuration of parameters was tested for both the full and down-sampled data to verify the accuracy of the down-sampled registration compared to the full-resolution registration and found very small differences in the results (cf. Fig. 2). Other configurations of the key parameters were tested on the down-sampled data.

### 3.4 Quantitative Evaluation

**Displacement Error.** To evaluate quantitatively the performance of each set of the parameters used for the iLogDemons with incompressibility on the velocity field set to 0 or 1, we calculated the ground truth displacement vector field from the deformation of the provided simulated meshes. We rasterized the displacement vectors to the image $\mathbf{u}_{GT}(\mathbf{x})$ in order to be able to compare them to the iLogDemons estimated displacement field $\mathbf{u}_e(\mathbf{x})$. The norm of the difference of the two vector fields $||\mathbf{u}_{GT}(\mathbf{x}) - \mathbf{u}_e(\mathbf{x})||$ is calculated. The global mean of this values over the whole left ventricle are calculated for each time frame in the cardiac cycle (cf. Fig. 3). Based on Fig. 3, the parameter $\sigma = 1.5$ without the incompressibility constraint gives the lowest maximum error for the first case. We calculated the LV volume of the ground truth deformed meshes in a cardiac cycle and we observed that the current electromechanical model is not incompressible. Fig. 4 shows the mean and standard deviation of the LV myocardium volume change in a cardiac cycle for the whole data-set. There is a 10% change of volume during the maximum contraction. In Fig. 5, we compare the ground truth displacement vector for each American Heart Association (AHA) region of the left ventricle. We compare it to the iLogDemons estimated displacement vector and calculated the difference for each AHA segment. Fig. 5 also shows the error for the basal (regions 1-6), mid (regions 7-12) and apical (regions 13-17) regions. More error is observed in the

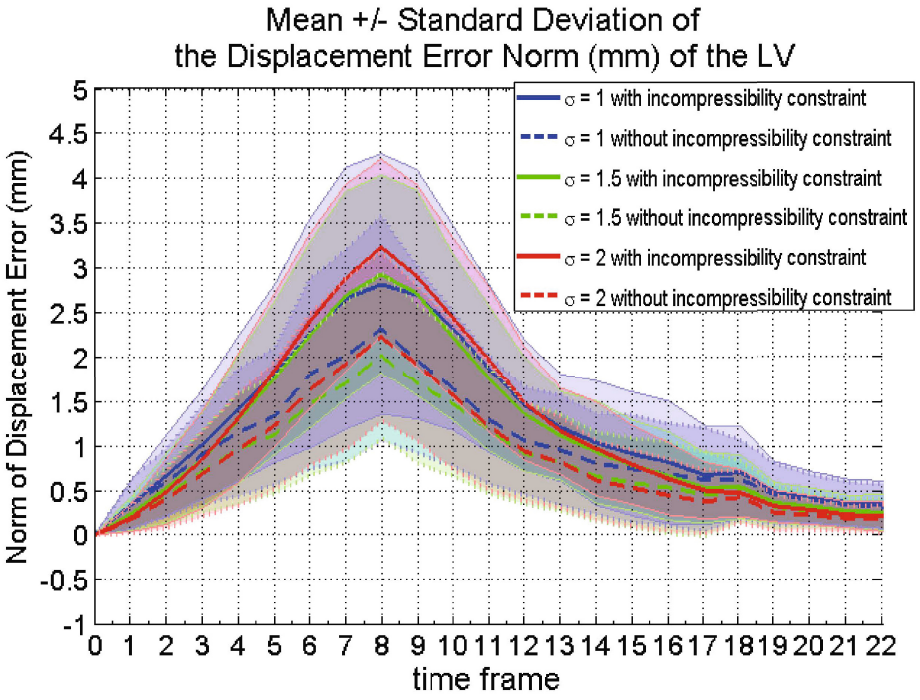


**Fig. 3.** The mean and standard deviation of the displacement error calculated on the whole left ventricle for varying values of $\sigma$ for the first case

apical region since the longitudinal motion of the apex toward the base changes the intensity of the apical region.

The result for the whole data-set processing is shown in Fig. 6. As also shown in Fig. 5 for the first case, the registration of each frame to its previous frame gives small error which is less than one voxel size. For the frame to reference result, we observe that there is an error accumulation during the maximum contraction.

**Strain Estimation.** From the iLogDemons estimated displacement field $\mathbf{u}(x)$, we computed the strain tensor and projected it to the local radial, circumferential and longitudinal directions. The strain tensor was calculated using the 3D Lagrangian finite strain tensor $E(x) = \frac{1}{2}[\nabla\mathbf{u}(x) + \nabla\mathbf{u}^T(x) + \nabla\mathbf{u}^T(x)\nabla\mathbf{u}(x)]$. The mean and standard deviation of the strain estimation of the whole data-set is shown in Fig. 7. The result using incompressibility has more realistic range of value (from -15% to 25%) of the estimated strain compared to the one without incompressibility (from 150% to 300%).

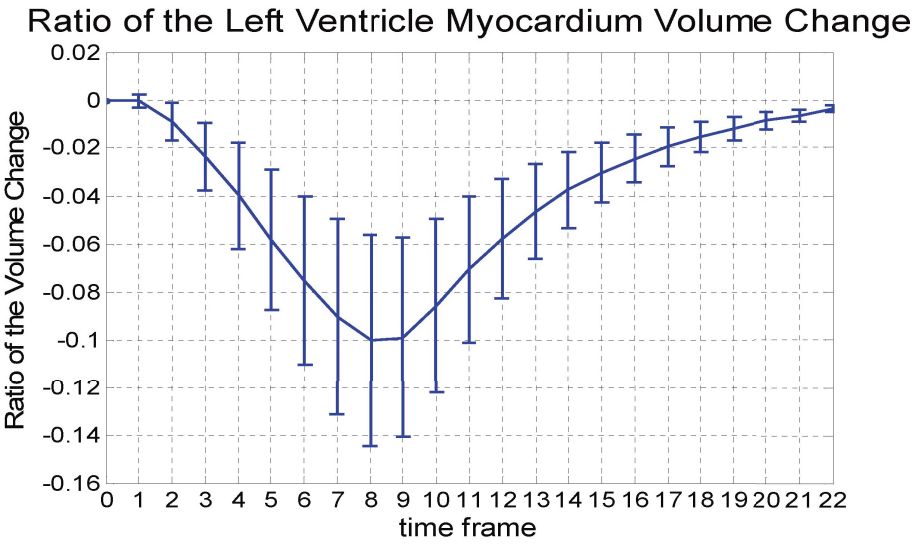


**Fig. 4.** The mean and standard deviation of the LV volume change of the ground truth deformed meshes during a cardiac cycle. Current electromechanical model is not incompressible since there is a 10% of volume change during the maximum contraction.

### 3.5 Myocardium Tracking

Qualitative evaluation of the algorithm is done by comparing the contour of the simulated mesh at the frame with maximum contraction with the deformation of the end diastolic mesh using the iLogDemons estimated displacement field at the same frame for the first case. Reasonable agreement of the contours can be observed in Fig. 8, which indicated that the algorithm is able to capture realistic deformations, even in the case of a synthetically simulated sequence.

## 4 Discussion

This evaluation shows that the iLogDemons with and without the incompressibility constraint were able to recover the simulated motion in the ultrasound synthetic sequence with reasonable accuracy. It is worth noting that the current electromechanical model is not incompressible, therefore enforcing incompressibility in the registration algorithm naturally does not improve the results, in comparison to the iLogDemons method without the incompressibility constraint. Furthermore, we also found that increasing or decreasing the sigma value does not always improve the result since the best value that we found here is $\sigma_u = 1.5$ while $\sigma_u = 1$ and $\sigma_u = 2$ do not yield significantly better results.

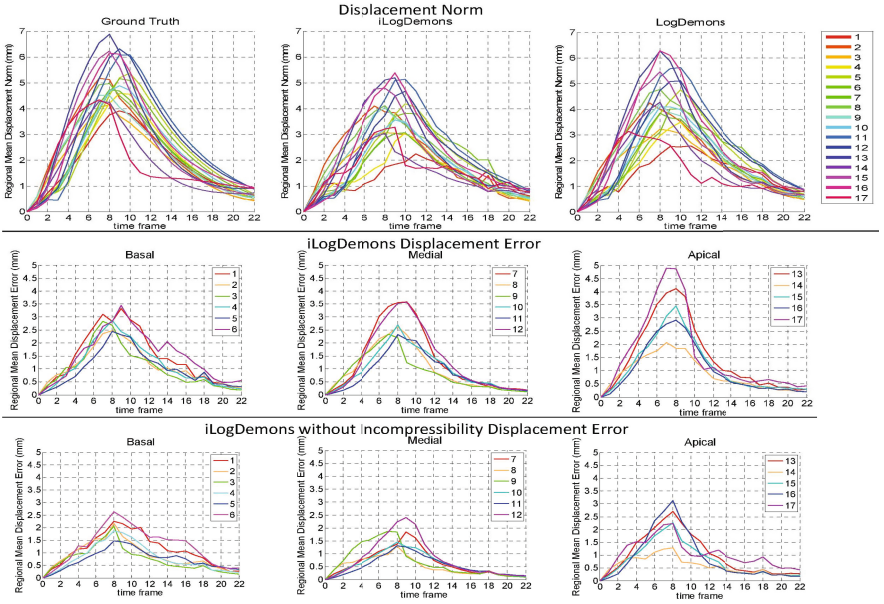


**Fig. 5.** The comparison of the ground truth, incompressible and non-incompressible iLogDemons estimated LV displacement norm for the first case on each American Heart Association (AHA) region. In both cases, $\sigma = 1.5$ was used. The mean displacement error is also calculated on each AHA region.

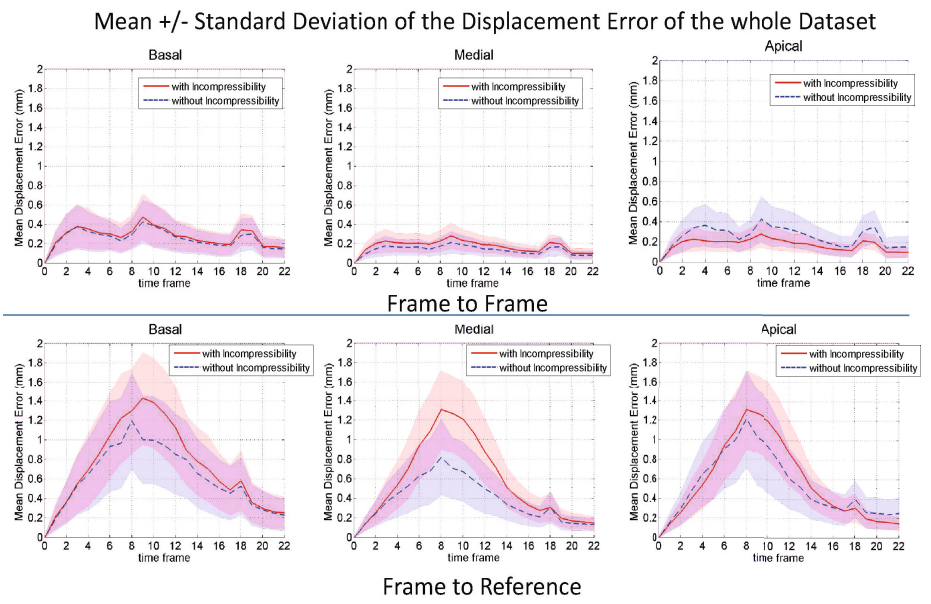


**Fig. 6.** The displacement error of the whole training data-set

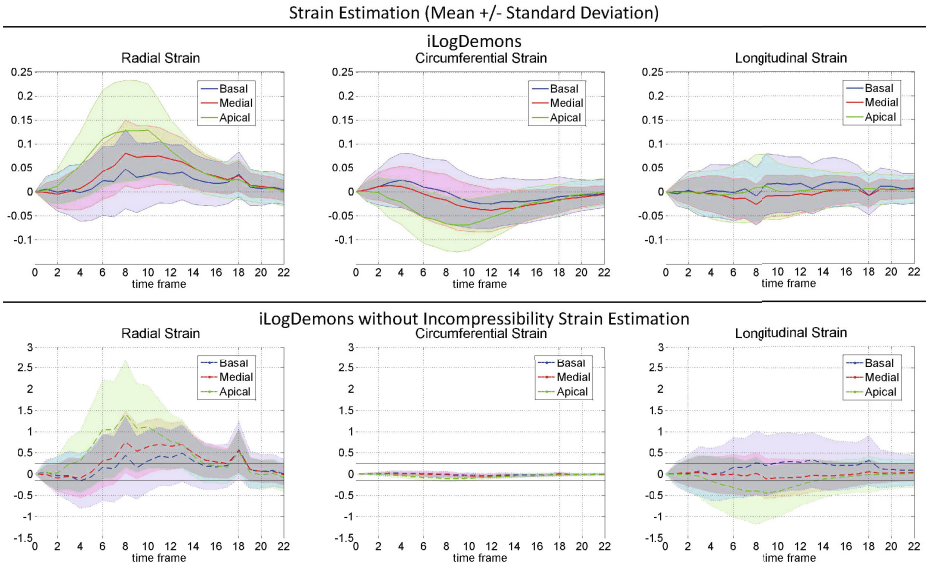


**Fig. 7.** The mean and standard deviation of the estimated strain for the whole training data-set with and without incompressibility constrain. Incompressibility constraint gives more realistic range of value of the estimated strain (from -15% to 25%). This range is shown as black horizontal lines on the result without incompressibility.

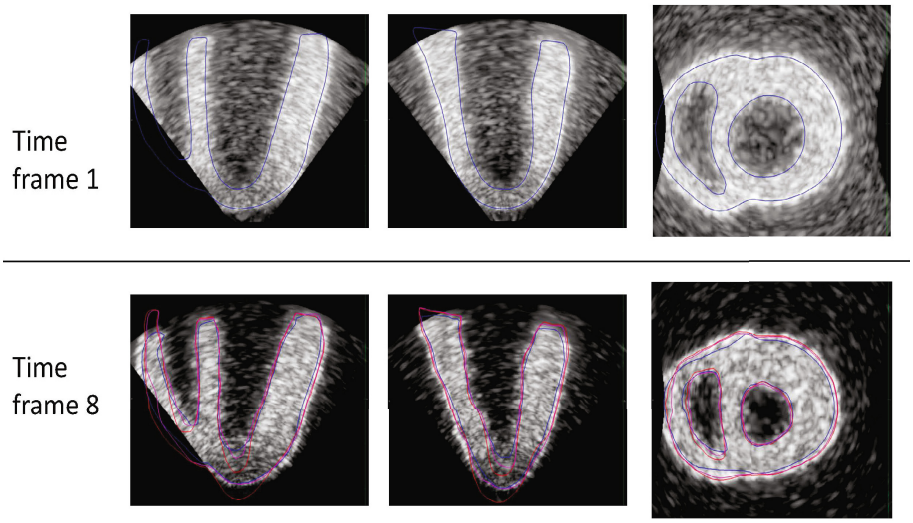


**Fig. 8.** Myocardium tracking result for the first case is shown (red for iLogDemons and purple for iLogDemons without incompressibility) and compared to the simulated ground truth (blue) at the time frame 8 which is at the maximum contraction. The tracking result follow the contour of the ground truth, indicating that the algorithm is able to capture reasonably well the dynamics of the motion.

## 5 Conclusion

The iLogDemons algorithm was applied to a data-set of synthetic ultrasound sequence with different motion and deformation pattern. The algorithm was able to reasonably estimate the ground truth deformation of the model. Since the provided data-set were created using an electromechanical model which is not incompressible, the incompressibility constraint does not improve the result. However, the incompressibility constraint gives more realistic range of estimated strain value. Future work is needed to deal with the error accumulation during the maximum of contraction.

**Acknowledgements.** This work was partially funded by the European Research Council (ERC) through the support of the MedYMA advanced grant 291080 and the European project euHeart.

## References

1. De Craene, M.: Statistical atlases and computational models of the heart (STACOM) 2012 cardiac motion analysis challenge (cMAC2) (2012), `http://www.physense.org/stacom2012/`
2. Mansi, T., Pennec, X., Sermesant, M., Delingette, H., Ayache, N.: iLogDemons: A demons-based registration algorithm for tracking incompressible elastic biological tissues. Int. J. of Comput. Vision 92, 92–111 (2011)
3. McLeod, K., Prakosa, A., Mansi, T., Sermesant, M., Pennec, X.: An Incompressible Log-Domain Demons Algorithm for Tracking Heart Tissue. In: Camara, O., Konukoglu, E., Pop, M., Rhode, K., Sermesant, M., Young, A. (eds.) STACOM 2011. LNCS, vol. 7085, pp. 55–67. Springer, Heidelberg (2012)
4. Moore, C., Lugo-Olivieri, C., McVeigh, E., Zerhouni, E.: Three-dimensional systolic strain patterns in the normal human left ventricle: Characterization with tagged MR imaging. Radiology 214, 453–466 (2000)
5. Tobon-Gomez, C., De Craene, M., Dahl, A., Kapetanakis, S., Carr-White, G., Lutz, A., Rasche, V., Etyngier, P., Kozerke, S., Schaeffter, T., Riccobene, C., Martelli, Y., Camara, O., Frangi, A.F., Rhode, K.S.: A Multimodal Database for the $1^{st}$ Cardiac Motion Analysis Challenge. In: Camara, O., Konukoglu, E., Pop, M., Rhode, K., Sermesant, M., Young, A. (eds.) STACOM 2011. LNCS, vol. 7085, pp. 33–44. Springer, Heidelberg (2012)
6. Vercauteren, T., Pennec, X., Perchant, A., Ayache, N.: Symmetric Log-Domain Diffeomorphic Registration: A Demons-Based Approach. In: Metaxas, D., Axel, L., Fichtinger, G., Székely, G. (eds.) MICCAI 2008, Part I. LNCS, vol. 5241, pp. 754–761. Springer, Heidelberg (2008)

# An Atlas for Cardiac MRI Regional Wall Motion and Infarct Scoring

Pau Medrano-Gracia[1], Avan Suinesiaputra[1], Brett Cowan[1], David Bluemke[2], Alejandro Frangi[3], Daniel Lee[4], João Lima[5], and Alistair Young[1]

[1] Auckland Bioengineering Inst., University of Auckland, New Zealand
[2] NIH Clinical Ctr., Bethesda, MD, USA
[3] Dept. of Mechanical Engineering, University of Sheffield, United Kingdom
[4] Feinberg Cardiovascular Research Inst., Northwestern University, Chicago, IL, USA
[5] Donald W. Reynolds Research Ctr., Johns Hopkins University, Baltimore, MD, USA

**Abstract.** Regional wall motion and infarct scoring of MR images are routine clinical tools to grade performance and scarring in the heart. The aim of this paper is to provide a framework for automatic scoring to alert the diagnostician to potential regions of abnormality. We investigated different shape and motion configurations of a finite-element cardiac atlas of the left ventricle. Two patient populations were used: 300 asymptomatic volunteers and 105 patients with myocardial infarction, both randomly selected from the Cardiac Atlas Project database. Support vector machines were employed to estimate the boundaries between the asymptomatic control and patient groups for each of 16 standard anatomical regions in the heart. Ground truth visual wall motion scores from standard cines and infarct scoring from late enhancement were provided by experienced observers. From all configurations, end-systolic shape best predicted wall motion abnormalities (global accuracy 78%, positive predictive value 85%, specificity 91%, sensitivity 60%) and infarct scoring (74%, 72%, 91%, 44%). In conclusion, computer assisted wall motion and infarct scoring has the potential to provide robust identification of those segments requiring further clinical attention; in particular, the high specificity and relatively low sensitivity could help avoid unnecessary late gadolinium rescanning of patients.

## 1 Introduction

Visual wall motion and infarct scoring by magnetic resonance imaging (MRI) is routine in clinical practice to assess ventricular function and regions of scar for patients with ischemic heart disease [12]. The left ventricular (LV) myocardium is typically partitioned into 17 segments according to guidelines set by the American Heart Association (AHA) [4]. Typically cine MRI (a sequence of MR images of the heart in different stages of contraction and relaxation) is qualitatively assessed using a five point scale from normal to dyskinetic, which is then used for patient management. However, visual assessment has significant inter- and intra-observer variability due to its subjective nature (for example, a *kappa* mean of

O. Camara et al. (Eds.): STACOM 2012, LNCS 7746, pp. 188–197, 2013.

0.43 for inter-observer agreement is reported in [7]). To reduce this variability, several authors have proposed various approaches to detect regional wall motion abnormalities (RWMA) automatically, e.g. by using parametric images [13], measuring the distance between abnormal and normal segment distributions [11, 5] or by integrating contraction patterns into point distribution models [9, 15]. Only [15] used clinical wall motion scores for validation of a proposed automatic detection framework and they reported relatively low accuracy results (64%, 67%, and 67% for basal, middle and apical levels when visual wall motion scoring was used as reference) for 45 patients.

In this study, we made use of large collections of Finite Element Models (FEMs) of the LV from the Cardiac Atlas Project[1], to create both shape and motion atlases. We investigated which combination of shape and motion best represented the wall motion features required to automatically detect and classify abnormal wall motion according to the standard clinical scale. Additionally, we sought to determine whether the atlas could predict segments with infarction by late gadolinium enhancement (LGE). If so, a clinical protocol could perform standard cine MRI and test whether infarcted or scarred segments were likely based on wall motion and shape, and if so, a LGE scan could then be performed. If no regions of infarction were likely, the patient could be saved an additional scan and intravenous contrast administration, thereby reducing risk, cost and discomfort. The aim of this paper is therefore not to replace LGE scanning but rather to detect when it is likely to be necessary on the basis of the common cine imaging.

The contribution of this paper is three-fold: (1) we quantitatively correlate gold standard clinical motion and infarct score data from a large-population study to the predictions of a learning system derived from a semi-automatic atlas; (2) we investigate the minimum size of the dataset (in particular the number of positive samples), required to obtain high classification power and, (3) we demonstrate that the end-systolic shape (minimum blood volume) is more useful than end-diastolic shape (maximum blood volume) alone or a combination of both end-systolic and end-diastolic shape in scoring RWMA and LGE.

## 2 Methodology

### 2.1 The Left-Ventricular Atlas

In order to build the atlas, guide-point modelling [18] was used to adaptively optimise a time-varying 3D finite element model of the left ventricle to fit each subject's images using custom software (CIM version 6.0). The model was interactively fitted to "guide points" provided by the analyst, as well as computer-generated data points calculated from the image using an edge detection algorithm, by linear least-squares. The model comprised 16 bicubic elements with $C^1$ continuity, defined in a prolate spheroidal coordinate system. Fiducial landmarks were manually defined at the hinge points of the mitral valve on the long

[1] `http://www.cardiacatlas.org`

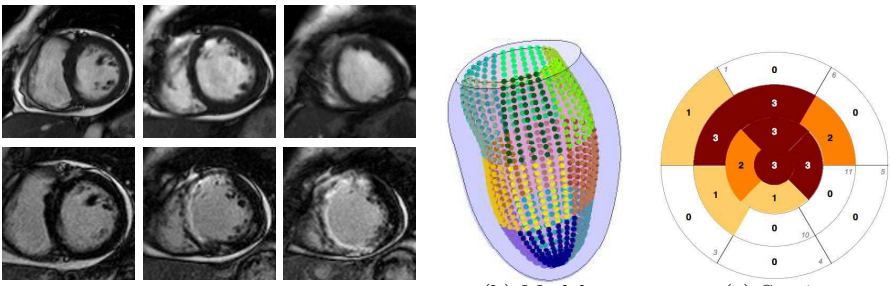

(a) MR acquisition (b) Model (c) Scoring

**Fig. 1.** Clinical work-flow for RWMA and LGE scoring, (a) acquisition, (b) LV finite element model (AHA regions appear highlighted by differently coloured points in the endocardium) and (c) the scoring on a *bull's eye* plot where each AHA region is scored visually by a specialist. Three examples of cine MRI (upper) and LGE MRI (lower) are shown in (a), for the base, mid and apical slices.

axis images, and at the insertions of the right ventricular free wall into the interventricular septum. These were used to define the atlas coordinate system and position of the model control points consistently aligned to the anatomy of the heart. Therefore, point correspondences between subjects were inherently formulated through the mathematical description of the model. This method has been previously validated against autopsy LV mass, in patients against manually drawn contours and in healthy volunteers against flow-derived measurements of cardiac output [18].

Shape parameters of the 3D finite element model were provided by Bézier bicubic control points for each of the epicardial (outer surface of the muscle) and endocardial surfaces. Each surface was represented by 16 bicubic elements each with 16 Bézier control points (four per node). The control points intuitively represent the position and slope of the model at the element boundaries. The surfaces were represented in a prolate spheroidal coordinate system enabling an efficient representation of the shape of the left ventricle with only 215 parameters.

### 2.2 Data

The control group was constructed from 300 asymptomatic patients from the MESA (Multi-Ethnic Study of Atherosclerosis) cohort [2]. We assumed that the cardiac motion of this group was normal in order to define a normal wall motion model. To test the RWMA and LGE classification methods, 105 patients with coronary artery disease and prior myocardial infarction were randomly selected from the DETERMINE (Defibrillators To Reduce Risk by Magnetic Resonance Imaging Evaluation) cohort [8]. Clinical characteristics and demographics of the study population are given in Table 1.

**Regional Wall Motion Abnormalities (RWMA).** A consensus was reached by two expert observers who quantitatively scored wall motion visually [10],

**Table 1.** Patient and control group characteristics (mean ± standard deviation)

| | Controls (n=300) | Patients (n=105) |
|---|---|---|
| Sex (M/F/Unknown) | 136/158/6 | 85/19/1 |
| Age | 60.5±10.5 | 62.0±11.9 |
| EDV (ml) | 115.7±24.1 | 194.6±52.3 |
| ESV (ml) | 45.5±14.1 | 113.3±49.6 |
| LV mass (g) | 136.0±36.3 | 162.9±39.4 |
| EF (%) | 61.1±6.0 | 43.8±11.5 |

on each of the 16 AHA regions (AHA region 17, the myocardial apical tip, was ignored in this work), and these were used as ground truth. RWMA was scored using a short-axis cine loop (i.e. by inspecting an animated image of all cardiac phases) into 5 grades of increasing abnormality: (0) normokinetic, (1) mildly hypokinetic, (2) severely hypokinetic, (3) akinetic (i.e. no motion) and (4) dyskinetic (i.e. paradoxical outward motion).

**Late Gadolinium Enhancement (LGE).** Areas of LGE were analogously examined and categorised into 5 grades according to the transmural thickness of enhancement on the LGE scan: (0) 0%, (1) 1-25%, (2) 26-50%, (3) 51-75% and (4) 76-100% of the wall thickness.

### 2.3 Motion Model Configurations

For each of the 16 regions, the atlas was sampled with a lattice of $10 \times 10$ evenly distributed points per region for both the endocardial and epicardial surfaces, yielding 200 points per region (100 per surface), thus facilitating the dimensional consistency needed for prediction. These points, expressed in rectangular Cartesian atlas coordinates, were used as features for classification (see Section 2.4).

The motion model was constructed from two cardiac frames: end diastole (ED) when the heart is full of blood and at its largest dimension and end systole (ES) when the heart is fully contracted and at its smallest dimension. In an attempt to find a suitable model to represent shape or motion, five configurations were investigated:

| | |
|---|---|
| ED | Features from the raw ED surface sample points without any transformation. |
| ES | Features from the raw ES surface sample points without any transformation. |
| EDES | Features calculated by subtracting ES points from ED points. |
| ESW | Features from the ES surface sample points after application of a thin-plate spline warp which mapped epicardial ES points to a mean shape of epicardial ED points [14]. |
| EDESW | Similar to EDES, but making use of the thin-plate spline ED-warped ESW points. |

### 2.4 Predictors

The sampled points, from the ED and ES regions were used as features for the classifiers in the different model configurations as described in 2.3. Two references were used for labelling: RWMA and LGE scores, as described in 2.2.

Support vector machines (SVM) [16] are popular learning systems that have formed their own field in machine learning. They have been widely used in the field of bioengineering and other fields because of their superior performance in terms of classification power. In this work, we applied SVM with a linear kernel to predict the RWMA or LGE scores from the atlas coordinates and compared these with the expert-derived gold standard. We used the library developed by [6] for both the training and classification. For each of the five configurations described in 2.3, the input was a raw matrix of 200 points $\times$ 105 cases and their corresponding labels for each region.

## 3 Experimental Results

The leave-one-out experiments were set up as follows. The classifiers were trained with the full dataset, leaving out one abnormal case from the patient group. Subsequently, the case was then predicted as an unseen example. This process was then repeated for all patients.

All subjects from the control group were considered as class "0" (normokinetic and no LGE scar) for all regions. Since we focused on the prediction of positive, or clinically abnormal segments, controls were not included in the leave-one-out experiments.

To gauge the overall performance of the classifier, the statistics presented in this section were computed globally across all leave-one-out experiments, as though it were a single global cross-validation experiment. Positive samples were identified by score values 1-4 (both for wall motion and infarct transmurality scores), and negative samples by 0. The accuracy was computed as $(TP + TN)/N$ where $TP$ stands for number of *true positives*, $TN$ for *true negatives* and $N = 1680$ (105 cases $\times$ 16 regions). Positive predictive value (PPV), specificity and sensitivity follow the standard definitions [1]. Also, for each type of label (RWMA and LGE), we provide regional scores for these experiments (Figures 2 and 4). For RWMA results, we use the term *prediction* whereas we use *inference* for LGE results, since enhancement thickness cannot be directly predicted by the surrounding surfaces (endocardium and epicardium) and must therefore be inferred.

Table 2 summarises the results of the different configurations for estimating RWMA/LGE scores in terms of overall accuracy, PPV, specificity and sensitivity, as defined before.

### 3.1 RWMA Prediction

RWMA results from Table 2 show how the ES configuration achieves the best result. In Fig. 2, the regional accuracy and PPV achieved by the SVM

**Table 2.** Global summary statistics for RWMA prediction and LGE inference (across all regions and cross-validation experiments) for the five atlas configurations

| Atlas | Accuracy | | PPV | | Specificity | | Sensitivity | |
|---|---|---|---|---|---|---|---|---|
| | RWMA | LGE | RWMA | LGE | RWMA | LGE | RWMA | LGE |
| ED | 61.1 | 65.1 | 70.0 | 55.3 | 92.4 | 94.5 | 22.2 | 12.1 |
| ES | 77.5 | 73.9 | 84.9 | 72.0 | 91.4 | 90.5 | 60.2 | 44.1 |
| EDES | 76.6 | 73.6 | 84.6 | 72.1 | 91.5 | 90.8 | 58.1 | 42.6 |
| ESW | 71.0 | 71.5 | 74.2 | 63.6 | 85.1 | 84.8 | 53.4 | 47.6 |
| EDESW | 71.3 | 70.8 | 79.0 | 63.7 | 89.7 | 86.4 | 48.3 | 42.9 |

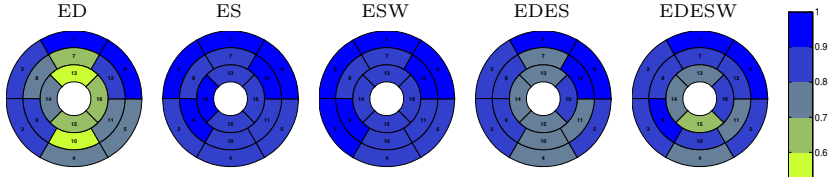


(a) RWMA detection accuracy

(b) RWMA positive predicted value

**Fig. 2.** RWMA regional leave-one-out results in terms of accuracy and PPV. For each AHA region, we present the colour-coded (a) accuracy and (b) PPV according to the scale on the right. ES and ESW appear to be the best configurations.

classifiers using the RWMA labels is presented in *bull's eye* plots as it is commonly presented in cardiac MR analysis.

We also investigated the minimum number of positive samples needed to obtain a robust classifier for each score. We took the ES model, which was the best configuration tested from the previous experiment, and plotted the PPV for the RWMA scores against the number of samples. Figure 3a shows this result for each score. A line through the origin has been fitted to each label of severity to assist in the interpretation.

As the number of positives grows (or as the sample grows in size for each case), so does the PPV. This is perhaps most clear in the mildly hypokinetic case, where a sufficient amount of positives is available. The same behaviour is observed in the rest of the cases, and they all report positive slopes. However the slopes tend to be steeper as the pathology worsens or becomes more distant from normal. This indicates that abnormal regions are easier to classify than normokinetic (to achieve the same level of PPV, fewer cases are needed) and is further discussed in Section 4.

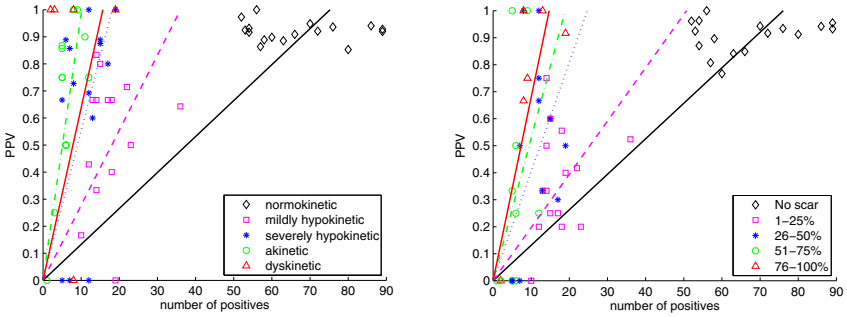


(a) RWMA (b) LGE

**Fig. 3.** PPV values grouped by wall motion class with the ES configuration, irrespective of the region. For each point, the $x$-coordinate represents the number of positives found in a region with a specific (a) wall motion label or (b) LGE score and the $y$-coordinate represents the corresponding PPV.

### 3.2 LGE Inference

Table 2 also shows the results of the different configurations for the estimation of LGE scores. In Fig. 4, the regional accuracy and PPV achieved by the SVM classifiers using the LGE labels is presented in *bull's eye* plots.

As it can be observed by comparing the RWMA and LGE results in Table 2, LGE's are generally lower. This is further discussed in Section 4 and is consistent with the fact that LGE scores (infarct regions) would be better inferred from the pixel intensity variation rather than from the surface point positions.

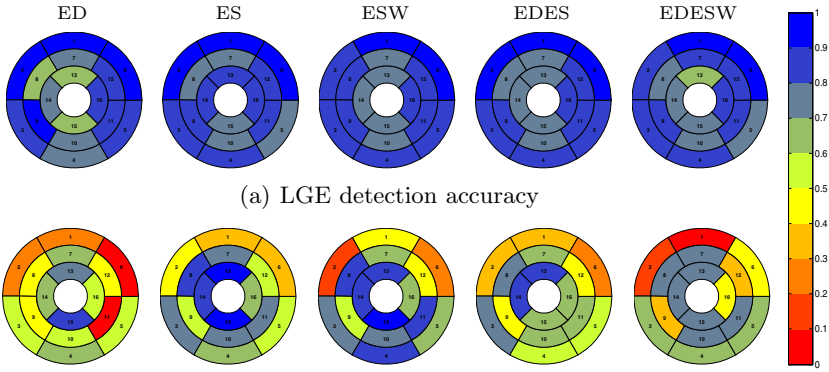


(a) LGE detection accuracy

(b) LGE positive predicted value

**Fig. 4.** LGE regional leave-one-out results in terms of accuracy and PPV. For each AHA region, we present the colour-coded (a) accuracy and (b) PPV according to the scale on the right. Again ES and ESW appear to be the best configurations.

Also in this case we examined the PPV per scar severity in Figure 3b which shows similar results to those of RWMA, albeit slightly lower.

## 4 Discussion and Future Work

From Table 2, virtually all atlas configurations show better classification of RWMA than LGE scores. The sampling of surface points at one or two time-points in the cardiac cycle represents a direct measurement of wall motion and therefore would be expected to robustly detect regions of motion abnormality (RWMA). Delayed enhancement (LGE) on the other hand is a measure of scar in the myocardium, and as no image contrast features were included in the model, the presence of hyperenhanced intensity areas must be inferred by its effect on wall motion; that is, regions of scar do not move well. As the scar becomes more transmural, the wall motion decreases and this is reflected in the use of higher or more abnormal wall motion scores. However the reverse may not be true since stunned or hibernating myocardium can show wall motion abnormalities without the presence of scar [3]. In such cases an LGE scan would also typically be performed.

Our tool shows high specificity but relatively low sensitivity. This is largely due to the limited number of regions of positive wall motion or scar score ($\geq 1$) in the sample (see for example Figure 3a). However, a high specificity is desired in this application since it means that if the predicted score is 0 it is likely that the true score is also 0, and an LGE scan is not warranted in this case.

The highest performance was achieved when the motion was modelled by the ES time-point only. Contrary to the expectation of enhancing the model by having more information in the data, adding ED surface points actually degraded the classification performance in most cases. The primary reason is that at the ED phase (when the heart is in its most relaxed state or not yet contracting) most hearts present no abnormalities. Therefore by adding this non-discriminative information, the classifier loses prediction power. This is supported clinically by the fact that ES volume is a better predictor of adverse outcome or prognosis than ejection fraction [17].

Considering epicardium-registered models (comparing ES with ESW and EDES with EDESW in Figures 2 and 4), it is clear that there was no significant improvement when registering the epicardial surfaces to a common fixed position. It is therefore sufficient to use surface sample points directly without non-rigid registration. Further work is required to determine whether a full motion atlas would improve the classifier.

In the experiment to estimate the minimum number of positive samples required in the training dataset to obtain a reliable classification result, we found that this number increases as the abnormality becomes less dramatic and therefore more difficult to distinguish from normal. This is shown for example in Figure 3a where to achieve $> 80\%$ classification accuracy for a specific label, 28 mildly hypokinetic cases, 14 severely hypokinetic cases and only 8 akinetic cases are required.

From Fig. 3a, the classifier was powerful enough to detect almost 100% positives in dyskinetic segments, even with a low number of positive samples. A dyskinetic segment shows very impaired wall motion during contraction, thus providing wide separation from other abnormal wall motion types. Clearly more cases are required to reliably classify mildly hypokinetic segments, especially where they are bordering on normal segments. The same sort of behaviour is observed in Fig. 3b even though the classifier can only infer from the available data.

In this study, we used a baseline kernel (linear) for the SVM classifier. This does not mean that SVM is the most optimal classification method for detecting RWMA and LGE scores, but it shows that SVM is capable of detecting RWMA and LGE scores with at least 78% accuracy using an ES atlas. We performed the same experiment with another classifier (Naive Bayes), but it produced worse classification results (maximum global PPV of 56% was achieved with the ES configuration for RWMA scores). Further work is required to determine optimal classifiers.

In conclusion, a motion atlas of the LV has great potential to predict RWMA and LGE scores, thus assisting clinicians during visual assessment. The most important application is to alert a clinician to the need for contrast administration and a LGE scan based on the initial standard cine images. An SVM classifier trained by features from ES surface points produces promising results. However, improvements are still necessary to make the automated RWMA/LGE classification system acceptable in clinical practice. These include optimising the kernel, adding more useful features such as more temporal resolution, regional LV functions (such as regional volume or statistical modes of variation) and intensity variations from LGE. These are all topics of future research.

**Acknowledgements.** This work was supported by Award Number R01HL087773 from the National Heart, Lung, and Blood Institute. The content is solely the responsibility of the authors and does not necessarily represent the official views of the National Heart, Lung, and Blood Institute or the National Institutes of Health. The National Institutes of Health (5R01HL091069) and St. Jude Medical provided grant support for the DETERMINE trial.

We also thank the reviewers for their insightful remarks and comments.

## References

[1] Altman, D., Bland, J.: Diagnostic tests 2: Predictive values. BMJ: British Medical Journal 309(6947), 102 (1994)

[2] Bild, D.E., Bluemke, D.A., Burke, G.L., et al.: Multi-ethnic study of atherosclerosis: objectives and design. Am. J. Epidemiol. 156(9), 871–881 (2002)

[3] Canty Jr., J.M., Fallavollita, J.A.: Hibernating myocardium. Journal of Nuclear Cardiology 12(1), 104–119 (2005)

[4] Cerqueira, M.D., Weissman, N.J., Dilsizian, V., et al.: Standardized myocardial segmentation and nomenclature for tomographic imaging of the heart. Circulation 105(4), 539–542 (2002)

[5] Duchateau, N., De Craene, M., Piella, G., Silva, E., Doltra, A., Sitges, M., Bijnens, B., Frangi, A.: A spatiotemporal statistical atlas of motion for the quantification of abnormal myocardial tissue velocities. Medical Image Analysis (2011)
[6] Fan, R., Chang, K., Hsieh, C., Wang, X., Lin, C.: Liblinear: A library for large linear classification. The Journal of Machine Learning Research 9, 1871–1874 (2008)
[7] Hoffmann, R., von Bardeleben, S., Kasprzak, J.D., et al.: Analysis of regional left ventricular function by cineventriculography, cardiac magnetic resonance imaging, and unenhanced and contrast-enhanced echocardiography: A multicenter comparison of methods. J. Am. Coll. Cardiol. 47(1), 121–128 (2006)
[8] Kadish, A.H., Bello, D., Finn, J.P., et al.: Rationale and design for the Defibrillators to Reduce Risk by Magnetic Resonance Imaging Evaluation (DETERMINE) trial. J. Cardiovasc. Electrophysiol. 20(9), 982–987 (2009)
[9] Lekadir, K., Keenan, N.G., Pennell, D.J., Yang, G.Z.: An inter-landmark approach to 4-D shape extraction and interpretation: application to myocardial motion assessment in MRI. IEEE Trans. Med. Imaging 30(1), 52–68 (2011)
[10] Ortiz-Pérez, J.T., Rodríguez, J., Meyers, S.N., et al.: Correspondence between the 17-segment model and coronary arterial anatomy using contrast-enhanced cardiac magnetic resonance imaging. JACC Cardiovasc. Imaging 1(3), 282–293 (2008)
[11] Punithakumar, K., Ben Ayed, I., Ross, I.G., et al.: Detection of left ventricular motion abnormality via information measures and bayesian filtering. IEEE Trans. Inf. Technol. Biomed. 14(4), 1106–1113 (2010)
[12] Reddy, G.P., Pujadas, S., Ordovas, K.G., Higgins, C.B.: MR imaging of ischemic heart disease. Magn. Reson. Imaging Clin. N. Am. 16(2), 201–212 (2008)
[13] Redheuil, A.B., Kachenoura, N., Laporte, R., et al.: Interobserver variability in assessing segmental function can be reduced by combining visual analysis of CMR cine sequences with corresponding parametric images of myocardial contraction. J. Cardiovasc. Magn. Reson. 9(6), 863–872 (2007)
[14] Suinesiaputra, A., Frangi, A.F., Kaandorp, T.A.M., et al.: Automated regional wall motion abnormality detection by combining rest and stress cardiac MRI: Correlation with contrast-enhanced MRI. J. Magn. Reson. Imaging 34(2), 270–278 (2011)
[15] Suinesiaputra, A., Frangi, A.F., Kaandorp, T.A.M., et al.: Automated detection of regional wall motion abnormalities based on a statistical model applied to multislice short-axis cardiac MR images. IEEE Trans. Med. Imaging 28(4), 595–607 (2009)
[16] Vapnik, V.: The nature of statistical learning theory. Springer (2000)
[17] White, H., Norris, R., Brown, M., Brandt, P., Whitlock, R., Wild, C.: Left ventricular end-systolic volume as the major determinant of survival after recovery from myocardial infarction. Circulation 76(1), 44–51 (1987)
[18] Young, A., Cowan, B., Thrupp, S., Hedley, W., Dell'Italia, L.: Left Ventricular Mass and Volume: Fast Calculation with Guide-Point Modeling on MR Images. Radiology 216(2), 597 (2000)

# Real-Time Catheter Extraction from 2D X-Ray Fluoroscopic and 3D Echocardiographic Images for Cardiac Interventions

Xianliang Wu[1], James Housden[2], Yingliang Ma[2],
Daniel Rueckert[1], and Kawal S. Rhode[2]

[1] Department of Computing, Imperial College London, SW7 2AZ, UK
[2] Division of Imaging Sciences & Biomedical Engineering,
King's College London, SE1 7EH, UK
x.wu11@imperial.ac.uk

**Abstract.** X-ray fluoroscopic images are widely used for image guidance in cardiac electrophysiology (EP) procedures to diagnose or treat cardiac arrhythmias based on catheter ablation. However, the main disadvantage of fluoroscopic imaging is the lack of soft tissue information and harmful radiation. In contrast, ultrasound (US) has the advantages of low-cost, non-radiation, and high contrast in soft tissue. In this paper we propose a framework to extract the catheter from both X-ray and US images in real time for cardiac interventions. The catheter extraction from X-ray images is based on SURF features, local patch analysis and Kalman filtering to acquire a set of sorted key points representing the catheter. At the same time, the transformation between the X-ray and US images can be obtained via 2D/3D rigid registration between a 3D model of the US probe and its projection on X-ray images. By backprojecting the information about the catheter location in the X-ray images to the US images the search space can be drastically reduced. The extraction of the catheter from US is based on 3D SURF feature clusters, graph model building, A* algorithm and B-spline smoothing. Experiments show the overall process can be achieved in 2.72 seconds for one frame and the reprojected error is 1.99 mm on average.

**Keywords:** Catheter Extraction, Cardiac Intervention, X-ray Fluoroscopy, Transesophageal Echocardiography.

## 1 Introduction

In image-guided interventions, X-ray and ultrasound (US) are two dominant modalities, in particular for real-time cardiac interventional procedures. X-ray images have already been widely used to guide standard cardiac electrophysiology (EP) procedures which try to diagnose or treat cardiac arrhythmias such as atrial fibrillation (AF). However, the drawbacks are its lack of soft tissue information and harmful radiation. In contrast, US has the advantages of low cost, high soft tissue contrast and non-ionizing radiation. It is used in many interventional procedures such as structural heart

O. Camara et al. (Eds.): STACOM 2012, LNCS 7746, pp. 198–206, 2013.

disease repair. However, the main drawbacks of US imaging are the difficulties in catheter visualization where identification of the tip can be especially challenging due to acoustic artifacts. This means that US imaging is less explored in standard EP procedures to actually guide ablation therapy.

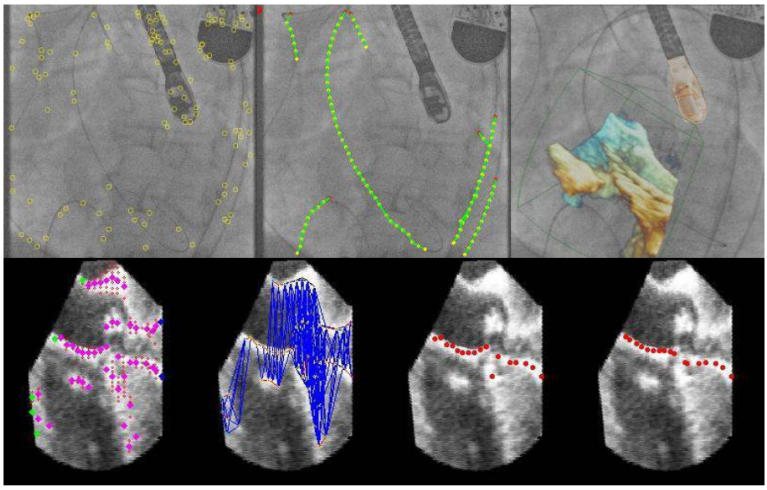

**Fig. 1.** An example of the system. From top left to bottom right are SURF detection in X-ray, catheter extraction by patch analysis and Kalman Filter, 2D/3D registration, 3D SURF detection and clustering in US, graph construction, shortest path finding and B-spline smoothing.

Recent research on catheter tracking has mainly focused on X-ray fluoroscopic imaging. An earlier approach trying to track a mapping catheter has been proposed in [1]. In this work, catheter tracking was accomplished by 3D catheter model generation, filter-based segmentation and 2D/3D registration using biplane X-ray imaging. Another approach for tracking the coronary sinus (CS) catheter to correct respiratory motion has been proposed in [2]. Electrodes are detected and a CS catheter is selected based on a cost function. In order to distinguish catheters of different size and remove catheter-like structures effectively, a learning-based approach has been proposed in [3], which segments the circumferential mapping catheter by training a cascade of boosted classifiers. Another recent technique also based on learning has been proposed in [4]. The tip and electrodes of the CS catheter are detected by trained binary classifiers and catheter hypotheses are generated based on aligning detections with a template. The topic of catheter detection and tracking in US imaging has not received as much attention as in X-ray imaging. Some research has already discussed the possibility of tracking devices in US [5, 6]. Recent work has proposed a real-time 3D tool tracking system based on US images in [7]. The coordinates of the US sensors mounted on a tool have been computed by analyzing US signals impinging on the sensors.

In this paper, we present a framework to extract catheters both in 2D X-ray images and 3D US images. The motivation of this research is to introduce soft tissue information

from US as well as minimize the X-ray exposure. The extraction from X-ray images is performed by SURF feature detection [8], local patch analysis and Kalman Filtering [9]. After that, the transformation between X-ray and US images is acquired through 2D/3D registration proposed in [10]. This allows the use of a ray casting approach to extract a curved surface in the US volume, which corresponds to the likely location of the catheter in the US volume. Finally, the catheter along this surface is extracted based on 3D SURF detection, feature clustering, graph model construction, shortest path finding and B-spline smoothing. An example of the whole process is shown in Fig. 1. The whole framework has been tested on both a pair of phantom images and a real patient sequence. The results show a total calculation time of 2.72s and around 1.99 mm re-projected error.

## 2 Catheter Extraction from X-Ray Images

### 2.1 SURF Feature Detection

The features we use are *S*peed *U*p *R*obust *F*eatures [8], also known as SURF, which is based on the integral image. The integral image provides a fast way to calculate the sum of intensity values inside a rectangular region on an image. The response of the SURF detector is an approximation of the determinant of the Hessian matrix.

### 2.2 Patch Analysis

Given a small square patch on an X-ray image, it is essential to determine whether a catheter passes through and get measurements pointing to the next patch.

First of all, the border of the catheter in the patch should be detected using a Haar detector along x- and y-directions. For each Haar feature $\mathbf{e}_i = (R_i, \theta_i)$, the gradient magnitude $R_i$ and direction $\theta_i$ are also calculated. Then, in order to extract the border of each side of the catheter, a classification is performed. A histogram of the value of $(\theta_i \, mod \, \pi)$ from 0 to $\pi$ is built and the two values of $\theta_i$ corresponding to the maximum quantity with an acceptable range (normally within $\pm\frac{1}{6}\pi$ ) are set as the threshold to classify those Haar features. There are two values because we use $(\theta_i \, mod \, \pi)$ instead of only $\theta_i$. These values, which we denote as $\theta^+$ and $\theta^-$, satisfy $\theta^+ - \theta^- = \pi$. The edge points can then be classified into three basic categories:

$$\mathbf{e}_i \in \begin{cases} \boldsymbol{E}^+, \ if \ \theta_i \in \left[\theta^+ - \frac{1}{6}\pi, \ \theta^+ + \frac{1}{6}\pi\right] \ mod \ 2\pi \\ \boldsymbol{E}^-, \ if \ \theta_i \in \left[\theta^- - \frac{1}{6}\pi, \ \theta^- + \frac{1}{6}\pi\right] mod \ 2\pi \\ \boldsymbol{E}^0, \ if \ others \end{cases} \quad (1)$$

The classes of Haar features can be fitted using two line equations corresponding to the borders of the catheter. Random Sample Consensus (RanSaC) [11] is used to remove outliers from $\boldsymbol{E}^{\pm}$ to $\boldsymbol{E}^0$. The ratio of the size of $\boldsymbol{E}^{\pm}$ to $\boldsymbol{E}^0$ is used to determine whether the catheter passes through the patch. A final central line equation is then determined using these two data sets $\boldsymbol{E}^+$and $\boldsymbol{E}^-$ using Singular Value Decomposition (SVD). After

the parameters of the central line are decided, the direction $\theta_p$ of the line and the intersection $\mathbf{x}_p = \left(x_p, y_p\right)^T$ of the central line with the perpendicular line via the center of the patch can be determined through their geometric relationship.

### 2.3 Catheter Extraction through Kalman Filter

By integrating patch analysis into a Kalman Filter framework [9], the whole catheter can be extracted from an initial SURF feature. Considering the whole catheter on the X-ray image as a path, and each SURF as a start point, a motion model is defined.

The state vector is denoted by $\mathbf{x}(k) = \left(x(k), y(k), \theta(k), \omega(k)\right)^T$, where $x(k)$ and $y(k)$ denote the spatial coordinates while $\theta(k)$ and $\omega(k)$ denote angular displacement and velocity at $k$th time respectively. System equations are defined as follows:

$$\begin{cases} x(k+1) = x(k) + T(v(\omega(\mathrm{k})\cos(\theta(k)))) \\ y(k+1) = y(k) + T(v(\omega(\mathrm{k})\sin(\theta(k)))) \\ \theta(k+1) = \theta(k) + T\omega(\mathrm{k}) \\ \omega(k+1) = \omega(k) + T\sigma(\mathrm{k}) \end{cases} \tag{2}$$

where $T$ is the sampling period and $\sigma(\mathrm{k}) \sim \mathrm{N}(0, \sigma^2)$. The relationship between absolute velocity $v(k)$ and angular velocity $\omega(k)$ can be denoted by:

$$v\left(\omega(k)\right) = (M - N)\, exp(-\alpha\omega(k)^2) + N \tag{3}$$

Where the velocity should be constrained in $[N, M]$ and $\alpha$ denotes how sensitive the velocity is in response to the change of $\omega(k)$. In addition, $\theta_p$ and $\mathbf{x}_p = \left(x_p, y_p\right)^T$ obtained from patch analysis can be considered as the direct measurements of the state variables $\theta(k)$ and $(x(k), y(k))^T$, i.e.

$$\mathbf{z}(k) = \left(\theta_p(k), x_p(k), y_p(k)\right)^T \tag{4}$$

After defining the system model and the measurement model, a sequence of positions $(x(k), y(k))^T$ can be easily acquired by applying Extended Kalman Filter equations. By checking the size of the sequence of positions, it can be decided whether or not these are the proper representation of the real catheter on the X-ray image.

## 3 Catheter Extraction from Echocardiography

Because of the low contrast of US images, it is very challenging to extract the catheter from US directly. However, the extraction of the catheter from X-ray images and the registration between US and X-ray provide strong priors on the location of the catheter in the US, enabling the search space to be narrowed dramatically.

### 3.1 Registration of TEE and X-Ray Fluoroscopy

The transformation between TEE and X-ray images can be acquired through registering a 3D TEE probe model to its projection on the 2D X-ray fluoroscopy, as proposed in [10]. The transformation matrix $\mathbf{T}_{US\to X-ray}$ mapping each TEE volume from the TEE coordinate system to the X-ray coordinate system consists of three terms:

$$\mathbf{T}_{US\to X-ray} = \mathbf{T}_{proj}\mathbf{T}_{probe}\mathbf{T}_{US\to probe} \tag{5}$$

where $\mathbf{T}_{US\to probe}$ transforms the 3D US volume to the probe space, $\mathbf{T}_{probe}$ denotes the 3D position of the US probe in X-ray space, and $\mathbf{T}_{proj}$ denotes the projection of the 3D position in X-ray space to the 2D X-ray image. $\mathbf{T}_{US\to probe}$ and $\mathbf{T}_{proj}$ can be acquired from the corresponding imaging devices directly or through calibration, while $\mathbf{T}_{probe}$ is calculated by a GPU accelerated 2D/3D registration between the 3D model of the TEE probe and its projection in the X-ray image.

### 3.2 Feature Detection in Reduced TEE Search Space

The extracted catheter in the X-ray image is represented by a set of sorted 2D key points with their homogeneous coordinates: $\mathbf{l}^i_{X-ray} = (x^i_{X-ray}, y^i_{X-ray}, 1)^T, i = 1, \cdots, n$ where $n$ is the size of the set. Suppose the US voxels corresponding to each key point on the X-ray image are denoted as $\mathbf{l}^i_{US} = (x^i_{US}, y^i_{US}, z^i_{US}, 1)^T, i = 1, \cdots, n$, then the transformation can be denoted by:

$$\mathbf{l}^i_{X-ray} = \mathbf{T}_{US\to X-ray}\mathbf{l}^i_{US} \tag{6}$$

Equation (6) defines a set of rays through the US volume, each of which corresponds to a key point on the X-ray image. Thus, the search strategy for the features is to search along each ray instead of the whole space, which reduces the searching cost dramatically. Because of registration and extraction errors, the search space cannot be limited only to each ray. Instead, the small space surrounding each ray, within an acceptable threshold, is also searched. The features we used are also SURF, however we use 3D rather than 2D SURF. For each ray, the detected features are also clustered with each other if they are within a certain distance along the direction of the ray. Thus after searching for the $i\,th$ ray, a set of clusters $C^i_j, j = 1, \cdots, n^i$ is also generated automatically, where $n^i$ is the number of clusters corresponding to the $i\,th$ ray. For each cluster $C^i_j$ containing a number of features $f^i_j$, a key feature set is defined as:

$$S^i_j = \{f^i_{j,Xmax}, f^i_{j,Ymax}, f^i_{j,Zmax}, f^i_{j,Xmin}, f^i_{j,Ymin}, f^i_{j,Zmin}, f^i_{j,mean}\} \tag{7}$$

each of which corresponds to the maximal or minimal x, y, or z coordinates, and a mean center respectively. The standard deviation $d^i_j$ of all features is also calculated.

### 3.3 Catheter Extraction Based on Graph Model and A* Algorithm

After a group of clusters has been generated, the next is to find which clusters are located on the catheter. The approach is to build a graph and find the shortest path.

Considering each cluster as a node on the graph model, all nodes are divided into two groups: active and passive. For active nodes, each is linked to only one node on the next adjacent ray with zero weight. Each passive node is linked to several nodes on adjacent rays. The purpose of doing this is to guarantee the shortest path can pass through as many active nodes as possible and can go back to an active node even if it reaches a passive one. Nodes near the border and having no active nodes on the last ray linking them are considered as starting nodes while those near the opposite border with no active node in the next ray linking it can be considered as end nodes.

The initial weight $W_{i,j\to p,q}^{ini}$ of edge from node $C_j^i$ to $C_q^p$is designed as a linear weighted combination of the 3D space distance $d_{i,j\to p,q}^{ini}$ between the corresponding clusters and two standard deviations of both the nodes $d_j^i$ and $d_q^p$:

$$W_{i,j\to p,q}^{ini} = \alpha d_{i,j\to p,q}^{ini} + (1-\alpha)(\, d_j^i + d_q^p) \tag{8}$$

where $\alpha$ can be set manually for different situations. In most of our experiments, we empirically set it to 0.5. $d_{i,j\to p,q}^{ini}$ can be determined using the smallest distance between any pair coming respectively from feature sets $S_j^i$ and $S_q^p$.

After allocating the initial weights, active nodes are selected by thresholding the initial weight. Then the final weight will be updated based on the following equation:

$$W_{i,j\to p,q}^{final} = \begin{cases} 0 & if\ active \\ W_{i,j\to p,q}^{ini} & if\ passive \end{cases} \tag{9}$$

In order to obtain a standard one-start-one-end graph, all start nodes are linked to a virtual start and all end nodes to a virtual end with zero weights. Thus the problem to extract the catheter is equivalent to finding the shortest path, which can be solved by the A* algorithm [12]. Finally, smoothing is performed through B-spline.

## 4 Experimental Results

The algorithm was first evaluated on a pair of phantom images, comprising a 2D X-ray fluoroscopic image and a 3D TEE image. It was then tested on real patient data, comprising a 321 frame X-ray sequence at 30 fps and a 216 frame TEE sequence at approximately 6 fps. All of the X-ray images, acquired with a Philips Allura Xper FD10 C-arm, have the same size of $512 \times 512$ pixels while the TEE images, acquired using a Philips X7-2t TEE probe, are $144 \times 160 \times 208$ voxels. The patient was undergoing an aortic valve implant via the minimally-invasive trans-aortic approach. 2D/3D registrations were carried out under Window 7, on a 2.66GHz, 4GB computer with a NVIDIA GeForce GTX 280 graphics card, and all other experiments were carried out under the Ubuntu Linux system on a 3.40GHz, 8GB desktop.

Our experiments are concerned with calculation time and accuracy. The calculation time of extractions in X-ray and US data are denoted by $t_{X-ray}$ and $t_{US}$ respectively. The registration time $t_{reg}$ is less than 1s. The overall time can be calculated as:

$$t_{overall} = \max\,(t_{X-ray}, t_{reg}) + t_{US} \tag{10}$$

Because the features are detected not only on the surface but within a margin, it is feasible to evaluate accuracy through re-projecting the coordinates of the 3D points representing the catheter to the X-ray image and comparing them with the original 2D points extracted from the X-ray image directly. The error can be formulated as:

$$\text{error} = \left(\sqrt{\sum_{i=1}^{n} \left\| \mathbf{x}_i - \mathbf{x}_i' \right\|^2}\right) / n \tag{11}$$

where $\mathbf{x}_i$ denotes the projection of the $i$th point in TEE space to the X-ray plane and $\mathbf{x}_i'$ denotes the nearest point to $\mathbf{x}_i$ on the catheter detected in the X-ray image.

The phantom experiment was undertaken in a tank of water. The extraction is relatively fast: 0.15s and 1.4s for the X-ray and TEE image respectively. The overall time was around 2.4s and the re-projected error was 1.60mm. Fig. 2 (Left) shows the phantom results. The real patient data are used to estimate the average performance. The last ten frames in the TEE sequence (the registrations are more accurate) were paired with up to 3 X-ray frames which are most likely to be their correspondences. 20 pairs were formed and the results are shown in Fig. 3. The last frames of both X-ray and TEE were also paired and the results are shown in Fig. 2(Right). For the patient sequence, the average re-projected error and overall time are 1.99mm and 2.72s.

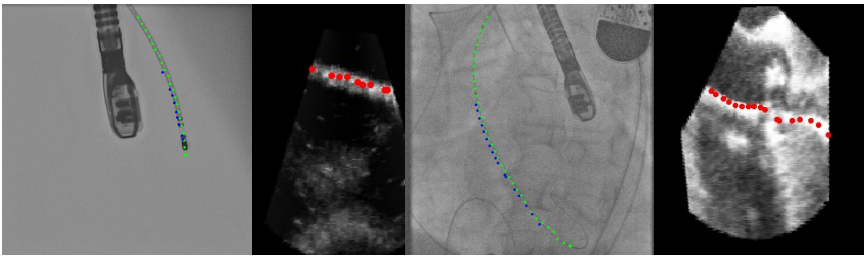

**Fig. 2.** Catheter Extraction. Left: phantom results. Right: real patient results. The red dots denote the catheter extraction in US. The green dots denote the original extraction from X-ray while the blue ones denote the back-projections from US to X-ray planes.

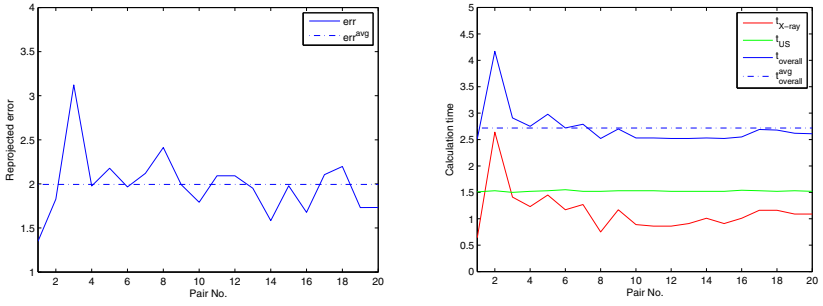


**Fig. 3.** Performance on 20 pairs from real patient data. Left: re-projected errors with an average error of 1.99mm. Right: the calculation times with an average overall time of 2.72s.

## 5 Conclusion and Future Work

We presented a new framework to extract catheters from both X-ray and TEE images in real-time. Our experiments show the process for one frame can consume less than 3s and the re-projected error is around 2 mm. Catheter extraction from X-ray is based on SURF, which are used as seed points. A Kalman Filter is used to extract the whole catheter based on patch analysis. This process takes around 1s. Meanwhile, the transformation between X-ray and TEE space can be obtained through 2D/3D registration between a probe model and its projection on the X-ray image. The registration takes less than 1s. Based on this registration, a curved surface can be extracted in the TEE images and the catheter can be extracted more easily. The 3D SURF are detected and clustered along rays corresponding to the catheter points on the X-ray image. The clusters are formulated as a graph and the problem to extract the catheter is transformed to the shortest path problem, which can be solved by A* Algorithm. Future work includes tracking catheters in both X-ray and TEE sequences in real-time.

## References

1. Brost, A., Liao, R., Hornegger, J., Strobel, N.: 3-D Respiratory Motion Compensation during EP Procedures by Image-Based 3-D Lasso Catheter Model Generation and Tracking. In: Yang, G.-Z., Hawkes, D., Rueckert, D., Noble, A., Taylor, C. (eds.) MICCAI 2009, Part I. LNCS, vol. 5761, pp. 394–401. Springer, Heidelberg (2009)
2. Ma, Y., King, A.P., Gogin, N., Rinaldi, C.A., Gill, J., Razavi, R., Rhode, K.S.: Real-Time Respiratory Motion Correction for Cardiac Electrophysiology Procedures Using Image-Based Coronary Sinus Catheter Tracking. In: Jiang, T., Navab, N., Pluim, J.P.W., Viergever, M.A. (eds.) MICCAI 2010, Part I. LNCS, vol. 6361, pp. 391–399. Springer, Heidelberg (2010)
3. Brost, A., Wimmer, A., Liao, R., Hornegger, J., Strobel, N.: Catheter Tracking: Filter-Based vs. Learning-Based. In: Goesele, M., Roth, S., Kuijper, A., Schiele, B., Schindler, K. (eds.) DAGM 2010. LNCS, vol. 6376, pp. 293–302. Springer, Heidelberg (2010)
4. Wu, W., Chen, T., Barbu, A., et al.: Learning-Based Hypothesis Fusion for Robust Catheter Tracking in 2D X-Ray Fluoroscopy. In: CVPR, pp. 1097–1104 (2011)
5. Nichols, K., Wright, L.B., Spencer, T., Culp, W.C.: Changes in Ultrasonographic Echogenicity and Visibility of Needles with Changes in Angles of Insonation. J. Vasc. Interv. Radiol. 14(12), 1553–1557 (2003)
6. Cheung, S., Rohling, R.: Enhancement of Needle Visibility in Ultrasound-Guided Percutaneous Procedures. Ultr. Med. Biol. 30(5), 617–624 (2004)
7. Mung, J., Vignon, F., Jain, A.: A Non-disruptive Technology for Robust 3D Tool Tracking for Ultrasound-Guided Interventions. In: Fichtinger, G., Martel, A., Peters, T. (eds.) MICCAI 2011, Part I. LNCS, vol. 6891, pp. 153–160. Springer, Heidelberg (2011)
8. Bay, H., Tuytelaars, T., Van Gool, L.: SURF: Speeded Up Robust Features. In: Leonardis, A., Bischof, H., Pinz, A. (eds.) ECCV 2006. LNCS, vol. 3951, pp. 404–417. Springer, Heidelberg (2006)
9. Kalman, R.E.: A New Approach to Linear Filtering and Prediction Problems. Transaction of the ASME—Journal of Basic Engineering, 35–45 (1960)

10. Gao, G., Penney, G., Gogin, N., Cathier, P., Arujuna, A., Wright, M., Caulfield, D., Rinaldi, A., Razavi, R., Rhode, K.: Rapid Image Registration of Three-Dimensional Transesophageal Echocardiography and X-ray Fluoroscopy for the Guidance of Cardiac Interventions. In: Navab, N., Jannin, P. (eds.) IPCAI 2010. LNCS, vol. 6135, pp. 124–134. Springer, Heidelberg (2010)
11. Fischler, M.A., Bolles, R.C.: Random Sample Consensus: A Paradigm for Model Fitting with Applications to Image Analysis and Automated Cartography. Commun. ACM 24, 381–395 (1981)
12. Hart, P.E., Nilsson, N.J., Raphael, B.: A Formal Basis for the Heuristic Determination of Minimum Cost Paths. IEEE Transactions on Systems Science and Cybernetics 4(2), 100–107 (1968)

# Measurement of Myocardial Structure: 3D Structure Tensor Analysis of High Resolution MRI Quantitatively Compared to DT-MRI

Stephen Gilbert[1,3], Mark Trew[4], Bruce Smaill[4], Aleksandra Radjenovic[2], and Olivier Bernus[1,3]

[1] Multidisciplinary Cardiovascular Research Centre
[2] NIHR Leeds Musculoskeletal Biomedical Research Unit University of Leeds, UK
{s.h.gilbert,a.radjenovic,o.bernus}@leeds.ac.uk
[3] L'Institut de ryhtmologie et modélisation cardiaque, Unité Inserm 1045, Centre de Recherche Cardio-Thoracique, Université Bordeaux Segalen, 33076 Bordeaux, France
olivier.bernus@u-bordeaux2.fr
[3]Auckland Bioengineering Institute, The University of Auckland, Auckland, New Zealand
{m.trew,b.smaill}@auckland.ac.nz

**Abstract.** The ventricular myocardium has a structure of branching laminae through which course regularly orientated fibers, an architecture important in excitation and contraction. DT-MRI is used to measure the fiber and laminar orientations. We quantify the performance of DT-MRI and structure tensor (ST) analysis of 3D high resolution MRI in five rat hearts and validate these against manual measurements. The ST and DT data are more similar for measures of the fiber orientation than laminar orientation. The average angle differences of elevation angles are 2.3±27.2˚, R = 0.57 for the fiber, 3.62±36.2˚, R = 0.24 for the laminae and 10.7±37.9˚, R = 0.32 for the laminae normal. The difference between DT and manually measured laminar orientation is 17±15˚ for DT and 5±10˚ for ST. DT and ST are comparable measures of the fiber orientation but ST is a better measure of myolaminar orientation.

**Keywords:** myocardium, structure tensor, diffusion tensor, ventricles, small animal imaging, diffusion tensor, structure tensor.

## 1 Introduction

The mammalian ventricles have a unique and specialized architecture consisting of a regular fiber-orientation which courses through a conserved and complex myolaminar arrangement. Due to the role of these structural features in electrophysiological and biomechanical function in both health and disease, their accurate measure is important. Changes in fiber orientation and myolaminar sliding are thought to be the principle mechanisms of myocardial thickening in systole [1]. Fiber orientation has long been known to influence the spread of myocardial activation [2], and furthermore, laminar organization has recently been shown to substantially influence activation [3]. Myofiber and myolaminar structure are present throughout the myocardium (except in

O. Camara et al. (Eds.): STACOM 2012, LNCS 7746, pp. 207–214, 2013.

the immediate sub-epicardium) and three principal orthogonal structural directions can be defined: (i) along the fiber axis; (ii) perpendicular to the fiber axis in the sheet plane; and (iii) normal to the sheet plane. This structural arrangement is known as orthotropy [3] (Fig. 1).

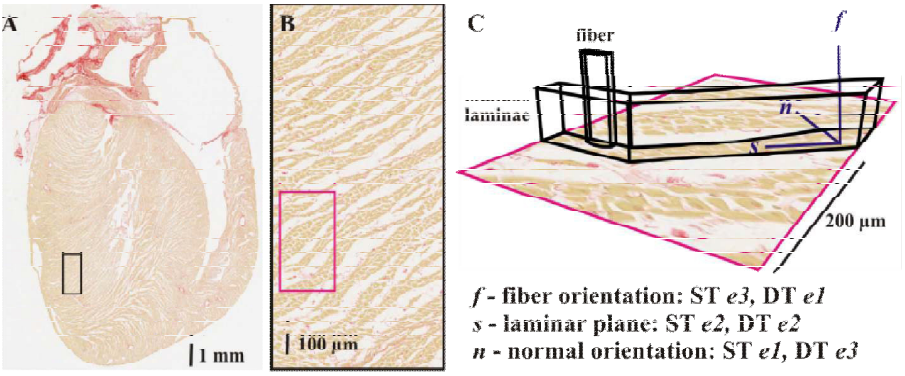


**Fig. 1.** Cardiac laminar and fiber architecture. (A) coronal long-axis section stained with Picrosirius Red. Cleavage planes – white, myolaminae – rust-red, collagen and fibroblasts – scarlet. (B) magnified region of A. (C) magnified region of B, with a representation of the 3D continuation of myofibers and laminae. The size of a 200 µm voxel is shown and the orientation of the myofibers and myolaminae are labeled, with the corresponding eigenvectors from ST and DT.

Whole-heart computational modeling requires detailed structural atlases [4]. Ideally these would be from accurate high-throughput 3D imaging but current methods have important limitations. 3D histology provides unparalleled spatial-resolution and can be used with molecular labeling but it is only applicable *post mortem* and destroys tissue [5,6]. DT has been widely applied and has been validated for fiber and laminar measurement against 2D methods but it: (i) has limited spatial resolution [7]; (ii) has limited accuracy for laminae [8]; (iii) has not been validated against 3D methods; (iv) is SNR sensitive [7]; (v) the microstructural feature imaged is controversial [9]; and, (vi) the influence of *b*-value has not been fully explored [9]. MicroCT has high spatial-resolution and is fast but has not yet been validated in the myocardium. HR-MRI has high spatial-resolution, is applicable to the beating heart and it has been validated against 2D-histology [10,11]. Structure tensor (ST) analysis is an image analysis method which derives a tensor from the distribution of gradient directions within the neighbourhood of an image voxel [12]. We hypothesized that ST analysis could be applied to HR-MRI images to quantify fiber and laminar orientation, and furthermore that myolaminar orientations from ST would be more accurate and reliable than those from DT as the largest eigenvalue in ST corresponds to the sheet normal direction, whereas in DT the largest eigenvalue corresponds to the fiber direction.

# 2 Methods

## 2.1 Heart Preparation and Perfusion Fixation

Male Wistar rats (N = 5) weighing 200 –220 g were euthanized in accordance with the UK Home Office Animals (Scientific Procedures) Act 1986, the hearts were removed and retrograde perfused (as in [11]) with: (i) HEPES-Tyrodes to clear blood; (ii) BDM to prevent contraction; then (iii) MRI contrast agent (0.1% Gd-DTPA) and fixative (4% formaldehyde). Hearts were imaged within 12 hours of fixation.

## 2.2 HR-MRI and DT-MRI Acquisition and Reconstruction

All hearts were imaged at 20°C using a FLASH (Fast Low Angle SHot) MRI sequence in a Bruker (Ettlingen, Germany) 9.4T spectroscope with 20 averages, echo time (TE) = 7.9 ms, and repetition time (TR) = 50 ms, taking 18h to acquire at a resolution of 50 x 50 x 50 µm. DT was carried out using the same spectroscope on the same hearts with a set of 6 optimized directions using a 3D diffusion-weighted spin-echo sequence with TE = 15 ms, TR = 500 ms, taking 2h to acquire at a resolution of 200 x 200 x 200 µm.

## 2.3 Structure Tensor Analysis of High Resolution MR Images

A binary mask was created slice-wise from the segmented images by thresholding intensity values and fractional anisotropy and performing a sequence of morphological operations in the following order: clean (removing isolated foreground pixels), bridge (connect pixels separated by one background pixel), fill (fill isolated background pixels), open (binary opening) and a thicken (add pixels around the exterior of an object but do not connect previously unconnected pixels.) Myostructural orientations were computed from the cleaned images by computing intensity gradients with an optimal 5×5×5 point derivative template [13]. The template was applied to the full 3D image using 1D FFT convolution. The structure tensor (the outer product of the intensity gradient vectors) was computed for each voxel in the 3D image. A sequence of structure tensors at progressive resolution doubling (i.e. 100 µm, 200 µm, 400 µm, etc.) was determined using a level 4 binomial filter. These calculations are completed in around 1 minute. The 200 µm smoothed structure tensor data set (64×64×128 tensors) was used to best match the expected DT resolution. Eigenanalysis was used to extract the principal directions from the structure tensor at each discrete point (the calculation requires < 10 s). The eigenvector corresponding to the largest magnitude eigenvalue was taken as the sheet/laminae normal direction and the eigenvector corresponding to the smallest magnitude eigenvalue was taken as the fiber direction (Fig. 1).

## 2.4 Comparison of Structure Tensor and Diffusion Tensor Orientations

A model cardiac geometry, with a manually fitted LV long-axis, was registered to each heart MRI by affine registration (using the Insight Tool Kit fast affine registration

implemented in Slicer3) with 20 histogram bins, 40000 spatial samples and 4000 iterations. The registered model hence defines: (i) the long-axis (LA) centroid of a cylindrical coordinate system for which the elevation and azimuth angles of the eigenvectors were calculated. and, (ii) selected regions of interest (ROI) for quantification. The orientation angles reported are defined in detail in [14]. Elevation angles are measured from the cardiac short-axis (SA) plane. The fiber helix angle ($\alpha_H$) is the angle between the transverse plane and the projection of the fiber vector onto the circumferential-longitudinal plane. The fiber transverse angle ($\alpha_T$) is the angle between the circumferential-longitudinal plane and the projection of the fiber vector onto the transverse plane. The angle between the transverse plane and the projection of the laminar vector onto the radial-longitudinal plane *is* $B'_S$. The angle between the longitudinal—radial plane and the projection of the laminar vector onto the transverse plane $B''_S$. The angles $B'_N$ and $B''_N$ correspond to $B'_S$ and $B''_S$ but are the orientations of the normal of the laminar plane. A mid-heart coronal long-axis plane was selected for visualization and quantification, and within this a ROI measuring 5.1 x 5.1 mm was selected and ST and DT $B'_S$ was visualised. ST and DT $B'_S$ was compared to manually measured laminar orientation in a 1.1 x 1.1 mm sub-region, by using ImageJ to measure orientation in 200 µm grid squares in the HR-MRI data.

## 3 Results

Fig. 2 shows unprocessed HR-MRI SA and LA images and alongside these are LA $\beta'$ and $\alpha_H$ maps and SA $\alpha_H$ and $\alpha_T$ maps. As previously demonstrated [10,11] the laminar organization can be clearly observed in the HR-MRI images. The $\alpha_H$ and $\alpha_T$ maps show that the values and spatial distribution of the fiber orientation measured by ST and DT is strikingly close. The $\beta'$ maps reveal related values with some differences between the ST and DT determined sheet elevation angle. These differences are in regions where the myocardium is compact and cleavage planes difficult to discern. The angle distributions (Fig. 2E&F) reflect these observations.

The ST and DT determined orientations were compared in the selected equatorial SA slice (Table 1). The mean angle differences are low for the fiber orientation angles (2.3° for $\alpha_H$, 1.7° for $\alpha_T$) and there is good correlation between the ST and DT $\alpha_H$ (circular correlation coefficient R = 0.57). The correlation of ST and DT $\alpha_T$ is weaker (R = 0.29). The average angle difference and correlation coefficients for the sheet orientation measures are likewise weaker but all correlations are significant.

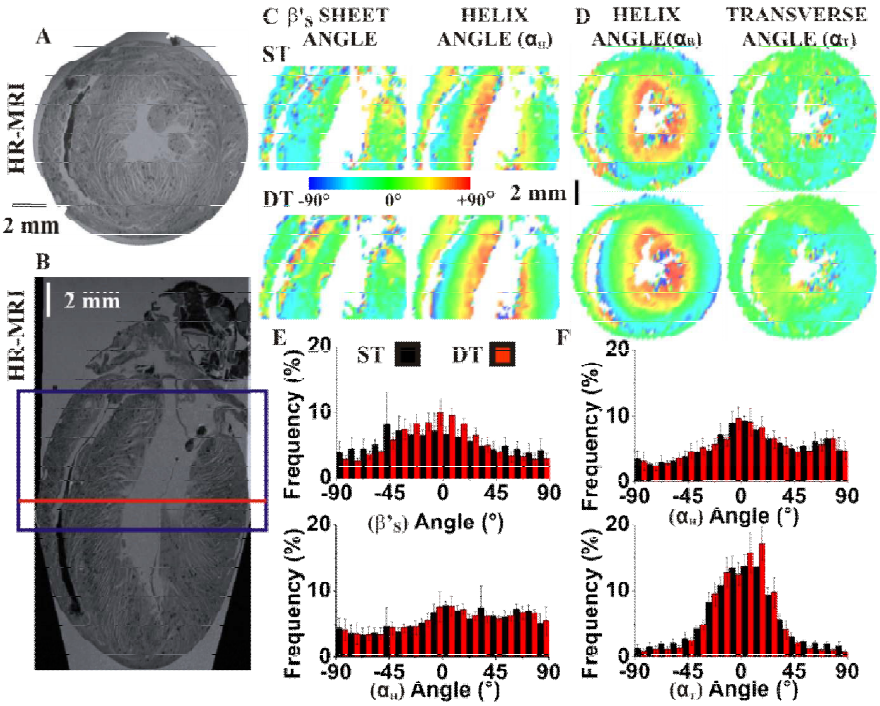


**Fig. 2.** Visualization of DT and ST $\alpha_H$, $\alpha_T$ and $\beta'$ maps and associated angle distributions. (**A**) SA HR-MRI image of ROI. (**B**) LA HR-MRI image, with the LA ROI highlighted in the blue box and the SA ROI highlighted by the red line. (**C**) LA $\beta_S'$ and $\alpha_H$ for ST (top panel) and DT (lower panel). (**D**) SA $\alpha_H$ and $\alpha_T$ for ST (top panel) and DT (lower panel). (**E**) Angle distributions corresponding to images in LA maps, $\beta'_S$ upper panel, $\alpha_H$ bottom panel. (**F**) Angle distributions corresponding to images in SA maps, $\alpha_H$ – upper panel, $\alpha_T$ bottom panel.

**Table 1.** The average difference (*mean* **Δ**) angles pooled the selected equatorial slice in the five hearts. * - correlation statistically significant at $p < 0.05$.

| | | $\alpha^H$ | $\alpha^T$ | $\beta'_S$ | $\beta''_S$ | $\beta'_N$ | $\beta''_N$ |
|---|---|---|---|---|---|---|---|
| ***mean Δ*** | ***x*** | 2.3 | 1.7 | 3.6 | 4.8 | 10.7 | 6.4 |
| | ***σ*** | 27.2 | 29.1 | 36.2 | 36.0 | 37.9 | 35.2 |
| ***corr.*** | ***R*** | 0.57* | 0.29* | 0.24* | 0.24* | 0.32* | 0.34* |

Fig. 3 compares the performance of DT and ST against manual measurement from HR-MRI. The magnified regions in Fig. 3E&F allow the visual assessment of the performance of ST and DT. In regions where the laminae are clearly defined by cleavage planes ST performs better than DT. It is not possible to assess the performance of the methods in the regions where laminar structure is not clearly defined (such as Fig 3E, top left of image).

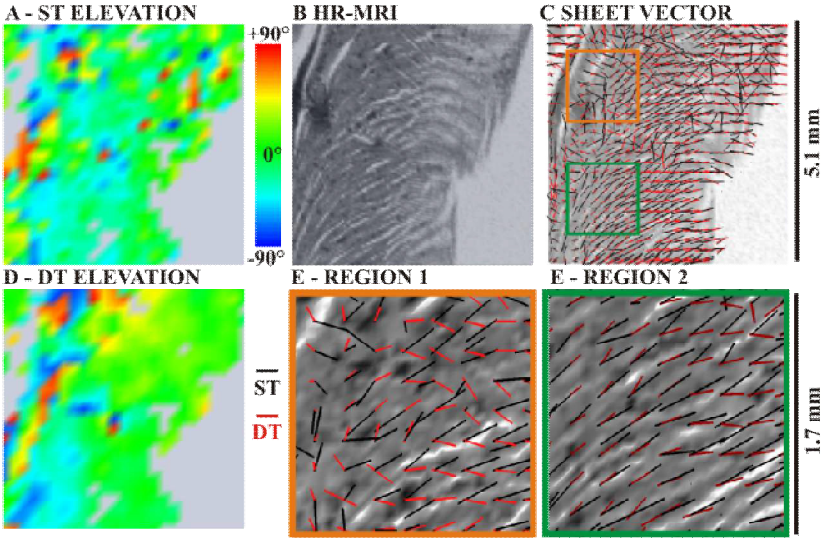


**Fig. 3.** Quantitative validation of DT and ST against manual measurements of sheet elevation angle (β') in HR-MRI images. A region was selected from the LA ROI in Fig. 2. (**A**) ST $\beta$' map. (**B**) The HR-MRI of the ROI. (**C**) The 3D orientation of the sheet vector within individual voxels in the ROI is shown by line glyphs, black for ST, red for DT. (**D**) DT $\beta$' map. (**E**) magnified orange box from panel B. (**F**) magnified green box from panel B.

Laminar elevation in the ROI in Fig. 3F was manually measured and the angle difference between the manual measurements (mean ± standard deviation) is 17±15° for DT and 5±10° for ST.

## 4 Discussion

DT and ST produce similar maps of fiber orientation. The maps of laminar orientation from DT and ST are related but ST is a consistently more acceptable measure, as shown by both visual comparison and by manual measurements. We demonstrate that the distinct approaches of DT and of ST produce globally and locally similar maps of fiber orientation. Although fiber orientation measurement by ST of myocardial images has been proposed [15] this is the first whole heart demonstration of the method. The quality of the ST $\alpha_H$ and $\alpha_T$ maps and the similarity to the DT maps is striking, particularly as the HR-MRI spatial resolution is not high enough to allow the manual identification of myocytes. Indeed, due to this resolution limitation it is not possible to directly validate DT or ST against manual measurements of fiber orientation from the HR-MRI data. DT and ST produce maps of laminar orientation which share some similarities, but there are also regions of marked difference. We show that the average difference between manual and DT $\beta$' measurement is 17±15°, while it is only 5±10° for ST $\beta$' measurement in a selected ROI. On this basis we propose that ST of HR-MRI is a useful method for measurement of whole heart laminar orientation and

performs superiorly to DT. Based on our data, DT provides limited accuracy when assessed in myocardium with easily discernible laminae and cleavage plane directions. An important question for the choice of method used to measure laminar orientation is the degree of accuracy required. Until recently the histological validation of DT in the measurement of laminar orientation has been small scale and 2D [16] or using an unconventional 2D ink-blot approach [17]. In a recent study the difference between histologically and DT determined sheet angles was reported as 8° ± 27° and the authors concluded that the measurement of myolaminae by the DT corresponds to histology [8]. Therefore, [8] reported a better performance of DT (albeit with high standard deviation) than we found. This is particularly of note as in [8] DT was assessed against histology and we assessed DT against HR-MRI. The accuracy of DT claimed by [8] is strikingly positive, particularly considering the substantial distortion of tissue, which accompanies sectional histological laminar orientation. It is our view that DT can be much more reliably assessed against the volumetric HR-MRI method as the same tissue preparation is sequentially imaged in the MRI scanner with no myocardial distortion or damage. There are some limitations in this preliminary study. It is possible that greater numbers of diffusion directions, greater numbers of repetitions, alternative b-values or alternative voxel sizes may increase the accuracy of DT applied to the myocardium, and a detailed sensitivity analysis has not yet been reported. In this study we assess the performance of 6 directions DT, but recent evidence suggests that this has comparable robustness to 30- or 60-direction data [18]. Future studies will incorporate sensitivity analysis of both ST and DT.

## References

1. Costa, K.D., Takayama, Y., McCulloch, A.D., Covell, J.W.: Laminar fiber architecture and three-dimensional systolic mechanics in canine ventricular myocardium. Am. J. Physiol. 276, H595–H607 (1999)
2. Arisi, G., Macchi, E., Baruffi, S., Spaggiari, S., Taccardi, B.: Potential fields on the ventricular surface of the exposed dog heart during normal excitation. Circ. Res. 52, 706–715 (1983)
3. Hooks, D.A., Trew, M.L., Caldwell, B.J., Sands, G.B., LeGrice, I.J., Smaill, B.H.: Laminar arrangement of ventricular myocytes influences electrical behavior of the heart. Circ. Res. 101, 103–112 (2007)
4. Sermesant, M., Chabiniok, R., Chinchapatnam, P., Mansi, T., Billet, F., Moireau, P., Peyrat, J.M., Wong, K., Relan, J., Rhode, K., Ginks, M., Lambiase, P., Delingette, H., Sorine, M., Rinaldi, C.A., Chapelle, D., Razavi, R., Ayache, N.: Patient-specific electromechanical models of the heart for the prediction of pacing acute effects in CRT: a preliminary clinical validation. Med. Image. Anal. 16, 201–215 (2012)
5. Sands, G.B., Gerneke, D.A., Hooks, D.A., Green, C.R., Smaill, B.H., LeGrice, I.J.: Automated imaging of extended tissue volumes using confocal microscopy. Microsc. Res. Tech. 67, 227–239 (2005)
6. Smith, R.M., Matiukas, A., Zemlin, C.W., Pertsov, A.M.: Nondestructive optical determination of fiber organization in intact myocardial wall. Microsc. Res. Tech. 71, 510–516 (2008)

7. Jiang, Y., Pandya, K., Smithies, O., Hsu, E.W.: Three-dimensional diffusion tensor microscopy of fixed mouse hearts. Magn. Reson. Med. 52, 453–460 (2004)
8. Kung, G.L., Nguyen, T.C., Itoh, A., Skare, S., Ingels Jr., N.B., Miller, D.C., Ennis, D.B.: The presence of two local myocardial sheet populations confirmed by diffusion tensor MRI and histological validation. J. Magn. Reson. Imaging 34, 1080–1091 (2011)
9. Hsu, E.W., Buckley, D.L., Bui, J.D., Blackband, S.J., Forder, J.R.: Two-component diffusion tensor MRI of isolated perfused hearts. Magn. Reson. Med. 45, 1039–1045 (2001)
10. Köhler, S., Hiller, K.H., Waller, C., Jakob, P.M., Bauer, W.R., Haase, A.: Visualization of myocardial microstructure using high-resolution T*2 imaging at high magnetic field. Magn. Reson. Med. 49, 371–375 (2003)
11. Gilbert, S.H., Benoist, D., Benson, A.P., White, E., Tanner, S.F., Holden, A.V., Dobrzynski, H., Bernus, O., Radjenovic, A.: Visualization and quantification of whole rat heart laminar structure using high-spatial resolution contrast-enhanced MRI. Am. J. Physiol. Heart. Circ. Physiol. 302, H287–H298 (2012)
12. Jähne, B.: Digital image processing, 6th edn. Springer, The Netherlands (2005)
13. Farid, H., Simoncelli, E.P.: Differentiation of discrete multidimensional signals. IEEE Trans. Image Process. 13, 496–508 (2004)
14. Benson, A.P., Gilbert, S.H., Li, P., Newton, S.M., Holden, A.V.: Reconstruction and Quantification of Diffusion Tensor Imaging-Derived Cardiac Fibre and Sheet Structure in Ventricular Regions used in Studies of Excitation Propagation. Math. Model. Nat. Pheno. 3, 101–130 (2008)
15. Burton, R.A., Plank, G., Schneider, J.E., Grau, V., Ahammer, H., Keeling, S.L., Lee, J., Smith, N.P., Gavaghan, D., Trayanova, N., Kohl, P.: Three-dimensional models of individual cardiac histoanatomy: tools and challenges. Ann. N. Y. Acad. Sci. 080, 301–319 (2006)
16. Scollan, D.F., Holmes, A., Winslow, R., Forder, J.: Histological validation of myocardial microstructure obtained from diffusion tensor magnetic resonance imaging. Am. J. Physiol. 275, H2308–H2318 (1998)
17. Tseng, W.Y., Wedeen, V.J., Reese, T.G., Smith, R.N., Halpern, E.F.: Diffusion tensor MRI of myocardial fibers and sheets: correspondence with visible cut-face texture. J. Magn. Reson. Imaging 17, 31–42 (2003)
18. Lebel, C., Benner, T., Beaulieu, C.: Six is enough? Comparison of diffusion parameters measured using six or more diffusion-encoding gradient directions with deterministic tractography. Magn. Reson. Med. (2011) (in press)

# A Fast and Noise-Robust Method for Computation of Intravascular Pressure Difference Maps from 4D PC-MRI Data

Sebastian Meier[1], Anja Hennemuth[1], Johann Drexl[1], Jelena Bock[2], Bernd Jung[2], and Tobias Preusser[1,3]

[1] Fraunhofer MEVIS, Bremen, Germany
[2] Department of Medical Physics, University of Freiburg, Germany
[3] School of Engineering and Science, Jacobs University, Bremen, Germany

**Abstract.** Noninvasive blood flow measurements by 4D flow-sensitive MRI can be used to compute the intravascular distribution of blood pressure. In this work, we present an efficient algorithm for this task, based on the Navier-Stokes equations including zero-divergence condition for the velocity field. Its accuracy and robustness is investigated on two different CFD-based software phantoms. The method has been integrated into research software for analysis of clinical 4D flow measurements, and is tested on six patients with aortic coarctation. The pressure drop across the stenosis is quantified and coincides well with published results from a previously validated solution algorithm.

## 1 Introduction

The pressure drop across a stenosed blood vessel is an important marker for assessment of the severity of a cardiovascular disease such as arteriosclerosis or aortic coarctation. Invasive catheter measurement, which is the current clinical gold standard, burdens the patient with radiation and a non-vanishing risk of severe side effects. Noninvasive methods to quantify intravascular pressure gradients would be a highly valuable tool for therapy decision or follow-up studies. For vessels close to the body surface, Doppler ultrasound provides an estimate via the simplified Bernoulli formula, but this method is subject to errors by operator dependence and strong model simplifications.

4D flow-sensitive phase-contrast MRI (4D PC-MRI) provides the opportunity to measure time- and spatially resolved velocity vectors without the need of catheterization, radiation or contrast agents [1,2]. Recently, it has been suggested to use a three-dimensional mathematical flow model (Navier-Stokes equations) to compute blood pressure maps from the MRI data, relative to a fixed position within the vessel [3]. The method is based on an iterative solution of the Pressure Poisson Equation (PPE) using spatial and temporal derivatives of the measured flow velocities as input. Its principal feasibility has been validated using flow phantoms [3] and animal studies [4], and the methods shows consistent results also for human volunteers and patients [5,6]. Despite of this success, in [7] it is

O. Camara et al. (Eds.): STACOM 2012, LNCS 7746, pp. 215–224, 2013.

indicated that the choice of the mathematical model and algorithm details may have a large influence on the results. In general, a systematic underestimation of pressure differences is to be expected. This is also consistent with recently reported reported good correlation, but systematic underestimation compared to Doppler ultrasound [5].

In the present work, the problem of determining the pressure field from noisy velocity measurements is put into the framework of mathematical optimization methods. The resulting optimization problem is approximately solved by a two-step procedure, in which first the divergent part is removed from the measured velocity field. Afterwards, the PPE with physically correct boundary conditions is solved. Both steps are solved by the finite element (FE) method [8]. A similar two-step procedure was also suggested in [9], but suffered from high computation times already for two-dimensional data sets. The fast pressure computation method presented in the present paper is built into a software demonstrator and is thus readily available for clinical evaluation.

In order to test the accuracy of the method, we present a comparison with two different software phantoms generated by computational fluid dynamics (CFD). Additional noise is added to provide realistic input to the pressure solvers and to test noise robustness. Moreover, the method is tested on six patients with aortic coarctation.

## 2 Navier-Stokes Model

### 2.1 Constrained Optimization Problem

The problem of recovering physiological information from noisy velocity measurement can be cast into a mathematical optimization framework: Given a noisy space- and time-varying vector field $\mathbf{v}_\varepsilon(\mathbf{x}, t)$ inside an image bounding box $\Omega_\mathrm{B} \subset \mathbf{R}^3$, we are searching a pressure field $p(\mathbf{x}, t)$ and a velocity field $\mathbf{v}(\mathbf{x}, t)$, which is close to the measurements and fulfills as an additional constraint the incompressible Navier-Stokes equations within the time-varying flow domain $\Omega_\mathrm{F}(t)$,

$$\rho\left(\frac{\partial \mathbf{v}}{\partial t} + \mathbf{v}\cdot\boldsymbol{\nabla}\mathbf{v}\right) - \mu\boldsymbol{\nabla}^2\mathbf{v} + \boldsymbol{\nabla}p = 0, \qquad \boldsymbol{\nabla}\cdot\mathbf{v} = 0. \tag{1}$$

The density $\rho$ and dynamic viscosity $\mu$ of blood are considered as constants known from literature; gravity has been neglected. This so-called partial differential equation (pde) constrained optimization problem can be tackled using state-of the art optimization methods. However, this approach would have two important shortcomings:

– The precise location of the pulsating vessel boundaries is not known a-priori. Typically, only a time-averaged segmentation of the vessel lumen is available for post-processing of 4D PC-MRI data (so-called phase-contrast angiography, PC-MRA).

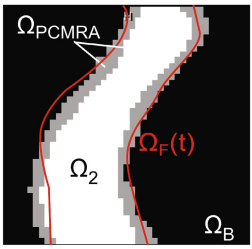


**Fig. 1.** Illustration of original lumen $\Omega_{\mathrm{F}}(t)$, time-averaged PCMRA segmentation $\Omega_{\mathrm{PCMRA}}$ (white+grey) and the reduced computational domain $\Omega_2$ (white)

– The computational complexity of a four-dimensional optimization problem constrained by the Navier-Stokes equations is even on parallel computer architectures prohibitively large to be applied for a single image analysis.

### 2.2 Two-Step Algorithm

In this work, we suggest a more efficient two-step procedure to approximately solve the above optimization problem. In a first step, we eliminate the divergent part of $\mathbf{v}_\varepsilon$. This step is expected to significantly enhance the measurements, since the true velocity field must be divergence-free and hence, its divergent part can be completely attributed to noise and artifacts [10]. In a second step, the divergence-free velocity field $\mathbf{v}$ is used to solve for the PPE for the unknown pressure field $p$. It turns out that both problems have very similar structure and can be efficiently solved using the same algorithm with minor modifications. For both steps, the precise time-resolved definition of the flow domain is not necessary, and is replaced by fixed domains $\Omega_2 \subset \Omega_1 \subset \Omega_{\mathrm{B}}$. Note that this does *not* imply a rigid-wall assumption for the vessel wall, since the pressure computation including the evaluation of all boundary conditions is performed fully inside the lumen.

*Step 1: Divergence-Filter.* For a fixed time point $t$ in the cardiac cycle, find a vector field $\mathbf{v}(\mathbf{x}, t)$ minimizing the functional

$$J_1(\mathbf{v}) = \frac{1}{2} \int_{\Omega_1} |\mathbf{v} - \mathbf{v}_\varepsilon|^2 \, \mathrm{d}\mathbf{x} \longrightarrow \min!$$

subject only to the constraint $\boldsymbol{\nabla} \cdot \mathbf{v} = 0$ inside a fixed domain $\Omega_1 \subset \Omega_{\mathrm{B}}$. If no boundary conditions are specified, the corresponding Euler-Lagrange system is a Poisson equation with homogeneous Dirichlet conditions [10], which is to be solved for each time sample $t$:

$$\boldsymbol{\nabla}^2 \lambda = \boldsymbol{\nabla} \cdot \mathbf{v}_\varepsilon \quad \text{in } \Omega_1, \qquad \lambda|_{\partial\Omega_1} = 0, \tag{2}$$

$$\mathbf{v}(\mathbf{x}, t) = \mathbf{v}_\varepsilon - \boldsymbol{\nabla}\lambda \tag{3}$$

*Step 2: Pressure-Poisson Equation.* For each time point $t$ at which the velocity field $\mathbf{v}(\mathbf{x}, t)$ was computed, find a pressure field $p(\mathbf{x}, t)$ minimizing the functional

$$\mathbf{r}(\mathbf{x}, t) := -\rho \left( \frac{\partial \mathbf{v}}{\partial t} + \mathbf{v} \cdot \boldsymbol{\nabla} \mathbf{v} \right) + \mu \boldsymbol{\nabla}^2 \mathbf{v}, \tag{4}$$

$$J_2(p) = \frac{1}{2} \int_{\Omega_2} \left| \boldsymbol{\nabla} p - \mathbf{r} \right|^2 \mathrm{d}\mathbf{x} \longrightarrow \min! \tag{5}$$

In general, a given vector field does not possess a potential field, hence problem (5) is truly an (unconstrained) minimization problem. Its unique solution (up to an additive constant) is obtained by solving a Poisson problem with Neumann boundary condition [8]:

$$\boldsymbol{\nabla}^2 p = \boldsymbol{\nabla} \cdot \mathbf{r} \quad \text{in } \Omega_2, \qquad \frac{\partial p}{\partial \mathbf{n}} = \mathbf{r} \cdot \mathbf{n} \quad \text{at } \partial\Omega_2 \tag{6}$$

*Choice of domains $\Omega_1$ and $\Omega_2$.* For simplicity and in order to avoid interpolation errors, all computations are performed directly on the voxel grid. All domains can therefore by defined and processed as image masks.

The filter formulated in step 1 eliminates the divergence of the velocity field only in the *interior* of the domain $\Omega_1$ and not on $\partial\Omega_1$. To avoid artifacts, $\Omega_1$ must therefore be larger than $\Omega_2$. Candidates for $\Omega_1$ are either the PC-MRA segmentation $\Omega_{\mathrm{PCMRA}}$ or the image bounding box $\Omega_{\mathrm{B}}$; in this work we use $\Omega_1 = \Omega_{\mathrm{B}}$.

The PPE computation is sensitive with respect to numerical errors from inaccurate first and second-order gradients close to the vessel boundaries. Therefore, these voxels should be excluded from the computation. In this work, the $\Omega_2$ is therefore created from the segmentation $\Omega_{\mathrm{PCMRA}}$ by morphological erosion of 1-2 voxels.

*Implementation.* The scalar quantities $v_{\varepsilon,i}$, $v_i$ $(i = x, y, z)$ and $\lambda$, $r$, $p$ are expanded into FE shape functions. The FE mesh coincides with the voxel grid by choosing trilinear eight-node hexahedral element functions.

The implementation of problem (2) for $\lambda(\mathbf{x}, t)$ is straight-forward and leads to a linear equation system with symmetric positive definite system matrix, which is solved efficiently by the preconditioned conjugate gradient method. Then $\mathbf{v}(\mathbf{x}, t)$ and $\mathbf{r}(\mathbf{x}, t)$ are computed using central difference quotients for the time derivatives and FE matrices of the form $\mathbf{L}_{i,j}^{(l)} := \int_{\Omega_1} \varphi_i \partial_{x_l} \varphi_j \, \mathrm{d}\mathbf{x}$ for the spatial derivatives within the flow domain. Finally, problem (6) is solved using an analogous solver as for problem (2). Typical computation times for in-vivo image data is about 5-10 seconds per time sample on a standard desktop computer. For a typical time resolution of 20 points, this amounts to a total computation time of 2-3 minutes for the whole cardiac cycle.

## 3 Software Flow Phantoms

The computed pressure field is effected by three different contributions from the Navier-Stokes equations: acceleration, convection, and viscous terms. For pulsatile

flow in the aorta, the acceleration and convection terms are dominant, while flow in straight narrow vessels is dominated by the viscous terms. In the creation of meaningful test data sets, it is therefore important to account for all three terms. For this study, we suggest two different flow scenarios: (1) steady flow in a straight stenosed vessel, and (2) steady and pulsatile flow in a pipe bend. Both models were simulated using the commercial software package COMSOL Multiphysics. The solutions were extracted at a realistic temporal resolution of 0.05 s and were linearly interpolated to an isotropic voxel grid of size 1 mm. Gaussian white noise with realistic signal-to-noise ratio (SNR) values of 3-20 was added to the data in order to test the robustness of the suggested algorithms. In the results presented in this work, SNR was equal to 3.

*1) Steady Flow in a Stenosis.* A stenotic vessel software phantom was created (Fig. 2). The vessel length was 750 mm and the minimal and maximal diameter was 10.3 and 33.5mm, respectively, which results in a stenosis degree of 90%. The dynamic blood viscosity was estimated as 0.00424 Pa s, and the density by $1060\,\mathrm{kg/m^3}$. The mean flow velocity at the inlet was 3.89 cm/s, which gives a moderate inlet Reynolds number of 163. Inside the stenosis, a velocity of 25 cm/s was achieved, which corresponds to a Reynolds number of 625. At the outlet, zero reference pressure was adopted.

*2) Steady and Pulsatile Flow in a Pipe Bend.* As a non-axisymmetric test data set, a 180° pipe bend model is chosen (Fig. 2), which has fluid mechanical properties comparable to the human aorta [11]. The geometry is designed for experiments with water, so the simulations are done with fluid properties of water ($\rho = 1000\,\mathrm{kg/m^3}$ and $\mu = 0.001\,\mathrm{Pa\,s}$). The lumen diameter was 8 mm and the bend radius was 72 mm. In the inlet, a fully developed laminar velocity profile was specified. For the steady simulation, mean velocity was 20 cm/s and Reynolds number was 1600. For the non-steady, pulsatile simulation, the mean velocity was periodically varying in time with time mean 21.5 cm/s, time peak 30.6 cm/s and frequency 1.79 1/s [11]. At the outlet, zero reference pressure was assumed, which results in an inlet pressure oscillating with the same frequency. The corresponding time-mean Reynolds number was 1713 and the Womersley number was 13.4. Both values are comparable to blood flow in a normal human aorta.

## 4 PC-MRI Image Data

The described algorithm was tested on PC-MRI measurements from six patients after aortic coarctation repair [5]. Flow sensitive 4D PC-MRI measurements covering the entire thoracic aorta were acquired on a 3T system (Magnetom Trio, Siemens AG) using a navigator respiration controlled and ECG-gated rf-spoiled gradient echo sequence [1]. Spatial resolution was $1.9-2.4 \times 1.7-1.8 \times 2.0-2.5\,\mathrm{mm^3}$, temporal resolution was $39.2-40.8$ ms, velocity encoding was $150-230$ cm/s. No contrast agent was used for this MRI sequence.

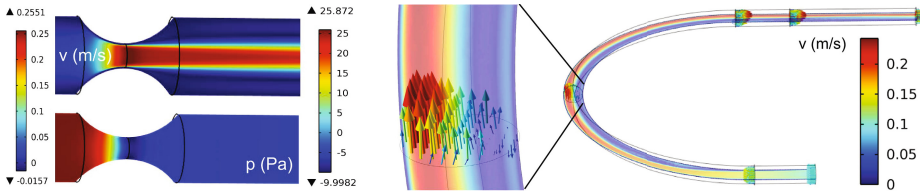


**Fig. 2.** CFD solutions of the two software phantoms. Left:; velocity magnitude and pressure fields for the stenosis flow model. Right: Velocity magnitude for the pulsatile pipe bend flow model.

Data processing was done using research software for analysis of 4D PC-MRI image data [12]. After correction for eddy-currents and phase-wraps, time-averaged segmentation of the aorta was done on the PC-MRA image using an interactive watershed algorithm. After application of the described finite-element solvers, the resulting pressure field was smoothed and calibrated to zero for all time steps at a reference point chosen in the abdominal aorta.

## 5 Results

### 5.1 Software Flow Phantoms

In order to quantify the accuracy and robustness of the method, computed and CFD phantom pressure maps were extracted on the vessel centerline and at single locations inside the vessel. In addition, the time averaged relative RMS errors over the whole (reduced) vessel mask were evaluated.

For the steady flow stenosis phantoms, the pressure field on the centerline coincides very well with the CFD solution (Fig. 3), with a relative RMS error

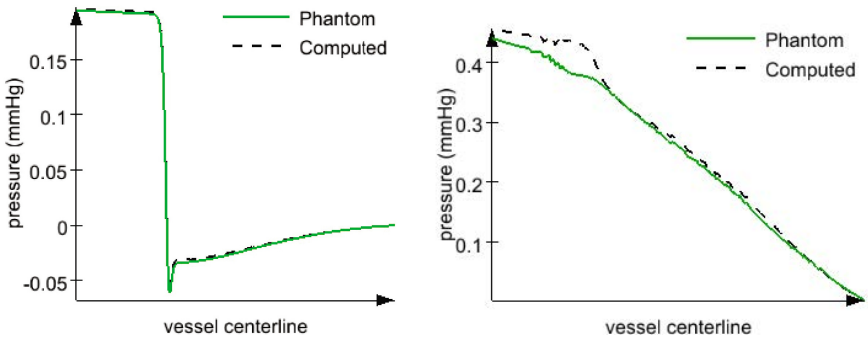


**Fig. 3.** Computed pressure curves for the steady phantoms. Left: Pressure profile along the vessel centerline for the straight stenosis model. Right: Pressure profiles along the centerline for the steady pipe bend model.

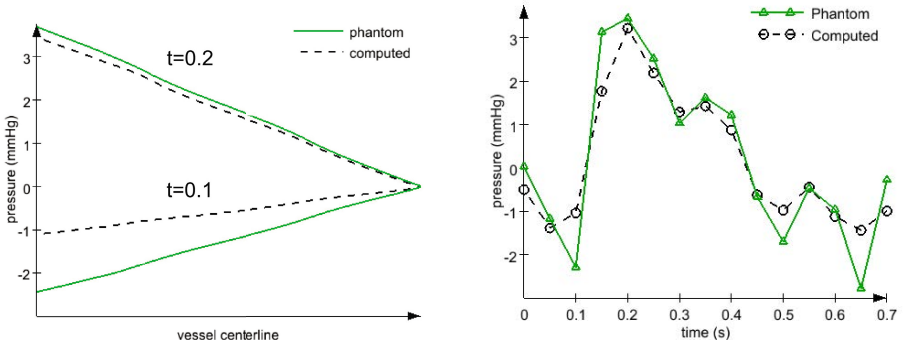


**Fig. 4.** Computed pressure curves for the pulsatile pipe bend phantom. Left: Pressure profiles along the centerline at time points $t = 0.1$ and $t = 0.2$. Right: Temporal evolution of the inlet pressure.

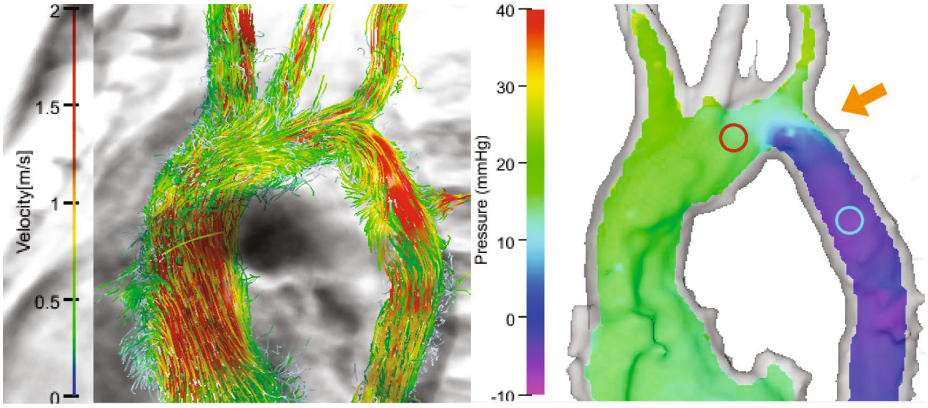


**Fig. 5.** Flow pathlines and pressure difference in a patient with aortic coarctation. The arrow indicates the location of the stenosis; the colored markers specify the two positions where the pressure time curves were extracted (Fig. 6).

of 12% for the stenosis case and 7% for the pipe bend. For the pulsatile pipe bend flow phantom, the error in the centerline pressure varies strongly with the temporal position within the periodic cycle (Fig. 4, left). This phenomenon is also seen in the evaluation of the inlet pressure (Fig. 4, right) and results in a time-averaged relative RMS error of 38%.

### 5.2 Patient Image Data

For the patient data sets, relative pressure maps were computed with and without divergence filter as the first step in the algorithm. The filter caused a correction of the velocity field by $11.4\% \pm 2.7\%$, as measured by the RMS difference

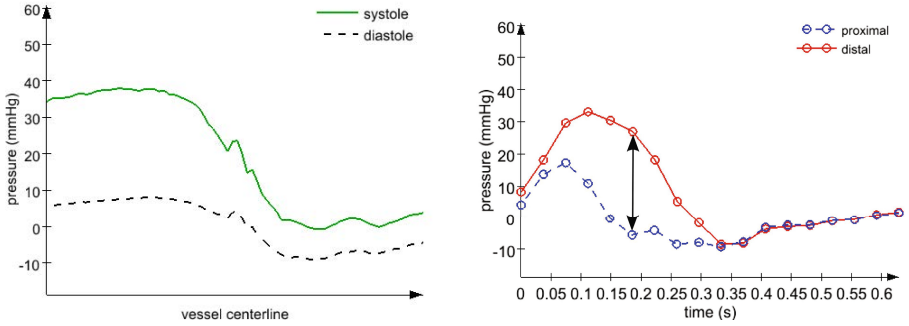


**Fig. 6.** Pressure differences along the centerline of the aortic arch (left image) and pressure over cardiac cycle at two positions distal and proximal to the stenosis. The black arrow visualizes the pressure drop evaluation.

**Table 1.** Pressure drop (in mmHg) across the stenosis in six patient data sets compared to previously published data

| method | Pat. 1 | Pat. 2 | Pat. 3 | Pat. 4 | Pat. 5 | Pat. 6 |
|---|---|---|---|---|---|---|
| our method | 36 | 19 | 3 | 16 | 6 | 8 |
| our method, no divergence filter | 33 | 20 | 3 | 20 | 8 | 8 |
| iterative PPE solver [5] | 34 | 16 | 12 | 28 | 11 | 18 |
| Doppler US (simplif. Bernoulli) | 37 | 19 | 16 | 29 | 8 | 17 |

between the original and the filtered velocity field. The pressure drop over the stenosis was quantified in a similar fashion as done in [5]. In Fig. 5, velocity pathlines and pressure maps during systole are shown for a single patient. Two points inside the aorta proximal and distal to the coarctation were chosen and the time-resolved pressure relative to the reference point was extracted (Fig. 6, right). The peak mean pressure gradient across the coarctation as described in [5] was determined as the maximum of the difference of the two curves. The spatially resolved pressure behavior is shown in the centerline pressure curves (Fig. 6, left).

The pressure drop values for all six patients are summarized in Table 1 and compared to previously published values computed from the same data by an iterative PPE solver, and from echocardiography using the simplified Bernoulli formula.

## 6 Discussion

We presented a new method for fast computation of pressure difference maps from 4D PC-MRI data. The key new aspect is the enhancement of the velocity field by elimination of the divergent part and the use of the finite-element method for accurate and fast solution of the differential equations. The tests on complex

CFD-based software phantoms suggest that the method is highly accurate for steady data sets. The results are robust against noise of realistic SNR. The main source of inaccuracy is the typically coarse time resolution of PC-MRI data sets.

The application for the patient data sets was feasible in all cases and gives consistent results in very short computation times with only minimal user interaction. The comparison with previously reported values obtained with a different PPE solver shows good correlation, but also significant varying results for single patients. Since no ground truth is available, the accuracy of the pressure drop estimation cannot be assessed on the basis of this data. The employment of the divergence filter slightly influences the resulting pressure drops across the coarctation region. One source of the difference may be the different locations inside the vessel, where the pressure values are evaluated. Since the pressure drop is highly sensitive to these positions, we suggest to employ an analysis of the centerline pressure curves extracted from the 3D pressure map instead, for a more robust estimation of the pressure drop. A systematic comparison of solvers and evaluation methods on a larger patient group remains for future research.

## References

1. Markl, M., Harloff, A., Bley, T.A., Zaitsev, M., Jung, B., et al.: Time-resolved 3D MR velocity mapping at 3T: Improved navigator-gated assessment of vascular anatomy and blood flow. J. Magn. Reson. Imaging 25(4), 824–831 (2007)
2. Markl, M., Kilner, P.J., Ebbers, T.: Comprehensive 4D velocity mapping of the heart and great vessels by cardiovascular magnetic resonance. J. Cardiov. Magn. Reson. 13 (2011)
3. Tyszka, J., Laidlaw, D., Asa, J., Silverman, J.: Three-dimensional, time-resolved (4D) relative pressure mapping using magnetic resonance imaging. J. Magn. Reson. Imaging 12(2), 321–329 (2000)
4. Lum, D., Johnson, K., Paul, R., Turk, A., Consigny, D., Grinde, J., Mistretta, C., Grist, T.: Transstenotic pressure gradients: measurement in swine–retrospectively ECG-gated 3D phase-contrast MR angiography versus endovascular pressure-sensing guidewires. Radiology 245(3), 751–760 (2007)
5. Bock, J., Frydrychowicz, A., Lorenz, R., Hirtler, D., Barker, A.J., Johnson, K., Arnold, R., Burkhardt, H., Hennig, J., Markl, M.: In Vivo Noninvasive 4D Pressure Difference Mapping in the Human Aorta: Phantom Comparison and Application in Healthy Volunteers and Patients. Magn. Reson. Med. 66(4), 1079–1088 (2011)
6. Meier, S., Hennemuth, A., Friman, O., Markl, M., Preusser, T.: Noninvasive 4D Blood Flow and Pressure Quantification in Central Blood Vessels via PCMRI. Online Archives of Computing in Cardiology 37, 903–906 (2010)
7. Ebbers, T., Farneback, G.: Improving computation of cardiovascular relative pressure fields from velocity MRI. J. Magn. Reson. Imaging 30(1), 54–61 (2009)
8. Gresho, P.M., Sani, R.L.: Incompressible Flow and the Finite Element Method. Isothermal Laminar Flow, vol. 2. John Wiley & Sons (2000)
9. Bolin, C., Raguin, L.: Methodology to estimate the relative pressure field from noisy experimental velocity data. J. Phys.: Conf. Series 135, 012020 (2008)

10. Song, S., Napel, S., Glover, G., Pelc, N.: Noise reduction in Three-dimensional Phase-Contrast MR Velocity Measurements. J. Magn. Reson. Imaging 3, 587–596 (1993)
11. Weston, S., Wood, N., Tabor, G., Gosman, A., Firmin, D.: Combined MRI and CFD Analysis of Fully Developed Steady and Pulsatile Laminar Flow through a Bend. J. Magn. Reson. Imaging 8, 1158–1171 (1998)
12. Hennemuth, A., Friman, O., Schumann, C., Bock, J., Drexl, J., et al.: Fast interactive exploration of 4D MRI flow data. In: Wong, K.H., Holmes, D.R. (eds.) Medical Imaging 2011: Visualization, Image-Guided Procedures and Modeling, vol. 7964, p. 79640E. SPIE (2011)

# Robust and Accurate Diaphragm Border Detection in Cardiac X-Ray Angiographies

Simeon Petkov[1], Adriana Romero[2], Xavier Carrillo Suarez[3], Petia Radeva[2], and Carlo Gatta[1]

[1] Centre de Visió per Computador, Bellaterra, Spain
[2] Universitat de Barcelona, Barcelona, Spain
[3] University Hospital "Germans Trias i Pujol", Badalona, Spain

**Abstract.** X-ray angiography is the most common imaging modality employed in the diagnosis of coronary diseases prior to or during a catheter-based intervention. The analysis of the patient X-Ray sequence can provide useful information about the degree of arterial stenosis, the myocardial perfusion and other clinical parameters. If the sequence has been acquired to evaluate the perfusion grade, the opacity due to the diaphragm could potentially hinder any kind of visual inspection and make more difficult a computer aided measurements. In this paper we propose an accurate and robust method to automatically identify the diaphragm border in each frame. Quantitative evaluation on a set of 11 sequences shows that the proposed algorithm outperforms previous methods.

**Keywords:** X-Ray angiography, diaphragm.

## 1 Introduction and Related Works

Cardiac X-Ray angiography is an imaging modality widely used in the analysis of cardiac diseases prior or during catheterization interventions. Besides the estimation of stenosis degree, other qualitative and quantitative analysis can be performed: in the last five years, some semi-automatic tools for the quantitative computer assisted measurement of the myocardial perfusion level (known as MBG or TIMI-MPG) have been proposed [3,6,8,5]. All of these methods are negatively affected by the diaphragm motion. In [3], authors make explicit use of a method for diaphragm border detection [2] to improve the quality of the region-of-interest tracking that is used to measure the myocardial perfusion. In [6], authors claim that the breathing movements can hide staining patterns, showing that the diaphragm movement, and the consequent gray-level variation in an area, can reduce the method ability to measure the myocardial staining. In [8], authors impose the angiography sequence acquisition to be done while the patient holds breath and show that the diaphragm movement introduces artifacts in the resulting analysis. It has to be noted that not all the patients can hold breath for the time required to a complete myocardial perfusion analysis sequence. In the preliminary work in [5], authors claim that one limitation of their method is that the manually delineated perfusion area must be isolated from the diaphragm, so that the method applicability is reduced for certain angiographies projections. All these methods can benefit of a pre-processing step able to accurately detect and digitally remove the diaphragm border. Moreover,

O. Camara et al. (Eds.): STACOM 2012, LNCS 7746, pp. 225–234, 2013.

in the future, the digital removal of the diaphragm can be used as a tool to enhance visualization during catheter-based interventions.

To the best of our knowledge, only one method for automatic detection of the diaphragm border has been proposed so far [2]. Authors model the diaphragm border as an arc of a circle. Their method is based on the following pipeline: (1) pre-processing the frame with a morphological closing operator to remove arteries; (2) apply the Canny edge detector; (3) use the Hough transform to detect the circle that best fits with the highlighted edges; (4) apply an active contour model (snake) to refine the result.

Up to now several methods are proposed for delineating the lungs in X-Ray images [11,1]. However, they are not applicable to the projections used for heart angiographies, because the lungs boundaries are not visible there.

The main contributions of our paper are: (1) a method which outperforms the state of the art, exploiting the diaphragm appearance, motion and morphological properties in a better way and (2) the proposal of a public validation dataset together with a protocol for a quantitative performance evaluation.[1]

## 2 Method

The proposed method has been developed exploiting the characteristics of the diaphragm in both spatial and temporal dimensions. We define a set of assumptions that will be used to obtain a robust and accurate diaphragm detection: (1) the diaphragm border appears as a vertical transition (edge) from brighter (above) to darker (below) gray-scale levels; (2) the diaphragm movement is continuous; (3) the diaphragm has a moving pattern which differs from the cardiac motion pattern and that pattern could significantly change from patient to patient; (4) the diaphragm border is a continuous smooth curve in the image domain. These assumptions have been exploited in an algorithm whose steps can be summarized as follows: (1) Roughly remove the arteries by means of a morphological closing operator; (2) Compute an *Edgeness* measure based on vertical multi-scale gradients; (3) Extract a set of paths traversing high (and at the same time similar) *Edgeness* values through the temporal axis; (4) Perform an unsupervised clustering to determine the set of paths that composes the diaphragm; (5) For each frame, interpolate the optimal diaphragm shape while removing outlier paths.

### 2.1 Artery Removal

As claimed in [2], the arterial staining can disturb the identification of the diaphragm border leading to vertical edges that locally resemble the diaphragm border appearance. Moreover, edges caused by arteries are normally stronger than the ones due to the diaphragm border. To deal with this problem, we apply a morphological closing operator as in [2], using as structuring element a disk of radius $R$ pixels on each sequence frame separately. Having an average resolution of 0.34 mm/pixel, to roughly remove arteries up to a diameter of 6 mm, the optimal radius is $R = 6\,[mm]/0.34\,[mm/pixel] = 20[pixel]$; this is sufficient to remove even thick left main arteries [4]. Fig. 1 (b) shows

[1] The validation dataset is available here: `https://sites.google.com/site/diaphragmdetection/engineering-docs`

an example of the closing filtering. It can be noticed that the removal is not very accurate; however this is not critical since the diaphragm border is maintained and successive steps of our algorithm allow to delineate it robustly.

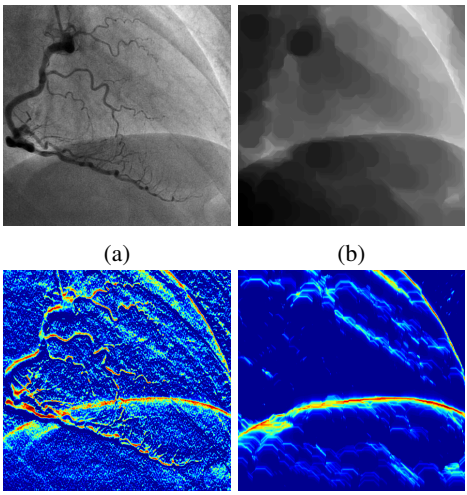


**Fig. 1.** Effect of closing operator on the *Edgeness* result: (a) input frame; (b) after applying the morphological closing; (c) the *Edgeness* measure applied on frame in (a); (d) the *Edgeness* measure applied on filtered frame in (b)

### 2.2 Edgeness

Let us define a gray-level sequence as a volume where two coordinates correspond to the image plane and the third coordinate is time, so that we can write it as a function $I(x, y, t) \in \mathbb{R}$. With the aim of exploiting the first assumption, we compute the normalized vertical derivative of all sequence frames at different scales as follows: $V_\sigma(x, y, t) = \sigma I(x, y, t) * \frac{\partial G(0;\sigma)}{\partial y}$, where the symbol $*$ denotes the convolution operator and $G$ is a Gaussian kernel with zero mean and standard deviation $\sigma$. We use the Lindeberg normalization [9] so that derivatives at different scales are comparable. Since we are searching for edges where the upper part is brighter than the lower part, we can modify $V_\sigma(x, y, t)$ to cancel its values for edges with the opposite pattern as follows:

$$\tilde{V}_\sigma(x, y, t) = \begin{cases} V_\sigma(x, y, t) & \text{if } V_\sigma(x, y, t) > 0 \\ 0 & \text{if } V_\sigma(x, y, t) \leq 0. \end{cases}$$

To discriminate between noisy edges and consistent edges over scales, we compute the average vertical modified *Edgeness* as follows:

$$\tilde{E}(x, y, t) = \frac{1}{|\Phi|} \sum_{\sigma \in \Phi} \tilde{V}_\sigma(x, y, t)$$

where the set of scales is $\Phi = \{1, 2, 4, 8, 16\}$ pixels. The scales have been defined in octaves to cover all possible sizes of edges caused by the diaphragm border; values larger than 16 do not provide relevant information and would merely increase the computational cost of the algorithm. Moreover, thanks to the averaging process, only clear edges will have large positive values of $E$. We apply the non-linear transformation to the *Edgeness* map $E(x, y, t) = 1 - \exp(-\tilde{E}(x, y, t))$. $E(x, y, t) \in [0\,1]$ has higher values at edges resembling a diaphragm border. Fig. 1(c-d) shows two examples of *Edgeness* map respectively for the frames (a-b) - it can be seen that the closing operator performs a sufficient artery removal.

### 2.3 From *Edgeness* to Paths

Let us denote a path $p$ as a curve with a fixed $x$ coordinate and a $y$ coordinate varying as a function of time: $p = \{x_p, y_p(t)\}$. From the first frame, we select all pixels having a value $E(x, y, 1) > \mu(E)$, i.e. above the average *Edgeness* for the sequence and use them as starting points. For each starting point from the first frame ($t = 1$), we draw a path by vertically tracking that point from frame to frame (sequentially from $t = 2$ to the end of the sequence $t = T$). The tracking maximizes the path quality defined with the following formula:

$$Q_{\text{path}}(p) = \frac{1}{T} \sum_{t=1}^{T} E(x_p, y_p(t), t) \cdot S(y_p(t), y_p(t-1)) \cdot M(y_p(t), \tilde{y}_p(t-1)) \quad (1)$$

This formula can be split in three parts, which account for different aspects. The rational behind the first term $E(\cdot, \cdot, \cdot)$ is to encourage the path to transverse points with high *Edgeness* values. However, this alone can lead to scattered paths jumping from one maxima to another in the next frame. The second (similarity) term $S(y_p(t), y_p(t-1)) = 1 - |E(x_p, y_p(t), t) - E(x_p, y_p(t-1), t-1)| \in [0\,1]$, imposes minimal *Edgeness* value variation between consecutive path points. The third term $M(y_p(t), \tilde{y}_p(t)) = e^{-\frac{(\tilde{y}_p(t) - y_p(t))^2}{2\sigma_M^2}}$ has been designed to add a smoothness criterion to the path construction. Here $\tilde{y}_p(t)$ is the expected value for the time location $t$, based on the linear approximation of previous values as Basically, the use of a Gaussian (with its $\sigma_M$ parameter) centered around the expected location $\tilde{y}_p(t)$ adds a constraint, so that paths are restricted from changing their trajectories in a way that does not resemble a continuous movement. All of the three terms are bounded in $[0\,1]$, so that their product ensures that only points fulfilling the three criteria at once are selected. The smoothness parameter $\sigma_M$ has been defined by cross-validation. Fig. 2 shows the plotted error for different $\sigma_M$ values using a training set of 9 images. As it can be seen $\sigma_M = 5$ [pixels] is the optimal choice. Changing the linear model for predicting $\tilde{y}_p(t)$ with a second order degree polynomial resulted in lower performance. Since the proposed path building is based on local decisions maximizing equation (1), we allow the construction of multiple paths given an $x$. However, to avoid path proliferation, if two paths collide, only the one with higher path quality is retained, so that at the end of the process we have a set of non-intersecting continuous paths $\mathcal{P}$. Fig. 3(c) depicts an example of resulting paths. Fig. 3(a) shows an example of paths construction over-imposed on the values of $E(x, y, t)$

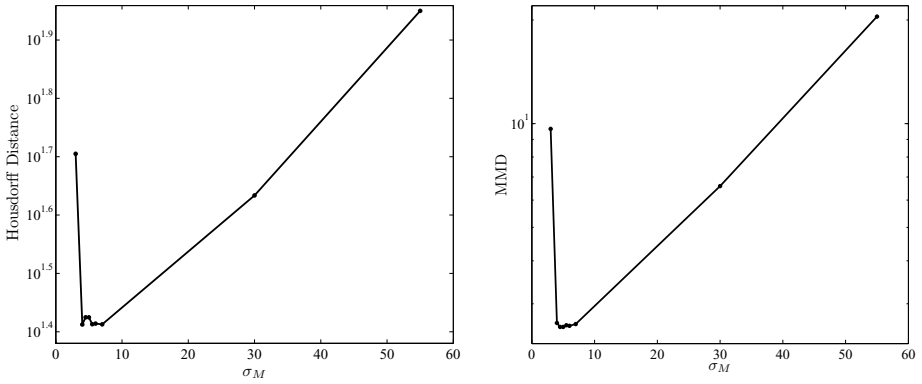


Hausdorff distance MMD

**Fig. 2.** Average distances over the training set when varying $\sigma_M$

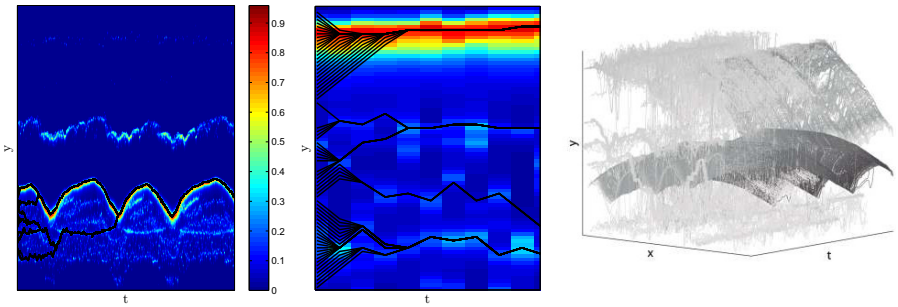


(a) (b) (c)

**Fig. 3.** Paths construction: (a) an example of paths construction for a given $x$; (b) Detail of the bottom left plot in (a); (c) A 3D plot of all the paths, where darker paths correspond to higher quality paths

for a specific $x$. As it can be noticed, the paths are smooth while accurately following the local shape of $E(x, y, t)$; moreover, the paths quickly collapse to a limited number of paths (see Fig. 3(b)).

### 2.4 Diaphragm Border Surface as a Collection of Paths

The previous step generates a set of paths $\mathcal{P}$. Each path $p$ has its own trajectory $y_p(t)$ and a quality measure $Q_{\text{path}}(p)$. We want to select a subset $\mathcal{D} \subseteq \mathcal{P}$ which contains paths that move in a similar way, so that we make use of the assumption that the diaphragm has a specific motion pattern. Moreover, we want to retain high quality paths and discard low quality paths, which normally correspond to false positive detections. To accomplish these two steps in a unified way, we perform an unsupervised clustering of both

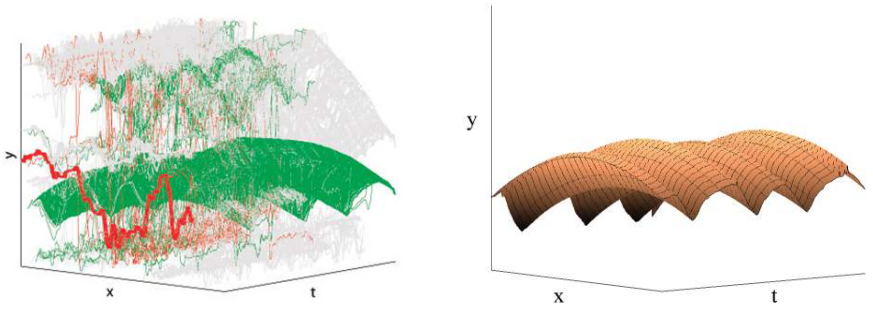


(a) (b)

**Fig. 4.** (a) The paths of Fig. 3(c) colored in accordance to their clusters; the green cluster is the selected one. (b) The resulting surface after fitting the polynomial function to all the sequence frames.

motion characteristics and quality measure: (1) Each path is modified so that we remove its bias, $\hat{y}_p(t) = y_p(t) - \mu(y_p(t))$, where $\mu$ is the mean operator. This step removes the average vertical position of the paths so that the clustering will not be influenced by (vertical) proximity of paths. (2) A feature vector $\boldsymbol{v}_p = [\hat{y}_p(1) \ldots \hat{y}_p(T)\, Q_{\text{path}}(p)]$ made of $T + 1$ elements is built. This vector contains information on path motion (first $T$ elements) and information on the path quality (last element). (3) We build a matrix $\boldsymbol{V}$ where each row contains a feature vector $\boldsymbol{v}_p$ for each path in $\mathcal{P}$. Since vertical positions and quality measure are incommensurable we need to normalize $\boldsymbol{V}$ such that every column has zero mean and unitary standard deviation. (4) We apply an unsupervised k-means[2] clustering; the cluster with the highest mean quality is the one which most probably defines the diaphragm border as a collection of paths. The use of unsupervised clustering is the most suited way to group paths into a consistent result since the actual diaphragm motion is unpredictable: a sequence can be acquired while the patient is holding the breath, or the patient can have irregular breathing pattern. On the other way, k-means requires the definition of the number of clusters, which we set to three. The rational behind this setting is to allow the clustering to find one cluster for the diaphragm, one cluster for noisy low quality paths and a third cluster which has a motion pattern that is a mixture of the diaphragm and cardiac patterns. This latter case has been considered since the morphological operator is not able to eliminate non-tubular structures that move according to the cardiac cycle. Fig. 4(a) shows the result of clustering for the case in Fig. 3(c); different clusters are depicted in different colors.

### 2.5 Imposing Diaphragm Border Smoothness on Image Plane

The previous step defines the diaphragm border evolving curve as a surface composed by a collection of paths having similar motion and high quality. Nonetheless, the

[2] Since the k-means is based on random centroids initialization, and it is not computational costly, we perform 100 trials keeping the solution with the lowest objective function.

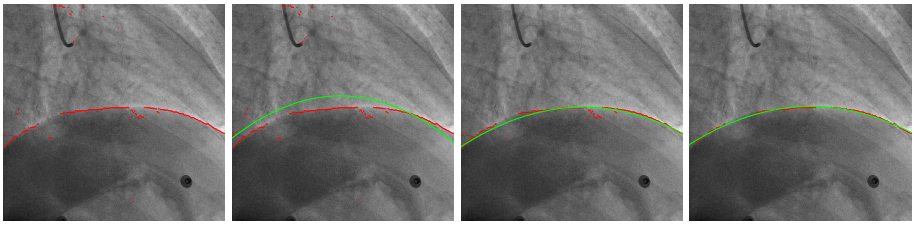

Initial points $1^{th}$ iteration $50^{th}$ iteration $155^{th}$ iteration (last)

**Fig. 5.** An example of iterative fitting of a polynomial function to the clustered points

clustering could be suboptimal and paths actually not belonging to the diaphragm border can fall into the set $\mathcal{D}$. Moreover, up to this point, no smoothness in the image plane has been imposed. The algorithm's last step is devoted to these two goals: imposing smoothness in the image plane while removing outlier paths. The diaphragm border is modelled as a polynomial function $f(x) = ax^2 + bx + c$. To estimate the optimal triplet $\{\hat{a}, \hat{b}, \hat{c}\}$ for a given frame at time $t$, we employ the following iterative algorithm. We define a set of points $\mathcal{C} \triangleq \{(x_i, y_i)\}$ taken from the paths of the diaphragm cluster at time $t$. At each iteration the optimal parameters are estimated minimizing the fitting squared error $E = \sum_{(x_i,y_i)\in\mathcal{C}}(f(x_i) - y_i)^2$; If the Thompson Tau outliers detector [10] on the signed error distribution finds at least one outlier, the point $(x_j, y_j) = \arg\max_i |f(x_i) - y_i|$ is removed from the set $\mathcal{C}$ and the iterative algorithm continues. If no outliers are found, the algorithm stops. Fig. 5 shows an example of this algorithm while Fig. 4(b) shows the final surface result.

## 3 Validation

### 3.1 Material

We defined a validation set of 16 frames taken from 11 sequences (11 patients, from which only one is completely holding breath throughout the whole video). The diaphragm border in each frame has been marked blindly by two experts. All sequences have been acquired using a Philips Allura Xper FD20, at 12.5 fps and with an image resolution of 0.34×0.34 mm. The C-arm position varies from -41° to 97° for the primary angle and from -17° to 33° for the secondary angle.

### 3.2 Methods

We compare our proposed method with the diaphragm detection algorithm described in [2]. We also compute the inter-observer variability between the two ground truth annotations. Moreover, we also provide intermediate evaluations of algorithms.

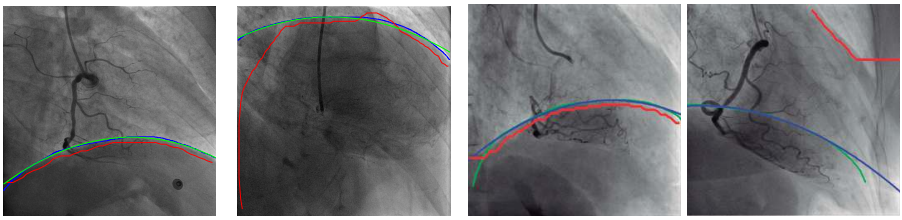

(a) (b) (c) (d)

**Fig. 6.** Four visual results. Blue is the ground truth, red is the method in [2] with snakes and green is our final detection.

### 3.3 Validation Protocol

Let $GT$ be the set of points forming the ground truth curve and $P$ be the set of points predicted by a given method. Considering all the points from each set we use two different measures to validate the prediction against the ground truth:

(1) The Hausdorff distance [7] is the distance between the two most faraway points from the two sets of points. This measure is very sensitive to predicted points laying far from the ground truth points but gives little information about the overall precision of the prediction, thus making it useful in measuring robustness.

(2) The Mean Minimal Distance:

$$MMD(P, GT) = \frac{1}{|P|} \sum_{i \in P} \min_{j \in GT} ||(x_i^P, y_i^P) - (x_j^{GT}, y_j^{GT})||$$

on the other hand, provides information about the overall precision of the predicted result. It has to be noted that the $MMD$ is not symmetric.

### 3.4 Results

Table 1 shows the error results using the Hausdorff and the MMD distances for the following cases (one for each row): inter-observer variability; the method in [2] before and after the application of the snake; our method prior to the clustering (Our-PC), prior to the curve fitting (Our-PF) and the final result (Our). For each distance, tables report its mean, standard deviation, minimum and maximum values. An interesting fact is that the use of snakes, as expected, can help the method in [2] to improve the results but in a very limited extent. Regarding our method, it can be noticed that each step improves the results. Once the paths are built, before the clustering, the method is limited in the fact that the sequence is analyzed mainly in its temporal dimension, so that a large number of incorrect paths can be generated. The clustering step selects a set of paths that potentially represent the diaphragm border; this decreases consistently the MMD error (three times), but is not able to reduce the Hausdorff distance since few erroneous paths far from the solution could be maintained. The polynomial fitting ensures a consistent solution imposing smoothness in the image domain and, at the same time, rejects erroneous paths thanks to the outlier detection; this results in a huge improvement in both

**Table 1.** Quantitative results. All measures are in pixels.

| | Hausdorff distance | | | MMD | | |
|---|---|---|---|---|---|---|
| | Avg±Std | min | max | Avg±Std | min | max |
| *O1 vs O2* | 25.82±22.75 | 4 | 86.33 | 2.03±2.07 | 0.78 | 7.84 |
| *O2 vs O1* | 25.82±22.75 | 4 | 86.33 | 1.41±0.66 | 0.75 | 3.35 |
| [2] (no snakes) | 83.36±124.37 | 22.14 | 429.17 | 32.09±50.65 | 14.24 | 233.49 |
| [2] | 84.71±120.73 | 17.03 | 407.12 | 28.04±54.42 | 10.71 | 234.17 |
| Our-PC | 364±48.5 | 287 | 440 | 132±19.7 | 108 | 185 |
| Our-PF | 302±58.1 | 188 | 385 | 43.7±25.5 | 16.7 | 85.0 |
| Our | **29.1±23.5** | **5.4** | **97.2** | **3.00±1.81** | **1.34** | **9.55** |

the Hausdorff and MMD distances (more than one order of magnitude). Results confirm that taking advantage of temporal and spatial properties of the diaphragm in an unified way produces far better results than relying only on frame based appearance. The average errors with their corresponding standard deviations are close to the inter-observer variability, which is a common way to evaluate a method's performance related to a medical expert behavior.

Fig. 6 shows four results; in case (a), both methods detect the diaphragm robustly, while our (in green) shows a higher accuracy. Case (b) is more difficult and the method in [2] fails to detect a segment of the diaphragm border. Cases (c) and (d) show that sometimes the diaphragm parabolic model might be too simple.

## 4 Conclusions

In this paper we proposed an algorithm for the robust and accurate detection of the diaphragm border in X-ray angiographies plus a validation methodology for quantitative performance evaluation. Results show that the proposed method is both robust and accurate. However, further investigation on how to deal with highly challenging cases is required. As future works, we want to increase the validation dataset and propose a digital diaphragm removal algorithm based on the detection proposed herein.

**Acknowledgements.** The work of Simeon Petkov is funded by a FI AGAUR grant and the work of Carlo Gatta is funded by a Ramon y Cajal grant. The authors would like also to thank the University Hospital "Germans Trias i Pujol" for the data and consultation they provided us with.

## References

1. Brown, M.S.: Knowledge-based method for segmentation and analysis of lung boundaries in chest x-ray images. Computerized Medical Imaging and Graphics 22, 463–477 (1998)
2. Condurache, A., Aach, T., Eck, K., Bredno, J., Stehle, T.: Fast and robust diaphragm detection and tracking in cardiac x-ray projection images. In: SPIE MI, vol. 5747, pp. 1766–1775 (2005)

3. Condurache, A., Aach, T., Kaiser, A., Radke, P.: User-defined ROI tracking of the myocardial blush grade. In: 7th IEEE SSIAI, Denver, CO, March 28-30, pp. 66–70. IEEE Computer Society (2006)
4. Funabashi, N., Kobayashi, Y., Perlroth, M., Rubin, G.: Coronary artery: quantitative evaluation of normal diameter determined with electron-beam ct compared with cine coronary angiography initial experience. Radiology 226(1), 263–271 (2003)
5. Gatta, C., Gomez Valencia, J.D., Ciompi, F., Rodriguez Leor, O., Radeva, P.: Toward Robust Myocardial Blush Grade Estimation in Contrast Angiography. In: Araujo, H., Mendonça, A.M., Pinho, A.J., Torres, M.I. (eds.) IbPRIA 2009. LNCS, vol. 5524, pp. 249–256. Springer, Heidelberg (2009)
6. Gil, D., Rodriguez-Leor, O., Radeva, P., Mauri, J.: Myocardial perfusion characterization from contrast angiography spectral distribution. IEEE TMI 27(5), 641–649 (2008)
7. Henrikson, J.: Completeness and total boundedness of the hausdorff metric. MIT Undergraduate Journal of Mathematics 1, 69–80 (1999)
8. Liénard, J., Vaillant, R.: Quantitative Tool for the Assessment of Myocardial Perfusion during X-Ray Angiographic Procedures. In: Ayache, N., Delingette, H., Sermesant, M. (eds.) FIMH 2009. LNCS, vol. 5528, pp. 124–133. Springer, Heidelberg (2009)
9. Lindeberg, T.: Principle for automatic scale selection. Technical report, RIT (1998)
10. Thompson, R.: A note on restricted maximum likelihood estimation with an alternative outlier model. Journal of the Royal Statistical Society. Series B 47, 53–55 (1985)
11. van Ginneken, B., et al.: Automatic segmentation of lung fields in chest radiographs. Medical Physics 27(10) (2000)

# Modeling of the Optical Behavior of Myocardial Fibers in Polarized Light Imaging

Paul Audain Desrosiers[1,2], Gabrielle Michalowicz[1], Pierre-Simon Jouk[1], Yves Usson[1], and Yuemin Zhu[2]

[1] CNRS, UMR 5525, Université Joseph Fourier de Grenoble
[2] CREATIS, CNRS UMR 5220, INSERM U1044, INSA de Lyon, Université de Lyon, Villeurbanne

**Abstract.** Many cardiovascular diseases are linked to anomalies in myocardial fibers. The purpose of this paper is to model the birefringence of myocardial fibers in polarized light imaging (PLI) with future application to measurements on real myocardial tissues. The method consists in modeling the behavior of a uni-axial birefringent crystal by means of the Muller matrix, and measuring the final intensity of polarized light and consequently the orientation of myocardial fibers, by using crossed polarizers. The method was illustrated with a tissue modeled as a volume of $100\times100\times500\mu m^3$. This volume was divided into cubes of size $20\mu m$ close to cell diameter. The fiber orientation within the cube was defined by azimuth and elevation angles. The results showed that the proposed modeling enables us to find the optimal conditions for the PLI of 3D fiber orientations and design a model for the myocardial tissue measurement from PLI.

**Keywords:** myocardial fibers, fiber architecture, human heart, fiber orientation, polarizers, polarized light.

## 1 Introduction

Cardiovascular disease is the first cause of mortality in the world. According to the OMS in 2030 the number of death will reach more than 17.3 million. Disorders in the heart being linked to myocardial fibers, many studies have tried to understand the architecture of myocardial fibers in the ventricular mass. Some old techniques used fiber peeling of the heart from pericardium to endocardium. Mac Callum (1900) peeled the heart of the pig and human in order to study the fibers structure. Other techniques were dissection methods, such as those of Mall [1], Robb [2], and Torrent-Guasp [3], while Hort [4] and Streeter [5] developed histological methods. More recent imaging techniques include diffusion tensor magnetic resonance imaging (DT-MRI or DTI) [6], [7], [8], [9] and microscopic techniques using the polarized light imaging (PLI) have been developed. The use of polarized light has been introduced in biology since the end of the 19th century as a method for studying the structure of the human tissue. The authors of [10] used the polarized light to study the light scattering in Bacillus subtilis. PLI was also

O. Camara et al. (Eds.): STACOM 2012, LNCS 7746, pp. 235–244, 2013.

used to visualize superficial layers of tissue where cancer arises in the skin [11], to analyze the healing after myocardial infarction [12], to establish the cartography of the pattern of myofibres in the second trimester fetal human heart [13], to study the architecture of the ventricle during fetal and neonatal life [14], to make an analysis of the collagen network [15], to investigate the topography of myocardial cells during embryonic and fetal life development [16], and to characterize the myocardium, including healthy, infarcted, and stem-cell-regeneration tissues using polarized light [17]. We used polarized light for many years in order to extract information in heart in neonatal life. In prior works on cot death, we analyzed the structure of autopsied hearts in the selected region such as the apex, the right ventricle and the left ventricle using polarized light, and have been able to observe the presence of heterogeneity of myocardial cells with a confocal microscopy [18]. However with the confocal microscopy, only a small and two-dimensional region was observed. More generally speaking, only PLI provides a very robust angular accuracy and 3D orientation map of myocardial cells with a high spatial resolution 0.1mm×0.1mm×0.5mm. Also PLI does not involve any human operation during the measurement process. However PLI cannot be used on the living human heart. Meanwhile, Some other techniques like DT-MRI or DTI can be used on the living human heart, but are limited in spatial resolution. On the other hand, although many researches were reported that are focused on the orientation of the myocardial fibers in polarized light, there is not yet work that addresses the degree of homogeneity of myocardial fibers.

In this paper, we propose to model the behavior of myocardial fibers in polarized light under controlled condition, and investigate the degree of homogeneity of the myocardial cells.

## 2 Materials and Methods

### 2.1 Sample Preparation

After removing the heart from the thorax, the hearts were perfused and fixed in a solution of 4% neutral buffered formaldehyde, and then immersed for 1 week in the same condition. The ventricles were then removed by severing the atria 1 mm proximal to the auriculo-ventricular groove and the great vessels of 3 mm from the ventricle. The ventricles were embedded in a resin of methyl methacrylate (MMA) using a protocol [16]. The specimens were infiltrated under vacuum (10 mbar) at room temperature in a series of mixtures of glycol methacrylate (GMA) and MMA in which the concentration of MMA was gradually increased to obtain pur MMA. The heart was then embedded by polymerization of MMA at 25° C. After polymerization, the heart was clearly seen through the transparent resin. It can be oriented according to the prerequisite referential system : coronal transversal, or sagittal. This was done by polishing the base of the block, which was mounted on the saw stage and determines the plane of serial sectioning, and a series of thick sections (500 $\mu$m) were cut with a diamond wire saw. The rate of penetration of the rotatory saw was set to a low speed (one hour per section) in order to avoid mechanical stress and distortions. By canceling the

optical properties of the collagen network, MMA embedding guarantee that PLI information was only due to the orientation of the myocardial cells [18].

To study fiber orientation with polarized light, an experimental PLI system was designed and constructed using the following elements:

a) A light source (unpolarized light i.e. the electric field E vibrating in all directions).
b) A linear polarizer whose vibration axis vibrates parallel to the West-East position, with reference to the stage of the virtual optic bench.
c) The birefringent sample to be tested.
d) A second linear polarizer whose vibration axis is perpendicular to the vibrating axis of the first polarizer.
e) A CCD camera that records the amount of transmitted light.

The optical bench was controlled and monitored by software we developed in C/C++. Light is an electromagnetic wave; the electric field vector E vibrates perpendicular to the direction along which it propagates. The light beam is composed of waves whose vibration axes are randomly distributed. The polarizer is an optical part which selects a specific vibration direction of the light. When the vibration axes of two polarizers are perpendicular to each other, without any birefringent sample between them, the light is blocked and the amplitude of light is down to zero. When a birefringent sample is rotated between crossed polarizers, it interferes with the light vibrating axis, and some light is transmitted across the second polarizer.

### 2.2 Optical Element Modeling

Thus, the amount of transmitted light is a function of the birefringence of the sample, and this birefringence is a function of the physico-chemical characteristics of the sample and its orientation with respect to the light. The myocardial birefringence is due to different molecules : the myosin that behaves like uni-axial positive birefringent crystal, and collagen that creates a structural birefringence. In order to collect the myosin birefringence signal alone, we cancel out the collagen structure birefringence, the biological sample was embedded in MMA whose refractive index is the same as that of collagen. When a polarizer beam crosses a uni-axial birefringent sample, the ray is divided in two beams (ordinary and extraordinary) that vibrate perpendicular to each other with a difference of phase that depends on the structural properties of the sample [19]. The birefringence ($n_o$-$n_e$) of the uni-axial sample was measured as the difference of refraction indices of the ordinary ray $n_o$ and the extraordinary ray $n_e$.

In order to model the optic parts of the above-mentioned PLI system, we used the Muller matrix, which was initially proposed by Hans Muller in 1940 for representing any optic element by a 4×4 matrix [20]. The Muller matrix is based on Stokes' parameters. The light can be described by four parameters, the first one is the total intensity of the light and the three others describe the polarization state. If we know the Stokes' parameters in $S_{(in)}$ and Stokes' parameters out $S_{(out)}$ of an optic part, the Muller matrix is expressed as

$$S_{(out)} = MS_{(in)}. \tag{1}$$

So, each element can be represented by a specific Muller matrix as follows.

$$\begin{pmatrix} S'_0 \\ S'_1 \\ S'_2 \\ S'_3 \end{pmatrix} = \begin{pmatrix} m_{00}\ m_{01}\ m_{02}\ m_{03} \\ m_{10}\ m_{11}\ m_{12}\ m_{13} \\ m_{20}\ m_{21}\ m_{22}\ m_{23} \\ m_{30}\ m_{31}\ m_{32}\ m_{33} \end{pmatrix} \begin{pmatrix} S_0 \\ S_1 \\ S_2 \\ S_3 \end{pmatrix} \tag{2}$$

The Muller matrix $M_d$ for the depolarizer which insures that the light is not polarized, can be written as

$$M_d = \begin{pmatrix} 1\ 0\ 0\ 0 \\ 0\ 0\ 0\ 0 \\ 0\ 0\ 0\ 0 \\ 0\ 0\ 0\ 0 \end{pmatrix} \tag{3}$$

where $M_d(1,1)$ represents the amplitude of unpolarized light.

The Muller matrix $M_p$ for the polarizers is characterized by $\alpha$ the rotation angle about the z-axis. It can be expressed as

$$M_p = \frac{1}{2} \begin{pmatrix} 1 & cos2\alpha & sin2\alpha & 0 \\ cos2\alpha & cos^2 2\alpha & cos2\alpha sin2\alpha & 0 \\ sin2\alpha & cos2\alpha sin2\alpha & sin^2 2\alpha & 0 \\ 0 & 0 & 0 & 0 \end{pmatrix} \tag{4}$$

The uni-axial birefringent sample is represented as a stack rotator and phase shifter

$$M_s = M(2\theta)M(\varphi(\Phi)). \tag{5}$$

The phase $\varphi(\Phi)$ of the birefringent sample depends on the birefringence ($n_o$-$n_e$), the wavelength $\lambda$, the thickness e of the sample, and the elevation angle $\Phi$. Therefore, the ellipticity state $\varepsilon$ of the sample represents the polarization degree of the light; it varies from $0<\varepsilon<1$. Empirically, the uni-axial birefringent of the sample can be represented by

$$M_s = \begin{pmatrix} 1 & 0 & 0 & 0 \\ 0 & d^2 - e^2 - f^2 + g^2 & 2(de + fg) & 2(df + eg) \\ 0 & 2(de - fg) & -d^2 + e^2 - f^2 + g^2 & -2(dg - ef) \\ 0 & 2(df - eg) & 2(dg + ef) & -d^2 - e^2 + f^2 + g^2 \end{pmatrix} \tag{6}$$

$d = \cos(2\varepsilon)\cos(2\theta)\sin(\varphi/2)$
$e = \cos(2\varepsilon)\sin(2\theta)\sin(\varphi/2)$
$f = \sin(2\varepsilon)\cos(2\theta)\sin(\varphi/2)$
$g = \cos(\varphi/2)$

with

$$\varphi(\Phi) = \frac{2\pi}{\lambda}(n_o - n_e)e. \tag{7}$$

and

$$(n_o - n_e) = 1.5 \left( \frac{1}{\sqrt{1 - \frac{2(n_o - n_e)_{max} \cos^2 \Phi}{1.5}}} - 1 \right) \tag{8}$$

where
$\varphi$ = phase shift
$\lambda$ = wavelength of light
$e$ = thickness of the sample
$n_o$-$n_e$ = birefringence of the sample
$\alpha$ = rotation angle of the polarizers
$\theta$ = azimuth angle
$\Phi$ = elevation angle
$\epsilon$ = Ellipticity (flattening measure of the ellipse).

After calculating the Muller matrix of each optic part, equation 9 was used to simulate the behavior of the uni-axial birefringent sample in optical bench, so all our simulation were run with GNU/Octave.

## 3 Results and Discussion

Based on the above modeling based on optical laws, we are now able to infer the mean spatial orientation of the myosin filaments for each pixel of the section. This orientation in space can be described by means of two angles : the azimuth and elevation angles. The azimuth angle is the angle between the west-east axis of the stage (x-axis) and the projection of the uni-axial sample direction on the stage plane, and the elevation angle corresponds to the obliquity of the uni-axial sample with respect to the plane of the section.

### 3.1 Light Amplitude Variation with Elevation or Azimuth Angle

The two polarizers were rotated at the same time. The first polarizer angle $\alpha_1$ is rotated from 0° to 90° and the second polarizer angle $\alpha_2$ is rotated from $\alpha_1$+90° (so forming two crossed polarizers) with the uni-axial birefringent sample ($\epsilon$= 0.02) between them. Figure 1a shows how the amplitude of the light varies with elevation angle for a given azimuth angle (45°). Note that The amplitude of 1.0 corresponds to the initial amplitude of the depolarized light source. Each curve corresponds to an elevation angle $\Phi$ (from 0° to 90°) of the birefringent sample. All the curves pass through the same corresponding point, that is the 45° point. At 45°, the amplitude of the light is dropped to zero, no light coming out of the second polarizer. That means, at this point, the azimuth angle $\theta$ is not depending on the rest of the system. The mathematical expression of amplitude of the polarized light in the setup is

$$M(1,1) = M_{p1}(\alpha_1) M_s(\theta, \varphi(\Phi)) M_{p1}(\alpha_2). \tag{9}$$

M(1,1) : represents the amplitude of the light in the system.

From the simulation based on the physical equation 9, we deduced a phenomenological model, that can be expressed as

$$y(\alpha) = Bcos\left(2\left(\alpha + \frac{\pi}{4} - \theta\right)\right)^2 \tag{10}$$

Least squares method allowed to fit the phenomenological model, that means the equation 10 with the curves of figure 1a, 1b (fitting at 99%) which come from the physical equation 9. In turn, equation 10 was used to extract the real parameter of the system under polarized light, such as the amplitude of the light, and the orientation of the myocardial cell.

where

B : represents the amplitude of the light (which depends on the elevation and the homogeneity)

$\theta$ : the azimuth angle of the birefringent sample

$\alpha$ :the rotation angle of the linear polarizer couple.

In Figure 1b, we represent the variation of the azimuth angle $\theta$ of the uniaxial birefringent sample ($\epsilon = 0.02$) from 0° to 180° (with a 20° step) with an elevation angle $\Phi$ set to a fixed value (0°). In this figure, all the curves have the same behavior except a phase shift that depends on the corresponding azimuth angle $\theta$.

Note that all the curves are modulo 90° about azimuth angle. Moreover, all the curves dropped to zeros at their corresponding azimuth angle $\theta$. For example, for an azimuth of 0°, the corresponding curve passes through its maximum at 45°.

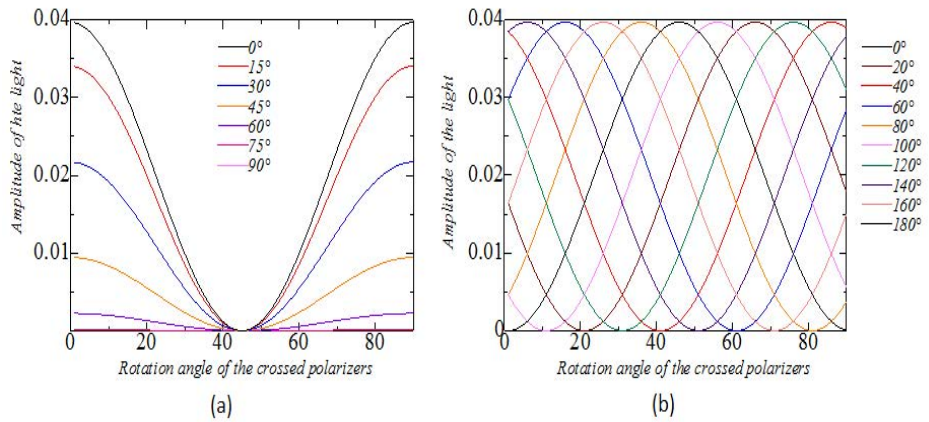


**Fig. 1.** a) Variation of the light amplitude as a function of rotation angles of the two polarizers when varying elevation angles and fixing azimuth angle; b) Variation of the light amplitude as a function of rotation angles of the two polarizers when varying azimuth angles and fixing elevation angle

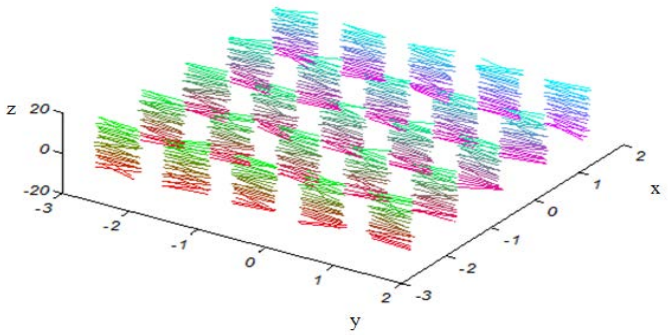


**Fig. 2.** Simulated volume with fibers having a dispersion angle of 15°, each vector is shown with a color of its own

### 3.2 Tissue Element of $100\times100\times500\mu m^3$

After simulating the behavior of a uni-axial birefringent sample, we now apply the same modeling method to a simulated tissue which was modeled as a mixture of small uni-axial birefringent elements. The tissue was modeled as a volume of $100\times100\times500\mu m^3$, which is divided into 25 cubic elements, each of which is formed of 25 cells (of 20 $\mu$m). For each cubic element, we set the local 3D orientation (azimuth and elevation) such that various conditions are experienced: homogeneous volume (all fibers are parallels) and heterogeneous volume (with solid angular dispersion, as shown in figure 2). The solid angle defines the angle dispersion of fibers.

### 3.3 Homogeneity with Parallels Fibers

In this configuration, the volume is composed of perfectly parallel fibers, without any variability. We used equation 9 with the same condition, and the uni-axial birefringent sample was replaced by the volume. The azimuth angle $\theta$ of the volume was set to a fixed value (45°), with a variation of the elevation angle $\Phi$ from 0° to 90°. As expected, since the fibers run perfectly parallel and are homogeneous, the corresponding curves pass through a minimum value at 45°, and at this point the amplitude of the light is dropped to zero, which is consistent with the result shown in figure 1a.

We obtain here exactly the same results as those physically measured with the real optical bench [21].

### 3.4 Heterogeneity with Solid Angle Dispersion

In this configuration, cell direction variability has been added to the volume. The cell orientation of the myocardial fibers is normally distributed and centered, with a standard deviation $\sigma$ (solid angle) of dispersion of 15° (figure 2 ). The azimuth angle $\theta$ is still set to a fixed value (45°) and the elevation angle $\Phi$

is set to 0°. As the volume is not homogeneous, all the curves begin to detach (offset) from abscissas at 45° as far as the solid angle increases. Moreover the amplitude of the light is decreased, and different from zero at 45°. This light leakage in the second polarizer depends on the summation of the disorders of the myocardial fibers. So, this offset depends on the standard deviation of the myocardial fibers; this is a consequence of the usual dispersion of fibers orientation around the mean orientation. Since we introduced variability in a stochastic manner, the subsequent results are the statistical measurements obtained after the simulation of 10 data sets. In figure 3a, only one data set is shown. Figures 3b to 3c show, respectively, the variation of the amplitude of the light (parameter B), the variation of the azimuth angle (parameter $\theta$), and the offset angle (parameter A) with an angular dispersion that varied from 0° to 40°. So, all these curves can be summarized by the following model

$$y(\alpha) = A + Bcos\left(2\left(\alpha + \frac{\pi}{4} - \theta\right)\right)^2 \tag{11}$$

$A$ = offset which characterized the heterogeneity; $B$ = estimates amplitude of the light that depends on both the elevation; $\theta$ = azimuth angle; $\alpha$ = rotation angle of the couple linear polarizer.

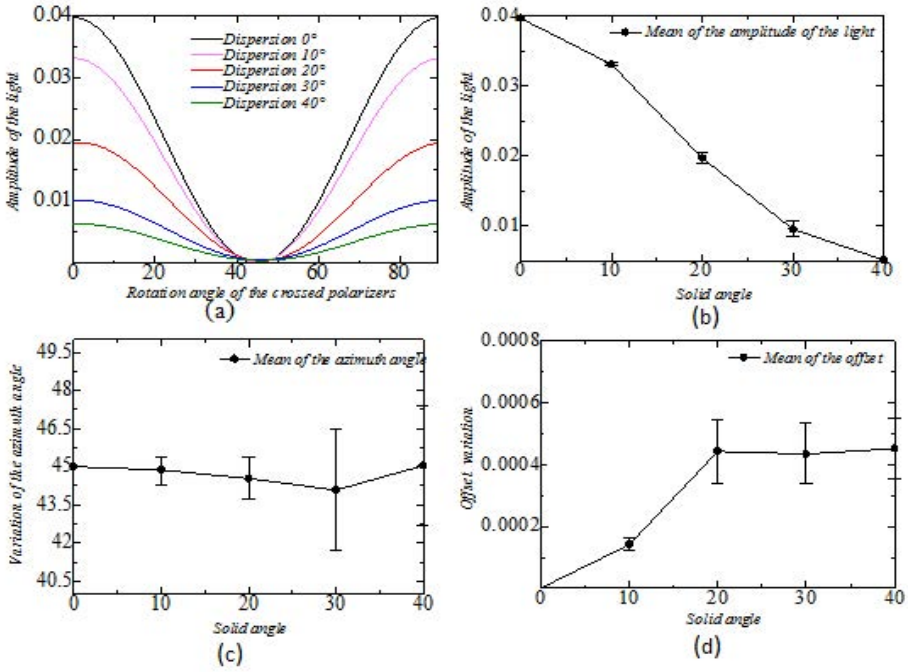


**Fig. 3.** Behavior of the volume in the presence of fiber angle dispersion (solid angle)

With the modeling results presented above, we can see that it is possible to predict the degree of homogeneity of the myocardial fibers with three parameters such as the amplitude of the light, weak variation of the azimuth angle, and the emergence of an offset.

## 4 Conclusion

The proposed PLI system modeling allowed us to understand the optical behavior of myocardial fibers in polarized light, and will help us to develop an adequate strategy to extract unambiguously the local 3D orientation (azimuth and elevation angles) on real myocardial tissues. We are working on applying the modeling to true human hearts in order to better physically measure the actual orientation of myocardial fibers.

**Acknowledgements.** Funding for this project was provided by a grant from the Région Rhône-Alpes France under the project CIBLE 2010.

## References

1. Mall, F.P.: On the muscular architecture of the ventricles of the human heart. Am. J. Anat. 11, 211–266 (1911)
2. Robb, J.S., Robb, R.C.: The normal heart-anatomy and physiology of the structural units. Am. Heart J. 23, 455–467 (1942)
3. Torrent-Guasp, F.: Organizacion de la musculeta cardiaca ventricular. In: Zarco, P., Perez, J. (eds.) El Mecanico del Corazon, pp. 3–36. Ediciones toray, Barcelona (1975)
4. Hort, W.: Quantitative morphology and structural dynamics of the myocadium. Methods Achiev. Exp. Pathol. 5, 3–21 (1971)
5. Streeter Jr., D.D.: Gross morphology and fiber geometric of the heart. The Cardiovascular (1979)
6. Basser, P., Pierpaoli, C.: Microstructural and Physiological Features of Tissues Elucidated by Quantitative-diffusion-tensor MRI. J. Magn. Reson. Imaging 111(3), 209–219 (1996)
7. Wu, M.T., Tseng, W.Y., Su, M.Y., et al.: Diffusion Tensor Magnetic Resonance Imaging Mapping the Fiber Architecture Remodeling in Human Myocardium After Infarction. Circulation 114(10), 1036–1045 (2006)
8. Frindel, C., Robini, M., Schaerer, J., Croisille, P., Zhu, Y.M.: A graph-based approach for automatic cardiac tractography. MRM 64, 1215–1229 (2010)
9. Scmid, P., Jaermann, T., Boesiger, P., Niederer, P.F., Lunkenheimer, P.P., Cryer, C.W., Anderson, R.H.: Ventricular myocardial architecture as visualized in postmortem swine hearts using magnetic resonance diffusion tensor imaging. Eur. J. Cardiothorac. Surg. 27, 468–472 (2005)
10. Bickel, W.S., Davidson, J.F., Huffman, D.R., Kilkson, R.: Application of polarization effects in light scattering: a new biophysical tool. Proc. Natl. Acad. Sci. USA 73, 486–490 (1976)
11. Jacques, S.L., Roman, J.R., Lee, K.: Imaging Superficial Tissues With Polarized Light (2000)

12. Whittaker, P., Boughner, D.R., Kloner, R.A.: Analysis of Healing After Myocardial Infarction Using Polarized Light Microscopy (1989)
13. Jouk, P.-S., Usson, Y., Michalowicz, G., Grossi, L.: Three dimensional cartography of the pattern of the myofibres in the second trimester fetal human heart. Anat. Embriol. 202, 103–118 (2000)
14. Jouk, P.-S., Mourad, A., Misilic, V., Michalowicz, G., Raoul, A., Caillerie, D., Usson, Y.: Analysis of the fiber architecture of the heart by quantitative polarized light microscopy, accurancy, limitations and contribution to the study of the fiber architecture of the ventricles during fetal and neonatal life. Journal of Cardiothoracic Sugery, 916–922 (2007)
15. Rieppo, J., Hallikainen, J., Jurverlin, J.S., Kiviranta, I., Helminen, H.J., Hyttinen, M.M.: Practical considerations in use of polarized light microscopy in the analysis of the collage Network in cartilage. Microscopy Research and Technique 71, 279–287 (2008)
16. Jouk, P.-S., Brugal, G.: Etude de la topographie des cellules myocardiques au cours du développement embryonnaire et fœtal (1994)
17. Wood, M.F.G., et al.: Polarization birefringence measurement for characterizing the myocardium, including healthy, infarcted, and stem-cell-regeneration tissues (2010)
18. Usson, Y., Parazza, F., Jouk, P.-S., Michalowicz: Method for the study of the three dimensional orientation of the nuclei of myocardial cells in fetal human heart by means confocal scanning laser microscopy. Journal of Microscopy 174(pt. 2), 101–110 (1994)
19. Walter, et al.: Polarized light microscopy
20. Brehat, F., Wyncke, B.: Répresentation des états de polarisation des ondes lumineuses (2003)
21. Methods for mapping of the orientation of myocardial cells by means of polarized light. Assessment by confocal scanning laser microscopy

# Quantification of Transvalvular Flow through Composite Gaussian Surfaces from Temporally Interleaved Multi-view 3D Colour Doppler Images

Alberto Gómez[1,⋆], Daniel Giese[1], Kuberan Pushparajah[1,2], John Simpson[2], Tobias Schaeffter[1], and Graeme P. Penney[1]

[1] King's College of London, Division of Imaging Sciences, London, UK
[2] NHS Trust, Guy and St Thomas' Hospital, London, UK

**Abstract.** We propose an angle independent method for quantification of flow through composite surfaces covering the cross section of cardiac inflow and outflow tracts. We interleave trigger-delayed 3D colour Doppler sequences to increase frame rate and use multiple views to increase coverage.

Our method is applied to four patients with Hypoplastic Left Heart Syndrome (HLHS). Flow and velocity measurement are compared to Phase Contrast Magnetic Resonance Imaging (PC-MRI). Results are highly time-resolved and agree well with PC-MRI and show superior performance compared to standard measurements. Mean dissimilarity with respect to PC-MRI was found to be $7.35\% \pm 3.72\%$ (neoaortic outflow) and $10.15\% \pm 2.72\%$ (tricuspid inflow).

## 1 Introduction

Pathological changes to intracardiac blood flow are a frequent occurrence in many forms of congenital heart disease, like Hypoplastic Left Heart Syndrome (HLHS). This may be due to valvular stenosis or regurgitation and the presence of septal defects. Echocardiography is the most frequently used imaging modality in clinical practice to assess cardiac morphology and function. Quantification of intracardiac blood flow would assist in the calculation of important clinical parameters such as cardiac output and intracardiac shunts.

Patient specific cardiac models are currently an intensive active area of research. These models provide new cardiac metrics and complement measurements [1], e.g. calculation of systemic to pulmonary shunt [2], estimation of valvular regurgitation [3] or calculations of cardiac efficiency [4]. These models are built on data measured using a wide range of techniques, mainly non-invasive imaging modalities such as MRI and Spectral Pulsed-Wave Doppler (sPWD). In particular, accurate time-resolved flow rate can be used as validation or input to patient-specific cardiac models.

⋆ This research is founded by the euHeart Project from the FP7.

O. Camara et al. (Eds.): STACOM 2012, LNCS 7746, pp. 245–252, 2013.

Accurate flow quantification is often carried out with Phase Contrast Magnetic Resonance Imaging (PC-MRI) [5]. Apart from being very expensive, PC-MRI is incompatible with some cardiac implants, can require a general anaesthetic for infants, and has a comparably long scan time for 3D imaging so is prone to motion artefacts.

sPWD is one of the most widely used cardiac flow quantifying techniques and the standard method for velocity measurements in echocardiography. It is widely available, inexpensive compared to PC-MRI, and images can be acquired in a few cardiac cycles. However, the method can have low accuracy and repeatability because flow is computed at a single point and assumed constant over the luminal cross section and because the echo beam direction must be aligned with the flow direction. Consequently the measurement is not adequate for cases in which the cross section is wide because the errors are deemed to be too large. Furthermore, even small errors in measurement of vessel diameters make a large difference to the calculated flow volume.

We propose a novel technique which provides angle independent and highly time-resolved flow quantification. Our proposed method uses multiple 3D colour Doppler images to estimate flow through a composite surface. Although the idea of integrating colour Doppler images over Gaussian surfaces was first proposed two decades ago[6], the potential of this technique has been scarcely investigated. A few papers have proposed surface velocity integration of 2D colour Doppler images[7, 8]. More recent work reports flow estimation from integrating 3D colour Doppler images, showing increase of interest in the potential of these techniques [9–11]. These approaches were limited by low temporal resolution and small Field of View (FoV) which reduces the applicability of the method to small regions with relatively simple flow patterns. In particular, flow measurements in large valves such as tricuspid or mitral, especially in adults or pathological subjects, are impracticable with a single view.

The novelty of our approach lies in combining a method to obtain accurate angle independent flow from 3D colour Doppler with a) increasing the FoV by using multiple views, which allows coverage of regions impossible with a single view and b) increasing the temporal resolution by interleaving trigger-delayed echo Doppler sequences.

## 2 Description of the Method

Our method can be split into three steps:

1. Temporally interleave data to increase frame rate (Sec. 2.1).
2. Combine two views to increase FoV (Sec. 2.2).
3. Compute flow for every frame (Sec. 2.3).

### 2.1 Sequence Interleaving

A 3D echo Doppler sequence can be acquired in a few heart beats. However, the frame-rate is limited by depth and FoV and is generally not fast enough to analyse dynamic flow behaviour.

We propose to acquire several sequences $i$, from the same view, delaying the acquisition trigger by a short time $\Delta t_i$, and then interleave these sequences. Instantaneous flow rate is computed frame by frame and then placed at its time location $t$ within the output interleaved cardiac cycle as follows. Let $f_i$ be the frame rate and $h_i$ the heart rate for sequence $i$. Let $h_r$ be the heart rate of the output interleaved sequence. The time $t'_i(k)$ at which the frame $k$ of the sequence $i$ is located within the output interleaved sequence is:

$$t'_i(k) = \left(k\frac{1}{f_i} + \Delta t_i\right)\frac{h_i}{h_r}$$

We impose that the output heart rate $h_r$ is the same as the heart rate of one of the input sequences, denoted *reference* (i.e. the other input sequences are temporally registered to the time frame of the reference sequence). The choice of the reference does not have a significant impact in the result.

### 2.2 Combining Two Views

Colour Doppler images have a limited FoV, especially in 3D. Therefore, it is sometimes impossible to achieve full coverage of the region of interest in a single acquisition. In particular, in congenital diseases like HLHS in which right heart is abnormally dilated, tricuspid valve is often difficult to cover with a single view.

We propose a method to extend the FoV by combining two views and producing composite spherical surfaces (CSS). The two views were registered using the B-Mode images with a phase-based registration algorithm [12].

Figure 1 shows the process of combining two views. First a standard B-Mode image (which has a wider FoV) is used to segment the region of interest (e.g. the tricuspid valve shown in Fig. 1 (a)). The centre of mass $P$ of the segmentation, which is in the overlap of both views, and the vector between the two beam sourcesdirection from the Beam Source (BS) of one view to the BS of the other define the plane from which each segment of the composite surface will be built (Fig. 1 (b)). Then, a spherical surface (coincident with the frontwave of the asociated BS passing by $P$) is extended at each side of $P$ (Fig. 1 (c)). Finally, The segmentation is used to clip the composite surface (Fig. 1 (d)).

### 2.3 Angle Independent Flow Rate from Velocity Integration

Flow rate, $\Phi(S)$ is defined as the amount of blood that passes through a surface $S$ per time unit. Using Gauss' theorem, flow rate can be computed as

$$\Phi(S) = \iint_S \boldsymbol{v} \cdot d\hat{n} = \iint_S \|\boldsymbol{v} \cdot \boldsymbol{n}\| dS$$

where $\boldsymbol{v}$ is the instantaneous velocity vector of blood at each point $s \in S$ and $\boldsymbol{n}$ is the vector normal to $S$ at $s$. In other words, only the component of the velocity along the vector normal to the surface contributes to flow computation. Since intensity in colour Doppler images measures the component of the blood velocity

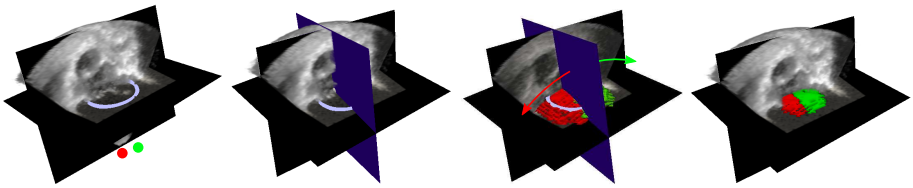

(a) Segmentation. (b) Separation plane. (c) Sphere extension. (d) CSS

**Fig. 1.** Combination of two views. (a) Segmentation of TV using a BMode image. Green and red dots represent the BS of each view. (b) Separation plane between views, defined by the centroid of the segmentation and the vector between the two beam sources. (c) Spherical surfaces are extended at each side of the separation plane. (d) The extended surfaces are clipped with the segmentation producing the final CSS.

along the echo beam direction, i.e. orthogonal to the family of spherical front surfaces, one concludes that flow rate can be computed from integrating colour Doppler intensities over spherical surfaces centred at the BS. These surfaces are obviously restricted to the frustum-shaped FoV of the images.

As a result, integrating colour Doppler images over the Composite Spherical Surface (CSS) defined in Sec. 2.2 yields flow rate with independence of the insonation angle.

## 3 Experimental Protocol

Echo Doppler and 2D PC-MRI data were acquired on four patients with HLHS. For both PC-MRI and echo image acquisition was triggered by the $R$ wave of the electrocardiogram. Colour Doppler was acquired using a Philips iE33 with a X3-1 3D probe, which produced colour Doppler sequences with a spatial resolution of $0.7mm$ (scan converted) isotropic and a temporal resolution of 14 to $16fps$. PC-MRI data was acquired on a Philips Achieva 1.5T, during free breathing using 3 averages to suppress breathing motion artefacts. Scan time was in the order of 1.5 minutes. 2D PC-MRI data had in-plane spatial resolution of $1.05mm$ isotropic and a temporal resolution of 40 phases per cardiac cycle. Data was automatically corrected for phase offsets due to eddy currents [13].

Clinical parameters of interest for HLHS are typically triscuspid valve (TV) inflow and neoaortic (NaV) outflow. For the inflow, two apical views were acquired covering the full cross-section of the TV. For the outflow, full coverage was achieved with a single view. In all three views, 3 separate sequences were acquired with $\Delta t = 0, 20, 40\ ms$. Each Doppler image was acquired in 7 cardiac cycles. As routinely done in the clinics, a sPWD was only aquired for the neoaortic outflow. The full echocardiographic exam lasted less than 10 min.

Flow rate was calculated in post-processing using 2D PC-MRI and our method. Flow was computed from PC-MRI data by manually segmenting the TV and NaV for each phase. Four experiments were carried out with colour Doppler data: 1) flow computed using temporal interleaving only, 2) flow computed using combined

views but no temporal interleaving, 3) flow computed by using combined views and temporal interleaving, and 4) flow computed from a single sequence, with no interleaving and a single view. Cardiac input and output volumes were calculated by integrating flow rate with respect to time.

## 4 Results

Figure 2 shows the estimated flow rate calculated using our method and PC-MRI, through the NaV and the TV, for patients #1 to #4. Temporal resolution is similar in both cases, due to temporal interleaving. In general, the echo and PC-MRI outflow curves can be seen to agree more closely than the inflow curves.

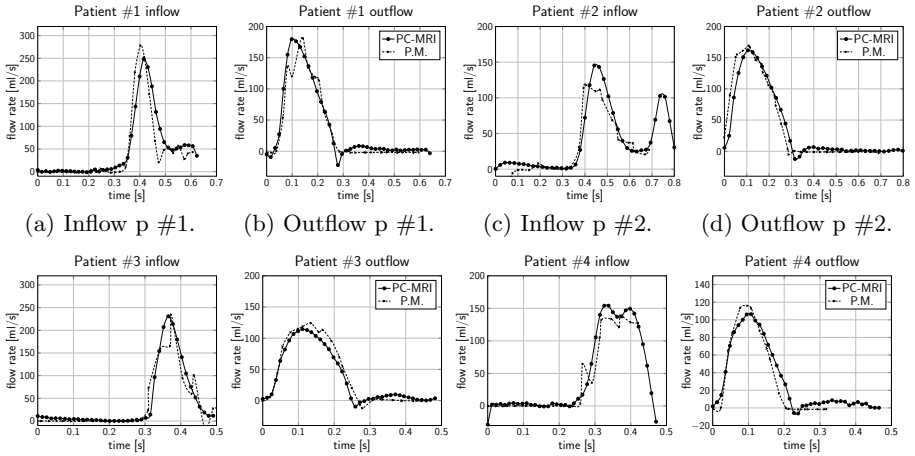


(a) Inflow p #1. (b) Outflow p #1. (c) Inflow p #2. (d) Outflow p #2.

(e) Inflow p #3. (f) Outflow p #3. (g) Inflow p #4. (h) Outflow p #4.

**Fig. 2.** TV and NaV flow rate curves on four HLHS patients. PC-MRI is shown in a solid lines, and our proposed view-combined, temporally interleaved flow from colour Doppler is shown in dashed lines.

Volume through the both valves (i.e. stroke volume) was calculated by integrating the flow rate throughout the whole cardiac cycle. Figure 3 shows mean dissimilarity with respect to PC-MRI in total volume, for each patient and for all averaged, calculated with four cases: 1) our proposed method (view combination + sequence interleaving), 2) temporal interleaving only, 3) view combination only, and 4) no temporal interleaving or view combination. For NaV outflow, averaging through all patients, mean dissimilarity increases from $7.35\% \pm 3.75\%$ to $8.50\% \pm 6.74\%$ if no temporal interleaving is used.

If we consider TV inflow, using our proposed method yields an average dissimilarity of $10.15\% \pm 2.72\%$. When using view combination only, mean dissimilarity increases to $13.98\% \pm 8.98\%$. If temporal interleaving is used but no

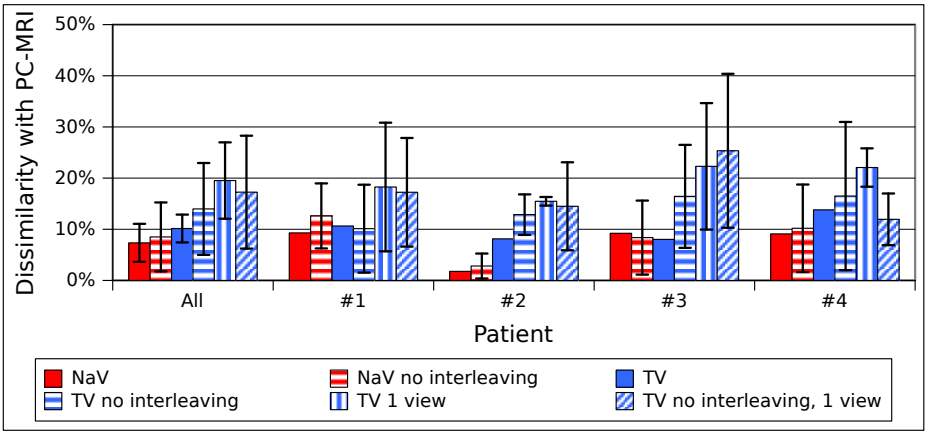


**Fig. 3.** Dissimilarity in NaV and TV volumes on four HLHS patient, compared to PC-MRI. Volumes estimated from integrating flow rate curves from Fig. 2. Four cases are covered: using our proposed method with temporal interleaving and view combination (TV); using view combination but no temporal interleaving (TV no interleaving); using 1 view with temporal interleaving (TV 1 view and NaV); and using 1 view and no temporal interleaving (TV no interleaving, 1 view and NaV no interleaving).

view combination, dissimilarity increases to $19.53\% \pm 7.46\%$. Dissimilarity is $17.25\% \pm 11.03\%$ when just a single sequence is used, without any interleaving or view combination.

## 5 Discussion

We have shown a method to provide accurate quantitative flow measurements using 3D colour Doppler sequences. We use multiple views to increase the coverage when needed, and interleave delayed sequences to increase temporal resolution. In our experiments, NaV was completely covered with one view, therefore view combination was only used for the TV.

Standard approaches need to assume simple flow patterns, because they lack temporal resolution, and are restricted to relatively small structures, like aortic or pulmonary outflow. Our approach increases temporal resolution, and increases the FoV. This allows us to compute both cardiac inflow and outflow.

In general, our results agreed well with values obtained from PC-MRI, with a mean dissimilarity close to 10% in patient data. To analyse the significance of this number, we take into account that although 2D PC-MRI is the gold standard for non-invasive flow measurement, several parameters such as breathing, inter-cardiac cycle variability, remaining eddy currents or vessel wall segmentation introduce errors of up to 10% in flow rate computation [13].

The error is in general larger for TV inflow than for NaV outflow. This can be due to several reasons. Inflow present more complex flow patterns than outflow (which is very close to laminar) and therefore difficult to measure with both PC-MRI and echo due to the fine scale flow features. Also, the plane through which flow is computed is not as well anatomically defined as for the outflow, which makes it difficult to select the same plane in both modalities. Additionally, this plane is kept in the same place during all the acquisition, while the TV moves vertically, which incorporates motion artefacts into flow rate. Finally, in HLHS patients, tricuspid regurgitation is a common issue. Regurgitation produces very fast jets which will produce aliasing and affect accuracy of flow computation.

Indeed, we believe that the main limitation of our method is the velocity range that can be measured. In pathological hearts, where high velocity jets can occur, aliasing cannot always be avoided because the maximum measurable velocity changes with depth and width of the 3D echo frustum, and in general cannot go above $150cm/s$. This limitation requires the use of dealiasing techniques. Further investigation is also needed in order to asses reproducibility, repeatability and robustness against errors in segmentation and registration.

In this work we have limited ourselves to computing flow through a single surface. However, we can compute flow through an arbitrary number of parallel surfaces within the extended FoV. This has the potential to increase SNR, e.g. by weighting the contribution of contiguous surfaces. In addition, if we assume that maximum velocity occurs at the valve plane, because it is the narrowest section, using several planes can help correcting for in-plane motion by tracking the plane of maximum velocity.

Our method for combining two views can be extended to 3+ views, which allow increased coverage and would provide higher flexibility in surface selection.

## 6 Conclusions

We have presented a new method for cardiac flow quantification from multi-view, trigger-delayed and time interleaved 3D colour Doppler images, which is independent of the view angle.

Although four patient datasets have been processed so far, and results are still preliminary, we have shown that the method provides flow quantification close to 10% error compared to the current gold standard, 2D PC-MRI. In addition, the proposed method overcomes the limitation of quantifying flow in large regions, such as the T.V., by combining several views using CSS.

The method shows potential to rapidly acquire quantitative, high temporal resolution flow measurements using a standard echo machine. Therefore this method has the potential to help quantify several cardiac parameters related, for example, to regurgitation or cardiac insufficiency, and be used for modelling as input boundary conditions or for validation of patient specific cardiac models.

## References


1. Ge, L., Ratcliffe, M.: The use of computational flow modeling (CFD) to determine the effect of left ventricular shape on blood flow in the left ventricle. Ann. Thorac. Surg. 87, 993–994 (2009)
2. Migliavacca, F., Yates, R., Pennati, G., Dubini, G., Fumero, R., de Leval, M.R.: Calculating blood flow from Doppler measurements in the systemic-to-pulmonary artery shunt after the norwood operation: a method based on computational fluid dynamics. Ultrasound Med. Biol. 26(2), 209–219 (2000)
3. Quaini, A., Canic, S., Guidoboni, G., Glowinski, R., Igo, S., Hartley, C., Zoghbi, W., Little, S.: A three-dimensional computational fluid dynamics model of regurgitant mitral valve flow: Validation against *in vitro* standards and 3D color Doppler methods. Cardiovascular Engineering and Technology 2, 77–89 (2011)
4. de Vecchi, A., Nordsletten, D., Remme, E., Bellsham-Revell, H., Greil, G., Simpson, J., Razavi, R., Smith, N.: Inflow typology and ventricular geometry determine efficiency of filling in the hypoplastic left heart. Ann. Thorac. Surg. (2012)
5. Bryant, D.J., Payne, J.A., Firmin, D.N., Longmore, D.B.: Measurement of flow with NMR imaging using a gradient pulse and phase difference technique. J. Comput. Assist. Tomogr. 8(4), 588–593 (1984)
6. Utsunomiya, T., Ogawa, T., Tang, H.A., Doshi, R., Patel, D., Quan, M., Henry, W.L., Gardin, J.M.: Doppler color flow mapping of the proximal isovelocity surface area: a new method for measuring volume flow rate across a narrowed orifice. J. Am. Soc. Echocardiogr. 4, 338–348 (1991)
7. Li, J., Li, X., Mori, Y., Rusk, R.A., Lee, J.S., Davies, C.H., Hashimoto, I., El-Sedfy, G.O.M., Li, X.N., Sahn, D.J.: Quantification of flow volume with a new digital three-dimensional color Doppler flow approach: an in vitro study. J. Ultrasound Med. 20, 1303–1311 (2001)
8. Mori, Y., Rusk, R.A., Jones, M., Li, X.N., Irvine, T., Zetts, A.D., Sahn, D.J.: A new dynamic three-dimensional digital color Doppler method for quantification of pulmonary regurgitation: Validation study in an animal model. J. Am. Coll. Cardiol. 40, 1179–1185 (2002)
9. Pemberton, J., Ge, S., Thiele, K., Jerosch-Herold, M., Sahn, D.J.: Real-time three-dimensional color doppler echocardiography overcomes the inaccuracies of spectral doppler for stroke volume calculation. J. Am. Soc. Echocardiogr. 19, 1403–1410 (2006)
10. Thavendiranathan, P., Liu, S., Datta, S., Walls, M., Nitinunu, A., Van Houten, T., Tomson, N., Vidmar, L., Georgescu, B., Wang, Y., Srinivasan, S., De Michelis, N., Raman, S., Ryan, T., Vannan, M.: Automated quantification of mitral inflow and aortic outflow stroke volumes by three-dimensional real-time volume color-flow Doppler transthoracic echocardiography: comparison with pulsed-wave doppler and cardiac magnetic resonance imaging. J. Am. Soc. Echocardiogr. 1, 56–65 (2012)
11. Ge, S.: Automated measurement of stroke volumes by real-time three-dimensional doppler echocardiography: Coming of age? J. Am. Soc. Echocardiogr. 1, 66–67 (2012)
12. Grau, V., Becher, H., Noble, J.A.: Registration of multiview real-time 3-D echocardiographic sequences. IEEE Trans. Med. Imag. 26, 1154–1165 (2007)
13. Gatehouse, P.D., Rolf, M.P., Graves, M.J., Hofman, M.B., Totman, J., Werner, B., Quest, R.A., Liu, Y., von Spiczak, J., Dieringer, M., Firmin, D.N., van Rossum, A., Lombardi, M., Schwitter, J., Schulz-Menger, J., Kilner, P.J.: Flow measurement by cardiovascular magnetic resonance: a multi-centre multi-vendor study of background phase offset errors that can compromise the accuracy of derived regurgitant or shunt flow measurements. J. Cardiov. Magn. Reson. 12 (2010)

# What a Difference in Biomechanics Cardiac Fiber Makes

Debora Gil[1], Agnés Borràs[1], Ruth Aris[2], Mariano Vázquez[2], Pierre Lafortune[2], Guillaume Houzeaux[2], Jazmin Aguado[2], Manel Ballester[3], Chi Hion Li[4], and Francesc Carreras[4]

[1] Comp Vis Center-UAB
[2] Barcelona Supercomputing Center-CNS
[3] Med Dep, Lleida Univ.
[4] Cardiac Imag Unit, Hosp Santa Creu i Sant Pau, IIB, Spain

**Abstract.** Computational simulations of the heart are a powerful tool for a comprehensive understanding of cardiac function and its intrinsic relationship with its muscular architecture. Cardiac biomechanical models require a vector field representing the orientation of cardiac fibers. A wrong orientation of the fibers can lead to a non-realistic simulation of the heart functionality.

In this paper we explore the impact of the fiber information on the simulated biomechanics of cardiac muscular anatomy. We have used the John Hopkins database to perform a biomechanical simulation using both a synthetic benchmark fiber distribution and the data obtained experimentally from DTI. Results illustrate how differences in fiber orientation affect heart deformation along cardiac cycle.

## 1 Introduction

Simulation of cardiac biomechanics requires the definition of a vector field representing the orientation of cardiac fibers inside a mesh of the geometry of the heart anatomy. Fiber information plays a key role, since an alteration of its distribution or orientation may lead to non-realistic incomplete models. There are two options for obtaining complete vector fields over the whole myocardial volume. Either using experimental measurements or relying on a rule-based mathematical model.

Experimental fiber orientation can be extracted from either histological studies or processing of DTI volumes. Histological cuts provide high resolution measurements of the local orientation of myocites [21,7,17]. Given that they provide sparse set of measurements, their use in cardiac mechanics simulations requires interpolation in order to obtain dense fields [7]. Such interpolation introduces artifacts in fiber orientation that are prone to hinder the simulation of biomechanics [4]. During the last decade, DT-MRI [16] has been established as the reference imaging modality for the rapid measurement of the whole cardiac architecture [5,14,3]. These models are dense and, thus, enable efficient solution of numerical problems. However, they provide a coarse representation that omits finer details

O. Camara et al. (Eds.): STACOM 2012, LNCS 7746, pp. 253–260, 2013.

at some areas (such as papillary muscles) which might play a significant role in cardiac electrophysiology and mechanics. Whole-heart models with such fine details might be achieved by co-registering structural MR and DTMR data with histological data [11]. Still, a common limitation of fiber models obtained from experimental data is that they only provide *ex-vivo* measurements. Therefore they require volume registration for a general use in geometries different from the ones used for their computation.

Mathematical models of fiber orientation are defined in terms of the coordinates of myocardial material points in local systems. Among existing methods [18,9,12], the one described in [18] is the preferred for biomechanical simulations [1,19,4] because it allows defining fiber orientations in both ventricles. A main advantage of mathematical models of fibers is that they can be consistently computed *in-vivo* on any myocardial geometry. A main shortcoming is the validity of the mathematical assumptions for fully describing the complexity of cardiac fiber orientations everywhere. For instance, accurate definition of fibers at the septum or where both ventricles meet remains unknown [1].

In order to select the most appropriate model for simulations, it is mandatory to assess the impact that different fiber orientations have on final simulations. Recent studies have validated the mathematical model described in [18] for the simulation of the electrical propagation [1,19]. The model has been successfully applied to the detection of arrythmia [19] and in [1] the authors report a qualitative comparison to DTI-based fibers. The comparison visually assesses discrepancies in, both, fiber orientation and simulated electrical propagations.

Even if it is presumed that discrepancies in fiber structure may significantly influence the simulation of the cardiac mechanics [1], as far as we know, there is a lack of quantitative studies. This paper explores the impact of the fiber information on the simulated biomechanics of cardiac muscular anatomy. We compare the canine DTI fiber model of the John Hopkins University, JHU, public data base [1] with the Streeter synthetic model [18]. The two fiber models are used in an electro-mechanical simulation of the heart [20]. Discrepancies between deformations are measured and related to differences in fiber orientations. Results show that the synthetic model presents a large discrepancy in the z-component of fibers that underestimates the longitudinal shortening of the left ventricle.

## 2 Computational Biomechanics

### 2.1 Cardiac Mesh Generation

Heart anatomy is given by the right and left ventricles and should exclude the atria. Atria and ventricles are separated by the basal loop, which complex geometry makes it difficult a fully automatic segmentation. Like existing approaches [13,19,4] we have developed a semi-automated solution using the open source software platform Seg3D [2]. A medical expert placed a set of key-points to locate

[1] `http://gforge.icm.jhu.edu`

[2] Seg3D: Volumetric Image Segmentation and Visualization, SCI.

the heart valves on the MR image stack that conform the atrioventricular border. Key-point location was done on a set of image slices in coronal and sagittal views. Finally, a spline interpolation was used to segment the remaining slices of the volume. A list of voxels uniformly sampled over the volume mask was meshed as described in Section 2.3.

### 2.2 Fiber Distribution

We have chosen the following two approaches representative of mathematical and experimental fiber models:

**Mathematical Fiber Model.** The local fiber orientation for each node has been calculated using the simulation package Chaste [10] as described in [12]. First, a map of the minimal distance from each node of the mesh to endocardium ($d_{endo}$) and epicardium ($d_{epi}$) is constructed, and the normalized thickness parameter e is defined:

$$e = \frac{d_{endo}}{d_{endo} + d_{epi}}$$

From that, the gradient of distance in each element is used to calculate the transmural direction. Finally, the so-called helix angle $\alpha$ is calculated to define the rotation of the fibre along transmural direction:

$$\alpha = R(1 - 2e)^n$$

where $R = \pi/3$ for the left ventricle and $R = \pi/4$ for the right ventricle. The parameters of this function are chosen to fit the observations reported in [18]. Following [1] we have considered a cubic ($n = 3$) and a linear ($n = 1$) model.

**DTI-Derived Fibers.** DT-MRI data is provided as a volume of three dimensional tensors. The primary eigenvector denotes the orientation of myocites on the given voxel. In this work we have used the public database of the JHU. This database provides MR data and such corresponding DTI information captured on a set of canine anatomies.

### 2.3 Efficient Biomechanical Model

The computational framework used is Alya System for Large Scale Computational Mechanics [6] which allows solving problems for nonhomogeneous anisotropic excitable media in thousands of processors running in parallel.

Electrophysiology and mechanical deformation are governed by sets of partial differential equations which are coupled via the free intracellular concentration and the stretch of the muscle fibers. The electrophysiology is modelled using the propagation equation of FitzHugh-Nagumo by a diffusion equation with nonlinear source terms [2] using the computational scheme described in [20]. The mechanical model implemented is based on a large strain total Lagrangian formulation. The total stress is the sum of a passive and an active contributions. The passive behavior is considered hyperelastic, orthotropic and compressible.

A local fiber-sheet-normal coordinate system is defined for every node of the mesh. The active part is transversely isotropic, with the active stress generated along the fiber direction [8].

A tetrahedra mesh of the list of voxels sampled on the segmented volume was generated using Tetgen [3]. Fiber field coming from DTI is defined at each node. In this way both problems, electrophysiology and mechanical deformation, are simulated on the same mesh, which in turn carries the original information of the DTI fibers. This procedure avoids interpolation errors that appears when each problem is solved in a different discrete mesh. Simulation models are implemented using explicit schemes with non-structured FEM meshes. In order to efficiently solve both problems the parallel coupled multi-physics solver of the Alya System was used. The parallelization of the code is based on automatic domain decomposition for distributed memory facilities.

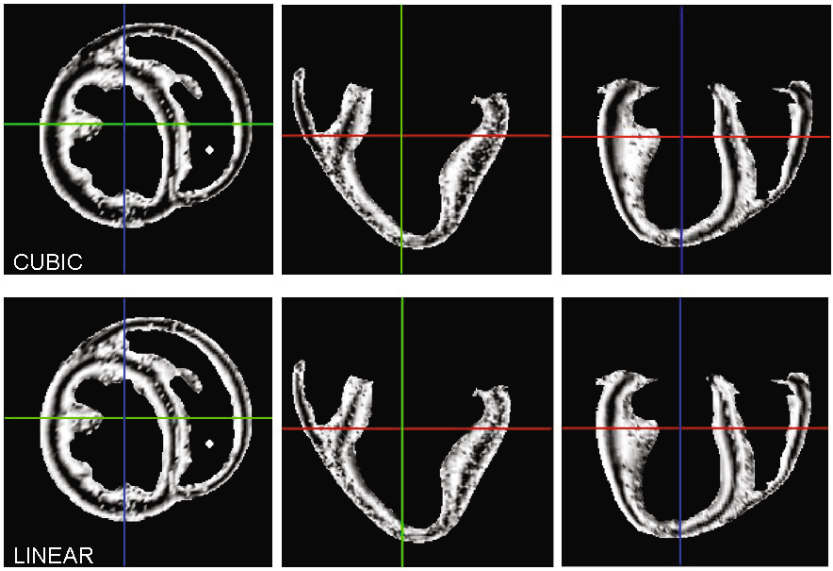


**Fig. 1.** Discrepancy between synthetic fibers and DTI

## 3 Experiments

The goal of our experiments is to compare the cubic and linear fiber models with the fibers extracted from the DTI studies of the JHU public database in the context of cardiac mechanics simulations. In order to quantify the impact of discrepancies on simulated cardiac deformation, our experiments focus on two issues: discrepancies in fiber orientation and impact on simulated cardiac deformation.

[3] `http://tetgen.berlios.de/`

### 3.1 Discrepancies in Fiber Orientation

Fibers computed using cubic and linear models have been compared to the fibers extracted from the DTI studies. For all models, fibers are given over the cardiac mesh segmented in Section 2.1. For each point in the mesh, synthetic fiber orientations are compared to DTI by means of the magnitude of the vector product, which, in the case of unitary vectors, corresponds to the sinus of the angle between them. Therefore it indicates the perpendicularity between fibers, 0 corresponding to parallel orientations and 1 to perpendicular ones. We will note this measure by $\mathcal{VP}_c$, $\mathcal{VP}_l$ for cubic and linear models, respectively.

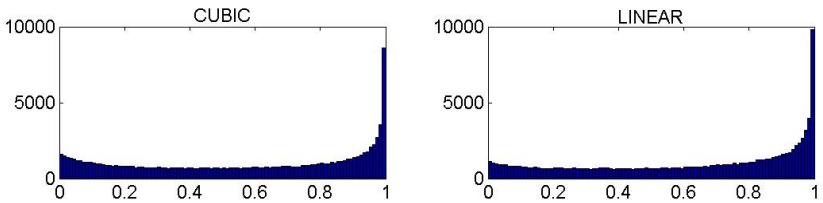


**Fig. 2.** Distribution of the discrepancy between synthetic fibers and DTI

Figure 1, shows a Short Axis, SA, cut at basal level and a Long Axis, LA, cut of $\mathcal{VP}_c$ (top images) and $\mathcal{VP}_l$ (bottom images). We also show histograms of $\mathcal{VP}_c$ and $\mathcal{VP}_l$ for the whole myocardial volume in fig.2. We observe that, in both cases, there is a large discrepancy with DTI fibers. Synthetic orientations are in general perpendicular to DTI fibers (as shown in the histograms of fig.2). The difference in orientations is within $40.7 \pm 27.6$ degrees for the cubic model and within $44.6 \pm 27.0$ degrees for the linear one. Images in fig.1 indicate that discrepancies mainly occur at myocardial walls, septal unions, papillary muscles and trabeculae. Meanwhile, the similarity at mid-wall is high everywhere.

Figure 3 (a) visually compares the fiber directions for the 3 models for a sub-sampling of the myocardial mesh in SA (top) and LA (bottom) views. It is worth noticing that the main source of discrepancy is in the z-component of fibers, while x-y components follow similar orientations. The histograms in fig.3 (b) show the distribution of the z-component inside the myocardial volume. The cubic model is the one that differs most from DTI with a low z-component in general. Although the linear distribution is closer to DTI it fails to cover the most vertical vectors, mostly at trabeculae (see fig.1).

### 3.2 Impact on Simulated Cardiac Deformation

The 3 fiber models have been used to run the electro mechanical simulation described in Section 2.3. The deformation vector was computed every 4.2 ms for a period of 0.8 s. This time gap includes the whole systolic cycle and the beginning of the diastole. For each time $t$ of the cardiac cycle, the simulation provided a

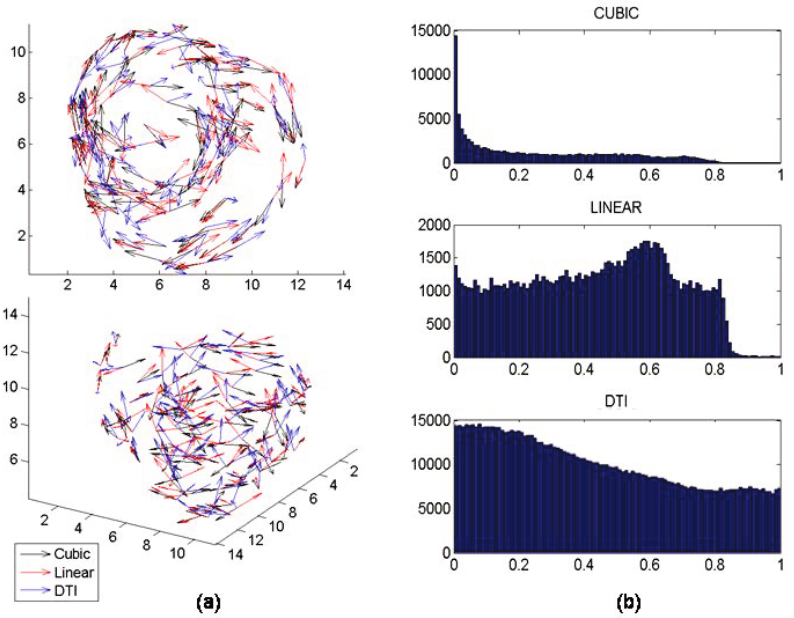


**Fig. 3.** Comparison of fibers for the three models

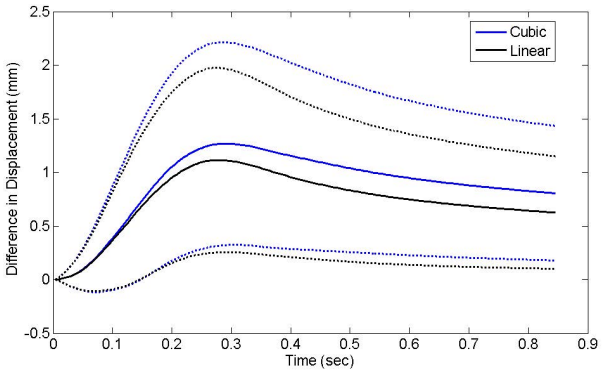


**Fig. 4.** Rank of displacements difference

vector field over each point of the segmented cardiac mesh that describes the deformation from time 0 to time t.

For each point in the mesh and time, we have computed the magnitude of the difference (in mm) between synthetic displacement vectors and DTI-based. Figure 4 shows the ranks (given by the mean ± standard deviation) of this differences as a function of time. The largest difference is achieved, for both models, around 0.3 seconds, which corresponds to the maximal myocardial contraction at end systole.

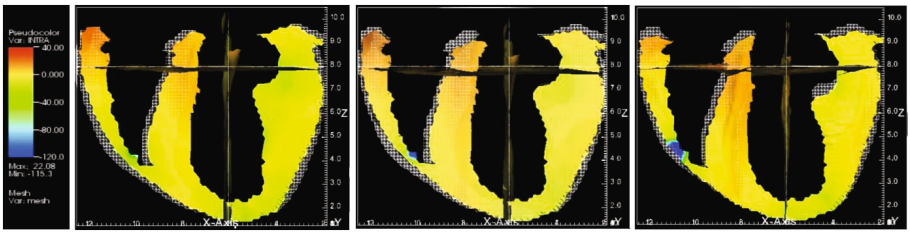

**Fig. 5.** Snap shot in LA view of the simulated deformations

Figure 5 shows a snap shot of the deformed mesh at $t = 0.3$ seconds in LA view. The mesh at time 0 is also shown as a gray grid. Colors in the deformed mesh correspond to the potential of the electrical propagation. As reported in the literature [1], we do not observe significant differences in the electrical part, but a small delay the synthetic models. As suspected, fiber structure are decisive in the modelling of cardiac mechanics. The cubic model fails short in longitudinal contraction compared to the linear and DTI models. This is a direct consequence of its lack of z-component (see histogram in fig. 3). The longitudinal shortening of the linear model is closer to DTI shortening at basal level, although it underestimates the overall shortening. The basal septal level and papillary muscles undergo a significant motion in the DTI model that it is absent in the linear one. We attribute this discrepancy to a lack of the most vertical fibers in the linear model (see histogram in fig. 3).

## 4 Conclusions

Accurate fiber orientation is crucial for getting realistic simulations of heart mechanics. Cubic and linear models underestimate the z component of fibers and, thus, motion at basal level (cubic) and papillary muscles (linear). It follows that such synthetic models produce simulations that do not correctly match the true motion. Our future research includes exploring the impact of discrepancies in clinical scores of the cardiac function (such as torsion) and analyzing recent mathematical models [15] based on the helical structure of the heart.

**Acknowledgements.** This work was supported by the Spanish projects TIN2012-33116, TIN2009-13618. The 1st author has been supported by The Ramon y Cajal Program.

## References

1. Bishop, M.J., Hales, P., Plank, G., Gavaghan, D.J., Scheider, J., Grau, V.: Comparison of Rule-Based and DTMRI-Derived Fibre Architecture in a Whole Rat Ventricular Computational Model. In: Ayache, N., Delingette, H., Sermesant, M. (eds.) FIMH 2009. LNCS, vol. 5528, pp. 87–96. Springer, Heidelberg (2009)

2. Fitzhugh, R.: Impulses and physiological states in theoretical models of nerve membrane. Biophysical Journal 1(6), 445–466 (1961)
3. Frindel, C., Schaerer, J., Gueth, P., Clarysse, P., Zhu, Y.-M., Robini, M.: A global approach to cardiac tractography. In: ISBI, pp. 883–886 (2008)
4. Gurev, V., Lee, T., Constantino, J., et al.: Models of cardiac electromechanics based on individual hearts imaging data. Biomech. Mod. Mechanobiology 10(3), 295–306 (2011)
5. Helm, P., Faisal, M., Miller, M.I., Winslow, R.L.: Measuring and mapping cardiac fiber and laminar architecture using diffusion tensor MR imaging. Ann. N. Y. Acad. Sci. 1047, 296–307 (2005)
6. Houzeaux, G., Aubry, R., Vázquez, M.: Extension of fractional step techniques for incompressible flows: The preconditioned orthomin(1) for the pressure schur complement. Computers and Fluids 44(1), 297–313 (2011)
7. Nielsen, P., Le Grice, I., Smail, B., Hunter, P.: Mathematical model of geometry and fibrous structure of the heart. Am. J. Physiol. 260(29), H1365–H1378 (1991)
8. Vázquez, M., Lafortune, P., Aris, R., Houzeaux, G.: Coupled parallel electromechanical model of the heart. Int. J. Num. Meth. Biomed. Eng. 28(1), 72–86 (2012)
9. Peskin, C.S.: Fiber architecture of the left ventricular wall: An asymptotic analysis. Comm. on Pure and App. Math. 42(1), 79–113 (1989)
10. Pitt-Francis, J.M., Pathmanathan, P., Bernabeu, M.O., et al.: Chaste: a test-driven approach to software development for biological modelling. Comp. Phys. Comm. 180(12), 2452–2471 (2009)
11. Plank, G., Burton, R., Hales, P., et al.: Generation of histo-anatomically representative models of the individual heart: tools and application. Phil. Trans. Royal Soc. 367, 2257–2292 (1896)
12. Potse, M., Dube, B., Richer, J., et al.: A comparison of monodomain and bidomain reaction-diffusion models for action potential propagation in the human heart. Trans. Biomed. Eng. 53(12), 2425–2435 (2006)
13. Quinn, T.A., Casero, R., Burton, R.A.B., et al.: Cardiac valve annulus manual segmentation using computer assisted visual feedback in three-dimensional image data. In: EMBC, WeBPo10.7 (2010)
14. Rohmer, D., Sitek, A., Gullberg, G.: Reconstruction and visualization of fiber and laminar structure in the normal human heart from ex vivo diffusion tensor magnetic resonance imaging DTMRI data. Invest. Radiol. 42(11), 777–789 (2007)
15. Savadjiev, P., Strijkers, G.J., Bakermans, A.J., et al.: Heart wall myofibers are arranged in minimal surfaces to optimize organ function. Proc. Natl. Acad. Sci. 109(24), 9248–9253 (2012)
16. Scollan, D.F., Holmes, A., Winslow, R., Forder, J.: Histological validation of myocardial microstructure obtained from diffusion tensor magnetic resonance imaging. Am. J. Physiol. 275(6 Pt 2), H2308–H2318 (1998)
17. Stevens, C., Remme, E., LeGrice, I., Hunter, P.: Ventricular mechanics in diastole: material parameter sensitivity. J. Biomech. 36, 737–748 (2003)
18. Streeter, D.D., Spotnitz, H.M., Patel, D.P., et al.: Fiber orientation in the canine left ventricle during diastole and systole. Circ. Res. 24(2), 339–347 (1969)
19. Vadakkumpadan, F., Arevalo, H., Prassl, A.J., et al.: Image-based models of cardiac structure in health and disease. Wiley Interdiscip. Rev. Syst. Biol. Med. 2(4), 489–506 (2010)
20. Vazquez, M., Aris, R., Hozeaux, G., et al.: A massively parallel computational electrophysiology model of the heart. Int. J. Num. Meth. Biomed. Eng. 27, 1911–1929 (2011)
21. Vetter, F.J., McCulloch, A.D.: Three-dimensional analysis of regional cardiac function: a model of rabbit ventricular anatomy. Prog. Biophys. Mol. Biol. 69, 157–183 (1998)

# Generalized Step Criterion Edge Detectors for Kalman Filter Based Left Ventricle Tracking in 3D+T Echocardiography

Engin Dikici[1] and Fredrik Orderud[2]

[1] Norwegian University of Science and Technology, Trondheim, Norway
engin.dikici@ntnu.no
[2] GE Vingmed Ultrasound, Oslo, Norway
fredrik.orderud@ge.com

**Abstract.** Step criterion edge detector (STEP) has been employed for the detection of endocardial edges in a Kalman filter based left ventricle tracking framework in previous studies. STEP determines the endocardial edge positions by fitting piecewise constant functions to intensity profiles, which are extracted on a tracked surface's normal directions. In this study, we generalize STEP using higher order piecewise polynomial functions. The generalized STEP detectors make different assumptions about the endocardial edge representations, and their accuracies vary over the endocardial surface and cardiac cycle positions. Accordingly, we combine the responses of the generalized detectors using a maximum likelihood (ML) approach. Unlike previously proposed ML approaches, our combined edge detector provides a real-time tracking solution as the majority of regressive functions for the polynomial fitting can be computed offline. Comparative analyses showed that the combined detector (1) outperforms each of the generalized STEP detectors, and (2) provides a comparable accuracy with the previously defined slower ML approach.

## 1 Introduction

3D+T echocardiography is a valuable tool for assessing cardiac function, as it enables real-time, non-invasive and low cost acquisition of volumetric images of the heart. The automated analysis methods for the echocardiography recordings have received considerable attention over the recent years [1,2]. However, the automated segmentation and tracking of heart chambers remain challenging tasks due to imaging artifacts; including speckle noise, shadows and signal dropouts [3]. Furthermore, the *real-time* detection of endocardial borders might be desirable for the invasive procedures and intensive care applications.

State-space analysis using Kalman filtering can be utilized for the tracking of heart chambers in time dependent recordings. The approach uses a sequential prediction and update strategy, where surface deformations are first predicted by a kinematic model, followed by an update step based on information provided by image measurements. Maximum gradient (MG) [4], step criterion (STEP) [5], local-phase [6] and max flow/min cut (MFMC) [7] edge detectors were previously employed for the detection of the left ventricle's (LV) endocardial edges in a Kalman tracking framework. In [8], a

O. Camara et al. (Eds.): STACOM 2012, LNCS 7746, pp. 261–269, 2013.

maximum likelihood (ML) edge detector combining the responses of multiple base detectors via learned statistical inferences was introduced. The ML detector was shown to be more accurate than the base detectors, however it offered a slower tracking solution due to the high computational complexity of a utilized base detector, MFMC.

The motivation for our study is to define an accurate and real-time ML endocardial edge detector. Accordingly, we first define a new set of base detectors that generalize STEP to higher order piecewise polynomials. The $k^{th}$ order STEP detector (1) fits multiple piecewise $k^{th}$ order polynomial functions to a given intensity profile, which is extracted on a tracked surface's normal direction, then (2) selects the optimal piecewise function in the least-squares (LS) sense. Each generalized STEP detector makes different assumptions about the intensity distribution characteristics of the myocardium and blood-pool; the accuracies of these detectors vary depending on the endocardial surface and cardiac cycle positions. Accordingly, we combine the responses of the generalized STEP detectors utilizing a space-time position dependent ML method described in [8]. The combined detector provides a real-time tracking solution as the majority of regressive functions for the polynomial fitting can be computed offline. The effectiveness of the introduced method is represented via comparative analyses among the $0^{th}$, $1^{st}$, $2^{nd}$ order generalized STEP detectors, proposed ML and previously defined ML approaches.

## 2 Tracking Framework

The tracking framework is built around a deformable subdivision model parametrized by a set of control vertices with associated displacement direction vectors. Model deformations are handled by a composite transform, where local shape deformations are obtained by moving control vertices in the subdivision model together with a global transformation that translates, rotates and scales the model as a whole. A manually constructed Doo-Sabin surface is used as a template for representing the endocardial borders, where the model control vertices are allowed to move in the surface normal direction to alter the shape.

The tracking framework consists of five separate stages, namely (1) state prediction, (2) evaluation of tracking model, (3) edge measurements, (4) measurement assimilation, and (5) measurement update [9].

Endocardial edge detection methods are employed during the *edge measurements* stage of the framework. First, $N$ 1D intensity profiles $(I_1, I_2, \ldots I_N)$ are extracted, where each profile is centered by an endocardial surface point and oriented in a surface normal direction. $I_{i,k}$ is used for referring to the intensity value of the $i^{\text{th}}$ profile's $k^{\text{th}}$ sample, and $M$ gives the total number of samples in each profile. Next, an edge detection method is employed for estimating the endocardial edge positions by processing the intensity profiles. Generalized STEP detectors, and a ML detector combining the responses of multiple generalized detectors are described in the following subsections.

### 2.1 Generalized Step Criterion Edge Detectors

The classical step criterion edge detector assumes that the intensity profile $I_i$ forms a transition from one intensity plateau to another. It calculates the heights of the two

plateaus for each index value, and selects the index with the lowest sum of squared differences between the criteria and the image data. For each profile, the edge index is estimated as:

$$\hat{\theta}_i^{STEP} = argmin_{\alpha} \sum_{t=1}^{\alpha} \left( \left( \frac{1}{\alpha} \sum_{j=1}^{\alpha} I_{i,j} \right) - I_{i,t} \right)^2 + \sum_{t=\alpha+1}^{M} \left( \left( \frac{1}{M-\alpha} \sum_{j=\alpha+1}^{M} I_{i,j} \right) - I_{i,t} \right)^2. \quad (1)$$

If the plateau heights for the determined edge index are similar ($\hat{\theta}_i^{STEP} = \alpha$ *and* $\frac{1}{\alpha}\sum_{j=1}^{\alpha} I_{i,j} = \frac{1}{M-\alpha}\sum_{j=\alpha+1}^{M} I_{i,j}$), then the edge index is reset to the profile center by $\hat{\theta}_i^{STEP} = \frac{M}{2}$.

The minimization task in Equation 1 can alternatively be represented as,

$$\hat{\theta}_i^{STEP} = argmin_{\alpha \in \{1,2 \ldots M\}} \left( \sum_{j=1}^{M} \left[ I_{i,j} - f_{\alpha}(j) \right]^2 \right), \quad (2)$$

with a piecewise constant function $f_\alpha$ minimizing,

$$min_{\beta_0^{\omega}, \beta_0^{\varpi}} \left( \sum_{j=1}^{\alpha} \left[ I_{i,j} - \beta_0^{\omega} \right]^2 + \sum_{j=\alpha+1}^{M} \left[ I_{i,j} - \beta_0^{\varpi} \right]^2 \right). \quad (3)$$

The STEP detector optimizes three unknown variables: (1) $\beta_0^{\omega}$ giving the estimated intensity value for the blood pool, (2) $\beta_0^{\varpi}$ giving the estimated intensity value for the myocardium, and (3) $\alpha$ giving the expected endocardial position. More explicitly, the STEP detector (1) fits an optimal single knot piecewise constant function to an intensity profile for each knot position (Equation 3), (2) then selects the optimal knot position (Equation 2). Both the function fitting and knot selection procedures are optimal in the LS sense.

The idea can be generalized to $k^{th}$ order, such that $\text{STEP}_k$ fits an optimal single knot piecewise $k^{th}$ order polynomial function for each knot position instead. Using the notations from Equations 2 and 3, the generalized $k^{th}$ order detector computes,

$$\hat{\theta}_i^{STEP_k} = argmin_{\alpha \in \{1,2 \ldots M\}} \left( \sum_{j=1}^{M} \left[ I_{i,j} - f_{\alpha}^{k}(j) \right]^2 \right), \quad (4)$$

with a piecewise $k^{th}$ order polynomial function $f_\alpha^k$ minimizing,

$$min_{\beta_0^{\omega}, \beta_1^{\omega}, \ldots \beta_k^{\omega}} \left( \sum_{j=1}^{\alpha} \left[ I_{i,j} - \left( \beta_0^{\omega} + j \cdot \beta_1^{\omega} + j^2 \cdot \beta_2^{\omega} + \ldots j^k \cdot \beta_k^{\omega} \right) \right]^2 \right) + \quad (5)$$

$$min_{\beta_0^{\varpi}, \beta_1^{\varpi}, \ldots \beta_k^{\varpi}} \left( \sum_{j=\alpha+1}^{M} \left[ I_{i,j} - \left( \beta_0^{\varpi} + j \cdot \beta_1^{\varpi} + j^2 \cdot \beta_2^{\varpi} + \ldots j^k \cdot \beta_k^{\varpi} \right) \right]^2 \right).$$

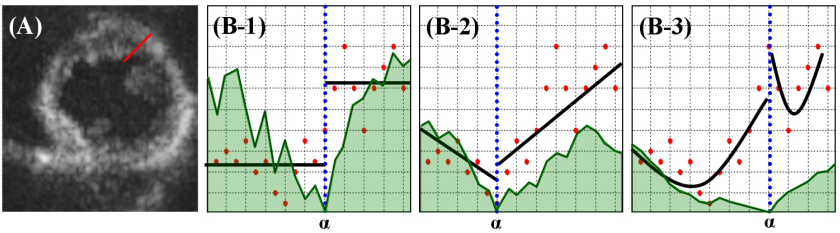


**Fig. 1.** The endocardial edge detection with generalized STEP detectors. (A) The target image and the intensity profile (red) are represented. (B-1) $0^{th}$ , (B-2) $1^{st}$ and (B-3) $2^{nd}$ order STEP edge detections are shown; $x$ axis gives the spatial position, $y$ axis gives the intensity, red dots show the image intensity values on the intensity profile, black lines (curves) are the fitted piecewise polynomial functions, green regions show the minimized energy functions from Equation 4, and $\alpha$ shows the detected edge position.

The regression task of finding the optimal parameters can be performed solving $\beta^{\omega} = \left(\mathbf{D}_{\alpha}^{T}\mathbf{D}_{\alpha}\right)^{-1}\mathbf{D}_{\alpha}^{T}\mathbf{y}$, where

$$\beta^{\omega} = [\beta_0^{\omega}, \beta_1^{\omega}, \ldots, \beta_k^{\omega}]^T, \mathbf{D}_{\alpha} = \begin{bmatrix} 1 & j & \cdots & j^k \\ 1 & j & \cdots & j^k \\ \vdots & \vdots & \ddots & \vdots \\ 1 & j & \cdots & j^k \end{bmatrix}, \mathbf{y} = [I_{i,1}, I_{i,2}, \ldots, I_{i,\alpha}]^T. \quad (6)$$

$\mathbf{D}_{\alpha}$ is a $\alpha \times (k+1)$ constant design matrix that can be computed offline for all possible $\alpha$ values ($\leq M$). Please note that the computation of $\beta^{\varpi} = \left[\beta_0^{\varpi}, \beta_1^{\varpi}, \ldots, \beta_k^{\varpi}\right]^T$ follows a similar method as the $\beta^{\omega}$'s (see Figure 1).

### 2.2 Maximum Likelihood Edge Detector

$\text{STEP}_k$ makes an assumption that the myocardium and blood pool sections of a given intensity profile can be represented using $k^{th}$ order polynomial functions. However, this assumption might only be valid for parts of the endocardial surface and cardiac cycle. As an example, $\text{STEP}_0$ might be a proper detector for the apical region, while performing poor for the basal anterior region at the end systole (ES). On the other hand, $\text{STEP}_2$ might outperform other generalized detectors for the apical region at ES, and produce highly biased detection results at the end diastole (ED). The responses of the generalized STEP detectors with orders $\leq p$ can be combined using a statistical learning approach, where the *learned* confidences of the base detectors for a given spatial and temporal position determine their weights.

The system can be described for the $i^{th}$ intensity profile at cardiac cycle position $\zeta \in [0 : ES, 1 : ED]$ using a general linear model as:

$$\mathbf{s}_{\mathbf{i},\zeta} = \mathbf{1}\theta_{\mathbf{i},\zeta} + \mathbf{b}_{\mathbf{i},\zeta} + \mathbf{w}_{\mathbf{i},\zeta}, \quad (7)$$

where

1. $\theta_{\mathbf{i},\zeta}$ is the unknown endocardial edge position (scalar valued),
2. $\mathbf{s}_{\mathbf{i},\zeta} = \left[\hat{\theta}_{i,\zeta}^{STEP_0}, \hat{\theta}_{i,\zeta}^{STEP_1}, \ldots \hat{\theta}_{i,\zeta}^{STEP_p}\right]^T$ is the measurement vector for the base edge detectors,
3. $\mathbf{b}_{\mathbf{i},\zeta} = \left[Bias_{i,\zeta}^{STEP_0}, Bias_{i,\zeta}^{STEP_1}, \ldots Bias_{i,\zeta}^{STEP_p}\right]^T$ is the learned bias vector,
4. $\mathbf{w}_{\mathbf{i},\zeta}$ is the noise vector with a learned Gaussian probability distribution function $N\left(0, C_{i,\zeta}\right)$ for the $i^{th}$ intensity profile at time $\zeta$.

Note that $C_{i,\zeta}$ is a $p \times p$ symmetric matrix holding the error covariances between the base detectors (e.g. $C_{i,\zeta}(q,q)$ holds the error variance of $\text{STEP}_q$ edge estimations, and $C_{i,\zeta}(q,r)$ holds the error covariance between $\text{STEP}_q$ and $\text{STEP}_r$ edge estimations for the $i^{th}$ intensity profile at $\zeta$). The bias vector can be merged with the measurement vector giving,

$$\mathbf{y}_{\mathbf{i},\zeta} = \mathbf{1}\theta_{\mathbf{i},\zeta} + \mathbf{w}_{i,\zeta}. \tag{8}$$

Maximum likelihood estimator of $\theta_{i,\zeta}$ can be derived as [8]:

$$\hat{\theta}_{i,\zeta}^{ML} = \frac{\mathbf{1}^T C_{i,\zeta}^{-1}}{\mathbf{1}^T C_{i,\zeta}^{-1}\mathbf{1}}\mathbf{y}_{\mathbf{i},\zeta}. \tag{9}$$

$\hat{\theta}_{i,\zeta}^{ML}$ is an unbiased estimator with the variance of $\sigma_{i,\zeta}^2 = \left(\mathbf{1}^{\mathbf{T}} C_{i,\zeta}^{-1}\mathbf{1}\right)^{-1}$. The estimator variance can be utilized as the measurement noise in the Kalman filter. ML endocardial edge estimations for the model at $\zeta$ are given as,

$$\hat{\theta}_{i,\zeta}^{ML} \sim N\left(\theta_{\mathbf{i},\zeta}, \sigma_{i,\zeta}^2\right), \qquad i = 1, \ldots, N. \tag{10}$$

Please see Figure 2 for an overview of the ML training and testing processes.

## 3 Results

3D echocardiography was performed on 10 healthy subjects and 19 subjects with recent first time myocardial infarction, using a Vivid 7 (26 recordings) or a Vivid E9 (3 recordings) ultrasound scanner (GE Vingmed Ultrasound, Norway) with a matrix array (3V) transducer. The endocardial border segmentation of the recordings was performed by a trained medical doctor using a semi-automatic segmentation tool (4D AutoLVQ, GE Vingmed Ultrasound, Norway).

An $N$-fold cross validation (CV) was applied for the evaluation of the ML method (*STEP-ML*) using the $\text{STEP}_0$, $\text{STEP}_1$ and $\text{STEP}_2$ as the base detectors. For each testing fold, the other folds were used for learning a ML model at the ED and ES frames. The ML model included bias, covariance and corresponding ML weights for the base detectors at 528 evenly distributed endocardial surface positions (see Figure 3). The learned model was later interpolated between ED and ES through the cardiac cycle using a linear interpolation. For the testing, (1) STEP-ML detector was used in connection to the Kalman tracking framework with the learned ML model. The error measurements

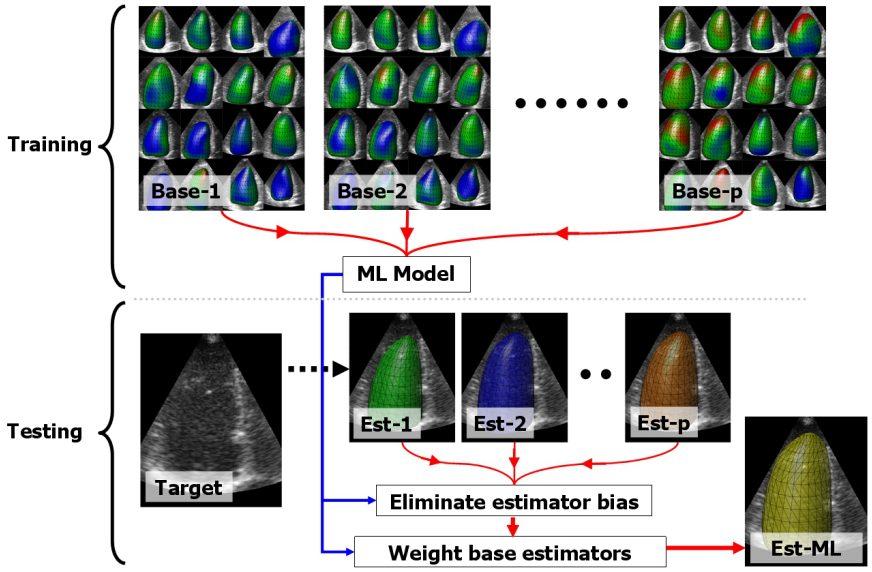


**Fig. 2.** Overview of the ML estimator. Training stage produces a ML model. For a given test image, (1) the base detectors produces their estimates (green, blue and orange meshes), (2) the bias of the estimates are eliminated using the ML model, and (3) the base estimators are weighted and fused using the ML model (yellow mesh).

including the (a) *absolute surface point error (ASPE)* giving the average absolute distance of predicted surface points to a ground truth surface, (b) *squared surface point error (SSPE)* giving the average squared distance of predicted surface points to a ground truth surface, and (c) *absolute volume error (AVE)* giving the average absolute volume error of predicted surfaces were computed. Similar error measurements were also computed for the $STEP_0$, $STEP_1$ and $STEP_2$ detectors using all 29 recordings directly without a CV *(as these base detectors do not require a training)*. For a comparison, a previously defined ML method (*CLS-ML*) [8], which uses MG, STEP and MFMC as the base detectors, was also evaluated via *N*-fold CV (see Table 1).

**Table 1.** Absolute surface point (in *mm*) , squared surface point (in $mm^2$), and absolute volume (in percentages) errors at ED and ES frames, [ED error - ES error], for the Kalman tracking framework using $STEP_0$, $STEP_1$ and $STEP_2$, STEP-ML and CLS-ML edge detectors

| | ASPE [*mm*] | SSPE [$mm^2$] | AVE [%] |
|---|---|---|---|
| $STEP_0$ | 2.211 – 2.153 | 8.862 – 8.274 | 15.718 – 13.674 |
| $STEP_1$ | 2.019 – 2.326 | 7.467 – 9.949 | 10.166 – 19.421 |
| $STEP_2$ | 2.268 – 2.941 | 10.831 – 15.428 | 13.137 – 30.547 |
| STEP-ML | 1.982 – 2.057 | 8.164 – 8.129 | 12.346 – 13.562 |
| CLS-ML | 1.999 – 2.043 | 7.542 – 7.545 | 12.592 – 14.298 |

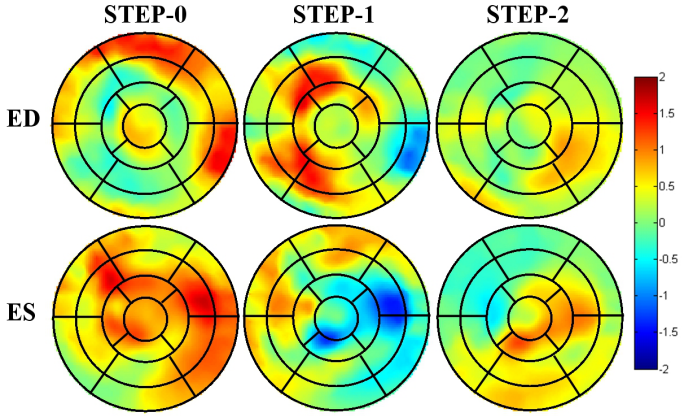


**Fig. 3.** 17-segment model representations for the learned ML weights for the base detectors: +2 weight is red, -2 weight is blue, 0 weight is green. Please note that the base detector weights vary spatially and temporarily. For a given endocardial surface and cardiac cycle position, the sum of the weights is always 1, where the negative weights are allowed.

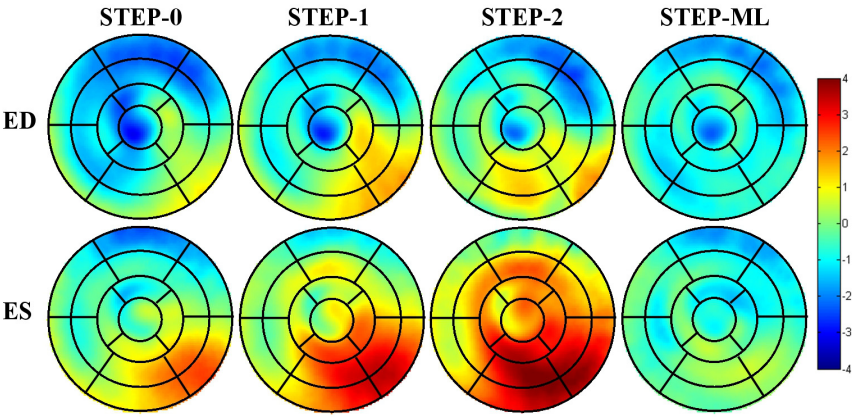


**Fig. 4.** 17-segment model representations for the signed surface error: 4mm overestimation is red, 4mm under-estimation is blue, 0mm no-error is green

*Signed surface error polar plots*, showing the average signed distances between the predicted and ground-truth surfaces using 17-segment model of the American Heart Association [10], for the $STEP_0$, $STEP_1$, $STEP_2$ and STEP-ML detectors are represented in Figure 4.

In the Kalman tracking framework, a handcrafted Doo-Sabin endocardial model consisting of 20 control points was used as LV model [9]. Edge measurements were performed in 528 intensity profiles distributed evenly across the endocardial surface. Each profile consisted of 30 samples, spaced 1 *mm* apart. During the edge detection, normal displacement measurements that were significantly different from their neighbors were

discarded as outliers. The tracking framework is implemented in C++, and processed each frame in 15.5*ms* with $STEP_0$, 16.3*ms* with $STEP_1$, 17.7*ms* with $STEP_2$, 46.6*ms* with STEP-ML, and 81*ms* with CLS-ML when executed on a 2.80 GHz Intel Core 2 Duo CPU.

## 4 Discussion and Conclusion

In this paper, we first introduced the generalized step criterion edge detectors, then combined the responses of these generalized detectors using a space-time dependent ML approach. To our knowledge, step criterion edge detector has not been generalized to higher order polynomial functions prior to this study.

Our analyses showed that $STEP_1$ and $STEP_0$ outperform the other generalized STEP detectors at ED and ES frames respectively (see Table 1, rows 1,2 and 3). These results suggest that the intensity distribution of myocardium and blood pool can be modeled better by constant functions at ES, and linear functions at ED. The sole application of $STEP_2$ leads to worse segmentation results (see Table 1, row 3). However, the relatively high ML weight of $STEP_2$ at mid inferolateral segment during ED shows the positive contribution of this base detector (see Figure 3, row 1). Accordingly, the combined usage of generalized STEP detectors, STEP-ML, produces better tracking results compared with the individual applications of the generalized detectors (see Table 1, row 4). Furthermore, STEP-ML introduces a significantly lower regional estimation bias (see Figure 4). This is due to the learned bias information stored in the ML model, which is factored in during the ML estimation.

STEP-ML produced comparable results with the previously defined ML detector, CLS-ML, [8] (see Table 1, rows 4 and 5). This shows that the linear combination of generalized STEP detectors can generate close results to MG and MFMC detectors, which are utilized in CLS-ML. Furthermore, STEP-ML reduces the processing time for each frame over 42% with respect to CLS-ML.

The current and previously proposed ML based approaches seek for an optimal linear combination of multiple base detectors. The non-linear detector fusion approaches might be investigated in a future study. Utilizing base detectors with well defined energy functions, such as the generalized STEP and MFMC, allows the definition of unified energy functions for the endocardial edge detection process. The unified energy functions might help us understand the visual perception process for this specific task; the derivation and usage of these functions might also be investigated in a future study.

## References

1. Zhang, Z., Sahn, D.J., Song, X.: Temporal Diffeomorphic Motion Analysis from Echocardiographic Sequences by Using Intensity Transitivity Consistency. In: Camara, O., Konukoglu, E., Pop, M., Rhode, K., Sermesant, M., Young, A. (eds.) STACOM 2011. LNCS, vol. 7085, pp. 274–284. Springer, Heidelberg (2012)
2. Pearlman, P., Tagare, H., Lin, B., Sinusas, A., Duncan, J.: Segmentation of 3d radio frequency echocardiography using a spatio-temporal predictor. Medical Image Analysis 16, 351–360 (2012)

3. Noble, J.A., Boukerroui, D.: Ultrasound image segmentation: a survey. IEEE Transactions on Medical Imaging 25, 987–1010 (2006)
4. Blake, A., Isard, M.: Active contours: the application of techniques from graphics, vision, control theory and statistics to visual tracking of shapes in motion. Springer-Verlag New York, Inc., Secaucus (1998)
5. Rabben, S.I., Torp, A.H., Støylen, A., Slørdahl, S., Bjørnstad, K., Haugen, B.O., Angelsen, B.: Semiautomatic contour detection in ultrasound m-mode images. Ultrasound in Medicine & Biology 26, 287–296 (2000)
6. Venkatesh, S., Owens, R.: On the classification of image features. Pattern Recogn. Lett. 11, 339–349 (1990)
7. Dikici, E., Orderud, F.: Graph-cut based edge detection for Kalman filter based left ventricle tracking in 3d+t echocardiography. In: Computing in Cardiology, pp. 205–208 (2010)
8. Dikici, E., Orderud, F., Torp, H.: Best linear unbiased estimator for Kalman filter based left ventricle tracking in 3d+t echocardiography. In: IEEE Workshop on Mathematical Methods in Biomedical Image Analysis (MMBIA), pp. 201–208 (2012)
9. Orderud, F., Rabben, S.: Real-time 3d segmentation of the left ventricle using deformable subdivision surfaces. In: IEEE Conference on Computer Vision and Pattern Recognition (CVPR), pp. 1–8 (2008)
10. Cerqueira, M.D., Weissman, N.J., Dilsizian, V., et al.: Standardized myocardial segmentation and nomenclature for tomographic imaging of the heart: a statement for healthcare professionals from the Cardiac Imaging Committee of the Council on Clinical Cardiology of the American Heart Association. Circulation 105, 539–542 (2002)

# Multi-resolution DT-MRI Cardiac Tractography

Ferran Poveda[1], Debora Gil[1,2], and Enric Martí-Godia[1]

[1] Computer Science Department, Universitat Autònoma de Barcelona, Spain
{ferran.poveda,enric.marti}@uab.es
[2] Computer Vision Center, Universitat Autònoma de Barcelona, Spain
debora@cvc.uab.es

**Abstract.** Even using objective measures from DT-MRI no consensus about myocardial architecture has been achieved so far. Streamlining provides good reconstructions at low level of detail, but falls short to give global abstract interpretations. In this paper, we present a multi-resolution methodology that is able to produce simplified representations of cardiac architecture. Our approach produces a reduced set of tracts that are representative of the main geometric features of myocardial anatomical structure. Experiments show that fiber geometry is preserved along reductions, which validates the simplified model for interpretation of cardiac architecture.

## 1 Introduction

The myocardium presents a distinctly complex architecture compared to the rest of voluntary muscles. There is an ongoing controversy on how this architecture translates into a generic geometric model and its correlation between this form and the function of the cardiac muscle. However, it is widely accepted that myocardial muscular architecture plays a critical role in key functional aspects as electrical propagation and force production. Researchers have proposed several interpretations of different conceptual models of cardiac architecture [1, 2] from either dissection or histology procedures. Still, many researchers reject these conceptual models due to the inherent complexity and subjectivity of the procedures used [3, 4]. Indeed, some recent works disagree in their architectural interpretation of the heart [2, 5]; the argument is nowhere near to a settlement.

Computer analysis of Diffusion Weighted Magnetic Resonance Imaging (DW-MRI) is the preferred approach for an objective representation of cardiac architecture. Among DW-MRI techniques, Diffusion Tensor MRI (DT-MRI) has been established as the reference imaging modality for the rapid measurement of the whole cardiac architecture. This technique provides objective discrete measurement of the spatial arrangement of myocytes by observing local anisotropic water diffusion of water molecules [6]. Due to the high level of detail of these modalities, extraction of the global architecture of the heart is not feasible by visual analysis. Currently, most research focuses on the reconstruction and representation of this data through tractography [7–11]. This technique represents spatial coherence of the tensors information through mathematical integration

O. Camara et al. (Eds.): STACOM 2012, LNCS 7746, pp. 270–277, 2013.

of the curves defined by DT-MRI primary eigenvector. These fully detailed tractographic reconstructions have proved their validity for low-level descriptions, but might fail on a higher level of analysis because of their inherent complexity. As a consequence, interpretation may still be biased.

In this paper we introduce a multi-resolution tractography-based methodology for a comprehensive description of the myocardial fiber architecture. We use pyramidal decomposition to represent fiber spatial disposition at several levels of detail. Each reduction level takes into account fiber orientation in order to better preserve anatomical features across decreasing resolutions. Our experiments show that fiber geometry is preserved along reductions, which validates the simplified model for interpretation of cardiac architecture.

## 2 Multi-resolution Tractography

Heart tractography [8] reconstructs cardiac muscular fibers composed by several streamlines (or fiber tracks) associated to DTI primary eigenvector. A streamline is a curve tangential to the vector field at any point of such curve. These curves cannot be solved analytically. For this reason, we reconstruct fibers using a fifth order Runge-Kutta-Fehlbert integration method with adaptive integration steps based on an estimation of the integration error. Unlike other methods, our tractographies ensure data completeness in the sense that the basal loop and the apex are reconstructed [12].

In any context, it is difficult, or even impossible, to understand the gross geometric features just by examining object details at a small scale. If we step away from the object we can get a more contextual view, providing us the opportunity to understand higher-level architectures. Computationally, this can translate in a multi-resolution approach. Multi-resolution strategies have been widely applied to process gross detail of data [13, 14], but their potential for getting abstract representations has been never used. We propose to build a multi-resolution tractography based on the reconstruction of multi-scale data.

The standard multi-scale generation approach is the linear Gaussian pyramidal representation. This technique applies a Gaussian filtering and later linear reduction via regular subsampling of the full-scale input. Reduced representations summarize the original information and represent it at different levels of detail. The reductions are statistically complete in such a way that the Gaussian smoothing keeps local information before applying subsampling.

A main concern of Gaussian approaches is that information is equally processed for any dimensions. Nevertheless, in a DT-MRI application we have structural information that can be taken as a reference for anisotropic filtering. For this reason, we argue that more robust filtering approaches should consider the anatomical directions of the muscle.

We propose using a Structure Preserving Diffusion (SPD) operator [15] oriented along DT-MRI primary eigenvector, $\xi_1$. Given the original volume to be filtered, $Vol(x, y, z)$, the diffusion process is given by the following heat diffusion equation in divergence form:

$$SPD_t = \text{div}(J \nabla SPD) \quad \text{with} \quad SPD(x, y, z, 0) = Vol(x, y, z) \tag{1}$$

for $\nabla$ denoting the gradient direction of the divergence operator, and $J$ a symmetric tensor driving the diffusion process. In order to restrict diffusion to $\xi_1$, $J$ is defined as:

$$J = Q \Lambda Q^t = \begin{pmatrix} \xi_1^1 & \xi_1^2 & \xi_1^3 \\ \xi_2^1 & \xi_2^2 & \xi_2^3 \\ \xi_3^1 & \xi_3^2 & \xi_3^3 \end{pmatrix} \begin{pmatrix} 1 & 0 & 0 \\ 0 & 0 & 0 \\ 0 & 0 & 0 \end{pmatrix} \begin{pmatrix} \xi_1^1 & \xi_2^1 & \xi_3^1 \\ \xi_1^2 & \xi_2^2 & \xi_3^2 \\ \xi_1^3 & \xi_2^3 & \xi_3^3 \end{pmatrix} \tag{2}$$

for $\xi_i$ DT-MRI eigenvectors. In our case, (1) is applied to each of $\xi_1$ components. In [15] it is shown that (1) has a unique solution that corresponds to solving the heat equation along the integral curves of $\xi_1$.

Decimation is obtained as in the Gaussian aproach, by the posterior linear reduction via regular subsampling of the full-scale input.

### 2.1 Implementation Details

The volume diffusion defined by equation (1) is implemented using 1-dimensional Gaussian kernels for weighting the values of the volume $Vol$ along the direction given by $\xi_1$. We observe that this would imply integrating the field $\xi_1$ for large times (scales). In order to avoid such integration, we will iterate the basic diffusion operator given by the volume diffused a minimal time unit $t_0$ (scale) as seen in Fig. 1. By uniqueness of solutions to parabolic PDE [16], the k-th iteration corresponds to the solution to (1) at time $kt_0$. For each voxel, $(x, y, z)$, the volume diffused at the minimal scale, $SPD(x, y, z, t_0)$, is given by:

$$\begin{aligned} SPD(x, y, z, t_0) = {} & g_{-1} SPD(x - \xi_1^x, y - \xi_1^y, z - \xi_1^z, 0) + g_0 SPD(x, y, z, 0) \\ & + g_1 SPD(x + \xi_1^x, y + \xi_1^y, z + \xi_1^z, 0) \end{aligned} \tag{3}$$

for $(g_j)_{j=-1}^1$ the coefficients of a 1-dimensional gaussian kernel of size 3. By iterating (3) k times:

$$\begin{aligned} SPD(x, y, z, kt_0) = {} & g_{-1} SPD(x - \xi_1^x, y - \xi_1^y, z - \xi_1^z, (k-1)t_0) \\ & + g_0 SPD(x, y, z, (k-1)t_0) \\ & + g_1 SPD(x + \xi_1^x, y + \xi_1^y, z + \xi_1^z, (k-1)t_0) \end{aligned} \tag{4}$$

we compute the solution to (1) at time $kt_0$. In the case of DTI primary eigenvector, the iteration (4) is applied to each of its components.

As in any diffusion process, boundary values deserve special treatment. In our case, due to DTI acquisition, the most undesired artifacts could appear at myocardial boundaries as a consequence of blending anatomical information with arbitrary adjacent data. A common way of coping with boundary artifacts is by propagating the values of the diffused function outside their domain of definition, that is, the myocardium. This propagation has to be performed across the domain boundaries in order to produce consistent extensions. We propose a boundary propagation based on the gradient of the distance map to a mask of the myocardial volume. Each non-anatomic voxel value is replaced by the closest boundary voxel value in the direction of the gradient.

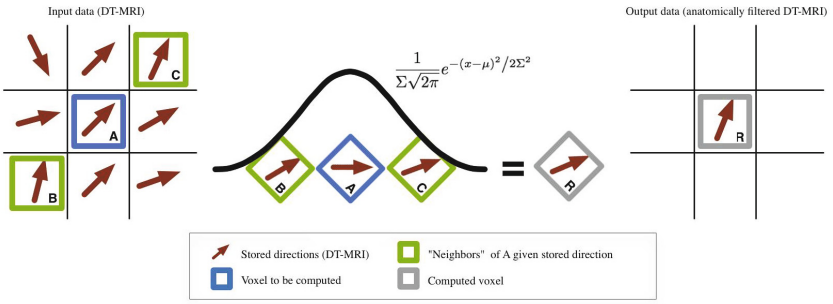


**Fig. 1.** Schematic example of anatomical filtering procedure

## 3 Results

There are two potential sources of error in a multi-resolution tractography. Losing anatomical information in the filtering step, and errors in the tractography integration introduced by the decimation of the resolution.

The loss of information in the filtering step strongly depends on the capability of the diffusion for preserving anatomical structures. In this context, SPD is more suitable than Gaussian reductions, at least for intensity volumes. Concerning errors in the tractography integration, they are a consequence from working in the discrete domain. The tractographic integration operates on a continuous vector field extrapolated from the original discrete domain, by linear interpolation. Therefore, the impact of such interpolation on reduced scale level should be determined.

In order to asses the above sources of error, we have applied our methodology to seven ex-vivo healthy canine studies from the JHU public database [17]. The data set was arranged in about 256 x 256 x 108 array (depending on the scanned heart) where each voxel in the array consisted of 3 eigenvalues and 3 eigenvectors. Two experiments have been performed:

- **Impact of volume filtering:** The original primary eigenvector has been compared to its filtered version using Gaussian kernels and SPD. This experiment validates which filtering is better suited for the full-scale tractography.
- **Impact of interpolation in reduced tractography:** The reduced volumes (previously filtered) have been up scaled using linear interpolation and compared to the filtered full scale volumes. This experiment allows us to compare our simplified tractographic reconstruction performance in front of the reconstruction on original data.

In order to compare vectors we have computed voxel-wise angular differences as reported in the literature [18, 19]. Results are statistically summarized using histograms for each canine study, as well as, the central quartile of the distribution.

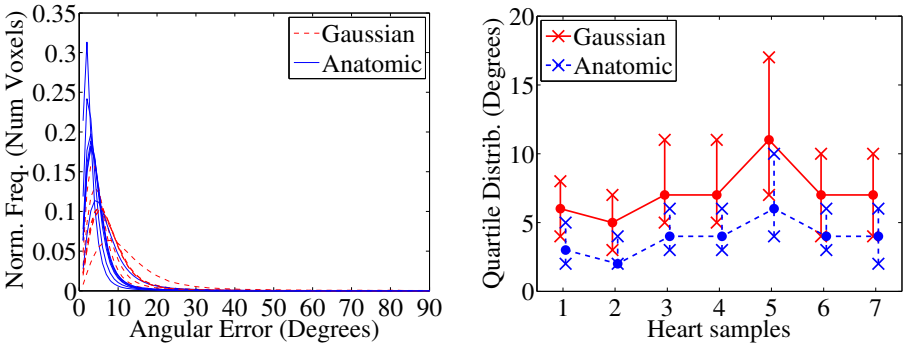


(a) Histogram traces of angular error

(b) Quartiles of angular error

**Fig. 2.** Voxel-wise statistics between original and filtered volumes

### 3.1 Impact of Volume Filtering

Figure 2 shows the histograms for Gaussian and SPD (Anatomic) filtering applied to all the canine samples, and the ranks given by the central, second and third quartiles of the distribution. First, we observe in Fig. 2(a) that the SPD histograms are the most stable ones. This is probably due to a better contextualization of myocardial anatomy. Gaussian filtering histograms significantly vary across canine anatomies. Additionally, ranges in Fig. 2(b) show that our anatomical filter performs better, having its central quartile ranging from 2 to 6 degrees. In contrast, Gaussian has considerably higher values, second quartile ranges from 5 to 11 degrees. This selects SPD as the best filtering for full-scale representations.

### 3.2 Impact of Interpolation in Reduced Tractography

Figure 3 show the same description as Fig. 2 but applied to the comparison of filtered with sub-sampled volumes. Gaussian pyramidal representation its still offering an inferior performance than the SPD approach. However, in the histogram traces shown in Fig. 3(a) it is difficult to appreciate any significant difference between the two methodologies. Figure 3(b) reveals more precise differences between the two methodologies. In this experiment, SPD have medians in the range of 6 to 7 degrees of angular error. Gaussian presents a similar behavior ranging from 6 to 8 degrees. It is clear that the linear interpolation applied on the tractography have an stronger impact in the non-isotropic methodology. The effect of sub-sampling on the Gaussian approach is clearly smaller. At this point, we attribute the loss of power of the SPD method to the isotropic nature of the re-interpolation that is used by the integration method to obtain a continuous vector field.

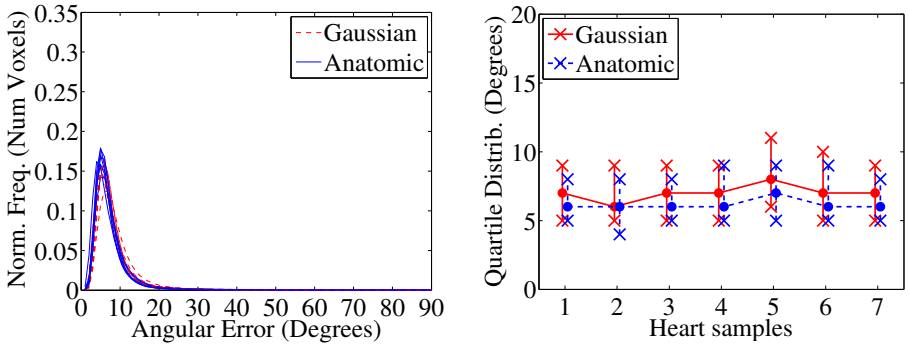


(a) Histogram traces of angular error (b) Quartiles of angular error

**Fig. 3.** Voxel-wise statistics between sub-sampled (filtered and sub-sampled) and filtered volumes

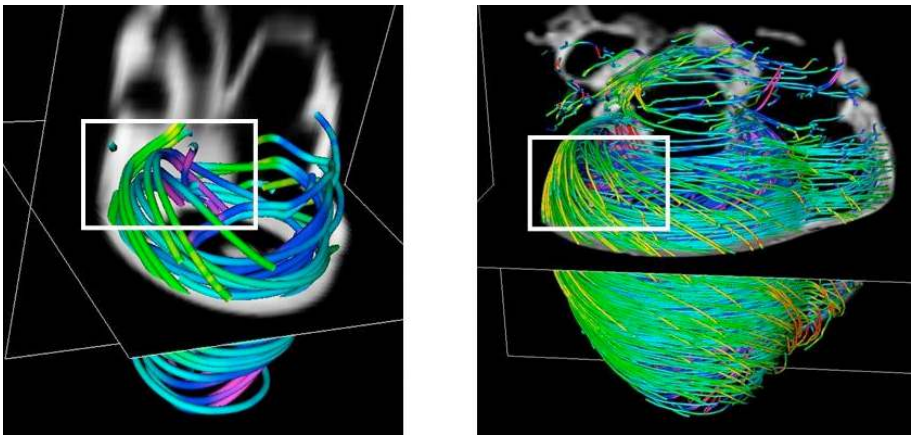

**Fig. 4.** Reduced (left) and full-scale (right) tractographic reconstructions of the same heart sample and a detail of the reconstruction of the complex structure of the Basal Ring

### 3.3 Cardiac Architecture Interpretation

The application of this work in terms of easing the interpretation of tractography can be visually assessed. Figure 4 shows our multi-resolution tractographic reconstruction of a sample canine heart, full-scale, and simplified. The simplified model keeps the main geometric features of fibers allowing an easier identification of global tendencies. It is important to notice that differences between Gaussian and SPD reductions are not easily identifiable with naked eye. However, SPD reductions are guaranteeing us more precision for future analysis.

## 4 Conclusions

Tractography of Diffusion Tensor MRI has enabled a new approach for an automatic and objective representation of the heart anatomy with high detail. However, the medical research to understand cardiac form and function depends on the interpretation of the essential structures of myocardial muscular architecture. These gross structures are not easily extrapolated from micro-architectural detail.

For that reason, we have considered a multi-resolution methodology that takes into account anatomical properties from DT-MRI to represent simplified tractographies of the cardiac anatomy.

The experiments show that this physiologically informed multi-scale representation gives remarkably higher performance than the application of classical Gaussian pyramidal decompositions for the full-scale tractographic reconstruction. The volumes sub-sampled using the anatomical filtering provide slightly better results than the Gaussian approach. However, we consider that the linear isotropic nature of the bilinear interpolation used by the integration method can not take advantage of the inherent anisotropy of the anatomical filetring. Given the observed results, we are currently focusing our work on the study of the impact of multi-resolution schemes to the reconstruction. Our aim is to obtain more complete results from a geometrical study of reconstructions.

**Acknowledgements.** This work was supported by the Spanish projects TIN2009-13618, TIN2012-33116, and CONSOLIDER - INGENIO 2010 (CSD2007-00018). The 2nd author has been supported by The Ramon y Cajal Program. We also want to thank Drs. Patrick A. Helm and Raimond L. Winslow at the Center for Cardiovascular Bioinformatics and Modeling and Dr. Elliot McVeigh at the National Institute of Health for provision of data.

## References

1. Gilbert, S.H., Benson, A.P., Li, P., Holden, A.V.: Regional localisation of left ventricular sheet structure: integration with current models of cardiac fibre, sheet and band structure. European Journal of Cardio-thoracic Surgery 32, 231–249 (2007)
2. Anderson, R., Smerup, M., Sanchez-Quintana, D., Loukas, M., Lunkernheimer, P.P.: The three-dimensional arrangement of the myocytes in the ventricular walls. Clinical Anatomy 22, 64–76 (2009)
3. Lev, M., Simkins, C.: Architecture of the human ventricular myocardium; technic for study using a modification of the mall-maccallum method. Laboratory Investigation 5(5), 396–409 (1956)
4. Grant, R.P.: Notes on the muscular architecture of the left ventricle. Circulation 32, 301–308 (1965)
5. Gao, C., Lu, K., Ye, W., Li, L., Cheng, L.: Reconstruction of the architecture of ventricular myocardial fibers in ex vivo human hearts. The Heart Surgery Forum 12(4), 225–229 (2009)

6. Scollan, D.F., Holmes, A., Winslow, R., Forder, J.: Histological validation of myocardial microstructure obtained from diffusion tensor magnetic resonance imaging. Am. J. Physiol. 275(6 Pt 2), H2308–H2318 (1998)
7. Basser, P., Pajevic, S., Pierpaoli, C., Duda, J.: In vivo fiber tractography using dt-mri data. Magnetic Resonance in Medicine 44(4), 625–632 (2000)
8. Zhukov, L., Barr, A.: Heart-muscle fiber reconstruction from diffusion tensor mri. In: Visualization, VIS 2003, pp. 597–602. IEEE (2003)
9. Helm, P., Beg, M.F., Miller, M.I., Winslow, R.L.: Measuring and mapping cardiac fiber and laminar architecture using diffusion tensor mr imaging. Ann. N. Y. Acad. Sci. 1047, 296–307 (2005)
10. Peeters, T., Vilanova, A., Strijkerst, G., ter Haar Romeny, B.: Visualization of the fibrous structure of the heart. In: Vision, Modelling and Visualization, pp. 309–316 (2006)
11. Rohmer, D., Sitek, A., Gullberg, G.: Reconstruction and visualization of fiber and laminar structure in the normal human heart from ex vivo diffusion tensor magnetic resonance imaging (dtmri) data. Investigative Radiology 42(11), 777–789 (2007)
12. Poveda, F., Gil, D., Andaluz, A., Marti, E.: Multiscale tractography for representing heart muscular architecture. In: Workshop on Computational Diffusion MRI, MICCAI (2011)
13. Williams, L.: Pyramidal parametrics. Proceedings of SIGGRAPH 17(3), 1–11 (1983)
14. Loeckx, D., Slagmolen, P., Maes, F., Vandermeulen, D., Suetens, P.: Nonrigid image registration using conditional mutual information. IEEE Transactions on Medical Imaging 29(1), 19–29 (2010)
15. Gil, D., Hernandez-Sabate, A., Brunat, M., Jansen, S., Martínez-Vilalta, J.: Structure-preserving smoothing of biomedical images. Pat. Rec. 44(9), 1842–1851 (2010)
16. Evans, L.: Partial Differential Equations. Berkeley Math. Lect. Notes (1993)
17. Johns Hopkins University: Public dtmri dataset (January 2011), `http://gforge.icm.jhu.edu/gf/project/dtmri_data_sets/`
18. Peyrat, J.M., Sermesant, M., Pennec, X., Delingette, H., Xu, C., McVeigh, E., Ayache, N.: A computational framework for the statistical analysis of cardiac diffusion tensors: Application to a small database of canine hearts. IEEE Transactions on Medical Imaging 26(11), 1500 (2007)
19. Lombaert, H., Peyrat, J.-M., Croisille, P., Rapacchi, S., Fanton, L., Clarysse, P., Delingette, H., Ayache, N.: Statistical Analysis of the Human Cardiac Fiber Architecture from DT-MRI. In: Metaxas, D.N., Axel, L. (eds.) FIMH 2011. LNCS, vol. 6666, pp. 171–179. Springer, Heidelberg (2011)

# From Image to Personalized Cardiac Simulation: Encoding Anatomical Structures into a Model-Based Segmentation Framework

Hannes Nickisch[1], Hans Barschdorf[1], Frank M. Weber[1], Martin W. Krueger[2], Olaf Dössel[2], and Jürgen Weese[1]

[1] Philips Research Hamburg, Germany
hannes.nickisch@philips.com
[2] Institute of Biomedical Engineering, Karlsruhe Institute of Technology (KIT), Karlsruhe, Germany

**Abstract.** Whole organ scale patient specific biophysical simulations contribute to the understanding, diagnosis and treatment of complex diseases such as cardiac arrhythmia. However, many individual steps are required to bridge the gap from an anatomical scan to a personalized biophysical model. In biophysical modeling, differential equations are solved on spatial domains represented by volumetric meshes of high resolution and in model-based segmentation, surface or volume meshes represent the patient's geometry. We simplify the personalization process by representing the simulation mesh and additional relevant structures relative to the segmentation mesh. Using a surface correspondence preserving model-based segmentation algorithm, we facilitate the integration of anatomical information into biophysical models avoiding a complex processing pipeline. In a simulation study, we observe surface correspondence of up to 1.6 mm accuracy for the four heart chambers. We compare isotropic and anisotropic atrial excitation propagation in a personalized simulation.

**Keywords:** model-based segmentation, electrophysiological structures, biophysical modeling and simulation.

## 1 Introduction

Personalized simulations of the heart [18] require – in addition to patient anatomy – structures such as the fast conduction tracts or muscle fibre directions hardly visible in clinical images but key for excitation propagation. Given the patient's heart anatomy, this information may be reconstructed by rule-based approaches [19,9] or by mapping a specific atlas to the patient [12]. Model-based segmentation (MBS) [5,21] allows to directly link this information to the generic model subsequently personalized by adaptation to an image. Good surface correspondence after the adaptation process (as suggested by [8]) is a prerequisite.

We propose a generic interface for MBS, in which meshes carry additional information such as fast conduction tracts or muscle fibre directions. Anatomical personalization is achieved by representing relevant structures *relative to*

O. Camara et al. (Eds.): STACOM 2012, LNCS 7746, pp. 278–287, 2013.

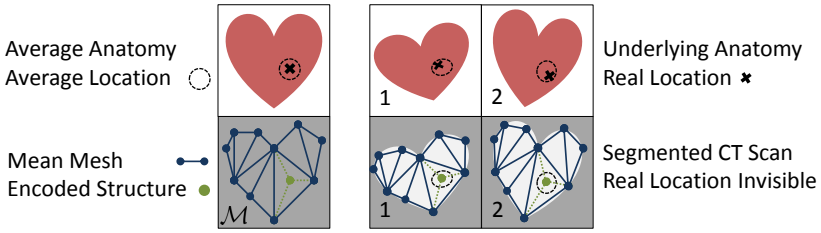


**Fig. 1.** Interface for structure encoding. **Left:** Functional structures (green) are encoded by linear combinations (thin dotted lines) of vertices of the segmentation mesh (blue) elements such as triangles or tetrahedra. **Right:** The mesh can be adapted to patient anatomies and the encoded structures transform accordingly.

the (partly volumetric) segmentation mesh prior to adaptation, see Fig. 1 (bottom left). During the adaptation of the segmentation mesh to image data, the structures are deformed in the same way as the mesh, see Fig. 1 (bottom right). The positions of the structures in an average anatomy can be obtained from histological studies or specialized measurements beforehand. For fast conduction tracts, this information is qualitative rather than quantitative [13] and cannot be obtained from CT scans. Relative encoding or atlas-based approaches do not capture variations across patients per se; these have to be modeled on top.

We investigate for the MBS approach presented in [5], to what extent vertex positions of the generic model are mapped to corresponding positions. Because a dense set of thousands of manual landmarks as ground truth can hardly be defined with sufficient accuracy, we perform MBS of a patient's dataset using the heart shape derived from other individuals as starting point. As metric, we compare the distance of corresponding vertices along the mesh surface. We map muscle fibre directions and fast conduction tracts to the right atrium and simulate atrial excitation propagation on a patient-specific mesh.

Previous approaches use a pipeline of segmentation, marching cubes meshing, mesh decimation and atlas registration [16] or surface correspondence matching, subsampling and thin plate spline warping [7,11]. We avoid these steps.

## 2 Encoding of Simulation Structures

Since the resolution of segmentation meshes is optimized for segmentation and not for biophysical simulations, we cannot simply attach structures to mesh vertices. In order to decouple mesh resolution from simulation structure positions, we use local coordinates (relative to the segmentation mesh) $\boldsymbol{\alpha} \in \mathbb{R}^d_+$ instead of global coordinates. A segmentation mesh $\mathcal{M}$ is composed of a set of vertices $\mathcal{V}_\mathcal{M}$ and a set of elements $\mathcal{E}_\mathcal{M}$. Every element $\mathbf{e} \in \mathcal{E}_\mathcal{M}$ is a convex combination of a small set of vertices $\{\mathbf{v}_1, .., \mathbf{v}_d\} \subset \mathcal{V}_\mathcal{M}$. Triangles and tetrahedra are very common mesh elements. As the elements $\mathbf{e}$ are convex sets of points, we can represent any of their interior points $\mathbf{x} \in \mathbf{e} \subset \mathbb{R}^3$ in terms of local coordinates $\mathbf{x} = \sum_{i=1}^{d} \alpha_i \mathbf{v}_i$

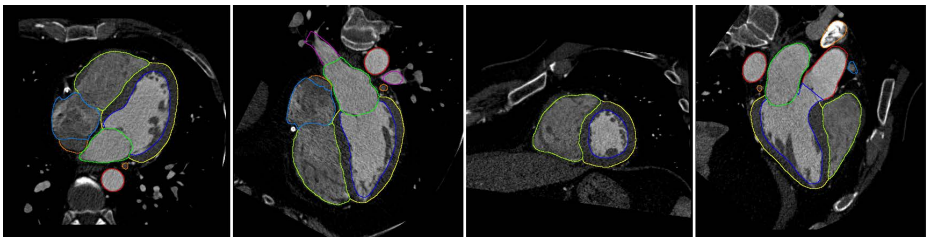

**Fig. 2.** Four views on one out of the 37 segmented CT data sets

where $\alpha_i \geq 0$ and $1 = \sum_{i=1}^{d} \alpha_i$. For a point $\mathbf{x}$ outside the mesh $\mathcal{M}$ we have two options: On the one hand, its projection $\mathbf{z} = P_{\mathcal{M}}(\mathbf{x}) = \arg\min_{\mathbf{z} \in \mathbf{e} \in \mathcal{E}_{\mathcal{M}}} \|\mathbf{x} - \mathbf{z}\|$ can be used (discarding small numerical deviations). On the other hand, we can explicitly encode finite wall thickness in (or height above) a triangulated surface by the scaled normal $\tilde{\mathbf{n}} = \mathbf{n}/\sqrt{\|\mathbf{n}\|}$, $\mathbf{n} = (\mathbf{v}_2 - \mathbf{v}_1) \times (\mathbf{v}_3 - \mathbf{v}_1)$ using the relation $\mathbf{x} = \sum_{i=1}^{3} \alpha_i \mathbf{v}_i + \alpha_4 \cdot \tilde{\mathbf{n}}$. The factor $\sqrt{\|\mathbf{n}\|}$ (unlike $\|\mathbf{n}\|$) rescales the wall thickness linearly and not quadratically as the normal $\mathbf{n}$ would.

We represent directions (and not positions) of muscle fibers $\mathbf{f} \in \mathbb{R}^3$ as vectors starting at $\mathbf{e}$'s center by $\mathbf{f} = \sum_{i=1}^{d} (\alpha_i - \frac{1}{d}) \mathbf{v}_i$.

## 3 Analysis of Surface Correspondence

In the following, we empirically assess the surface correspondence achieved by the segmentation algorithm [5] after different shape initialisations. First, we describe our evaluation approach (3.1), next, we discuss the distance measures used (3.2) and then, we present results on a dataset of 37 CT scans (example shown in Fig. 2) acquired by a Philips iCT scanner (3.3 and 3.4). Finally, we describe a simulation of excitation propagation in the human atria (3.5).

### 3.1 Approach

An assessment of the surface correspondence by a densely sampled set of ground truth landmark points is practically impossible. Therefore, we follow an indirect approach where we look at the positional error of the segmentation algorithm itself instead of the anatomical variation in a group of patients.

The segmentation algorithm [5] applies a sequence of parametric, multi-affine and deformable adaptation steps to an average initial shape balancing attraction by the initial shape and the image features. The final nonrigid adaptation of the mesh (as done in [5]) is driven by two energies: an internal energy provides the mesh with stiffness along the surface and keeps the vertex distribution similar to the mean mesh (surface curvature is not penalised) and an external energy pulls the mesh along its normals towards edges with features similar to the ones in the training set. There is no explicit mechanism to enforce surface correspondence

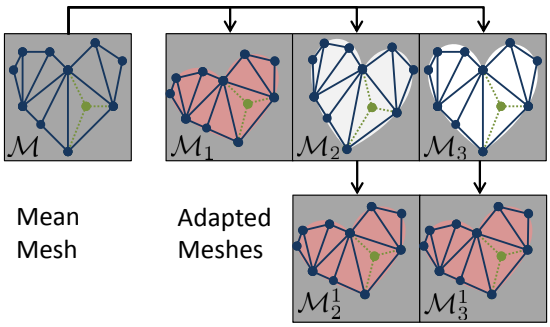


**Fig. 3.** Surface correspondence is validated by adapting a mean mesh $\mathcal{M}$ to different anatomies and using the resulting meshes $\mathcal{M}_j$ as mean meshes for a second adaptation step whose outputs are compared to each other

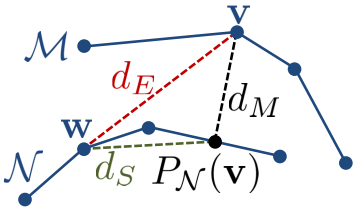


**Fig. 4.** Distance measures between corresponding vertices $\mathbf{v}$ and $\mathbf{w}$ of topologically identical meshes $\mathcal{M}$ and $\mathcal{N}$: Euclidean distance $d_E$, mesh-to-mesh distance $d_M$ (after projection) and surface distance $d_S$

but correspondence is implicitly preserved because the external energy acts along the surface only.

We vary the intial shape model and analyze the surface correspondence of the resulting segmentations. The initial shapes cover the possible anatomical variations in a group of patients, hence, we obtain a faithful measure of surface correspondence that can be evaluated for every vertex of the segmentation mesh. The shape variations in a group of patients tend to be overestimated by this approach because the difference between initial shape and adapted mesh is bigger than the difference between mean shape and adapted mesh on average.

We have a set of anatomical images $I_1, .., I_N$ (see Fig. 3), a mean mesh $\mathcal{M}$ and a segmentation algorithm $S : (\mathcal{M}, I_i) \mapsto \mathcal{M}_i$ using the mean mesh as a soft geometrical constraint [5] and returning an adapted mesh $\mathcal{M}_i$. Then we use the adapted mesh $\mathcal{M}_j$ as new mean mesh, compute $\mathcal{M}_k^j \leftarrow S(\mathcal{M}_j, I_k)$ and compare the vertex distances between the meshes $\mathcal{M}_k$ and $\mathcal{M}_k^j$ adapted to the same image $I_k$. Small distances along the surface and simultaneously a high segmentation quality indicate good surface correspondence across different images $\mathcal{I}$.

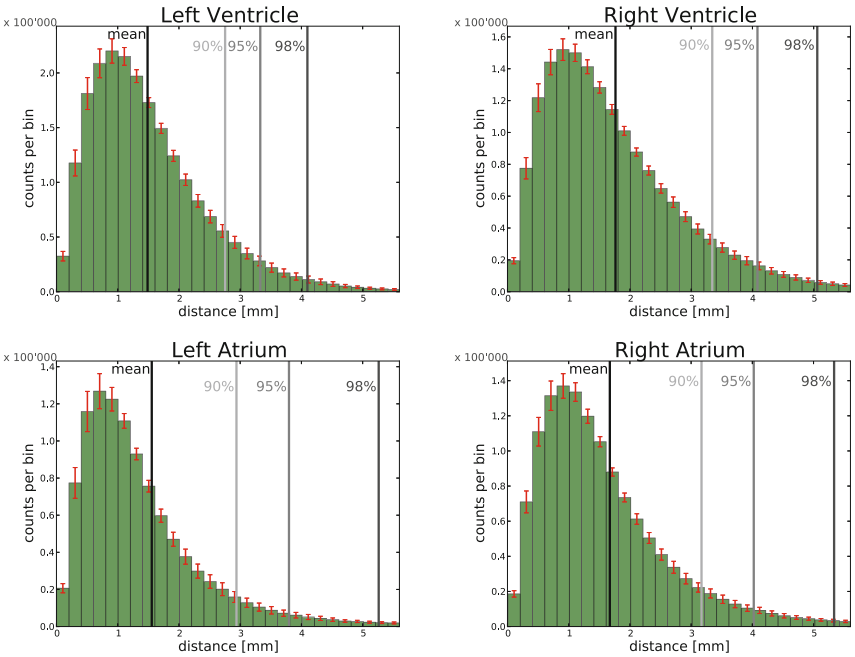


**Fig. 5.** Surface error histograms $d_S$ for $N = 37$ patients at the same heart phase (diastasis). We show results for the four heart chambers: left/right ventricle/atrium. We computed histograms for all $N = 37$ scans individually and visualize the mean (green bar) and two times its standard error (red) capturing 95% of the variance.

### 3.2 Distance Measures

There are several distance measures between topologically identical meshes $\mathcal{M}$ and $\mathcal{N}$ with corresponding vertices $\mathbf{v} \in \mathcal{M}$, $\mathbf{w} \in \mathcal{N}$, see Fig. 4. Segmentation quality is assessed by the mesh-to-mesh distance $d_M$ focusing on the differences *between* the surfaces. Absolute deviations between corresponding vertices are quantified by the Euclidean distance $d_E$. Our validation experiments use $d_S$ to measure the shift *along* the surface defined by the mesh.

### 3.3 Analysis of the Results

We composed a dataset of $N = 37$ CT scans acquired at the same heart phase (diastasis/reduced filling) yielding very good segmentation quality, see Fig. 2. "Very good" means that we require a mesh-to-mesh distance $d_M$ between segmentations with different initial shapes below 5 mm for 99% of the vertices. We obtained an average mesh-to-mesh distance of 0.6 mm. All $j = 1..37$ scans were segmented and we used the results $\mathcal{M}_j$ as initial shapes for the final segmentation of other datasets as explained in section 3.1 yielding $\mathcal{M}_k^j$. As a next step,

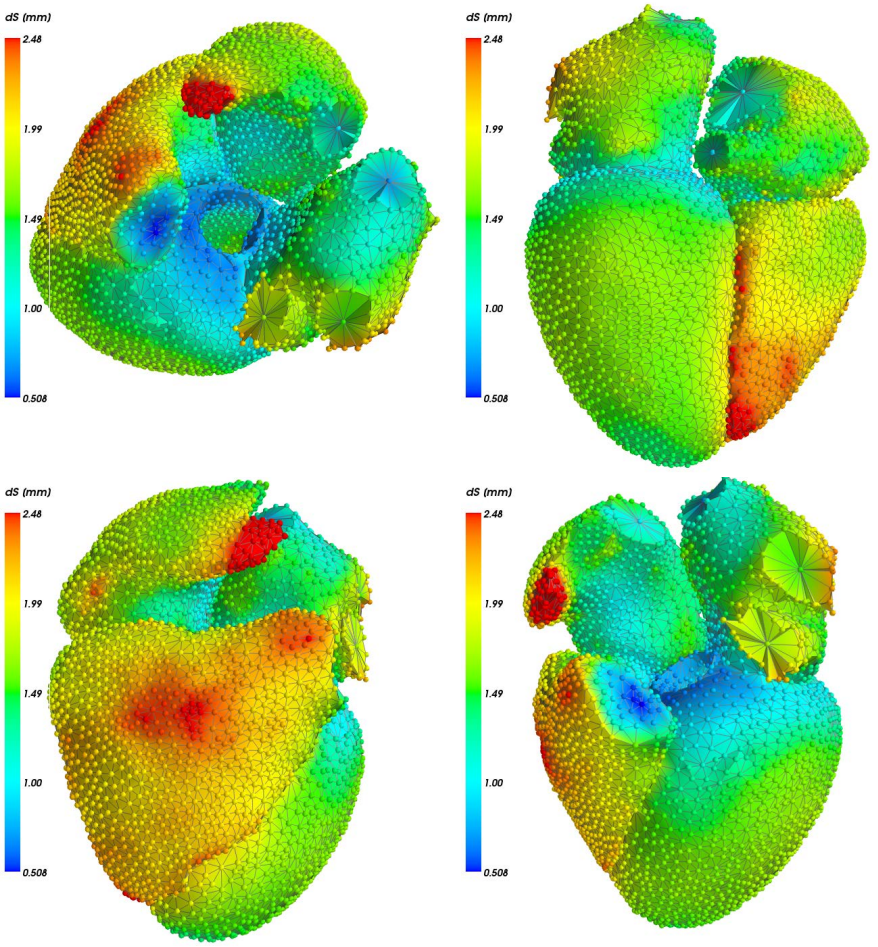


**Fig. 6.** Spatial distribution of the surface errors $d_S$ averaged over a subgroup of $N = 24$ patients (segmented with the same mesh) at the same heart phase (diastasis)

we computed surface distances $d_S$ between $\mathcal{M}_k^j$ and the segmentation $\mathcal{M}_k$ from the initial shape to assess the degree of surface correspondence.

Error histograms for the vertices of the four heart chambers are shown in Fig. 5. The average surface error over the four heart chambers amounts to 1.6 mm. Note that since $d_E$, $d_M$ and $d_S$ form a triangle, a small mesh distance $d_M$ implies $d_E \approx d_S$. It can be seen that the surface error $d_S$ is smallest for the left ventricle. Further, most of the vertices have an error of 1 mm since the histograms have a peak around that value and there are some outliers (in the order of a few percent) that show larger errors. Also, the histograms are very consistent across different scans as indicated by the small error bars.

Looking at the spatial distribution of the errors (Fig. 6), we see outliers in right atrial high curvature regions and in the lower part of the right ventricle.

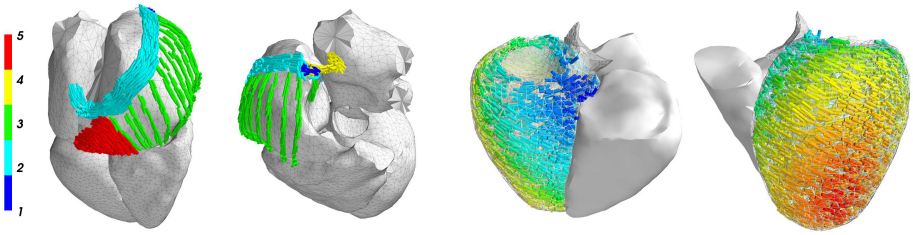


**Fig. 7.** Encoded structures. **Left** Rule-based atrial fast conduction pathways [9], where the colors of the fibers correspond to 1) Sinus Node, 2) Crista Terminalis, 3) Pectinate Muscles, 4) Bachman Bundle, and 5) Inferior Isthmus. **Right** Rule-based muscle fiber directions [19] encoded in volumetric left ventricular mesh.

### 3.4 Examples of Encoded Structures

We used our approach to encode muscle fiber directions in a volumetric left ventricle mesh using a rule-based approach [19] needed for electrophysiological and mechanical simulations, see Fig. 7 left. As shown by Figs. 5 (upper left) and 6, the surface correspondence error in the left ventricle is 1.5 mm on average.

Secondly, we encoded the sinus node (SN), Crista Terminalis (CT), pectinate muscles (PM), Bachmann bundle (BB), and right atrial inferior isthmus (II) as placed by the rule-based approach of [9] in the right atrium, see Fig. 7 left.

| Average distance | SN | CT | PM | BB | II |
|---|---|---|---|---|---|
| Euclidean distance $d_E$ [mm] | 1.95 | 1.83 | 1.82 | 1.79 | 1.86 |
| Mesh-to-mesh distance $d_M$ [mm] | 0.50 | 0.51 | 0.48 | 0.56 | 0.48 |
| Surface distance $d_S$ [mm] | 1.95 | 1.84 | 1.83 | 1.79 | 1.87 |

Summarizing the table, we find the average surface correspondence error $d_S$ (see Fig. 4) for all five structures to be below 2 mm.

### 3.5 Simulating Atrial Excitation Propagation

To demonstrate our pipeline from image to simulation, we encode three things into the segmentation mesh: the location and fiber directions $\mathbf{f_x}$ along the Crista Terminalis (see Fig. 7) and the simulation mesh itself, which has a four times higher resolution than the segmentation mesh. Excitation propagation is modeled by the anisotropic eikonal equation $1/v_{\mathbf{x}}^2 = \nabla\tau_{\mathbf{x}}^\top \mathbf{D_x} \nabla\tau_{\mathbf{x}}$, which we solve by a fast marching algorithm [17]. Here $v_{\mathbf{x}} \in \mathbb{R}_+$ is the local propagation velocity, $\tau_{\mathbf{x}} \in \mathbb{R}_+$ is the resulting local activation time and the local tensor $\mathbf{D_x} \in \mathbb{R}^{3\times3}$ models the anisotropy caused by different conduction velocities along fiber directions $\mathbf{f_x}$ and orthogonal to them. In Fig. 8, we compare an isotropic and an anisotropic simulation as done in [9]. We use a velocity of $v_{\mathbf{x}} = 0.9\frac{m}{s}$, and $\mathbf{D_x} = \mathbf{I}$ in the isotropic case (upper row) as well as $\mathbf{D_x} = \frac{3}{2}\mathbf{f_x}\mathbf{f_x}^\top + \frac{1}{2}\mathbf{I}$ in the anisotropic case (lower row). This corresponds to a velocity of $2v_{\mathbf{x}}$ along the fibers and $v_{\mathbf{x}}/2$ orthogonal to the fibers in the anisotropic case. One can clearly see that

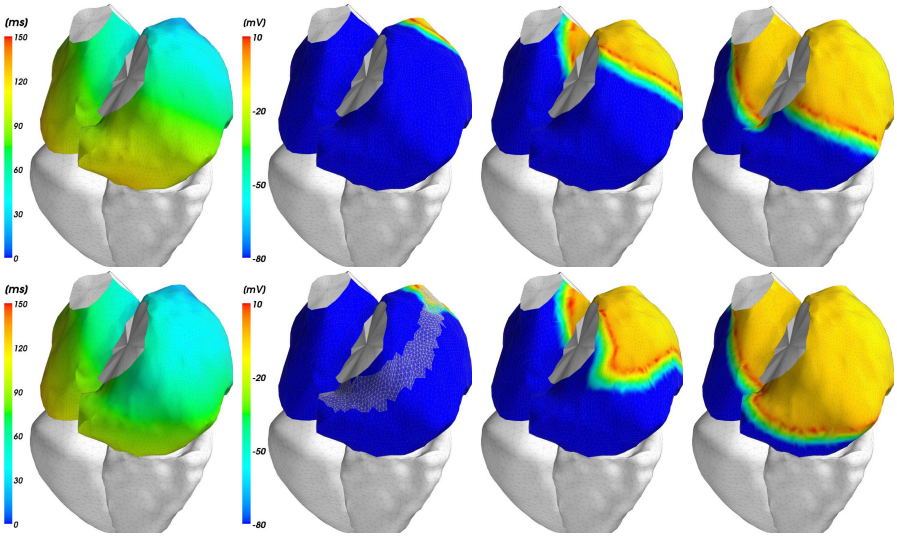


**Fig. 8.** Excitation propagation in the human atria. **Upper row** isotropic and **lower row** anisotropic propagation using the Crista Terminalis. **Left column** local activation times $\tau_{\mathbf{x}}$, **right columns** membrane potential after 30, 60, and 90 ms.

the shape of the wavefront distinctively differs (as in [9]) and the personalized anisotropy is important.

## 4 Discussion and Conclusion

In this paper we have presented a generic interface allowing to encode information in mesh models used for model-based segmentation. Once the mesh models are adapted to data, we obtain a personalised model for subsequent biophysical simulations. Experiments performed for the segmentation approach of [5] show that vertex positions of the generic model are mapped to corresponding positions after adapting the model to $N = 37$ CT scans with an average overall accuracy of 1.6 mm for the heart chambers. These errors exclude anatomical variations in position across patients and they are larger than the segmentation error assessed by point-to-surface distances with an average of 0.55 mm. However, these errors are much smaller than the typical size of, for example, fast conducting pathways in the atria. We have demonstrated our pipeline from image data to biophysical model in a atrial excitation propagation simulation. The resulting models can be further used, for example to quantify the influence of myocardial structures on the excitation propagation in the atria [1].

The segmentation approach may be further optimized to better reconstruct corresponding positions after model adaptation, e.g., by locally adjusting the mesh resolution or locally modifying the internal energy. In contrast, it does not handle variations of these structures between different individuals. However,

if the structures are visible in the image, their position may be refined on an individual basis. This has been done similarly for detecting the coronary ostia on the aortic bulbus [20] or modeling the Purkinje system [4,15] or for personalising Purkinje terminals [2].

Beyond structure encoding, we also attached a mesh optimized for biophysical simulations directly to the model (host mesh fitting e.g.[14,6]) and simulated atrial excitation propagation. This is an alternative to registering a mesh for biophysical simulations to a binary segmentation result [10]. We could also use FieldML [3] to formalize the coupling of a simulation to a personalized anatomy. Thus, the direct encoding of simulation structures provides a simple processing pipeline paving the way for the integration into clinical workflows.

**Acknowledgment.** The research leading to these results has received funding from the European Community's Seventh Framework Programme (FP7/2007-2013) under grant agreement number 224495 (euHeart project).

## References

1. Burdumy, M., Luik, A., Neher, P., Hanna, R., Krueger, M.W., Schilling, C., Barschdorf, H., Lorenz, C., Seemann, G., Schmitt, C., Dössel, O., Weber, F.M.: Comparing measured and simulated wave directions in the left atrium - a workflow for model personalization and validation. Biomedical Engineering (2012)
2. Camara, O., Pashaei, A., Sebastian, R., Frangi, A.F.: Personalization of Fast Conduction Purkinje System in Eikonal-Based Electrophysiological Models with Optical Mapping Data. In: Camara, O., Pop, M., Rhode, K., Sermesant, M., Smith, N., Young, A. (eds.) STACOM-CESC 2010. LNCS, vol. 6364, pp. 281–290. Springer, Heidelberg (2010)
3. Christie, G.R., Nielsen, P.M., Blackett, S.A., Bradley, C.P., Hunter, P.J.: FieldML: concepts and implementation. Philosophical Transactions of the Royal Society A 367(1895), 1869–1884 (2009)
4. Dux-Santoy, L., Sebastian, R., Felix-Rodriguez, J., Ferrero, J.M., Saiz, J.: Interaction of specialized cardiac conduction system with antiarrhythmic drugs: A simulation study. IEEE Transactions on Biomedical E 58(12), 3475–3478 (2011)
5. Ecabert, O., Peters, J., Schramm, H., Lorenz, C., von Berg, J., Walker, M.J., Vembar, M., Olszewski, M.E., Subramanyan, K., Lavi, G., Weese, J.: Automatic model-based segmentation of the heart in CT images. IEEE Transactions on Medical Imaging 27(9), 1189–1201 (2008)
6. Fernandez, J.W., Mithraratne, P., Thrupp, S.F., Tawhai, M.H., Hunter, P.J.: Anatomically based geometric modelling of the musculo-skeletal system and other organs. Biomechanics and Modeling in Mechanobiology 2, 139–155 (2004)
7. Hoogendoorn, C., Pashaei, A., Sebastian, R., Sukno, F.M., Cámara, O., Frangi, A.F.: Sensitivity Analysis of Mesh Warping and Subsampling Strategies for Generating Large Scale Electrophysiological Simulation Data. In: Metaxas, D.N., Axel, L. (eds.) FIMH 2011. LNCS, vol. 6666, pp. 418–426. Springer, Heidelberg (2011)
8. Kaus, M.R., Pekar, V., Lorenz, C., Truyen, R., Lobregt, S., Weese, J.: Automated 3-d PDM construction from segmented images using deformable models. IEEE Transactions on Medical Imaging 22(8), 1005–1013 (2003)

9. Krueger, M.W., Schmidt, V., Tobón, C., Weber, F.M., Lorenz, C., Keller, D.U.J., Barschdorf, H., Burdumy, M., Neher, P., Plank, G., Rhode, K., Seemann, G., Sanchez-Quintana, D., Saiz, J., Razavi, R., Dössel, O.: Modeling Atrial Fiber Orientation in Patient-Specific Geometries: A Semi-automatic Rule-Based Approach. In: Metaxas, D.N., Axel, L. (eds.) FIMH 2011. LNCS, vol. 6666, pp. 223–232. Springer, Heidelberg (2011)
10. Lamata, P., Niederer, S., Nordsletten, D., Barber, D.C., Roy, I., Hose, D.R., Smith, N.: An accurate, fast and robust method to generate patient-specific cubic Hermite meshes. Medical Image Analysis 15(6), 801–813 (2011)
11. Neher, P., Barschdorf, H., Dries, S., Weber, F.M., Krueger, M.W., Dössel, O., Lorenz, C.: Automatic Segmentation of Cardiac CTs - Personalized Atrial Models Augmented with Electrophysiological Structures. In: Metaxas, D.N., Axel, L. (eds.) FIMH 2011. LNCS, vol. 6666, pp. 80–87. Springer, Heidelberg (2011)
12. Peyrat, J.M., Sermesant, M., Pennec, X., Delingette, H., Xu, C., McVeigh, E.R., Ayache, N.: A computational framework for the statistical analysis of cardiac diffusion tensors: Application to a small database of canine hearts. IEEE Transactions on Medical Imaging 26(10), 1–15 (2007)
13. Sakamoto, S., Nitta, T., Ishii, Y., Miyagi, Y., Ohmori, H., Shimizu, K.: Interatrial electrical connections: The precise location and preferential conduction. Journal of Cardiovascular Electrophysiology 16(10), 1077–1086 (2005)
14. Schulte, R.F., Sands, G.B., Sachse, F.B., Dössel, O., Pullan, A.J.: Creation of a human heart model and its customisation using ultrasound images. Biomedical Engineering 46, 26–28 (2001)
15. Sebastian, R., Zimmerman, V., Romero, D., Frangi, A.F.: Construction of a computational anatomical model of the peripheral cardiac conduction system. IEEE Transactions on Biomedical En. 58, 3479–3482 (2011)
16. Sermesant, M., Delingette, H., Ayache, N.: An electromechanical model of the heart for image analysis and simulation. IEEE Transactions on Medical Imaging 25, 612–625 (2006)
17. Sermesant, M., Konukoğlu, E., Delingette, H., Coudière, Y., Chinchapatnam, P., Rhode, K.S., Razavi, R., Ayache, N.: An Anisotropic Multi-front Fast Marching Method for Real-Time Simulation of Cardiac Electrophysiology. In: Sachse, F.B., Seemann, G. (eds.) FIHM 2007. LNCS, vol. 4466, pp. 160–169. Springer, Heidelberg (2007)
18. Smith, N., de Vecchi, A., McCormick, M., Nordsletten, D., Camara, O., Frangi, A.F., Delingette, H., Sermesant, M., Relan, J., Ayache, N., Krueger, M.W., Schulze, W.H.W., Hose, R., Valverde, I., Beerbaum, P., Staicu, C., Siebes, M., Spaan, J., Weese, P.H.J., Chapelle, H.L.D., Rezavi, R.: euHeart: personalized and integrated cardiac care using patient-specific cardiovascular modelling. Interface Focus 1(3), 349–364 (2011)
19. Streeter, D., Spontnitz, H., Patel, D., Ross, J., Sonnenblick, E.: Fiber orientation in the canine left ventricle during diastole and systole. Circulation Research 24, 339–347 (1969)
20. Waechter, I., Kneser, R., Korosoglou, G., Peters, J., Bakker, N.H., van der Boomen, R., Weese, J.: Patient Specific Models for Planning and Guidance of Minimally Invasive Aortic Valve Implantation. In: Jiang, T., Navab, N., Pluim, J.P.W., Viergever, M.A. (eds.) MICCAI 2010, Part I. LNCS, vol. 6361, pp. 526–533. Springer, Heidelberg (2010)
21. Zheng, Y., Barbu, A., Georgescu, B., Scheuering, M., Comaniciu, D.: Four-chamber heart modeling and automatic segmentation for 3d cardiac CT volumes using marginal space learning and steerable features. IEEE Transactions on Medical Imaging 27(11), 1668–1681 (2008)

# A Near-Incompressible Poly-affine Motion Model for Cardiac Function Analysis

Kristin McLeod[1], Christof Seiler[1,2], Maxime Sermesant[1], and Xavier Pennec[1]

[1] INRIA Méditerranée, Asclepios Project, Sophia Antipolis, France
[2] Institute for Surgical Technology and Biomechanics, University of Bern, Switzerland

**Abstract.** Understanding the motion of the heart through the cardiac cycle can give useful insight for a range of different pathologies. In particular, quantifying regional cardiac motion can help clinicians to better determine cardiac function by identifying regions of thickened, ischemic or infarcted tissue. In this work we propose a method for cardiac motion analysis to track the deformation of the left ventricle at a regional level. This method estimates the affine motion of distinct regions of the myocardium using a near incompressible non-rigid registration algorithm based on the Demon's optical flow approach. The global motion over the ventricle is computed by a smooth fusion of the deformation in each segment using an anatomically aware poly-affine model for the heart. We apply the proposed method to a data-set of 10 volunteers. The results indicate that we are able to extract reasonably realistic deformation fields parametrised by a significantly reduced number of parameters compared to voxel-wise methods, which better enables for statistical analyses of the motion.

## 1 Introduction

Better understanding the motion of the heart through the cardiac cycle is crucial in aiding diagnosis and therapy planning for patients with heart defects and in particular for those that are known to have deformed ventricular shape. However, tracking cardiac motion from 3D images is a difficult task due to the complex movement of the myocardium through the cardiac cycle.

The clinical challenge is to capture the apparent cardiac motion from the available data (i.e 3D cine MRI sequences), and for this we can apply non-rigid registration algorithms. In this case we require methods that are not only fast but also reproducible and robust (able to handle noisy and low resolution images). In order to compare the heart beat motion of a number of patients, we also require the tracked motion deformation to be characterised by a small number of parameters. Rigid-body or affine motion would do this but is not sufficient in capturing the observed dynamics. Therefore we are interested in finding a compromise between rigid (or affine) and non-rigid deformations.

A recently proposed method for tracking cardiac motion using cine MRI is the incompressible log-domain Demons algorithm (iLogDemons for short) [1].

O. Camara et al. (Eds.): STACOM 2012, LNCS 7746, pp. 288–297, 2013.

This method has the nice advantage of ensuring near incompressibility in the myocardial region; a realistic constraint for the heart given that the myocardial muscle volume changes by around 5-10% during the cycle. However, the motion is highly localised since the deformation is considered on a voxel-by-voxel basis making the method sensitive to image noise and constrained by a high number of degrees of freedom. Therefore we are interested in tracking the motion in a more regional manner to capture a more realistic global deformation as well as including some anatomical priors in the regional regularisation process.

For that purpose, an interesting regional regularisation method was proposed in [2] to register mandibles by using the log-domain Demons algorithm [3] and in each region estimating the affine transformation from the resulting deformation field and fusing to a global deformation using the poly-affine model proposed by Arsigny et. al [4]. A poly-affine model was applied in cardiac imaging in [5] for 2D+t multi-modal images. In this last work the poly-affine model is based on an adaptive grid to determine the poly-affine regions. When going to 3D, interpretation of the results could be made easier with a lower number of regions that are anatomically grounded. In [5] the regions are determined on the fly by the images, and are thus without inter-subject reproducibility. A 3D combination of locally affine transformations was used in [6] as an initialisation step to a free-form deformation for cardiac image segmentation. This approach could be improved by coupling the poly-affine deformation with the non-rigid deformation rather than using only as an initialisation.

Inspired by the method of Seiler et. al [2], we propose in this paper to track cardiac motion by estimating an affine transformation in given regions of the left ventricle (LV) myocardium from a computed Log-Demons velocity field [3], with added penalisation to control the compressibility of the tissue. We apply the proposed method to estimate the left-ventricular motion of a 3D data-set of 10 volunteers from the STACOM 2011 MICCAI workshop motion tracking database [7]. We compare the results to the iLogDemons algorithm to deduce that we are able to obtain similar results at a significantly lower degree of parametrisation, which enables statistical analyses to be applied directly to the reduced parametrisation rather than the full iLogDemons velocity field.

## 2 Cardiac Motion Tracking with a Near-Incompressible Log-Domain Poly-affine Model

We propose an algorithm for regional cardiac motion tracking that utilises the log-domain Demons algorithm (LogDemons) to estimate the motion of the left ventricle at a local level, in a given set of physiologically meaningful regions. This way, we can define a diffeomorphic transformation from one image to another. From this deformation, we estimate the affine parameters in each region to determine a global affine transformation to give a more regional based motion for each segment. The regional deformation fields are fused in a smooth manner using the poly-affine model. The key contribution of this work is an added penalisation term to the affine parameter estimation to control the amount of

compressibility we allow in each region, as well as an added regularisation term to control the similarity between regions, both formulated as efficient quadratic criteria.

**AHA Left Ventricle Segmentation.** Using the American Heart Association (AHA) standardised myocardial segmentation, we can define anatomically meaningful regions of the ventricle [8]. The recommendation given by the AHA is to divide the left ventricle of the heart into 17 regions with six regions for the basal area (1-6), six regions for the mid area (7-12) and five for the apical areas (13-17).

**Log-Domain Demons Registration.** We are interested in tracking the motion of the heart from a reference time point (in this case we use end diastole as the reference) to the remaining time points along the cardiac sequence. To do this we want to estimate the transformation $\phi$ that minimises the distance between the reference image $R$ and the target image $T$. For this we employ the Log-Demons algorithm which has the key property that the transformations are constrained to be diffeomorphic (therefore don't allow folding and are invertible), as well as enabling efficient computation in the log-domain by integrating stationary velocity fields using the exponential scaling and squaring method [3].

**Poly-affine Registration.** The poly-affine registration algorithm proposed in [4] and extended further in [9] allows to fuse locally affine transformations into a global diffeomorphism using weight functions. The method is suitable for cardiac motion tracking due to the fact that the deformations are computed in the log-Euclidean framework and therefore has the advantage that the transformations are invertible (and the inverse is also a poly-affine transformation).

**Poly-affine LogDemons.** In Seiler et.al [2], the authors propose a method to estimate a poly-affine model from a log demons deformation field. Using homogeneous co-ordinates, the parameters of the poly-affine model can be defined for points $x$ in Cartesian co-ordinates as

$$\log(T) \stackrel{\text{def}}{=} \log \begin{pmatrix} A & t \\ 0 & 1 \end{pmatrix} = \begin{pmatrix} M \\ 0 \end{pmatrix} \tag{1}$$

where log is a principal matrix logarithm, $A$ is the linear part of the transformation, $t$ its translation, and $M$ a $3 \times 4$ matrix. For each segment the affine deformation fields parameterised by the $M_i$ matrices are fused to a global deformation field using the poly-affine model:

$$\boldsymbol{v}_{poly}(x) = \sum_i \omega_i(x) M_i x, \tag{2}$$

where $\omega_i$ is a parameter controlling the weight of the $i^{th}$ region for each voxel $x$. Eqn. 2 can be estimated by a linear least squares problem with the least squares

error with respect to the observed velocity field $\boldsymbol{v}(x)$ (in this case computed using the LogDemons algorithm) given by:

$$C(M_1, M_2, \cdots, M_N) = \int_\Omega \parallel \sum_i \boldsymbol{v}_{poly}(x) - \boldsymbol{v}_{obs}(x) \parallel^2 dx. \tag{3}$$

$\Omega$ defines the mask to restrict the estimation within the myocardium (1 inside the binary mask of the myocardium, 0 outside). As shown in [2] the log affine parameters $M_i$ can be estimated by the least-squares minimisation problem given in Eq. 3 to give

$$M = B\Sigma^{-1}, \tag{4}$$

where $M = [M_1 M_2 \cdots M_3]$, $B_i = \int \omega_i(x) \cdot \boldsymbol{v}(x) \cdot x^T dx$ and $\Sigma_{ij} = \int \omega_i(x) \cdot \omega_j(x) \cdot x \cdot x^T dx$. Equivalently, the least-squares solution can be written in terms of vectors:

$$\bar{M} = (\Sigma \otimes I_3)^{-1} \cdot \bar{B}, \tag{5}$$

where $\bar{M}$ (resp. $\bar{B}$) is the standard matrix vectorisation of $M$ (resp. $B$), $\otimes$ is the Kronecker Product.

### 2.1 Left-Ventricle Poly-affine Model

The weights $\omega_i(x)$ can be defined by a simple Gaussian function as

$$\omega_i(x) = -\exp\left(\frac{1}{2}(x - \bar{x}_i)^T \phi_i^{(-1)}(x - \bar{x}_i)\right), \tag{6}$$

with $\bar{x}_i$ the barycentre (centre point) of zone $i$ and $\phi_i$ the corresponding covariance matrix as in [2].

**Incompressibility Penalisation.** In order to control the compressibility of the myocardium to be within physiological ranges, an added penalisation term is needed. Given that a transformation is incompressible if its Jacobian determinant is equal to one, for an infinitesimal transformation $T = I + \boldsymbol{v}_{poly}$ with $\nabla T = I + \nabla \boldsymbol{v}_{poly}$ we have

$$\det(\nabla T) = \det(I + \nabla \boldsymbol{v}_{poly}) = Tr(\nabla \boldsymbol{v}_{poly}) + \mathcal{O}(\parallel \nabla \boldsymbol{v}_{poly}) \parallel^2). \tag{7}$$

Here $\mathcal{O}(\cdot)$ represents higher order terms. Therefore the velocity field $\boldsymbol{v}_{poly}$ is locally incompressible if the trace of $\nabla \boldsymbol{v}_{poly}$ is zero. A penalisation term can then be derived as:

$$\alpha \int_\Omega Tr(\nabla \boldsymbol{v}_{poly})^2 dx. \tag{8}$$

The parameter $\alpha$ is used to control the strength of the penalisation. Incorporating this term into the least squares minimisation (3) gives the penalised least squares formula:

$$C(M_1, M_2, \cdots, M_N) = \int_\Omega \parallel \sum_i \omega_i(x) \cdot M_i \cdot x - \boldsymbol{v}_{obs}(x) \parallel^2 dx + \alpha \int_\Omega Tr(\nabla \boldsymbol{v}_{poly})^2 dx \tag{9}$$

To incorporate the new term into the least squares computation, (8) needs to be re-formulated to obtain a quadratic form of $\bar{M}$. Taking the partial derivative of the poly-affine velocity field with respect to $x$ gives

$$\frac{\partial \boldsymbol{v}_{poly}(x)}{\partial x} = \sum_i \left( \omega_i(x) M_i \begin{bmatrix} I_3 \\ 0 \end{bmatrix} + M_i \cdot x \cdot \frac{\partial \omega_i(x)}{\partial x} \right). \tag{10}$$

Using $T = \text{vect}[I_3; 0])$ to extract the diagonal elements from the matrix, we have

$$Tr(\nabla \boldsymbol{v}_{poly}(x)) = \sum_i \left( \omega_i(x) \cdot T^T \cdot \text{vect}(M_i) + g_i(x)^T \cdot \text{vect}(M_i) \right), \tag{11}$$

with $g_i(x) = \text{vect}(\nabla \omega_i(x) \cdot x^T)$. A penalisation term can then be derived as:

$$\alpha \int_\Omega Tr(\nabla \boldsymbol{v}_{poly})^2 dx = \alpha \sum_{i,j} \text{vect}(M_i)^T \cdot V_{ij} \cdot \text{vect}(M_j) \tag{12}$$

with $V_{ij} = \int_\Omega (\omega_i(x) \cdot T + g_i(x))(\omega_j(x) \cdot T + g_j(x))^T dx$. Seemingly, this could be simplified to consider only the first order terms: $V_{ij} = \int_\Omega (\omega_i(x) \cdot T)(\omega_j(x) \cdot T)^T dx$. This is sufficient to penalise the trace per region, but does not take into account the directional information meaning that neighbouring regions can have high deformations in opposing directions, causing problems in the overlap.

**Regularisation Term.** We can also define a regularise term to control how neighbouring regions influence one another. The weights $\omega_i(x)$ control how smooth the transition is between two regions, however we would also like to control how similar the affine matrices are, as an addition regularisation. To do this we can add an additional term:

$$\sum_{ij} \pi_{ij} dist(M_i, M_j). \tag{13}$$

Defining a matrix $Q$ such that $Q = \left[\begin{array}{c|c} I_3 & 0 \\ \hline 0 & \mu \end{array}\right]$ allows to account for the different scaling between the rotation/sheering part of the affine matrix and the translation part. The distance term can be written as:

$$\begin{aligned} dist^2(M_i, M_j) &= Tr[(M_i - M_j)^T \cdot Q \cdot (M_i - M_j)] \\ &= Tr(M_i^T Q M_i) + Tr(M_j^T Q M_j) - 2Tr(M_i^T \cdot Q \cdot M_j), \end{aligned} \tag{14}$$

with

$$Tr(M_i^T Q M_j) = \text{vect}(M_i^T Q)^T \cdot \text{vect}(M_j) = \text{vect}(M_i)^T \cdot (Q \otimes I_3) \cdot \text{vect}(M_j). \tag{15}$$

Setting

$$l_{ij} = \begin{cases} -\pi_{ij} = -\int_\Omega \omega_i(x) \omega_j(x) dx & \text{for } i \neq j \\ \sum_{k \neq i} \pi_{ij} = \sum_{k \neq i} \int_\Omega \omega_i(x) \omega_k(x) dx & \text{for } i = j \end{cases}$$

we can account for the correlation between regions. Thus we obtain

$$\sum_{i,j} l_{ij} Tr(M_i^T \cdot Q \cdot M_j) = \bar{M}^T \cdot L \otimes (Q \otimes I_3) \cdot \bar{M}. \quad (16)$$

For $R = L \otimes (Q \otimes I_3)$ the penalised least squares error is given by:

$$C(M) = \bar{M}^T (\Sigma \otimes I_3) \bar{M} - \bar{M}^T \cdot \bar{B} + \alpha \cdot \bar{M}^T \cdot V \cdot \bar{M} + \beta \cdot \bar{M}^T \cdot R \cdot \bar{M}, \quad (17)$$

where $\beta$ controls the strength of the regularisation. We want to find the optimum by solving $\nabla C_M = 0$.

$$\nabla C_M = (\Sigma \otimes I_3 + \alpha V + \beta R) \bar{M} - \bar{B}. \quad (18)$$

Therefore the solution for $M$ is given by:

$$\bar{M} = (\Sigma \otimes I_3 + \alpha V + \beta R)^{-1} \cdot \bar{B} \quad (19)$$

**Algorithm 1.** Heart Poly-Affine Near-Incompressible Log-Domain Demons (Regional iLogDemons)

- Segment LV into 17 AHA zones
- Let $\boldsymbol{v}_{poly}(x) = I$ (identity transformation)

**Require:** Let $\boldsymbol{v}^0 = v_{poly}(x)$

**loop** {*over n until convergence*}

- Compute the update velocity: $\delta \boldsymbol{v}^n$ given $\boldsymbol{v}^{n-1}$.
- Update the correspondence velocity field: $\boldsymbol{v}^n \leftarrow Z(\boldsymbol{v}^{n-1}, \delta \boldsymbol{v}^n)$.
- Estimate affine transformation of each segment from $\boldsymbol{v}^n$ by solving (2) under the incompressibility penalisation (19).
- Let $\boldsymbol{v}_{poly}(x) \leftarrow \sum_i \omega_i(x) M_i x$

**return** $\boldsymbol{v}$, $\phi = \exp(\boldsymbol{v})$ and $\phi^{-1} = \exp(-\boldsymbol{v})$.

## 3 Left-Ventricular Motion Tracking in Healthy Volunteers

*Patient Data and Preparation.* We illustrate these tools on 10 volunteers (3 females, mean age ± SD = 28±5) obtained from the STACOM 2011 MICCAI cardiac motion tracking challenge database [7]. Steady-state free precision cine MRI were acquired using a 3T scanner (Philips Achieva System, Philips Healthcare) in the short axis view covering entirely both ventricles (12-15 slices; isotropic in-plane resolution:1.21x1.21mm to 1.36x1.36mm; slice thickness: 8mm; 30 frames).

*Myocardium Mask and AHA Segment Delineation.* We extract a binary mask image to define the left ventricle myocardium where the least squares minimisation is computed. To do this we to define a surface mesh of the myocardium by

annotating the boundary of the ventricle directly on the given patient images, and create a surface mesh (and related binary mask) from these annotations. This was done with a 3D interactive segmentation tool based on implicit variational surfaces and provided within the CardioViz3D package[1]. Each LV mesh was then divided into 17 regions according to the AHA recommendations using a semi-automatic C++ segmentation tool that required just the input of four landmarks to define the base, apex, LV-RV junction on anterior and LV-RV junction on posterior.

### 3.1 Results

In order to determine a suitable range of parameters for $\alpha$ and $\beta$ a set of simulations were run for one patient fixing $\alpha$ (resp. $\beta$) and ranging $\beta$ (resp. $\alpha$) (see Fig. 1). From this analysis, the values for $\alpha$ and $\beta$ were set for all patients as $\alpha = 1$ and $\beta = 10$. Higher values of $\beta$ give better values for the Jacobian determinant, but result in over regularisation of the field, converging towards a single affine transformation and thus restricting the global motion. Values of $\alpha$ greater than 10 (towards an incompressibility constraint rather than projection) result in numerical instabilities in the matrix inversion of Eq. 19.

From each of the computed frame-to-reference deformation fields, the corresponding Jacobian determinant images were computed. The average value within each of the AHA regions was calculated and the average per region for all patients is shown in Fig 2 (left), to show the amount of regional compression (or expansion) in the myocardium. The strain was computed over the cycle in each of the circumferential, radial and longitudinal directions, and averaged over each of the AHA regions. In Fig. 2 we show the average strain in each direction of all patients per region.

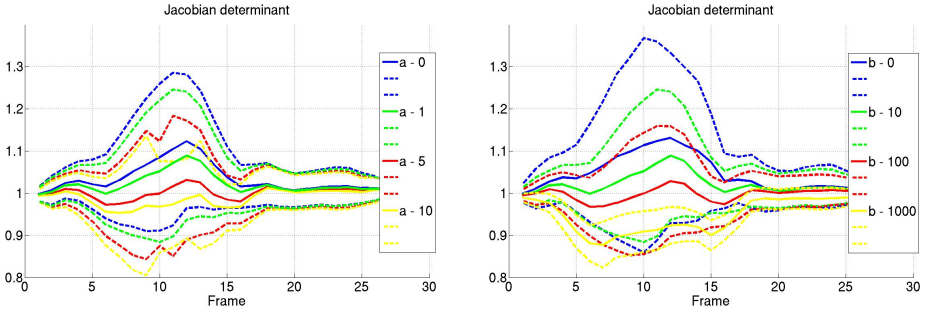


**Fig. 1.** Mean and standard deviation of the Jacobian determinant for one patient computed as an average over each AHA zone with varied values of $\alpha$ (left) and $\beta$ (right). A reasonable trade-off between the range and smoothness of the Jacobian determinant is given for $\alpha = 1$, $\beta = 10$.

[1] http://www-sop.inria.fr/asclepios/software/CardioViz3D/

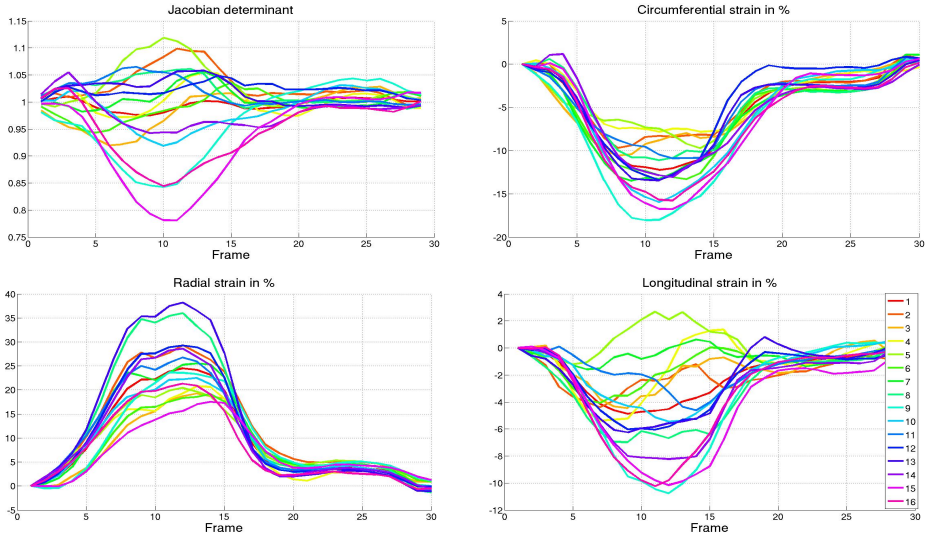


**Fig. 2.** Left: Plot of the average Jacobian determinant per AHA region averaged for all patients, shown at each frame of the cycle. The plot shows that the volume change of the left ventricle is maintained with 15% over the cycle (each region shown in a different colour). Regional strain curves computed in the circumferential (centre-left), radial (centre-right), and longitudinal (right) directions for each of the 17 AHA regions then averaged over the patients.

The values of the strain, Jacobian determinant and the apparent registration accuracy based on the figures shown in Fig. 4, can be compared directly to the results obtained from the STACOM 2011 MICCAI workshop cardiac motion tracking challenge algorithms applied to the same data-set [7]. The left ventricular volume was compared between the iLogDemons algorithm and the proposed algorithm (see Fig. 3) showing an ejection fraction of 50% and 58% resp. (note the normal range is $55-70\%$ and typical value is 58% [10]). These results suggest that the method is able to obtain comparable registration, strain curves, and left ventricular volume to those for the iLogDemons algorithm [11].

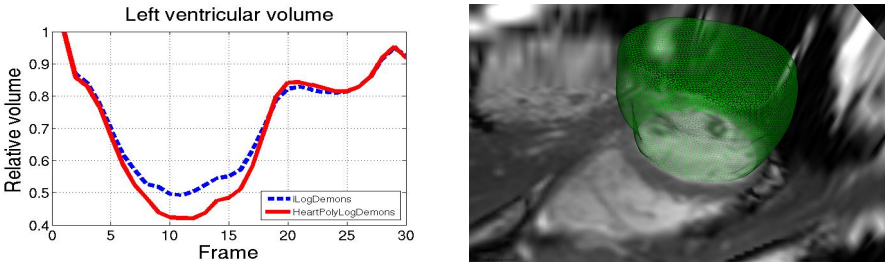


**Fig. 3.** Left ventricular volume along the cardiac cycle for the iLogDemons algorithm (blue dashed line), and proposed algorithm (red solid line) shown in relative measures to the end-diastolic volume (left), computed from deforming the 3D segmented end-diastolic volume mesh (right).

To exemplify the results of the registration for one individual, the mesh segmented at the reference frame (end diastole) is overlaid on the reference image (see Fig. 4 top row). The same mesh is deformed by the poly-affine deformation field computed from peak contraction to reference, and the resulting mesh is overlaid on the peak contraction image (see Fig. 4 bottom row). The results show good alignment between the deformed peak systole mesh and the image.

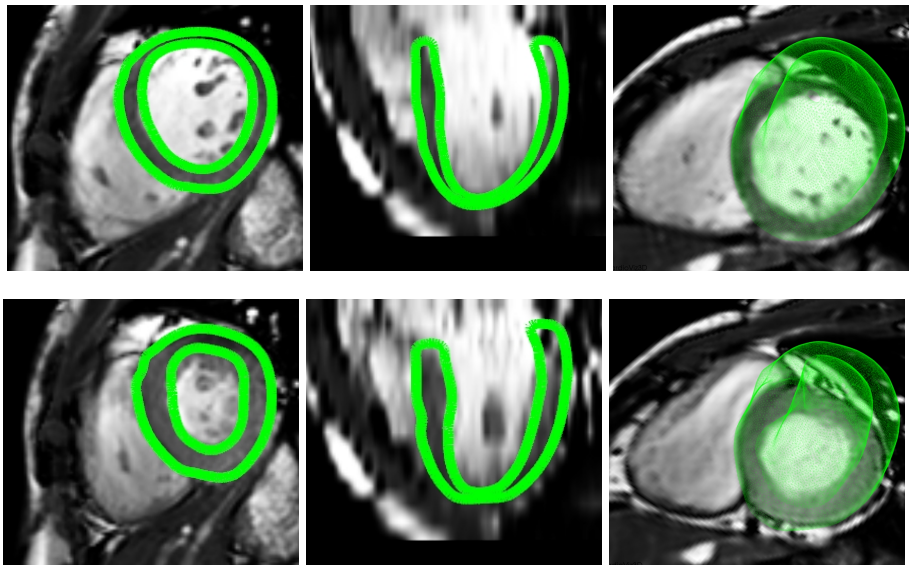

**Fig. 4.** Top row: Three views of the reference frame (end diastole) with segmented mask over-laid in green. Bottom row: Same views of peak systole with the segmented reference mask deformed by the computed poly-affine deformation field. The results in the bottom row indicate that the registration provides reasonable deformation fields that capture the motion of the heart.

## 4 Discussion and Future Work

The results suggest that the method is able to track the cardiac motion reasonably well and with less than 20% volume change in the myocardium for all patients and all regions. Moreover, we are able to parameterise the deformation by 204 parameters, as opposed to over 5 million parameters for the iLogDemons algorithm (or similarly for other registration algorithms parameterised at the voxel level). Full incompressibility can only be achieved in this model with a global affine incompressible deformation, thus with so few degrees of freedom, the volume change is penalised within reasonable ranges. Using more regions may possibly improve the results with respect to the incompressibility.

This paper describes a proof of concept of the method. More work is needed to better understand the weight functions, the choice of suitable regions, as well as

the optimal number of regions. Given that the definition of the regions is consistent in this work from subject to subject, we expect to obtain reproducible and powerful clinical scores to characterise different heart conditions. A long term objective is to use the computed parameters as clinical scores to aid in quantifying healthy heart motion and then to analyse the motion in the pathological case.

**Acknowledgements.** This project was partially funded by the Care4Me ITEA2 project and the Swiss National Science Foundation.

## References

1. Mansi, T., Pennec, X., Sermesant, M., Delingette, H., Ayache, N.: iLogDemons: A demons-based registration algorithm for tracking incompressible elastic biological tissues. Int. J. of Comp. Vision 92(1), 92–111 (2011)
2. Seiler, C., Pennec, X., Reyes, M.: Capturing the multiscale anatomical shape variability with polyaffine transformation trees. Medical Image Analysis (2012) (in press)
3. Vercauteren, T., Pennec, X., Perchant, A., Ayache, N.: Symmetric Log-Domain Diffeomorphic Registration: A Demons-Based Approach. In: Metaxas, D., Axel, L., Fichtinger, G., Székely, G. (eds.) MICCAI 2008, Part I. LNCS, vol. 5241, pp. 754–761. Springer, Heidelberg (2008)
4. Arsigny, V., Commowick, O., Ayache, N., Pennec, X.: A fast and log-euclidean polyaffine framework for locally linear registration. J. of Math. Imaging and Vision (JMIV) 33(2), 222–238 (2009)
5. Zhang, W., Brady, J.M., Becher, H., Noble, J.A.: Spatio-temporal (2d+t) non-rigid registration of real-time 3d echocardiography and cardiovascular mr image sequences. Physics in Medicine and Biology 56(5), 1341 (2011)
6. Zhuang, X., Rhode, K., Razavi, R., Hawkes, D., Ourselin, S.: A registration-based propagation framework for automatic whole heart segmentation of cardiac mri. IEEE Transactions on Medical Imaging 29(9), 1612–1625 (2010)
7. Tobon-Gomez, C., De Craene, M., Dahl, A., Kapetanakis, S., Carr-White, G., Lutz, A., Rasche, V., Etyngier, P., Kozerke, S., Schaeffter, T., Riccobene, C., Martelli, Y., Camara, O., Frangi, A.F., Rhode, K.S.: A Multimodal Database for the $1^{st}$ Cardiac Motion Analysis Challenge. In: Camara, O., Konukoglu, E., Pop, M., Rhode, K., Sermesant, M., Young, A. (eds.) STACOM 2011. LNCS, vol. 7085, pp. 33–44. Springer, Heidelberg (2012)
8. Cerqueira, M., Weissman, N., Dilsizian, V., Jacobs, A., Kaul, S., Laskey, W., Pennell, D., Rumberger, J., Ryan, T., Verani, M.: Standardized myocardial segmentation and nomenclature for tomographic imaging of the heart. Circulation 105, 539–542 (2002)
9. Commowick, O., Arsigny, V., Isambert, A., Costa, J., Dhermain, F., Bidault, F., Bondiau, P.Y., Ayache, N., Malandain, G.: An efficient locally affine framework for the smooth registration of anatomical structures. Medical Image Analysis 12(4), 427–441 (2008)
10. Talley, N., O'Connor, S.: Clinical Examination: A Systematic Guide to Physical Diagnosis. Churchill Livingstone, Elsevier Health Sciences (2009)
11. McLeod, K., Prakosa, A., Mansi, T., Sermesant, M., Pennec, X.: An Incompressible Log-Domain Demons Algorithm for Tracking Heart Tissue. In: Camara, O., Konukoglu, E., Pop, M., Rhode, K., Sermesant, M., Young, A. (eds.) STACOM 2011. LNCS, vol. 7085, pp. 55–67. Springer, Heidelberg (2012)

# Towards Real-Time Computation of Cardiac Electrophysiology for Training Simulator

Hugo Talbot[1,2], Christian Duriez[2], Hadrien Courtecuisse[2], Jatin Relan[1], Maxime Sermesant[1], Stéphane Cotin[2], and Hervé Delingette[1]

[1] ASCLEPIOS Group, INRIA Sophia-Antipolis, France
[2] SHACRA Group, INRIA Lille North Europe, France

**Abstract.** This work aims at developing a training simulator for interventional radiology and thermo-ablation of cardiac arrhythmias. To achieve this, a real-time model of the cardiac electrophysiology is needed, which is very challenging due to the stiff equations involved. In this paper, we detail our contributions in order to obtain efficient cardiac electrophysiology simulations. First, an adaptive parametrisation of the Mitchell-Schaeffer model as well as numerical optimizations are proposed. An accurate computation of both conduction velocity and action potential is ensured, even with relatively coarse meshes. Second, a GPU implementation of the electrophysiology was realised in order to decrease the computation time. We evaluate our results by comparison with an accurate reference simulation using model parameters, personalized on patient data. We demonstrate that a fast simulation (close to real-time) can be obtained while keeping a precise description of the phenomena.

## 1 Introduction

Cardiac arrhythmias are characterised by a pathological electrical activity in the myocardium (heart muscle) which can be lethal. Catheter thermo-ablation is a minimally invasive technique that can prevent fibrillation by removing the substrate or the trigger of such a phenomenon through the ablation of the responsible cardiac cells. This procedure is performed by highly skilled and experienced interventional cardiologists, yet the success rate remains limited due to the complexity of such pathologies. Moreover, due to population ageing, an important increase is predicted in such arrhythmias, without an associated increase in interventional cardiologists. Therefore, there will be an important need for novel tools in learning, training and planning, such as simulators.

One important missing step towards the development of such a simulator is the ability to simulate the electrophysiology of the heart in real-time. The electrical wave propagating inside the cardiac walls corresponds to ion exchanges between the cells and through the cell membrane. The myocardial cells are polarised, i.e. there is a potential difference between the inside and the outside of the cells. This potential difference is called action potential (AP) or transmembrane potential. Before a thermo-ablation, cardiologists first carry out a diagnostic electrophysiological study (programmed electrical stimulation) allowing a

O. Camara et al. (Eds.): STACOM 2012, LNCS 7746, pp. 298–306, 2013.

definitive diagnosis. From the acquired data, the ablation intervention can be planned. We focus here on the training of cardiologists for these catheter-based ablation of cardiac tissues in the context of cardiac arrhythmias.

Research on cardiac electrophysiology models is very active. The proposed models can be divided into three different classes: (i) biophysical models, which are complex models including the different ionic concentrations and channels, involving many parameters and simulating the electrophysiology close to the cellular scale [14]; (ii) phenomenological models, which are simplified models [13], [1], [7], [10] derived from the biophysical models, involving less parameters and capturing the AP shape and its propagation at the organ scale; (iii) Eikonal models [8], which correspond to static non-linear partial differential equations for the depolarization time derived from the previous models. These models enable to simulate wave propagation but cannot accurately account for complex physiological states and the parameters have no direct physiological meaning.

This paper addresses the problem of real-time simulation of electrophysiology thanks to a new modelling approach adapted to efficient computational strategies. The approach relies on one of the phenomenological models from Mitchell-Schaeffer (MS) [10]. The following sections presents the MS model, the model parameters and the numerical settings. Then we detail how we adapt the model parameters and numerical settings in order to recover patient-specific features, namely the conduction velocity (CV) and the action potential duration (APD, denoting APD90). To further improve our computation times, we propose an efficient GPU implementation with CUDA. Finally, we present our first results on patient-specific data and we conclude with some ideas for future work.

## 2 Real-Time Cardiac Electrophysiology Simulation

### 2.1 Discretisation of the Cardiac Electrophysiology Model

**Mitchell-Schaeffer Model.** For the last fifty years, numerous models were proposed for the cardiac cell AP. Regarding the features of the model categories presented previously, the phenomenological models meet best our requirements in terms of computational efficiency at the organ scale. The model that we chose is the MS model [10] because of the following reasons:(*i*) it has only 5 parameters that we detail below, (*ii*) each parameter has a physiological meaning and (*iii*) it provides a better estimation of the AP compared to other phenomenological models (as the Aliev-Panfilov model [1]).

The MS model is a two-variable model derived from the Fenton Karma model [7]. The equations describing the model are written in 1:

$$\begin{cases} \partial_t u = div(D\nabla u) + \dfrac{zu^2(1-u)}{\tau_{in}} - \dfrac{u}{\tau_{out}} + J_{stim}(t) \\ \partial_t z = \begin{cases} \dfrac{(1-z)}{\tau_{open}} & \text{if} \quad u < u_{gate} \\ \dfrac{-z}{\tau_{close}} & \text{if} \quad u > u_{gate} \end{cases} \end{cases} \tag{1}$$

where $u$ is a normalized transmembrane potential[1] and $z$ is the gating variable associated to the sodium ion influx, thus depicting the repolarization phase. The extra-cellular potential can be recovered using the method described in [4]. The diffusion term is defined by an 3x3 anisotropic diffusion tensor $D = d{\cdot}diag(1, r, r)$ so that the planar conduction velocity in the fiber direction is 2.5 times greater than in the transverse plane ($r = \frac{1}{(2.5)^2}$). $d$ is the diffusion coefficient. The parameters $\tau_{in}$ and $\tau_{out}$ define the repolarization phase whereas the constants $\tau_{open}$ and $\tau_{close}$ manage the gate opening or closing depending on the change-over voltage $u_{gate}$. The term $J_{stim}(t)$ is the stimulation current applied in the pacing area. The default values (describing the common action potential) of these parameters are given in [10]. The initial conditions of our simulation were set as Dirichlet conditions. The pacing area ($u_0 = 1$ and $z_0 = 1$) has been extracted from the depolarization time map.

**Patient-Specific Spatial Discretisation.** The cardiac geometry that we used in this study is an anatomy segmented from a patient MRI. This patient suffers from chronic ischemia and a left bundle branch block (noted LBBB).

The method used for the spatial discretization of the model is the finite element method which requires a volumetric mesh of the myocardium. The volumetric bi-ventricular geometry has been meshed with linear tetrahedra using CGAL (www.cgal.org) algorithms. The edge size used is about $dx = 4\ mm$ and implies 65547 tetrahedra which is already substantial for real-time simulation. Usually the usual edge size required for cardiac electrophysiology is $dx < 0.1\ mm$. However the element size has to be fine enough to correctly model the wave propagation, especially in the grey zones around scars. Scar regions are known to be very unstable electrical zones and can be responsible for cardiac reentries. These areas therefore need to be discretized with accuracy.

A LBBB abnormal conduction implies a late activation of the left ventricle. Regarding this pathology, the edge size of 4 $mm$ should be sufficient for our simulation since only the times of depolarization and repolarization have to be computed accurately. However to model a possible ventricular tachycardia induced by an isthmus the edge size should be finer. As demonstrated in [9], a 0.8 $mm$ edge size must be used for accurate simulation.

**Time Integration Scheme.** For all our simulations, we use the second-order semi-implicit solver called Modified Crank Nicholson/Adams Bashforth (MCNAB), detailed in [6]. This solver defines an implicit integration of the diffusion term and an explicit integration of the ionic current. The construction of the matrix system leads to a symmetric definite positive case that we can solve using many existing algorithms.

In our GPU simulations, we work with a conjugate gradient (CG) to solve the resulting linear system (written $\mathbf{A}x = b$). To improve the convergence rate, we

[1] The MS is a monodomain model since it is expressed according to the transmembrane potential whereas bidomain models depends on both intra- and extra-cellular potential.

use a preconditioner Jacobi. The Jacobi method computes the inverse matrix of the diagonal of the system matrix **A**. Since our matrix **A** is diagonal dominant, the use of this preconditioner is straightforward. The factorization provided by the Jacobi method can be updated when needed, thus allowing to interact with the model (e.g. thermo-ablation).

### 2.2 Numerical Study

To achieve our performance goal, the numerical settings of our simulation need to be optimized. In the literature about cardiac electrophysiology simulation, it is shown that both element size and time step have to be small enough to capture the cardiac phenomenon. Usual values for the edge size are defined such that $dx \leq 0.1\ mm$ and the time step is lower than $dt \leq 0.01\ ms$ (see [11]). However meshing a heart geometry with such small elements would imply millions of tetrahedra. Such small elements as well as very small time steps prevent real-time simulations. To achieve real-time performances, we have to use larger time steps and larger finite-element. In this part, we study the impact of using large elements, the limitation in terms of time step as well as solutions to reach real-time performances.

**Locally-Adapted Model Parameters.** To ensure the reliability of the training simulation, we need a relatively accurate computation of the CV. Nevertheless using large elements will affect the diffusion effect, i.e. the wave propagation and its CV. We studied the influence of the element size on the CV with the lumping using the MS model on a 3D bar ($15cm \times 2.5cm \times 2.5cm$, regularly meshed) on which the wave is propagating along the bar axis with a planar front. A similar study was conducted in [11] where they also considered other integration method for the ionic term than the lumping method. The results are compared to a very accurate computation of the MS model in 1D using Matlab with a time step $dt = 10^{-5}\ s$ and a spatial step $dx = 5 \cdot 10^{-6}\ m$ that provides a CV reference value: $CV_{ref} = 0.5124\ m/s$. In the Fig. 1, the results show that the CV decreases when the mesh becomes coarse.

A way to compensate this integration error is to artificially increase the diffusion coefficient $d$. Based on this idea, a personalization of the diffusion coefficient $d$ and the opening and closing time constants $\tau_{open}$ and $\tau_{close}$ has been computed to fit measured patient data, using the personalization method of [12]. This personalization step gave us values of the diffusion coefficient for each tetrahedron, as well as values of opening and closing time constants on each vertex.

**Time-Step Limitations.** Even if the time step does not affect the electrophysiology features, the explicit formulation of the ionic term implies a stability condition on the time step. This limitation of the time step has already been pointed out in [6] and [5]. Since the diffusion is computed implicitly the limiting term is the ionic term. Following [5], we should define $dt \leq \frac{1}{|inf(\partial f)|} = \frac{\tau_{in}\tau_{out}}{\tau_{in}+\tau_{out}} = 0.286\ ms$, if we would use a semi-implicit Euler solver ($f$ denoting the ionic term).

Using the MCNAB, we measured $dt \leq 0.59\ ms$. For more stability, we will use $dt = 0.4\ ms$.

**Optimization on CG Tolerance.** As detailed in 2.1, we use a CG to solve our system. Our solver stops when the difference between the results given by two successive iterations is below the tolerance, noted $tol$. The tolerance $tol_{ref} = 10^{-10}$ ensures us to reach the "exact" solution. However to improve the computation performances, we computed the optimal tolerance value. We found the tolerance $tol_{opt} = 10^{-6}$ giving a $L^2$-error about $err = 3.79 \cdot 10^{-5}$ on the action potential field, which is fully acceptable. In the results part, we will show performances using both tolerances $tol_{ref} = 10^{-10}$ and $tol_{opt} = 10^{-6}$ in section 3.

### 2.3 GPU Implementation

The GPU architecture consists in several multi-processors able to carry out highly parallel tasks independently. The complexity of GPU programming results in defining an optimal distribution of the threads and minimizing the memory access latency. In our approach, we relied on the CUDA toolkit (dedicated to NVidia's GPUs) to develop the GPU version of the method. Similar results could be obtained using OpenCL and other GPU models.

The implementation of the ionic term of MS is based on classical parallelization methods. Using the lumping integration method, the ionic term is computed on each vertex. Therefore each thread is dedicated to one vertex and computes the contribution of the MS term for this vertex. However our computation strategy ensures a tiled access in memory in our GPU code.

The diffusion term $div(D \cdot grad(u))$ is more complicated to implement in parallel. The contribution of the diffusion term is computed from the edges and summed on each vertex. In a parallel computation, this algorithm can lead to writing conflicts: two threads solving two adjacent edges could write on the same point simultaneously. New GPUs supporting CUDA 2.0 handle now these atomic operations. Nevertheless a solution to this problem is detailed in [2] which

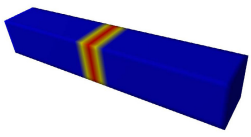

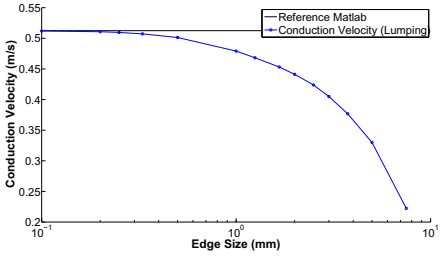


**Fig. 1.** (Left) initial conditions on the 3D bar (Right) Evolution of the CV $(m/s)$ against element size $(mm)$

is twice faster than atomic functions from CUDA. We decided to adapt this algorithm, originally designed for deformable finite element equations, to our diffusion model. This technique consists in first computing the neighborhood of each node. Then the contribution of the diffusion is computed and saved on all the edges. Finally, the contribution on each vertex is obtained by accumulating the values computed on the edges with the neighborhood information. In this last accumulation step, a parallel reduction is carried out using several threads by vertex as explained in [2].

Our GPU implementation also includes a conjugate gradient and a Jacobi preconditioner that are used to solve very quickly the electrophysiology model on the whole mesh. Only single float precision has been considered since it is sufficient regarding the electrophysiology accuracy. Moreover simulations using single float precision are about two times faster than simulations using double precision as detailed in [3].

Finally, it must be stressed that this GPU implementation is a novel application of an efficient method originally proposed by [2] for deformable finite element computations. This parallel implementation will be crucial in our performance results.

## 3 Results and Discussion

The local adaptations on the MS model that we detailed in 2.2 will still generate some errors. We now want to evaluate this error in comparison with our ground-truth data. Moreover a GPU implementation has been done to improve the computation time of our simulation. The performances using the optimized model parameters will also be assessed with this implementation.

### 3.1 Depolarization Times and APD Error Maps

We compared our results with the reference simulation using very small time step ($dt = 10^{-5}\ s$) and model parameters fitting patient data. We computed an average error on depolarization time of 4.05 $ms$ ($\sim 5.48\%$) and an average error on APD of 19.1 $ms$ ($\sim 5.62\%$). These results shows that the errors are bounded. As future work, the restitution analysis of this patient-specific case seems to be compulsory to fully validate our simulation.

### 3.2 GPU Performances

Using the optimization presented previously would not be sufficient for fast computations. However, when combined to a GPU implementation, we obtain a significant speedup. Table 3.2 sums up computation times and other metrics of performance on the CPU and on the GPU (GeForce GTX580 with 512 cores). The processor used for CPU computations is a Intel Xeon W3550.

From this table, we clearly notice the performance gain offered by the parallel implementation. The GPU simulation is more than 10 times faster than the

**Table 1.** Performance comparison between CPU and GPU

| | CPU | GPU | GPU (using $tol_{opt}$) |
|---|---|---|---|
| Mean computation time for one time step (ms) | 25.4 | 3.89 | 2.17 |
| real-time ratio (slower than real-time) | 75.8 | 7.04 | 2.95 |

CPU one. The computation time spent in the computation of diffusion and MS becomes negligible. Now the limitation of our simulation is now the solver, since it is the most time-consuming part of our computation. We notice that reasonably decreasing the tolerance of the CG significantly improves the performances.

To discuss these results, it can be stressed that 65547 tetrahedra represent a large amount of computation in a real-time context. A first solution would be to use on a coarser mesh. It must be stressed that the electrical wave of this patient was especially fast implying a small time step. Next generation GPU cards could also be most helpful.

### 3.3 User Interaction

A simulation dedicated to a training system assumes that cardiologists will interact with it. Our simulations already allow to stimulate any area of the heart in real-time (constraint with $u = z = 1$). This allows to simulate the stimulation done by the surgeon before the ablation in order to set the definitive diagnosis.

The procedure of thermo-ablation is also handled by our computations. The cardiac cells treated by thermo-ablation can not conduct the current anymore. These cells can be seen as zero conductivity area. To take this change into account, we update the factorization computed by the Jacobi method. This thermo-ablation step can therefore be done without affecting the computation times.

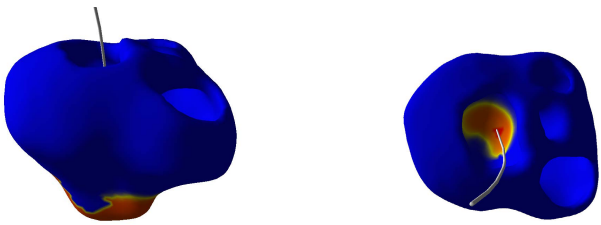

**Fig. 2.** Two different views of an electrical stimulation (with a catheter) applied by the user on a two-chamber geometry (ventricles)

## 4 Conclusion

In the coming years, the growing number of cardiology students implies to improve the training methods. Medical training simulators are an efficient solution to answer this need. Their main advantage is that simulators enable to train on virtual patient, thus avoiding to early operate on patients. Moreover such simulators could be a way of improving the course of medical studies.

In this paper, we presented some contributions to speed up simulations of cardiac electrophysiology. First, we locally modified time constant parameters from the Mitchell-Schaeffer model in order to use larger time steps and a coarser mesh. Then, we calculated the optimal time step and tolerance value for our iterative solver. Finally, we implemented a GPU version of the code modeling the diffusion and the Mitchell-Schaeffer model. With these optimizations, we reached an interactive simulation close to real-time based on 3D patient-specific data. This work is a very encouraging step toward the development of a training simulator.

In this work, only monocycle simulations have been considered, i.e. simulating only one cardiac cycle. A multicycle study needs to be carried out to analyze the restitution curves of our model and to validate our simulations. This paper presents a personalized simulation using data from a patient suffering from LBBB.

In the future, we want to address the challenging issue of simulating the electrophysiology of patients suffering from a ventricular tachycardia with an isthmus. This would lead to compute models with finer elements around the regions of interest (scars and isthmus) in order to accurately capture the electrical activity around these regions. To do so, we plan to implement innovative numerical method to use finer meshes without altering our performances.

## References

1. Aliev, R.R., Panfilov, A.V.: A simple two-variable model of cardiac excitation. Chaos, Solitons and Fractals 7(3), 293–301 (1996)
2. Allard, J., Courtecuisse, H., Faure, F.: Implicit fem solver on gpu for interactive deformation simulation. In: GPU Computing Gems, vol. 2. NVIDIA Elsevier (2011)
3. Bartocci, E., Cherry, E.M., Glimm, J., Grosu, R., Smolka, S.A., Fenton, F.H.: Toward real-time simulation of cardiac dynamics. In: Proceedings of the 9th International Conference on CMSB, pp. 103–112. ACM (2011)
4. Chhay, M., Coudière, Y., Turpault, R.: How to compute the extracellular potential in electrocardiology from an extended monodomain model. Research Report RR-7916, INRIA (2012)
5. Coudière, Y., Pierre, C.: Stability and convergence of a finite volume method for two systems of reaction-diffusion equations in electro-cardiology. Nonlinear Analysis: Real World Applications 7(4), 916–935 (2006)
6. Ethier, M., Bourgault, Y.: Semi-implicit time-discretization schemes for the bidomain model. SIAM J. Numerical Analysis 46, 2443–2468 (2008)
7. Fenton, F., Karma, A.: Vortex dynamics in three-dimensional continuous myocardium with fiber rotation. Chaos 8(1), 20–47 (1998)

8. Keener, J.P.: An eikonal-curvature equation for action potential propagation in myocardium. Journal of Mathematical Biology 29, 629–651 (1991)
9. Lamecker, H., Mansi, T., Relan, J., Billet, F., Sermesant, M., Ayache, N., Delingette, H.: Adaptive tetrahedral meshing for personalized cardiac simulations. In: CI2BM 2009 - MICCAI Workshop on Cardiovascular Interventional Imaging and Biophysical Modelling, pp. 149–158 (2009)
10. Mitchell, C., Schaeffer, D.: A two-current model for the dynamics of cardiac membrane. Bulletin of Mathematical Biology 65, 767–793 (2003)
11. Pathmanathan, P., Mirams, G., Southern, J., Whiteley, J.: The significant effect of the choice of ionic current integration method in cardiac electro-physiological simulations. International Journal for Numerical Methods in Biomedical Engineering (2011)
12. Relan, J., Sermesant, M., Delingette, H., Pop, M., Wright, G., Ayache, N.: Quantitative comparison of two cardiac electrophysiology models using personalisation to optical and mr data. In: IEEE International Symposium, pp. 1027–1030 (2009)
13. FitzHugh, R.: Impulses and physiological states in theoretical models of nerve membrane. Biophysical Journal 1(6), 445–466 (1961)
14. Tusscher, K.H.W.J.T., Noble, D., Noble, P.J., Panfilov, A.V.: A model for human ventricular tissue. American Journal of Physiology - Heart and Circulatory Physiology 286(4), 1573–1589 (2004)

# Automated Personalised Human Left Ventricular FE Models to Investigate Heart Failure Mechanics

Vicky Y. Wang[1], Corné Hoogendoorn[2], Alejandro F. Frangi[2,3], B.R. Cowan[4], Peter J. Hunter[1], Alistair A. Young[1,4], and Martyn P. Nash[1,5]

[1] Auckland Bioengineering Institute, University of Auckland, New Zealand
{vicky.wang,p.hunter,a.young,martyn.nash}@auckland.ac.nz
[2] Center for Computational Imaging & Simulation Technologies in Biomedicine: Dept. of Info. and Communication Tech., Universitat Pompeu Fabra, Barcelona, Spain
{corne.hoogendoorn,alejandro.frangi}@upf.edu
[3] Department of Mechanical Engineering, University of Sheffield, Sheffield, UK
[4] Centre for Advanced MRI, University of Auckland, New Zealand
b.cowan@auckland.ac.nz
[5] Department of Engineering Science, University of Auckland, New Zealand

**Abstract.** We have developed finite element modelling techniques to semi-automatically generate personalised biomechanical models of the human left ventricle (LV) based on cardiac magnetic resonance images. Geometric information of the LV throughout the cardiac cycle was derived via semi-automatic segmentation using non-rigid image registration with a pre-segmented image. A reference finite element mechanics model was automatically fitted to the segmented LV endocardial and epicardial surface data at diastasis. Passive and contractile myocardial mechanical properties were then tuned to best match the segmented surface data at end-diastole and end-systole, respectively. Global and regional indices of myocardial mechanics, including muscle fibre stress and extension ratio were then quantified and analysed. This mechanics modelling framework was applied to a healthy human subject and a patient with non-ischaemic heart failure. Comparison of the estimated passive stiffness and maximum activation level between the normal and diseased cases provided some preliminary insight into the changes in myocardial mechanical properties during heart failure. This automated approach enables minimally invasive personalised characterisation of cardiac mechanical function in health and disease. It also has the potential to elucidate the mechanisms of heart failure, and provide new quantitative diagnostic markers and therapeutic strategies for heart failure.

**Keywords:** Personalised FE modelling, left ventricle, *in vivo* myocardial mechanics, myocardial stiffness, maximum activation level, heart failure.

## 1 Introduction

Heart failure (HF) is a leading cause of morbidity and mortality with increasing prevalence. Whilst HF symptoms have been conventionally linked with compromised

O. Camara et al. (Eds.): STACOM 2012, LNCS 7746, pp. 307–316, 2013.

pump function (known as systolic HF), it has recently been recognised that equal numbers of patients with HF symptoms appear to have normal systolic function, but impaired diastolic filling, which has been termed diastolic HF. The inter-relationship between diastolic and systolic HF is poorly understood. To investigate changes in ventricular mechanics, personalised heart mechanics models have been used to characterise ventricular mechanical behaviour with the development of advanced cardiac imaging techniques. Such methods typically utilise geometric information of the heart derived from 3D cardiac magnetic resonance images (MRI) to build 3D mechanics models, then use them to estimate myocardial mechanical properties using dynamic MRI. Previous studies have compared healthy and diseased hearts by estimating either the passive tissue stiffness [1] or the myocardial contractility [2][3] in isolation. The primary aim of this study was to develop automated methods for creating personalised biomechanical finite element (FE) models of the heart from 3D cardiac image data and to use these models to estimate tissue stiffness and systolic contractile properties in the same hearts to investigate mechanisms of cardiac dysfunction.

This paper describes the automated fitting of a 3D cardiac mechanics model to human left ventricular (LV) surface data extracted from the Sunnybrook Cardiac database [5]. A semi-automated segmentation method was used to generate ventricular surface data for individual human hearts. The reference LV FE mechanics model was customised to surface data defined at the unloaded state (diastasis) using a nonlinear least squares fitting technique. After incorporating fibre orientations from the Auckland canine heart model [11] and cavity pressure boundary constraints, the LV FE model was used to solve the governing equations for finite deformation continuum mechanics to simulate ventricular deformation throughout the cardiac cycle. Estimations of the diastolic tissue stiffness and systolic contractile properties of the heart were derived by fitting to the geometric data extracted at the end-diastolic (ED) and end-systolic (ES) LV states, respectively. Personalised estimates of the distributions of myocardial fibre extension and stress were also obtained using this modelling framework. We demonstrate this approach using cine magnetic resonance (MR) images from hearts of a healthy human and patient diagnosed with non-ischaemic HF to investigate the underlying mechanisms of dysfunction.

## 2 Methodology

### 2.1 Cardiac Images and Segmentation

The LV geometries were extracted using an active shape model (ASM) based approach [6] developed specifically for segmentation of sparse image data. The training set for the statistical shape model was obtained from Computed Tomography studies and comprised shapes of 100 subjects, with 15 shapes per subject sampled throughout the cardiac cycle [7]. The MR image intensity model was obtained from 30 cardiac MR data sets, independent from the Sunnybrook database, after fitting the shape model to their manual segmentations.

The sparse ASM, or SPASM algorithm uses the fact that a 3D image data set is often merely a set of image slices rather than a contiguous 3D volume [8]. It generates shape update steps initially at the intersections of the image slices with the model mesh (the sources), producing update vectors coplanar with the image slices. Through two propagation steps and weighted averaging of update vectors from different sources, this information is 'smeared out' over a larger portion of the model surface. The resulting shape update step thus deforms the shape only near image slices, and consequently is likely to produce implausible shapes. The constraints imposed by the statistical shape model ensure that the resulting shape continues to be a valid LV shape.

Initialisation of the algorithm for the first cardiac phase was done by manual identification of the LV apex and the centroids of the aortic and mitral valves. From these landmarks the initial size and orientation of the model mean mesh were computed. For later cardiac phases, the segmentation of the previous phase was used for initialisation. We constrained the shape model to three standard deviations from the mean in each of its 138 modes.

## 2.2 Automated Personalisation of the LV Mechanics Model

We adapted an existing canine model with embedded myocardial fibre orientation fields [9], and fitted it to the human LV surface geometry data used in this study.

**Data Transformation.** The segmented LV surface data were rigidly transformed to a conventional cardiac coordinate system, in which the x-axis is aligned with the long-axis of the LV (passing from the centroid of the LV base through the LV apex); the y-axis is directed from the centroid of the LV to the centroid of the RV (near the mid-ventricle); and the z-axis is oriented in the anterior-to-posterior direction. This transformation procedure was also applied to the ED and ES surface data.

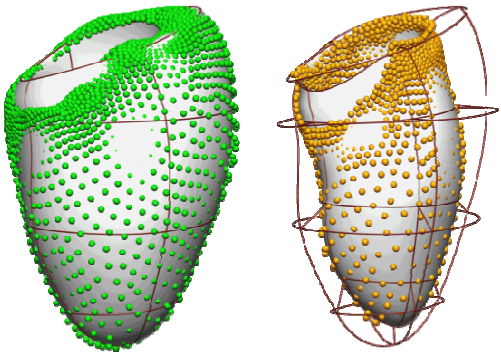

**Fig. 1.** Personalised LV FE model (brown lines and surfaces) fitted to epicardial (left: green) and endocardial (right: gold) surface points at diastasis of a normal human LV

**Geometric Model Creation.** We fitted the reference canine FE mechanics model to surface data segmented from the diastasis image using the methods detailed in [10]. Briefly, the FE model consisted of 16 hexahedral finite elements (4 circumferential, 4

longitudinal and 1 radial element) interpolated using $C^1$ continuous tricubic Hermite basis functions. The human LV surface data were separately projected onto the epicardial and endocardial surfaces of the scaled canine FE model. Nonlinear least-squares optimisation was used to adjust the geometric parameters of each FE model surface to best match the corresponding LV surface data (Fig. 1).

**Ventricular Fibre Structure.** In order to account for the LV myocardial architecture, we incorporated histologically derived fibre-sheet orientation data from the Auckland canine LV model [9,11]. This choice was primarily due to the lack of detailed *in vivo* or *ex vivo* measurements on human muscle fibre orientation.

**Boundary Constraints.** LV cavity pressures and displacement boundary constraints were applied during the simulations. The epicardial basal nodes of the model were constrained to match the motion of the segmented surface data, whereas the apex was unconstrained. Due to the lack of *in vivo* cavity pressure data in this study, pressure loading constraints were taken from the literature. During diastolic filling, a LV cavity pressure of 1.48 kPa [12] was applied to the endocardial surface of the reference FE model, whilst the afterload was set to 15.1 kPa [13].

**LV Mechanics.** LV mechanics was simulated in two phases: 1) passive diastolic filling (slow filling) to ED; and 2) active systolic contraction to ES, which included the isovolumic contraction (IVC) and ejection phases of the cycle. The governing equations of finite deformation elasticity were solved using the FE method.

**LV Passive Mechanics and Passive Property Estimation.** The passive inflation phase was simulated by incrementally applying pressure to the LV endocardial surface of the model until the preload was reached. The passive mechanical behaviour was modelled using a transversely-isotropic constitutive equation (Eq. 1) [14].

$$W = C_1 \exp(Q)$$
$$\text{where } Q = C_2 E_{ff}^2 + C_3 (E_{cc}^2 + E_{rr}^2 + 2E_{cr}^2) + 2C_4 (E_{fc} E_{cf} + E_{fr} E_{rf}) \quad (1)$$

where $E_{\alpha\beta}$ are the components of Green's (Lagrange) strain tensor referred to fibre ($f$), cross-fibre ($c$) and radial ($r$) material coordinates, and $C_1$ - $C_4$ are the passive myocardial constitutive parameters. An estimate of the tissue stiffness ($C_1$) was obtained after matching the inflated FE mechanics model to the segmented ED surface data. During this optimisation, the segmented data were projected onto their corresponding FE model surfaces, and the overall root-mean-squared error of the projections was then minimised by varying $C_1$. Other parameters describing the anisotropy ($C_2$ - $C_4$) were not included in the estimation due to the lack of regional strain information in the segmented data. Instead, their values were taken from our previous study based on MR tagging in canine hearts [9].

**LV Systolic Mechanics and Active Property Estimation.** After tuning the passive properties, the simulation was continued through IVC, to the end of ejection. Contraction of the LV model was driven by a calcium-dependent activation transient ($T_{Ca}$) throughout systole as part of a steady-state model for contractile stress ($T_a$) [15]:

$$T_a = T_{Ca}\left(1+\beta(\lambda-1)\right) \tag{2}$$

where $\lambda$ is the fibre extension ratio and $\beta$ is a material parameter that describes the length-dependence of the activation level. Note that this model is independent of the velocity of muscle shortening. Following the end of inflation, the activation level, $T_{Ca}$, was gradually increased to represent the release of calcium from the sarcoplasmic reticulum. During IVC, the LV cavity pressure was raised to counteract the contractile force in order to hold the cavity volume constant at its ED value. Simulations ran until the LV cavity pressure reached an afterload of 15.1 kPa [13]. The maximum activation level at ES ($T_{Ca\_max}$) was estimated by matching the model predicted ES state to the segmented human ES data.

## 3 Results

Fig. 2 illustrates the segmented ED (top) and ES (bottom) epicardial (green) and endocardial (gold) surface points derived from the automatic segmentation procedure described in section 2.1. Global geometric and functional measurements, such as wall volume, EDV, ESV and ejection fraction (EF) were calculated from geometric models fitted to the surface contours at ED and ES. These indices are summarised in Table 1.

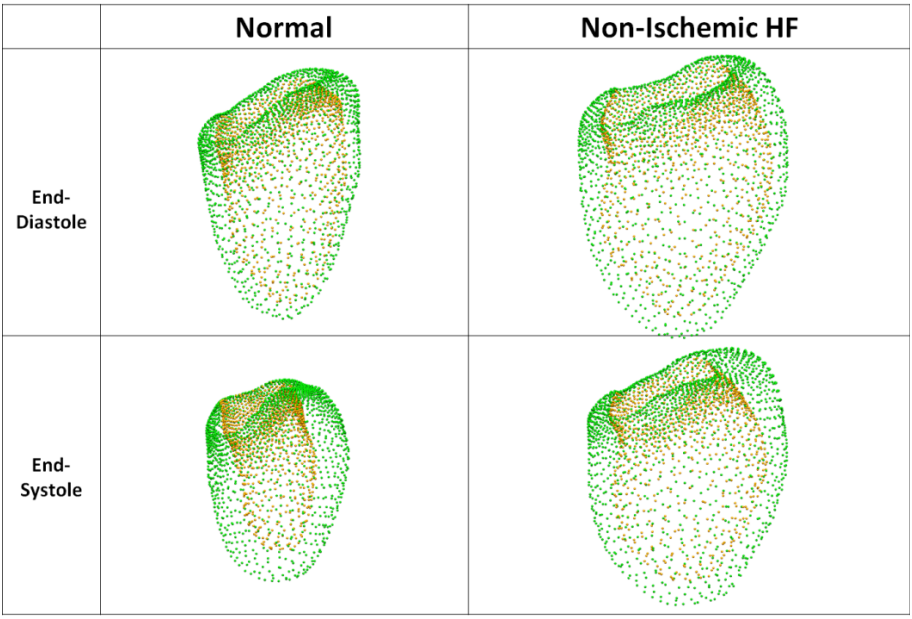


**Fig. 2.** Epicardial (green) and endocardial (gold) surface points at end-diastole (top) and end-systole (bottom) for LVs from a normal human (left) and non-ischaemic HF patient (right)

For the two cases studied in this paper, both the wall volume and the EDV for the non-ischaemic HF case were approximately double the values for the normal, indicating severe remodelling of the LV geometry with both wall thickening and

ventricular dilatation. The non-ischaemic HF case also exhibited a larger ESV compared to the normal, but the stroke volumes between the two cases were only moderately different (81ml versus 62 ml). The significant reduction in EF seen in the non-ischaemic HF case was primarily due to its increased EDV. Fig. 3 shows the error projections of the segmented data at ED and ES onto the corresponding surfaces of the associated predicted models.

The estimated passive tissue stiffness parameter ($C_1$) was substantially larger for the non-ischaemic case (Table 2). In contrast, estimated values of the maximum activation level ($T_{Ca\_max}$) were relatively similar. As indicated in Fig. 4, fibre extent of shortening was lower for the non-ischaemic HF case compared to the normal case. This resulted in an increased active fibre stress ($T_a$) at ES, due to its dependence upon length (the Frank-Starling mechanism), even though the estimated activation levels ($T_{Ca}$) were similar for the two cases.

**Table 1.** Geometric and functional data for normal and non-ischaemic heart failure LVs

| | Normal | Non-ischaemic Heart Failure |
|---|---|---|
| Wall Volume (ml) | 105 | 194 |
| EDV (ml) | 119 | 247 |
| ESV (ml) | 38 | 185 |
| EF (%) | 68 | 25 |

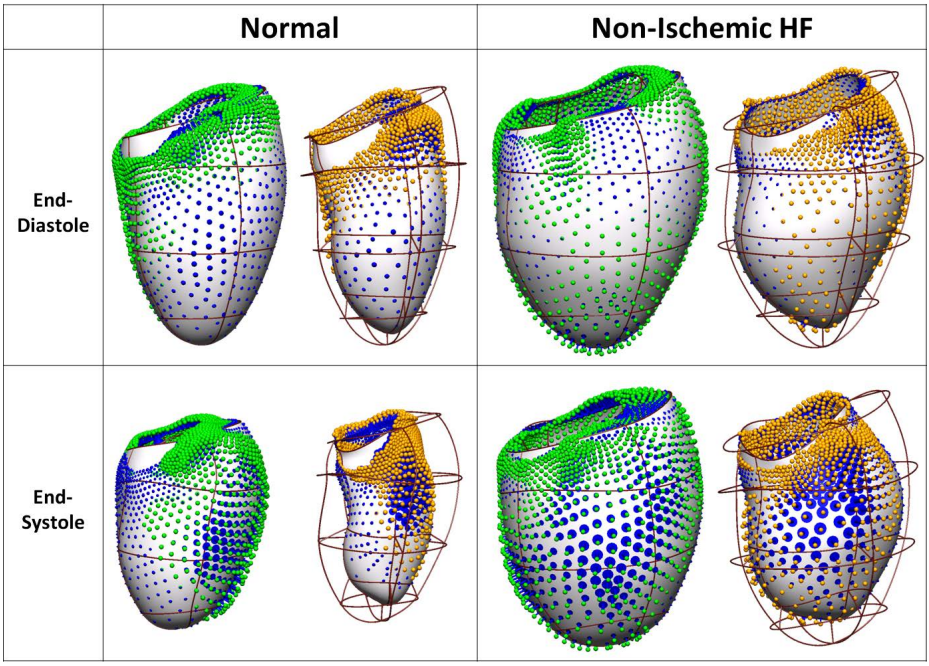


**Fig. 3.** Predicted ED FE models following passive parameter estimation (upper), and ES models following active contractile parameter estimation (lower). Epicardial (green) and endocardial (gold) surface data error projections (blue) are shown for a normal human LV (left), and a LV of a non-ischaemic heart failure patient (right).

**Table 2.** Estimated passive and active mechanical properties for normal and non-ischaemic heart failure LVs

| | Normal | Non-ischaemic HF |
|---|---|---|
| Passive Stiffness ($C_1$ *(kPa)*) | 2.3 | 7.6 |
| ED Fibre Extension Ratio ($\lambda$) | 1.1 ± 0.03 | 1.04 ± 0.02* |
| ED Passive Fibre Stress *(kPa)* | 4 ± 1.9 | 4 ± 2.6 |
| Maximum Activation Level ($T_{Ca\_max}$ *(kPa)*) | 93 | 94 |
| ES Fibre Extension Ratio ($\lambda$) | 0.89 ± 0.07 | 0.95 ± 0.07* |
| ES Active Fibre Stress *(kPa)* | 70 ± 14 | 81 ± 13* |

* indicates significant difference (P<0.05) compared to the normal case.

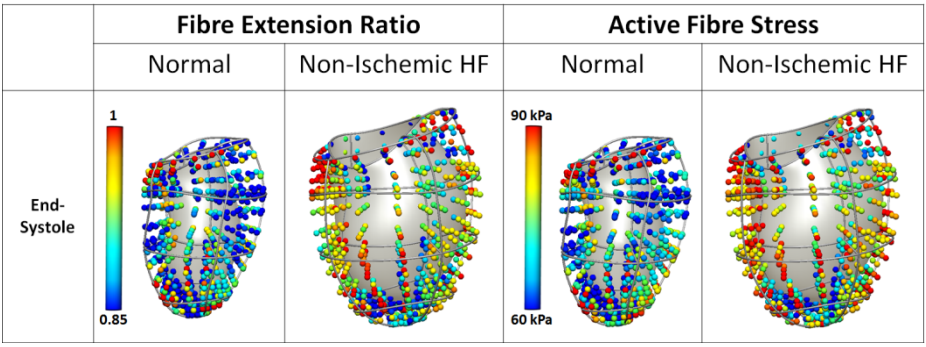


**Fig. 4.** FE model predictions of end-systolic fibre extension ratio and active fibre stress for two case studies

## 4 Discussion

This paper presents a workflow to construct LV surface segmentations from cardiac MR images, and to create personalised FE biomechanical models to characterise global mechanical properties of the LV. Although a manual step was required to start the segmentation process by identifying a small number of landmarks, the automatic detection of landmarks is currently feasible and could be applied to produce a fully automated method. These models were used to generate personalised estimates of passive and active mechanical properties by matching model predictions to the kinematic information derived from the cardiac MR images. These methods not only provided estimates of global mechanical function, but also estimates of regional fibre stretch and stress.

A key limitation of this study was the lack of subject-specific cavity pressure measurements, which were not recorded. Therefore, we assumed the same diastolic (preload) and systolic (afterload) blood pressures for both the normal and HF cases. Estimated mechanical properties were shown to be correlated with preload and afterload (data not shown). Lack of pressure transient measurements also limited our mechanical analysis to consider only two time-points for both phases of the cardiac

cycle. If personalised pressure recordings were available, these data could be readily incorporated into this workflow to provide estimates of the activation level transients throughout the cardiac cycle.

A second limitation was the lack of subject-specific microstructural information for the human hearts studied. This may have been particularly limiting for the analysis of the failing hearts. *In vivo* imaging of the myofibre architecture may be made possible using *in vivo* diffusion tensor MR imaging (DTMRI) techniques. Recent attempts to acquire *in vivo* DTMRI of beating heart include [16][17], however the data collected are still rather sparse and the techniques require extensive validation before *in vivo* DTMRI becomes a clinical routine. This framework is capable of incorporating *in vivo* fibre orientation data should they be available in future studies. In [18], statistical atlases of human myocardial fibre orientations for both healthy and abnormal hearts were proposed based on *ex vivo* DTMR imaging of 10 healthy and 6 abnormal hearts. Incorporating the data from this atlas into this modelling framework was beyond the scope of the present study, partly because the physical conditions of these hearts remain unclear. However, in a separate study we are presently underway to investigate the sensitivity of strain predictions on the underlying fibre structure [19] by embedding the fibre data extracted from normal human hearts [18] into the LV mechanics model.

For this paper, we focused on only the LV. The next stage of this study is to extend the analysis to consider both ventricles, and this inclusion can potentially improve the RMSE during parameter estimation.

We tuned the mechanical properties to match the shapes of the LV at ED and ES, and assumed that the distributions of these properties were homogeneous. This assumption may be violated for diseased cases where tissue remodelling (e.g. due to myocardial infarction) may induce regional variation of mechanical properties. However, this choice was made solely due to the lack of regional motion data because the 3D MR images used in this study only allowed derivation of surface information of the LV. To incorporate heterogeneity, regional kinematic data are required. This framework could be readily extended to estimate material parameters on a regional basis.

By applying this automated method to LV images from a normal heart, and the LV of a non-ischaemic HF patient, we were able to compare the estimated mechanical properties. For this study, we focused on the effects of geometric remodelling during HF on mechanical properties estimates. Using this modelling workflow, the estimated passive tissue stiffness for the LV with non-ischaemic HF was greater than that for the normal LV. This is consistent with the fibrosis that is known to occur during HF [12]. The estimated maximum activation levels ($T_{Ca\_max}$) were similar for the two cases, suggesting that non-ischaemic HF is not associated with a change in the systolic mechanical properties of the myocardium. In this study, the geometric remodelling as a result of non-ischaemic HF was fully accounted for by an increase in passive stiffness. We speculate that the increased active fibre stress ($T_a$) for the non-ischaemic HF case may be responsible for triggering myocardial tissue and chamber remodelling.

## 5 Conclusions

We have developed an automated segmentation and FE modelling workflow to generate personalised human LV mechanics models using geometric and kinematic information derived from semi-automatic segmentation of cardiac images. The methods presented will be used in a larger-scale study to generate personalised FE mechanics models, and extract patient-specific mechanical properties of hearts from patients with HF. Determining more specific variations in mechanical properties between diseased and normal human hearts will help in the understanding of the underlying mechanisms of HF.

**Acknowledgements.** This work is funded by the European Commission's Ricordo project (FP7-ICT-248502), within the 7th Framework Programme. CH and AFF have been partially funded by the Industrial and Technological Development Center (CDTI) CENIT-cvREMOD program, by the Spanish Ministry Science and Innovation under grant STIMATH (TIN2009-14536-C02-01), and by the European Commission's project euHeart (FP7-ICT-224495).

## References

1. Xi, J., Lamata, P., Shi, W., Niederer, S., Land, S., Rueckert, D., Duckett, S.G., Shetty, A.K., Rinaldi, C.A., Razavi, R., Smith, N.: An Automatic Data Assimilation Framework for Patient-Specific Myocardial Mechanical Parameter Estimation. In: Metaxas, D.N., Axel, L. (eds.) FIMH 2011. LNCS, vol. 6666, pp. 392–400. Springer, Heidelberg (2011)
2. Imperiale, A., Chabiniok, R., Moireau, P., Chapelle, D.: Constitutive Parameter Estimation Methodology Using Tagged-MRI Data. In: Metaxas, D.N., Axel, L. (eds.) FIMH 2011. LNCS, vol. 6666, pp. 409–417. Springer, Heidelberg (2011)
3. Chabiniok, R., Moireau, P., Lesault, P.-F., Rahmouni, A., Deux, J.-F., Chapelle, D.: Trials on Tissue Contractility Estimation from Cardiac Cine MRI Using a Biomechanical Heart Model. In: Metaxas, D.N., Axel, L. (eds.) FIMH 2011. LNCS, vol. 6666, pp. 304–312. Springer, Heidelberg (2011)
4. Sermesant, M., Billet, F., Chabiniok, R., Mansi, T., Chinchapatnam, P., Moireau, P., Peyrat, J.-M., Rhode, K., Ginks, M., Lambiase, P., Arridge, S., Delingette, H., Sorine, M., Rinaldi, C.A., Chapelle, D., Razavi, R., Ayache, N.: Personalised Electromechanical Model of the Heart for the Prediction of the Acute Effects of Cardiac Resynchronisation Therapy. In: Ayache, N., Delingette, H., Sermesant, M. (eds.) FIMH 2009. LNCS, vol. 5528,
pp. 239–248. Springer, Heidelberg (2009)
5. Radau, P., Lu, Y., Connelly, K., Paul, G., Dick, A.J., Wright, G.A.: Evaluation Framework for Algorithms Segmenting Short Axis Cardiac MRI. The MIDAS Journal - Cardiac MR Left Ventricle Segmentation Challenge, `http://hdl.handle.net/10380/3070`
6. Cootes, T.F., Taylor, C.J., Cooper, D.H., Graham, J.: Active shape models - their training and application. Comput. Vis. Image Underst. 61(1), 8–59 (1995)
7. Ordás, S., Oubel, E., Leta, R., Carrera, F., Frangi, A.F.: A statistical shape model of the heart and its application to model-based segmentation. In: Proc. SPIE Medical Imaging, article no. 65111K (2004)

8. van Assen, H.C., Danilouchkine, M.G., Frangi, A.F., Ordás, S., Westenberg, J.J.M., Reiber, J.H.C., Lelieveldt, B.P.F.: SPASM: A 3-D ASM for segmentation of sparse and arbitrarily oriented cardiac MRI data. Med. Imag. Anal. 10(2), 286–303 (2006)
9. Wang, V.Y.: Modelling In Vivo Cardiac Mechanics using MRI and FEM. PhD thesis. The University of Auckland, New Zealand (2011)
10. Wang, V.Y., Lam, H.I., Ennis, D.B., Cowan, B.R., Young, A.A., Nash, M.P.: Modelling passive diastolic mechanics with quantitative MRI of cardiac structure and function. Med. Imag. Anal. 13(5), 773–784 (2009)
11. Nielsen, P.M.F., Le Grice, I.J., Smaill, B.H., Hunter, P.J.: Mathematical model of geometry and fibrous structure of the heart. Am. J. Physiol. 260(4), H1365–H1378 (1991)
12. Honda, H., Nakaya, S., Kamada, H., Hasegawa, H., Demachi, J., Chikama, H., Sugimura, K., Yamamoto, Y., Kumasaka, N., Takita, T., Ikeda, J., Kanai, H., Koiwa, Y., Shirato, K.: Non-invasive estimation of human left ventricular end-diastolic pressure. Med. Eng. Phys. 6, 485–488 (1998)
13. McKay, R.G., Aroesty, J.M., Heller, G.V., Royal, H.D., Warren, S.E., Grossman, W.: Assessment of the end-systolic pressure-volume relationship in human beings with the use of a time-varying elastance model. Circ. 74, 97–104 (1986)
14. Guccione, J.M., McCulloch, A.D., Waldman, L.K.: Passive material properties of intact ventricular myocardium determined from a cylindrical model. J. Biomech. Eng. 113, 43–55 (1991)
15. Hunter, P.J., McCulloch, A.D., ter Keurs, H.E.D.J.: Modelling the mechanical properties of cardiac muscle. Prog. Biophys. Mol. Bio. 69, 289–331 (1998)
16. Dou, J., Tseng, W.I., Reese, T.G., Wedeen, V.J.: Combined diffusion and strain MRI reveals structure and function of human myocardial laminar sheets in vivo. Magnet. Reson. Med. 50(1), 107–113 (2003)
17. Toussaint, N., Sermesant, M., Stoeck, C.T., Kozerke, S., Batchelor, P.G.: *In vivo* Human 3D Cardiac Fibre Architecture: Reconstruction Using Curvilinear Interpolation of Diffusion Tensor Images. In: Jiang, T., Navab, N., Pluim, J.P.W., Viergever, M.A. (eds.) MICCAI 2010, Part I. LNCS, vol. 6361, pp. 418–425. Springer, Heidelberg (2010)
18. Lombaert, H., Peyrat, J.-M., Fanton, L., Cheriet, F., Delingette, H., Ayache, N., Clarysse, P., Magnin, I., Croisille, P.: Statistical Atlas of Human Cardiac Fibers: Comparison with Abnormal Hearts. In: Camara, O., Konukoglu, E., Pop, M., Rhode, K., Sermesant, M., Young, A. (eds.) STACOM 2011. LNCS, vol. 7085, pp. 207–213. Springer, Heidelberg (2012)
19. Wang, V.Y., Casta, C., Croisille, P., Clarysse, P., Zhu, Y.M., Cowan, B.R., Young, A.A., Nash, M.P.: Estimation of in vivo human myocardial fibre strain by integrating diffusion tensor and tagged MRI using FE modelling. In: 9th IEEE International Symposium on Biomedical Imaging (ISBI), pp. 46–49 (2012)

# Feasibility Study of Looped-Catheter-Based 2D-3D Image Registration of CT and X-Rays for Cardiac Catheterization Procedures in a Phantom Experiment

Michael V.N. Truong, Graeme P. Penney, and Kawal S. Rhode

Division of Imaging Sciences and Biomedical Engineering,
King's College London, London, England, UK
{michael.truong,graeme.penney,kawal.rhode}@kcl.ac.uk

**Abstract.** For X-ray guided cardiac catheterisations it is desirable to overlay pre-operative 3D-CT information for additional guidance. A common technique to obtain an overlay is to loop a catheter inside a target chamber and then manually align CT-derived surface models using multiple X-ray views. We propose and test a fully automatic algorithm for this purpose. The algorithm aligns the images by first estimating the pose of the CT relative to the X-ray table using the supine and isocentre constraints. Subsequently the pose is refined using an iterative optimisation strategy that maximises the intersection between the loop and projected target chamber, while minimising the separation between the X-ray cardiac border and the projected ventricles, in two X-ray views. Validation was carried out using a geometrically-realistic plastic heart phantom with two looped-catheter configurations formed inside the left atrium. The algorithm executes in under five minutes and yields average 3D-TREs between 2.4 and 5.4 mm over various regions of the heart, and 4.0 mm over the four chambers. Preliminary evaluation of this novel approach indicates feasibility for clinical interventional guidance and merits thorough validation using further phantom and clinical images.

**Keywords:** 2D-3D image registration, cardiac imaging, image-guided catheterisation, CT, X-ray, data fusion.

## 1 Introduction

Cardiac catheterisations are minimally invasive procedures to treat pathologies of the heart and are routinely guided using X-ray fluoroscopy. This modality is suitable for this due to its real-time imaging capabilities and excellent device visibility. However, the images suffer from a complete loss of depth information and provide poor visualisation of the heart itself. Therefore it is highly desirable to overlay the X-rays with improved soft-tissue 3D-CT information acquired pre-operatively during the diagnostic and treatment planning phase of the procedure [1-10]. This lends itself to a 2D-3D image registration solution for cardiac images.

Currently, registration can be performed automatically and in real-time using a hybrid X-ray/MR guidance system proposed in [1] to within 5-mm accuracy. However,

O. Camara et al. (Eds.): STACOM 2012, LNCS 7746, pp. 317–325, 2013.

this requires a specially designed hardware that is not available in many hospitals. The use of fiducial skin markers or other surrogate structures is another approach to registration [4, 5], but accuracy may be lost if there is motion between the heart and the markers. This source of error can be avoided by using anatomical landmarks from the heart itself for registration, such as vessel bifurcation points and ostia [6], or the cardiac shadow [7]. However, repeat contrast agent injections may be needed for their reliable segmentation. In cardiac catheterisations, the use of the catheters for registration is attractive since these devices are the main instruments of the procedure and are placed directly into the heart with excellent visibility in X-ray [8, 9, 10, 11]. In current clinical settings, a common registration technique is to insert a catheter and loop it inside a target chamber, such as the left atrium (LA), and then manually aligning the pre-operative CT data from several X-ray views (EPNavigator, Philips Healthcare, Best, Netherlands) [11].

In this manuscript, a fully automatic algorithm is proposed for this purpose; i.e., to use catheter loops created inside a target chamber as a constraint in order to register pre-operative CT data onto intra-operatively acquired X-ray. To improve accuracy and robustness necessary for automation, the cardiac shadow adds an additional constraint as in [7], but in order to avoid the need for a contrast agent injection, only the upper border of the shadow is used since it is readily visible in X-ray images of the heart without contrast agents.

## 2 Methods

The proposed algorithm relies on the formation of a catheter loop inside the target chamber of the heart and iteratively searches for the rigid-body transformation (RBT) $T_{\text{reg}}$ that aligns the CT data to X-ray images. This is achieved by maximising the area,

$$A = \left(A_{1,\text{pa}} + A_{1,\text{ao}}\right) - \left(A_{2,\text{pa}} + A_{2,\text{ao}}\right). \tag{1}$$

$A_1$ is the intersecting area enclosed by points manually picked along the loop $\boldsymbol{L}_{2\text{D}}$ from the two X-ray views, one posterior-anterior (PA) and the other in either left or right anterior-oblique (AO), and projections of the target chamber surface $\boldsymbol{C}_{3\text{D}}$ segmented semi-automatically from CT. $A_2$ is the area between points manually picked along the upper cardiac X-ray border $\boldsymbol{S}_{2\text{D}}$ and the projections of the combined surfaces of the segmented left and right ventricles (LRV) $\boldsymbol{V}_{3\text{D}}$ segmented semi-automatically from CT (fig 1a, b, c). To ensure points picked on the catheter loop and the cardiac shadow correspond to one another in both X-ray views, points are first picked in PA and then in AO using epipolar constraints [10]:

$$\boldsymbol{L}_{\text{ao}} \in P_{\text{ao}} P_{\text{pa}}^{+} \boldsymbol{L}_{\text{pa}} \quad \boldsymbol{S}_{\text{ao}} \in P_{\text{ao}} P_{\text{pa}}^{+} \boldsymbol{S}_{\text{pa}}, \tag{2}$$

where $P$ are the camera calibration matrices encoding the pose and projection parameters of the X-ray views [10], and $P^{+}$ is the Moore-Penrose pseudoinverse of $P$. Another view can be chosen instead of PA if the catheter loop appears more circular.

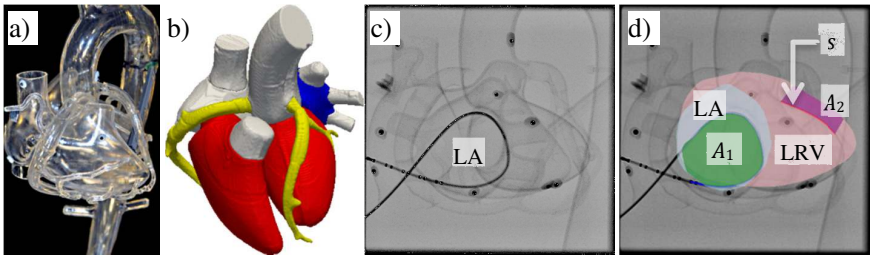


**Fig. 1.** a) Photograph of the plastic heart phantom. b) Surface rendering of its CT scan after segmentation. c) X-ray of phantom in PA view of 1st catheter loop configuration. d) Same PA view highlighting the upper cardiac border from X-ray (*red solid line, labelled s*) and the projected convex hulls of the LA (*blue*) and combined LRV (*red*). The algorithm attempts to maximise the intersection of the catheter loop in X-ray and the projected LA (*green, $A_1$*) while minimising the gap between the upper cardiac border from X-ray and the projected LRV (*purple, $A_2$*).

**Loop Area $A_1$.** To quantify how much the catheter loop is contained within the target chamber, the algorithm first projects this chamber onto the X-ray images (fig 1d) and extracts their convex hulls $\boldsymbol{C}$ using a fast radial sweep hull routine [12].

$$\boldsymbol{C}_{\mathrm{pa}} = \text{convex hull}\left(P_{\mathrm{pa}} T_{\mathrm{reg}} \boldsymbol{C}_{\mathrm{3D}}\right), \quad \boldsymbol{C}_{\mathrm{ao}} = \text{convex hull}\left(P_{\mathrm{ao}} T_{\mathrm{reg}} \boldsymbol{C}_{\mathrm{3D}}\right). \tag{3}$$

The intersecting area between the loop and the hull is computed by taking the points $\boldsymbol{l}$ along the catheter loop that lie inside the hull, and points $\boldsymbol{c}$ along the convex hull that lie inside the catheter loop, using a point-in-polygon routine [13] (fig 2a),

$$\begin{aligned} \boldsymbol{l}_{\mathrm{pa}} &= \boldsymbol{L}_{\mathrm{pa}} \text{ inside } \boldsymbol{C}_{\mathrm{pa}}, \quad \boldsymbol{l}_{\mathrm{ao}} = \boldsymbol{L}_{\mathrm{ao}} \text{ inside } \boldsymbol{C}_{\mathrm{ao}}, \\ \boldsymbol{c}_{\mathrm{pa}} &= \boldsymbol{C}_{\mathrm{pa}} \text{ inside } \boldsymbol{L}_{\mathrm{pa}}, \quad \boldsymbol{c}_{\mathrm{ao}} = \boldsymbol{C}_{\mathrm{ao}} \text{ inside } \boldsymbol{L}_{\mathrm{ao}}, \end{aligned} \tag{4}$$

and treating the union of these as a closed polygon in each view to obtain the areas:

$$\begin{aligned} A_{1,\mathrm{pa}} &= \textstyle\sum_i x_i y_{i+1} - x_{i+1} y_i \,;\, (x_i, y_i) = \boldsymbol{c}_{\mathrm{pa}} \cup \boldsymbol{l}_{\mathrm{pa}}, \\ A_{1,\mathrm{ao}} &= \textstyle\sum_i x_i y_{i+1} - x_{i+1} y_i \,;\, (x_i, y_i) = \boldsymbol{c}_{\mathrm{ao}} \cup \boldsymbol{l}_{\mathrm{ao}}. \end{aligned} \tag{5}$$

**Border Area $A_2$.** The gap between the upper cardiac border in X-ray and ventricle projections is the measure to be minimised in eq 1 and calculated by first finding the convex hull of the projection of the combined surfaces of the LRV,

$$\boldsymbol{V}_{\mathrm{pa}} = \text{convex hull}\left(P_{\mathrm{pa}} T_{\mathrm{reg}} \boldsymbol{V}_{\mathrm{3D}}\right), \quad \boldsymbol{V}_{\mathrm{ao}} = \text{convex hull}\left(P_{\mathrm{ao}} T_{\mathrm{reg}} \boldsymbol{V}_{\mathrm{3D}}\right). \tag{6}$$

Cubic splines are fitted through the convex hulls using periodic boundary conditions, and through the upper cardiac border using natural boundary conditions. The splines are resampled at an interval of $\Delta = 0.5$ px separation distance.

$$\boldsymbol{w}_{\mathrm{pa}} \subset \boldsymbol{v}_{\mathrm{pa}} \text{ closest to } \boldsymbol{s}_{\mathrm{pa}}, \quad \boldsymbol{w}_{\mathrm{ao}} \subset \boldsymbol{v}_{\mathrm{ao}} \text{closest to } \boldsymbol{s}_{\mathrm{ao}}. \tag{7}$$

For each X-ray view, a point $\boldsymbol{v}_{\mathrm{m}}$ belonging to $\boldsymbol{v}$ is selected that is closest to the middle point of $\boldsymbol{s}$, $\boldsymbol{s}_{\mathrm{m}}$, rounding the point index down if there is an even number of points. The contiguous set of points $\boldsymbol{w}$ from $\boldsymbol{v}$ is taken such that $\#(\boldsymbol{w}) = \#(\boldsymbol{s})$, where $\#(\boldsymbol{x})$ represents the number of points in $\boldsymbol{x}$, and $\boldsymbol{v}_{\mathrm{m}}$ is the midpoint of $\boldsymbol{w}$ and (fig 2b).

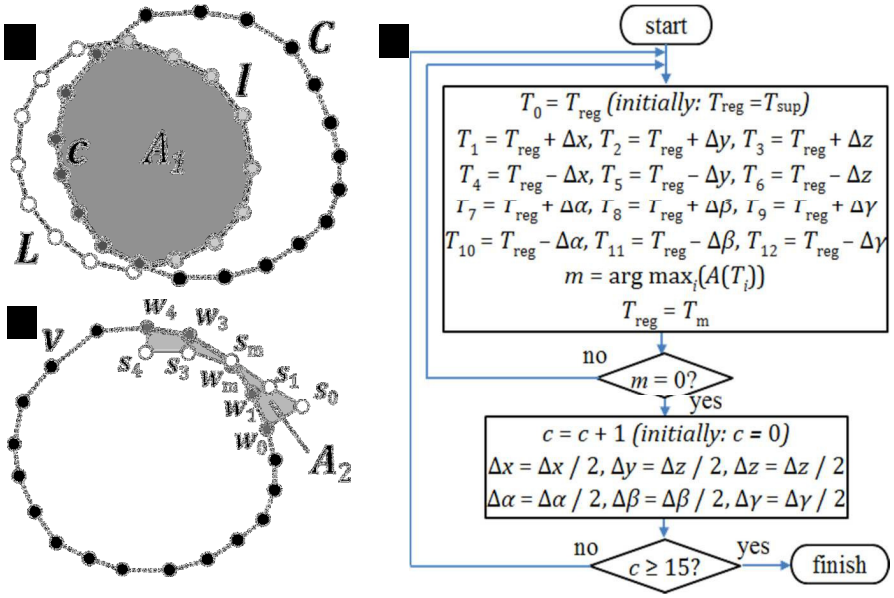


**Fig. 2.** a) Intersecting area $A_1$ (shaded grey) of catheter loop $\boldsymbol{L}$ (white circles on dashed line) and convex hull of target chamber $\boldsymbol{C}$ (black circles on dotted line). Points $\boldsymbol{l} \subset \boldsymbol{L}$ inside $\boldsymbol{C}$ shaded light grey and points $\boldsymbol{c} \subset \boldsymbol{C}$ inside $\boldsymbol{L}$ shaded dark grey. b) Separation area $A_2$ (shaded light grey) between X-ray cardiac border $\boldsymbol{s}$ (white circles) and points $\boldsymbol{w}$ on ventricle hull (dark grey circles) closest to $\boldsymbol{s}$. Rest of the hull $\boldsymbol{v}$ (black circles) lie on the dotted line. c) Flowchart of algorithm used to find $T_{\text{reg}}$ that minimises $A$ in eq 1. T + Δx shorthand for T(x + Δx, y, z, α, β, γ).

$$\boldsymbol{w}_{\text{pa}} \subset \boldsymbol{v}_{\text{pa}} \text{ closest to } \boldsymbol{s}_{\text{pa}}, \quad \boldsymbol{w}_{\text{ao}} \subset \boldsymbol{v}_{\text{ao}} \text{closest to } \boldsymbol{s}_{\text{ao}}. \tag{8}$$

Since $\boldsymbol{s}$ and $\boldsymbol{w}$ are evenly spaced, the area the two curves enclose is computed with:

$$\begin{aligned} A_{2,\text{pa}} &= \Delta \textstyle\sum_i \sqrt{\boldsymbol{s}_{i,\text{pa}} - \boldsymbol{w}_{i,\text{pa}}}\,, \\ A_{2,\text{ao}} &= \Delta \textstyle\sum_i \sqrt{\boldsymbol{s}_{i,\text{ao}} - \boldsymbol{w}_{i,\text{ao}}}\,. \end{aligned} \tag{9}$$

**Iterative Search Strategy.** The algorithm begins with an initial guess of $T_{\text{reg}}$, which is composed of six parameters: three translational (x, y, z) and three rotational (α, β, γ),

$$T = T(x, y, z, \alpha, \beta, \gamma) = \begin{bmatrix} R(\alpha, \beta, \gamma) & (x, y, z) \\ (0,0,0)^{\text{T}} & 1 \end{bmatrix}. \tag{10}$$

The initial guess assumes that the X-rays were taken with the heart lying in the iso-centre of the C-arm, and that the patient is lying in a supine position, $T_{\text{reg}} = T_{\text{sup}}$. The area $A$ in eq 1 is then computed using 13 variants of $T_{\text{reg}}$: six variants include a small positive change in each one of its six parameters, $\Delta x$, $\Delta y$, $\Delta z$, $\Delta\alpha$, $\Delta\beta$ and $\Delta\gamma$, for example, $T_{+\Delta x} = T(x + \Delta x, y, z, \alpha, \beta, \gamma)$; six negative changes in each parameter, $-\Delta x$, $-\Delta y$, $-\Delta z$, $-\Delta\alpha$, $-\Delta\beta$ and $-\Delta\gamma$; and in the last variant there is no change (fig 2c). The variant $T_{\text{reg}}$ that maximises the computed area is then used as the new guess and this is repeated until the largest area is due to the no-change variant. In this case, the

incremental amounts are halved and iteration resumes until the increments have been halved 15 times, at which point the algorithm ends and is said to converge.

### 2.1 Phantom Experiment

In order to validate the proposed algorithm, a phantom experiment was carried out with a geometrically-realistic plastic model of the heart (LFA 5000, Lake Forest Anatomicals, Lake Forest, IL, US) (fig 1a, b). Eight radio-opaque 0.25-mm diameter lead balls were adhered around the heart to provide a gold standard registration followed by a 0.488×0.488x0.625-mm$^3$-voxel-resolution 512×512×416 CT scan (Discovery STE, GE Healthcare, Little Chalfont, UK). The heart was subsequently catheterised in two configurations via the inferior vena cava (IVC) and into the LA where it forms a loop around the chamber's interior wall. In the 1$^{st}$ configuration, the catheter exited the LA via the right lower pulmonary vein (RLPV) and in the 2$^{nd}$ configuration exiting the left upper pulmonary vein (LUPV). Once the catheter loop was in place, a sequential biplane X-ray pair of the heart is taken from PA and RAO 45° views (Allura Xper FD10, Philips Healthcare, The Netherlands) (fig 1c, 3a, c).

The surfaces of the LA and LRV chambers of the CT image were segmented semi-automatically using an active contour method [14] for use as $\boldsymbol{C}_{3D}$ and $\boldsymbol{V}_{3D}$ in eqs 3, 6 (fig 1b) with $\#(\boldsymbol{C}_{3D}) = 39960$ and $\#(\boldsymbol{V}_{3D}) = 132384$: 61014 from LV, 71370 from RV. From X-ray, the looped portion of the catheter and the upper-left border of the cardiac shadow were selected in PA and subsequently in RAO using epipolar constraints for use as $\boldsymbol{L}_{pa}$, $\boldsymbol{L}_{ao}$, $\boldsymbol{S}_{pa}$ and $\boldsymbol{S}_{ao}$ in eq 4 and summarised in table 1.

The accuracy of the algorithm is quantified in terms of mean 3D target registration errors (3D-TRE) found by comparing the $T_{reg}$ to a gold standard RBT $T_{gs}$ between the CT scan and the X-ray table space. $T_{gs}$ is found by applying the method in [15] without scaling between the eight fiducial markers picked from CT and corresponding markers in the two X-ray views reconstructed using epipolar geometry and back projection [10]. The TREs can be computed by applying the two RBTs to points in the regions of interest of the heart obtained using [14]:

$$\text{mean 3D-TRE} = \frac{1}{n}\sum_{i=1}^{n}\left\| T_{gs}\boldsymbol{r}_i - T_{reg}\boldsymbol{r}_i \right\| \;\; \forall\, \boldsymbol{r}_i \in \text{region of interest}\,. \tag{11}$$

The iterative registration algorithm was applied to both catheter loop configurations using isocentre and supine constraints and with $\Delta x = \Delta y = \Delta z = \pm 3$ mm and $\Delta\alpha = \Delta\beta = \Delta\gamma = \pm 5°$ as the initial increments.

**Table 1.** Number of points that make up each curve in X-ray and their 2D arclengths $\ell$

| configuration | curve | # | $\ell$ in PA (px) | $\ell$ in RAO (px) |
|---|---|---|---|---|
| 1: IVC-LA-RLPV | $\boldsymbol{L}$ | 15 | 489.79 | 354.49 |
| | $\boldsymbol{S}$ | 5 | 90.52 | 58.36 |
| 2: IVC-LA-LUPV | $\boldsymbol{L}$ | 17 | 394.58 | 244.29 |
| | $\boldsymbol{S}$ | 7 | 107.44 | 86.82 |

## 3 Results

Eight lead fiducials provided a $T_{gs}$ with fiducial registration error of 0.87 mm which indicates a suitable gold standard. Using the supine and isocentre constraints as an initial guess and ±3 mm, ±5° for the initial increments, the algorithm was able to align the CT and X-ray data to within a mean 3D-TRE of 3.0 mm over the four chambers of the heart for the 1st catheter loop configuration, and 4.9 mm with the 2nd. The average TREs of the two configurations were between 2.4 and 5.4 mm over various regions of the heart and 4.0 mm over the four chambers (table 2). The algorithm took 35 and 43 steps to converge respectively, and required on average 269.30 s (C#; Intel Core 2 Extreme, 2×3.06 GHz, 4 GB ram, 64-bit Win 7).

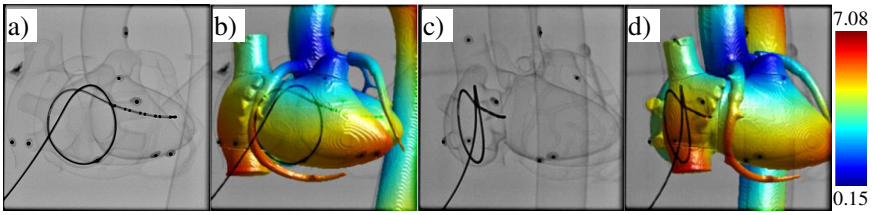


**Fig. 3.** a) PA and c) RAO 45° X-ray views of the plastic heart with 2nd looped catheter configuration. b, d) Segmented surface rendering of CT data overlaid onto the views. Colour map showing spatial distribution of 3D-TRE over heart phantom between 0.15 and 7.08 mm.

**Table 2.** Number of points (#) from segmentations of the heart, and the mean 3D-TRE obtained for the various regions listed for each loop configuration, and the average between the two

| region of interest | | # | mean 3D-TRE (mm) | | |
|---|---|---|---|---|---|
| | | | 1: RLPV | 2: LUPV | average |
| chambers | left atrium | 39960 | 4.1 | 2.5 | 3.3 |
| | left ventricle | 61014 | 4.5 | 2.2 | 3.3 |
| | right atrium | 44608 | 5.2 | 3.8 | 4.5 |
| | right ventricle | 71370 | 5.9 | 3.6 | 4.8 |
| | 4-chamber average | 216952 | 4.9 | 3.0 | 4.0 |
| small vessels | coronary sinus ostium | 4024 | 5.0 | 3.9 | 4.5 |
| | left coronary artery | 13560 | 5.4 | 2.7 | 4.0 |
| | right coronary artery | 20502 | 6.2 | 3.8 | 5.0 |
| large vessels | ascending aorta | 35304 | 4.6 | 2.2 | 3.4 |
| | inferior vena cava | 15958 | 5.8 | 5.0 | 5.4 |
| | superior vena cava | 15096 | 4.2 | 3.3 | 3.8 |
| | pulmonary trunk | 11002 | 5.4 | 1.2 | 3.3 |
| pulmonary veins (PV) | left lower PV | 3676 | 4.0 | 0.9 | 2.4 |
| | left upper PV | 4704 | 4.1 | 1.8 | 3.0 |
| | right lower PV | 3328 | 4.9 | 4.2 | 4.6 |
| | right upper PV | 3800 | 4.4 | 4.0 | 4.2 |

## 4 Discussion and Conclusion

A 2D-3D image registration algorithm was developed that can align 3D-CT data onto biplane X-ray images of the heart by using a catheter looped inside a target chamber and the upper cardiac border to constrain the registration. The algorithm requires the segmentation of the target chamber and the left and right ventricles from CT, and segmentation of the loop part of the catheter and upper border of the cardiac shadow from X-ray. The algorithm registers the data by projecting the segmented chambers onto both X-ray views, and maximises the area of intersection between the projected target chamber and catheter loop, while minimizing the gap formed between the upper border of the cardiac shadow and the project ventricles. Using isocentre and supine constraints, an initial guess RBT is established to align the CT-data to the X-rays, and subsequently uses an iterative search strategy that perturbs the transformation, one parameter at a time, by a small increment until a local maximum area is found.

To test this algorithm, a phantom experiment was carried out with two catheter loop configurations formed inside the LA via the IVC, with one exiting the RLPV and the other exiting the LUPV (fig 1c, fig 3a, c). The accuracy was measured in terms of mean 3D-TREs against a fiducial-based gold standard with a 0.87-mm FRE. The average TRE between the two configurations was between 2.4 and 5.4 mm over various regions of the heart, and 4.0 mm over the four chambers (table 2).

Results show that the LUPV configuration yielded lower TREs than the RLPV configuration for all regions of interest. A possibility is that the while the target chamber was the same size in both configurations, the catheter loop formed in PA in the RLPV configuration was only 19070 $px^2$ while the in the LUPV configuration the loop was 25334 $px^2$, suggesting that the larger the catheter loop, the better constraint that the loop and chamber can provide, and hence a more accurate registration.

While the experiment shows that registration with a plastic phantom can yield TREs within the 5-mm clinical tolerance, the phantom is rigid and stationary and therefore no errors are introduced to the reported TREs due to cardiac and respiratory motions. Although the main cause of error in rigid registration methods are not simulated, the experiment carried out in this manuscript is still valid and applicable to a cardiac catheterisation procedure by adding the requirement that the intra-operative X-ray images are phase-matched to the pre-operative CT image with respect to the cardiac and respiratory cycle, typically in end-diastole and end-systole.

Another limitation to using a plastic phantom model is the absence of the pericardial sac that would contribute to the upper cardiac shadow when imaging a live heart. To account for this when working with patient data the pericardial sac should be included in the ventricle segmentation.

The automatic registration algorithm can be performed in less than five minutes. While this is a reasonable execution time under clinical settings, the speed of the algorithm can potentially be improved by using optimized iterative search strategies found in [16], and by using a multi-resolution approach to reduce the number of points used in the CT segmentation during the initial alignment when the increments are relatively large, and then restore the number of points when the increments are small and finer resolution is needed.

Preliminary evaluation of the algorithm yields mean-3D-TREs below the 5-mm clinical tolerance, demonstrating feasibility for clinical interventional guidance and meriting thorough validation using further phantom and clinical images.

## References

1. Rhode, K., Ma, Y., Housden, J., Karim, R., Rinaldi, A., Cooklin, M., Gill, J., O'Neill, M., Schaeffter, T., Relan, J., Sermesant, M., Dilingette, H., Ayache, N., Kruger, M., Schulze, W., Seemann, G., Doessel, O., Razavi, R.: Clinical Applications of Image Fusion for Electrophysiology Procedures. In: Proc. ISBI, vol. 2127 (2012)
2. Markelj, P., Tomaževič, D., Likar, B., Pernuš, F.: A review of 3D/2D registration methods for image-guided interventions. Medical Image Analysis 16(3), 642–661 (2012)
3. Rhode, K.S., Sermesant, M., Brogan, D., Hegde, S., Hipwell, J., Lambiase, P., Rosenthal, E., Bucknall, C., Qureshi, S.A., Gill, J.S., Rezavi, R., Hill, D.L.G.: A system for real-time XMR guided cardiovascular intervention. IEEE Trans. Med. Imag. 24(11), 1428–1440 (2005)
4. Gutiérrez, L.F., de Silva, R., Ozturk, C., Sonmez, M., Stine, A.M., Raval, A.N., Raman, V.K., Sachdev, V., Aviles, R.J., Waclawiw, M.A., McVeigh, E.R., Lederman, R.J.: Technology preview: X-ray fused with magnetic resonance during invasive cardiovascular procedures. Catheter. Cardiovasc. Interv. 70, 773–782 (2007)
5. Rhode, K., Ma, Y., Chandrasena, A., King, A., Gao, G., Chinchapatnam, P., Sermesant, M., Hawkes, D., Schaeffter, T., Gill, J., Razavi, R.: Evaluation of the use of multimodality skin markers for the registration of pre-procedure cardiac MR images and intra-procedure x-ray fluoroscopy images for image guided cardiac electrophysiology procedures. In: Proc. SPIE, vol. 6918 (2008)
6. Ector, J., De Buck, S., Huybrechts, W., Nuyens, D., Dymarkowski, S., Bogaert, J., Maes, F., Heidbüchel, H.: Biplane three-dimensional augmented fluoroscopy as single navigation tool for ablation of atrial fibrillation: accuracy and clinical value. Heart Rhythm 5(7), 957–964 (2008) (Epub. March 25, 2008)
7. Daul, C., Lopez-Hernandez, J., Wolf, D., Karcher, G., Ethévenot, G.: 3-D multimodal cardiac data superimposition using 2-D image registration and 3-D reconstruction from multiple views. Image and Vision Computing 27(6), 790–802 (2009)
8. Sra, J., Ratnakumar, S.: Cardiac image registration of the left atrium and pulmonary veins. Heart Rhythm 5(4), 609–617 (2008)
9. Truong, M.V.N., Aslam, A., Ginks, M., Rinaldi, C.A., Rezavi, R., Penney, G.P., Rhode, K.: 2D-3D Registration of Cardiac Images Using Catheter Constraints. In: Proc. CinC, p. 0605 (2009)
10. Truong, M., Gordon, T., Razavi, R., Penney, G., Rhode, K.S.: Analysis of Catheter-Based Registration with Vessel-Radius Weighting of 3D CT Data to 2D X-ray for Cardiac Catheterisation Procedures in a Phantom Study. In: Camara, O., Konukoglu, E., Pop, M., Rhode, K., Sermesant, M., Young, A. (eds.) STACOM 2011. LNCS, vol. 7085, pp. 139–148. Springer, Heidelberg (2012)
11. Ma, Y., Duckett, S., Chinchapatnam, P., Gao, G., Shetty, A., Rinaldi, C.A., Schaeffter, T., Rhode, K.S.: MRI to X-ray Fluoroscopy Overlay for Guidance of Cardiac Resynchronization Therapy Procedures. In: Proc. CinC, vol. 37, pp. 229–232 (2010)
12. Sinclair, D.: S-hull: a fast sweep-hull routine for Delaunay triangulation (2010), http://www.s-hull.org

13. Finley, D.R.: Point-In-Polygon Algorithm – Determining Whether a Point Is inside a Complex Polygon (2007), http://alienryderflex.com/polygon
14. Zhang, H., Goodlett, C., Burke, T., Tustison, N.: ITK-SNAP (2011), http://www.itksnap.org
15. Horn, B.K.P.: Closed-form solution of absolute orientation using unit quaternions. J. Opt. Soc. Am. A 4, 629–642 (1987)
16. Press, W.H., Teukolsky, S.A., Vetterling, W.T., Flannery, B.P.: Numerical Recipes: The Art of Scientific Computing, 3rd edn. Cambridge University Press, Cambridge (2007)

# A Pre-clinical Framework to Characterize Peri-infarct Remodelling Using *in vivo* $T_1$ Maps and CARTO Data

Mihaela Pop[1,2,*], Samuel Oduneye[1], Nilesh Ghugre[2], Elnaz Shokrolahi[2], Jen Barry[2], Yuesong Yang[2], Sudip Ghate[2], Roey Flor[2], Ilan Lashevsky[2], Eugene Crystal[2], and Graham A. Wright[1,2]

[1] Deptartment of Medical Biophysics, University of Toronto
[2] Sunnybrook Research Institute, Toronto, Canada
mihaela.pop@utoronto.ca

**Abstract.** The purpose of this work was to use *in vivo* MR imaging and electro-anatomical maps to characterize dense scars and border zone, BZ (a mixture of collagen and viable fibers). To better understand how these measures might probe potentially arrhythmogenic substrates, we developed a preclinical swine model of chronic infarction and integrated *in vivo* MRI and electrophysiology (EP) data in five swine at 5-6 weeks post-infarction. Specifically, we first aligned and registered $T_1$-maps (from MR studies) and bipolar voltage maps (from CARTO-EP studies) using Vurtigo, an open source software. We then performed a quantitative analysis based on circumferential segments defined in the short-axis of MR images. Our results demonstrated a negative linear relation between bipolar voltage maps and $T_1$ maps within the first two mm of the endocardial surface. The results of our novel approach suggest that $T_1$-maps combined with limited EP measurements can be used to evaluate the biophysical properties of healing myocardium post-infarction, and to distinguish between the infarct categories (i.e., dense scar vs. BZ) with remodelled electrical characteristics.

**Keywords:** cardiac MRI, T1 maps, CARTO bipolar voltages, border zone.

## 1 Introduction

The arrhythmogenic substrate for potentially lethal heart rhythms in patients with prior myocardial infarction is typically located at the so-called border zone (BZ), which is found between the normal and scarred tissue [1]. Currently, in the clinics, the chronic infarct areas are identified using contact (e.g. CARTO-XP electro-anatomical system, Biosense, Diamond, USA) and non-contact systems (e.g. Ensite system, St Paul, MN, USA). These systems record unipolar voltage values (between the catheter tip and a reference electrode) which reflect the global electrical activity and are influenced by far fields, as well as bipolar voltage values (i.e., difference between two unipolar electrograms recorded by adjacent rings of 1-2 mm separation) which

* Corresponding author.

O. Camara et al. (Eds.): STACOM 2012, LNCS 7746, pp. 326–335, 2013.

represent more accurately the local activity. In the CARTO bipolar voltage recordings, the voltage cut-off used to delineate the normal myocardium from infarct areas is arbitrarily set to values greater than 1mV or 1.5mV [2, 3]. A further categorization of the infarcted area is done by setting the cut-off thresholds to dense scar $\leq$ 0.5 mV (which comprises electrically inactive, fibrotic areas) and 0.5 mV < BZ < 1-1.5 mV. Although the electrical signals help identify some of the arrhythmogenic foci, these electro-anatomic voltage maps (EAVM) are only surfacic and do not provide transmural information. Thus, an important task for the clinicians is to determine the location, extent and transmurality of the infarct scar, and this is done non-invasively by employing MR imaging methods [4]. The conventional delayed-enhanced DE-MRI method is based on the elevation of signal intensity (SI) values within infarct regions, measured approximately 10-15 min after the contrast agent administration. The observed signal enhancement is due to different concentrations and kinetics of the Gadolinium-based molecules in the extracellular space within the healthy tissue and the infarcted areas; thus the infarct appears brighter than the surrounding structures as the Gd-based contrast agents alter MR relaxation properties and shorten the $T_1$ relaxation time [5]. Moreover, by using certain pulse sequences (e.g. the inversion-recovery gradient echo IR-GRE) and manipulating some MR parameters (e.g. inversion time, TI), one can obtain images with almost null MR signal from the healthy tissue and a clearly distinguishable infarct area.

Several studies aimed to characterize the scar and BZ using DE-MRI and CARTO maps and demonstrated that critical sites of post-infarction arrhythmias are usually confined to areas of elevated signal intensity (SI) in DE-MR images [6,7]. However, they also suggested that discrepancies between peri-infarct sites detected by DE-MRI and CARTO could be due to: far-field influences from normal myocardium, manual delineation of scar, poor wall/catheter contact. Notably, in most of these studies, SI threshold was set at 2 SD or 3 SD (standard deviation) higher than the mean SI selected from remote/normal myocardium. However, all these algorithms proposed to categorize infarct heterogeneities into dense scar and BZ are affected by noise, which is inherent in the MR signal and can significantly affect the reproducibility of results. An alternative method involves $T_1$-mapping and is based on a multi-contrast late enhancement (MCLE), in which a simultaneous nulling of MR signal from healthy myocardium and blood is employed. In particular, this method might be superior to the conventional delayed-enhanced MR method in delineating the subendocardial infarcted tissue from the blood pool [8].

However, to date, combined *in vivo* EP-MRI studies aiming to correlate infarct regions identified in $T_1$-maps from MCLE with bipolar voltage maps from CARTO studies have not been performed. Such investigation could provide a better characterization of electrical and structural properties infarcted myocardium. Therefore, the specific purpose of this paper was to characterize the heterogeneous infarct areas (i.e., dense scar and BZ) using *in vivo* CARTO bipolar voltage maps and *in vivo* MCLE-MRI methods, in a pre-clinical swine model of chronic infarction.

## 2 Materials and Methods

A diagram of the proposed framework is shown in Figure 1. We first acquired the *in vivo* MRI and EP data. Secondly, we performed data post-processing to segment the LV, to categorize tissue heterogeneities, and to fuse (align and register) MR images with EAV maps. Thirdly, we analyzed the correlation between T1-maps and bipolar voltage maps. We described below these three steps in more detail.

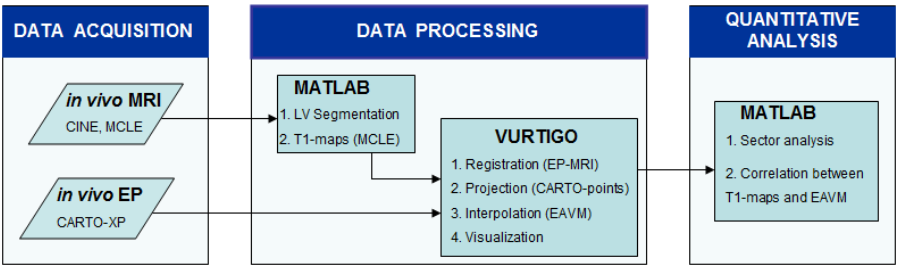


**Fig. 1.** Flow-chart of the three major steps performed: a) *in vivo* MRI and EP data acquisition; b) data processing (tissue classification, CARTO-to-MRI fusion); and c) quantitative analysis (correlation between bipolar voltage values and $T_1$-maps)

### 2.1 *In vivo* MRI Study and *in vivo* CARTO-EP Study

All experiments included in this pre-clinical framework were approved by Sunnybrook Research Institute, Toronto, CA. For the correlation between T1 maps and CARTO maps we used five swine with chronic infarction. The infarction was generated using an occlusion-reperfusion method and the scar was allowed to heal for 5-6 weeks, as previously described [9, 10]. In the current work, for the purpose of calibrating the threshold for the bipolar voltage values in healthy myocardial tissue, we also included CARTO-EP data collected in five control/healthy swine.

The MR imaging studies were performed on a dedicated 1.5T research scanner (GE SignaExcite) using a 5-inch surface coil. The MR scans had the following parameters: TE=1.9 ms, TR=5.5 ms, NEX=1, FOV=26 cm, 256x256 acquisition matrix, and 5-mm slice thickness. Delayed enhancement imaging was started 10-15 minutes after the injection of a Gd-DTPA bolus. Several short-axis MCLE images were acquired through the infarct volume, with the inversion pulse placed such that the infarct-enhanced images were acquired with minimal motion during diastole, for which TI (inversion time) ranged from 175 to 250 ms. A clinical expert verified in select images (based on manual contours) that there was indeed minimal motion within this range, especially in the infarct area where the collagenous scar losses contractility. The MCLE used steady-state free precession (SSFP) readouts during the inversion recovery IR process, producing 20 images over the cardiac cycle each at a different TI*. The MCLE images at early inversion times have varying contrast where the infarct can be visualized as an area of fast $T_1^*$ recovery (where $T_1^* < T_1$ due to the

continuous SSFP readout). Figures 2a-d show four (out of 20) MCLE images corresponding to one 2D short-axis MR slice.

Further, approximately six images (per heart cycle) were selected and used to extract the signal intensity (SI) recovery curve for each pixel within the LV (including the blood pool pixels), given that signal intensity obeys the equation (1):

$$SI\ (time) = SS * [1\text{-}2exp(-time/T_1^*)] \quad (1)$$

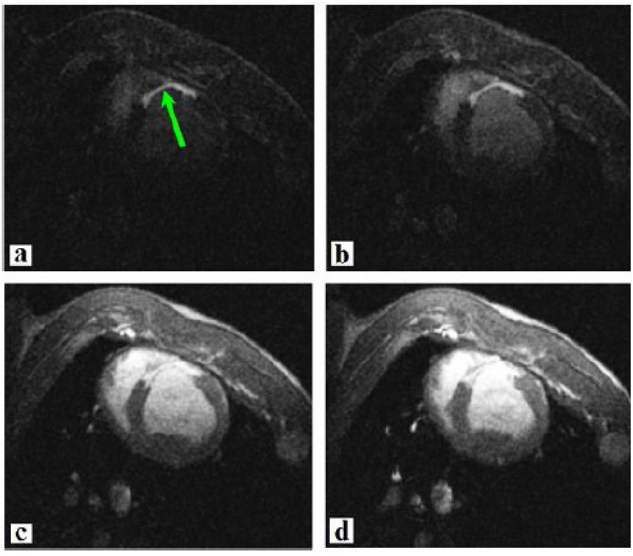


**Fig. 2.** Four consecutive short-axis MCLE images (a-d) acquired in a swine with the infarct visualized as a hyper-enhanced region (indicated by arrow)

Next, each *in vivo* EP study was performed after the MRI scan using the CARTO-XP electro-anatomical system. The bipolar voltage maps were acquired using either QwikStar or Navistar contact catheters inserted into the cavity of the LV under X-ray fluoroscopy, and the recordings were performed in the normal sinus rhythm or in paced conditions.

## *2.2* Data Processing: Tissue Segmentation and Fusion of in vivo MRI and EAVM

For the LV segmentation, the LV endocardial and epicardial surfaces were traced in short-axis image series of conventional cine SSFP during all phases of the heart, using an algorithm previously developed by our group [11]. For the 2D MCLE images, a corresponding spatial map of the various tissue types was generated using automated fuzzy clustering analysis [12]. The fuzzy clustering algorithm determines the probability of each pixel belonging to each of the three clusters based on a distance metric derived from the scatter plot ($T_1^*$ versus steady-state (SS)) as described in [12]. A scatter plot of $T_1^*$ versus steady-state value for each pixel was then used as the

input to a fuzzy C-means algorithm to automatically classify each pixel as: either infarct, or healthy myocardium, or blood.

Next, the (X,Y) coordinates of endocardial and epicardial contours were extracted and imported into VURTIGO software [13]. The LV endocardial and epicardial contours were used to generate 3D meshes by converting the myocardial contours into 3D coordinates, based on the 3D spatial location and pixel (voxel) size in MR images. All CARTO points were imported into VURTIGO, where each EAVM was aligned to its corresponding MR endocardial surface using anatomical markers; we then registered these maps by matching these reference points from both imaging modalities. Note that all landmark points (i.e., apex, mitral valve, etc) were manually selected by a clinical expert, similarly to the registration described in [6] and [7] where the CARTO-MERGE software was used. For the interpolation step, a triangulation approach was employed to obtain a surface description of myocardial walls from the recorded EAV points. The registration error (i.e., fiducial registration error, FDE) was calculated using:

$$FRE = \frac{\sum_{i=1}^{N_{landmarks}} dist(S_i, T_i)}{N_{landmarks}} \tag{2}$$

where: $N_{landmarks}$ is the number of landmark pairs, $S_i$ is the i'th source landmark and $T_i$ is the i'th target landmark.

### 2.3 Quantitative Analysis

We correlated the $T_1$ values from selected 2D MCLE data (i.e., 3-5 images per animal) with the bipolar voltage amplitude values from the corresponding CARTO points by using a sector analysis. All select short-axis MCLE slices were segmented circumferentially into 12 equal sectors (instead of 6 basal and 4 apical proposed in the AHA guidelines); this was done to decrease the potential mismatch between the values of CARTO points projected onto either BZ or scar segments defined from $T_1$ maps. Further, each sector was divided in sub-sectors (i.e., sub-segments) defined from the endocardium to the epicardium by drawing concentric circles at 2 mm of endocardium surface, as well as on epicardium (at whole thickness). Next, we calculated the percentage of each tissue type (in pixels) in each sub-segment within the first two mm of endocardium and within the full thickness, respectively, and further categorized each sub-segment into: healthy or BZ or dense scar, depending on the majority of pixels calculated within that sub-segment. Each endocardial segment was also assigned a bipolar voltage value from the CARTO points projection. Finally, a comparison between EP and MRI was performed as per the 'points by segment' method proposed in [7]. Note that, if more than 1 CARTO point was projected onto a segment, we calculated an average bipolar voltage value for that segment.

Figure 3 shows a hypothetical example of correlating the EP signal and MR tissue characteristics using sectors categorized from $T_1$-maps, where a CARTO 'scar' point of 0.4 mV bipolar voltage value is projected onto an endocardial segment from the

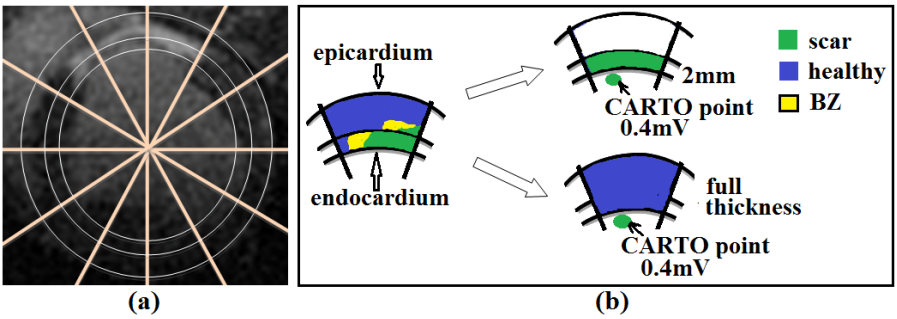


**Fig. 3.** Schematic example of the sector analysis in the LV of a heart with anterior infarct: (a) LV segmentation into 12 sectors and further sub-sectors at different depths; and (b) hypothetical tissue categorization from MCLE images based on $T_1$ relaxation values, with different transmural categorization (based on number of pixels in that sub-sector) at 2 mm depth of endocardium and at full thickness, respectively, and further correspondence between these categories and the bipolar voltage value of a segment (following projection of a CARTO point onto it).

left ventricle. At 2 mm depth of endocardium, this voltage value would correspond correctly to a sector categorized as 'scar' in a $T_1$-map, whereas at full thickness, it would incorrectly correspond to a 'healthy' sector.

## 3 Results

Figure 4 shows example results from the step 2 (data processing) obtained in one of the animals. Fig 4a shows a scatter plot of T1* versus SS values for all pixels within the LV (for the MCLE images presented in Fig 2). The resulted 2D spatial map of various tissue types classified using the automated fuzzy clustering algorithm is shown in Fig 4b.

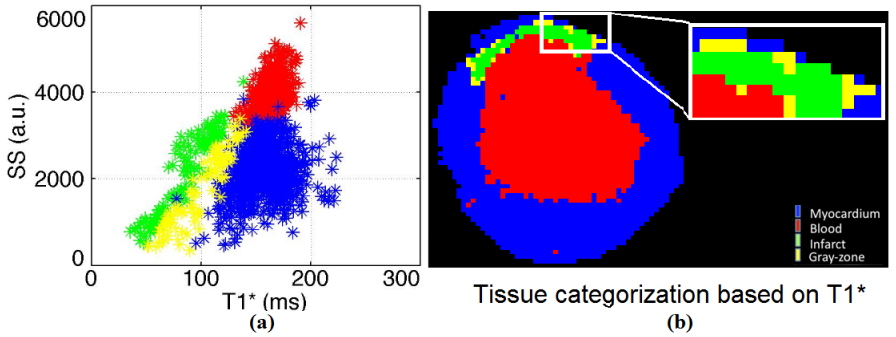


**Fig. 4.** Example of realistic categorization from MCLE images: (a) scatter plot of $T_1^*$ versus steady-state (SS) values for all pixels within the LV; and (b) corresponding spatial map of various tissue categories classified using the fuzzy clustering algorithm: infarct (green), BZ (yellow), healthy tissue (blue), and blood (red)

Figure 5 shows an example result from the integration of EAVM and MR images performed using VURTIGO. A snapshot of the endocardial contours (white dots) generated from the cine MR images is shown in Fig 5a. The bipolar voltage map projected onto this endo-surface (after landmark registration) is shown in Fig 5b, and corresponding tissue heterogeneities as defined by $T_1$-maps in Fig 5c. The mean *FRE* was calculated to be 5 mm (averaged over all infarcted animals).

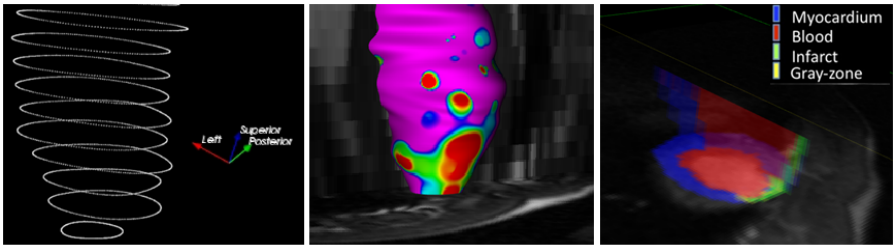


**Fig. 5.** Integration and visualization of bipolar voltage maps with MR images using VURTIGO: (a) segmented endocardial surface from cine-MR images; (b) a bipolar voltage map projected onto the LV-endocardium after registration; and (c) a 3D volume rendering from a 2D stack of MCLE images after categorization.

Figure 6 shows the results of the quantitative analysis performed in all five animals, demonstrating a strong correlation between $T_1$-maps and bipolar voltage values. Figure 6 suggests that, based on the correspondence between bipolar voltages cut-off in BZ and dense scar categorized in healthy, BZ and dense scar, the catheter sensitivity decreases with the depth of endocardium. Furthermore, we derived negative linear relationships with the following correlation coefficients: r = -0.86 at 2mm-1mm depth, and r = - 0.73 at whole myocardium, respectively (note: we excluded the first 1 mm from the radial circle corresponding to 2 mm of endocardium, as some slices had blood pixels due to the automatic segmentation algorithm of endocardium from cine images). In addition, we calculated the median values for the bipolar voltages measured in the five control/healthy swine (not included in the figure), and thus confirmed that 1.5 mV is a valid threshold to differentiate between healthy and infarcted myocardium.

Statistical analysis performed using two-tailed *t*-test between the different categories plotted in Fig 6a, reveals statistical significant differences between the bipolar values corresponding to the following categories identified by MCLE: a) healthy areas and either BZ or scar areas (both had $p < 0.001$). b) BZ at 2mm-1mm and BZ at whole thickness ($p< 0.024$); and c) BZ and scar at 2mm-1mm ($p < 0.0001$), as well as BZ and whole thickness ($p < 0.0025$), respectively. The calculated p value between the scar at 2mm-1mm and whole thickness was found to be not significant ($p<0.2$), which was expected due to the transmural extent of scar.

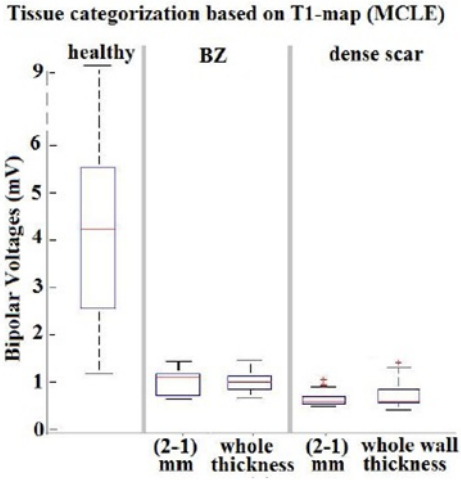


**Fig. 6.** Correlation between bipolar voltage values and T1-maps: median bipolar voltage values of the segments corresponding to different tissue categories (based on T1 map) within 2mm–1mm of endocardium, and whole-thickness of myocardium (note: box plots have the 25th and 75th percentiles in the distribution score)

## 4 Discussion

Accurate myocardial characterization in post-infarction remodelling is an important task in order to identify potential arrhythmogenic foci. This clearly motivates the development of pre-clinical experimental frameworks and novel non-invasive imaging methods and image analysis algorithms to assess tissue viability and biophysical properties of ischemic areas, in order to supplement the limited EP measures. A superior non-invasive imaging method is the MCLE method used in this work, which allowed us to generate accurate $T_1$ maps that were used to detect infarcted tissue without the need to estimate the TI for nulling myocardium as in the conventional DE-MRI. In general, we demonstrated that our method provided an accurate classification of the infarct heterogeneities and identification of subtle endocardial lesions in a swine model of chronic infarction. The $T_1$ maps reflected the structural changes in healing myocardium, that is an increase in extracellular space and in collagen deposition in the infarcted areas, as well as the presence of heterogeneous areas in the peri-infarct (a hallmark of patchy fibrosis in the chronic infarction). These structural changes were also accompanied by alteration in electrical properties and signal morphologies (e.g. the amplitude of bipolar voltage values) as observed in the EP experiments.

Our study is the first to evaluate the relation between MR tissue properties based on $T_1$ relaxation maps and local voltage values using EAVM and MCLE to characterize infarct heterogeneities (i.e., dense scars and ischemic BZ areas). Specifically, we demonstrated that the infarct categorization (healthy, dense scar and border zone) determined in $T_1$ maps correlated very well with bipolar voltage values. On the basis of our experimental results, this study also supports the validity of

conventional voltage criteria: 0.5-1.5 mV for delineation of scar and BZ region, as well as > 1.5 mV for the healthy areas. Note that our results are in agreement with those reported in a recent study [7] which integrated MRI-derived scar maps with EAVM in fifteen patients undergoing ablation VT ablation, and similarly found that bipolar voltage values significantly decrease with the increase in scar transmurality for core infarct and BZ. Notably, for the segments categorized as BZ in our $T_1$ maps, our bipolar voltage values showed a better correlation at the first 2 mm depth of endocardium compared to the whole thickness, as well as a significant decrease in bipolar values with the increase in depth of endocardium, reflecting the sensitivity of the recording catheter at these locations. However, the same significant difference was not observed for the segments containing mainly dense scar, and was attributed to the (almost) full transmurality of the infarct in these segments.

The registration between the CARTO and MRI was performed in Vurtigo using anatomical landmarks selected by clinical experts, in a similar way the fusion of MRI and contact-EP data is performed in the clinical settings with the CARTO-MERGE software, yielding a 5 mm fiducial registration error which is clinically acceptable. In our method, each slice was divided into 12 segments and this likely provided a more accurate correlation between T1 and CARTO maps compared to a segmentation into 4-6 AHA segments (per apical/base slices). We believe that the registration step did not introduce large errors in the analysis since each segment (getting assigned 1 CARTO value or an average of few values) was relatively large; however, future work will address this in more detail. Moreover, future work will also focus on extending this type of EP-$T_1$ analysis using electrical signal amplitude in bipolar voltage maps recorded in real-time under MR guidance, in an infarcted swine model. A recent study from our group has reported the feasibility of recording electrophysiology data (i.e., depolarization maps) in a swine study [14]; such approach minimizes the registration error since the EP data is collected in the same coordinate system as of the MR images.

Finally, a limitation of this study is the relatively small sample size (i.e., n=5 animals); however, there were between 3-5 MR images (slices) containing infarcted tissue selected per each heart, that is 36 to 60 sectors analyzed per animal (at each depth), which was enough for accurate statistical analysis.

To conclude, $T_1$ maps can be used to evaluate the biophysical properties of healing myocardium post-infarction, and to distinguish between infarct categories (i.e., dense scar vs. BZ) with remodelled electrical characteristics. Moreover, $T_1$ maps contain transmural information and thus supplement the information currently given by the limited/surfacic EP measurements.

**Acknowledgement.** This work was financially supported in part by a grant from the Canadian Institutes of Health Research (MOP93531).

## References

1. Stevenson, W.G.: Ventricular scars and VT tachycardia. Trans. Am. Clin. Assoc. 120, 403–412 (2009)
2. Wrobleski, D., Houghtaling, C., Josephson, M.E., Ruskin, J., Reddy, V.: Use of electrogram characteristics during sinus rhythm to delineate the endocardial scar in a porcine model of healed myocardial infarction. J. Cardiovasc. Electrophysiol. 14, 524–529 (2003)

3. Callans, J.D., Ren, J.-F., Michele, J., Marchlinski, F., Dillon, S.: Electroanatomic left ventricular mapping in the porcine model of healed anterior myocardial infarction. Correlation with intracardiac echocardiography and pathological analysis. Circulation 100, 1744–1750 (1999)
4. Bello, D., Fieno, D.S., Kim, R.J., et al.: Infarct morphology identifies patients with substrate for sustained ventricular tachycardia. J. Am. College of Cardiology 45(7), 1104–1110 (2005)
5. Kim, R.J., Fieno, D.S., Parrish, T.B., Harris, K., Chen, E.L., Simonetti, O., Bundy, J., Finn, J.P., Klocke, F.J., Judd, R.M.: Relationship of MRI delayed contrast enhancement to irreversible injury, infarct age, and contractile function. Circulation 100, 1992–2002 (1999)
6. Codreanu, A., Odille, F., Aliot, E., et al.: Electro-anatomic characterization of post-infarct scars comparison with 3D myocardial scar reconstruction based on MR imaging. J. Am. Coll. Cardiol. 52, 839–842 (2008)
7. Wijnmaalen, A., van der Geest, R., van Huls van Taxis, C., Siebelink, H., Kroft, L., Bax, J., Reiber, J., Schalij, M., Zeppenfeld, K.: Head-to-head comparison of contrast-enhanced magnetic resonance imaging and electroanatomical voltage mapping to assess post-infarct scar characteristics in patients with ventricular tachycardias: real-time image integration and reversed registration. European Heart Journal 32, 104 (2011)
8. Detsky, J.S., Stainsby, J.A., Vijayaraghavan, R., Dick, A.J., Wright, G.A.: Inversion-recovery prepared SSFP for cardiac-phase-resolved delayed-enhancement MRI. Magnetic Resonance in Medicine 58(2), 365–372 (2007)
9. Pop, M., Sermesant, M., Mansi, T., Crystal, E., Ghate, S., Peyrat, J.-M., Lashevsky, L., Qiang, B., McVeigh, E.R., Ayache Wright, G.A.: Correspondence between simple 3D MRI-based computer models *and invivo* EP measurements in swine with chronic infarctions. IEEE Trans. Biomed. Eng. 58(12), 3483–3486 (2011)
10. Ghugre, N.R., Ramanan, V., Pop, M., Yang, Y., Barry, J., Qiang, B., Connelly, K., Dick, A., Wright, G.A.: Quantitative tracking of edema, hemorrhage and microvascular obstruction after acute myocardial infarction by MRI. Magnetic Resonance in Medicine 66(4), 1129–1141 (2011)
11. Lu, Y., Radau, P., Connelly, K., Dick, A., Wright, G.A.: Segmentation of Left Ventricle in Cardiac Cine MRI: An Automatic Image-Driven Method. In: Ayache, N., Delingette, H., Sermesant, M. (eds.) FIMH 2009. LNCS, vol. 5528, pp. 339–347. Springer, Heidelberg (2009)
12. Detsky, J.S., Paul, G., Dick, A.J., Wright, G.A.: Reproducible classification of infarct heterogeneity using fuzzy clustering on multicontrast delayed enhancement magnetic resonance images. IEEE Trans. Med. Imaging 28(10), 1606–1614 (2009)
13. Radau, P.E., Pintilie, S., Flor, R., Biswas, L., Oduneye, S.O., Ramanan, V., Anderson, K.A., Wright, G.A.: VURTIGO: Visualization Platform for Real-Time, MRI-Guided Cardiac Electroanatomic Mapping. In: Camara, O., Konukoglu, E., Pop, M., Rhode, K., Sermesant, M., Young, A. (eds.) STACOM 2011. LNCS, vol. 7085, pp. 244–253. Springer, Heidelberg (2012)
14. Oduneye, S.O., Biswas, L., Ghate, S., Ramanan, V., Barry, J., Laish-FarKash, A., Kadmon, E., Zeidan Shwiri, T., Crystal, E., Wright, G.A.: The feasibility of endocardial propagation mapping using MR guidance in a swine model and comparison with standard electro-anatomical mapping. IEEE Trans. Med. Imaging 31(4), 977–983 (2012) (Epub. November 4, 2011)

# Exercise Induced Inter-individual Variation of Right Ventricular Pressures: Simulations Using a Modular Model of the Cardiovascular System

Catalina Tobon-Gomez[1], Georgina Palau-Caballero[1], Marta Sitges[2], and Bart H. Bijnens[1,3]

[1] PhySense - N-RAS, Universitat Pompeu Fabra, Barcelona, Spain*
[2] Thorax Institute, Hospital Clinic, Universitat de Barcelona, IDIBAPS, Barcelona, Spain**
[3] Institució Catalana de Recerca i Estudis Avançats (ICREA), Barcelona, Spain

**Abstract.** In recent years, the response of, especially, the right ventricle to intense exercise has gained increased interest. In this study, we use the CircAdapt model to evaluate the influence of inter-individual variation of pulmonary vascular resistance during exercise on cardiovascular hemodynamics. We modeled pulmonary vascular resistance as a nonlinear resistive module in which the resistance increases proportionally to stroke volume. We modeled inter-individual variation following normal random distributions. To evaluate the hemodynamic response to exercise, we computed pulmonary artery systolic pressure and end-systolic wall stress. With our modeling strategy, we were able to reproduce the phenomena observed clinically.

## 1 Introduction

In recent years, the response of, especially, the right ventricle (RV) to intense exercise has gained increased interest [2]. In professional athletes the incidence of arrhythmias originating from the RV has been shown to be significantly higher [3]. Several hypotheses have been suggested as a possible cause, among which is the inter-individual hemodynamic response of the RV to high-intensity exercise [1].

Modeling has long been used by researchers to study physiological phenomena. Using a model, a complex system can be interrogated for a variable of interest under controlled circumstances. In particular, the cardiovascular system has been studied for decades using in-vitro and animal models. More recently, computational models have also been adopted as a technique able to accurately reproduce cardiovascular dynamics. Due to their computational nature, a great number of scenarios can be simulated.

* This study was partially supported by the Subprograma de Proyectos de Investigación en Salud. Instituto de Salud Carlos III, Spain (FIS - PI11/01709).
** This study was partially supported by a grant of Sociedad Española de Cardiologia 2012-06-18.

O. Camara et al. (Eds.): STACOM 2012, LNCS 7746, pp. 336–344, 2013.

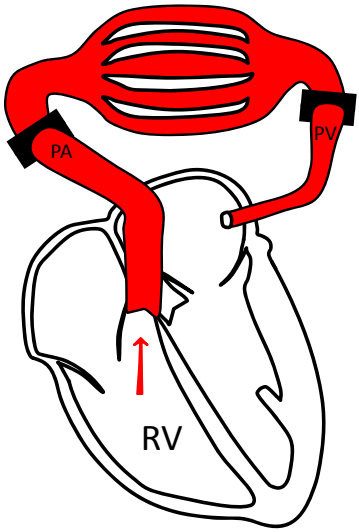


**Fig. 1.** Schematic of pulmonary circulation. A larger amount of blood circulating through the cardiovascular system is bottle-necked at pulmonary circulation. This bottle-neck effect is related to *pulmonary vascular resistance* (PVR). An increase of PVR leads to an increase of pressure at the inlet of pulmonary circulation: the pulmonary artery. Since the right ventricle pumps the blood into the pulmonary artery, the increase of pressure directly affects RV pressures. According to recent findings [1], during exercise some individuals are able to recruit and dilate more pulmonary vessels than other individuals (i.e. increased *pulmonary reserve*). In these individuals, blood flows easier through pulmonary circulation, thus overall PVR is reduced (see Sec. 2.1 and Sec. 2.2). PA= pulmonary artery; PV= pulmonary veins; RV= right ventricle.

A well validated computational model of circulation dynamics is CircAdapt [4, 5]. It represents the whole circulatory system as a combination of four types of modules: chambers, tubes, resistances and valves. The model simulates beat-to-beat dynamics of the four-chambers of the heart with systemic and pulmonary circulation.

Pulmonary circulation is an important modulator of cardiac output, both in pathological [6, 7] and healthy subjects [8]. During exercise, pulmonary vascular resistance (PVR) increases [8]. In this study, we use the CircAdapt model to evaluate the influence of inter-individual variation of PVR during exercise on cardiovascular hemodynamics.

## 2 Methods

### 2.1 Clinical Motivation

It was recently suggested that during exercise some individuals show transpulmonary crossing of ultrasound-contrast agent in larger quantities with respect to other individuals. This is known as low and high pulmonary transit of agitated contrast (low-PTAC and high-PTAC, respectively) [1]. This differentiation was shown to be independent of their hours of training per week (elite athletes or volunteers). This suggests that some individuals are able to recruit larger vessels in the pulmonary circulation while stroke volume (SV) increases, thus altering the overall PVR (see Fig. 1). We will refer to this ability to adapt to high demands of SV as increased *pulmonary reserve*. Therefore, our study focuses on the inter-individual differences in the RV pressure-volume relation during exercise, resulting from differences in pulmonary reserve.

**Table 1.** Modified input parameters at baseline and peak exercise

| Parameters | Units | Baseline | | Peak Exercise | |
|---|---|---|---|---|---|
| | | EA | NA | EA | NA |
| Hemodynamics | | | | | |
| Cardiac output | L/min | 8.2 | 7.8 | 18.7 | 23.3 |
| Stoke volume$^{\dagger}$ | mL | 139.0 | 110.0 | 156.0 | 130.0 |
| Heart rate$^{\dagger}$ | beats/min | 59.0 | 71.0 | 149.0 | 144.0 |
| Mean blood pressure$^{\dagger}$ | mmHg | 101.0 | 97.0 | 120.0 | 123.0 |
| Geometrical | | | | | |
| LV end-diastolic volume$^{\ddagger}$ | mL | 232.0 | 179.0 | *n.a.* | *n.a.* |
| RV end-diastolic volume$^{\ddagger}$ | mL | 264.0 | 198.0 | *n.a.* | *n.a.* |
| LV myocardial wall volume$^{\ddagger}$ | mL | 159.0 | 112.2 | *n.a.* | *n.a.* |
| RV myocardial wall volume$^{\ddagger}$ | mL | 45.8 | 28.1 | *n.a.* | *n.a.* |
| Inter-individual variation | | | | | |
| $\Delta P$ | mmHg | $3.1 \pm 1.4$ | | $25.7 \pm 7.4$ | |

EA= elite athlete; NA= non athlete; $^{\ddagger}$= Mean values in [2]; $^{\dagger}$= Mean values in [1]; $\Delta P$ = pulmonary arteriovenous pressure drop; *n.a.*= not applicable.

### 2.2 Modeling Strategy

**Circulation Hemodynamics.** To model circulation hemodynamics, we use the CircAdapt model [4, 5]. This model adapts to changes in mechanical load using a set of physical and physiological rules. Acute adaptation is obtained by vasodilation. Chronic adaptation is obtained by chamber dilation and/or wall hypertrophy.

CircAdapt has been previously used to simulate changes in PVR due to chronic pulmonary hypertension [9], where different PVR values are obtained by varying the instantaneous pulmonary arteriovenous pressure drop ($\Delta P$ = pulmonary artery pressure - pulmonary venous pressure). In this previous work, Lumens *et al.* simulate $\Delta P$ as a nonlinear resistive module, in agreement with pressure-flow relationships measured in human and dogs [10–12]. For our study, we use this same nonlinear resistive module, but we increase $\Delta P$ proportionally to SV (see Fig. 1 and next section for further details).

**Pulmonary Vascular Resistance (PVR) during Exercise.** We obtained a normal hemodynamic simulation at rest using the baseline values reported by La Gerche *et. al.* [1]. To simulate a state of exercise, we increased cardiac output from baseline to peak exercise values. Cardiac output (CO) changes were obtained by increasing three parameters in equally spaced increments: SV, heart rate (HR) and mean blood pressure (MBP). The chronic adaptation to exercise was simulated by modifying initial conditions of ventricular geometry. That is, larger cavity volumes and thicknesses (see next section for further details). Then, we studied the hemodynamic response to exercise only with acute adaptation. That is, allowing vasodilation without cavity enlargement or hypertrophy. Baseline and peak exercise values used in this study are summarized in Table 1.

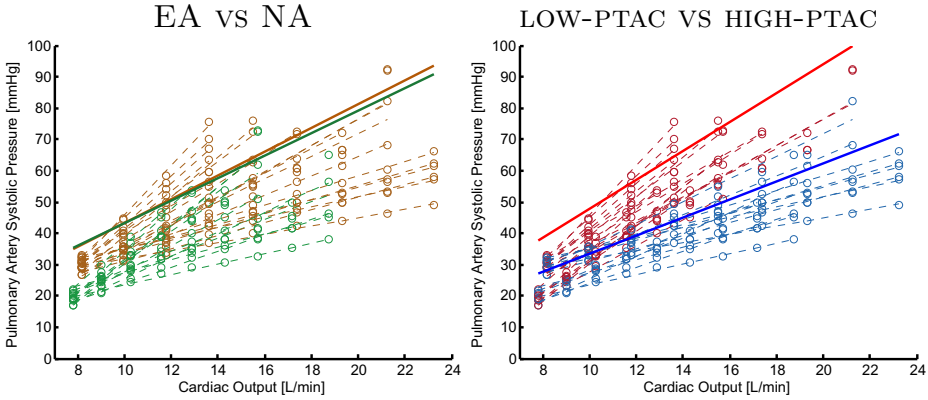


**Fig. 2.** Pulmonary artery systolic pressure (PASP) measurements computed from the clinical surrogate. (left) Each line represents one individual either with an elite athlete heart (brown) or a non athlete heart (green). (right) Each individual was classified as above (red) or below (blue) the mean slope reported in literature [1]. This classification corresponds to individuals with low-PTAC (red) and high-PTAC (blue). (left-right) Dark lines represent mean slope values reported in literature [1]. For further analysis see Sec. 3.

**Inter-individual Variation.** We generated 20 virtual individuals as follows. To generate each virtual individual, baseline $\Delta P_0$ was assigned a random value $X \sim \mathcal{N}(\mu, \sigma^2)$ with $\mu$ and $\sigma$ as summarized in Table 1.

For each individual, $\Delta P_0$ was increased with exercise as a function of SV, such that:

$$\Delta P_i = \Delta P_0 + \Delta P_0 \times fact * \frac{SV_i - SV_0}{SV_{peak} - SV_0} \tag{1}$$

where $i$ represents each CO increment, and $fact$ was assigned a random value $fact \sim \mathcal{N}(15, 15^2)$. Resulting $\Delta P$ values at peak exercise are also summarized in Table 1.

To each virtual individual, we assigned two types of heart geometries, corresponding to a non athlete (NA) heart and an elite athlete (EA) heart [1,2]. The geometry was imposed by modifying end-diastolic volumes and myocardial wall volumes (mL) for both LV and RV (see Table 1).

## 3 Results

### 3.1 Pulmonary Artery Systolic Pressure

To evaluate the effect of exercise on pulmonary hemodynamics, we computed pulmonary artery systolic pressure (PASP). CircAdapt provides this value as direct

**Table 2.** Measures of hemodynamic response at baseline and peak exercise in comparison to literature

| | | Units | Baseline | | | Peak Exercise | | |
|---|---|---|---|---|---|---|---|---|
| | | | low-PTAC | high-PTAC | $\Delta$ | low-PTAC | high-PTAC | $\Delta$ |
| PASP | La Gerche *et al.* [1] | mmHg | 22.0 ± 4.2 | 21.0 ± 3.4 | 1.0 | 62.6 ± 13.7 | 52.3 ± 9.8 | 10.3 |
| | Our study | mmHg | 26.2 ± 5.8 | 25.4 ± 5.5 | 0.6 | 69.1 ± 11.8 | 61.6 ± 13.7 | 7.5 |
| | | | LV | RV | | LV | RV | |
| ESWS | La Gerche *et al.* [2] | Kdynes/cm$^2$ | 243.4 ± 17.3 | 139.5 ± 10.9 | | 263.8 ± 25.6 | 282.9 ± 22.1 | |
| | Our study | Kdynes/cm$^2$ | 220.8 ± 33.6 | 98.3 ± 9.7 | | 338.6 ± 90.6 | 524.5 ± 245.7 | |

PASP= pulmonary artery systolic pressure;

ESWS= end systolic wall stress; LV= left ventricle; RV= right ventricle;

output of the simulation. However, to be able to compare with reported literature values [1], we computed the clinical surrogate measurement of PASP [13]:

$$PASP = mean(P_{VC}) + max(P_{RV}) - max(P_{RA}) \tag{2}$$

where $P$ = pressure, $VC$ = vena cava, $RV$ = right ventricle, $RA$ = right atrium.

Fig. 2 shows the results of PASP measurements, where each line represents one individual. The differences in slope represent the inter-individual variation of pulmonary reserve. Fig. 2-left shows PASP measurements for both types of hearts: EA and NA. It can be observed that there is no clear differentiation between the two groups. Fig. 2-right shows the results of PASP measurements where each individual was classified as above (red) or below (blue) the mean slope reported in literature [1]. This classification corresponds to individuals with low-PTAC (red) and high-PTAC (blue) [1]. We observe that the modeling approach is able to reproduce scopes of clinically reported PASP vs. CO values. Average values at baseline and peak exercise for these two groups are summarized in Table 2. Although the overall effect of inter-individual differences in pulmonary reserve was reproduced with our modeling strategy, both baseline and peak values were overestimated w.r.t. literature values. Note that we used only mean values reported in the literature. Most likely, computed PASP ranges will be improved by simulating inter-individual PVR differences with patient-specific parameters. That is, cavity volumes, wall thicknesses, cardiac output and pressure measurements. This will be our immediate future work.

### 3.2 End-Systolic Wall Stress

Another important hemodynamic measure is wall stress. Particulary, it has been shown that end-systolic wall stress (ESWS) at peak exercise is considerably higher on the RV with respect to the LV [2]. Based on Laplace's law, we computed ESWS as:

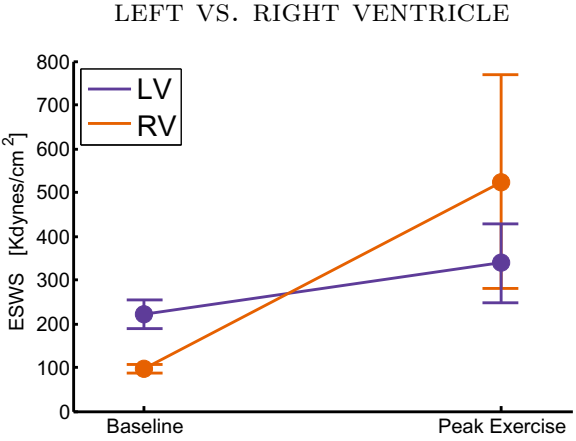


**Fig. 3.** End-systolic wall stress (ESWS) for the left ventricle (LV) and right ventricle (RV). Note the disproportionate higher load on the RV at peak exercise when compared with the LV. For further analysis see Sec. 3.

$$ESWS = \frac{Pr}{2h} \tag{3}$$

where $r$ = ventricular radius, and, $h$ = ventricular wall thickness. For LV, cavity pressure $P$ = systolic blood pressure LV pressure,while for RV $P$ = PASP calculated from the clinical surrogate, as described above. Results are displayed in Fig. 3. We can observe the disproportionate higher load on the RV at peak exercise when compared with the LV. Note also the larger dispersion of ESWS for the RV at peak exercise, due to a larger inter-individual variability of PVR. Average values at baseline and peak exercise are summarized in Table 2. Similarly to PASP values, we obtained a mismatch between computed and previously reported ESWS values [2]. However, the overall clinical phenomenon was successfully reproduced.

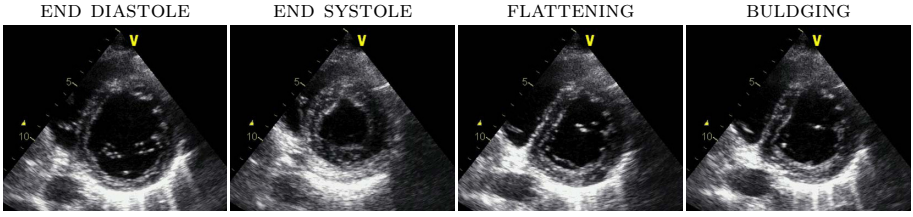


**Fig. 4.** 2D echocardiography of an elite athlete. We can clearly observe the effect of septal fattening and buldging (septum is displaced towards the LV cavity). Studying the simulations we can conclude that this happens due larger RV pressures immediately after LV end systole. For further analysis see Sec. 3.

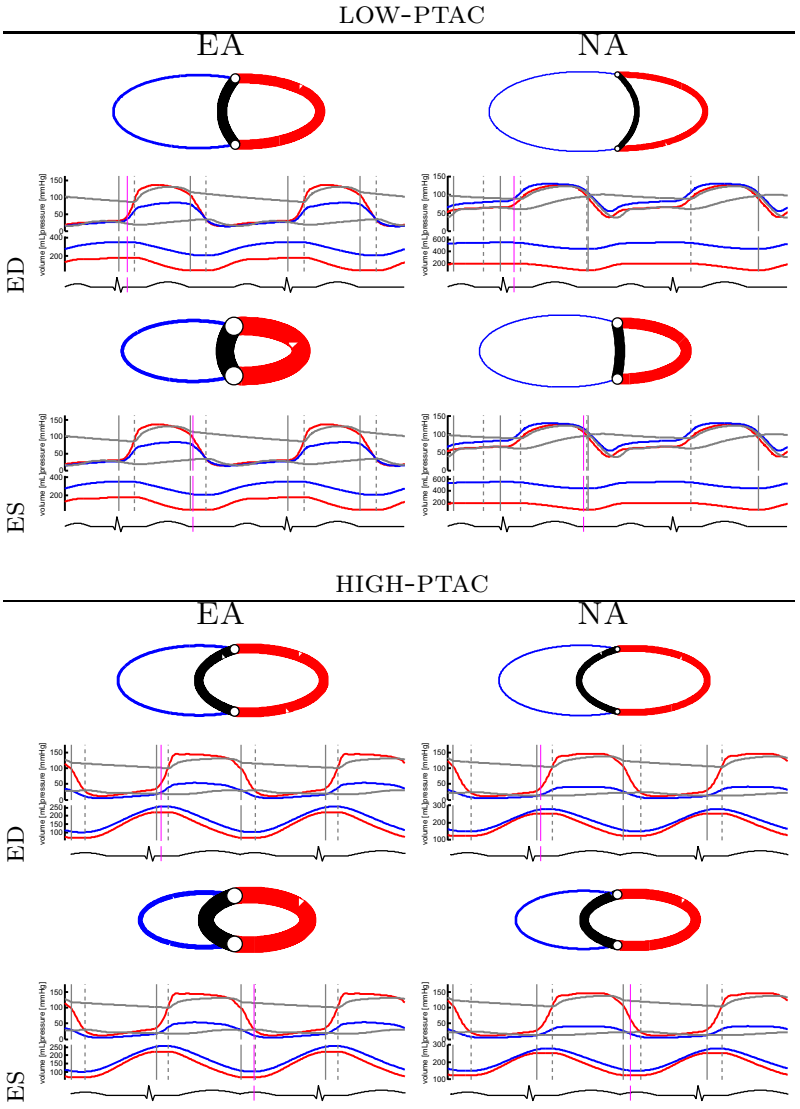


**Fig. 5.** Each figure displays (top) a schematic short-axis view of chamber anatomy and (bottom) a Wiggers diagram. In the schematic we can observe the proportion of cavity size, wall thickness and septal curvature. In the Wiggers diagram we can observe the relation of pressure and volume curves along the cardiac cycle. For further analysis see Sec. 3.

### 3.3 Schematic and Wiggers Diagram

To provide a better visualization of the hemodynamic effect of intense exercise, Fig. 5 shows a schematic short-axis view of chamber anatomy and a Wiggers diagram. The schematic was generated using the graphical user interface developed by Palau-Caballero *et al.* [14]. This figure was computed for the individual with the largest PASP vs. CO slope (Fig. 2-right). We can clearly observe the geometrical changes induced by exercise: RV enlargement and septal flattening. Also, due to the large increase of RV pressures the septum is displaced towards the LV cavity. Fig. 4 shows this effect in a 2D echocardiography dataset of an elite athlete. We can observe septal fattening and buldging.

## 4 Conclusions

This work studied the inter-individual differences in the RV pressure-volume relation during exercise, resulting from differences in pulmonary reserve. We modeled pulmonary vascular resistance as a linear resistive module in which the resistance increases proportionally to stroke volume. We modeled inter-individual variation following normal random distributions.

To evaluate the hemodynamic response to exercise, we computed pulmonary artery systolic pressure and end-systolic wall stress. With our modeling strategy, we obtained simulation results which reproduce reported clinical phenomena. Future work includes, an extensive sensitivity analysis of the simulation approach, and, an extension of the approach to fit patient-specific values from our in-house clinical population.

## References

1. La Gerche, A., MacIsaac, A.I., Burns, A.T., Mooney, D.J., Inder, W.J., Voigt, J.U., Heidbüchel, H., Prior, D.L.: Pulmonary transit of agitated contrast is associated with enhanced pulmonary vascular reserve and right ventricular function during exercise. J. Appl. Physiol. 109(5), 1307–1317 (2010)
2. La Gerche, A., Heidbuchel, H., Burns, A.T., Mooney, D.J., Taylor, A.J., Pfluger, H.B., Inder, W.J., Macisaac, A.I., Prior, D.L.: Disproportionate exercise load and remodeling of the athlete's right ventricle. Med. Sci. Sports Exerc. 43(6), 974–981 (2011)
3. La Gerche, A., Burns, A.T., Mooney, D.J., Inder, W.J., Taylor, A.J., Bogaert, J., Macisaac, A.I., Heidbuchel, H., Prior, D.L.: Exercise-induced right ventricular dysfunction and structural remodelling in endurance athletes. Eur. Heart J. 33(8), 998–1006 (2012)
4. Arts, T., Delhaas, T., Bovendeerd, P., Verbeek, X., Prinzen, F.W.: Adaptation to mechanical load determines shape and properties of heart and circulation: the CircAdapt model. Am. J. Physiol. Heart Circ. Physiol. 288(4), H1943–H1954 (2005)
5. Lumens, J., Delhaas, T., Kirn, B., Arts, T.: Three-wall segment (TriSeg) model describing mechanics and hemodynamics of ventricular interaction. Ann. Biomed. Eng. 37(11), 2234–2255 (2009)

6. Barr, R.G., Bluemke, D.A., Ahmed, F.S., Carr, J.J., Enright, P.L., Hoffman, E.A., Jiang, R., Kawut, S.M., Kronmal, R.A., Lima, J.A.C., Shahar, E., Smith, L.J., Watson, K.E.: Percent emphysema, airflow obstruction, and impaired left ventricular filling. N. Engl. J. Med. 362(3), 217–227 (2010)
7. Holverda, S., Rietema, H., Westerhof, N., Marcus, J.T., Gan, C.T.J., Postmus, P.E., Vonk-Noordegraaf, A.: Stroke volume increase to exercise in chronic obstructive pulmonary disease is limited by increased pulmonary artery pressure. Heart 95(2), 137–141 (2009)
8. Argiento, P., Chesler, N., Mulè, M., D'Alto, M., Bossone, E., Unger, P., Naeije, R.: Exercise stress echocardiography for the study of the pulmonary circulation. Eur. Respir. J. 35(6), 1273–1278 (2010)
9. Lumens, J., Blanchard, D.G., Arts, T., Mahmud, E., Delhaas, T.: Left ventricular underfilling and not septal bulging dominates abnormal left ventricular filling hemodynamics in chronic thromboembolic pulmonary hypertension. Am. J. Physiol. Heart Circ. Physiol. 299(4), H1083–H1091 (2010)
10. West, J.B., Dollery, C.T., Naimark, A.: Distribution of blood flow in isolated lung; relation to vascular and alveolar pressures. J. Appl. Physiol. 19, 713–724 (1964)
11. Janicki, J.S., Weber, K.T., Likoff, M.J., Fishman, A.P.: The pressure-flow response of the pulmonary circulation in patients with heart failure and pulmonary vascular disease. Circulation 72(6), 1270–1278 (1985)
12. Kondo, M., Washizu, M., Matsukura, Y., Washizu, T., Miyasaka, K., Takata, M.: Pressure-flow relationship and longitudinal distribution of pulmonary vascular resistance in heartworm-infected dogs. J. Vet. Med. Sci. 65(9), 965–970 (2003)
13. Jeon, D.S., Luo, H., Iwami, T., Miyamoto, T., Brasch, A.V., Mirocha, J., Naqvi, T.Z., Siegel, R.J.: The usefulness of a 10% air-10% blood-80% saline mixture for contrast echocardiography: Doppler measurement of pulmonary artery systolic pressure. J. Am. Coll. Cardiol. 39(1), 124–129 (2002)
14. Palau-Caballero, G., Tobon-Gomez, C., Balicevic, V., Butakoff, C., Loncaric, S., Sitges, M., Bijnens, B.H.: Improving Clinical Translation of Cardiovascular Circulatory Models through an Intuitive Graphical User Interface to CircAdapt, Presenting Simulation Results as Clinical Images and Signals. In: Camara, O., Mansi, T., Pop, M., Rhode, K., Sermesant, M., Young, A. (eds.) STACOM 2012. LNCS, vol. 7746, pp. 345–354. Springer, Heidelberg (2013)

# Improving Clinical Translation of Cardiovascular Circulatory Models through an Intuitive Graphical User Interface to CircAdapt, Presenting Simulation Results as Clinical Images and Signals

Georgina Palau-Caballero[1], Catalina Tobon-Gomez[1], Vedrana Balicevic[2], Constantine Butakoff[1], Sven Loncaric[2], Marta Sitges[3], and Bart H. Bijnens[1,4]

[1] PhySense, N-RAS, Universitat Pompeu Fabra, Barcelona, Spain*
[2] Faculty of Electrical Engineering and Computing, University of Zagreb, Zagreb, Croatia
[3] Thorax Institute, Hospital Clinic, Universitat de Barcelona, IDIBAPS, Barcelona, Spain**
[4] Institució Catalana de Recerca i Estudis Avançats (ICREA), Barcelona, Spain

**Abstract.** Despite the great potential of computational models, their clinical use is limited due to lack of clinical translation. It is, therefore, desirable to present and visualise simulation results as regular *imaging* data commonly used in clinical practice. The purpose of this paper is to present an implementation of a graphical user interface (GUI) for the lumped model CircAdapt. The GUI displays simulation results as: *1)* an animated schematic short-axis view of ventricular geometry, *2)* a Wiggers diagram relating pressure and volume curves with clear indication of the timing events within the cardiac cycle, *3)* a simulated Pulsed Wave Doppler echocardiographic image of mitral/aortic and tricuspid/pulmonary flow, and, *4)* a B-Mode echocardiographic image of short-axis ventricular geometry. We have modeled different physiological and pathological conditions to illustrate the applicability of the GUI: normal state, aortic stenosis and acute response to exercise with high pulmonary vascular resistance.

## 1 Introduction

Current modeling techniques have two primary objectives: *1)* fitting experimental data to better analyse it, or, *2)* capturing physiologic phenomena in order to predict results from further experiments. Unfortunately, physiological models are often developed in one laboratory and tailored for *in-house* needs. The models are sometimes shared among technical groups but hardly ever translated

* This study was partially supported by the Subprograma de Proyectos de Investigación en Salud. Instituto de Salud Carlos III, Spain (FIS - PI11/01709).
** Beca de la Sociedad Española de Cardiología 2012-06-18.

O. Camara et al. (Eds.): STACOM 2012, LNCS 7746, pp. 345–354, 2013.

into clinically understandable parameters, so that clinicians would get easily interested in using or applying them.

This hampers the widespread use of such models in a clinical environment. As a consequence, comparison of simulation results with data that is regularly available in clinical practice is difficult. In order to improve the clinical translation of such models, it is desirable to present and visualise simulation results as regular *imaging* data commonly used in clinical practice.

To achieve this, the first step is to make the model *understandable* for clinicians and non basic-experimental users. This requires to find a correspondence between the physical properties of the model and *typical* clinical parameters. Once this is accomplished, the model can be applied to interesting clinical hypotheses. This also helps the technical users to get clinical feedback on their models in order to judge relevance and realism.

The purpose of this work is to present an implementation of a graphical user interface (GUI) for the lumped model CircAdapt [1,2] to improve clinical translation of the model. The GUI displays simulation results as: *1)* schematic short-axis view, *2)* a Wiggers diagram, *3)* a Pulsed Wave Doppler echocardiographic image, and, *4)* a B Mode echocardiographic image.

## 2 Methods

### 2.1 The Model

The CircAdapt model [1,2] simulates the dynamics of heart and circulation, where heart and vessels geometry and properties are determined by adaptation rules to mechanical load. Acute adaptation is obtained, e.g., by vasodilation. Chronic adaptation is obtained by, e.g., chamber dilation and/or wall hypertrophy. The model is based on four types of modules, which are: cavities which make reference to left ventricle (LV), right ventricle (RV), left atrial (LA) and right atrial (RA); tubes which correspond to aortic and pulmonary arteries and, pulmonary and systemic veins; valves which basically are mitral, aortic, tricuspid and pulmonary valves; and resistances, which mean both pulmonary and blood systems.

### 2.2 Graphical User Interface

The implementation developed in this work is described below. In short, we made a clinical translation of technical parameters of CircAdapt. Also, we provide results as pressure, volume and flow curves. Finally, given that echocardiography is the most common imaging modality in cardiologic evaluations, we provide visualisation of the results as simulated echocardiographic images.

**Description.** In Fig. 1 the CircAdapt GUI is shown. The GUI has a panel (top-left) for input parameters. Currently, it is possible to change *mean arterial pressure*, *cardiac output*, *cycle time* and *pulmonary arteriovenous pressure drop*. The user can choose: to load the *Reference* simulation (normal physiological condition); to *Load* a previously computed simulation; to compute a *New*

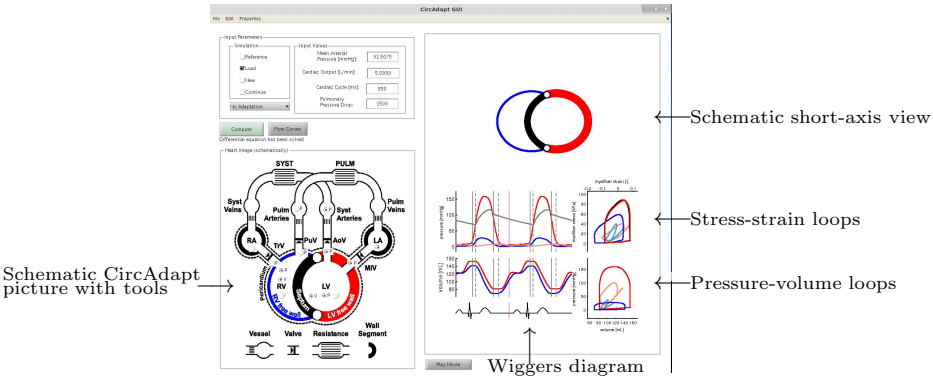


**Fig. 1.** Visualisation of the CircAdapt GUI for aortic stenosis simulation. The figure is displayed once the user clicks the *Compute* button. The figure shows the schematic short-axis view, the Wiggers diagram and pressure-volume and stress-strain loops. The Wiggers diagram will include the values enabled in the radio buttons on the left.

simulation with default physiological conditions; or to *Continue* the current simulation (more iterations to converge).

Besides the parameter values, the user can choose which curves to display on the visualisation panel. Thus, there are radio buttons for each component of the cardiovascular system. A schematic picture of CircAdapt is displayed on the GUI in order to make this selection easier. In the current version, the modules to be selected are: volume, pressure and flow of the LV and RV; pressure of the LA and RA; pressure of the Pulmonary and Aortic Arteries; closing and opening times of the mitral/tricuspid/aortic/pulmonary valves. The GUI is meant to be in continuous development to be flexible to user needs.

Once the user has chosen the desired parameters, the simulation is executed by clicking on the *Compute* button. After the simulation is finished, a realistic visualisation (animation) of the Wiggers diagram is displayed on the right panel, which can be played multiple times with the *Play Movie* button, to analyse cardiac dynamics. The movie can also be saved for later display.

**Clinical Translation.** For clinical translation, two steps are necessary: *1)* identification of the technical parameters critical for a correct simulation, and, *2)* conversion of these parameters into clinically measurable parameters.

For instance, the *pressure* [kPa] corresponds to *mean arterial pressure* [mmHg], the *flow* [mL/s] corresponds to *cardiac output* [L/min], and the *cycle time* [ms] is computed from *heart rate* [beats/min]. The type of adaption allowed by the model needs to be translated as well. *Rest* adaption is modeled as dilation of cardiac vessels. Therefore, it corresponds to an *acute* physiological response. *Exercise* adaption adds to vasodilation chamber size and wall thickness increase. Therefore, it corresponds to a *chronic* physiological response.

**Schematic Short-Axis View.** The schematic short-axis view displayed in the GUI aims to better visualise cardiac dynamics. The schematic includes three thick-walled spherical segments representing LV free wall (LW), RV free wall (RW) and septal wall (SW). They form a ventricular composite consisting of an LV cavity and an RV cavity. These walls meet in a junction margin to encapsulate the LV and the RV cavities.

The schematic short-axis displays the three walls from the midwall parameters values obtained from CircAdapt. The wall thicknesses were fitted proportionally to the line width of each wall. For each time point from the last two cycles, all parameter values are used in order to obtain one time frame of the animation. Finally all frames are put together to display the complete animation.

**Wiggers Diagram.** The Wiggers diagram is a standard diagram used by clinicians. The x-axis of the diagram corresponds to time [ms]. The diagram is divided in three axes. The top one displays pressure [mmHg], the middle one displays volume [mL] and the bottom one shows the electrocardiogram (ECG). In the pressure axis, LV pressure and RV pressure are both displayed, as well as aortic pressure and atrial pressure. In the volume axis, LV and RV volumes are displayed. In both axes aortic/mitral (or tricuspid/pulmonary) valve openings and closing times are displayed.

**Pulsed Wave Doppler Echocardiography.** Since Doppler techniques measure velocity of the flowing blood, the flow calculated by CircAdapt can be used to derive velocity profiles. Given that the mean velocity of the blood through the vessel $v_{mean}$ can be computed by $v_{mean} = q/A$, this inverse problem can be solved in two different ways depending on the Reynolds number ($Re$) of the blood flow through the vessel. In fluid dynamics it is known that when $Re < 2100$, the flow will be laminar, and when $Re > 4000$, the flow will be turbulent (the interval in between is a transitional flow). Velocity ratios of maximal value of the velocity in the center of the circular cross-section area and the mean value ($v_{max}/v_{mean}$) are experimentally obtained for fluids with different $Re$ values [3].

1. Laminar flow is the normal condition for blood flow throughout most of the circulatory system. In that case, the ratio $v_{max}/v_{mean}$ equals 2 [3]. The hydraulic gradient $I$, *i.e.,*the energy loss per unit length (of a vessel) equals:

$$I = \frac{8\eta}{gR^2} v_{mean} \tag{1}$$

and the velocity distribution is computed as:

$$v_r = \frac{Ig}{4\eta}(R^2 - r^2) \tag{2}$$

The expression in Eq.2 is known as Hagen-Poiseuille equation, where $g$ is the gravitational acceleration, $\eta$ is the blood viscosity, $R$ is the valve radius and $r$ is a range of values belonging to $[-R, R]$.

2. Turbulent flow is more likely to occur in a point where vessels divide or there is a sharp bend or narrowing of a vessel. This option is used in the model if explicitly requested by the user, because it depends on the type of the observed vessel. In that case, the ratio $v_{mean}/v_{max}$ equals 0.817 [3]. Now, the velocity distribution in turbulent flow is given approximately by Prandtl's one-seventh-power law equation:

$$v_r = \left(\frac{r}{R}\right)^{1/7} \tag{3}$$

In both cases, the width of the profile is the chosen Doppler width, and the pixel intensity in the profile is proportional to the corresponding velocity.

**B-Mode Echocardiography.** The synthetic echocardiographic images were generated using the convolutional approach [4] [5]. This approach assumes that the imaging system has a linear, space-invariant Point Spread Function (PSF) and the transducer is linear. Let $t(x, y)$ be an echogenicity model of the object being imaged (*i.e.,*a mask where different tissues are represented by different pixel intensities). The $x$ and $y$ variables are lateral and axial coordinates. The subresolution variations in object impedance are introduced by adding Gaussian white noise $G(\sigma_n; x, y)$ with zero mean and variance $\sigma_n$.

$$T(x, y) = t(x, y) \cdot G(\sigma_n; x, y) \tag{4}$$

The 2D ultrasonic echo dataset $V(x, y)$ can then be obtained by a convolution

$$V(x, y) = h(x, y) * T(x, y) \tag{5}$$

where

$$h(x, y) = h_l(x, \sigma_x) \cdot h_a(y, \sigma_z) \tag{6}$$

$$h_l(u, \sigma_u) = exp\left[-u^2/\left(2\sigma_u^2\right)\right] \tag{7}$$

$$h_a(v, \sigma_v) = sin(2\pi f_0 v/c)\, exp\left[-v^2/\left(2\sigma_v^2\right)\right] \tag{8}$$

and $c$ is the speed of sound in the tissue (usually 1540 m/s) and $f_0$ is the center frequency of the transducer.

The image of the envelope-detected amplitude, $A(x, y, z)$, is given by

$$A(x, y) = \left|V(x, y) + i\widehat{V}(x, y)\right| \tag{9}$$

where $\widehat{V}(x, y, z)$ is the Hilbert transform of $V(x, y, z)$.

The simulation parameters are as follows: $\sigma_z = 0.7mm$, $\sigma_x = 3mm$, $\sigma_n = 1.5$. The pixels intensity used for myocardium, in the echogenicity image, is 0.98 and for the background 0.2 to ensure a good contrast between the tissues (assuming the image intensities vary from 0 to 1).

### 2.3 Experiments

The user can interact with a schematic drawing of the model to enable different curves in the Wiggers diagram. We have modeled different physiological and

pathological conditions to illustrate the applicability of the GUI. The tested conditions were: normal state, aortic stenosis and acute response to exercise with high pulmonary vascular resistance, which was modeled by an increase in cardiac output, reduction of heart rate and a significant increase of pulmonary vascular resistance.

## 3 Results

Results for the normal state, aortic stenosis simulation and acute response to exercise are displayed in Fig. 2, Fig. 3 and Fig. 4, respectively. Fig. 2(a), Fig. 3(a) and Fig. 4(a) display the resulting PW Doppler Echocardiography of mitral/aortic and tricuspid/pulmonary flow velocities on each state. Additionally, Fig. 2(b) and Fig. 2(c), Fig. 3(b) and Fig. 3(c), and Fig. 4(b) and Fig. 4(c) show the resulting B-Mode Echocardiographic simulated image for each state at end diastole (ED) and at end systole (ES), respectively. In Fig. 2(d) and Fig. 2(e) healthy proportions of LV and RV are displayed. In Fig. 3(f) we can observe the difference in aortic pressure curve with respect to the normal state (Fig. 2(f)). In Fig. 4(d) and Fig. 4(e), we observe how a large increase of RV pressure is generated, which flattens and pushes the septum immediately after ES. Finally, Fig. 2(h), Fig. 3(h) and Fig. 4(h) display pressure-volume loops for normal state, aortic stenosis and acute exercise, respectively, while Fig. 2(g), Fig. 3(g) and Fig. 4(g) show myofiber stress-strain loops.

## 4 Conclusions

In this work we developed a graphical user interface to enable clinicians to interact with the CircAdapt model in a natural manner. The GUI displays simulation results as: *1)* an animated schematic short-axis view, *2)* a Wiggers diagram, *3)* a simulated Pulsed Wave Doppler echocardiographic image, and, *4)* a B Mode echocardiographic image. The GUI is meant to be in continuous development to be flexible to user needs. This tool shows great potential to improve the interaction of the modeling community with their clinical counterpart.

## Additional Material

Videos of all simulated conditions can be found in the following links:
*1)* Normal condition:
`https://dl.dropbox.com/u/15336366/NormalState_movie.avi`
*2)* Aortic stenosis:
`https://dl.dropbox.com/u/15336366/AortaStenosis_movie.avi`
*3)* Acute response to exercise:
`https://dl.dropbox.com/u/15336366/AcuteEx.avi`

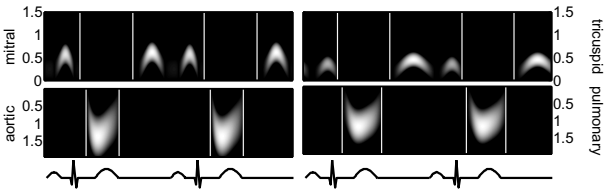


(a) PW Doppler Echo

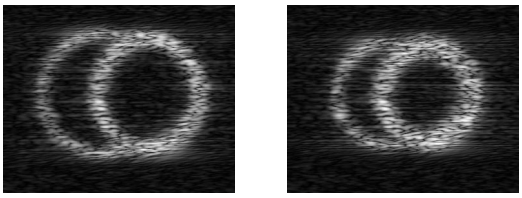

(b) B Mode Echo at ED (c) B Mode Echo at ES

(d) Schematic axis view at ED (e) Schematic axis view at ES

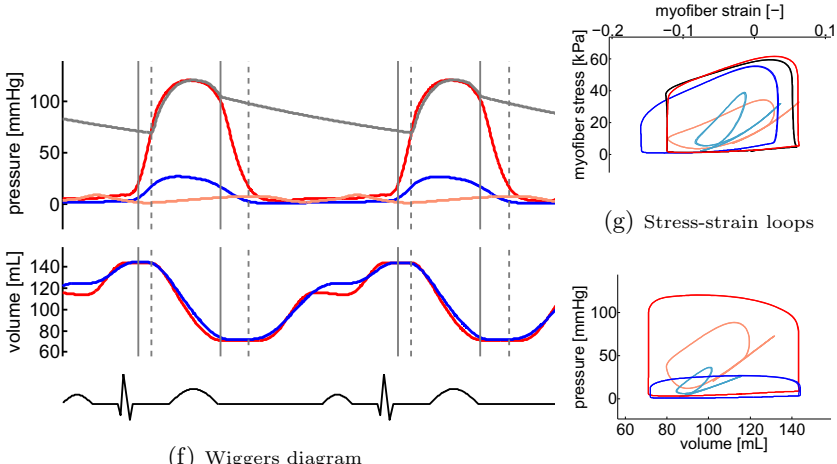


(f) Wiggers diagram (g) Stress-strain loops (h) Pressure-volume loops

**Fig. 2. Normal state**. In 2(a) the resulting PW Doppler Echocardiography of mitral/aortic and tricuspid/pulmonary flow velocities [m/s] is displayed. In 2(d) and 2(e) we can observe the proportion of cavity size, wall thickness and septal curvature. Healthy proportions of LV and RV, as well as a smooth curvature of the septum are displayed. Thicker cavity walls on ES than on ED are shown. In 2(f) we observe pressure (for aorta, LV, RV and LA) and volume (for LV and RV) curves along the cardiac cycle. In 2(g) stress-strain loops for LV, LA, RV, RA and septum are displayed, while in 2(h) pressure-volume loops for LV, LA, RV and RA are displayed. [Color map: LV, LA, RV, RA, septum, aorta]

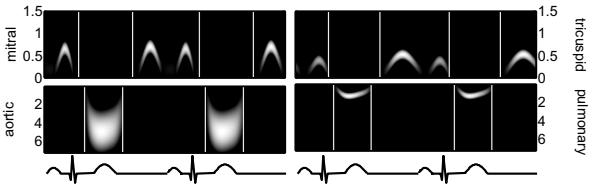


(a) PW Doppler Echo

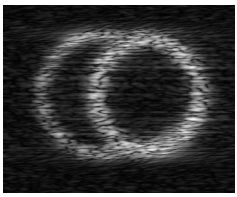

(b) B Mode Echo at ED

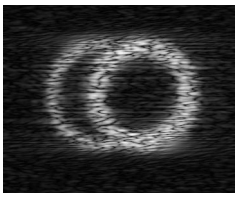

(c) B Mode Echo at ES

(d) Schematic axis view at ED

(e) Schematic axis view at ES

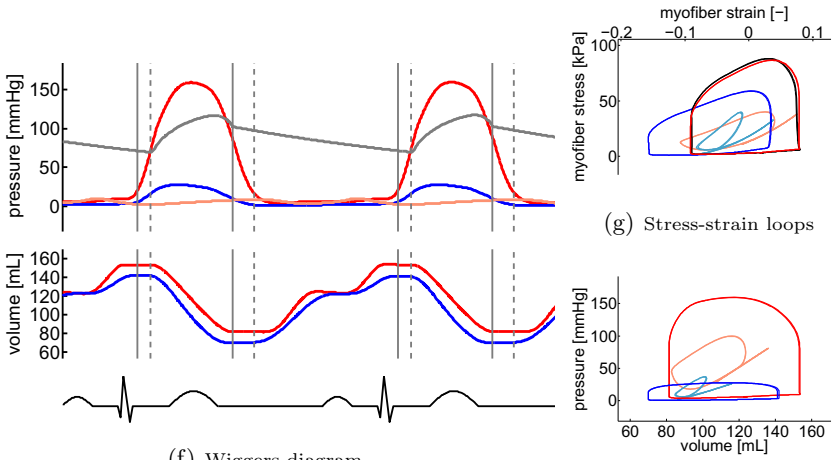


(f) Wiggers diagram

(g) Stress-strain loops

(h) Pressure-volume loops

**Fig. 3. Aortic stenosis**. In 3(a) we observe higher flow velocities [m/s] for aortic/mitral valves in comparison with the corresponding ones on normal state (Fig. 2(a)). In 3(d) and 3(e) we can observe the proportion of cavity size and wall thickness are similar to the normal state (Fig. 2). Thicker cavity walls on ES than on ED are shown. In 3(f) we observe pressure (for aorta, LV, RV and LA) and volume (for LV and RV) curves along the cardiac cycle. Note the difference in pressure between the LV and the aorta. In 3(g) stress-strain loops for LV, LA, RV, RA and septum are displayed, while in 3(h) pressure-volume loops for LV, LA, RV and RA are displayed. We observe that the pressure-volume loop for RV is displaced towards lower volume values in comparison with values from normal state (Fig. 2(h)). [Color map: LV, LA, RV, RA, septum, aorta]

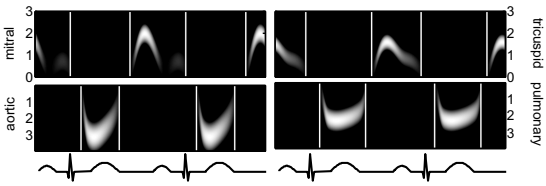


(a) PW Doppler Echo

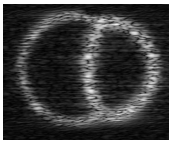

(b) B Mode Echo at ED

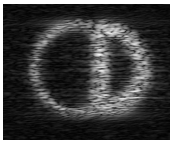

(c) B Mode Echo at ES

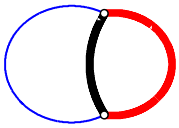

(d) Schematic axis view at ED

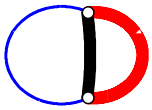

(e) Schematic axis view at ES

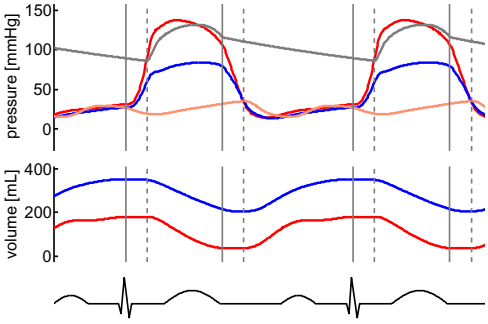


(f) Wiggers diagram

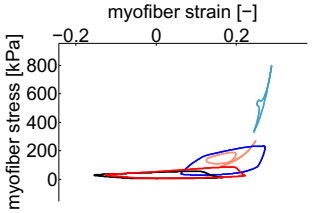


(g) Stress-strain loops

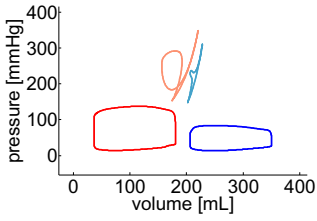


(h) Pressure-volume loops

**Fig. 4. Acute response to exercise.** In 4(a) we observe higher flow velocities [m/s] for all valves. In 4(d) and 4(e) we can observe how a large increase of RV pressure is generated, which flattens and pushes the septum immediately after ES. In 4(f) we observe pressure (for aorta, LV, RV and LA) and volume (for LV and RV) curves along the cardiac cycle. Aortic pressure is slightly lower than LV pressure while aorta valve is opened. It exists a constant difference of volume between LV volume and RV volume along all cardiac cycle. In 4(g) stress-strain loops for LV, LA, RV, RA and septum are displayed, while in 4(h) pressure-volume loops for LV, LA, RV and RA are displayed. The pressure-volume loops for LV and RV are below the ones for LA and RA. We observe that the pressure-volume loop for LV is completely displaced towards lower volume values in comparison with the one for RV. The same situation is observed for LA and RA. [Color map: LV, LA, RV, RA, septum, aorta]

## References

1. Arts, T., Delhas, T., Bovendeerd, P., Verbeek, X., Prinzen, F.W.: Adaptation to mechanical load determines shape and properties of heart and circulation: the circadapt model. Am. J. Physiol. Heart Circ. Physiol., 288 (2005)
2. Lumens, J., Delhaas, T., Kirn, B., Arts, T.: Three-wall segment (triseg) model describing mechanics and hemodynamics of ventricular interaction. Ann. Biomed. Eng., 2234–2255 (2009)
3. Coulson, J.M., et al.: Chemical Engineering Fluid Flow, Heat Transfer and Mass Transfer, pp. 83–85. Elsevier (1999)
4. Abbott, P., Braun, M.: Simulation of ultrasound image data by a quadrature method. In: Proc. Eng. Phys. Sci. Med. Health Conf., p. 209 (1996)
5. Bambre, J.C., Dickinson, R.J.: Ultrasonic B-scanning: A computer simulation. Phys. Med. Biol., 463–479 (1980)

# Integrating Fiber Orientation Constraint into a Spatio-temporal FEM Model for Heart Borders and Motion Tracking in Dynamic MRI

Răzvan Stoica[1], Jérôme Pousin[2], Christopher Casta[1], Pierre Croisille[1], Yue-Min Zhu[1], and Patrick Clarysse[1]

[1] Université de Lyon, CREATIS, CNRS UMR5220, INSERM U1044, INSA-Lyon
[2] Université de Lyon, ICJ, CNRS UMR5208, INSA-Lyon,
69621 Villeurbanne, France

**Abstract.** The dynamic deformable elastic template (DET) model has been previously introduced for the retrieval of personalized anatomical and functional models of the heart from dynamic cardiac image sequences. The dynamic DET model is a finite element deformable model, for which the minimum of the energy must satisfy a simplified equation of Dynamics. In this paper, we extend the model by integrating fiber constraints in order to improve the retrieval of cardiac deformations from cinetic magnetic resonance imaging (cineMRI). Evaluation conducted until now on cine MRI sequences shows an improvement of the recovery of the motion in images that present a low level of obvious rotation.

## 1 Introduction

The detailed analysis of cardiac images and retrieval of personalized anatomical and functional models from clinical cardiac images is still a challenging task. Magnetic resonance imaging (MRI) is a versatile imaging modality, able to provide the required data to reconstruct patient specific models. A few papers have targeted the spatio-temporal analysis of the heart function from dynamic image sequences. Montagnat proposed a dynamic framework based on simplex meshes to analyze 4D SPECT data [1], treating the temporal dimension geometrically. Sermesant proposed a bio-inspired electromechanical model of the heart designed both for the simulation of its electrical and mechanical activity, as well as for the segmentation of time series of medical images [2]. Billet extended this approach to cardiac motion recovery using the adjustment of the previous electromechanical model of the heart to cine MR images [3]. Recently, Lynch proposed a parametric motion model, using a priori knowledge about the temporal deformation of the myocardium that is embedded in a level-set scheme [4].

In a previous paper [5], we introduced the dynamic deformable elastic template model (Dynamic DET) for the automatic segmentation and motion tracking of the heart in dynamic cine MRI sequences. This spatio-temporal approach imposes temporal smoothness and periodicity constraints to improve the regularity and continuity of the extracted contours and motion throughout the cardiac cycle.

O. Camara et al. (Eds.): STACOM 2012, LNCS 7746, pp. 355–363, 2013.

In the present study, we propose to improve the accuracy of the obtained patient specific models by introducing orientation constraints to certain nodes of the mesh of the finite element (FE) DET model used in segmentation. We therefore adapt the DET taking into account the orientation of the myocardial fibers in order to enforce heart deformation in the direction of the fibers. The exact relation between the deformation and the fiber orientations will be not considered. Instead a simplified relation will be introduced in order to validate the proposed methodology. This paper presents a 2D approach for integrating the fiber orientation constraints. It is just a first step in the development of a complete 3D method and it allows to analyze the difficulties that can be encountered while implementing fiber orientation constraints in a simpler environment.

First, the principle of the Dynamic DET model is recalled. Then, the proposed methodology to implement the orientation constraints into Dynamic DET is introduced. In the last section, preliminary results on real human MRI sequences are presented.

## 2 Dynamic DET Model

The dynamic DET is a combination of a topological and geometrical model of the object to be segmented, a constitutive elasticity equation defining its behavior under applied external forces and a dynamic constrained scheme to track the deformable object throughout the sequence. A complete description of the dynamic DET model can be found in [5].

### 2.1 Model Main Equations

We assume the data is available as sequences of $N$-2D or -3D images, sampling the cardiac cycle. To simplify the mathematical treatment of the problem, we assume that the cardiac cycle is parameterized by $t \in [0, 1]$.

The DET model is a deformable volumetric model submitted to external constraints imposed by the image. The equilibrium of the model is obtained through the minimization of an energy $E$ which is the sum of an elastic deformation energy term $E_{elastic}$ and data energy term $E_{data}$ due to the action of external image forces $f$:

$$E(u) = E_{elastic}(u) + E_{data}(u) = \frac{1}{2}\int_{\Omega} \mathrm{tr}(\sigma\epsilon^T)\, d\Omega - \int_{\partial\Omega} f(u)\, d\gamma \qquad (1)$$

where $\sigma$ and $\epsilon$ are the 3D strain and deformation tensors, $u$ is the displacement belonging to the Sobolev space $(H^1(\Omega))^2$ quotiented with the rigid motions $H/_V$, $\varphi\epsilon\dot{\varphi} \Leftrightarrow \varphi = \dot{\varphi} + q$, $q\epsilon V$ and $\Omega$ is the *a priori* model domain at rest. The *a priori* left ventricular (LV) model is an annulus in 2D (a half-ellipsoid in 3D)(Figure 1). The material is considered to be isotropic, homogenous and completely defined by its Young modulus and its Poisson coefficient. $\partial\Omega$ is the border of the object domain $\Omega$.

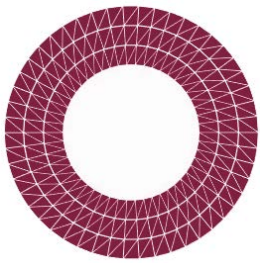

**Fig. 1.** Sample ring mesh used as initial template for 2D short-axis cardiac MR segmentation and motion tracking

These energy terms can be approximated by discretizing the displacement $u$ and the force $f$, using the finite element method (FEM). The displacement is approximated by linear functions on these elements, while the forces are sampled at nodal points. Under this approximation, the minimum of the energy must satisfy the following equation:

$$\mathbf{KU} = \mathbf{F}(\mathbf{U}) \tag{2}$$

where $\mathbf{K}$ is the stiffness matrix corresponding to the response of the elastic material, and $\mathbf{U}$ and $\mathbf{F}$ are respectively the displacement and force vectors on mesh nodes.

The model resulting from equation 2 is purely static. Extending this method to the spatio-temporal domain [5], the heart dynamics is controlled by the simplified Dynamics equation (where acceleration is neglected):

$$\mathbf{D}\dot{\mathbf{U}} + \mathbf{KU} = \mathbf{F}(\mathbf{U}, t) \tag{3}$$

, where $t$ is the time parameter, the span in which we assume a full heart cycle has occurred. The damping matrix $\mathbf{D}$ is represented by a unique scalar $\alpha$.

$$\alpha\dot{\mathbf{U}} + \mathbf{KU} = \mathbf{F}(\mathbf{U}, t) \tag{4}$$

### 2.2 Algorithm Implementation

Solution to equation (3) is achieved through a pseudo-instationary process [6]. Roughly speaking, it consists in introducing a parameter $\tau$, and considering a pseudo-instationary problem with respect to $\tau$ derived from the original problem. Let's define the operator $\mathbf{A} = \alpha\frac{d}{d\tau} + \mathbf{K}$ and consider,

$$\begin{cases} \frac{d\mathbf{U}}{d\tau} & = \mathbf{F}(\mathbf{U}) - \mathbf{AU} \\ \mathbf{U}(0) & = 0. \end{cases} \tag{5}$$

If $\mathbf{U}$ converges when $\tau \to +\infty$, then it tends towards a limit which is a solution of the nonlinear time dependent problem. Discretizing the previous equation with finite differences to solve the temporal equation leads to (see [5] for details):

$$(\frac{1}{\Delta\tau} + \frac{\alpha}{\Delta n} + \mathbf{K})\mathbf{U}_n^\tau = \mathbf{F}(\mathbf{U}_n^{\tau-1}) + \frac{1}{\Delta\tau}\mathbf{U}_n^{\tau-1} + \frac{\alpha}{\Delta n}\mathbf{U}_{n-1}^\tau \quad (6)$$

which is a linear system and thus straightforward to solve.

## 3 Integration of Fiber Orientation in DET Model

Cardiac fiber architecture is more and more studied as shown by the recent development of a human cardiac fiber atlas [7]. Fiber orientation from such an atlas can be attributed to a specific patient anatomy by deformable registration (fig 2, [8]). With the desire to enhance the cardiac architectural and dynamic information retrieval from standard cine MR Images, we seek to improve the DET model by integrating *a priori* information of the fiber orientation in such a way that we improve its abilities to track the motion during the segmentation. Studies show that there exists a rotation of the fibers through the ventricular wall, with an electrical propagation and mechanical contraction mainly along the fiber axis. In figure 2 we can observe fiber vectors that are superimposed onto a MR Short Axis (SA) at end diastole and they are displayed using CMGUI software (Auckland Bioengineering Instituite). The image and tensor are extracted from a database of ex-vivo DTI human hearts [8]. It is true that significant wall strain occurs in the cross-fiber direction i.e. in the radial direction in a short axis view. This results more from a re-arrangement of fiber bundles [9]. But at the fiber level, fibers extend along their main direction just as shown in figure 2.

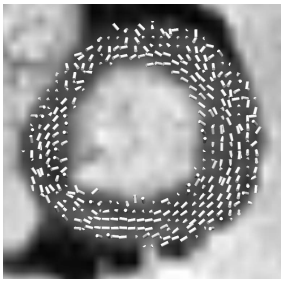

**Fig. 2.** Fiber orientation superimposed on a MR cardiac short axis image of the LV wall.(Image from CMGUI software, Auckland Bioengineering Institute)

### 3.1 Theoretical Aspects

In this section we present the modifications brought to the dynamic DET model in order to take into account the fiber orientation of the heart muscle. In order to keep the presentation simple, we first explain the constraint by considering the static problem 1. The ring mesh used as initial template for 2D short-axis cardiac MR segmentation tracking is composed of a certain number of triangles. In our approach we try to impose the deformation to selected triangles by using a vector

$w$ of the form $w = \begin{pmatrix} w_1 \\ w_2 \end{pmatrix}$. These vectors express the fiber orientation and we want to impose those directions as the principal directions for the deformation, that is to say that $w$ is the eigenvalue associated to the largest eigenvalue of the deformation in modulus: $\epsilon(u)w = \lambda w$. As a first step, a simpler problem is introduced. For:

$$\widetilde{w} = \begin{pmatrix} -w_2 \\ w_1 \end{pmatrix}. \tag{7}$$

a perpendicular vector to $w$, it is required that

$$\varepsilon(u)\widetilde{w} = 0. \tag{8}$$

This relation imposes that the deformations are proportional to vector $w$. The relation (8 ) is an equality constraint, thus the Lagrange's theory of multipliers applies. Let us write in a variational form the constraint (8 ). $\forall\ q \in \left(L^2(\Omega)\right)^2$ we have:

$$\int_\Omega \varepsilon(u)\widetilde{w}q\, dx = 0. \tag{9}$$

From Problem (1), we derive the Lagrangian $L(v, q)$ defined by:

$$L(v,q) = \frac{1}{2}\int_\Omega \mathrm{tr}(\sigma(v)\epsilon^T(v))\, d\Omega - \int_{\partial\Omega} f(v)\, d\gamma + \int_\Omega \epsilon(v)\widetilde{w}q\, d\Omega. \tag{10}$$

The displacement associated with its Lagrange's multiplier $\Lambda$ verify:

$$(u, \Lambda) = Argmin_{v\epsilon H}\ max_{q\epsilon(L^2(\Omega))^2} L(v, q). \tag{11}$$

By using a Galerkin first order Lagrange finite element approximation of optimality conditions for (11) (i.e. the derivative of the Lagrangian function has to be zero), and by keeping the same notations for the unknowns in the matrix formulation, optimality conditions for (11) becomes:

$$\begin{cases} \mathbf{KU} + \mathbf{B}^T\Lambda = \mathbf{F}(\mathbf{U}); \\ \mathbf{BU} = 0. \end{cases} \tag{12}$$

Here $B$ denotes the matrix associated to the bilinear form (9), where the basis functions for the Lagrangian multipliers, $\Lambda$, take a specific value for each triangle $T_k$ in the ring mesh. The form of the basis functions is

$$\hat{\psi}_i = \hat{x}\hat{y}(1 - \hat{x} - \hat{y}) \tag{13}$$

where $\hat{x}, \hat{y}$ are the coordinates of each of the node that constitutes the triangle of the mesh.

As stated in the description of the DET model, the equation of the form (12) describes the static behavior. The simplified Dynamics equations that control the heart dynamics can be rewritten to also take into account the above presented modifications:

$$\begin{cases} \mathbf{D}\dot{\mathbf{U}} + \mathbf{KU} + \mathbf{B}^T\Lambda = \mathbf{F}(\mathbf{U}, t) \\ \mathbf{BU} = 0 \end{cases} \tag{14}$$

### 3.2 Implementation Updates

We have to note also the differences that occur regarding the algorithm implementation, equation (5) has to take into account the contribution of the Lagrangian multipliers:

$$\begin{cases} \frac{d\mathbf{U}}{d\tau} &= \mathbf{F}(\mathbf{U}) - \mathbf{A}\mathbf{U} - \mathbf{B}^T\Lambda \\ \mathbf{B}\mathbf{U} &= 0 \\ \mathbf{U}(0) &= 0. \end{cases} \tag{15}$$

In order to solve the temporal equations, the finite difference formulation of (15) becomes:

$$\begin{cases} (\frac{1}{\Delta\tau} + \frac{\alpha}{\Delta n} + \mathbf{K})\mathbf{U}^{\tau}_{n+1} + \mathbf{B}^T\Lambda^{\tau}_{n+1} = \mathbf{F}(\mathbf{U}^{\tau-1}_{n}) + \frac{1}{\Delta\tau}\mathbf{U}^{\tau-1}_{n} + \frac{\alpha}{\Delta n}\mathbf{U}^{\tau}_{n-1} \\ \mathbf{B}\mathbf{U} = 0 \end{cases} \tag{16}$$

## 4 Results

### 4.1 Simple Example

The first simulations were conducted on simple meshes composed of a few number of triangles in order to reduce the degree of computational complexity while still in the phase of elaborating the numerical implementation. In figure 3 we present the way a simple structure reacts when under the effect of a diagonal force that is applied on every node, with the same intensity, except for the nodes marked with red circles. The marked nodes are fixed, so that the structure is able to react to the force otherwise it will simply float above the background image. As it can be observed from the triangle deformation, the evolution of the structures takes very well into account the deformation directions allowed through the implemented fiber orientations.

### 4.2 Preliminary Results on Cardiac Cine MRI

The experiments were conducted on 2D Cine MRI sequences of the human heart to study the impact on the segmentation and motion tracking results after integrating the fiber orientation information in the dynamic DET model. In the presented example, the Young modulus was set to 2.4 and the Poisson coefficient to 0.2 (this is to cope with the adaptation of the initial template to the data and the myocardial area variation during the cardiac cycle, in 2D). The center of the annulus and its radius were set using a manual initialization, and a contraction parameter was automatically set depending on the initialization on both ED and ES phases. The initial wall thickness was set to 6 pixels. The image was generated with 4 rings and divided into 40 sectors. The image resolution level was set to 3, the highest resolution, and the stopping criterion to $10^{-5}$.

A very important aspect is represented by the fact that not all and not any triangle of the mesh used in the dynamic DET model can be constrained to deform in prescribed directions. Border triangles are not constrained with a

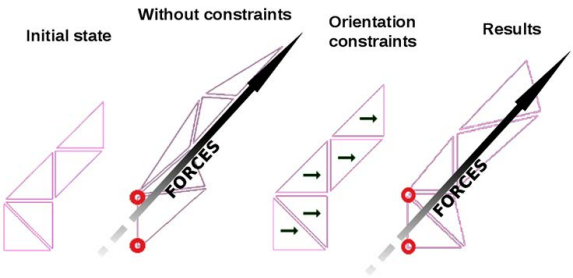


**Fig. 3.** Simple mesh composed of 5 triangles illustrating deformation evolution without and with implemented fiber orientation. Nodes marked with red circles are kept fixed.

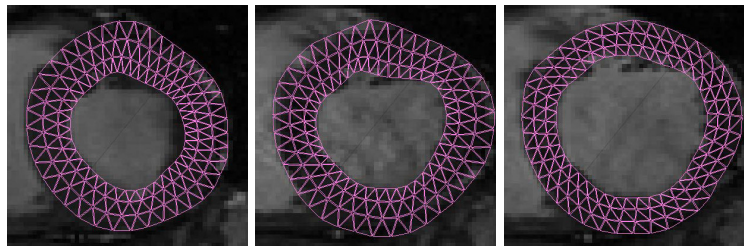

(a) (b) (c)

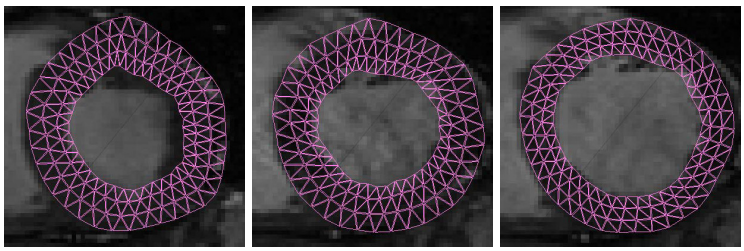

(d) (e) (f)

**Fig. 4.** DET model superimposed onto 3 cine MR images: end-diastole, mid-systole, end-systole, after the processing of a full sequence of 20 images. The pink mesh is the DET model. It is translucent so that correspondence between model and image contours can be evaluated. Figures (a), (b) and (c) correspond to a segmentation with no orientation constraint. Figures (d), (e) and (f) correspond to a segmentation with fiber orientation implementation.

deformation orientation because they already are constrained by the action of the external forces used by the model. The orientation constraints are mainly applied to the inner ring of triangles of the mesh, they assure a good spread of

the orientation constraints because of their connection to the neighbor triangles and they are not too constrained as would be the case if we were to apply the orientation constraints on the border triangles. Also, the model should take into account the fact that during the evolution of the heart motion the orientation of the fibers changes by a small degree from the first frame of the sequence until the last one.

Figure 4 shows the results of a LV segmentation on a sequence of cine MR images using the fiber orientation information in the dynamic DET model. In this static example, the difference can be noticed by comparing the border line of the images on the $1^{st}$ row with the images on the $2^{nd}$ row. One can notice the less regulate border line, a sign that the orientation constraints affect the orientation of the neighbor area of the constrained triangles. Through this we can achieve a higher degree of rotational information retrieval inside the mesh. Due to the fiber orientation, the mesh is able to better interpret the forces recovered from the cine MRI sequence and translate them into rotational motion rather than just an increase in the thickness of the mesh

## 5 Discussion

The results shown in figure 4 are first demonstrations of the improvements achieved with the help of fiber orientation information. It will have to be better studied on other cases and also quantitatively evaluated. The approach is potentially interesting because it may produce patient specific models which may reproduce more realistic heart dynamics. Indeed, the rotational component of the motion is usually not observable in conventional cardiac MRI. This work was conducted in the framework of the LabEx PRIMES ("Physics, Radiobiology, Medical Imaging and Simulation").

## References

1. Montagnat, J., Delingette, H.: 4D deformable models with temporal constraints: application to 4D cardiac image segmentation. Medical Image Analysis 9(1), 87–100 (2005)
2. Sermesant, M., Delingette, H., Ayache, N.: An Electromechanical Model of the Heart for Image Analysis and Simulation. IEEE Transactions in Medical Imaging 25(5), 612–625 (2006)
3. Billet, F., Sermesant, M., Delingette, H., Ayache, N.: Cardiac Motion Recovery and Boundary Conditions Estimation by Coupling an Electromechanical Model and Cine-MRI Data. In: Ayache, N., Delingette, H., Sermesant, M. (eds.) FIMH 2009. LNCS, vol. 5528, pp. 376–385. Springer, Heidelberg (2009)
4. Lynch, M., Ghita, O., Whelan, P.F.: Segmentation of the Left Ventricle of the Heart in 3D+t MRI Data Using an Optimised Non-Rigid Temporal Model. IEEE Transactions in Medical Imaging 27(2), 195–203 (2008)
5. Schaerer, J., Casta, C., Clarysse, P., Rouchdy, Y., Pousin, J.: A Dynamic Elastic Model for Segmentation and Tracking of the Heart in MR Image Sequences. Medical Image Analysis (in press)

6. Ciarlet, P.G., Lions, J.L.: Handbook of Numerical Analysis. Finite difference methods, Solution of equations in $\mathbb{Z}^n$, vol. 1. North-Holland (1990)
7. Lombaert, H., Peyrat, J., Croisille, P., Rapacchi, S., Fanton, L., Cheriet, F., Clarysse, P., Magnin, I., Delingette, H., Ayache, N.: Human Atlas of the Cardiac Fiber Architecture: Study on a Healthy Population. IEEE Transactions on Medical Imaging PP(99), 1 (2012)
8. Wang, V.Y., Casta, C., Croisille, P., Clarysse, P., Zhu, Y.-M., Cowan, B.R., Young, A., Nash, M.P.: Estimation of in vivo human myocardial fibre strain by integrating diffusion tensor and tagged MRI using FE modeling. Presented at the International Symposium of Biomedical Imaging, Barcelona, Spain, pp. 46–49. IEEE (2012)
9. Kroon, W., Delhaas, T., Bovendeerd, P., Arts, T.: Computational analysis of the myocardial structure: Adaptation of cardiac myofiber orientations through deformation. Medical Image Analysis 13(2), 346–353 (2009)

# *In vivo* Contact EP Data and *ex vivo* MR-Based Computer Models: Registration and Model-Dependent Errors

Mihaela Pop[1,2,*], Maxime Sermesant[3], Roey Flor[2], Charles Pierre[4], Tommaso Mansi[5], Samuel Oduneye[1], Jen Barry[2], Yves Coudiere[6], Eugene Crystal[2], Nicholas Ayache[3], and Graham A. Wright[1,2]

[1] Dept. Medical Biophysics, Univ. of Toronto
[2] Sunnybrook Research Institute, Toronto, Canada
[3] Inria - Asclepios Project, France
[4] University of Pau, France
[5] Siemens Corporation, Corporate Technology, Princeton, NJ, USA
[6] Inst. Mathematiques de Bordeaux, France
mihaela.pop@utoronto.ca

**Abstract.** Sudden cardiac death is a major cause of death in industrialized world; in particular, patients with prior infarction can develop lethal arrhythmia. Our aim is to understand the transmural propagation of electrical wave and to accurately predict activation times under different stimulation conditions (sinus rhythm and paced) using MRI-based computer models of normal or structurally diseased hearts. Parameterization of such models is a prerequisite step prior integration into clinical platforms. In this work, we first evaluated the errors associated with the registration process between contact EP data and MRI-based models, using *in vivo* CARTO maps recorded in three swine hearts (two healthy and one infarcted) and the corresponding heart meshes obtained from high-resolution *ex vivo* diffusion weighted DW-MRI (voxel size < $1mm^3$). We used the open-source software Vurtigo to align, register and project the CARTO depolarization maps (from LV-endocardium and epicardium) onto the MR-derived meshes, with an acceptable registration error of < 5mm in all maps. We then compared simulation results obtained with the macroscopic monodomain formalism (i.e., the two-variable Aliev-Panfilov model), the simple Eikonal model, and the complex bidomain model (TNNP model) under different stimulation conditions. We found small errors between the measured and the predicted activation times, as well as between the depolarization times using these three models (e.g., with a mean error of 3.4 ms between the A-P and TNNP model), suggesting that simple mathematical formalisms might be a good choice for integration of fast, predictive models into clinical platforms.

**Keywords:** electrophysiology, 3D computer modelling, cardiac DW-MRI.

* Corresponding author.

O. Camara et al. (Eds.): STACOM 2012, LNCS 7746, pp. 364–374, 2013.

# 1 Introduction

Integration of electrophysiology (EP) measurements with image-based computer models can help us understand the 3D transmural propagation of cardiac excitation wave and the vulnerability of individual hearts to lethal arrhythmias under different stimulation scenarios [1]. Cases associated with abnormal propagation of electrical wave in hearts with structural disease (e.g. myocardial infarct) are a major cause (>85%) of sudden cardiac death [2]. An important task is the identification of infarct location and extent. Currently, the infarct areas are identified during the EP study using contact or non-contact mapping systems, which are limited to surfacic endocardial and/or epicardial maps obtained invasively via catheters, often under fluoroscopy. Thus, there is a strong motivation to supplement the EP measures with non-invasive 3D information, such as: scar transmurality and location (from imaging) [3], and wave propagation through the heart (from modelling). Several image-based predictive computer models are already available and recent studies demonstrated the usefulness and predictive power of such models [4]; however, parameter estimation and model customization remain an important prerequisite prior to integration into clinical treatment planning platforms.

Our broad aim is to predict the propagation of electrical wave in pathologic hearts using 3D MRI-based computer models, enriched with electrophysiology measures. Recently, we demonstrated the feasibility of using *ex vivo* measures of action potential (recorded via optical fluorescence imaging) to calibrate the parameters of normal and pathologic hearts [5]. The next logical step is to perform similar calibrations using *in vivo* EP data; however, for accurate comparisons between experiment and predictions, we need:1) to register the measured EP maps with the MR images; and 2) to replicate in the model the experimental conditions. In this paper, we first investigated the feasibility of using Vurtigo[1] software to integrate CARTO depolarization maps into DW-MRI-based models. We then performed simulations: a) to predict the isochrones of depolarization times using a parameterized fast, macroscopic formalism (i.e., Aliev-Panfilov model); and b) to compare the isochrones predicted by the A-P model with those predicted by a simple Eikonal model and a complex bidomain model (e.g. Tusscher-Noble-Noble-Panfilov), respectively. Note that wee only performed a global adjustment of the conductivity parameter *d* (which tunes the speed of wave) for the A-P model, and then focused on testing the predictive power of these three models.

# 2 Material and Methods

## 2.1 The Experimental Data: *in vivo* EP Studies and *ex vivo* DW-MRI Studies

In this paper, we included three *in vivo* EP studies, which were performed in two healthy swine and a swine with a ~5 week old infarct (note: the methodology of generating chronic infarction was previously described [5]). A total of five maps of depolarization times (i.e., three LV-endocardial and two epicardial maps) were

[1] www.vurtigo.ca

recorded either in normal sinus rhythm or under pacing conditions by using a CARTO-XP electro-anatomical mapping system (Biosense Webster, Diamond, USA); the experimental procedures were approved by our institution, Sunnybrook Research Institute, Toronto). At the completion of the EP studies, the hearts were explanted, gently preserved in formalin, and imaged using a 1.5T (voxel size < $1mm^3$) with most of the MR parameters being similar to those used in [5]. For the construction of the 3D heart models, the anatomy of each heart was extracted from the un-weighted images and used to generate volumetric meshes; the myocardial fiber directions was extracted from DT-MRI and integrated into associated meshes. In the case of the infarcted heart, the 3D apparent diffusion coefficient (ADC) maps was further used to categorize tissue into two zones: healthy and infarct scar.

Then, for each heart, the experimental datasets (EP and MRI-derived meshes) were imported into the open-source software Vurtigo for further analysis. Each EP cloud of points (LV-endo and/or epicardium recordings) was registered with the 3D MRI-based model using a similarity transformation (rotation, translation and isotropic scaling). The registration alignment was done using markers (i.e., in our case, three or four anatomical landmarks such as the apex, mitral valve, etc) manually selected by a clinical expert in both EP maps and MR-meshes. This was done as per similar methods established and reported by clinical groups that used either the CARTO-MERGE or their own software [6, 7]. Note that the apex was also visible in the X-ray images, and that the CARTO signals around the valve (electrically inert) have distinct electrical signal morphology); these features helped with the alignment. In our experiment, we determined the registration error *FRE* by calculating the average distance between the corres-ponding pairs of these 'fiducial' points on the CARTO data and LV-endo/epi surfaces from MRI, after registration had been performed, by using the formula (1):

$$FRE = \frac{\sum_{i=1}^{N_{landmarks}} dist(S_i, T_i)}{N_{landmarks}} \tag{1}$$

where: $N_{landmarks}$ is the number of landmark pairs, $S_i$ is the i'th source landmark and $T_i$ is the i'th target landmark.

Each CARTO point was subsequently projected onto the closest point of the MR-derived surface mesh (LV-endo or epi) as in [8], and the resulting CARTO maps of depolarization times were interpolated over the surfacic meshes. The target registration error, *TRE* was calculated for each map using the following formula:

$$TRE = \frac{\sum_{i=1}^{N_{EP}} dist(EP_i, MeshSurface)}{N_{EP}} \tag{2}$$

where $N_{EP}$ is the number of CARTO-EP points.

### 2.2 Mathematical Models to Predict Depolarization Times in the Heart

**The Aliev-Panfilov (A-P) model** is based on reaction-diffusion type of equations and solves for the action potential ($V$) and recovery term ($r$) as described in [9]:

$$\frac{\partial V}{\partial t} = \nabla \cdot (D\nabla V) - kV(V-a)(V-1) - rV \tag{3}$$

$$\frac{\partial r}{\partial t} = -(\varepsilon + \frac{\mu_1 r}{\mu_2 + V})(kV(V-a-1) + r) \tag{4}$$

This simple model accounts for the heart muscle anisotropy via the diffusion tensor $D$ (which depends on tissue bulk conductivity, $d$). The anisotropy ratio ρ is set to 0.11 for a wave propagating three times faster along the fibers compared to the transverse direction.

The following relation is obeyed in 1D:

$$c = \sqrt{2 \cdot k \cdot d}\,(0.5 - a) \tag{5}$$

and thus a theoretical calibration curve can be used to adjust the global ('bulk') conductivity $d$ in the model, which can also be extended to the calculation of conduction velocity $c$ from associated surfacic measures [10]. Firstly, we performed here a set of simulations on a thin rectangular slab (element size 1mm), in which we varied $d$ and measured the resulted $c$. Secondly, we performed a fit of two parameters ($\alpha$ and $\beta$) to pairs of simulated data ($c$,$d$) based on the following one dimensional formula $c(d) = \alpha \cdot \sqrt{d} + \beta$. This step was done by minimizing the mean error in least square sense, using simple Matlab routines. Thirdly, we used this resulting calibration curve to further estimate $d$ from the mean $c$ value that was determined from the measured depolarization time maps (i.e., we computed $c$ at each mesh node from the projected CARTO map, and then calculated a mean speed value from the corresponding histogram) as per the method previously proposed in [11]. The *parameter estimation* of $d$ was done only for the LV-endo paced map (Heart #1). Note that we did not perform a 'personalization' step for each map, but specifically aimed to: 1) derive a 'generic' value for $d$ from the paced case for the A-P model; and 2) use this value as input into simulations performed for the other two hearts, in order to assess the *predictive* power of the A-P model.

The other input parameters in eq (3-4) were assigned in the model as in [12]. To solve for $V$, a Finite Element Method with explicit Euler time integration scheme, was implemented as in [13].

**The Eikonal (EK) model** is the simplest and fastest model; it computes only the wave front propagation (i.e., the depolarization phase $T_d$ of the electrical wave) based on the anisotropic Eikonal equation [14]:

$$c^2\left(\nabla T_d^t D \nabla T_d\right) = 1 \tag{6}$$

where the $c$ is the local speed of the wave, D is the diffusion tensor, and ρ is the anisotropy ratio (as in the A-P model described above).

**The bidomain model** offers the most complete description of the electrical behavior of myocardium, and explicitly accounts for the current flow in the two extra-/intercellular spaces through the non-linear PDEs (7) and (8):

$$A_m(C_m(\partial_t V_m + I_{ion}(V_m,y,c)\text{-}I_{stim}(x,t)) = div(G_i \nabla(V_m+\phi_e)) \quad (7)$$

$$div((G_i+G_e)\nabla\phi_e) + div(G_i \nabla V_m)) = 0 \quad (8)$$

where $V_m$ is the transmembrane potential, $c$ is the ion concentration (per specie), $A_m$ is the cellular surface to volume ratio, C$m$ is membrane capacitance, $G$ is the conductance of the extra- or intracellular space. For the computation of the current flowing between the two cellular spaces, we used the model proposed by Tusscher-Noble-Noble-Panfilov described in [15]. The evolution of $V_m$ is solved implicitly using the optimal pre-conditioner defined in [16]. For the boundary conditions of this system we used the following constraints: $G_i \nabla(V_m+\phi_e)\cdot n = 0$ and $G_e \nabla\phi_e \cdot n = 0$.

## 3 Results

### 3.1 Integration of *in vivo* EP Data and *ex vivo* MRI Using Vurtigo Platform

All results obtained for the registration between CARTO maps and MRI meshes, and the projection of CARTO points onto these meshes are included in Table 1. For all maps, FRE was < 5mm. For the TRE, we observed a larger average distance between CARTO epi-points and MR epi-surface (likely due to the heart motion during the open-chest procedure for the epicardial mapping).

**Table 1.** Registration errors between CARTO poits and MR-derived meshes using Vurtigo

| Heart # | Isochronal map from CARTO system | FRE (mm) | TRE (mm) |
|---|---|---|---|
| 1. Healthy (paced) | LV-endocardium | 2.7 | 5.8 ± 3.6 |
| 2. Healthy (sinus rhythm) | LV-endocardium | 2.1 | 4.0 ± 2.5 |
| | Epicardium | 2.8 | 4.2 ± 3.1 |
| 3. Infarcted (sinus rhythm) | LV-endocardium | 4.9 | 4.4 ± 3.3 |
| | Epicardium | 4.8 | 9.2 ± 4.9 |

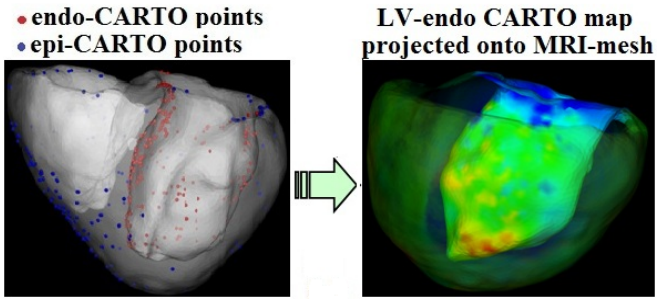


**Fig. 1.** Fusion of EP and MRI for heart #3: CARTO points projected onto the MR mesh *(left)*; LV-endo map interpolated and seen through the heart model (r*ight*)

An example highlighting the EP-MR data registration and maps' projection is given in Figure 1 (for heart # 3), with the epicardial CARTO points in blue and LV-endo points in red *(left)*, as well as the LV-endo isochronal map seen through the semi-transparent 3D MRI-derived model (*right*).

### 3.2 Comparison between Experimental vs. Simulated Depolarization Times

#### 3.2.1 Global Adjustment of Conductivity Using Precise Pacing Location

Figure 2 shows results from the healthy heart #1, which was paced at 500 ms using a pacing electrode, at the apex of RV. A recording catheter was inserted in the LV cavity and mapped the LV-endocardium (note: the pacing site was easily visualized under fluoroscopy, see Fig 2a). Fig 2b shows the replication of pacing location in the 3D model, and Fig 2c shows the reconstructed fiber directions from DT-MRI.

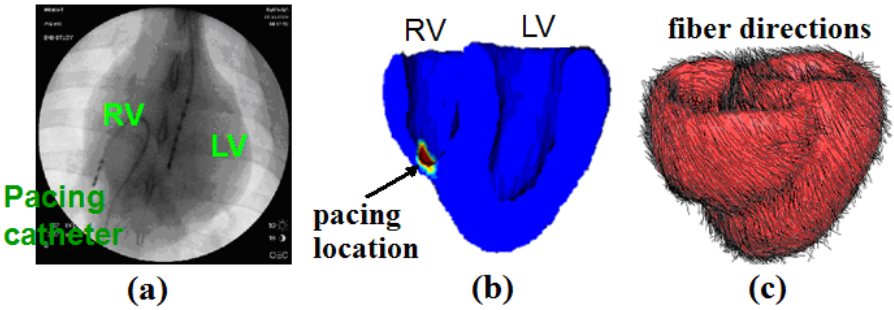


**Fig. 2.** MRI-based model construction and replication of EP experiment (see text for details)

Figure 3a shows the simulation results of depolarization times. The corresponding error map (absolute values, ms) between the A-P model output and the CARTO measurements is shown in Fig 3b, after the adjustment of *d* value. This adjustment used equation (5) to obtain the estimated function presented in Fig 3c.

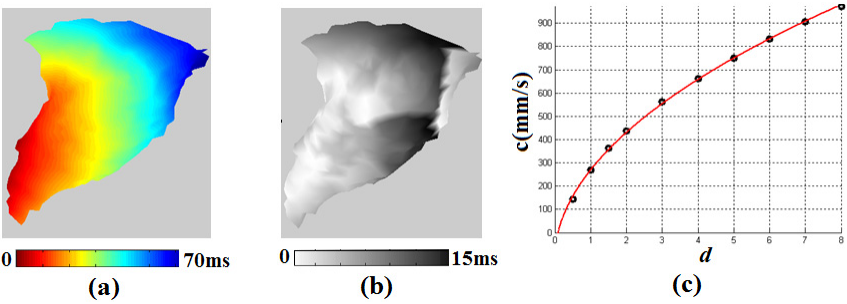


**Fig. 3.** Example of simple estimation of global conductivity from experimental EP data: (a) simulated depolarization times for LV-endo; (b) corresponding error between measured and simulated depolarization times after the estimation of *d* (using the calibration curve in (c) that relates conduction velocity to conductivity *d*.

### 3.2.2 Inter-models Errors in Predicting Activation Times

Figure 4 presents a comparison between A-P and bidomain models for heart #3, both models having the same mesh input and stimulation protocol (see Fig 4a). This protocol replicated the experimental observations that suggested a left branch block (QRS > 120 ms). For stimulation, a pulse $V$=1 was applied at the RV-apex for 5 ms and was followed by another similar short pulse applied on the anterior RV free-wall (see the small red areas in the RV in the top view through the 3D MRI-mesh). The resulting propagation as well as the early breakthrough epicardium mimicked the observations recoded in a human heart [17]. The qualitative difference between TNNP and A-P is shown in Fig 4b, whereas the quantitative error is shown in Fig. 4c (note that $d$ value in A-P model was set to 3.5 as determined in the paced case). A small error was obtained between the TNNP and A-P models, correlation coefficient 0.98, mean error = 3.4 ms (compared to 0.94 and mean error of 10.2 ms between TNNP and EK, not included in Fig. 4).

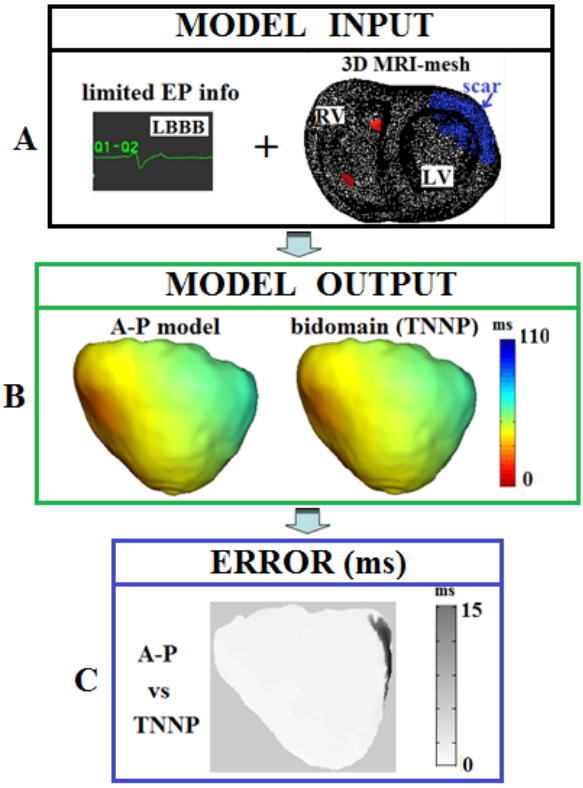


**Fig. 4.** 3D MRI-based models for the heart # 3: (a) the model *input* used limited prior EP info to apply two stimuli on the RV-endo (at apex and on the free wall); (b) qualitative comparison between the depolarization isochrones predicted by the A-P and bidomain (TNNP) models, respectively (note that red indicates early activation times, EAT, and blue indicates late activation times, LAT); and (c) the absolute errors between TNNP and A-P models (gray scale).

Figure 5 shows results obtained with the A-P and EK models, with the *d* value determined from the measured speed values using the experimental CARTO isochrones obtained on this heart, and the calibration curve presented in Fig 2c. We observed closer correspondence between simulated and measured isochronal maps (again for Heart #3). Fig 5a (*top*) shows the stimulus configuration for which we obtained the best match between experimental pattern of epicardial CARTO isochrones presented in Fig 5a (*bottom*) and the corresponding simulated depolarization times using the A-P and EK models (Fig 5b). A small difference (mean error of 12.33 ms and correlation coefficient 0.91) was found between the epicardial CARTO map and the isochrones predicted by A-P model.

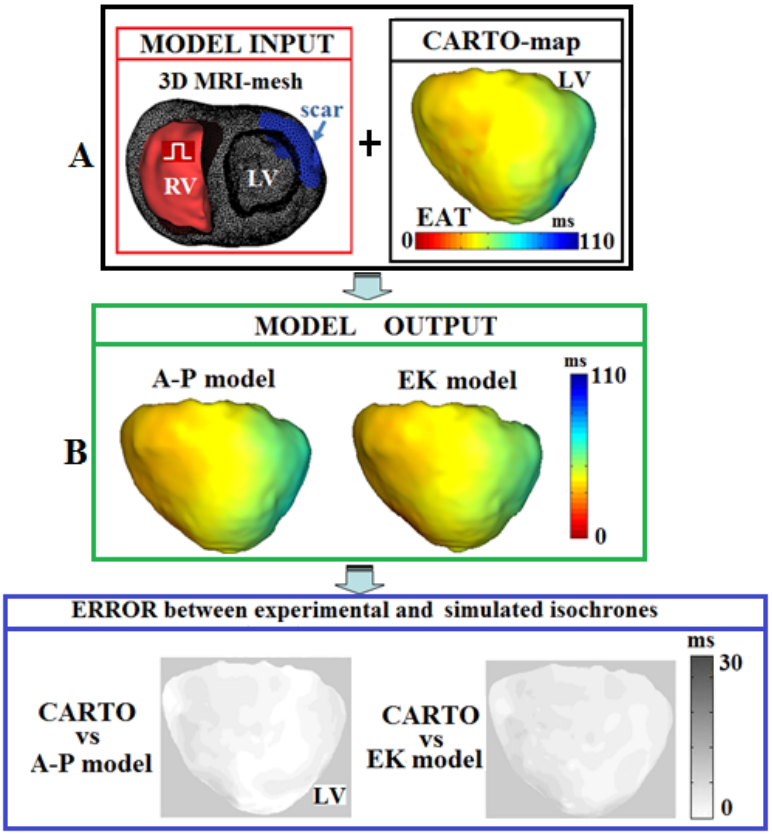


**Fig. 5.** Example result from the global adjustment using the forward approach: (a) *input* to the computer model *(top)* and measured CARTO isochrones *(bottom)*, (b) simulated isochronal maps obtained with the conductivity adjusted globally in the A-P and Eikonal models; and c) error maps of depolarization times (absolute values, ms) between CARTO and simulated isochrones using the A-P and EK models.

## 4 Discussion and Future Work

The evaluation of 3D image-based computer models performance and utility, as well as the customization using *in vivo* EP measurements will help us use such models correctly, and to properly target them for different clinical applications.

In this work, we first demonstrated the feasibility of using the versatile software Vurtigo to integrate surfacic *in vivo* CARTO isochronal maps into 3D MRI-based heart models built from high resolution *ex vivo* diffusion weighted MR images, with a clinically acceptable registration error (< 5mm). Vurtigo allowed the projection of LV-endocardial and epicardial CARTO points onto the MR-derived meshes, as well as the interpolation and the visualization of these maps.

Secondly, a global adjustment of $d$ value was successfully performed by minimizing the error between the A-P model *output* and the *in vivo* EP-CARTO measurements of depolarization times in the healthy paced heart. Further, this $d$ value was used as input into the model to assess its predictive power. After the global adjustment of the parameter $d$, we demonstrated the predictive power of several mathematical models by simulating the transmural activation times (i.e., depolarization isochrones) and by comparing the surfacic endocardial and epicardial isochrones with the CARTO isochrones. Our results suggested that for such forward computational approaches, a *minimal EP information* from measurements is also needed as *input* in order to obtain correct theoretical predictions, with isochronal maps having EAT/LAT ranges similar to those measured, as well as similar pattern of propagation wave. This information (i.e., either the pacing location for the Heart #1, or the electrical abnormality detected in the sinus rhythm for the Heart #3) was needed for the preparation of stimulation protocol in the models. The simulation results also suggested that a simple approximation with excitation stimuli on the surface only (i.e., RV-endo and LV-endo for Hearts #2, and RV-endo surface for Heart #3) seems feasible in the absence of a sophisticated cardiac conduction system with Purkinje-junctions integrated into the model. Nonetheless, the paced scenario in the healthy Heart #1 was the easiest to reproduce in simulations, and generated the most accurate results. Overall, we demonstrated that, although simple, the A-P model can provide good estimation of the conduction velocity and propagation of the excitation wave under different stimulation configurations.

Lastly, since the computational time is important in such applications, we should mention that for the A-P model the simulation time of 0.2s of the heart cycle on a mesh of approx. 190,000 elements (element size of ~1.2 mm), was about 10 min on an Intel ® Core™ 2 duo CPU, T5550 @1.83GHz, with 4 GB of RAM, compared to Eikonal model which takes < 1min, and > 7h for the TNNP model.

Future work will focus on simulating the repolarization phase as well as on estimating the critical parameters corresponding to this phase of action potential, including the restitution curve. This step will be performed by measuring the activation-recovery interval (a clinically accepted surrogate of action potential duration) from the extracellular/unipolar CARTO waves recorded in sinus rhythm and at different pacing frequencies. Also, future work will focus on refining the adjustment process using local AHA zones, to decrease locally the error between experiment and simulations, as per the method proposed in [18].

**Acknowledgement.** This work was financially supported in part by a grant from the Canadian Institutes of Health Research (MOP93531).

## References

1. Clayton, R.H., Panfilov, A.V.: A guide to modelling cardiac electrical activity in anatomically detailed ventricles. Progress in Biophysics & Molecular Biology - Review 96(1-3), 19–43 (2008)
2. Stevenson, W.G.: Ventricular scars and VT tachycardia. Trans. Am. Clin. Assoc. 120, 403–412 (2009)
3. Bello, D., Fieno, D.S., Kim, R.J., et al.: Infarct morphology identifies patients with substrate for sustained ventricular tachycardia. J. Am. College of Cardiology 45(7), 1104–1110 (2005)
4. Vadakkumpadan, F., Rantner, L., Tice, B., Boyle, P., Prassl, A., Vigmond, E., Plank, G., Trayanova, N.: Image-based models of cardiac structure with applications in arrhythmia and defibrillation studies. J. Electrocardiology 42(2), 15 (2009)
5. Pop, M., Sermesant, M., Liu, G., Relan, J., Mansi, T., Soong, A., Truong, M.V., Fefer, P., McVeigh, E.R., Delingette, H., Dick, A.J., Ayache, N., Wright, G.A.: Construction of 3D MRI-based computer models of pathologic hearts, augmented with histology and optical imaging to characterize the action potential propagation. Medical Image Analysis 16(2), 505–523 (2012)
6. Codreanu, A., Odille, F., Aliot, E., et al.: Electro-anatomic characterization of post-infarct scars comparison with 3D myocardial scar reconstruction based on MR imaging. J. Am. Coll. Cardiol. 52, 839–842 (2008)
7. Wijnmaalen, A., van der Geest, R., van Huls van Taxis, C., Siebelink, H., Kroft, L., Bax, J., Reiber, J., Schalij, M., Zeppenfeld, K.: Head-to-head comparison of contrast-enhanced magnetic resonance imaging and electroanatomical voltage mapping to assess post-infarct scar characteristics in patients with ventricular tachycardias: real-time image integration and reversed registration. European Heart Journal 32, 104 (2011)
8. Oduneye, S.O., Biswas, L., Ghate, S., Ramanan, V., Barry, J., Laish-FarKash, A., Kadmon, E., Zeidan Shwiri, T., Crystal, E., Wright, G.A.: The feasibility of endocardial propagation mapping using MR guidance in a swine model and comparison with standard electro-anatomical mapping. IEEE Trans. Med. Imaging 31(4), 977–983 (2012) (Epub. November 4, 2011)
9. Aliev, R., Panfilov, A.V.: A simple two variables model of cardiac excitation. Chaos, Soliton and Fractals 7(3), 293–301 (1996)
10. Chinchapatnam, P., Rhode, K.S., Ginks, M., Rinaldi, C.A., Lambiase, P., Razavi, R., Arridge, S., Sermesant, M.: Model-Based imaging of cardiac apparent conductivity and local conduction velocity for planning of therapy. IEEE Trans. Med. Imaging 27(11), 1631–1642 (2008)
11. Lepiller, D., Sermesant, M., Pop, M., Delingette, H., Wright, G.A., Ayache, N.: Cardiac Electrophysiology Model Adjustment Using the Fusion of MR and Optical Imaging. In: Metaxas, D., Axel, L., Fichtinger, G., Székely, G. (eds.) MICCAI 2008, Part I. LNCS, vol. 5241, pp. 678–685. Springer, Heidelberg (2008)
12. Nash, M.P., Panfilov, A.V.: Electromechanical model of excitable tissue to study reentrant cardiac arrhythmias. Prog. Biophys. Molec. Biol. 85, 501–522 (2004)
13. Sermesant, M., Delingette, H., Ayache, N.: An electromechanical model of the heart for image analysis and simulations. IEEE Transaction in Medical Imaging 25(5), 612–625 (2006)

14. Keener, J.P., Sneeyd, J.: Mathematical physiology. Springer (1998)
15. Ten Tusscher, K.H., Noble, D., Noble, P.J., Panfilov, A.V.: A model for human ventricular tissue. Am. J. Physiol. Heart Circ. Physiol. 286(4) (2004)
16. Pierre, C.: Preconditioning in bidomain model with almost linear complexity. Journal of Computational Physics 231, 82–97 (2012)
17. Durrer, D., VanDam, R.T., Freud, G.E., Janse, M.J., Meijler, F.L., Arzbaecher, R.C.: Total excitation of the heart. Circulation 41, 899–912 (1970)
18. Moreau-Villeger, V., Delingette, H., Sermesant, M., Ashikaga, H., McVeigh, E., Ayache, N.: Building maps of local apparent conductivity of the epicardium with a 2-D electrophysiological model of the heart. IEEE Transactions on Biomedical Engineering 53, 1457–1466 (2006)

# Understanding Hemodynamics and Its Determinant Factors in Type B Aortic Dissections Using an Equivalent Lumped Model

Paula Rudenick[1], Bart Bijnens[2,3], Constantine Butakoff[3], David García-Dorado[1], and Arturo Evangelista[1]

[1] University Hospital and Research Institute Vall d'Hebron, Universitat Autonoma de Barcelona, Barcelona, Spain
[2] ICREA
[3] Physense – N-RAS, Universitat Pompeu Fabra, Barcelona, Spain

**Abstract.** Despite successful initial treatment during the acute phase of aortic dissections, long-term morbidity and mortality of type B aortic dissections is still a clinical challenge. Therefore, the importance of the assessment and understanding of potential variables involved in their long-term outcome, such as flow patterns and pressure profiles in false and true lumen and across tears.

Hence, we developed an equivalent electric 0D model mimicking a type B aortic dissection. The model was calibrated and validated using in-vitro experimental data from a pulsatile flow circuit. We assessed the variation of pressure profiles in the lumina and flow patterns across the tears as a function of changes in tear size and wall compliance.

We found a good concordance between the in-vitro experiments and the predictions from the lumped model.

Therefore, a 0D model of aortic dissection is feasible and offers potential to study pressures and flow pattern alterations in clinical conditions.

**Keywords:** lumped model, type B aortic dissection, lumen haemodynamic.

## 1 Introduction

Despite success of acute treatment of aortic dissections, long-term results have revealed diminished life expectancy [1] and substantial morbidity because of false lumen (FL) expansion, re-dissection and eventually rupture [2].

To date, some in-vitro and in-silico studies [3-6] have been performed to address the effects of potential anatomic and physiologic factors involved in the progression of chronic type B aortic dissections. However, all of these studies are based on complex and costly models with limited potential to perform fast and easy studies on the influence of individual parameters.

An alternative method is based on the use of Windkessel models. The first quantitative formulation of a Windkessel model was given by Frank in 1899 [7]. Windkessel or lumped models help to recreate and understand several aspects of a system minimizing the need for complex in-silico, in-vivo or in-vitro experiments. Compared to

O. Camara et al. (Eds.): STACOM 2012, LNCS 7746, pp. 375–382, 2013.

these approaches, lumped models are able to describe pressure and flow phenomena without providing accurate solution on, mainly, local phenomena, but they do provide a reasonable mean to assess the overall system behavior.

A wide range of 0D models has been proposed to study the dynamics of the cardiovascular system. Although 0D models were at the beginning oriented to model the whole circulatory system through a mono-compartment description [7-9], they have been extended to describe characteristics of specific circulatory subsystems using multi-compartment descriptions [10].

The aim of this study is to contribute to the modeling of cardiovascular system pathologies by developing a multi-compartment electric analog 0D model of a chronic type B aortic dissection, which has not been done before. Experimental data from previously published work [5] was used to calibrate and validate the proposed lumped model. The developed analog 0D model is in turn used to: 1) study the variation of pressure gradients across the tears with changes in tear size; 2) study the variation of flow patterns across the tears with changes in wall compliance.

## 2 Materials and Methods

### 2.1 Anatomic Configurations to Be Modeled

Type B aortic dissections are modeled as 2 channels communicated by holes/resistances to represent the proximal and distal tears (Fig.1). We investigate anatomic or morphologic configurations with different combination of tear size, number and location within the dissection. In this study we assessed two morphologic configurations of type B dissections varying the tear size: a first one with small proximal and distal tears; a second one with large proximal and distal tears.

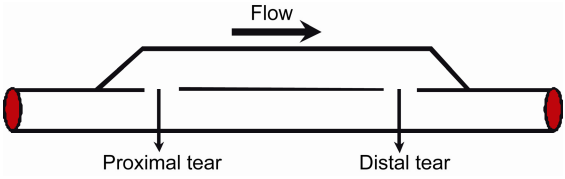


**Fig. 1.** Proposed model of a type B aortic dissection

### 2.2 In-vitro Experimental Model

Measurements from our previous in-vitro study [5] were used to provide suitable inputs to the lumped model, to calibrate it and test its validity. Type B aortic dissections were modeled by phantoms made of a compliant material and (clinically assumed) small and large tears were modeled as holes of 4 mm diameter and 10 mm diameter, respectively. A dynamic fluid circuit was created to reproduce the human cardiovascular system.

Pressures within the lumina were acquired via retrograde catheterization performed from an access distal to the model. FL and true lumen (TL) pressures were monitored at the proximal and distal sites of each dissected segment with a pressure transducer (SPC-350 5F, Millar Instruments, TX, USA). Velocities within the lumina were acquired using pulsed wave Doppler. Flow at the inlet of the model (15 cm before the beginning of the dissected segment) was measured using a flow probe connected to a flow meter system (Transonic Systems Inc, NY, USA). Pressures and flow waveforms were recorded using a PowerLab 16/30 together with LabChart Pro software (ADInstruments, Colorado Springs, CO, USA).

A more detailed description of the creation of the phantom and the circuit setting has previously been published [5].

### 2.3 Equivalent Electric Lumped Model

A diagram of the developed model is shown in Figure 2. An equivalent electric 0D model has been developed to recreate the haemodynamics aspects of a type B aortic dissection. For the modeling we limited the setup to the dissected segment. TL and FL were modeled as parallel subsystems connected by resistances to mimic (rigid) tears.

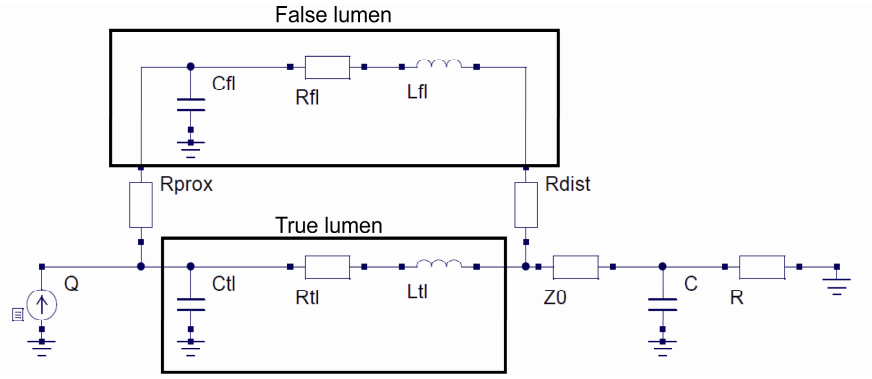


**Fig. 2.** Diagram of the equivalent electric 0D model for a type B aortic dissection. Lumina are modeled as parallel compartments connected by resistances mimicking the tears. (Q: input flow; tl: true lumen; fl: false lumen; prox: proximal tear; dist: distal tear).

Each lumen is modeled as an individual compartment by including the local resistance to blood flow ($R_{lumen}$), elasticity of the lumen ($C_{lumen}$) and inertia of blood ($L_{lumen}$). The peripheral connection of the dissection is represented by using a simple 3-element network of a resistance in series with a parallel arrangement of resistance and capacitance to describe the systemic vascular bed, where $R$ represents the peripheral resistance and $C$ is the total compliance of the distal vascular tree. Proximal and distal tears connecting the lumina in the aortic dissection are modeled through resistances: $R_{prox}$ and $R_{dist}$, respectively.

Parameters of the 0D model (Table 1) were manually estimated to reach an inlet pressure in the range of 80-120mmHg and with a visually similar profile to the inlet

pressure obtained in the in-vitro simulation. The estimated compliance of the distal vascular tree is much lower than values reported in literature, since the model was calibrated to the experimental circuit, which consisted of PVC tube connections with different compliance and length compared to the human peripheral circulation. We used the inlet flow waveform obtained from the in-vitro experiments as the input signal of the 0D model. For each anatomic configuration, we averaged 10 cardiac cycles during steady state.

The equivalent electric lumped model was implemented using Qucs [11] which is an integrated circuit simulator released under the GPL license. This program offers a friendly graphical user interface that allows connecting electrical components in the circuit to one another and running the simulation.

**Table 1.** Parameters' values of the 0D model

| Parameter | Value |
|---|---|
| *Rprox,Rdist* (mmHg/(ml/s)) | |
| *Small tear* | 40 |
| *Large tear* | 10 |
| *Rtl,Rfl* (mmHg/(ml/s)) | 0,0016 |
| *Ltl,Lfl* (mmHg/(ml/s$^2$)) | 0,0005 |
| *Ctl* (ml/mmHg) | 0,18 |
| *Cfl* (ml/mmHg) | |
| *Low compliance* | 0,0001 |
| *High compliance* | 0,005 |
| *Z0* (mmHg/(ml/s)) | 0,5 |
| *C* (ml/mmHg) | 0,001 |
| *R* (mmHg/(ml/s)) | 0,475 |

*prox:* proximal tear; *dist:* distal tear; *tl:* true lumen; *fl:* false lumen.

# 3 Results

## 3.1 Comparison between the Analog Electric 0D Model and the In-vitro Model

The results obtained with the lumped model are similar to the results obtained from the in-vitro experiments (Fig. 3). It was possible to recreate an inlet pressure profile in the range of 80-120 mmHg whose waveform approaches the experimental one. The obtained simulated flow profiles within the tears are also comparable to the pulsed wave Doppler measurements.

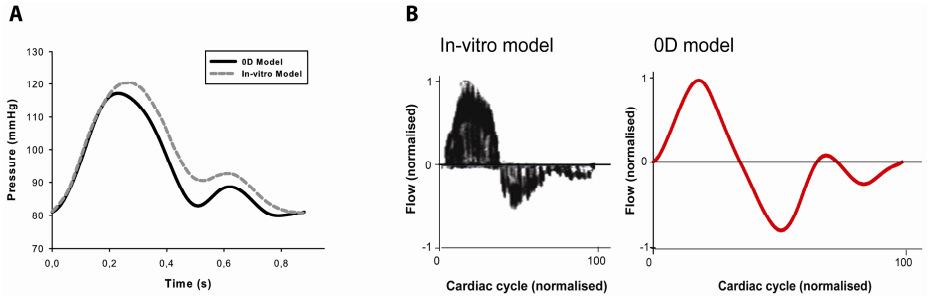


**Fig. 3.** A) Comparison between the inlet pressure profile obtained from the in-vitro model and the one predicted by the lumped model. B) Flow pattern comparison between the in-vitro model and the lumped model at the proximal tear for the anatomic configuration with 2 small tears.

### 3.2 Relation between Wall Compliance and Flow Patterns across the Tears

Figure 4 shows the influence of the FL wall compliance on flow profiles across the tears. When FL wall compliance is very low (i.e. when the FL is almost rigid), FL and TL behave as parallel chambers with the proximal tear only acting as an entry site and the distal tear only acting as an exit site. However, with increasing FL compliance, flow simultaneously goes into the FL at both proximal and distal tears during systole and vice-versa during diastole, so that both tears act as entry and distal sites during the cardiac cycle.

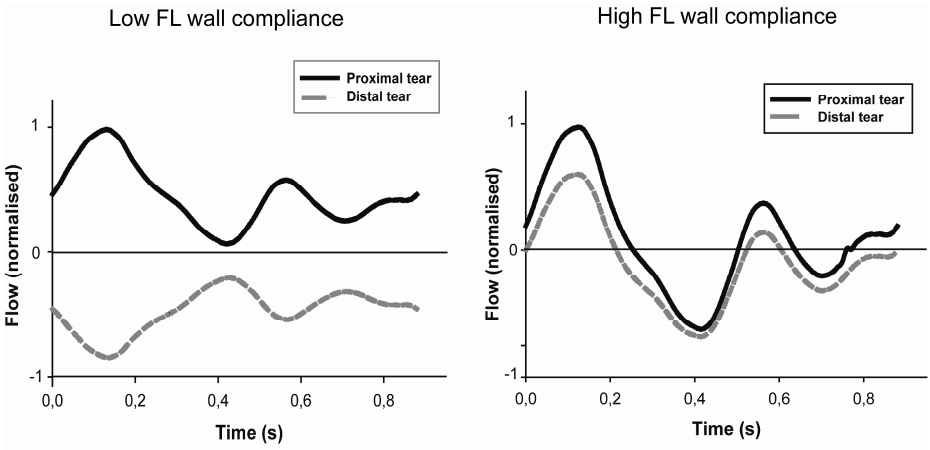


**Fig. 4.** Variation of flow profiles across proximal and distal tears with changes in FL wall compliance. Positive flow corresponds to flow from TL towards FL.

### 3.3 Relation between Tear Size and Pressure Gradient across the Tears

Figure 5 illustrates how pressure profiles vary with changes in tear size. As tear size is increased, TL and FL pressures equalize, decreasing the TL/FL pressure gradient

across the tears and increasing FL pressures. In the presence of small tears, the pressure gradient between TL and FL increases, resulting in more dampened FL waveforms and lower FL pressures. FL waves are displaced in the cardiac cycle compared to TL waves.

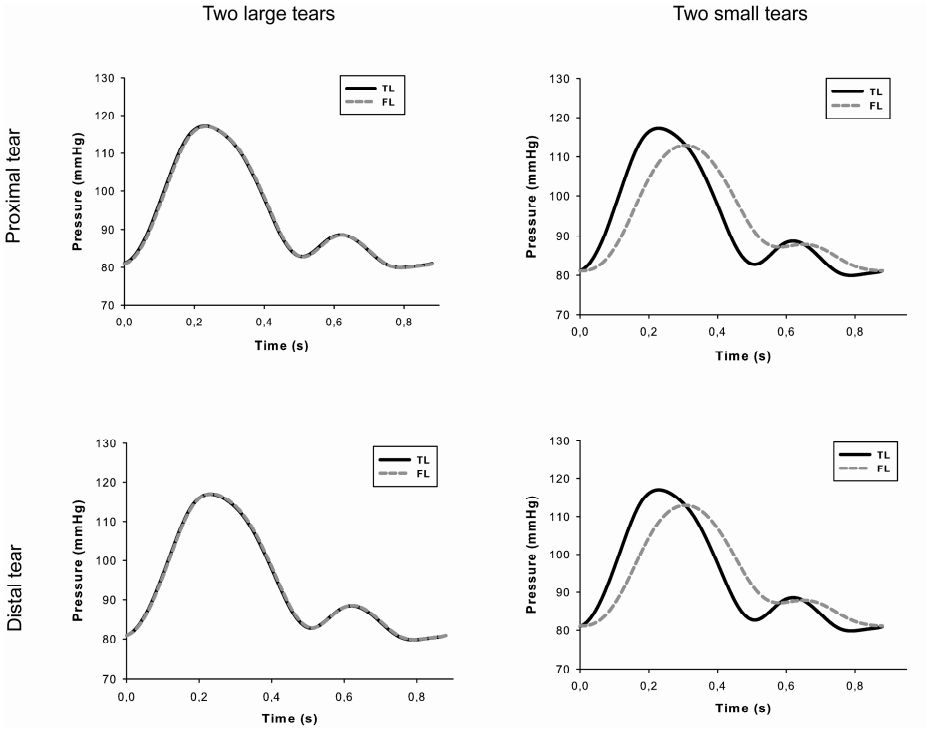


**Fig. 5.** Simulated TL and FL pressures profiles at the proximal and distal tears for the anatomic configuration with 2 small tears and the one with 2 large tears

## 4 Discussion

Knowledge of the haemodynamics in aortic dissections is of importance in diagnosis and better understanding of their chronic progression and outcome. We have developed a realistic lumped model of a type B dissection. This has the advantage that it allows the assessment of the factors affecting pressures and flows, in an easier and more exhaustive way that can be performed by complex in-silico, in-vitro and in-vivo approaches. The model was validated with previous experimental in-vitro data. We assessed the pressure variations across the tears with the changes in tear size and FL wall compliance effects on flow patterns through the tears.

A good correlation was found between the 0D model predictions and the experimental in-vitro data. The waveform and range of values of inlet pressure, pressure behavior across the tears with tear size changes, and flow patterns across the tears, were consistent with the experimental results of the in-vitro approach.

Additionally, when assessing the relationship between tear size and pressure gradient across the tears, in-silico results are in agreement with the experimental observations previously published [3-5]. The presence of large tears causes the equalization of TL/FL pressures across the tears with a consequent increment of FL pressures. This is also in line with a recent clinical study [1] where the presence of a large entry tear in chronic patients is related to long-term complications during the follow-up.

Moreover, the model allowed investigating the influence of properties that have not been studied before. Arterial compliance is a biomechanical property with an important influence on arterial hemodynamics and thus clinical evolution since it has clear effects on pressures and WSS [12,13]. Additionally, while the assessment of flows through the tears is rarely studied, it could play an important role in aortic remodeling and dissection progression and outcome [14,15]. Our model shows that FL compliance has major effects on the flow patterns across the tears. When the compliance of the FL wall is low, TL and FL behave as parallel chambers, so that the proximal tear only behaves as an entry and distal tear only behaves as an exit. However, when the compliance of the FL wall is increased, the tear flow dynamics totally change and both proximal and distal tears simultaneously behave as entry and exit sites during the cardiac cycle. This is additionally accompanied with significant flow reversals in the different compartments of the dissections, thus introducing more WSS variability. The scenario when both tears act as entry and exit sites simultaneously during a cardiac cycle could be a potential cause of simultaneous jets getting into the FL from several locations and the consequent presence of flow collisions and turbulence formations. Therefore, wall compliance should be taken into account at the moment of the assessment and study of the progression of aortic dissections.

These initial results seem promising to improve our understanding of hemodynamics in aortic dissections and can be further extended to study the effects of changes in morphologic configurations on lumen pressures and flows.

**Limitations.** At the moment, we only have implemented the lumped model using a graphics based simulator of the equivalent electric circuit which hampers its automatic calibration and restricts its extension, so that the parameter estimation was performed by trial-and-error. A more flexible and generalized implementation of the model and its calibration are parts of further studies.

## 5 Conclusion

In conclusion, the proposed electric analog 0D model seems to be a good approximation to examine and assess flow and pressure patterns in type B aortic dissections, with the advantage of being a more simplified option compared to complex in-silico, in-vitro or in-vivo models.

## References

1. Evangelista, A., Salas, A., Ribera, A., Ferreira-González, I., Cuellar, H., Pineda, V., González-Alujas, T., Bijnens, B., Permanyer-Miralda, G., Garcia-Dorado, D.: Long-Term Outcome of Aortic Dissection with Patent False Lumen: Predictive Role of Entry Tear Size and Location. Circulation 125(25), 3133–3141 (2012)

2. Tsai, T.T., Fattori, R., Trimarchi, S., Isselbacher, E., Myrmel, T., Evangelista, A., et al.: Long-term survival in patients presenting with type B acute aortic dissection: insights from the International Registry of Acute Aortic Dissection (IRAD). Circulation 114(21), 2226–2231 (2006)
3. Chung, J.W., Elkins, C., Sakai, T., Kato, N., Vestring, T., Semba, C.P., et al.: True-lumen collapse in aortic dissection: part I. Evaluation of causative factors in phantoms with pulsatile flow. Radiology. 214(1), 87–98 (2000)
4. Tsai, T.T., Schlicht, M.S., Khanafer, K., Bull, J.L., Valassis, D.T., Williams, D.M., et al.: Tear size and location impacts false lumen pressure in an ex vivo model of chronic type B aortic dissection. J. Vasc. Surg. 47, 844–851 (2008)
5. Rudenick, P., Bijnens, B., Garcia-Dorado, D., Evangelista, A.: An in-vitro phantom study on the influence of tear size and configuration on the haemodynamics of the lumina in chronic type B aortic dissections. J. Vasc. Surg. (2012) (in press)
6. Karmonik, C., Bismuth, J., Davies, M.G., Shah, D.J., Younes, H.K., Lumsden, A.B.: A computational fluid dynamics study pre- and post-stent graft placement in an acute type B aortic dissection. Vasc. Endovascular Surg. 45(2), 157–164 (2011)
7. Frank, O.: Die Grundform des arteriellen Pulses. Z Biol. 37, 483–526 (1899)
8. Landes, G.: Einige untersuchungen an elektrischen analogieschaltungen zum kreitslaufsystem. Z Biol. 101, 418–429 (1943)
9. Stergiopulos, N., Westerhof, B.E., Westerhof, N.: Total arterial inertance as the fourth element of the windkessel model. Am. J. Physiol. 276, H81–H88 (1999)
10. Milisic, V., Quarteroni, A.: Analysis of lumped parameter models for blood flow simulations and their relation with 1D models. ESAIM-Mathematical Modelling and Numerical Anslysis 38, 613–632 (2004)
11. Qucs project: Quite Universal Circuit Simulator, `http://qucs.sourceforge.net`
12. Nienaber, C.A., Haverich, A., Erbel, R.: Diseases of the aorta and trauma to the aorta and the heart. In: Camm, J., Lüscher, T.F., Serruys, P. (eds.) The ESC Textbook of Cardiovascular Medicine, 1st edn., pp. 993–1031. Blackwell Publishing, Oxford (2006)
13. Evangelista, A., González-Alujas, T.: Pathophysiology of aortic dissection. In: Rosseau, H., Verhoye, J.-P., Heautot, J.-F. (eds.) Thoracic Aortic Diseases, 1st edn., pp. 33–53. Springer, Heidelberg (2006)
14. Bernard, Y., Zimmermann, H., Chocron, S., Litzler, J.-F., Kastler, B., Etievent, J.-P., et al.: False lumen patency as a predictor of late outcome in aortic dissection. Am. J. Cardiol. 87, 1378–1382 (2001)
15. Tsai, T.T., Evangelista, A., Nienaber, C.A., Myrmel, T., Meinhardt, G., Cooper, J.V., et al.: Partial thrombosis of the false lumen in patients with acute type B aortic dissection. N. Engl. J. Med. 357, 349–359 (2007)

# Author Index


Acheampong, Prince 71, 97
Aguado, Jazmin 253
Albà, Xènia 62
Alessandrini, Martino 159
Allain, Pascal 125, 151
Arbel, Tal 80
Aris, Ruth 253
Ayache, Nicholas 364

Bächer, Moritz 17
Balicevic, Vedrana 345
Ballester, Manel 253
Barbosa, Daniel 142, 159
Barry, Jen 326, 364
Barschdorf, Hans 278
Bernard, Olivier 159
Bernus, Olivier 207
Bijnens, Bart H. 336, 345, 375
Bluemke, David 188
Bock, Jelena 215
Bordone, Maurizio 26, 53
Borràs, Agnés 253
Butakoff, Constantine 345, 375

Carreras, Francesc 253
Carrillo Suarez, Xavier 225
Casta, Christopher 355
Chen, Zhong 71, 97
Clarysse, Patrick 355
Claus, Piet 97, 142
Corsi, Cristiana 53
Cotin, Stéphane 298
Coudiere, Yves 364
Courtecuisse, Hadrien 298
Cowan, Brett R. 188, 307
Croisille, Pierre 355
Crystal, Eugene 326, 364
Curzen, Nick 53

Dadvand, Pooyan 26
De Craene, Mathieu 125, 134, 151
Delingette, Hervé 125, 298
Desrosiers, Paul Audain 235
D'hooge, Jan 125, 142
Dikici, Engin 261
Donini, Bruno 53
Dössel, Olaf 278
Drexl, Johann 215
Duchateau, Nicolas 134
Dufour, Cécile 151
Duriez, Christian 298

Evangelista, Arturo 375

Figueras i Ventura, Rosa M. 62
Flor, Roey 326, 364
Frangi, Alejandro F. 62, 134, 188, 307
Friman, Ola 87
Fu, Wenyu 1

Gao, H. 125
García-Dorado, David 375
Gatta, Carlo 225
Gavidia, Giovana 53
Gee, Michael W. 44
Ghate, Sudip 326
Ghugre, Nilesh 326
Giese, Daniel 245
Gil, Debora 253, 270
Gilbert, Stephen 207
Gill, Harminder 71, 97
Gill, Jaspal 71
Gómez, Alberto 245
González Ballester, Miguel A. 53

Henn, Thomas 34
Hennemuth, Anja 87, 169, 215
Herrero, Javier 53
Heuveline, Vincent 34
Heyde, Brecht 142
Hilpert, Loïc 125, 151
Hoogendoorn, Corné 307
Housden, R. James 97, 198
Houzeaux, Guillaume 253
Huellebrand, Markus 87
Hunter, Peter J. 307

Ismail, Mahmoud 44

Jolly, Marie-Pierre 105
Jouk, Pierre-Simon 235
Jung, Bernd 215

Karim, Rashed 71, 97
Karimaghaloo, Zahra 80
Kaxiras, Efthimios 17
Krause, Mathias J. 34
Krueger, Martin W. 278

Lafortune, Pierre 253
Lamberti, Claudio 53
Lanconelli, Nico 53
Lara, Laura 53
Lashevsky, Ilan 326
Lee, Daniel 188
Lekadir, Karim 62
Li, Chi Hion 253
Liebgott, Hervé 159
Lima, João 188
Loncaric, Sven 345
Lu, Xiaoguang 105

Ma, Ying-Liang 71, 97, 198
Madan, Shobhit 9
Maes, Frederik 142
Mahapatra, Dwarikanath 115
Makram-Ebeid, Sherif 125, 151
Manrique, Alain 125
Mansi, Tommaso 364
Marchesseau, S. 125
Martí-Godia, Enric 270
McLeod, Kristin 178, 288
Medrano-Gracia, Pau 188
Meier, Sebastian 215
Menon, Prahlad G. 9
Michalowicz, Gabrielle 235
Morgan, John 53
Morisi, Rita 53
Mory, Benoît 151

Nash, Martyn P. 307
Nickisch, Hannes 278

Obom, Samantha 71, 97
Oduneye, Samuel 326, 364
O'Neill, Mark 71, 97
Orderud, Fredrik 261

Palau-Caballero, Georgina 336, 345
Peitgen, Heinz-Otto 87, 169
Pekkan, Kerem 9
Pennec, Xavier 178, 288
Penney, Graeme P. 245, 317
Perez, Frederic 53
Peters Randles, Amanda 17
Petkov, Simeon 225
Pfister, Hanspeter 17
Piella, Gemma 134
Pierre, Charles 364
Pop, Mihaela 326, 364
Porras, Antonio R. 134
Pousin, Jérôme 355
Poveda, Ferran 270
Prakosa, A. 125
Prakosa, Adityo 178
Preusser, Tobias 215
Pushparajah, Kuberan 245

Qiao, Aike 1

Radeva, Petia 225
Radjenovic, Aleksandra 207
Razavi, Reza 71, 97
Relan, Jatin 298
Rhode, Kawal S. 71, 97, 198, 317
Rinaldi, C. Aldo 71
Ritterbusch, Sebastian 34
Rivaz, Hassan 80
Romero, Adriana 225
Rosengarten, James 53
Rossi, Riccardo 26
Rudenick, Paula 375
Rueckert, Daniel 198

Saloux, Eric 125, 151
Schaeffter, Tobias 71, 97, 245
Seiler, Christof 288
Sermesant, Maxime 125, 178, 288, 298, 364
Shokrolahi, Elnaz 326
Simpson, John 245
Sitges, Marta 336, 345
Smaill, Bruce 207
Somphone, Oudom 125, 151
Soudah, Eduardo 26, 53
Stoica, Răzvan 355
Suinesiaputra, Avan 188

Talbot, Hugo 298
Tautz, Lennart 169

Tobon-Gomez, Catalina 336, 345
Trew, Mark 207
Truong, Michael V.N. 317
Turco, Dario 53

Usson, Yves 235

Vázquez, Mariano 253
Vera, Sergio 53
Villain, Nicolas 125, 151

Wall, Wolfgang A. 44
Wang, Vicky Y. 307
Weber, Frank M. 278
Weese, Jürgen 278
Wright, Graham A. 326, 364
Wu, Xianliang 198

Yang, Yuesong 326
Young, Alistair A. 188, 307

Zhu, Yue-Min 235, 355